THE MODELING AND EXPERIMENTATION OF HYPERSONIC TURBULENT BOUNDARY LAYERS WITH AND WITHOUT THERMAL NONEQUILIBRIUM

A Dissertation

by

CASEY JOSEPH BROSLAWSKI

Submitted to the Graduate and Professional School of
Texas A&M University
in partial fulfillment of the requirements for the degree of

DOCTOR OF PHILOSOPHY

Chair of Committee,	Rodney Bowersox
Committee Members,	Simon North
	Diego Donzis
	Christopher Limbach
Head of Department,	Ivett Leyva

August 2022

Major Subject: Aerospace Engineering

ABSTRACT

Improved modeling of hypersonic turbulent shear layers is of national interest. The Reynolds numbers experienced preclude widespread use of high fidelity simulations, and the complexity of the flow is not captured by simpler techniques derived for low speed applications. The extreme temperatures characteristic of hypersonic environments and the thermochemical effects they engender remain a challenge for the current theory, but their accurate prediction is imperative for vehicle designers. This body of work covers the theory, modeling, and experimentation of a hypersonic turbulent boundary layers with and without thermal nonequilibrium. An existing low fidelity, low cost algebraic energy flux model was re-derived to great detail, allowing it to be more easily implemented, assessed, and extended to cases with thermal nonequilibrium. It was integrated into a simple numerical boundary layer solver, which was written to guide subsequent experiments. Experimental data for the validation of turbulence models was provided from a 2.75° half-angle wedge tested at $M = 5.7$ and $Re = 6 \times 10^6/\text{m}$ in the Actively Controlled Expansion tunnel. Specifically designed trips fomented turbulence over the test article and a 47W direct current glow discharge instilled vibrational nonequilibrium. Both on- and off-body visualization, temperature, frequency, and velocity data sets collected with a variety of techniques are included herein. Redundancy in the techniques ensured the veracity of the data, and allowed global trends to be identified. Of particular interest to turbulence model validation were mean and fluctuating velocity and temperature data collected using NO planar laser-induced fluorescence. This technique was also used to study the vibrational relaxation of $NO^{v=1}$ in the boundary layer along the test article. These data, the first known survey in a hypersonic turbulent boundary layer, suggested the vibrational relaxation and flow timescales were comparable, allowing the possibility the two separate mechanisms could interact. To summarize, an exhaustive database of boundary layer data was generated which could serve to validate existing and future turbulence models. These would allow better prediction of vehicle heating in hypersonic environments.

DEDICATION

To my mother, for my perseverance, and to my father, for my curiosity.

To my brothers, to Gregory, for teaching compassion, and to Michael, for teaching composure.

And to every foul-weather friend who gave me harbor in a storm.

We did it.

QUOTATION

Voyager, in case it's ever encountered by extraterrestrials, is carrying photos of life on Earth, greetings in fifty-five languages, and a collection of music from Gregorian chants to Chuck Berry, including "Dark Was the Night, Cold Was the Ground" by '20s blues man Blind Willie Johnson, whose stepmother blinded him at seven by throwing lye in his eyes after his father beat her for being with another man.

He died penniless of pneumonia after sleeping bundled in wet newspapers in the ruins of his house that burned down...

But his music just left the solar system.

"The Warfare of Genghis Khan." *The West Wing*, created by Aaron Sorkin, season 5, episode 13, Warner Bros. Television, 2004

ACKNOWLEDGMENTS

First and foremost, I would like to thank my advisor, Dr. Rodney Bowersox, for accepting me into this program and doggedly supporting me throughout my time at Texas A&M University. His expertise and consummate professionalism were inspirational, and he was a paragon of a university professor. All this stemmed from a sincere, genuine passion for aerospace engineering and a joy of teaching. I am most grateful for his optimism, which carried me over many experimental hurdles.

I have several a distinct memories of each member of my research committee helping me through a thorny problem. Dr. Simon North offered a constant stream of advice and guidance on the complex laser diagnostics contained in this report. Dr. Diego Donzis asked many probing questions about the flow physics and my models thereof, which made me think harder and ultimately work smarter. Dr. Christopher Limbach sat with me at many points throughout the program and discussed plasma physics and aerothermochemistry, from the most basic concepts in my first year to more complex problems later on. To have open access to such a breadth of knowledge made this project stronger and more successful. This extended to the rest of the faculty at Texas A&M University, who never failed to take time to answer questions about their fields; specifically, thank you to Dr. David Staack and Dr. Albina Tropina for their help with plasma experimentation and modeling respectively.

On a practical level, I am grateful for the tireless efforts of the staff associated with our lab. Thank you to Mr. Cecil Rhodes and Mr. John Kochan for keeping us safe, well-equipped, and productive; you both taught me countless lessons on tackling real-world problems, and I will miss your can-do attitudes. Of equal importance, thank you to Mrs. Rebecca Marianno, Ms. Kendall Lackey, and Mrs. Gail Rowe for your administrative work; it is no small task to keep our lab organized, on-task, and efficient. Thank you to Mr. John Pettit for attentively maintaining and diligently improving the lab's IT infrastructure. And of course thank you to Mr. Zahir Udovich and Mr. Will Seward for not only making so many beautiful custom parts for this work, but patiently teaching me about practical design and machining. This group made the world go 'round.

I am grateful for the research opportunities afforded to me as a member of the Pathways Internship Program at NASA Langley Research Center. Seeing the same research challenges being addressed in a professional environment was hugely validating. Every term I spent as a member of the Aerothermodynamics Branch made me a better engineer and the ideas and techniques I was able to translate to my work at the NAL tangibly improved my results. Thank you to Mrs. Kelly Murphy for taking a chance and accepting me as an intern, and for taking every opportunity to advocate on my behalf. Thank you as well to Mrs. Shelly Mason for her mentorship and guidance through several projects. Whatever may come in my career, I am thankful for this opportunity to begin on the best of terms.

I have seen the future of hypersonics, and it is my labmates at the NAL. Thank you to Ian Neel, whose enthusiasm was a large part of why I chose to go to Texas A&M. Thank you to Andrew Leidy, for setting the standards and tone during the early days of my research career. You both were mentors and role models to me as both a graduate student and later as a young professional. Thank you to my friend Maddie Smotzer, whose positive impact on this entire experience has been so profound I honestly don't think I could put into words; she's finally left me speechless. I'll never know if I could've done any of this without her, but I'm positive I wouldn't have wanted to. Thank you to Heather Kostak for her simple, invaluable act of friendship over these many years; our many conversations kept all the stresses of the graduate school in perspective, and I was consistently impressed by her skill in the lab. A special place must be held for Zach Buen, the labmate with whom I worked most closely. He is an outstanding chemist, a natural leader, and a true original. More importantly, however, he is a good person and a good friend. We don't get to choose who we work with every day, but I couldn't have asked for a better project partner.

In absolutely no order, thank you to: Farhan Siddiqui for his calm confidence when approaching research problems; Tyler Dean for his inspirational work ethic and for being the first person I'd go to with a question; Bryan Morreale for his brilliance and "dive in headfirst" approach to any problem life could throw; Ashley Moran, for the bright and positive energy she brought into the lab every day; Jack Shine, John Wirth, and Kate Melone for being the kind of "new hires" that

taught me more than I taught them; Joel White, for making me laugh and think every conversation we had. Thank you as well to Josh Winner, Brianne McManamen, Alton Hutchinson, Trevor Blair, McKenna Roberts, Joe Carlson, Eric Swinney, Donovan McGruder, Kyle Ruggles, and Taylor Best. When I came to Texas, I didn't know a soul for a thousand miles, but sure enough this group made it a home, and I can honestly say I haven't worked a day since I got here. For all the times I thought I had failed, when even a fool wouldn't wager a penny on me to win, thank you all for not once letting me give up. Here's to many more years of collaboration ahead.

Thank you to Daniel Sturman, for his unwavering friendship since my first day of college. He is the rare individual whose bold ambitions are consistently met through sheer tenacity. But what truly sets him apart is the joy and enthusiasm by which he sees the world. There have been many dark days walking this strange road, and there will be many more to come, but I am not afraid because he has shown time and time again I can always rely on his company.

And lastly, thank you to my family. I very nearly chose not to pursue a graduate degree for fear of failure. Even now, if someone were to ask my how I managed everything in this report, and everything out of it as well, I wouldn't know where to start. But somehow, so slowly that I didn't even notice, I've come to develop an aversion to "fine". A willingness to take risks. An acceptance that life is long, and strange, and not long enough. This was only possible because I have such deep roots, a family tree which loves me unconditionally. I fully understand now that wherever I go or whatever the circumstance, I will always have that. And it is invaluable. It is enough. Thank you to Mom, Dad, Gregory, and Michael.

CONTRIBUTORS AND FUNDING SOURCES

Contributors

This work was supported by a dissertation committee consisting of Drs. Rodney Bowersox (advisor), Diego Donzis, and Christopher Limbach from the Department of Aerospace Engineering and Dr. Simon North from the Department of Chemistry.

Several research endeavors were conducted alongside other students from the Departments of Aerospace Engineering (Aero) and Chemistry (Chem) as part of their doctoral research. Unless otherwise specified, the data were processed independently. The planar laser-induced fluorescence data were collected with Zachary Buen (Chem) and Madeline Smotzer (Chem); these data were processed by Zachary Buen and published in part in [48, 49]. The simulations shown in Chapter 3 were completed by Bryan Morreale (Aero) and published in [46]. The optical emission spectroscopy data were collected alongside Ashley Moran (Chem). The Pitot probe measurements were made with Joel White (Aero). Past and present members of the National Aerothermochemistry and Hypersonics Laboratory assisted with wind tunnel operation and maintenance.

All other work conducted for the dissertation was completed by the author independently.

Funding Sources

Graduate study was supported by Texas A&M University through a College of Engineering Engineering Graduate Merit Fellowship and a graduate research assistantship from the Department of Aerospace Engineering. The author gratefully acknowledges Dr. Bindu Nair and the Department of Defense Office of the Undersecretary of Defense for Research and Engineering Vannevar Bush Faculty Fellowship for awarding Grant Number N00014-18-1-3020 and Drs. Nafiz Karabudak, Barry Bauer, and John Rhoads and the Lockheed Martin Corporation for financial support and collaborative discussion for this project, Number S20-004. The contents herein are solely the responsibility of the author and do not necessarily represent the official views of Texas A&M University, the DoD OUSD(R&E), or the Lockheed Martin Corporation.

TABLE OF CONTENTS

Page

LIST OF FIGURES

FIGURE Page

LIST OF TABLES

TABLE Page

1. INTRODUCTION

Consider Figure 1.1, a schlieren image of a slender wedge in a wind tunnel. Several striking features are immediately apparent. As the flow moved downstream, there was a growing structure near the wall. This was a boundary layer, a viscosity dominated region of the flow which governs fluid-wall interaction; this interaction determines a vehicle's drag and heating, so boundary layers are intensely studied. Upon further inspection, beyond $\sim$ 130mm from the leading wedge, the boundary layer became chaotic, full of eddies and with a distinct ragged edge separating it from the freestream. In analyzing the flow's properties within this region, one would find both a wide range of relevant scales and instantaneous fluctuations forming a statistical distribution about a mean condition. This is a broad description of turbulent flow. Turbulent boundary layers effectively increase a vehicle's skin friction and thereby its drag and heating, so properly anticipating, and if possible controlling, their formation is often a key consideration for vehicle designers; Whitehead Jr. [294] found that if the proposed hypersonic National Aerospace Plane had a fully laminar boundary layer its payload-to-gross-weight would be double what it would be with a fully turbulent boundary layer.

A closer inspection of the data revealed other distinct features. The shock at the leading edge was at a shallow angle with respect to the rest of the body. Because of the low densities in the wind tunnel, discrete trips at $\sim$ 65mm were needed to foment turbulence. Also, the boundary layer was thicker than one would expect from a traditional analysis. It was difficult to see from the data, but at the blunted leading edge the shock was highly curved, which led to a gradient in the entropy behind it. Finally, electrodes mounted to the surface created a plasma which instilled thermal nonequilibrium.

Each of these five features are characteristics Anderson [6] uses to define hypersonic flow. Summarizing, they are 1) A thin shock layer due to small shock angles; 2) Low-density effects causing violations of the no-slip and continuum assumptions due to the high altitudes at which many hypersonic vehicles operate; 3) Thick boundary layers due to strong viscous interaction; 4)

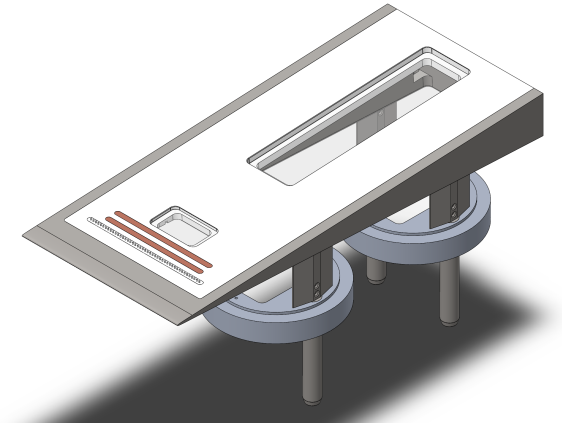

(a) CAD model

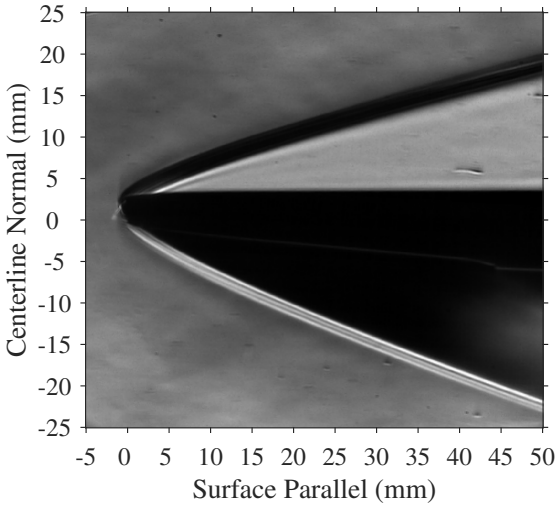

(b) Bow shock

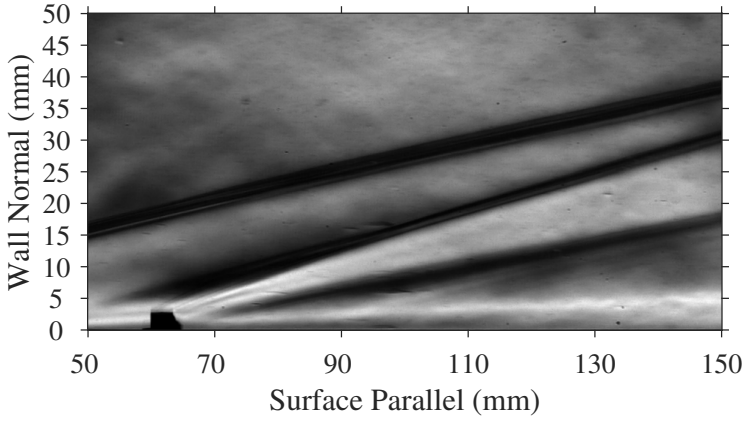

(c) Upstream view

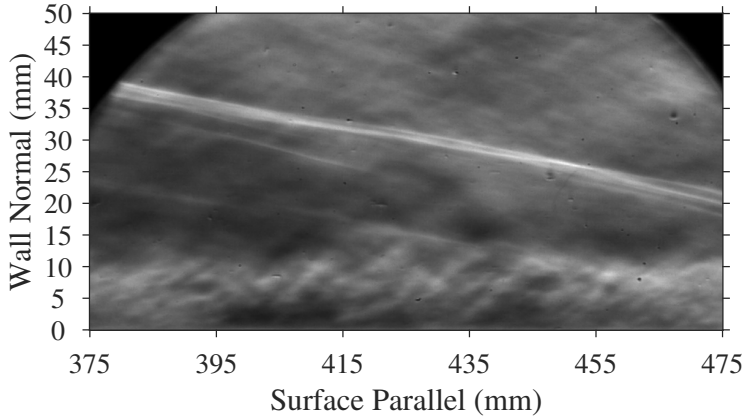

(d) Downstream view

Figure 1.1: Schlieren of a zero pressure gradient hypersonic turbulent boundary layer.

An entropy layer due to curvature of the bow shock; 5) Thermochemical nonequilibrium due to high temperatures from the strong shock and viscous boundary layer. These features are illustrated for a characteristic vehicle in Figure 1.2. A hypersonic flow is one where any of these traits become important; under flight conditions, typically this occurs around Mach five which leads to this limit often being used as the casual threshold for the hypersonic regime.

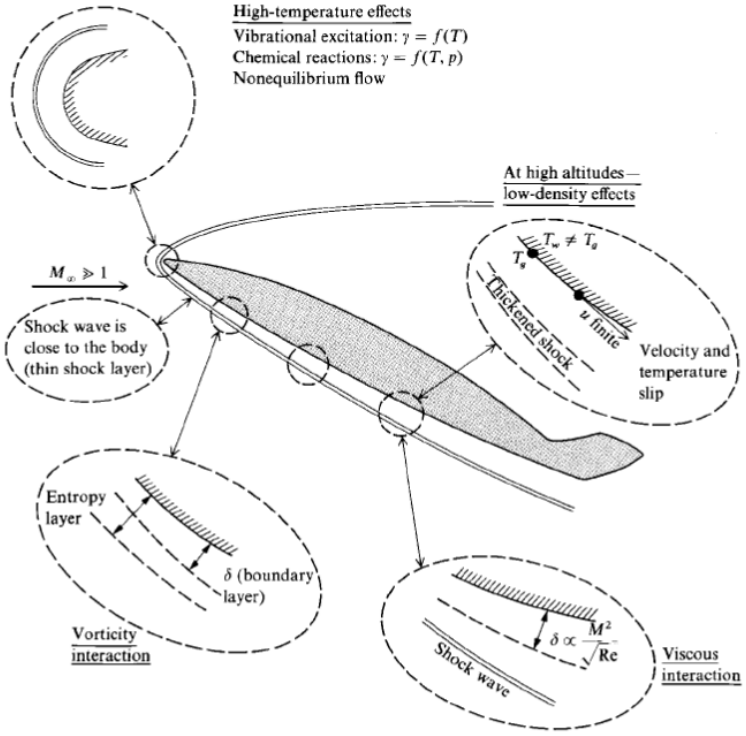

Figure 1.2: Characteristics of hypersonic flows; figure taken with permission from Anderson [6].

Hypersonic flows are perhaps the most extreme atmospheric flight environments, and as such they continue to defy the hegemony aerodynamicists enjoy over other regimes. Nevertheless, there exists an omnipresent desire to travel higher and faster which motives continued dedication to their research. Currently a principle concern is vehicle heating. The compression across a hypersonic vehicle's bow shock leads to temperatures on the same scale as the surface of the Sun [6], and viscous heating in the thick boundary layers contribute as well. As was mentioned before, turbulent boundary layers have even higher viscous effects [293], so they only act to exacerbate the problem.

At such extreme temperatures, air molecules begin to become internally excited, dissociate, and eventually ionize. This thermochemical nonequilibrium affects the thermodynamic environment around a vehicle so it must be well understood.

To explore this element of hypersonic flows, both computational and experimental approaches are employed. Consider the former. Ideally one could simply simulate the environment around a vehicle with maximum resolution, but this problem is currently intractable for even subsonic turbulent flows with length and timescales far more generous than high speed ones. This leads to the adoption of low cost, low fidelity, but fast return models of the turbulence's mean properties which can direct subsequent high fidelity calculations.

Bowersox [38] examined an algebraic energy flux addition to these simplified models which was found to improve their prediction in high speed flows even without considering internal excitation of the molecules [218, 118, 46]. Bowersox et al. [37] extended their model to include this effect, an analysis which revealed the timescales of vibrational and turbulent energy decay are distinct and thereby are able to impact one another. Fuller et al. [95] experimentally found this decay had a tangible impact on a subsonic turbulent channel flow exited by a radiofrequency plasma, and the work in [94] contextualized this effort within the energy flux theory. The pathways identified by Fuller et al. [95] were supported by the subsequent numerical exploration of Khurshid and Donzis [138]. Thus there existed a need for experimental data in a hypersonic environment to provide validation data as these theories and models were tested in high speed regimes. Ideally, these data would contain a high degree of detail, but involve relatively simple flows and modest thermodynamics (*ex.*- a two-temperature flow of air and $N_2^{v=1}$) to allow for incremental progress to be made.

Experiments on hypersonic turbulent boundary layers (TBLs) over canonical zero pressure gradient (ZPG) models have been conducted in the Actively Controlled Expansion (ACE) tunnel at Texas A&M University's National Aerothermochemistry and Hypersonics Laboratory (NAL) by Semper [243] and Leidy [160]. The former studied the generation of such a flow in a low density hypersonic environment while the latter used these results to refine the test article and study shock-

boundary layer interaction. In the present work the test article was again re-designed to include electrodes capable of producing a glow discharge plasma. This allowed the introduction of thermal nonequilibrium effects which introduced another element of the hypersonic environment to ZPG flows in the ACE tunnel. The ability to "turn on" turbulence or nonequilbrium using discrete trips or a plasma allowed the effect of each to be isolated and controlled.

The study of hypersonic flow is interdisciplinary and complex, and as is shown in Figure 1.3 this project covered several elements of the field. In the coming chapters, it is helpful to treat each specialty separately, but to remember all three are inter-related. It was endeavored that the present work make meaningful contributions to hypersonic turbulence modeling and experimentation and include thermal nonequilibrium effects in the study of both.

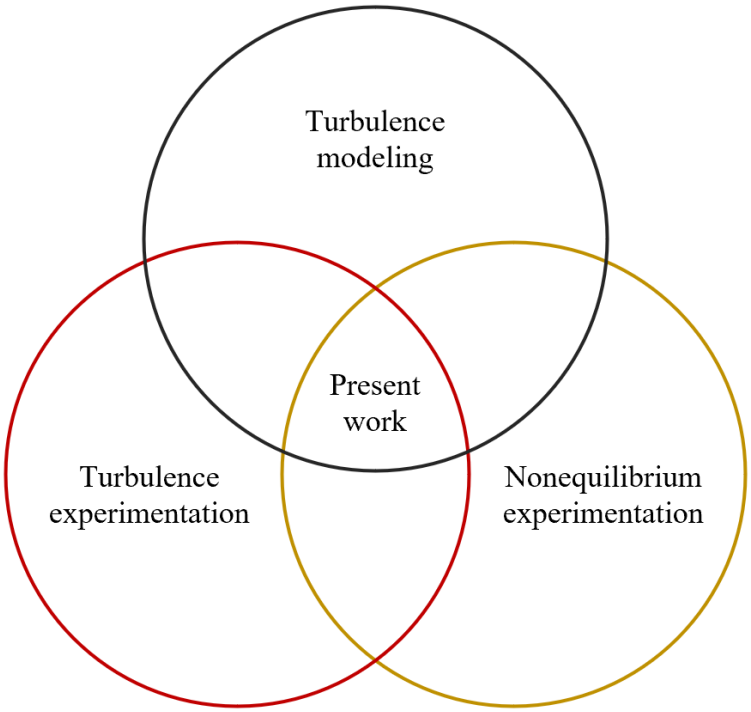

Figure 1.3: Venn diagram of the present research.

1.1 Research Objectives

The overarching objective was improved understanding and modeling of turbulence subject to hypersonic thermal nonequilibrium effects. The vibrational energy flux model in [37] provided mathematical context. The fundamental contribution of the present study was to provide quality experimental validation data for said model, and any other approaches. To that end, experiments were performed on the canonical "flat" plate (2.75° half-angle wedge) test article shown in Figure 1.1(a). This test article built off the designs of Semper et al. [244] and Leidy [160] by the introduction of trips and electrodes which produced a glow discharge for turbulence and vibrational nonequiliubrium activation as needed. This test article was designed to support both traditional diagnostic techniques as well as modern optical approaches. The research goals were, in order:

1. Design a test article which could produce a canonical hypersonic turbulent boundary layer
    - Allow laminar, transitional, and turbulent boundary layers to be produced
    - Allow thermal nonequilibrium to be introduced
    - Allow for both on- and off-body measurements, including laser diagnostics
2. Formalize the derivation for the algebraic energy flux model introduced in [38] to allow further development and easier extension to cases with thermal nonequilibrium, as in [37]
3. Provide experimental measurements to validate turbulence theories
4. Provide experimental measurements of vibrational energy through the boundary layer to explore how thermal nonequilibrium couples with hypersonic turbulence

1.2 Experimental Approach

The test article was designed following Semper [243] and Leidy [160]. Like their models, it used discrete trips to allow different boundary layers to be produced. A novel introduction, in addition to their recommended upgrades, were spanwise electrodes for the generation of a glow discharge. The plasma fomented vibrational nonequilibrium in a controllable manner, which let its

effect be isolated and studied. The new wedge also allowed for off-body optical diagnostics due to its flush windows and rigid yet translatable installation in the test section. All tests were conducted in the ACE tunnel at Texas A&M University's NAL. Each of the experimental diagnostics employed and the data they provide are summarized:

- Numerical boundary layer solver: Predicted boundary layer properties and tested turbulence theories
- Surface profilometery: Confirmed model uniformity and measured surface roughness
- Oil flow: Visualized streamlines to confirm there were no global spanwise pressure gradients, provided information on transition to turbulence, and informed subsequent sensor placement
- Schlieren imaging: Visualized boundary layer to confirm state and size, and also showed shocks around test article
- Infrared thermography: Provided surface temperature, heat flux, and Stanton number
- High-frequency surface pressure measurement: Checked for dominant frequencies in the boundary layer and confirmed fully developed turbulence
- Optical emission spectroscopy: Communicated which species were excited in the plasma and estimated its temperature
- Pitot surveys: Allowed for calculation of Mach number through the boundary layer. Through post-processing and under the right conditions could provide temperature and velocity maps, as well estimates of surface shear stress
- Planar laser-induced fluorescence: Instantaneous and direct measurement of mean and turbulent velocities and temperatures through the boundary layer. The technique was extended to probe vibrational temperatures. Mean and fluctuation profiles and images were produced

1.3 Contribution to the Field

Improved modeling of thermal nonequilibrium in TBLs will provide more accurate predictions of turbulent heating. This will allow more efficient use of thermal protection on hypersonic vehicles. At present, there is an extreme dearth of validation data for hypersonic TBLs in thermal nonequilibrium. Algebraic models are faster than large eddy (LES) or direct numerical (DNS) simulations, and they provide more information and accuracy than current Reynolds-Averaged Navier-Stokes (RANS) calculations. However, few detailed write-ups of algebraic turbulence models are offered in literature, especially for compressible flows. The algebraic approach provided in [37, 38] was amenable to both LES and RANS implementations, further justifying the need for its comprehensive derivation to be made readily accessible. Here only the procedure for the case of thermal equilibrium was provided, as there was direct and sustained interest in this approach from the community [218, 199, 200, 46] and clarifying its derivation would benefit both future equilibrium and nonquilibrium turbulence models.

The experiments conducted here were canonical, and so should provide validation data to a variety of CFD codes. Many measurements were made using a variety of techniques to provide a comprehensive and detailed database for the community to probe. Data were provided for laminar/turbulent and equilibrium/nonequilibrium cases to allow through comparison direct study of the effect of vibrational nonequilibrium on hypersonic TBLs. The data included the first known measurement of vibrational nonequilibrium development through a hypersonic TBLs.

1.4 Organization of Document

This research effort was expansive, so it is helpful to provide a guide for this text. The present chapter introduces the project and covers the problem statement, the research goals, and the steps taken to reconcile the two. The next chapter covers the theory behind turbulent boundary layers and their models, the high-temperature effects experienced during hypersonic flight, glow discharge plasmas, and the laser diagnostics used throughout the experimental campaign. When appropriate, a literature review of a particularly relevant experiment is provided.

At this point, the novel research begins. The proven algebraic energy flux model of Bowersox [38] is derived in great detail, formalizing and clarifying the process to allow for extension to flows with thermal nonequilibrium as was done in [37]. The theoretical work completed, the next chapter describes the physical facilities including the ACE tunnel and test article. The numerical and experimental methods used to study the test article are separately discussed, followed by the results from each. To better organize the data, they are split into separate sections by topic covering numerical simulation, model characterization, flow physics, and advanced optical techniques; these disparate experiments are compared in a final section to identify global trends in the off body variables, surface streaks, wall variables. The turbulence and nonequilibrium theory and experimentation from throughout the entire report are synthesized in a dedicated chapter to address the coupling between the two fields. Finally, conclusions are drawn and recommendations for future work are provided.

2. BACKGROUND

The present research effort had considerable breadth, so for the sake of clarity it is helpful to review each of its constituents in turn. The fluid mechanics can be split into four distinct parts: compressible turbulent boundary layers; Reynolds-averaged Navier-Stokes (RANS) modeling; high-temperature effects; and glow discharge physics. Due to its relative complexity and novelty it is also worthwhile to study the advanced laser diagnostics employed. Each of these five topics is covered to sufficient detail to follow the remainder of this report, though references are provided if further reading is desired. When available, a literature series pertaining to a relevant, modern characteristic experiment is summarized to contextualize the state-of-the-art.

2.1 Compressible Turbulent Boundary Layers

A boundary layer is a viscosity-dominated region of a flow occurring near the interface with a solid body. They encapsulate specialized physics which are of particular interest to hypersonic flight including heat transfer and drag, so they have been heavily studied [6]. White [293] offers a succinct description of the characteristics of TBLs: 1) Fluctuations are superimposed on mean variables; 2) There are eddies of various sizes; 3) Flow properties vary randomly but are distinct from true white noise; 4) Production can allow for self-sustaining turbulence; 5) Mixing, diffusion, entrainment, and dissipation are enhanced.

At its core, this research endeavor was a study of compressible TBLs. The test article was flat, smooth and had no mass transfer; said technically, it has ZPG, negligible roughness, an impermeable wall, and negligible stagnation at the leading edge. Such a simplified flow may appear restrictive, but because it allowed for a "single variable" study of turbulence while maintaining a practical application it remains an active area of model development. For those readers interested in a less-specialized study of turbulence Pope [221] and Tennekes [277] offer thorough analyses, and White [293], Schetz and Bowersox [239], and Smits and Dussauge [258] cover more generalized boundary layers.

2.1.1 Equations of Motion

The Navier-Stokes equations of motion for a compressible, viscous, heat-conducting perfect gas are, as reported by Cebeci and Smith [55] are

$$Continuity: \quad \rho_{,t} + (\rho u_j)_{,j} = 0 \tag{2.1}$$

$$Momentum: \quad (\rho u_i)_{,t} + (\rho u_i u_j)_{,j} = -P_{,i} + \tau_{ij,j} \tag{2.2}$$

$$Energy: \quad (\rho h)_{,t} + (\rho h u_j)_{,j} = P_{,t} + u_j P_{,j} + \tau_{ij} u_{i,j} - q_{j,j} \tag{2.3}$$

where $\tau_{ij} = \lambda \delta_{ij} u_{l,l} + \mu(u_{i,j} + u_{j,i})$, $\lambda = -\frac{2}{3}\mu$ and $q_j = -kT_{,j}$. The equations are universally applicable to any continuum flow, but for turbulence it is beneficial to split the variables into their mean and fluctuating components. There are two common ways to do this, and they were described in detail by Cebeci and Smith [55] and Schetz and Bowersox [239]. The definition of time, or Reynolds, averaging is $u = \frac{1}{t_{max}} \int_0^{t_{max}} u dt$ which leads to $u = \overline{u} + u'$. Favre, or mass, averaging, meanwhile, is defined as $\tilde{u} = \frac{\overline{\rho u}}{\overline{\rho}}$, which leads to $y = \tilde{u} + u''$ [89]. Some useful identities for relating the two approaches were provided by Cebeci and Smith [55] and Schetz and Bowersox [239], but the most important concept is that for Reynolds averaging, $\overline{u'} \equiv 0$ and $\overline{\rho u'} \neq 0$ while for Favre averaging $\overline{u''} \neq 0$ and $\overline{\rho u''} \equiv 0$. This explains why velocity (or temperature, pressure, *etc.*) by itself is often Reynolds averaged but the same variable multiplied by density is typically Favre averaged: during a subsequent time averaging the cancellations are advantageous [55].

This was first applied to the compressible Navier-Stokes equations by van Driest [282] and it remains a fundamental strategy to this day because it isolated the mean and fluctuating terms in a turbulent flow. A common strategy for analyzing the turbulent equations of motion is to apply the perturbations, then take the Reynolds average of the entire equation. Whatever terms remain constitute the mean equations, the "Reynolds-Averaged" equations. This process is straightforward but lengthy, so here only the end result for the mean conservation RANS equations, as derived by

Cebeci and Smith [55], are shown.

$$Continuity: \quad \overline{\rho}_{,t} + (\overline{\rho}\tilde{u}_j)_{,j} = 0 \tag{2.4}$$

$$Momentum: \quad (\overline{\rho}\tilde{u}_i)_{,t} + (\overline{\rho}\tilde{u}_i\tilde{u}_j)_{,j} = -\overline{P}_{,i} + \overline{\tau}_{ij,j} - (\overline{\rho u_i'' u_j''})_{,j} \tag{2.5}$$

$$Energy: \quad (\overline{\rho}\tilde{h})_{,t} + (\overline{\rho}\tilde{h}\tilde{u}_j)_{,j} = \overline{P}_{,t} + \tilde{u}_j\overline{P}_j + \overline{u_j'' P_{,j}} - \overline{q}_{j,j} - (\overline{\rho h'' u_j''})_{,j} + \overline{u_{i,j}\tau_{ij}} \tag{2.6}$$

These equations can be greatly simplified using Prandtl's [222] classic boundary layer assumptions; these are effectively an order-of-magnitude analysis and are roughly summarized with [293]: 1) $\overline{v} \ll \overline{u}$; 2) $\frac{\partial}{\partial x} \ll \frac{\partial}{\partial y}$; 3) $\overline{P}(x,y) \approx \overline{P}_e(x)$. One can further assume the flow is steady, so temporal gradients are zero. The first application of these concepts to compressible TBLs is attributed to van Driest [282]. A detailed walk-through of the full derivation is better left to textbooks (see [55, 258]), but some of the more central assumptions are briefly discussed here. The thermofluid properties like μ, c_p, k, and Pr all have mean and fluctuating components, but it reasonable to assume, for these terms only, $X' \ll \overline{X}$ so the fluctuating component can safely be neglected [293]; note that the state variables ρ, P, and T are excluded from this assumption. Those properties which are functions of temperature are evaluated at the mean temperature [55]. With these simplifications the compressible, RANS equations of motion for a turbulent 2D boundary layer are [55, 293]

$$Continuity: \quad (\overline{\rho}\,\overline{u})_{,x} + (\overline{\rho v})_{,y} = 0 \tag{2.7}$$

$$X-Momentum: \quad \overline{\rho}\,\overline{u}\,\overline{u}_{,x} + \overline{\rho v}\,\overline{u}_{,y} = \rho_e u_e \frac{du_e}{dx} + \tau_{,y} \tag{2.8}$$

$$Y-Momentum: \quad \overline{P}_{,y} = -\left(\overline{\rho v'' v''}\right)_{,y} \ll |P_{,x}| \tag{2.9}$$

$$Energy: \quad \overline{\rho}\,\overline{u}\overline{h}_{,x} + \overline{\rho v}\overline{h}_{,y} = \overline{u}\,\overline{P}_{,x} + q_{,y} + \tau\overline{u}_{,y} \tag{2.10}$$

Now $q = \frac{\overline{\mu}}{Pr}\overline{h}_{,y} - \overline{\rho}\,\overline{h'' v''}$, $\tau = \overline{\mu}\,\overline{u}_{,y} - \overline{\rho}\,\overline{u'' v''}$, and the Bernoulli approximation $\frac{dP_e}{dx} \approx -\rho u_e \frac{du_e}{dx}$ has been applied, an especially safe assumption for ZPG flows as the term is simply zero. It is noted that Equation 2.7 was used to pull the coefficients on the left hand side out of their respective derivatives; this common practice can be easily verified using the Multiplication Rule and will

be used regularly throughout this report. White [293] recommended also using Equation 2.7 to remove $\overline{\rho v}$ from Equation 2.8. For perfect gases, this leaves two equations for three variables, $\overline{u}$, $\overline{v}$, $\overline{T}$. The thermal ($\overline{P} = \overline{\rho} R_{air} \overline{T}$) and caloric ($\overline{h} = c_p T$) equations of state close the system [293]. The boundary conditions are: 1) No slip at the wall ($\overline{u}_w = \overline{\rho_w v_w} = 0$); 2) No temperature or density jump at the wall; 3) Edge conditions match the freestream for u, T, and ρ (there is no such requirement for v). It is also noted that these equations are written solely in terms of temporal stresses and Reynolds stresses, following van Driest [282].

The aspect that distinguishes these conservation equations from their laminar counterparts is the presence of the Reynolds stress $\tau^T \equiv -\overline{\rho}\,\overline{u''v''}$ and the turbulent heat flux $q^T \equiv -\overline{\rho}\overline{h''v''}$. These terms have added two new variables to the system and therefore require new equations for closure. As will be explored in depth in Section 2.2, the heat flux and shear stress are usually modeled as opposed to directly solved or measured.

To that end, it is useful to introduce the Boussinesq approximation for eddy viscosity and eddy conductivity in 2D boundary layers, $\tau^T \approx \mu_t \overline{u}_{,y}$ and $q^T \approx k_t \overline{T}_{,y}$ respectively. These relations are so named because Boussinesq modeled turbulent eddies simply as entities which alter the flow physics by changing the fluid's viscosity and thermal conductivity. For example, this allows $\tau = (\mu + \mu_t)\overline{u}_{,y}$. It is important to understand μ and k are inherent, material properties of the fluid while μ_t and k_t are properties of the flow's dynamics. The existence of these eddy terms implies there is a turbulent Prandtl number which relates them, $Pr_t = \frac{c_p \mu_t}{k_t}$. Reynolds [226] postulated that because τ^T and q^T are functions of mathematically similar quantities of the form (in their notation) $\overline{X''Y''}$, $Pr_t = f(Pr) = \mathcal{O}(1)$. This is a form of the now famous Reynolds Analogy, and per the data of Blackwell [33] it is acceptable to assume for air $Pr_t \approx 0.9$ for all flows considered here; deviation near the wall is considerable, but in this dissipation-dominated region μ_t and k_t are so small the flow becomes laminar [293].

For those disinterested in the Boussinesq approach, it is appropriate to write the compressible Reynolds stress transport equations for 2D boundary layers; freestream equations for Reynolds stress (τ_{ij}^T) and turbulent heat flux q_i^T transport are derived in Chapter 3, and some models for each

are provided in Section 2.2 and Chapter 3 respectively. Here each component of the Reynolds stress transport is shown individually as opposed to combining them with indicial notation in order to make full use of specific boundary layer simplifications. The proceeding equations are derived by Cebeci and Smith [55], and these authors used, for 2D boundary layers, $\frac{DX}{Dt} = \frac{\partial X}{\partial t} + \frac{\partial X\overline{u}}{\partial x} + \frac{\partial X\overline{v}}{\partial y}$

$$\frac{D\overline{\rho u''^2}}{Dt} = \overline{2Pu''_{,x}} - (\overline{v''\rho u''^2})_{,y} - 2\overline{\rho u''v''}\overline{u}_{,y} + \left(\overline{\mu}\overline{u''^2_{,y}}\right)_{,y} - 2\overline{\mu}\overline{u''_{,k}u''_{,k}} \tag{2.11}$$

$$\frac{D\overline{\rho v''^2}}{Dt} = \overline{2Pv''_{,y}} - 2(\overline{Pv''})_{,y} - (\overline{v''\rho v''^2})_{,y} + \left(\overline{\mu}\overline{v''^2_{,y}}\right)_{,y} - 2\overline{\mu}\overline{v''_{,k}v''_{,k}} \tag{2.12}$$

$$\frac{D\overline{\rho w''^2}}{Dt} = \overline{2Pw''_{,z}} - (\overline{v''\rho w''^2})_{,y} + \left(\overline{\mu}\overline{w''^2_{,y}}\right)_{,y} - 2\overline{\mu}\overline{w''_{,k}w''_{,k}} \tag{2.13}$$

$$\frac{D\overline{\rho u''v''}}{Dt} = \overline{P\left(u''_{,y} + v''_{,x}\right)} - (\overline{\rho u''v''^2})_{,y} - \overline{\rho v''^2}\overline{u}_{,y} + \left(\overline{\mu}\overline{u''v''_{,y}}\right)_{,y} - (\overline{Pu''})_{,y} - 2\overline{\mu}\left(\overline{u''_{,k}v''_{,k}}\right) \tag{2.14}$$

Under the boundary layer assumptions $\frac{D\overline{\rho u''w''}}{Dt} = \frac{D\overline{\rho v''w''}}{Dt} = 0$.

The case where $i = j$ corresponds to the turbulent kinetic energy $K \equiv \frac{1}{2}\overline{u''_i u''_i}$, sometimes called simply turbulent energy, equation for TBLs [55].

$$\underbrace{\overline{\rho}K_{,t}}_{\text{Local RoC}} + \underbrace{\overline{\rho}\,\overline{u}K_{,x} + \overline{\rho v}K_{,y}}_{\text{Convection}} = \underbrace{-\overline{\rho}\,\overline{u''v''}\overline{u}_{,y}}_{\text{Production}} + \underbrace{\left(\overline{\mu}\left(K + \overline{v''^2}\right)_{,y}\right)_{,y} - \left(\overline{\rho v''\frac{u''^2_i}{2}}\right)_{,y} - \left(\overline{v''P}\right)_{,y}}_{\text{Viscous, Kinetic, and Pressure Diffusion}} - \underbrace{\phi\overline{\rho}}_{\text{Dissipation}} \tag{2.15}$$

In Equation 2.15 the mean turbulent energy dissipation function is, neglecting bulk viscosity, $\phi \equiv \frac{1}{\overline{\rho}}\overline{\tau''_{ik}\frac{\partial u''_i}{\partial x_k}} \equiv \frac{1}{\overline{\rho}}\overline{\left(\frac{\partial u''_i}{\partial x_k} + \frac{\partial u''_k}{\partial x_i}\right)\frac{\partial u''_i}{\partial x_k}}$. "RoC" is the rate of change and, "Production" refers to the rate turbulent kinetic energy (TKE) is generated from the mean flow, "Dissipation" is the rate TKE is lost to internal energy via viscosity, and "Diffusion" is the rate TKE is transported within the fluid due to molecular processes ("Viscous"), turbulent fluctuations ("Kinetic"), and the pressure-velocity fluctuation correlation ("Pressure") [297]. With this the transport equation for each Reynolds stress $\overline{\rho u''_i u''_j}$ has been provided, but the dominant term for 2D flows is $\overline{\rho}\overline{u''v''}$ because of its direct presence in Equations 2.8 and 2.10.

2.1.2 Thermodynamic Relations

Two of the most important parameters to vehicle designers are drag and thermal load, so it follows that the early theoretical work in high speed flows centered around modeling the skin friction and Stanton number. There are several techniques to approach this problem for both laminar and turbulent flows well-reviewed by White [293], but two simple and useful techniques for predicting these and other such thermodynamic variables are discussed here.

2.1.2.1 Reference Temperature

A useful technique first proposed by Rubesin and Johnson [232] is that of the reference temperature. This concept attempts to find one temperature T^* which can be used in incompressible formulas to correct for all compressibility effects [239]. This is especially useful for flat plates where incompressible models have been proposed for a number of important parameters in adiabatic, conducting, laminar, turbulent, *etc.* flows. An empirical formula was proposed in [85]:

$$\frac{T^*}{T_e} \approx 0.5 + 0.39M^2 + 0.5\frac{T_w}{T_e} \tag{2.16}$$

For example, by evaluating $\rho(T^*) = \rho^*$, $k(T^*) = k^*$, $c_p(T^*) = c_p^*$, one can make use of the incompressible formulas for turbulent boundary layers $Pr^* \approx \frac{C_{fe}}{2St}$ and $c_f^* = \frac{0.0592}{(Re_x^*)^{\frac{1}{5}}}$ listed in [293]. Of particular interest is the Stanton number for a laminar, compressible boundary layer $St^* = \frac{q_w}{\rho^* u_e (h_{aw} - h_w)} = \frac{0.332}{(Re_x^*)^{\frac{1}{2}}}(Pr^*)^{-\frac{2}{3}}$ where $Pr^* = \frac{\mu^* c_p^*}{k^*}$ [6]. This is important because in the proceeding section the "van Driest II" method will be introduced to provide the Stanton number for turbulent compressible flows, so now the reference temperature method can act as a check. Anderson [6] notes that although the reference temperature method is easy to use and often very accurate, it should only be used for approximate analyses; White [293] suggests it is accurate to within a few percent of the exact solution.

2.1.2.2 The Crocco-Busemann Relations

The Crocco-Busemann [70, 51] relations provide a useful set of solutions for the conservation of energy for both laminar and turbulent flows under certain restrictions. White [293] summarized their derivation starting with the laminar forms of the compressible conservation of momentum and energy

$$\rho u u_{,x} + \rho v u_{,y} = -P_{e,x} + (\mu u_{,y})_{,y} \tag{2.17}$$

$$\rho u h_{,x} + \rho v h_{,y} = u P_{e,x} + \left(\frac{\mu}{Pr} h_{,y}\right)_{,y} + \mu \left(u_{,y}\right)^2 \tag{2.18}$$

or

$$\rho u H_{,x} + \rho v H_{,y} = \left(\frac{\mu}{Pr} H_{,y}\right)_{,y} + \left[\left(1 - \frac{1}{Pr}\right) \mu u u_{,y}\right]_{,y} \tag{2.19}$$

where $H = h + \frac{u^2}{2}$. Now one must assume that the flow is steady and that for air $Pr = Constant = 1$, which is a considerable but not unreasonable deviation from the accepted value for air, $Pr = 0.71$ [293].

For unity Prandtl number, Equation 2.19 has a particular solution $H = Constant$ which means $H_{,y} = 0$. This, coupled with the no-slip condition at the wall, implies $h_{,y} = 0$, or an adiabatic wall. This is the first Crocco-Busemann integral relation.

Now allow heat transfer, but assume steady flow, $Pr = 1$, and $P_{e,x} = 0$; neglecting the pressure gradient is acceptable for the current flat plate experiments. Following White [293], one can use Equation 2.17 and Equation 2.18 to derive the particular solution $h = -\frac{u^2}{2} + C_1 u + C_2$. Applying the boundary conditions $h = h_w$ and $u = 0$ at $y = 0$ and $h = h_e$ and $u = u_e$ at y_∞, one is left with the second Crocco-Busemann integral

$$H = h_w + (H_e - h_w)\frac{u}{u_e} \tag{2.20}$$

White [293] notes that the first Crocco-Busemann relation is contained as a special case of the second, when $H = H_e = h_w = Const$. If one further assumes a perfect gas such that $c_p = Constant$

the second Crocco-Busemann relation becomes, as written in [293] and [55] respectively,

$$T = T_w + (T_e + \frac{u_e^2}{2c_p} - T_w)\frac{u}{u_e} - \frac{u^2}{2c_p} = T_w + (T_o - T_w)\frac{u}{u_e} + (T_e - T_o)\left(\frac{u}{u_e}\right)^2 \tag{2.21}$$

Equation 2.21 is a powerful result because it implies if one solves Equation 2.17 to determine the velocity profile, the conservation of energy is immediately solved. However, any further analysis relies on the adiabatic wall temperature. This is commonly estimated using the recovery factor r, the amount of kinetic energy "recovered" at an adiabatic wall [239]. From White [293]

$$r = \frac{T_{aw} - T_e}{T_o - T_e} \approx f(Pr) \tag{2.22}$$

Ideally ($Pr = 1$), when a flow of a perfect gas is brought to rest adiabatically its stagnation temperature approaches the sum of the static temperature and the translational kinetic energy $T_o = T_e + \frac{u_e^2}{2c_p}$ [293]; alternatively, one could write $\frac{T_o}{T_e} = 1 + \frac{\gamma-1}{2}M_e^2$ [55]. Under these ideal conditions, all of the energy is recovered at the wall, so $r = 1$ and $T_{aw} = T_o$. It was found in practice that the measured adiabatic wall temperature fell below the stagnation temperature, but using the relations for T_o in Equation 2.22 one obtains a formula for T_{aw} accounting for $r \neq 1$

$$T_{aw} = T_e + r\frac{u_e^2}{2c_p} = T_e\left[1 + r\frac{\gamma-1}{2}M_e^2\right] \tag{2.23}$$

Either form of this equation is appropriate to calculate T_{aw}, though typically the latter is used throughout this report. Using a self-similar analysis Pohlhausen [219] showed $r_{lam} = Pr^{\frac{1}{2}}$ and if $Pr_t \approx 1$, which it is for gases, then for turbulent flows Dorrance [82] writes $r_{turb} \approx Pr^{\frac{1}{3}}$.

Reconsider Equation 2.21 under the newfound context of the recovery factor. It was derived assuming $Pr = 1$, so Equation 2.22 states $r = 1 \implies T_{aw} = T_o$. This changes Equation 2.21 into, as written in [293] and [55] respectively,

$$T = T_w + (T_{aw} - T_w)\frac{u}{u_e} - r\frac{u^2}{2c_p} = T_w + (T_{aw} - T_w)\frac{u}{u_e} + (T_e - T_{aw})\left(\frac{u}{u_e}\right)^2 \tag{2.24}$$

where $T_{aw} = T_e \left[1 + r\frac{\gamma-1}{2}M_e^2\right]$. It is critically important, and therefore repeated, that throughout the Crocco-Busemann derivation technically $r = 1$, which affected not only 2.24 but also the calculation of T_{aw}; now r has been written explicitly as a reminder that it was indeed present from the outset of the derivation. Cebeci and Smith [55] state that it is acceptable to use $r \neq 1$ to expand Equation 2.24 to non-unity Pr for flows with small heat transfer, but one cannot reproduce Equation 2.21 as printed in [293, 239] from 2.24 unless $r = 1$.

Returning to the Crocco-Busemann relation, White [293] differentiates Equation 2.21 to produce

$$q_w = k_w \left(\frac{\delta T}{\delta y}\right)_w = \frac{(T_{aw} - T_w)k_w \tau_w}{u_e \mu_w} \tag{2.25}$$

which leads to another form of the Reynolds analogy [226]

$$St = \frac{q_w}{\rho_e u_e c_p (T_{aw} - T_w)} = \frac{C_f}{2Pr^{\frac{2}{3}}} \tag{2.26}$$

Again, technically Pr should be used in the denominator of Equation 2.26, but a better fit is provided if $Pr^{\frac{2}{3}}$ is used [293]. Note that Pr is not forced to unity, even though this was an assumption during the derivation, because the Pr is a by-product of the derivation and the above result matches the traditional theory. Also note that this equation is applicable to both laminar and turbulent flows.

To that end, up to this point the the flow has been laminar. However, White [293] shows how the Crocco-Busemann relations for turbulent flows are exactly the same as the laminar results. White [293] wrote the conservation of momentum and energy as

$$\overline{\rho}\,\overline{u}\,\overline{u}_{,x} + \overline{\rho v}\,\overline{u}_{,y} = -\overline{P}_{e,x} + \left[(\mu + \mu_t)\overline{u}_{,y}\right]_{,y} \tag{2.27}$$

or

$$\overline{\rho}\,\overline{u}\,H_{,x} + \overline{\rho v}\,H_{,y} = \left[\left(\frac{\mu}{Pr} + \frac{\mu_t}{Pr_t}\right)H_{,y}\right]_{,y} + \left[\mu\left(1 - \frac{1}{Pr}\right) + \mu_t\left(1 - \frac{1}{Pr_t}\right)\right]_{,y}\left(\frac{\overline{u}^2}{2}\right)_{,y} \tag{2.28}$$

where $H = \overline{h} + \frac{\overline{u}^2}{2}$. For $Pr = 1$ and negligible pressure gradient flow these equations become identical so the particular solution is $H = C_1 + C_2\overline{u}$ (or $\overline{h} = \frac{\overline{u}}{2} + C_1\overline{u} + C_2$). Again, this means the solution is the same as that for the laminar case, so the second Crocco-Busemann integral and all its related formulas previously derived are still usable. Cebeci and Smith [55] concludes their analysis by deriving formulas from the Crocco-Busemann equations relating the state variables' fluctuations with one another, but although these results are interesting they were not all validated for $M > 5$, so for clarity they are not included here.

2.1.2.3 van Driest II Equation

Here the "van Driest II" equation [285] for calculation of the skin friction coefficient of a compressible, adiabatic, and turbulent flow over a flat plate is introduced. For flows following these criteria, it is widely regarded as the best such formula [293, 43]. It is useful because the calculation of Stanton number via the Reynolds analogy (Equation 2.26) requires C_{fe}.

$$\frac{\sin^{-1}A + \sin^{-1}B}{\sqrt{C_{fe}\left(\frac{T_{aw}}{T_e} - 1\right)}} \approx 4.15\log\left(Re_{xe}C_{fe}\frac{\mu_e}{\mu_w}\right) + 1.7 \tag{2.29}$$

where $A = \frac{2a^2-b}{\sqrt{b^2+4a^2}}$, $B = \frac{b}{\sqrt{b^2+4a^2}}$, $a = \sqrt{\frac{\gamma-1}{2}M_e^2\frac{T_e}{T_w}}$, and $b = \left(\frac{T_{aw}}{T_w} - 1\right)$.

2.1.3 Qualitative Characteristics

Morkovin hypothesized the fundamental physics of compressible shear flows will follow their incompressible analog [188]; if accurate, this assertion would allow the extension of the trends observed in incompressible TBLs into the compressible regime, though certain details would be modified. This hypothesis has been shown to hold up to Mach 5 [293] which was similar to the case considered in this report, especially because the ACE tunnel does not have meaningful high-temperature hypersonic effects. This is useful, because much of the early work on TBLs occurred in the subsonic regime and would otherwise be unusable here. Instead, classical experiments can be used to qualitatively describe the behavior of TBLs, perhaps the most famous [293, 239, 55, 258] of which being Klebanoff's [142] hot-wire surveys of an incompressible, smooth, and impermeable

ZPG TBL. The data are summarized in Figure 2.1.

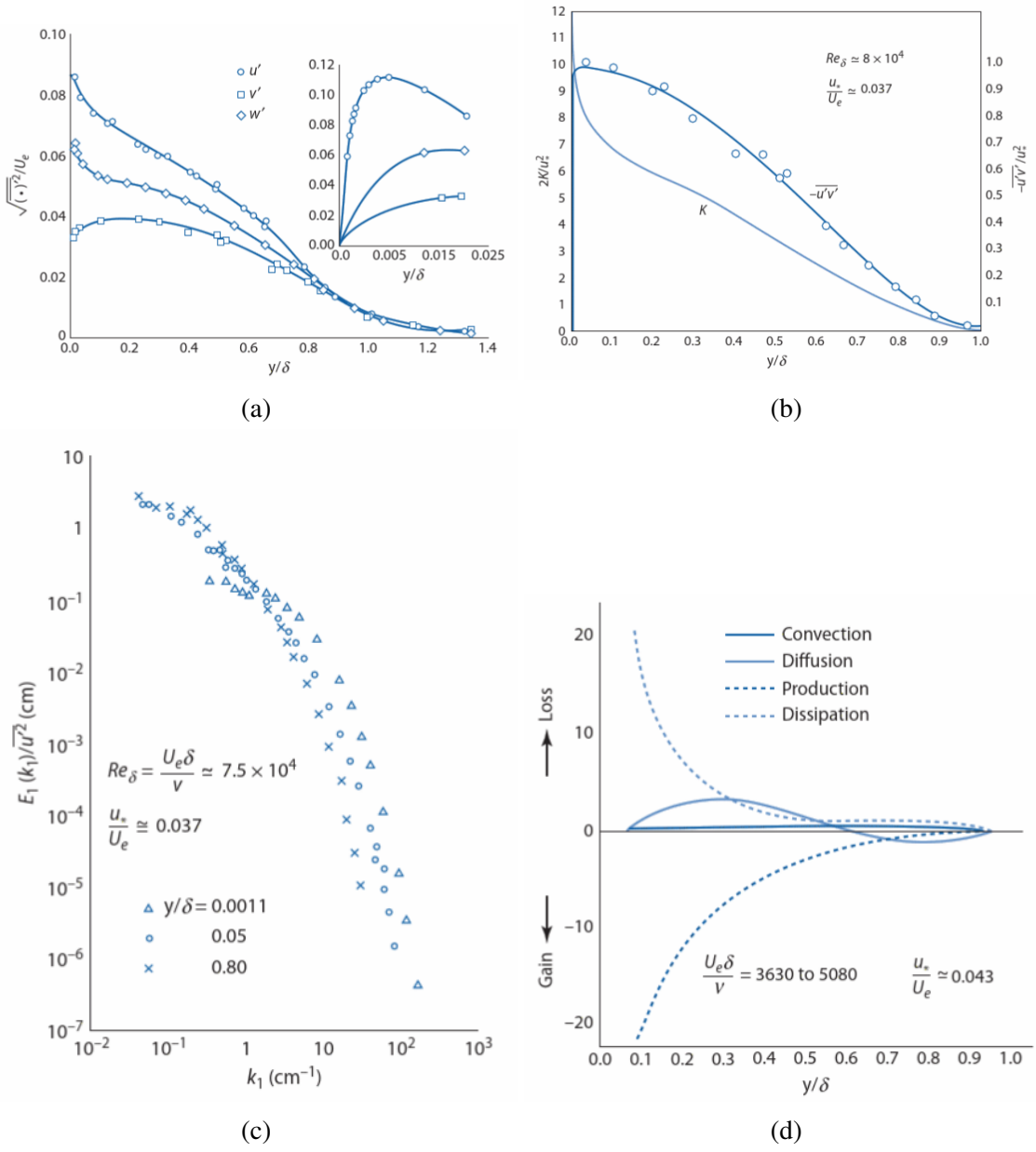

Figure 2.1: Standard incompressible hot-wire data from Klebanoff [142]; figures taken with permission from Schetz and Bowersox [239].

These plots visualize several important TBL concepts which apply regardless of compressibility effects. Figure 2.1(a) shows that despite a no-slip condition meaningful turbulent fluctuations

exist very near the wall. It is not surprising the fluctuations are strongest in the streamwise direction, but Schetz and Bowersox [239] further suggests the wall-normal fluctuations are the weakest due to the damping effect of the wall; the wall's effect fades as one moves farther away from it so the turbulence decays to isotropy. Plots of the Reynolds stress, Figure 2.1(b), show that it drops to zero very near the wall due to the wall-damping effect, but quickly maximizes just above the wall. This behavior implies peak turbulence production occurs in the buffer layer, but turbulence dissipation peaks in the viscous sublayer; both of these regions will be defined shortly. This is confirmed by the spectra in Figure 2.1(c) because small-scale structures near the wall are more susceptible to dissipation, while large-scale structures take energy from the mean flow farther from the wall [221]. Schetz and Bowersox [239] recommended using turbulent kinetic energy, described by Equation 2.15, as a convenient single parameter to describe turbulence intensity. The terms in this equation are commonly attributed to four mechanisms, production, dissipation, convection, and diffusion, especially in general turbulence [221]. These mechanisms are plotted in Figure 2.1(d) and the data suggest TBLs are dominated by dissipation and production, and that these two processes mostly balance one another [239].

A few relevant additional features are noted here. Mean TBL profiles are generally thicker than their laminar counterparts [55], but most of the velocity loss occurs very close to the wall while the slope is fairly shallow throughout the rest of the boundary layer [239]. A hypersonic laminar and turbulent boundary layer are compared in Figure 2.2 using data generated with the boundary layer solver and test conditions described later in Chapters 5 and 7 respectively. For turbulent flows, the sharp rise near the wall produces very strong wall-normal gradients which, coupled with the increased dissipation, leads to enhanced heat flux and drag [55, 239]. This is especially critical for hypersonic vehicles, where thermal loading can easily destroy a vehicle. van Driest [285] showed heat flux is significantly higher ($\mathcal{O}(1-10\times)$) for a turbulent flow than for a laminar one; their data is also shown in [293, 6].

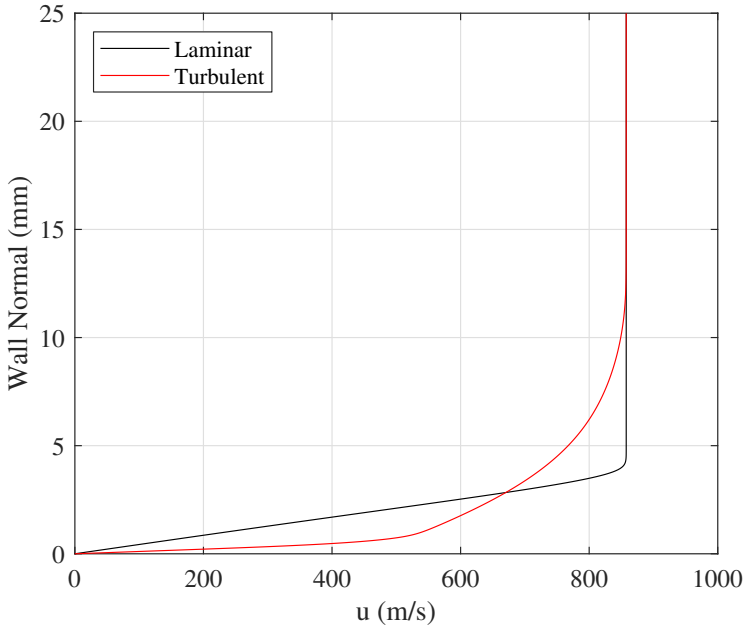

Figure 2.2: Simulated laminar and turbulent hypersonic boundary layers.

2.1.4 Structure and Nondimensional Scaling

It is shown in any viscous flow textbook (i.e.- [239, 293]) that, in the presence of different pressure gradients, flow geometries, and Reynolds numbers, the mean turbulent boundary layer profiles have unique, almost unrelated shapes. Insight was provided by Prandtl and von Kármán, who split these boundary layers into different regions dominated by different physics. Over time, these physics guided a dimensional analysis that resulted in a novel coordinate system purpose-built for turbulent flows. The three main regions are summarized here [293].

- Inner layer:
  - Dominated by viscous (molecular) shear
  - $\overline{u} = f(\tau_w, \rho, \mu, y)$
  - Attributed to Prandtl
  - Subdivided into the viscous sublayer (laminar flow) and buffer layer (transitional flow)
- Overlap/Log layer:

- Smoothly connects the two regions and blends viscous and molecular shear stresses such that $\overline{u}_{inner} \approx \overline{u}_{outer}$
- Sometimes called the log layer because it can be expressed logarithmically
- Fully turbulent flow
- Sometimes included in the definition of the inner layer because it can accurately be modeled with inner layer formulas

• Outer layer:

- Dominated by turbulent (eddy) shear
- $U_e - \overline{u} = f\left(\tau_w, \rho, y, \delta, \frac{dP_e}{dx}\right)$
- Attributed to von Kármán
- Wake-like flow

There is technically a fourth region as well. As one rises through a TBL one will begin to experience brief periods of laminar flow because distinct turbulent eddies give the upper edge of the boundary layer a ragged boundary. These laminar intrusions will grow in duration and frequency until one has left the boundary layer entirely. Even then, however, turbulent eddies can cause brief instances of instability in what is called the superlayer [66]. The data from [142] yields a useful empirical formula this so-called intermittency, mathematically defined as the ratio of time which a flow is turbulent to laminar [293] $\gamma = \left(1 + 5 * \left(\frac{y}{\delta}\right)^6\right)^{-1}$. The center for this Gaussian distribution, $\gamma = 0.5$, corresponds to $\frac{y}{\delta} = 0.78$ and the tails extend as far as $\frac{y}{\delta} \approx 1.2$. Klebanoff estimates the mean wavelength of the superlayer to be 2δ [142]. Often, as is the case here, the superlayer is included in the outer layer analysis.

2.1.4.1 Incompressible Foundation

Much of the early work in this field was conducted on incompressible flows. When the need and ability arose to study high-speed flows, these fundamental equations were effectively just modified.

For that reason, it is best to summarize the incompressible conclusions here. The present analysis follows White [293].

For the inner layer there are five unknowns $(\overline{u}, \tau_w, \rho, \mu, y)$ with only three dimensions, so dimensional analysis requires two additional nondimensional variables. These so-called inner variables are u^+ and the inner law Reynolds number y^+. They were related by $u^+ = \frac{\overline{u}}{v^*} = f(y^+)$ where $y^+ = \frac{yv^*}{\nu}$. The so-called friction velocity $\frac{v^*}{u_e} = \sqrt{\frac{\tau_w}{\rho u_e^2}} = \sqrt{\frac{C_f}{2}}$ is used for nondimensionalization in order to scale the outsized effect C_f has on the boundary layer profiles [239].

Following the same logic, the outer law equation must have three such variables, the velocity-defect $\frac{u_e - \overline{u}}{v^*} = g\left(\frac{y}{\delta}, \xi\right)$, $\frac{y}{\delta}$, and $\xi = \frac{\delta}{\tau_w}\frac{dP_e}{dx}$; often ξ will have a constant value, and here it is zero and thus neglected.

By definition the velocity profile in the overlap layer is found by equating the inner and outer equations. It can be expressed by both inner and outer layer variables respectively as

$$\frac{\overline{u}}{v^*} = A\ln(y^+) + C = \frac{1}{\kappa}\ln(y^+) + C \tag{2.30}$$

and

$$\frac{u - u_e}{v^*} = A\log\left(\frac{y}{\delta}\right) + B \tag{2.31}$$

where $A = 5.5$, $\kappa = \frac{\ln(10)}{A} = 0.41$, $B = -2.5$, and $C = 4.9$ [61]. Note the introduction of a logarithm in the overlap layer, making it linear on logarithmic plots $u^+ \, vs. \, \log(y^+)$ and giving rise to the specification of a "log layer". Converting TBL data to $u^+ \, vs. \, \log(y^+)$ plots immediately collapses the different profiles into a single line in the overlap regime ($30 \lesssim y^+ \lesssim 300$) accurately predicted by the log-law previously derived. What remains is to extend the predictive models to the inner and outer layers.

The Law of the Wall defines the behavior of the mean flow in the viscosity-dominated near-wall region. Very near the wall ($y^+ \lesssim 5$), viscosity dominates so well that there exists a linear relationship $u^+ = y^+$ (though it is not straight when plotted on logarithmic axes). Within this so-called viscous sublayer the flow is effectively laminar, a fact Schetz and Bowersox [239] attributes

to the small Reynolds number y^+ and the dominance of dissipation. This region is often defined by the viscous length scale $\frac{\nu}{v^*}$. The sublayer is smoothly merged to the overlap layer by the buffer layer between $5 \lesssim y^+ \lesssim 30$. In this region the flow is neither linear nor logarithmic, but a helpful fit provided by Spalding [262] accurately predicts the sub-, buffer, and overlap layers

$$y^+ = u^+ + e^{-\kappa B}\left[e^{\kappa u^+} - 1 - \kappa u^+ - \frac{(\kappa u^+)^2}{2} - \frac{(\kappa u^+)^3}{6}\right] \tag{2.32}$$

The Law of the Wake was proposed by Coles [65] when they described the pressure-dependent, wake-like velocity defect above the overlap layer's log-law as, with proper normalization, a function of $\frac{y}{\delta}$ alone. Essentially Coles added a wake function $W(\eta) \approx 2\sin^2\left(\frac{\pi}{2}\eta\right)$ to the inner variable log-law to create a composite function accurate for $y^+ \gtrsim 30$

$$\frac{\overline{u}}{v^*} = \frac{1}{\kappa}\ln(y^+) + C + \frac{\Pi}{\kappa}W\left(\frac{y}{\delta}\right) \tag{2.33}$$

where the wake parameter $\Pi = -\frac{\kappa B}{2} = 0.51$ (as reported in [293], though Coles [65] used 0.55).

With this a single, universal the velocity profile through an entire incompressible TBL over a smooth, impermeable wall has been defined through the use of nondimensional coordinates. For completeness, the nondimensionalized temperature profile is included below. Note that one must first solve the velocity profile before calculating the temperature profile; it will be seen this is a general trend for solving the turbulent conservation equations [293].

$$T^+ = Pr * y^+ \exp -\Gamma + \left(2.12\ln\left(\left(1+y^+\right)\frac{2.5\left(2-\frac{y}{\delta}\right)}{1+4\left(1-\frac{y}{\delta}\right)^2}\right) + \beta(Pr)\right)\exp -\frac{1}{\Gamma} \tag{2.34}$$

where $T^+ = \frac{T_w - \overline{T}}{T^*}$, $T^* = \frac{q_w}{\rho c_p v^*}$, $\beta(Pr) = \left(3.85Pr^{\frac{1}{3}} - 1.3\right)^2 + 2.12\ln(Pr)$, and $\Gamma = \frac{0.01\left(Pry^+\right)^4}{1+5Pr^3y^+}$.

The success of the inner wall coordinates is evident in Figure 2.3. These data were collected from a variety of experiments and the figure shows how with proper nondimensionalization they can be plotted on a single curve all the way to the wake region, where outer variables should be used. This is useful not only for literature reviews or code validation, but even for predictive

assessments. Here the viscous sublayer exists at $y^+ \lesssim 20$ (note it would be linear but for the logarithmic scale), the buffer layer between $20 \lesssim y^+ \lesssim 50$, the log layer from $50 \lesssim y^+ \lesssim 500$ (note that it is linear in the logarithmic scale), and the wake region above $y^+ \gtrsim 500$.

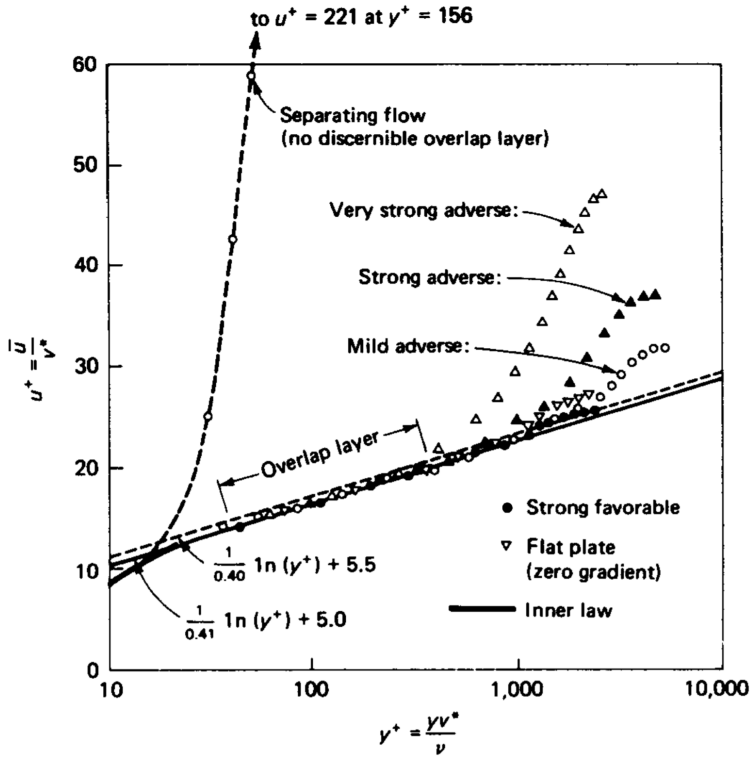

Figure 2.3: Turbulence data at various pressure gradients scaled with inner variables; figure taken with permission from White [293].

2.1.4.2 Compressible Modifications

Recalling Morkovin's hypothesis [188], it is acceptable to use the previously defined inner law variables, though they do need to be modified to account for property (ρ, μ, ν, *etc.*) variation through the boundary layer. Common practice is to simply evaluate these parameters at the wall so $v^* = \sqrt{\frac{\tau_w}{\rho_w}}$, $u^+ = \frac{\bar{u}}{v^*}$, and $y^+ = \frac{yv^*}{\nu_w}$ [239, 293]; this naturally leads to $u^+ = y^+$ in the viscous sublayer [239].

van Driest [282] used these modified inner variables to create a compressible version of the Law of the Wall now referred to as the "van Driest I" model. The analysis ignores the viscous sublayer and also follows Prandtl's mixing length theory $\tau = \tau^T = \overline{\rho} l \left(\frac{d\overline{u}}{dy}\right)^2$ where $l \approx \kappa y$. An alternate theory called "van Driest II" [285] is derived from the Kármán integral relation has been known to give slightly superior results [293, 239] but as it was originally applied to calculate skin friction it was not used here. The "van Driest I" approach assumes a perfect gas with $Pr \approx Pr^T \approx 1$ in order to make use of the Crocco-Busemann relation, which allows one to relate density to velocity [293].

$$\frac{\rho_w}{\overline{\rho}} = \frac{\overline{T}}{T_w} = 1 + \left(\frac{T_{aw}}{T_w} - 1\right)\frac{\overline{u}}{U_e} - \frac{\gamma - 1}{2} M^2 \frac{T_e}{T_w}\left(\frac{\overline{u}}{u_e}\right)^2 \tag{2.35}$$

Using this relation in the expression for τ and by making the flat plate assumption $\tau \approx \tau_w$ van Driest integrated to produce

$$u_{eq} = \frac{u_e}{a}\left(\sin^{-1}\left(\frac{2a^2\frac{\overline{u}}{u_e} - b}{Q}\right) + \sin^{-1}\left(\frac{b}{Q}\right)\right) = v^*\left(\frac{1}{\kappa}\ln y^+ + C\right) \tag{2.36}$$

where a and b were defined for Equation 2.29 and $Q = \sqrt{b^2 + 4a^2}$. As for the incompressible case $\kappa \approx 0.41$ and $C \approx 4.9$. For adiabatic flows, these parameters simplify to $u_{eq} = \frac{u_e}{a}\left(\sin^{-1} a\frac{\overline{u}}{u_e}\right)$, $a = \sqrt{1 - \frac{T_e}{T_w}}$, $b = 0$, and $Q = 2a$. u_{eq} is called the van Driest effective velocity [293], and its application produces a compressible Law of the Wall of the exact same form as the incompressible case. Fernholz and Finley [90] validated Equation 2.36 above $M = 7$ through the overlap layer.

Maise and Mcdonald [169] extended the imcompressible Law of the Wake for the adiabatic case by simply using the modified inner variables and van Driest's u_{eq},

$$\frac{u_{eq}}{v^*} \approx \frac{1}{\kappa}\ln\left(y^+\right) + C + \frac{2\Pi}{\kappa} W\left(\frac{y}{\delta}\right) \tag{2.37}$$

As before, $\Pi = -\frac{\kappa B}{2} = 0.51$, $B = -2.5$, $C = 4.9$, $\kappa = 0.41$, and $W(\eta) \approx \sin^2\left(\frac{\pi}{2}\eta\right)$. Fernholz and Finley [90] validated this compressible Law of the Wake on a flat plate above $M = 10$, but Schetz and Bowersox [239] reminds readers the agreement is poor for cases with heat transfer.

Finally, and for completeness, a single equation for the temperature throughout the entire boundary layer in inner variables is offered by Kader [133].

$$T^+ = Pr * y^+ \exp -\Gamma + \left(2.12 \ln\left[(1+y^+)\frac{2.5(2-y/\delta)}{1+4(1-y/\delta)^2}\right] + C_T(Pr)\right)\exp(-1/\Gamma) \qquad (2.38)$$

where $T^+ = \frac{T_w - \overline{T}}{T^*}$, $T^* = \frac{q_w}{\rho c_p v^*}$, $C_T(Pr) = (3.85 Pr^{1/3} - 1.3)^2 + 2.12\ln(Pr)$, and $\Gamma \equiv \frac{0.01(y^+ * Pr)^4}{1+5y^+ * Pr^3}$.

2.2 Reynolds-Averaged Navier Stokes (RANS) Turbulence Modeling

Recall the Reynolds-averaged conservation equations for turbulent boundary layers, Equations 2.7 - 2.10. Neglecting the continuity equation, there were three equations with five unknowns, u, v, and h as well as τ^T and q^T. Thus in order to close the system closure techniques are needed for the Reynolds stress $-\overline{\rho}\,\overline{u''v''}$ and the turbulent energy flux $-\overline{\rho}\overline{h''v''}$. The Boussinesq approximation is an example of one such technique, and while it continues to enjoy application for many boundary layer problems, especially the present ZPG flow over a smooth, impermeable wall, some more generalized approaches will be introduced.

Before proceeding, it is worthwhile to again outline the strategy for turbulence modeling with the Boussinesq approximation [36]. For a 2D boundary layer, by calculating μ_t with any of the models about to be presented, one can find $\tau^T \equiv -\overline{\rho}\overline{u''v''} \approx \mu_t \overline{u}_{,y}$ and solve the momentum equation. Once can then use the turbulent Prandtl number to calculate $q^T \equiv -\overline{\rho}\overline{h''v''} \approx k_t \overline{T}_{,y}$; this is the so-called gradient diffusion approach. Because k_t follows so easily from the μ_t, most of the modeling effort is expended on calculating the eddy viscosity. There are issues with this treatment of q_i^T, and they prompted the derivation of the energy flux model described in Chapter 3, but here the focus is finding μ_t with the assumption the gradient diffusion approximation is sufficient.

An implication of the Boussinesq approximation is the assumption that $\mu_t = f(l_u, V_u)$, or that it is a function of a length and velocity scale. How one calculates these two scales defines the order of the model. For example, if a separate transport equation is solved for each then one has a 2-equation model, but if instead one uses an arbitrarily defined or known scales, such as the distance from the wall for l_u and the mean velocity gradient for V_u then one has derived a 0-equation model.

Again, the X-equation models simply count the number of transport equations needed to find μ_t with the maximum necessary being two.

Within this section, the 0-equation models are included with proper coefficients for compressible application while all others are reported for incompressible flows. This is because the former are sufficient to accurately simulate the present boundary layer and some are eventually implemented into a numerical boundary layer solver while the later are provided for completeness and are therefore left in their original incompressible form for generalized applications. For a discussion of these RANS models as well as the more advanced techniques of LES and DNS, the reader is referred to the work by Wilcox [297].

2.2.1 0-Equation Models

Because these techniques solve the Boussinesq approximation without a transport equation, they are sometimes called algebraic models [297]. They have been shown to be tolerably accurate in simple boundary layers like the one studied here [293]. The numerical boundary layer solver described in in Chapter 5 was written using the 0-equation models because of their speed, simplicity, and tolerable fidelity, so some details on their application can be found therein. All of the coefficients used in this section only are confirmed to be appropriate for compressible flows.

2.2.1.1 Prandtl Mixing Length

Prandtl [222] assumed $\mu_t \approx \rho l^2 \left|\overline{u}_{,y}\right|$ where l is a characteristic length scale describing the diameter of the eddies within the flow; when l is large the eddy diameters are not constrained by the wall so there is a lot of mixing, and *vice versa*. The velocity scale used is the gradient of the mean flow velocity. Prandtl [222] originally expressed the mixing length as $l \approx \kappa y$ where $\kappa = 0.41$. Again, the linear relationship between l and y implies eddies are small near the wall, which makes sense as near the wall viscosity tends to be the dominant mechanism. van Driest [284] further emphasized the near-wall damping due to the strong viscous effects in this region with the introduction of a damping factor $l \approx \kappa y \left(1 + \exp\left(-\frac{y^+}{A}\right)\right)$ where $A = 26$. White [293] accepted Prandtl's mixing length in the inner layer, and recommended $l \approx 0.09\delta$ in the outer layer

where $\delta_{99.5\%}$ is the boundary layer thickness.

With this the full Pandlt mixing length model is

$$Inner\,layer: \quad \mu_t \approx \rho \left[\kappa y \left(1 + \exp\left[-\frac{y^+}{A} \right] \right) \right]^2 \left| \overline{u}_{,y} \right| \tag{2.39}$$

$$Outer\,layer: \quad \mu_t \approx \rho \left[0.09 \delta_{99.5\%} \right]^2 \left| \overline{u}_{,y} \right| \tag{2.40}$$

The listed constants and coefficients are valid for both incompressible and compressible flows [239, 54, 169].

Typically a blending function is used to smoothly transition between the two regimes as one moves up from the wall when $l_{inner} > l_{outer}$ [293]. Extending the same idea to the eddy viscosity, another popular option is to switch at the y-value when, as y increases, $\mu_{t,inner} > \mu_{t,outer}$, noting that $\mu_{t,inner}$ grows faster of the two [55]. When implemented in the code described in Chapter 5, the following equation was used:

$$\mu_t(y_n) \approx \rho \left(l_{inner} y_{blend} + l_{outer}(1 - y_{blend}) \right)^2 \left| \frac{y_{n+1} - y_{n-1}}{\Delta \eta} \frac{ab}{a+y} \right| \tag{2.41}$$

Here $y_{switch} = \frac{0.09\delta_{99.5\%}}{\kappa}$ and $y_{blend} = \left(1 + 10 \left(\frac{y_n}{y_{switch}} \right)^{10} \right)^{-1}$. a, b, and η are computational grid parameters and are discussed in detail in Chapter 5.

2.2.1.2 Clauser-Spalding Eddy Viscosity

Spalding [262] and Clauser [61] offered models for the inner and outer layers, respectively, which did not use Pandlt's mixing length. Spalding [262] did not use a length scale and instead modified the viscosity directly, while Clauser [61] used δ^* and $\overline{u}_e$ for the relevant scales.

$$Inner\,layer: \quad \mu_t \approx \mu \kappa e^{-\kappa B} (e^Z - 1 - Z - 0.5Z^2) \tag{2.42}$$

$$Outer\,layer: \quad \mu_t \approx C \rho \overline{u}_e \delta^*_{k,99.5\%} \tag{2.43}$$

Again $\kappa = 0.41$ and $B = 5.0$, and now $Z = \kappa u^+$ and $C = 0.018$. The Clauser constant is appli-

cable to both incompressible and compressible flows [239]. For incompressible flows, the 99.5% displacement thickness is used $\delta^* = \int_0^\delta \left(1 - \frac{\overline{\rho}\,\overline{u}}{\rho_e \overline{u_e}} dy\right)$ but for compressible flows this is replaced with the "kinematic" displacement thickness $\delta_k^* = \int_0^\delta \left(1 - \frac{\overline{u}}{\overline{u_e}}\right)$ [239]. It has been shown that δ_k^* provides reasonable accuracy in compressible flows, but an even better improvement is offered by Kiss and Schetz [141]. More information regarding the Clauser model is included in the following subsection.

2.2.1.3 Cebeci-Smith Combined

Techniques using different length scales in the inner and outer layers can be mixed and matched. Cebeci and Smith [55] used the Prandtl mixing length theory for the inner layer and the Clauser model in the outer layer, though the authors modified the latter to account for intermittency γ.

$$Inner\,layer: \quad \mu_t \approx \rho \left[\kappa y \left(1 + \exp\left[-\frac{y^+}{A}\right]\right)\right]^2 \left|\overline{u}_{,y}\right| \tag{2.44}$$

$$Outer\,layer: \quad \mu_t \approx \frac{C\rho u_e \delta^*_{k,99.5\%}}{\gamma} \tag{2.45}$$

where, for the current case, $\gamma = 1 + 1.2\left(\frac{\overline{u}}{\delta}^6\right)$. This model was put into the boundary layer solver using the same blending scheme as the entirely Prandtl model shown above

$$\mu_t(y_n) \approx \rho\gamma \left((l_{inner} y_{blend})^2 \left| \frac{y_{n+1} - y_{n-1}}{\Delta\eta} \frac{ab}{a+y} \right| + C u_e \delta_k^* (1 - y_{blend}) \right) \tag{2.46}$$

Again, a discussion of the a, b, ad η terms is reserved for Chapter 5. Note that γ can be applied to both the inner and outer layers, but its affect near the wall will be small.

2.2.1.4 Baldwin-Lomax Non-Iterative

In all of the above models, in order to calculate the eddy viscosity one must have $\overline{u}_i$ to calculate y^+ in τ_w or either δ_k^* or δ. Of course, if these parameters were known for the given TBL, then there would be no need for the model in the first place. The solution is an iterative process where one guesses a boundary layer profile such as the laminar profile or the result from the previous

streamwise node, solves the boundary layer equations, and if the solution is not tolerably accurate updates the necessary parameters and repeats. While the iteration for y^+ is unavoidable, Baldwin and Lomax [12] proposed a technique to omit boundary layer thickness from the outer layer formula, removing the need for iteration as well as any error in the calculation of δ_k^* or δ; this model is improved by coefficients provided by Granville [103]. The lack of iteration makes this model desirable in more complex flowfields like separated or shock flows [297]. For hypersonic boundary layers, Anderson [6] recommended using the Prandtl mixing length theory for the inner layer and the following for the outer layer:

$$Inner\,layer: \quad \mu_t \approx \rho \left[\kappa y \left(1+\exp\left[-\frac{y^+}{A}\right]\right)\right]^2 \left|\overline{u}_{,y}\right| \tag{2.47}$$

$$Outer\,layer: \quad \mu_t \approx \rho K C_{cp} F_{wake} F_{Kleb} \tag{2.48}$$

where the new coefficients are $C_{cp} = 1.6$ and $K = 0.0168$. The ancillary function is

$$F(y) = y\left|\frac{\partial \overline{u}}{\partial y}\right|\left(1-e^{-\frac{y^+}{A}}\right) \tag{2.49}$$

such that $F(y_{max}) = F_{max}$. Here y_{max} is the length scale and $F(y)$ is the velocity scale. F_{wake} is the lesser of $y_{max}F_{max}$ and $C_{wk}y_{max}U_{dif}^2/F_{max}$ where $C_{wk} = 0.25$ and $U_{dif} = \sqrt{\overline{u}^2+\overline{v}^2}$ and $F_{Kleb}(y) = \left[1+5.5\left(C_{Kleb}\frac{y}{y_{max}}\right)^6\right]^{-1}$ with $C_{Kleb} = 0.3$. According to Wilcox [297], there is little to choose between the Baldwin-Lomax and Cebeci-Smith models for boundary layer simulation.

2.2.2 1-Equation Models

These models introduce one new transport equations, either for turbulent kinetic energy (Equation 2.15) or eddy viscosity. The former are classified as "incomplete" because they rely on a model of the turbulent length scale while the latter are "complete" and solve for it directly. According to Wilcox [297], "incomplete" models are seldom used and therefore will not be explored here, though interested readers can find a review in Wilcox's textbook. With regard to the "complete models", it is important to recognize that by solving a transport equation for eddy viscosity they

fundamentally accept the Boussinesq approximation, but they circumvent solving for a distinct length and time scale with liberal use of empirical data. For many applications and especially for boundary layer flows, Wilcox [297] recommended a model for eddy viscosity owing to [261]. As a final general remark, for simple boundary layers 1-equation models offer only comparable accuracy to 0-equation models [239] and for complex boundary layers they are less accurate than 2-equation models, so they are not widely used [293]. Again, note that the coefficients shown here are generalized and may not be applicable to compressible flows.

2.2.2.1 Spalart-Almaras

Kalitzin et al. [134] showed that kinematic eddy viscosity ν_t grows linearly with y^+ in the log layer, but with y^{+4} in the viscous sublayer. This necessitates strong cell clustering near the wall. The Spalart-Almaras 1-equation model attempts to circumvent this issue by introducing a variable $\tilde{\nu}$ which for the special case of a flat plate is linear throughout the entire boundary layer; the authors proposed $\nu_t = \tilde{\nu} f_{v1}$ where viscous damping is modeled as $f_{v1} = \frac{\chi^3}{\chi^3 + C_{v1}^3}$ with $\chi = \frac{\tilde{\nu}}{\nu}$ and $C_{v1} = 7.1$ [261]. Wilcox [297] stated the constants, of which several more will be introduced, were calibrated for application to adverse pressure gradients like those on wings. For such flows with nonzero pressure gradients, one must solve a transport equation for $\tilde{\nu}$, but this is numerically tractable because the likely solution remains nearly linear throughout the domain. The boundary conditions are $\tilde{\nu} = 0$ at the wall and $\tilde{\nu} = \nu_t$ in the freestream. The transport equation is [261]

$$\tilde{\nu}_{,t} + u_j \tilde{\nu}_{,j} = \underbrace{C_{b1}\tilde{S}\tilde{\nu}}_{Production} + \underbrace{\frac{1}{\sigma}\left[(\nu + \tilde{\nu})\tilde{\nu}_{,k} + C_{b2}(\tilde{\nu}_{,k})^2\right]_{,k}}_{Diffusion} - \underbrace{C_{w1} f_w \left(\frac{\tilde{\nu}}{d}\right)^2}_{Sink} \tag{2.50}$$

where the constants are

$$C_{b1} = 0.1355; C_{b2} = 0.622; C_{v1} = 7.1; C_{w1} = \frac{C_{b1}}{\kappa^2} + \frac{1 + C_{b2}}{\sigma}; C_{w2} = 0.3; C_{w3} = 2; \sigma = \frac{2}{3}; \kappa = 0.41$$

the functions are

$$f_{v1} = \frac{\chi^3}{\chi^3 + C_{v1}^3}; \; f_{v2} = 1 - \frac{\chi}{1 + \chi f_{v1}}; \; f_w = g\left[\frac{1 + C_{w3}^6}{g^6 + C_{w3}^6}\right]^{\frac{1}{6}}$$

and the relations are

$$\chi = \frac{\tilde{\nu}}{\nu}; \; g = r + C_{w2}(r^6 - r); \; r = \frac{\tilde{\nu}}{\tilde{S}\kappa^2 d^2}; \; \tilde{S} = S + \frac{\tilde{\nu}}{\kappa^2 d^2} f_{v2}; \; S = \sqrt{2\Omega_{ij}\Omega_{ij}}; \; \Omega_{ij} = \frac{1}{2}(u_{i,j} - u_{j,i})$$

There are additional terms which account for transition, but they are beyond the current scope.

The left hand side follows the familiar form for transport equations. Production is tied to shear $\tilde{S}$ so locations with strong velocity gradients and thereby high rate of strain lead to eddy generation and turbulence. Diffusion acts to spread the eddies across the flow. What distinguishes the diffusion in Equation 2.50 is the presence of the nonlinear $C_{b2}(\tilde{\nu}_{,k})^2$ term. Spalart and Allmaras [261] included this term and calibrated the constant to account for wake spreading, which they modeled as the wake "diffusing". Wilcox [297] choose to separate the nonlinear term in order to reduce the diffusion to the standard form and instead modeled the spreading as an independent and explicit source term. Finally, the negative "Sink" term is defined by the inverse of the distance to the wall d^{-1} so that as one moves closer to the wall, the sink grows in amplitude as turbulent energy (here pressure fluctuations) succumbs to wall damping; note that f_w is scaled to prevent error when $d = 0$. This sink term only accounts for the inviscid damping; f_{v1} captures the energy loss due to viscous effects. Thus the system is closed and one can solve for $\tilde{\nu}$ and thereby ν_t.

2.2.3 2-Equation Models

As with 0- and 1-equation models, there are several branches of successful 2-equation turbulence models. This section is limited to the most popular and influential, while texts like [297] offer a more detailed examination of the field. Despite their additional complexity and the applicability to advanced, practical flow fields they offer, 2-equation models follow the same principals as their reduced-order counterparts in that they provide a means to calculate μ_t by now solving a transport

equation for a length and velocity scale and thereby close the specific Reynolds stress term.

Because this section is taken predominantly from [297], who considered general turbulent flows and not just boundary layers, here the Boussinesq assumption is defined as $\tau_{ij} = -\overline{u_i' u_j'} = 2\nu_t S_{ij} - \frac{2}{3} K \delta_{ij}$. Note that only Reynolds averaging is being used because Favre averaging is unnecessary for incompressible cases. It is also useful to here write, in Wilcox's notation, the mean rate of strain $S_{ij} = \frac{1}{2}\left(u_{i,j} + u_{j,i}\right)$ and rotation tensors $\Omega_{ij} = \frac{1}{2}\left(u_{i,j} - u_{j,i}\right)$, the turbulent kinetic energy $K = \frac{1}{2}\overline{u_i' u_i'}$, and the dissipation rate per unit mass $\varepsilon = \nu \overline{u_{i,k}' u_{i,k}'}$.

Most 2-equation models make use of the square root of the turbulent kinetic energy $\sqrt{K}$ as a velocity scale, so all that remains is the need for a suitable length scale. It is in the choice of length scale 2-equation models differentiate themselves; White [293] attributed the now-standard adoption of dissipation as a pseudo-length scale to the success of Jones and Launder's [130] seminal work. Kolmogorov [144] introduced the "specific dissipation rate" ω with units of $time^{-1}$ to produce $\nu_t \sim \frac{K}{\omega}$, $l_u \sim \frac{k^{\frac{1}{2}}}{\omega}$, and $\varepsilon \sim \omega K$. Chou [59] suggested directly modeling the dissipation ε via $\nu_t \sim \frac{K^2}{\varepsilon}$ and $l_u \sim \frac{k^{\frac{3}{2}}}{\varepsilon}$ and similarly Rotta [229, 230] proposed modeling the length scale with $\nu_t \sim \frac{K^{\frac{3}{2}}}{\varepsilon}$ and $\varepsilon \sim \frac{k^{\frac{3}{2}}}{l_u}$. There has also been some effort to model the "turbulence dissipation time scale" τ_u (the reciprocal of ω [297]), with Zeierman and Wolfshtein [306] suggesting $\nu_t \sim K\tau_u$, $l_u \sim k^{\frac{1}{2}}\tau_u$, and $\varepsilon \sim \frac{K}{\tau_u}$. Using the rate of dissipation (ε or ω), which takes place on the smallest scales, as a proxy for the larger characteristic length scale of turbulent production is tolerable because energy is passed from production to dissipation in a cascade [221], so a physically linking the two.

While 2-equation models improve accuracy in complex flow fields (wakes, jets, separation bubbles, *etc.*) with the introduction of transport equations for a length and velocity scale as opposed to models, there has been no great mathematical revelation. These transport equations need to be reduced to be solved, so in the end one still derives a heavily simplified model to solve for these parameters. Wilcox [297] emphasizes this point, that "we should avoid deluding ourselves by thinking the *drastic surgery* approach to something as complex as [the dissipation transport equation] is any more rigorous than dimensional analysis". In short, the fundamentals have not

changed, and complexity does not itself provide fidelity.

2.2.3.1 Standard $K-\varepsilon$

The first widely adopted 2-equation model was provided by Jones and Launder [130], though its coefficients were later enhanced in [154]. The conceit is

$$\nu_t \approx \frac{C_\mu K^2}{\varepsilon} \tag{2.51}$$

and the modeled kinetic energy and dissipation transport equations are

$$K_{,t} + u_j K_{,j} = \tau_{ij} u_{i,j} - \varepsilon + \left((\nu + \frac{\nu_t}{\sigma_k}) K_{,j} \right)_{,j} \tag{2.52}$$

$$\varepsilon_{,t} + u_j \varepsilon_{,j} = C_{\varepsilon 1} \frac{\varepsilon}{K} \tau_{ij} u_{i,j} - C_{\varepsilon 2} \frac{\varepsilon^2}{K} + \left((\nu + \frac{\nu_t}{\sigma_\varepsilon}) \varepsilon_{,j} \right)_{,j} \tag{2.53}$$

where $C_{\varepsilon 1} = 1.44$, $C_{\varepsilon 2} = 1.92$, $C_\mu = 0.09$, $\sigma_K = 1$, and $\sigma_\varepsilon = 1.3$. For completeness, $\omega = \frac{\varepsilon}{C_\mu K}$ and $l_u = \frac{C_\mu K^{\frac{3}{2}}}{\varepsilon}$. This is the so-called "Standard" model; an alternative model using renormalization group theory, the "RNG" model, was provided by Yakhot et al. [303]. The full transport equations for both energy and dissipation are provided by Wilcox [297]. Wilcox commented that not only is the equation for dissipation so complex that its model is only tenuously related to it, the modeling parameters are functions of large-eddy scales following the preceding dimensional analysis and not truly dissipation.

Just as the Prandtl mixing length model [222] required an empirical modification to add the effect of viscosity to the mixing length in the sublayer, so too are viscous corrections necessary for the Standard $K-\varepsilon$ model. The following were offered by Launder and Sharma [154]

$$f_1 = 1 \tag{2.54}$$

$$f_2 = 1 - 0.3 \exp\left(Re_t^2\right) \tag{2.55}$$

$$f_\mu = \exp\left(\frac{-3.4}{\left(1 + \frac{Re_t}{50}\right)^2} \right) \tag{2.56}$$

where $Re_t = \frac{\rho K^{1/2} l}{\mu} = C_\mu \frac{\rho K^2}{\mu \varepsilon}$, using $l = l_u$ as the characteristic length scale. The turbulent Reynolds number Re_t is the ratio of turbulent forces to viscous forces; for example, if Re_t is small then viscosity dominates. f_1 is multiplied with $C_{\varepsilon 1}$, f_2 is multiplied with $C_{\varepsilon 2}$, and f_μ is multiplied with ν_t. With the inclusion of these damping functions, one has a "high Reynolds number" model for the freestream and a "low Reynolds number" model near the wall. For the present boundary layer study, the low Reynolds number corrections are needed.

As a final comment, it is widely accepted that the proceeding 2-equation models are superior to the $K-\varepsilon$ model under a wide variety of conditions, especially for such aerospace applications like the strong adverse pressure gradients seen on wings and in diffusers. Furthermore, despite the use of empirical corrections, the near wall corrections cannot offer the same fidelity as the upcoming $K-\omega$ techniques. However, as the first widely implemented 2-equation, and due to its continued success in high Reynolds number flows, the $K-\varepsilon$ model is worth serious consideration for many applications [293, 297].

2.2.3.2 Wilcox $K-\omega$

As was seen with the $K-\varepsilon$ model, ε and ω can be readily related. So, if they are so similar, why is an entirely new transport equation for ω necessary? The damping functions needed to account for viscosity improve the near-wall behavior of $K-\varepsilon$ model, but they still do not provide the desired accuracy for adverse pressure gradient and separating flows. This is a major problem for airfoil applications, and one a new model could hopefully address.

Kolmogorov [144] is credited with the first 2-equation model of turbulence using the kinetic energy and a new variable for "the rate of dissipation of energy in unit volume and time", ω. Wilcox [297] analyzed Kolmogorov's likely thought process in the development of an equation for ω, the main takeaways being that the variable probably came solely from a dimensional analysis (ex.- a $1/time$ term such as ε/K was needed to close the kinetic energy transport equation) and that the transport equation was entirely empirical. In the decades since Kolmogorov's publication, production and molecular diffusion terms were added and varying explanations for the physical meaning of ω were offered, but that the core of the model remains, again emphasizing the power

of dimensional analysis and physical intuition in turbulence modeling.

Wilcox [297] provided a succinct timeline of the advancements made to the $K-\omega$ model from Kolmogorov to the present. One of the most widely accepted and up-to-date $K-\omega$ models was presented in 2006 by Wilcox [297]; note with this form Wilcox improves on previous iterations their own the model [295, 296], especially in free shear and strongly separated flows, so the date is worth distinguishing.

For the present model, Wilcox [297] defined $\omega \equiv \frac{\varepsilon}{\beta^* K}$, where $\beta^* = 0.09$ just as C_μ from the $K-\varepsilon$ model. This means ω is proportional of the ratio of dissipation to kinetic energy, giving it units of $\frac{1}{time}$ as compared to the dissipation rates $\varepsilon \sim \frac{length^2}{time^3}$. It can therefore be thought of as the so-called specific dissipation rate. Remember, 2-equation models need a length scale to match Prandtl's theory [222], so the close relationship between ε and ω allows both to be related to l_u.

Wilcox's model, as reported in [297] is as follows. For the kinematic eddy viscosity,

$$\nu_t = \frac{K}{\tilde{\omega}} \tag{2.57}$$

with $\tilde{\omega} = \max\left(\omega, C_{lim}\sqrt{\frac{2S_{ij}S_{ij}}{\beta^*}}\right)$ and $C_{lim} = \frac{7}{8}$. The turbulent kinetic energy and specific dissipation rate transport equations are, respectively,

$$K_{,t} + u_j K_{,j} = \tau_{ij} u_{i,j} - \beta^* K\omega + \left(\left(\nu + \sigma^* \frac{K}{\omega}\right) K_{,j}\right)_{,j} \tag{2.58}$$

$$\omega_{,t} + u_j \omega_{,j} = \alpha \frac{\omega}{K} \tau_{ij} u_{i,j} - \beta \omega^2 + \frac{\sigma_d}{\omega} K_{,j} \omega_{,j} + \left(\left(\nu + \sigma \frac{K}{\omega}\right) \omega_{,j}\right)_{,j} \tag{2.59}$$

where the constants are

$$\alpha = \frac{13}{25};\ \beta^* = 0.09;\ \sigma = 0.5;\ \sigma^* = 0.6;\ \sigma_{do} = 0.125;\ \beta_o = 0.0708$$

and the functions are

$$\beta = \beta_o f_\beta;\ f_\beta = \frac{1+85\chi_m}{1+100\chi_m};\ \chi_m \equiv \left|\frac{\Omega_{ij}\Omega_{jk}S_{ki}}{(\beta^*\omega)^3}\right|;\ \varepsilon = \beta^*\omega K;\ l_u = \frac{K^{1/2}}{\omega}$$

$$\sigma_d = \begin{cases} 0 & K_{,j}\omega_{,j} \leq 0 \\ \sigma_{do} & K_{,j}\omega_{,j} > 0 \end{cases}$$

There are two distinguishing features to the above model. The first is the presence of the cross diffusion term $K_{,j}\omega_{,j}$. A recurring issue with $K-\omega$ models is their sensitivity to the freestream turbulence boundary condition. For numerical stability, one cannot simply set $K_\infty = 0$, but instead must use a small number; Kok [143] showed how selection of this boundary condition ($K_\infty/u_\infty^2 = [10^{-6}, 10^{-8}, 10^{-10}]$) could lead to dramatic changes in the resulting ν_t. Speziale et al. [264] showed how inclusion of the cross-diffusion term could lessen this sensitivity. The success of this term led to its continued use here and in the upcoming "Menter SST $K-\omega$ model [181]. Wilcox [297] noted that while this addresses the boundary condition, it reduces the accuracy of $K-\omega$ models in free-shear applications, but the version discussed here has superior performance in this regime.

The stress-limiter dependence of ν_t on $\tilde{\omega}$ instead of ω directly is another new addition to the 2006 iteration of Wilcox's model. This correction was first suggested by Coakley [62] and shown by Huang [119] to improve performance in separation bubbles, incompressible, and transonic flows. Menter [181] implemented it in their "SST $k-\omega$" model. As a final comparison, Wilcox [297] added that this correction has been shown [135] to improve accuracy in the transonic regime without the need for cross diffusion, blending functions, and nonlinear constitutive relations like those used by Menter [181].

Wilcox [297] concluded the discussion of their model by stating it is one of only two 2-equation models applicable to both wall-bounded and free shear flows. Of particular interest is the claim that the model is appropriate, as written, for shock-separated flows all the way through the hypersonic regime. Verification and validation data is provided in [297] to abet these claims. Further modifications and information regarding its implementation are available on the Wilcox $K-\omega$ model are

available at the NASA Langley Research Center's Turbulence Modeling Resource[1].

2.2.3.3 Menter SST $K-\omega$

Consider the previous two 2-equation models. Launder and Sharma's [154] $K-\varepsilon$ model performs very well at high Reynolds number but requires empirical corrections near walls, while early versions of Wilcox's [295] $K-\omega$ excelled at the wall but struggled with the freestream turbulent boundary condition. It would be advantageous to play to the strengths of each model, switching from the $K-\omega$ model at the wall to the $K-\varepsilon$ model in the freestream. With a similar mathematical formulation and the proper blending function, the transition could be seamless. This is what Menter proposed in 1992 [181] and formalized with a journal publication in 1994 [182].

Recall that ε is related to ω via $\varepsilon = C_\mu K\omega$. So, one can use this relation to write the transport equation for ε in terms of ω. In doing so, one is left with

$$K_{,t} + u_j K_{,j} = \tau_{ij} u_{i,j} - \varepsilon + \left(\left(\nu + \frac{\nu_t}{\sigma_k} \right) K_{,j} \right)_{,j} \tag{2.60}$$

$$\omega_{,t} + u_j \omega_{,j} = \frac{\gamma}{\nu_t} \tau_{ij} u_{i,j} - \beta \omega^2 + \left(\left(\nu + \sigma \frac{K}{\omega} \right) \omega_{,j} \right)_{,j} + 2(1-F_1) \frac{\rho \sigma_{\omega\varepsilon}}{\omega} K_{,j} \omega_{,j} \tag{2.61}$$

Note the slightly different form from the Wilcox $K-\omega$ transport equation owing to some small modeling steps and the use of the "ε" form of the turbulent kinetic energy transport equation. The main novelty between the ε and ω transport equations is the introduction of the cross-diffusion term, the last term on the right hand side. It was previously discussed how Speziale et al. [264] used this term to lessen the impact of freestream turbulent kinetic energy boundary conditions, but here it serves a second function. Because the cross diffusion is all that separates $\frac{D\varepsilon}{Dt}$ from $\frac{D\omega}{Dt}$, [182] chose to add the blending function F_1 to toggle between the two models. This allows the code to automatically choose the proper model for the local conditions. A common correction suggested by Menter [183] is to apply a limiter to the production term ($\tau_{ij} u_{i,j}$) in the turbulent kinetic energy transport equation: $min(\tau_{ij} u_{i,j}, 20\beta^* \omega K)$.

[1] https://turbmodels.larc.nasa.gov/

The blending function used is $F_1 = \tanh(arg_1^4)$ to smoothly merge the two regimes, with

$$arg_1 = min\left[max\left(\frac{\sqrt{K}}{\beta^*\omega d}, \frac{500\nu}{d^2\omega}\right), \frac{4\rho\sigma_{\omega\varepsilon}K}{CD_{K\omega}d^2}\right] \tag{2.62}$$

where $CD_{K\omega} = max\left(2\rho\sigma_{\omega 2}\frac{1}{\omega}K_{,j}\omega_{,j}, 10^{-20}\right)$, d is the distance to the nearest wall, $\beta^* = 0.09$, and $\sigma_{\omega 2} = 0.856$. Similarly, it is necessary to blend all of the empirical constants between the two models, which is done with $\phi = F_1\phi_\omega + (1 - F_1)\phi_\varepsilon$ where ϕ_ω and ϕ_ε represent constants for the $K-\omega$ and $K-\varepsilon$ models respectively.

At this point, the above model is sometimes called the $K-\omega$ "Baseline Stress Transport" model. Menter's "Shear Stress Transport" (SST) model includes another correction to improve the results of separated flows,

$$\mu_t = \frac{a_1\rho K}{max(a_1\omega, VF_2)} \tag{2.63}$$

where $a_1 = 0.31$, V is the vorticity magnitude $V = \sqrt{2\Omega_{ij}\Omega_{ij}}$, $F_2 = \tanh(arg_2^2)$ with

$$arg_2 = max\left(2\frac{\sqrt{K}}{\beta^*\omega d}, \frac{500\nu}{d^2\omega}\right) \tag{2.64}$$

Near the wall the constants are: $\gamma_\omega = \frac{\beta_\omega}{\beta^*} - \frac{\sigma_{\omega 1}\kappa^2}{\sqrt{\beta^*}}$; $\sigma_{k\omega} = 0.85$; $\sigma_{\omega\omega} = 0.5$; $\beta_\omega = 0.075$. In the freestream the constants are: $\gamma_\varepsilon = \frac{\beta_\varepsilon}{\beta^*} - \frac{\sigma_{\omega\varepsilon}\kappa^2}{\sqrt{\beta^*}}$; $\sigma_{k\varepsilon} = 1.0$; and $\sigma_{\omega\varepsilon} = 0.856$; $\beta_\varepsilon = 0.0828$.

The improved accuracy of Menter's SST $k-\omega$ model for separated flows is especially beneficial for external aerodynamics. Further modifications and information regarding its implementation are available through NASA Langley Research Center's Turbulence Modeling Resource (see preceding section).

2.2.4 Non-Boussinesq Models

The underpinning of all of the models to this point has been the Boussinesq approximation, that Reynolds stress can be written in terms of a flow's eddy viscosity μ_t. As such, the objective of every model has been the estimation of μ_t, not the Reynolds stress directly.

There are two details in the previous statement which can cause problems. Because μ_t depends on the flow and is not an intrinsic fluid property like μ, it allows the effect of sudden flow anomalies to persist for unnaturally long periods [297]; for example, sudden changes in mean strain rate can be unrelated to mean flow processes and time scales, which is problematic for the Boussinesq approximation. Similarly, flows with unequal normal Reynolds stresses like those with significant streamline curvature can have inaccurate predictions. Additional problematic flows include rotating and 3D applications [297].

While these instances are not relevant to the current project, the Algebraic Energy Flux model derived in Chapter 3 does require individual calculation of each Reynolds stress component, which Boussinesq models cannot provide. Bowersox [38] circumvented this restriction by probing DNS databases to validate a model which relates eddy viscosity to Reynolds stress, and Broslawski et al. [46] directly used DNS results for the Reynolds stresses, but such *ad hoc* solutions are not universal. Two classes of models for direct calculation of the Reynolds stresses will be discussed. It is noted these models still rely on 2-equation relations, just not the eddy viscosity, and that the theoretical and numerical cost of direct Reynolds stress calculation is significant. Again, this section is included for illustrative purposes and the formulations seen here may not be appropriate for compressible flows.

It is noted that even if one directly solves for the Reynolds stress, one must still close the q_y^T term. This is often done with the gradient diffusion method, which itself relies on k_t, so the Boussinesq approximation persists. The model provided by Bowersox [38] and re-derived in Chapter 3 offers a way calculate q_y^T directly, thereby closing the loop on the turbulent terms and completely avoid the Boussinesq approximation.

2.2.4.1 Algebraic Stress Models (ASM)

ASMs are formally nonlinear constitutive relations and assume the Reynolds stress is just the first entry in a larger polynomial expansion of functionals. They are beneficial in that they do not introduce another transport equation to the system. Early attempts at such models, which are appropriate for flat plates, are well reviewed by Wilcox [297]; some successful examples include

Equations 2.65 [234] (modified in [297]) and 2.66 [298]

$$\tau_{ij} = -\frac{2}{3}K\delta_{ij} + 2\nu_t S_{ij} - D\frac{K}{\omega^2}\left(S_{ik}\Omega_{kj} + S_{jk}\Omega_{ki}\right) \tag{2.65}$$

$$\tau_{ij} = -\frac{2}{3}K\delta_{ij} + 2\nu_t\left(S_{ij} - \frac{1}{3}u_{k,k}\delta_{ij}\right) + \frac{8}{9}\frac{K\left(S_{ik}\Omega_{kj} + S_{jk}\Omega_{ki}\right)}{(\beta^*\omega^2 + 2S_{mn}S_{mn})} \tag{2.66}$$

The above models are not true ASMs because they do not derive from the Reynolds stress transport equation. Technically the name ASM only means the equation does not include a partial differential equation so such a derivation, while beneficial, is not strictly necessary.

Two models which do originate from the Reynolds stress transport equation are offered by Rodi [227] and Gatski and Speziale [96], an early (Equation 2.67) and improved form (Equation 2.68) respectively. In the former, a "standard" implicit ASM, the dissipation (ε_{ij}) and pressure-strain (Π_{ij}) terms are closed with complex 3D correlations. For the latter, an "explicit" EASM, the α terms are constants, $\zeta^2 = C_\zeta \frac{K}{\varepsilon}\sqrt{\Omega_{ij}\Omega_{ij}}$ and $\eta = C_\eta \frac{K}{\varepsilon}\sqrt{S_{ij}S_{ij}}$.

$$\frac{\tau_{ij}}{K}\left(\tau_{mn}u_{m,n} - \varepsilon\right) = -\tau_{ik}u_{j,k} - \tau_{jk}u_{i,k} + \varepsilon_{ij} - \Pi_{ij} \tag{2.67}$$

$$\tau_{ij} = -\frac{2}{3}K\delta_{ij} + \frac{3}{3 - 2\eta^2 + 6\zeta^2}\left[\alpha_1\frac{K^2}{\varepsilon}S_{ij} + \alpha_2\frac{K^3}{\varepsilon^2}(S_{ik}\Omega_{kj} + S_{jk}\Omega_{ki}) - \alpha_3\frac{K^3}{\varepsilon^2}(S_{ik}S_{kj} - \frac{1}{3}S_{mn}S_{mn}\delta_{ij})\right] \tag{2.68}$$

While the true ASMs offer improved accuracy in curved flows over their earlier counterparts and provide better predictions of the anisotropy of the normal Reynolds stress, their general success is erratic [297] and their overall use is limited [293]. As such, not much detail is warranted.

2.2.4.2 Reynolds Stress Models

As expected, so-called second-order closure models begin with the Reynolds stress $\tau_{ij} \equiv -\overline{u_i' u_j'}$ transport equation; note that this means Reynolds stress is no longer tied to μ_t through the Boussi-

nesq approximation. The form shown here was taken from [297]

$$\tau_{ij} + u_k \tau_{ij,k} = -\underbrace{\tau_{ik} u_{j,k} - \tau_{jk} u_{i,k}}_{Production} + \underbrace{\varepsilon_{ij}}_{Dissipation} - \underbrace{\Pi_{ij}}_{Pressure\,Strain} + \underbrace{\left(\nu \tau_{ij,k}\right)_{,k}}_{Diffusion} + \underbrace{\left(C_{ijk}\right)_{,k}}_{Transport} \tag{2.69}$$

where the pressure-strain correlation is $\Pi_{ij} \equiv \overline{\frac{P'}{\rho}(u'_{i,j} + u'_{j}, i)}$, the dissipation is $\varepsilon_{ij} \equiv 2\nu \overline{u'_{i,k} u'_{j,k}}$, and the turbulent transport is $\rho C_{ijk} \equiv \rho \overline{u'_i u'_j u'_k} + \overline{P' u'_i}\delta_{jk} + \overline{P' u'_j}\delta_{ik}$.

Wilcox [297] made several incisive observations regarding Equation 2.69 and how it addresses the main issues with the Boussinesq approximation. To start, the convective and diffusive terms allow for the flow history to be appropriately carried into the current time step. As a full transport equation, it is more generalized to account for a fuller range of applications. Finally, the normal stresses are dependent on the initial conditions and flow physics, so sudden changes in rate of strain are acceptable. Additionally, and most important to this work, the Reynolds stress tensor is directly solved for any flow condition.

In exchange for these benefits, however, there are now three terms on the right hand side that must each be closed (the production and diffusion terms are already written in terms of Reynolds stress). General solutions are provided for each, before a final, cumulative model for applicable to even compressible flows is provided.

Wilcox [297] described the philosophy behind the dissipation term. Because dissipation is dominant at the flow's smallest scales, many models take Kolmogorov's [145] assumption of local isotropy $\varepsilon_{ij} = \frac{2}{3}\varepsilon\delta_{ij}$. Hanjalić and Launder [106] improved on this by allowing anisotropy via the Reynolds stress anisotropy tensor $b_{ij} = (\overline{u'_i u'_j} - \frac{2}{3}K\delta_{ij})/(2K)$

$$\varepsilon_{ij} = \frac{2}{3}\varepsilon\delta_{ij} + 2 f_s \varepsilon b_{ij} \tag{2.70}$$

Here f_s is a low-Reynolds number damping function $f_s = (1 + 0.1 Re_t)^{-1}$, the turbulent Reynolds number is $Re_t \equiv k^2/(\varepsilon\nu)$, and $\varepsilon_{ij} \equiv \nu \overline{u'_{i,k} u'_{j,k}}$. In practice, ε and K are supplied by a $K-\varepsilon$ routine like those discussed above.

The turbulent transport term is supplied by Launder et al. [155] as

$$C_{ijk} = -C_s \frac{K}{\varepsilon} \left[\tau_{im}\tau_{jk,m} + \tau_{jm}\tau_{ik,m} + \tau_{km}\tau_{ij,m} \right] \tag{2.71}$$

where $C_s = 0.11$. This approach is supported by DNS data from [185] and is used the famous Speziale-Sarkar-Gatski (SSG) model [263]. Wilcox [297] noted that literature mostly ignores the fluctuating pressure terms when modeling C_{ijk}, and DNS supports this omission.

What remains is the pressure-strain correlation, and it is the most challenging term to model and validate [293]. Wilcox [297] reviewed the steps taken and subsequent modifications to derive the form used in the famous Launder-Reece-Rodi (LRR) model; the details of the application are too numerous to cover here, and the theory itself is best served by Pope's [221] text, but the main ideas are reported.

The process begins with Poisson's equation for fluctuating pressure,

$$\frac{1}{\rho} P'_{,kk} = -\underbrace{2\overline{u}_{i,j} u'_{j,i}}_{Rapid} - \underbrace{\left(u'_i u'_j - \overline{u'_i u'_j} \right)_{ij}}_{Slow} \tag{2.72}$$

Rapid pressure fluctuations are immediately affected by changes in the mean strain rate of the base flow due to the direct inclusion of $\overline{u}_{i,j}$ while this effect is secondary for the slow pressure term; again, Pope [221] covers this concept in detail. Using Green's functions to model both forms of pressure individually yields $\Pi_{ij} = A_{ij} + M_{ijkl}\overline{u}_{k,l}$. The integral forms of A_{ij} (slow pressure strain) and M_{ijkl} (rapid pressure strain) are both fairly complex, but the main takeaway is that the pressure-strain is not a local quantity; fluctuations in one region of the flow impact another far away. In order to proceed, one must assume the effect of distant eddies is negligible with the "locally-homogeneous turbulence" approximation. Using known physical constraints, Rotta [229] models the slow pressure strain integral equation as

$$A_{ij} = C_1 \frac{\varepsilon}{K} \left(\tau_{ij} + \frac{2}{3} K \delta_{ij} \right) \tag{2.73}$$

Data from Uberoi [281] suggests $1.4 < C_1 < 1.8$.

Modeling rapid pressure strain is more complex. The most popular solution is that of the LRR model [155]. The authors followed Rotta's [229] technique, writing the integral equation for M_{ijkl} in terms of tensors, then selecting the most general equation for the tensor which satisfied the practical constraints. The result is

$$M_{ijkl}\overline{u}_{k,l} = -\hat{\alpha}\left(P_{ij} - \frac{1}{3}P_{kk}\delta_{ij}\right) - \hat{\beta}\left(D_{ij} - \frac{1}{3}D_{kk}\delta_{ij}\right) - \hat{\gamma}KS_{ij} \tag{2.74}$$

where, from [155, 151], the functions are

$$P_{ij} = \tau_{im}\tilde{u}_{j,m} + \tau_{jm}\tilde{u}_{i,m};\ D_{ij} = \tau_{im}\tilde{u}_{m,j} + \tau_{jm}\tilde{u}_{m,i};\ P = 0.5P_{kk}$$

and the constants are

$$0.4 \le C_2 \le 0.6;\ \hat{\alpha} = (8+C_2)/11;\ \hat{\beta} = (8C_2-2)/11;\ \hat{\gamma} = (60C_2-4)/55$$

The model is further improved by the inclusion of a "pressure-echo" or "wall-reflection" term [42] arising from the behavior of the integral form of Poisson's equation (2.72) near the wall. This term, to be added to the right hand side, is

$$\Pi_{ij}^{(w)} = \left[0.125\frac{\varepsilon}{K}\left(\tau_{ij} + \frac{2}{3}K\delta_{ij}\right) - 0.015(P_{ij} - D_{ij})\frac{K^{3/2}}{\varepsilon n}\right] \tag{2.75}$$

where n is the distance to the surface.

For completeness, the famous Speziale-Sarkar-Gatski (SSG) pressure-strain model [263] is listed as well; the treatment of this term is all that differentiates the two models.

$$\begin{aligned}\Pi_{ij} = &-\left(C_{1\varepsilon} + C_1^*\tau_{mn}\overline{u}_{m,n}\right) + C_{2\varepsilon}\left(b_{ik}b_{kj} - \frac{1}{3}b_{mn}b_{mn}\delta_{ij}\right) + \left(C_3 - C_3^*\sqrt{II}\right)KS_{ij} \\ &+ C_4K\left(b_{ik}S_{jk} + b_{jk}S_{ik} - \frac{2}{3}b_{mn}S_{mn}\delta_{ij}\right) + C_5K\left(b_{ik}\Omega_{jk} + b_{jk}\Omega_{ik}\right)\end{aligned} \tag{2.76}$$

where the Reynolds stress anisotropy tensor b_{ij} was used in modeling the dissipation term and

$$C_1 = 3.4; C_1^* = 1.8; C_2 = 4.2; C_3 = 0.8; C_3^* = 1.3; C_4 = 1.25; C_5 = 0.4$$

There is no need for a pressure-echo correction [297].

Before presenting the final LRR RSM, a few concluding remarks are appropriate. So et al. [259] reviewed the low Reynolds number modifications needed in the sublayer for the dissipation transport equation; these are necessary for the same reason they are used in the $K-\varepsilon$ model. Wilcox [297] stated that due to the complex tensors involved in deriving RSM models, more mathematical rigor is used than during the derivation of the 2-equation models. That said, 2-equation models are still used for both ASM and RSM techniques, so their inherent limitations carry over. Nevertheless, White [293] was optimistic about the future of RSMs.

Finally, the full LRR model is provided in compressible form [155], following Wilcox's notation [297]. It is noted this is a high Reynolds number formulation, so like the $K-\varepsilon$ model its performance near the wall may be limited. It is worth noting that in the dissipation transport model, ν_t from the $K-\varepsilon$ model is replaced with its analog C_{ijk}. Again, this is necessary because the entire point of RSMs is the removal of the Boussinesq approximation.

$$\overline{\rho}\tau_{ij,t} + \overline{\rho}\tilde{u}_k\tau_{ij,k} = -\overline{\rho}P_{ij} + \frac{2}{3}\overline{\rho}\varepsilon\delta_{ij} - \overline{\rho}\Pi_{ij} - C_s\left[\frac{\overline{\rho}K}{\varepsilon}\left(\tau_{im}\tau_{jk,m} + \tau_{jm}\tau_{ik,m} + \tau_{km}\tau_{ij,m}\right)\right]_{,k} \tag{2.77}$$

$$\overline{\rho}\varepsilon_{,t} + \overline{\rho}\tilde{u}_j\varepsilon_{,j} = C_{\varepsilon 1}\frac{\overline{\rho}\varepsilon}{K}\tau_{ij}\tilde{u}_{i,j} - C_{\varepsilon 2}\frac{\overline{\rho}\varepsilon^2}{K} - C_\varepsilon\left[\frac{\overline{\rho}K}{\varepsilon}\tau_{km}\varepsilon_{,m}\right] \tag{2.78}$$

$$\Pi_{ij} = C_1\frac{\varepsilon}{K}\left(\tau_{ij} + \frac{2}{3}K\delta_{ij}\right) - \hat{\alpha}\left(P_{ij} - \frac{2}{3}P\delta_{ij}\right) - \hat{\beta}\left(D_{ij} - \frac{2}{3}P\delta_{ij}\right) - \hat{\gamma}K\left(S_{ij} - \frac{1}{3}S_{kk}\delta_{ij}\right) + \ldots$$
$$\left[0.125\frac{\varepsilon}{K}\left(\tau_{ij} + \frac{2}{3}K\delta_{ij}\right) - 0.015(P_{ij} - D_{ij})\frac{K^{3/2}}{\varepsilon n}\right] \tag{2.79}$$

where the functions are

$$P_{ij} = \tau_{im}\tilde{u}_{j,m} + \tau_{jm}\tilde{u}_{i,m};\ D_{ij} = \tau_{im}\tilde{u}_{m,j} + \tau_{jm}\tilde{u}_{m,i};\ P = 0.5P_{kk}$$

n is the distance normal to the surface, and the constants are

$$\hat{\alpha} = (8+C_2)/11;\ \hat{\beta} = (8C_2-2)/11;\ \hat{\gamma} = (60C_2-4)/55;$$

$$C_1 = 1.8;\ C_2 = 0.60;\ C_s = 0.11;\ C_\varepsilon = 0.18;\ C_{\varepsilon 1} = 1.44;\ C_{\varepsilon 2} = 1.92$$

2.3 High-Temperature Effects

Hypersonic flows are perhaps the most extreme aerodynamic environments a vehicle may encounter. Their excessive speeds introduce complexities into the system's thermodynamics, and the high temperatures involved mean there is little margin of error for vehicle designers. Consider Figure 2.4 which tracks the velocity and altitude of NASA's Space Shuttle as it returned from orbit. At speeds approaching $10\frac{\text{km}}{\text{s}}$ viscous effects in the boundary layer and compression across the strong shocks produce temperatures sufficient to not only excite the air's internal energy modes, but fully dissociate N_2 and O_2; not shown is that once atomic N exists, it can react with atomic O to form NO. The presence of these high-temperature effects invalidates many of the foundational equations used to analyze flows up to supersonic speeds.

Consider for example Figure 2.5. If one takes the traditional assumption that $\gamma = Constant = 1.4$ ("calorically perfect gas") and solves for the post-shock temperature using the standard shock relations (see [128]), one will produce ludicrous results. However, if one takes into consideration high-temperature effects such as dissociation, recombination, and internal mode excitation more reasonable, albeit complex, temperatures are predicted. This is because energy is being "spent" breaking the air's molecular bonds and exciting its internal modes instead of its kinetic energy.

The temperatures at which each new energy mode becomes important are shown in Figure 2.6; it is again noted that NO formation begins as soon as atomic N exists. Of special interest is

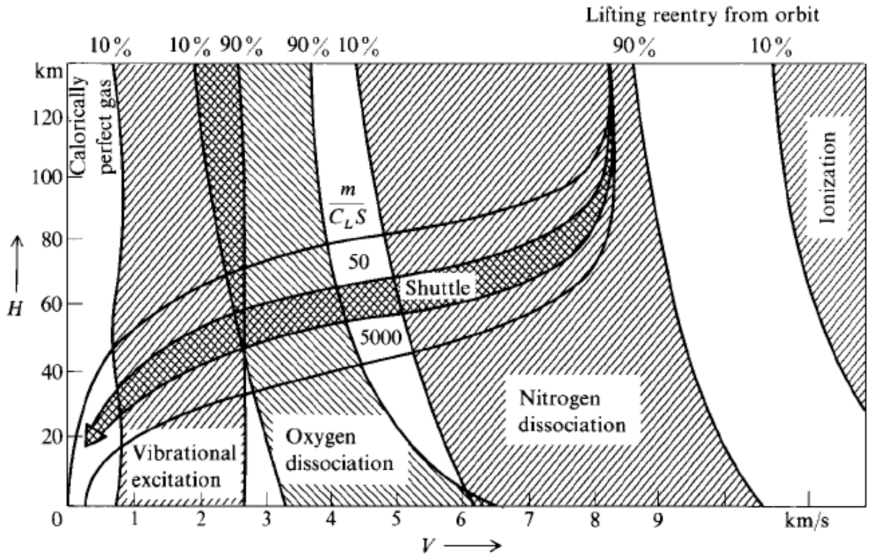

Figure 2.4: Gas regimes encountered during Shuttle reentry; data from Tauber et al. [276], figure taken with permission from Anderson [6].

the vibrational excitation. It occurs at a relatively low temperatures, and so it is the first internal mode to be excited (rotational excitation is generally assumed to be equilibrated with the external translational mode). Because vibrational excitation states are more greatly spaced than rotational and translational modes, even activating the air's lower vibrational levels stores a disproportionate amount of the flow's energy and has a large impact on the system's thermodynamics.

This section covers both thermal equilibrium and nonequilibrium. For clarity, each of these concepts are covered separately and to the depth required for the present application. It begins by introducing the relevant definitions and requisite thermodynamics for a meaningful review of each regime. For complete coverage of the topics reviewed, see [6, 41].

2.3.1 Classification of the Gas

Because the there are many different elements to hypersonic flows and their descriptors are precise, it is necessary to clearly define the system; the lexicon adopted here is from Anderson [6]. It was hypothesized the proposed flow field would be a mixture of thermally perfect gases with caloric imperfections. Furthermore, the anticipated thermochemical regime was one of chemical equilibrium throughout the domain, thermal equilibrium at the wall due to quenching, and

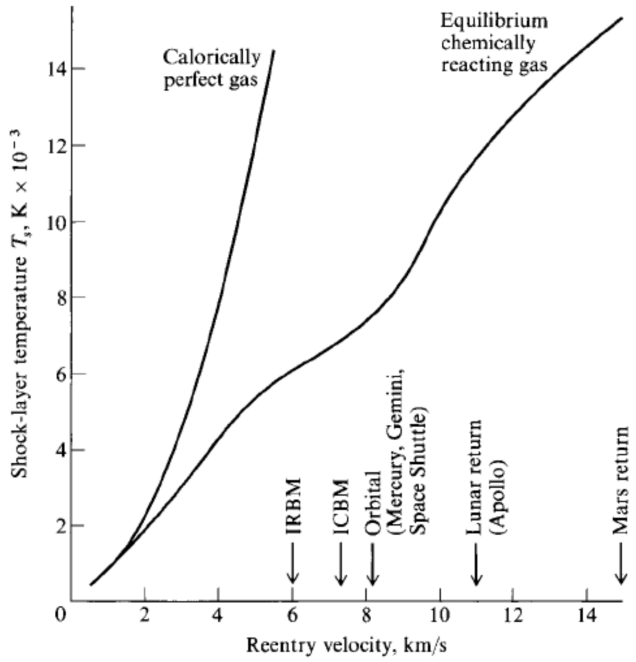

Figure 2.5: Temperature behind normal shock for hypersonic vehicles at 52km; data from Anderson [5], figure taken with permission from Anderson [6].

thermally frozen vibrational nonequilibrium in the freestream due to the plasma and low collision frequency in the ACE tunnel; thus some transition from equilibrium to frozen flow through the boundary layer was predicted. Each of these terms is defined in turn below, and these hypotheses will be tested throughout this report, especially in Chapter 8.

A gas in thermal equilibrium can be described by a single temperature; in other words, its external (translational) temperature and internal (rotational, vibrational, electronic) temperatures are all the same. A gas in chemical equilibrium is one not undergoing any spontaneous reactions. Past a strong hypersonic shock, rotational and translational temperatures equilibrate rapidly while the vibrational temperature requires far more collisions to match the bath (see Table 2.1). Similarly, the reaction rate for N_2 dissociation or ionization can match a representative flow time scale, so the chemical composition changes as the fluid travels over the vehicle. These are respective examples of thermal and chemical nonequilibrium typical of hypersonic flight.

Anderson [6] further defines local thermal equilibrium as the case where a Boltzmann distri-

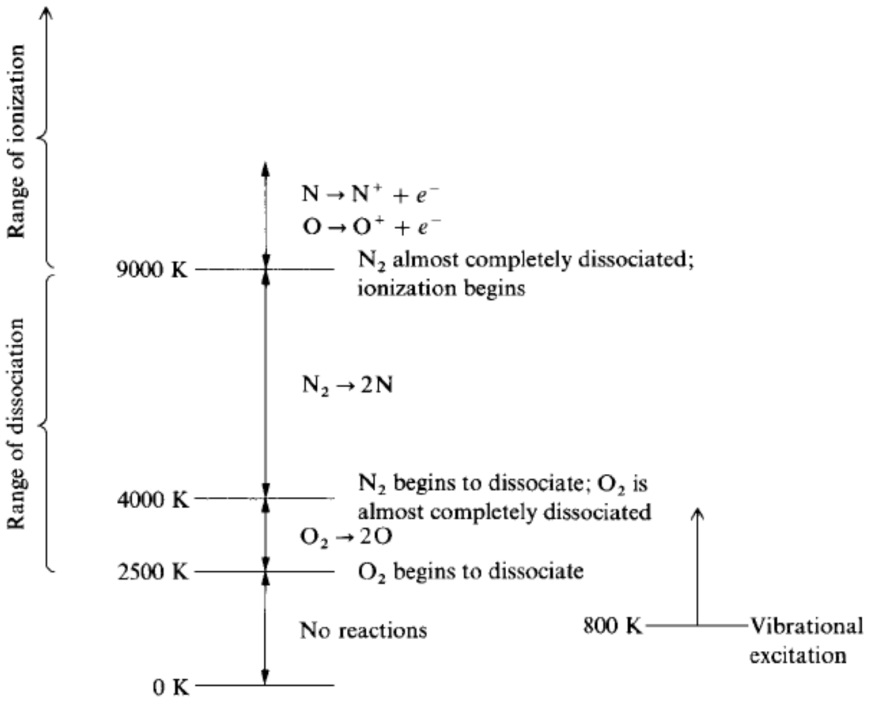

Figure 2.6: Characteristics of hypersonic flows; figure taken with permission from Anderson [6].

	Translation	**Rotation**	**Vibration**
Translation	1	10	10^6
Rotation	10	10	10^5
Vibration	10^6	10^5	$< 10^6$

Table 2.1: Estimate of collisions necessary for equilibration.

bution at local temperature can be fit to each species at each point in the flow. Similarly, they define local chemical equilibrium as the case where, at each point in the flow, the chemistry is in equilibrium for the local temperature and pressure. Note that equilibrium is distinct from a frozen flow, wherein the rates for thermal or chemical equilibration are long enough to consider the nonequilibrium temperature or chemistry as constant for the relevant flow time scale.

A thermally perfect gas is one where real gas effects such as the volume of the molecules and intermolecular forces are negligible. The most general form of the thermal equation of state is $P = P(V,T)$. A common form for hypersonic flows is $P\hat{V} = Z\hat{\mathscr{R}}T \rightarrow P = Z\rho R_{specific}T$ where a hat

$\hat{X}$ denotes a unit molar quantity and Z is the compressibility factor. Real gas effects are typically only important at low temperatures or high pressures (high densities), and so for simplicity they are generally and safely neglected for here. If $Z = 1$ the familiar Perfect (Ideal) Gas Law is recovered. The caloric equations of state are $e = e(V,T)$ and $h = h(P,T)$. For a calorically perfect gas, the specific heats C_v and C_v, and by extension their ratio γ are constant. This allows $e = C_vT$ and $h = C_pT$, but due to the presence of internal energy excitation caloric perfection is seldom experienced in hypersonic flight.

A simple model for hypersonic flows may contain five gas species, N_2, O_2, N, O, and NO. It is helpful to assume a mixture of thermally perfect gases, which requires that all species have the same volume and are not affected by intermolecular forces. This allows one to treat each species independently at the system's temperature and volume in accordance with Dalton's Law of Partial Pressures, and then produce a bulk property by summing each species' contribution scaled by its mass or molar average.

2.3.1.1 Vibrational Profile Assumptions

It was previously stated the expected vibrational temperature would be frozen in the freestream and in equilibrium at the wall. Here both of those cases are more rigorously considered.

The effect of plasma-initiated vibrational nonequilibrium on a turbulent freestream (channel) was studied by Fuller et al. [95] (see section 2.3.5). They showed that energy released by relaxing vibrational modes has a strong impact on $T^{rot-trans}$, viscosity, and ultimately Reynolds stress; this experiment and its affiliated work will be revisited in detail in Section 2.3.5. Thus accurate prediction of vibrational decay is critical. In addition to performing the experimental measurements described in [94, 95], Hsu [116] conducted an extensive simulation of the collisional kinetics of the channel flow. Their model contained six species (N_2, O_2, NO, O, H_2O, and CO_2) and 52 reactions covering chemical, vibration-vibration, and vibration-translation energy exchange collisions; the relevant rate constants Hsu calculated for their experiment are provided in Table 2.2. Neglecting the results in the presence of H_2O and CO_2, Hsu found N_2, O_2, and NO had a vibrational relaxation lifetimes of $\mathcal{O}(100\text{ms})$, $\mathcal{O}(100\text{ms})$, and $\mathcal{O}(0.1\text{ms})$ respectively. They attributed the rapid decay of

NO to its rate constants being orders of magnitude larger than those for the other species, and noted that for both VT and VV collisions N_2 is the longest-lived molecule by orders of magnitude. This was critical, because it suggested air moving at $u = 850\text{m/s}$, a realistic speed for the ACE tunnel, will travel 85m before significantly decaying, but seeded NO will decay within 0.085m of excitation. Of course, the present test has different conditions than Hsu [116], but they are close enough that it is safe to assume the air is thermally frozen along the entire length of the test article, but the NO will decay somewhat. This assumption will be analyzed through an analogous analysis in Chapter 8.

Reaction	**Forward Rate Constant** $(cm^3/molec/s)$	**Ref.**	**Rxn No.**
V-V Relaxation			
$N_{2,v=1} + O_2 \rightarrow O_{2,v=1} + N_2$	7.58×10^{-18}	[15]	1
$N_{2,v=1} + NO \rightarrow NO_{v=1} + N_2$	1.04×10^{-15}	[53]	2
$NO_{v=1} + O_2 \rightarrow O_{2,v=1} + NO$	1.00×10^{-14}	[131]	3
V-T Relaxation			
$N_{2,v=1} + N_2 \rightarrow N_2 + N_2$	4.13×10^{-24}	[53]	4
$N_{2,v=1} + O_2 \rightarrow N_2 + O_2$	4.13×10^{-24}	[53]	5
$N_{2,v=1} + NO \rightarrow N_2 + NO$	4.13×10^{-24}	[53]	6
$O_{2,v=1} + O_2 \rightarrow O_2 + O_2$	5.77×10^{-19}	[15]	7
$NO_{2,v=1} + N_2 \rightarrow O_2 + N_2$	5.58×10^{-19}	[15]	8
$O_{2,v=1} + NO \rightarrow O_2 + NO$	6.55×10^{-19}	[53]	9
$NO_{v=1} + NO \rightarrow NO + NO$	7.52×10^{-14}	[147]	10
$NO_{v=1} + O_2 \rightarrow NO + O_2$	2.58×10^{-14}	[147]	11
$NO_{v=1} + N_2 \rightarrow NO + N_2$	1.30×10^{-16}	[147]	12

Table 2.2: Relevant relaxation rate constants for the conditions in [116]

For the continuum flows in the ACE tunnel velocity and external temperature slip at the wall is infeasible, but slip in the vibrational temperature profile is possible. Here vibrational slip analyzed analogously to the Maxwell model for velocity slip (see [238]), following Nompelis et al. [207]

$$e_{v,slip} - e_{v,wall} = \frac{2 - \sigma_v}{\sigma_v} \lambda_v \left(\frac{\partial e_v}{\partial y} \right)_{wall} \tag{2.80}$$

Here $\lambda_v = \lambda = 2/\mu/\rho\bar{c}$ is equivalent to the momentum mean free path with $\bar{c} = \sqrt{8R_{specific}T/\pi}$. $e_{v,wall}$ is the vibrational energy of the wall, and $e_{v,slip}$ is the vibrational energy of the gas at the wall, with slip allowed; thus the degree of slip is controlled by the vibrational accommodation factor σ_v. When $\sigma_v = 0$, the above equation is meaningless, the wall is vibrationally adiabatic and e_v is uncorrelated to the wall. Conversely, when $\sigma_v = 1$ the flow is completely correlated. This is perhaps more clearly explained by the definition in [304], who wrote that σ_v is the portion of the energy accommodated so $\sigma_v e_{v,wall}$ energy is accommodated by the wall and $(1-\sigma_v)e_{v,wall}$ is reflected back into the flow.

The macroscopic effect of vibrational accommodation is to increase wall heat flux; as $\sigma_v \to 1$ the wall absorbs more vibrational energy and becomes hotter, and *vice versa* [207, 237]. Furthermore, Yu et al. [304] showed a vibrational temperature boundary layer can only form when $\sigma_v \neq 0$, otherwise the frozen temperature will extend to the wall; their flat plate shock tunnel simulations showed no change in the external boundary layer profile regardless of the vibrational accommodation used. Sauerwein and Hruschkaand [237] compared their own simulations to shock tunnel data over a cone and found vibrational accommodation has no effect on surface pressure, and that its effect on heat flux is inversely proportional to density.

Estimation of σ_v is important but difficult because it depends on both flow and material properties [304]. In their CFD replication of shock tunnel data over a double cone, Nompelis et al. [207] found a value of $\sigma_v = 0.001$ following the measurements of Black et al. [31] for stainless steel provided excellent agreement with the data (directly better than $\sigma_v = 0.1$), though its effect was coupled with other high-temperature corrections to the simulation; Moss and Bird [189] independently found that when adjusting σ_v alone better results were attained with full vibrational accommodation for the same experimental data set, though both the $\sigma_v = 0$ and 1 data were within the experimental uncertainty. Evidence for negligible vibrational accommodation is provided by the literature survey in [184]. Boyd et al. [40] also used $\sigma_v = 0.1$ for their calculations.

Thus it would seem vibrational equilibrium cannot be assumed at the wall. However, the previous studies were mostly concerned with high-temperature shock tube experiments, and none

considered a turbulent boundary layer. The ACE tunnel runs at modest Mach numbers, relatively negligible vibrational excitation, and comparatively (see [237]) high densities. Finally, here a glow discharge was used to locally seed in weak vibrational nonequilibrium. As such there is currently no truly analogous study of the vibrational slip condition in the literature. It was decided the best course of action would be to perform the experiment and for now accept the modest assumption that the vibrational excitation is collisionally quenched at the wall so $\sigma_v = 1$. This open question will be probed with optical techniques as part of the current work; discussions are available in Section 7.4.2.2 and Chapter 8.

2.3.2 Statistical Thermodynamics

Statistical thermodynamics are useful because they allow one to calculate thermodynamic properties from first principles while the classical approach defines most properties only relative to one another and often relies on empirical or experimental results. The proceeding analysis is summarized from Anderson [6]. It is applicable only to a single species in chemical equilibrium, but in a later section it is extended to a mixture of thermally perfect gases with caloric imperfections.

2.3.2.1 Energy Modes, Levels, and States

To begin, recall that atoms and molecules have distinct energy modes corresponding to their translational, rotational, vibrational, and electronic behavior. Picture a linear diatomic molecule: it can translate in space (three degrees of freedom); meaningfully rotate about two axes (two degrees of freedom); vibrate inwards and outwards (two degrees of freedom); and each electron stores both potential and kinetic energy. For atoms (N and O), rotational and vibrational energy are negligible. These behaviors lead to distinct energy levels for each energy mode, and they are pictorialized in Figure 2.7. Qualitatively, this figure shows there are many translational levels, rotational levels become farther spaced at higher energies, and that vibrational levels become more closely spaced at higher energies.

Each of the ε'_X exists as the sum of the zero-point energy $\varepsilon'_{0,X}$ and it measurable, or "sensible" energy ε_X; the zero-point energy corresponds to the value at 0K. Using the Schrödinger

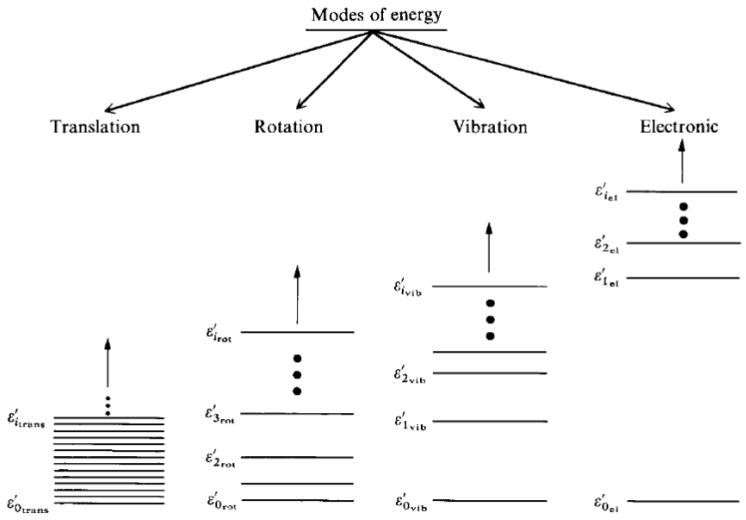

Figure 2.7: Energy level diagram for each excitation mode; figure taken with permission from Anderson [6].

Wave Equation, one can derive directly from quantum mechanics equations for the total energy of each energy mode. This process is too complex to be shown here, relies on some minor physical simplifications such as a rigid rotor for diatomic molecules, and cannot easily be extended to the electronic energy, but the results for the remaining modes are:

- Translation:
  - Assume particle in a box of size a_1, a_2, a_3
  - $\varepsilon'_{trans} = \frac{h^2}{8m}\left(\frac{n_1^2}{a_1^2} + \frac{n_2^2}{a_2^2} + \frac{n_3^2}{a_3^2}\right)$ where m is mass, h is Plank's constant, and n are integral quantum numbers for each dimension.
  - Assume $\varepsilon'_{trans,0} \approx 0$ so $\varepsilon_{trans} \approx \varepsilon'_{trans}$
- Rotation:
  - Assume rigid rotor of moment of inertia I
  - $\varepsilon'_{rot} = \frac{h^2}{8\pi^2 I} J(J+1)$ where h is Plank's constant and J is the integral quantum number
  - At $J = 0$ $\varepsilon'_{rot,0} = 0$, so $\varepsilon_{rot} = \varepsilon'_{rot}$

- Vibration:
  - Assume harmonic oscillator
  - $\varepsilon'_{rot} = h\nu(n+\frac{1}{2})$ where h is Plank's constant, ν is the particle's funcamental vibrational frequency, and n is the integral quantum number
  - At $n = 0$ $\varepsilon'_{vib,0} = \frac{1}{2}h\nu$, so $\varepsilon_{vib} = nh\nu$

Values for I and ν are provided from spectroscopic measurement and are usually read from tabulated data [109, 214]. An expression for the electronic energy will be provided shortly.

The total energy of an energy level ε'_J is the sum of a set of internal and external energy modes. As a reductive example, a particle translating very quickly could have the same total energy as one vibrating somewhat slowly. Put another way, two molecules rotating at the same rate but in different orientations have the same energy, but different angular momentum vectors. Thus a particle cannot completely be described by the energy level alone, one must also consider the number of unique combinations of energy modes which can produce it and other defining factors. The total number of these so-called energy states is called the degeneracy g_J of ε'_J. The degeneracy can also be thought of as a statistical weight; a state with a higher g_J is more likely to occur than one with a lower value.

This concept is extended to a system of N molecules. The system itself will have distinct energy levels ε'_J of degeneracy g_J, but now instead of energy states it will have macrostates. A macrostate is the instantaneous distribution of molecules N_J over all of the available energy levels. The most probable macrostate is the one which is achieved most frequently when the system is in thermochemical equilibrium. As such it is desirable to predict this most probable macrostate. This relies on one final parameter, the microstate. A microstate defines how the N_J molecules in a energy level ε'_J distribute themselves over the g_J macrostates; W is the number of microstates for a given macrostate. Microstates have uniform probability, so the macrostate with the largest W is the most probable, and its particle distribution is denoted as N^*_J.

Calculation of W is beyond the scope of the present work, but is shown in detail in [6]. Suffice

it to say that the case of gases above $\sim$ 5K, which well describes the present application and thus will be used hereafter, $g_J \gg N_J$ and

$$N_J^* = N\frac{g_J e^{-\varepsilon_J/k_B T}}{\sum_J g_J e^{-\varepsilon_J/kT}} = N\frac{g_J e^{-\varepsilon_J/k_B T}}{Q} \tag{2.81}$$

This is the famous Bolztmann distribution, well described by Anderson [6]: "For a system of N molecules at a given temperature T and volume V, Equation 2.81 tells us how many molecules or atoms N_J^* are in each energy level ε_J when the system is in thermodynamic equilibrium". Note that here it has been written in terms of the sensible energy ε_J, and k_B is the Boltzmann constant.

2.3.2.2 Partition Functions

The partition function $Q = Q(V,T)$ is used to provide the macroscopic thermodynamic state variables from statistical results, linking the two approaches. Physically, it represents the average number of active energy levels for a given energy mode; these functions use the atomic/molecular structure to predict how a particle will distribute energy between the different energy levels in the translational, rotational, vibrational, and electronic modes. Nitrogen, for example, will only have $Q_{vib} \approx \mathcal{O}(1)$ until $T \gtrsim 600$K. From the definition of the Boltzmann distribution, $Q = \sum_J g_J e^{-\varepsilon_J/kT}$, so using the results for the sensible energy for each mode one can derive

$$\begin{aligned}
\frac{Q_{trans}}{V} &= \left(\frac{2\pi m k_B T}{h^2}\right)^{3/2} \\
Q_{rot} &= \frac{8\pi^2 I k_B T}{h^2} \\
Q_{vib} &= \frac{1}{1-e^{-h\nu/k_B T}} \\
Q_{el} &= g_0 + g_1 e^{-\varepsilon_{el,1}/k_B T} + g_2 e^{-\varepsilon_{el,2}/k_B T}
\end{aligned} \tag{2.82}$$

It is noted that Q_{el} is simply the definition of the partition function (see Equation 2.81) truncated at three terms, which Anderson [6] deemed sufficiently accurate, with the sensible energy taken from spectroscopic data [109, 214]. Furthermore, for symmetric molecules like N_2 the wave function is also symmetric, which means the same states are predicted twice; this is remedied by simply

multiplying Q_{rot} by $\frac{1}{2}$ for symmetric molecules. All of these separate functions are combined with $\frac{Q}{V} = \frac{Q_{trans}}{V} Q_{rot} Q_{vib} Q_{el}$.

In practice, $\frac{\delta Q}{\delta T}$ is usually needed, and using $\ln(Q)$ helps to simply the algebra. With this adjustment $\frac{\partial \ln(Q/V)}{\partial T} = \frac{\partial \ln(Q_{trans}/V)}{\partial T} + \frac{\partial \ln(Q_{rot})}{\partial T} + \frac{\partial \ln(Q_{vib})}{\partial T} + \frac{\partial \ln(Q_{el})}{\partial T}$ and

$$\begin{aligned}
\frac{\partial \ln(Q_{trans}/V)}{\partial T} &= \frac{3/2}{T} \\
\frac{\partial \ln(Q_{rot})}{\partial T} &= \frac{1}{T} \\
\frac{\partial \ln(Q_{vib})}{\partial T} &= -\frac{h\nu}{k_B T^2} \frac{e^{-h\nu/k_B T}}{1 - e^{-h\nu/k_B T}} \\
\frac{\partial \ln(Q_{el})}{\partial T} &= \left(\frac{1}{\sum_{l=0}^{2} g_l e^{-\varepsilon_{el,l}/k_B T}} \right) \underbrace{\sum_{l=0}^{2} \left[\frac{g_l \varepsilon_{el,l}}{T^2 k_B} e^{-\frac{\varepsilon_{el,l}}{k_B T}} \right]}_{\partial Q_{el}/\partial T}
\end{aligned} \tag{2.83}$$

$\frac{\delta^2 \ln(Q_{el})}{\delta T^2}$ is also needed

$$\begin{aligned}
\frac{\partial^2 \ln(Q_{el})}{\partial T^2} = &- \left(\frac{\partial Q_{el}/\partial T}{\sum_{l=0}^{2} g_l e^{-\varepsilon_{el,l}/k_B T}} \right)^2 + \ldots \\
&\left(\frac{1}{\sum_{l=0}^{2} g_l e^{-\varepsilon_{el,l}/k_B T}} \right) \underbrace{\sum_{l=0}^{2} \left[\frac{-\varepsilon_{el,l} g_l}{k_B T^2} e^{-\varepsilon_{el,l}/k_B T} \left(\frac{2}{T} - \frac{\varepsilon_{el,l}}{k_B T^2} \right) \right]}_{\partial^2 Q_{el}/\partial T^2}
\end{aligned} \tag{2.84}$$

Anderson [6] showed how Q directly relates to thermodynamic properties. They used $E = \sum_J \varepsilon_J N_J^*$ to derive an equation for the specific internal sensible energy for a Boltzmann distribution of molecules

$$e = R_{specific} T^2 \left(\frac{\partial \ln Q}{\partial T} \right)_V = \frac{3}{2} R_{specific} T + R_{specific} T + \frac{h\nu/k_B T}{e^{h\nu/k_B T} - 1} R_{specific} T + e_{el} \tag{2.85}$$

The terms on the right hand side correspond to the translational, rotational, vibrational, and electronic contributions, respectively. For atoms, the rotational and vibrational energy terms are neglected. The specific enthalpy, making use of the Ideal Gas Law $PV = R_{specific} T$, falls natu-

rally from the energy equation: $h = e + PV = R_{specific}T^2\left(\frac{\partial \ln Q}{\partial T}\right)_V + R_{specific}T$. Also, because $c_v \equiv \left(\frac{\partial e}{\partial T}\right)_v$ and $c_p = c_v + R_{specific}$, this equation explains why for diatomic molecules like N_2 and O_2 ("air") from $\sim 3-600$K, when only ro-translational modes are excited, $\gamma = \frac{c_p}{c_v} = Const = 1.4$.

2.3.2.3 Derivation of the Perfect Gas Law from First Principles

Here a crucial link between classical and statistical thermodynamics is introduced. It stands to reason that entropy, or disorder, is maximized when the particle's in the system can distribute themselves as broadly as possible. This corresponds to a high number of microstates. Boltzmann related the macroscopic parameter, entropy, to the statistical theory with the equation

$$S = k_B \ln(W_{max}) \tag{2.86}$$

This is the origin of the Bolztmann constant k_B.

Anderson [6] showed how Equation 2.86 leads to

$$S = Nk_B\left(\ln\frac{Q}{N} + 1\right) + Nk_BT\left(\frac{\partial \ln Q}{\partial T}\right)_V \tag{2.87}$$

From classical mechanics, $TdS = dE + PdV$. For a thermally perfect single species system $dE = 0$, which leaves

$$P = Nk_BT\left(\frac{\partial \ln Q}{\partial V}\right)_T \tag{2.88}$$

Only $\ln(Q_{trans})$ is a function of V. Performing the differentiation yields

$$PV = Nk_BT \tag{2.89}$$

Thus the Perfect (Ideal) Gas Law is derived from first principles.

2.3.3 Flows in Thermochemical Equilibrium

As an application of the above concepts, consider the case of five-species air (N_2, O_2, NO, N, and O) in thermochemical equilibrium immediately downstream of a hypersonic vehicle's bow

shock, before any relaxation can yield nonequilibrium. Treat the system as a mixture of thermally perfect gases with caloric imperfections, and neglect ionization, vibrational-rotational coupling, high-order rotational effects (the molecular diameter is constant). It should be clear from the above analyses that chemical and thermal reactions will take place across the shock which alter the enthalpy and specific heats, rendering a traditional shock analysis completely inaccurate.

2.3.3.1 Calculation of Species

The main challenge is calculation of the amounts of the species present, which is a function of both temperature and pressure. Knowledge of $N_{species} = N_{(n)}$, where N is the amount of each species in moles, is critical for the calculation of the macroscopic thermodynamics of the mixture and thereby the flow variables. Furthermore, $N_{(n)}$ directly depends on the partition functions, which introduces statistical mechanics to the flow.

The governing chemical reaction is $0.79N_2 + 0.21O_2 \leftrightarrows N_{N_2}N_2 + N_{O_2}O_2 + N_{NO}NO + N_N N + N_O O$. There are two atoms, but five species, so in order to find the concentration of all five species two atom balance equations and three additional subreactions are needed. The exact equations used does not matter so long as they are linearly independent, but as an example take $N_2 \leftrightarrows 2N$, $O_2 \leftrightarrows 2O$, and $NO \leftrightarrows N + O$. With this the system is closed.

Because chemical equilibrium is assumed, one must find the equilibrium rate constants from

$$k_{nd}(T) = \prod_n \left(\frac{Q_{(n)}}{V}\right)^{\left(\nu''_{(n)} - \nu'_{(n)}\right)} \exp\left(\frac{-\Delta\hat{\varepsilon}^o_o}{\hat{\mathscr{R}}T}\right) \tag{2.90}$$

$$k_p(T,P) = \left(\frac{k_B T}{P^*}\right)^{\Sigma_{(n)}\left(\nu''_{(n)} - \nu'_{(n)}\right)} * k_{nd} \tag{2.91}$$

$$k_N(T,P) = \prod_n \left(X_{(n)}\right)^{\left(\nu''_{(n)} - \nu'_{(n)}\right)} = \left(\frac{P_{(n)}}{P^*}\right)^{-\sigma_\nu} * k_p \tag{2.92}$$

In these equations, a hat $\hat{X}$ denotes a variable per unit mole, $\Delta\varepsilon^o_o \equiv \sum_{(n)}\left(\nu''_{(n)} - \nu'_{(n)}\right)\varepsilon^o_o$ is the formation energy at 0K ($\varepsilon^o_{f(n)o}$, available from spectroscopic tables [109, 214]) for the species, and P^* is a reference pressure. The $\nu''_{(n)} - \nu'_{(n)}$ term relates the stoichiometric coefficients of each of the

species present in the subreaction (single prime for reactants, double prime for products), and σ_ν is the sum of all of these terms for a given subreaction. For example, for the $N_2 \leftrightarrows 2N$ subreaction $\sigma_\nu = (0-1)+(2-0)$ for N_2 and N respectively. The subscripts for the three equilibrium constants denote number density (nd), pressure (P), and amount (N) respectively. Here the chemistry, captured by the rate constants k, is related to the statistical thermodynamics via Q.

By defining k_N in terms of the molar concentration $X_{(n)} = N_{(n)}/N_{tot}$ as well as k_P, one can calculate $N_{(n)}$ from the equilibrium constants. At this point the problem has become an $n \times n$ system of equations for the amount of each species. Two equations are provided from the atom balance, and the remainder come from the equilibrium rate constants of the subreactions. An algorithm to rapidly solve this system is offered by Gordon and McBride [102]. The Gordon-McBride algorithm relies on an assumptions for each type of equation. Respectively,

$$\begin{aligned}
\varepsilon^a_{(n)} &= \frac{\Delta N^a_{(n)}}{\Delta N^{a-1}_{(n)}} = \frac{\Delta X^a_{(n)} N^a_{(tot)}}{\Delta X^{a-1}_{(n)} N^a_{(tot)}} = \frac{\Delta X^a_{(n)}}{\Delta X^{a-1}_{(n)}} \left(1 + \frac{\Delta N^{(tot)}}{N^{a-1}_{(tot)}}\right) \approx \frac{\Delta X^a_{(n)}}{\Delta X^{a-1}_{(n)}} \\
&\implies N^a_{(n)} = N^{a-1}_{(n)} + \Delta N^a_{(n)} = N^{a-1}_{(n)}(1+\varepsilon^a_{(n)}) \\
\varepsilon^a_{(n)} &= \frac{\Delta N^a_{(n)}}{\Delta N^{a-1}_{(n)}} \approx \delta \ln N^a_{(n)} \approx \frac{\Delta X^a_{(n)}}{X^{a-1}_{(n)}} \approx \Delta X^a_{(n)} \\
&\implies \ln N^a_{(n)} = \ln N^{a-1}_{(n)} + \varepsilon^a_{(n)}
\end{aligned} \tag{2.93}$$

Here ε denotes error and $\varepsilon = \sqrt{\sum_n \varepsilon^2_{(n)}}$ and a is the iteration. Once all of the equations have been rewritten using the form outlined above, the system be written in the form $[A]\{\varepsilon_i\} = \{b_i\}$ with $\ln N^a_i = \ln N^{a-1}_i + \varepsilon_1$ and solved iteratively until the error drops below a threshold.

As an example for each type of equation, consider the N atom balance $2N_{N_2} + N_{NO} + N_N = 2 * 0.79$ and the N_2 dissociation subreaction $N_2 \leftrightarrows 2N$. The former can be written

$$2N^{a-1}_{N_2}\varepsilon^a_{N_2} + N^{a-1}_{NO}\varepsilon^a_{NO} + N^{a-1}_N \varepsilon^a_N = 2 * 0.79 - \left(2N^{a-1}_{N_2} + N^{a-1}_{NO} + N^{a-1}_N\right) \tag{2.94}$$

The latter must be written in terms of its mole fractions as $k_{n,N_2} = X^2_N / X_{N_2}$ to be equated to k_n

via Equation 2.92. With this on can take the logarithm, separate the division and exponents using logarithmic identities, and expand over the iteration indices to produce $2\ln(X_N)^{a-1} + 2\Delta\ln(X_N)^a - \ln(X_{N_2})^{a-1} + \Delta\ln(X_{N_2})^a = \ln k_{n,N_2}$. Under the Gordon-McBride assumptions, this becomes

$$2\varepsilon_N - \varepsilon_{N_2} = \ln\left(\frac{k_{n,N_2}}{k_{n,N_2}^{n-1}}\right) \tag{2.95}$$

where on the right hand side the numerator is evaluated from Equation 2.92 and the denominator is $k_{n,N_2}^{a-1} = \left(\frac{X_N^2}{X_{N_2}}\right)^{a-1}$. For the entire system the equations become

$$\begin{bmatrix} 2 & 0 & 0 & -1 & 0 \\ 0 & 2 & 0 & 0 & -1 \\ 1 & 1 & -1 & 0 & 0 \\ N_N^{a-1} & 0 & N_{NO}^{a-1} & 2N_{N_2}^{a-1} & 0 \\ 0 & N_O^{a-1} & N_{NO}^{a-1} & 0 & 2N_{O_2}^{a-1} \end{bmatrix} \begin{Bmatrix} \varepsilon_N^a \\ \varepsilon_O^a \\ \varepsilon_{NO}^a \\ \varepsilon_{N_2}^a \\ \varepsilon_{O_2}^a \end{Bmatrix} = \begin{Bmatrix} \ln k_{n_{N_2}}^a - \ln k_{n_{N_2}}^{a-1} \\ \ln k_{n_{O_2}}^a - \ln k_{n_{O_2}}^{a-1} \\ \ln k_{n_{NO}}^a - \ln k_{n_{NO}}^{a-1} \\ 2*0.79 - 2N_{N_2}^{a-1} - N_{NO}^{a-1} - N_N^{a-1} \\ 2*0.21 - 2N_O^{a-1} - N_{NO}^{a-1} - N_{NO}^{a-1} \end{Bmatrix} \tag{2.96}$$

It is advised to keep the diagonal of the Jacobian nonzero to aid convergence.

Initial conditions are provided using the Law of Mass Action for a mixture of thermally perfect gases

$$k_p = \exp\left(\frac{-\Delta G^o}{\hat{\mathscr{R}}T}\right) = \left(\frac{P}{P^*}\right)^{\sigma_\nu} \prod_n X_{(n)}^{(\nu''_{(n)} - \nu'_{(n)})} \tag{2.97}$$

$\Delta G^o = \sum_n g^o_{(n)} \left(\nu''_{(n)} - \nu'_{(n)}\right)$ is the total change in Gibb's free energy from a reference state and is provided in thermodynamics texts [280], so the left hand side is known. The strategy for the right hand side is to assume a low temperature and pressure where the mole fractions are known to be $N_{N_2} = 0.79$ and $N_{O_2} = 0.21$ and the remaining species are present only in trace amounts. Using the two atom balance equations, the bulk species can be substituted out of N_{tot} so $X_{(n)}$ is a function of the trace species alone. The equation is also linearized by assuming $N_{trace} * N_{trace} \approx 0$. With this one has an explicit system of equations for the three subreactions, as well as the known values of N_{bulk}. This system can then be solved to provide the moles of the trace species. Note that this

approach is not applicable at high temperatures, when the amount of the bulk species is unknown and the trace species are not negligible.

With the initial conditions set and an algorithm provided, a code can loop through an array of temperatures and pressures to provide an array of $N_{(n)}$ which can be interpolated at any temperature and pressure. This solves the chemistry problem, but it is important to remember the internal energy modes' effects are built in via the partition functions in Equation 2.92. Anderson [6] plots the results for five-species air at 1atm in Figure 2.8.

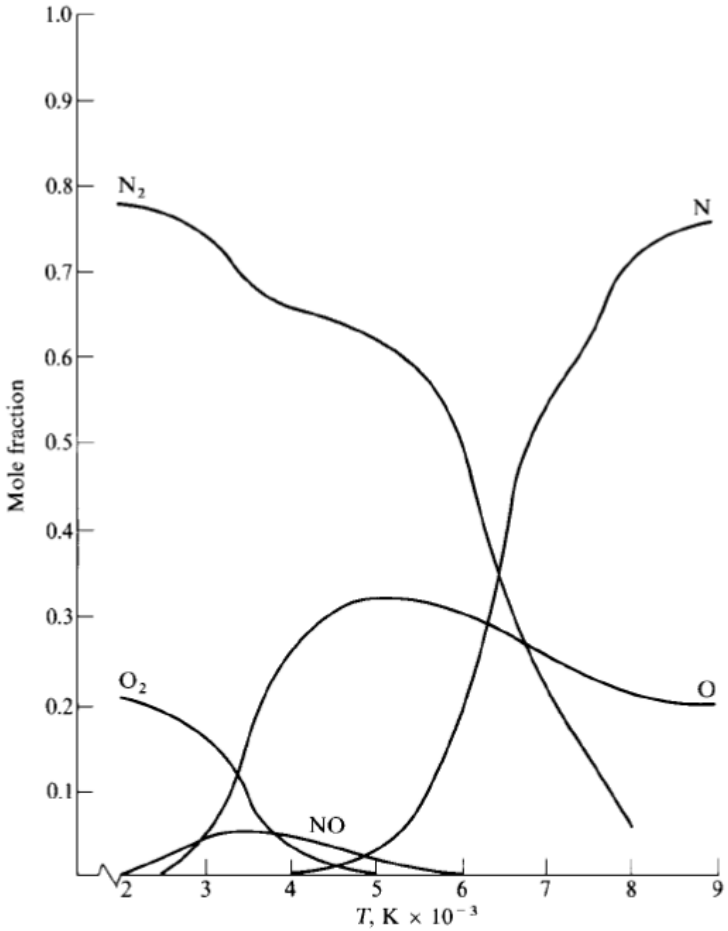

Figure 2.8: Equilibrium species of high temperature air in thermochemical equilibrium at 1atm; figure taken with permission from Anderson [6].

2.3.3.2 Application to Fluid Dynamics

The preceding analysis should provide a table of species amounts as a function of temperature and pressure. With these parameters known, one can calculate the mixture's enthalpy, entropy, and specific heat according to

$$h = \sum_n Y_{(n)} * \left[h^o_{f,(n)o} + R_{(n)}T + R_{(n)}T^2 \left(\frac{\partial \ln Q_{(n)}}{\partial T} \right)_V \right] \tag{2.98}$$

$$s = \sum_n Y_{(n)} * \left[R_{(n)} * \ln \left(\frac{Q_{(n)}}{V} \frac{k_B T}{P} \right) - R_{(n)} \ln \left(X_{(n)} \right) + \frac{h_{(n)} - h^o_{f,(n)o}}{T} \right] \tag{2.99}$$

$$c_v = \sum_n Y_{(n)} * \left[\frac{3}{2}R_{(n)} + R_{(n)} + \frac{(h\nu/k_BT)^2 e^{h\nu/k_BT}}{(e^{h\nu/k_BT}-1)^2} R_{(n)} + \left(2TR_{(n)} \frac{\partial Q_{el}}{\partial T} + T^2 R_{(n)} \frac{\partial^2 Q_{el}}{\partial T^2} \right) \right] \tag{2.100}$$

Here $Y_{(n)}$ is the mass fraction $N_{(n)}\hat{m}_{(n)} / \sum_n N_{(n)}\hat{m}_n$ and the enthalpy of formation $h^o_{f,(n)o}$ is available in thermodynamics texts [280]. It is noted that for atomic molecules, the second and third terms on the right hand side of Equation 2.100 are identically zero when (n) corresponds to atomic molecules as they represent the contributions of the rotational and vibrational energies'. From these quantities $c_p = R_{Mix} + c_v$ where $R_{Mix} = \frac{\hat{\mathscr{R}}}{\hat{m}}$ with $\hat{m} = \sum_n X_{(n)}\hat{m}_{(n)}$; γ remains $\frac{c_p}{c_v}$.

Applying all of the above concepts to the bow shock example is a highly iterative process. Assuming the flow conditions and chemistry are known in the upstream (X_1) location the steps are

1. Guess u_2
    - $u_2 = 0$ is a tolerable initial guess; it assumes the flow stagnates at the vehicle's surface
2. Calculate P_2 from the conservation of momentum $P_2 = P_1 + \rho_1 u_1^2 - \rho_2 u_2^2$
3. Calculate enthalpy with the conservation of energy $h_2 = h_1 + u_1^2/2 - u_2^2/2$
4. Iterate to find T_2
5. Calculate density using the equation of state $\rho = \frac{P_2}{ZR_1T_2}$

- Compressibility $Z = \frac{\hat{m}_1}{\hat{m}}$ is a measure of real gas effects and the deviation the ideal (thermally and calorically perfect) gas law they cause. It is included to account for chemical and thermal nonequilibrium and real gas effects across the shock, which does not meet the broader equilibrium assumption.

6. Calculate u_2 from the conservation of mass $u_2 = \rho_1 u_1 / \rho_2$.

7. Compare $u_{2,Guess}$ to $u_{2,Calc}$

   - If they do not satisfy a set tolerance, repeat with $u_{2,Calc}$ as the next iteration's guess
   - If they do satisfy a set tolerance, all of the values from the current iteration are acceptable and the problem is solved. Calculate any secondary variable desired (ex.- Mach number using γ and R_{Mix} for the mixture)

High-temperature effects are explicitly included in the calculation of h_2 and ρ_2, and the former requires further explanation. Enthalpy is fist calculated using the conservation of energy. This is passed into a zero-point Newton-Raphson iteration for T_2

$$T_2^{i+1} = T_2^i - \frac{\Delta h_2^i}{\frac{\Delta h_2^i - \Delta h_2^{i-1}}{T_2^i - T_2^{i-1}}} \tag{2.101}$$

where $\Delta h = h_{Cons\,of\,Energy} - h_{Stat\,Thermo}$ and $h_{Stat\,Thermo}$ is the enthalpy calculated from Equation 2.98. This iteration is unique because formally one is iterating T_2 but the convergence criteria is $\Delta h < Tolerance$. The error in Δh is updated because with each new value for T_2, Equation 2.98 provides a new value for $h_{Stat\,Thermo}$. Thus temperature is used to "unite" the classical and statistical theories and ensure the right mixture enthalpy is used. The Newton-Raphson technique requires two initialization guesses for T_2; the temperature from the calcorically perfect caloric equation of state ($T_{2,CPG} = h_{Cons\,of\,Energy} / c_{p,298K}$) and $95\% T_{2,CPG}$ are recommended, though another option if species data is not available at this point is to just use the maximum value for which species data was tabulated as "$T_{2,CPG}$".

Both the theory and implementation of high-temperature effect are complex, even for flows in thermochemical equilibrium. That said, as was shown in Figure 2.5, ignoring the physics is not an option. In practice, because strong shocks excite internal energy modes which "store" energy and lower the fluid's translational temperature, hypersonic vehicles where heating is excessive (ex.- re-entry vehicles) are often designed with blunted surfaces to encourage strong bow shock structures.

2.3.4 Flows in Thermochemical Nonequilibrium

In order to model a flow in thermochemical nonequilibrium, one must add conservation equations for both species conservation and the different energy modes to model chemical and thermal effects respectively. This is a direct departure from the above case of equilibrium, where no new conservation equations were introduced and the thermodynamic variables were calculated using the standard conservation laws supplemented with statistical thermodynamics results. The equations of motion shown below are for a weakly ionized plasma and were provided by Bowersox et al. [37]; to view the derivation of analogous forms see [60, 286]. In these equations n represents the species, m represents the energy modes, and $Y_{(n)}$ represents the mass fraction of each species.

- Global Conservation of Mass

$$\rho_{,t} + (\rho u_k)_{,k} = 0 \tag{2.102}$$

- Global Conservation of Momentum

$$(\rho u_i)_{,t} + (\rho u_i u_k)_{,k} = \sigma_{ik,k} + F_{bi} \tag{2.103}$$

  - Here $\sigma_{kl} = -P\delta_{ik} + \tau_{ik}$ and the body force due to electromagnetic forces is $F_{bi} = \sum_{(n)} \rho Y_{(n)} f_{b(n)}$

- Global Conservation of Energy

$$(\rho e)_{,t} + (\rho e u_k)_{,k} = -\left[q_k + \sum_n J_{(n)k}\left(h^{(ex)}_{(n)} + h^o_{f(n)}\right)\right]_{,k} + \sigma_{kl}u_{l,k} + \dot{W}_{F_b} - Q_{rad} \tag{2.104}$$

– Here $q_k = -kT_{,k}$ and the three terms on the right hand side outside of the brackets represent, from left to right, work due to pressure and viscous forces, the rate of change of energy due to body forces, and radiation. The second bracketed term is the energy exchange due to species diffusion with, following Fick's Law, $J_{(n)k} = \rho_{(n)} u_{(n)k} \approx -D_{(n)(m)} Y_{(n),k}$ where $D_{(n)(m)}$ is the binary diffusion coefficient. $h^o_{f(n)}$ is the formation enthalpy.

- Conservation of Species

$$(\rho Y_{(n)})_{,t} + (\rho Y_{(n)} u_k)_{,k} = \dot{\omega}_{(n)} - J_{(n)k,k} \tag{2.105}$$

– Here $\dot{\omega}_{(n)}$ represents the rate of species change due to chemical reaction

- Conservation of External Energy of Heavy Particles

$$\begin{aligned} &\left(\rho_{(h)} e^{(ex)}_{(h)}\right)_{,t} + \left(\rho_{(h)} e^{(ex)}_{(h)} u_k\right)_{,k} = \\ &-\left[q^{(ex)}_{(h)k} + \sum_{n \neq e} J_{(n)k}\left(h^{(ex)}_{(n)} + h^o_{f(n)}\right)\right]_{,k} + \sigma_{(h)kl} u_{l,k} + \dot{W}^{(ex)}_{F_b(h)} + Q^{(ex)}_{(h)} + \dot{W}^{(ex)}_{d(h)} \end{aligned} \tag{2.106}$$

– Here $Q^{(ex)}_{(h)} = \sum_{(m)} \rho_{(h)} q^{(ex)-(m)}_{(h)} + Q^{(ex)}_{rad(h)}$; it covers energy exchange between external and internal energy modes and radiation.

– Here $\dot{W}^{(ex)}_{d(h)} = \dot{W}_{(h)} - \left[\rho_{(h)}\left(u_i u_{(h)k} + u_{(h)i} u_k + u_{(h)i} u_{(h)k}\right)\right]_{,k}$; the first term covers the work due to collisions, force field interactions, and chemical reactions while the second term covers the effects of diffusion using the diffusion velocity $u_{(h)i}$. For weakly ionized plasmas $\dot{W}^{(ex)}_{d(h)} \approx 0$.

- Conservation of External Energy of Electrons

$$\begin{aligned} &\left(\rho_{(e)} e^{(ex)}_{(e)}\right)_{,t} + \left(\rho_{(e)} e^{(ex)}_{(e)} u_k\right)_{,k} = \\ &-\left[q^{(ex)}_{(e)k} + J_{(e)k} e^{(ex)}_{(e)}\right]_{,k} + \sigma_{(e)kl} u_{l,k} + \dot{W}^{(ex)}_{F_b(e)} - \sum_{n=ions} I_{(n)} \dot{\omega}_{(n)} + Q^{(ex)}_{(e)} + \dot{W}^{(ex)}_{d(e)} \end{aligned} \tag{2.107}$$

- Terms generally follow same interpretation as those of Equation 2.106.
- $\sum_{n=ions} I_{(n)} \dot{\omega}_{(n)}$ represents energy transferred to an ion's potential energy during an ionizing collision between a neutral particle and an electron.

- Conservation of Internal Energy of Heavy Particles

$$\left(\rho_{(n)} e^{(in)}_{(n)}\right)_{,t} + \left(\rho_{(n)} e^{(in)}_{(n)} u_k\right)_{,k} = -\left[q^{(in)}_{(n)k} + J_{(n)k} e^{(in)}_{(n)}\right]_{,k} + e^{(in)}_{(n)} \dot{\omega}_{(n)} + Q^{(in)}_{(n)} \tag{2.108}$$

- Terms generally follow same interpretation as those of Equation 2.106.
- $e^{(in)}_{(n)} \dot{\omega}_{(n)}$ represents the rate of internal energy transfer during chemical reactions.
- $Q^{(in)}_{(n)} = \sum_{(m)} \rho_{(n)} q^{(in)-(m)}_{(n)} + Q^{(in)}_{rad(n)}$. The radiation for the electric mode can manifest as visible light in a weakly ionized plasma, as is observed in the positive column of a glow discharge.

The above equations are generalized to be applicable to a variety of flows. However, for the present case of chemical equilibrium downstream of a weakly ionized plasma, several simplifications were appropriate; a similar philosophy, of reduction of the general form to suit a specific case, was employed by Fuller [94]. To begin, no electrons or ions were present, so Equation 2.107 and the heavy particle subscript (h) were removed. Without the presence of charged particles and an electric field, the body force terms were removed. Technically, in the absence of chemical reactions one could remove Equation 2.105 and $e^{(in)}_{(n)} \dot{\omega}_{(n)}$, but for now these terms were kept for those who consider each internal energy mode and corresponding level to be a distinct species. Finally, the sum of the internal and external energy should be equal to the global energy (assuming perfect modeling), so Equation 2.104 was redundant. With these changes the equations of motion for the present case of thermal nonequilibrium were

- Conservation of Mass

$$\rho_{,t} + (\rho u_k)_{,k} = 0 \tag{2.109}$$

- Conservation of Momentum

$$(\rho u_i)_{,t} + (\rho u_i u_k)_{,k} = \sigma_{ik,k} \tag{2.110}$$

- Conservation of Species

$$(\rho Y_{(n)})_{,t} + (\rho Y_{(n)} u_k)_{,k} = \dot{\omega}_{(n)} - J_{(n)k,k} \tag{2.111}$$

- Conservation of External Energy

$$\begin{aligned} &\left(\rho_{(n)} e^{(ex)}_{(n)}\right)_{,t} + \left(\rho_{(n)} e^{(ex)}_{(n)} u_k\right)_{,k} = \\ &- \left[q^{(ex)}_{(n)k} + \sum_n J_{(n)k}\left(h^{(ex)}_{(n)} + h^o_{f(n)}\right)\right]_{,k} + \sigma_{(n)kl} u_{l,k} + \sum_{(m)} \rho_{(n)} q^{(ex)-(m)}_{(n)} \end{aligned} \tag{2.112}$$

- Conservation of Internal Energy

$$\left(\rho_{(n)} e^{(in)}_{(n)}\right)_{,t} + \left(\rho_{(n)} e^{(in)}_{(n)} u_k\right)_{,k} = -\left[q^{(in)}_{(n)k} + J_{(n)k} e^{(in)}_{(n)}\right]_{,k} + e^{(in)}_{(n)} \dot{\omega}_{(n)} + \sum_{(m)} \rho_{(n)} q^{(in)-(m)}_{(n)} \tag{2.113}$$

It is important to be explicit when defining the "external" and "internal" modes included in Equations 2.112 and 2.113 respectively. Because the translational and rotational modes equilibrate in just $\mathscr{O}(10)$ collisions, it is appropriate to include the rotational internal energy mode in Equation 2.112. Furthermore, for the present application one can assume there is no electronic excitation outside of the plasma, so the only active internal mode is vibrational excitation, but going forward this term is kept general to allow for electronic excitation. As a compromise, assume there is only one "internal" temperature covering both the vibrational and electronic modes as in [100].

Similarly, one must be clear in the definition of n. One could follow Deiwert and Candler [78] and assume each species is in vibrational nonequilibrium, whereby Equation 2.113 would need to be solved for each species. Alternatively, Park [214] and Gnoffo et al. [100] assumed

all species are in vibrational equilibrium, so only one equation was needed and therefore one could completely drop the species subscript n; justification for this simplification is provided in the former publication. The same decision can be applied to the external energy equation as well, especially because it is far safer to assume inter-species equilibrium. Here, for generality and based off the rate constants provided in [116], no inter-species equilibrium was assumed and the species subscript remained.

It is noted that n could further represent each energy level of each energy mode of each species. Such a treatment is explored in [165, 212, 190, 213, 167]. Here the authors used rate and thermodynamics data tabulated [57, 240, 123, 124, 125] for 20 million N_2 and N subreactions to precisely study several classical assumptions for hypersonic flows, like ro-translational equilibrium and Boltzmann population distributions of internal modes within a set energy level. Even in these advanced studies, only N_2 and N were considered, and energy pools were developed to cluster internal energy levels into a tractable number for simulation. Again, the present study was limited to only include vibrationally excited molecules as distinct species (n) via the inclusion of Equation 2.111 despite the absence of chemical reactions; put another way, vibrationally excited molecules were assumed to be a separate species from the ground state bath, and only one internal temperature was considered.

There are several new terms introduced which differentiate the above equations for a flow in thermal nonequilibrium from an equilibrium flow. $J_{(n)k}$ can be modeled with Fick's Law, and $\dot{\omega}_{(n)}$, which formally is only applicable to flows in chemical nonequilibrium, will be addressed as part of a later model. What remains is the energy exchange term, which is explored in the next section.

2.3.4.1 Vibrational Energy Relaxation

For the present application all of the internal energy was vibrational; there was no electronic excitation (or it was otherwise well described with a single internal temperature), and ro-translational equilibrium was assumed. Thus a model is needed to couple the vibrational and (ro-)translational modes. The Landua-Teller model [150] has been adopted as the standard model [202] for such relaxation between diatomic molecules. It is noted that in general the Landau-Teller approach is not

limited to vibrational-translational relaxation, but can be extended to other internal energy modes, namely rotational-translational relaxation when equilibrium cannot be assumed [213].

Consider the following example from Vincenti and Kruger [286], noting that it assumes diatomic harmonic oscillators [286] and that it ignores all collisions except vibration-translation exchanges [6]. Begin with the rate equation for vibrational relaxation

$$\frac{de_{vib}}{dt} = \frac{1}{\tau}\left(e_{vib}^{eq} - e_{vib}\right) \tag{2.114}$$

where τ is a characteristic relaxation time. If one assumes the equilibrium temperature is constant and lets $e_{vib} = e_{vib_0}$ at $t = 0$, then the ordinary differential equation can be solved analytically

$$\frac{e_{vib} - e_{vib}^{eq}}{e_{vib_0} - e_{vib}^{eq}} = \exp\left(\frac{-t}{\tau}\right) \tag{2.115}$$

With this one can see that τ is the time required to let the vibrational energy reach $\frac{1}{e}$ its initial value. However, Vincenti and Kruger [286] noted that practically e_{vib_0} varies, especially as energy is brought into rotational and translational states. This means the rate equation becomes

$$\frac{de_{vib}}{dt} = \frac{1}{\tau(T,P)}\left(e_{vib}^{eq}(T) - e_{vib}\right) \tag{2.116}$$

While $e_{vib}^{eq}(T)$ can be calculated from theoretical expressions, here it is not necessary as the main goal is to find a model for τ so vibrational decay can be predicted; note that due to the dependency on temperature and pressure, Vincenti and Kruger [286] stated that τ loses its exponential behavior and cannot formally be called a relaxation time, so instead they called it a local relaxation time.

It is at this point the Landau-Teller model [150] for τ is introduced,

$$\tau = \frac{K_1 T^{\frac{5}{3}} \exp\left(\frac{K_2}{T}\right)^{\frac{1}{3}}}{P\left(1 - \exp\left(-\frac{\Theta_v}{T}\right)\right)} \tag{2.117}$$

wherein K_1 and K_2 are molecule dependent constants, $\Theta_v \equiv \frac{h\nu}{k_B}$, h is Plank's constant, and ν is the

fundamental frequency of the oscillator. For low temperatures, a simpler form is acceptable [286]

$$\tau = \frac{C_1}{P} \exp\left(\frac{C_2}{T}\right)^{\frac{1}{3}} \tag{2.118}$$

where the constants are determined from experimental data. For a pure N_2 environment, Blackman [32] provided $7.21 \times 10^8 \text{Pa} \cdot \text{s}$ and $1.91 \times 10^6 \text{K}$ for C_1 and C_2 respectively; these values were taken for the temperature range of $800 - 6000\text{K}$.

While the given constants far exceed the equilibrium temperatures in the ACE tunnel, the underlying theory was applicable. The development of the time constant for vibrational temperature decay is useful in closing the energy coupling terms in Equations 2.112 and 2.113. A calculation for the local relaxation time at the test conditions using another form of the Laundau-Teller equation is included in Chapter 8.

2.3.5 Classic Experiment: Decaying Mesh Turbulence in Vibrational Nonequilibruim

The doctoral work of Fuller [94] and Hsu [116], also conducted at the NAL, included a study of the effect of a radiofrequency (RF) plasma on subsonic, decaying mesh turbulence in a channel. The former focused on the design of the facility and plasma, the turbulence theory, and turbulence measurements using particle imaging velocimetry (PIV) while the latter delivered optical measurement techniques including *NO* PLIF thermometry, optical emission spectroscopy, coherent anti-Stokes Raman spectroscopy (CARS), and theory regarding vibrational energy relaxation. These works were synthesized in a joint journal publication [95], and this work is the main source discussed here. There are obvious distinctions between this publication and the experiment described in this report: a subsonic channel flow *versus* a hypersonic boundary layer; an RF plasma *versus* a DC glow discharge; densities high enough to perform PIV and CARS (CARS is well described in [84], who shows that as a rule of thumb signal $I \propto \rho^2$ so that $\mathcal{O}(100\times)$ less signal is expected in the present work than the published data). Furthermore, the system nominally operated at 30Torr, room temperature, $30\frac{\text{m}}{\text{s}}$ in the test section, and with either a 300 or 150W plasma. Nevertheless, the quality of the data, breadth of the techniques, and analysis of the direct role the

plasma played in stabilization all warranted inspection. Indeed, Fuller et al. [95] began with a discussion of documented relaminarization mechanisms. Of particular interest was the effect of bulk heating via the plasma, which increased viscosity and lowered the Reynolds number; this could either occur through direct heating of the external energy modes, or by the decay of excited internal energy modes downstream of the plasma.

The optical measurements are now reviewed. Optical emission spectroscopy was used to determine the ro-translational and vibrational temperatures of N_2, which were 335K and $\sim$ 2900K respectively; it was noted that the vibrational temperature corresponds to the C electronic state, and so did not correlate to the ground electronic state vibrational temperature experienced outside of the plasma [116]. Furthermore, no NO or OH peaks were observed in the spectra, which implied that the plasma could not produce these species; NO peaks were faintly present when the gas was seeded for PLIF measurements, however [116].

CARS was employed to measure the N_2 and O_2 vibrational temperatures in the ground electronic state; the N_2 temperatures were 1230 and 1540K just downstream of the 150 and 300W plasmas respectively, and the O_2 data was below the noise floor. The absence of O_2 spectra was taken to imply a two-temperature flow outside of the plasma in the test domain, which in turn lent credence to this assertion for the present glow discharge experiment. The CARS data showed a significant decay in vibrational temperature along the streamline, which the authors demonstrated could be mostly attributed to the presence of water vapor in the humid room air. Modeling the decay with $N_2 - H_2O$ collisions produced strong agreement with the data while $N_2 - N_2$ collisions were found to be too ineffective to produce the observed decay on their own; more detail on modeling the kinetics was provided by Hsu [116]. Notably, in these models the N_2, O_2, and NO were assumed to be at an initial equilibrium vibrational temperature of 2000K after an electron collisional cross section calculation in the plasma put their estimated vibrational temperatures at 1700, 800, and 2000K respectively; NO was included as it was present for PLIF measurements.

As the vibrational temperature decreased, NO PLIF ($\sim 1\%$ NO by mass) showed an increase in rotational temperature, which was assumed to be in equilibrium for all species. This was attributed

to energy exchange between the internal and external modes and was explained by the equation $h_o = 2.73k_BT + 0.77e_{N_2}^{vib} + \frac{1}{2}u^2$, which assumed $h_o = Constant$ and a two-temperature only flow.

To summarize, the thermal analysis showed that the plasma only weakly heated the external modes (to 335K), but due to the presence of H_2O the vibrationally excited species, N_2 and NO, were able to relax and heat up the bulk gas' external modes. Thus vibrational decay along the test domain, not Joule or cathode heating of the bath gas' ro-translational states in the plasma proper, was the dominant thermal mechanism in the experiment. Using Rayleigh theory for low Mach numbers to relate temperature and velocity ratios and then comparing PIV velocimetry and PLIF thermometry data yielded an estimate of 40% for the ratio of plasma power put into external energy modes; it was written $\sim 12\%$ of the N_2 molecules were vibrationally excited.

As an aside, it was previously stated that the densities in the ACE tunnel are too low for easy CARS implementation, though Montello et al. [187] was able to make CARS measurements in an ACE tunnel-like Mach 5 freestream. It is noted that one could theoretically measure N_2^{vib} using a total temperature probe, Fuller's energy balance equation for h_o, and assuming a calorically perfect gas, though this approach is sensitive to electrical interference. As was mentioned, optical emission spectroscopy can only provide the vibrational temperature of excited electronic states which were not present outside of the plasma. Using Fuller's [95] CARS data, one can only assume $T_{N2}^{vib} \approx \mathcal{O}(1000\text{K})$, though this will be re-visited in Chapter 8. It will be shown in Section 2.5 that T_{NO}^{vib} can be measured with PLIF, and this may be used for the vibrational temperature measurements required for the theories in this report.

With the thermal effect of the plasma thus understood, PIV was employed to understand its impact on the turbulence. The mean velocity data were presented first. To begin, a decrease and increase in velocity before and after the electrodes respectively, and growing more pronounced as the plasma power was increased, was present and attributed to a pressure rise in the vicinity of the hot plasma. Along the channel, the peak velocity grew, which was expected for a relaminarizing channel flow. Indeed, plots of the normalized mean velocity profiles show they become more parabolic the farther one moves downstream, indicative of a classic Poiseuille flow [293]; when

plotted in wall coordinates, the farther one moved downstream the more closely the data matched a theoretical laminar boundary layer plot.

Across the electrodes, the Reynolds axial and shear stresses dropped 15 and 30% for the 150W case, and 30 and 50% for the 300W case, as compared to the "Off" condition. The Reynolds shear stress and molecular (laminar) stresses were plotted in wall coordinates at both the first and last test locations. At the first location, the molecular and Reynolds stresses were collapsed onto two separate curves for all three plasma cases ("Off", 150W, 300W). At the final location, the molecular stresses remained clustered together and of similar magnitude to before, but the Reynolds stresses were progressively reduced as the plasma strength was increased. Plots of the individual velocity components showed that the axial turbulence intensity (u') was reduced $10-15$, 30, and 40% at the final location for the "Off", 150W, 300W plasma cases respectively; there was not dependence on the plasma for reduction in the spanwise turbulence quantity. For the same three test locations, the Reynolds stress fell 60, 75, and 85%. These two decays followed power law trends in the streamwise coordinate. The reduction in turbulence intensity and Reynolds stress even in the absence of a plasma was indicative of natural turbulence dissipation, and was supported by an analysis of the correlation coefficient $C_{xy} = \tau_{xy}/(-\tau_{xx})(-\tau_{yy})$; this quantity was reduced 30, 50, and 70% for the three plasma cases between the first and last test location. However, the increasing reduction of all included turbulence quantities after the introduction and strengthening of the plasma suggested it was causing relaminarization.

Following the approaches of Bowersox et al. [37] and Bowersox [38], an effort was made to explain the flow physics via the transport equations for axial, spanwise, and mixed Reynolds stresses as well as turbulent energy flux $\theta_i^T = \rho\overline{e'u_i'}$ (to be introduced in Chapter 3). The analysis is too detailed to include here, but there is value in the technique; additional detail for the vibrational energy flux case was provided by Fuller et al. [95]. The authors started with a complex transport equation, simplified it to suit their application, then analyzed each term independently to try and isolate its effect and reconcile it with the bulk behavior experimentally observed. This lets one attempt to identify the exact function the nonequilibrium plays in relaminarization.

In summary, though the experiment differed for the proposed conditions, the effect of plasma on turbulence is clear. When facilitated by a rapid-relaxer like H_2O, plasma-seeded vibrational energy can sufficiently relax to heat the gas enough to meaningfully increase the viscosity and reduce Reynolds stress. As the present experiment is expected to be vibrationally frozen in the freestream and potentially at least partially equilibrated at the wall, where turbulent boundary layers are the most sensitive, there is reason to believe interesting physics should develop. Furthermore, the techniques and data in [95] led to the adoption of identical or analogous methodologies here.

2.3.6 Classic Experiment: ACE Tunnel-Like Vibrational Nonequilibrium (NEQ) Experiments and Simulations

Of particular interest to the present work was vibrational NEQ in the ACE tunnel's freestream. Hypersonic tunnels are particularly susceptible to this complexity due to the high temperatures required to prevent liquefaction of oxygen, low densities, and short time scales. Taken together, it is possible for the gases to be vibrationally frozen at or near the stagnation temperature. Both computational and experimental works studying this effect and its impact are reviewed here.

- Candler and Perkins [52] (1991): A computational paper which studied the effect of vibrational nonequilibrium has on the performance of a hypersonic nozzle. Most simulations were of a $M = 17$ nozzle with stagnation temperatures > 1500K, far more extreme than the ACE tunnel. The simple harmonic oscillator and Landau-Teller models were used for vibrational energy modeling and exchange. The effect of viscous boundary layers, both laminar and turbulent, were included, as well as possible mitigation effects. For a diatomic gas $\gamma_{neq} = 7/5$ while $7/9 \leq \gamma_{eq}(T) \leq 7/5$ as the flow equilibrates, so Mach numbers should naturally be higher in a nonequilibrium flow; exacerbating this effect, the external temperature should be lower in the equilibrium case if the flow freezes as energy becomes trapped in the internal mode (see [6]). Indeed, the simulations showed the cases for $\gamma = 7/5$ and γ_{neq} produced higher Mach numbers than the γ_{eq} case. The similarity between the $\gamma = 7/5$ and γ_{neq} cases was also established and occurred due to the vibrational energy freezing to $90\%T_o$

near the throat, effectively removing itself from relevancy in the subsequent thermodynamics. Still, in both cases the nozzle did not reach its specified performance; it was observed that the growing boundary layers caused recompression upstream of the nozzle exit which made the Mach number fall. The performance was worsened for thicker turbulent boundary layers. This prompted the authors to explore the validity of the Method of Characteristics nozzle design, specifically its assumption of perfect shock reflection at a thick boundary layer. They also showed that lengthening the nozzle's throat and increasing the stagnation pressure can both decrease the amount of energy stored in internal modes from 81%T_o to 66 and 68% respectively, but the nonequilibrium remained strong.

- Neville et al. [197] (2014), Bowersox et al. [37] (2008), and Khurshid and Donzis [138] (2015): Fujii and Hornung [93] and Wagnild [290] numerically studied the effect vibrational nonequilibrium has on a single acoustic wave. They found that when the wave's frequency matched the vibrational timescale, there was optimal damping of the turbulent quantities. Neville et al. [197] and Neville et al. [198] extended this concept to compressible, isotropic turbulence and turbulent shear layers respectively. They varied the Mach numbers (turbulent [197] and convective [198]), as well as ratio between the large eddy and vibrational relaxation timescales from frozen to fully equilibrated; the latter was described by a vibrational Damköhler number $Da_v = \tau_{flow}/\tau_{vib}$. For the case of isotropic turbulence, the authors found there was indeed an optimal timescale ratio for damping between the two extremes related to the inverse of the turbulent Mach number (i.e.- for $Ma_t = 0.5$, $Da_{v(opt)} = 2$). This implied for higher turbulent Mach numbers, greater nonequilibrium was necessary to cause damping. Neville et al. [197] found the damping mechanism matched that in [93, 290]. Again, if vibrational energy lagged behind turbulent fluctuations in ro-translational temperature, energy could be stored in the internal modes during external temperature crests, and then dissipated back into the external mode during troughs; overall this dampened the turbulent fluctuations. For the case of a turbulent shear layer, again there existed some optimal Da_v which supported the claim that vibrational decay must be tuned to the flow timescale. Here the effect of vibra-

tional relaxation was most pronounced in the dilatational energy mode, and because higher Mach numbers have stronger waves it was in these flows the physics were the clearest. In both cases the effect of vibrational relaxation was limited to temperature fluctuations; there was no significant effect on kinetic energy. It is noted all of the aforementioned works used CO_2 as the working medium.

In their model Bowersox et al. [37] showed how a vibrational relaxation and turbulence (energy flux) timescale can mathematically communicate, which supports the experimental findings

$$\left(\frac{\delta_{ik}}{\overline{\tau}^{(vib)}_{(n)}} + \frac{\delta_{ik}}{\tau_{\theta^{T(ex)}_{(n)}}} + \tilde{u}_{i,k} \right) \theta^{T(in)}_{(n)k} \approx \tilde{Y}_{(n)} \tau^{T}_{(n)ik} \tilde{e}^{(vib)}_{(n),k} + \frac{\theta^{T(in)}_{(n)i,eq}}{\overline{\tau}^{(vib)}_{(n)}} \tag{2.119}$$

where $\tau^{(vib)}_{(n)} \approx C_{(n)1} e^{(C_{(n)2/T_1})^{1/3}}/P$, C is the energy flux correlation coefficient $C_i = \theta^T_i / \sqrt{-\tau^T_{(i)(i)}} \overline{\rho} \overline{(e'')}^2$, θ^T_i is the turbulent energy flux $\theta^T_i \equiv \overline{\rho e'' u''_i}$ (discussed extensively in Chapter 3), and the remainder of lexicon is taken from the conservation equations in Section 2.3.4. Though these timescales were unique to this paper and the simplicity of Equation 2.119 belies the derivation's complexity and assumptions, the point here is to show that one can derive a link between vibrational and turbulence timescales. Indeed, in their paper Bowersox et al. [37] outlines the chain of dependencies which does indeed link their $\tau^{(vib)}_{(n)}$ to the Reynolds shear stress.

Khurshid and Donzis [138] further explored the effect of NEQ on decaying compressible turbulence through DNS simulations. They derived a nondimensional parameter β which combined the degree of initial NEQ and the ratio of the turbulent decay and vibrational and relaxation timescales. This allowed the study of regimes where the flow was vibrationally ($\beta \ll 1$) or mechanically ($\beta \gg 1$) frozen. In the latter case, the results matched those of Neville et al. [197] in that there was little effect of NEQ on the kinetic energy, though the authors attributed this moreso to the lack of NEQ at the outset of their simulations than the energy exchange itself. If the vibrational decay rate exceeded the turbulent time scale, then as the initial amount of NEQ was increased the more rapid its effect on the flow. This effect

was identified as a decrease in the flow's kinetic energy; in the same process outlined in Section 2.3.5, the relaxing vibrational energy passed energy into the ro-translational states, which increased the temperature and thereby the viscosity which damped the turbulence. An asymptotic limit for the increase in viscosity as a function of increasing β was identified.

Khurshid and Donzis [138] also described the effect of turbulent fluctuations on the vibrational energy $\langle E_{vib} \rangle$; here angular brackets denoted a volume average. For $\langle E_{vib}^{eq} \rangle$ it was determined that approaching equilibrium $\langle E_{vib} \rangle < \langle E_{vib}^{eq} \rangle$ because equilibrating energy from vibrationally cold regions produced by the turbulent fluctuations required longer timescales than those for vibrationally hot regions because transferring energy from the ro-translational state into the vibrational state lowered the bath temperature, increasing τ_{vib} and decreasing $(E_{vib} - E_{vib}^{eq})$. The turbulent fluctuations have a greater effect on the equilibrium vibrational energy $\langle E_{vib}^{eq} \rangle$ than the vibrational relaxation time constant $\langle \tau_{vib} \rangle$, which Donzis and Maqui [81] traced back to the lag between E_{vib} and E_{vib}^{eq}. In the same paper, Donzis and Maqui [81] also write that for equilibrium ($\tau_v \ll \tau_{turb}$), and especially NEQ ($\tau_v \gg \tau_{turb}$) flows, a greater proportion of the total energy is stored in vibrational modes in the presence of bulk temperature fluctuations than in their absence (turbulent *versus* laminar flow). Put another way, with all other parameters fixed, a turbulent flow will have a higher mean vibrational temperature than a laminar flow.

- Nishihara et al. [205] (2012) (journal, conference (2010) [203]) and Nishihara et al. [204] (2010): Papers outlining the development and characterization of a Mach 5 blowdown wind tunnel at The Ohio State University which uses a combination of pulsed and DC plasmas in the settling chamber to instill vibrational nonequilibrium. The tunnel's run time is $5 - 10$s and stagnation pressure is $50.66 - 101.33$kPa. Gases can be injected downstream of the plasma to act as a vibrational energy sink, furthering the thermal nonequilibrium. Nominal test articles were cylinders. Schlieren imaging and high speed (custom burst-mode laser) *NO* PLIF were used to visualize the flow, and the system's thermodynamics were studied with optical emission spectroscopy, PLIF thermometry (for both rotational and vibrational

temperature measurements), and picosecond CARS (best described in [186]). The work was also supported by CFD.

Calculations showed most of the plasma energy was stored in vibrational modes, and that in the absence of a "rapid-relaxer" species (ex.- H_2, H_2O, NO) it was frozen even after passing through the strong bow shock (recall this is a low temperature, low Mach number facility). The later CARS work in [186] showed how plasma power and relaxer species can be used to tailor the degree of nonequilibrium; notably, O_2 had little effect, which was important because the present experiment was conducted in air. Similarly, Nishihara et al. [206] showed how the injection of CO_2 could cause sufficiently fast relaxation to alter the trajectory of a free shear layer. In the settling chamber, theory and measurements showed $T_o = 300-400$K and $T_{o(v)}$ up to 2000K while in the test section $T_o = 300$K and $T_o = 500$K (stagnation at cylinder, plasma off and on respectively) and $T_v = 1000$K (freestream, plasma on); the calculated T_v of N_2 was 850K. No detectable change in the freestream ro-translational temperature in the presence of vibrational nonequilibrium was reported. The CARS work in [187], commendably performed at low density, showed there was no vibrational relaxation across a shock, which is expected in a low temperature, density, and Mach number flow. Calculations suggested as much as $50-80\%$ of the DC discharge's power went into vibrationally exciting the N_2 molecules, and very little went into its electronic modes; this was mostly confirmed by the CARS measurements in [186]. It was noted sufficient NO was generated by the plasma that weak PLIF was possible even without gas injection. Furthermore, spectroscopy showed between $200-300$nm $NO\,\gamma$ bands dominated the signal, and there was evidence of NO_2 chemoluminescence between $400-1000$nm.

These works showed that vibrational nonequilibrium is present in blowdown wind tunnels even without intentional excitation, and it can have a serious impact on the flow. While the temperatures and techniques used to generate the nonequilibrium were far greater than what is experienced in the ACE tunnel, the underlying physics persist. The gas should have some vibrational energy near the throat conditions, and it should be mostly frozen in the freestream and through shocks. However,

equilibrating the gas by the injection of relaxer species could have a significant impact on the fluid dynamics. If well-tuned to the turbulence, vibrational decay can significantly dampen temperature fluctuations, which matched the findings in [95]. Thus link between the current experiment's thermodynamics and turbulence was established, both experimentally and mathematically [37].

2.4 Direct Current Glow Discharges

A plasma is a state of matter wherein an equal balance of electrons, ions, and neutral atoms or molecules maintain quasi-neutrality but permit the passage of electrical current. Figure 2.9 shows several different forms of plasma and each has its own distinct characteristics, but here the discussion shall be limited to a direct current (DC) glow discharge.

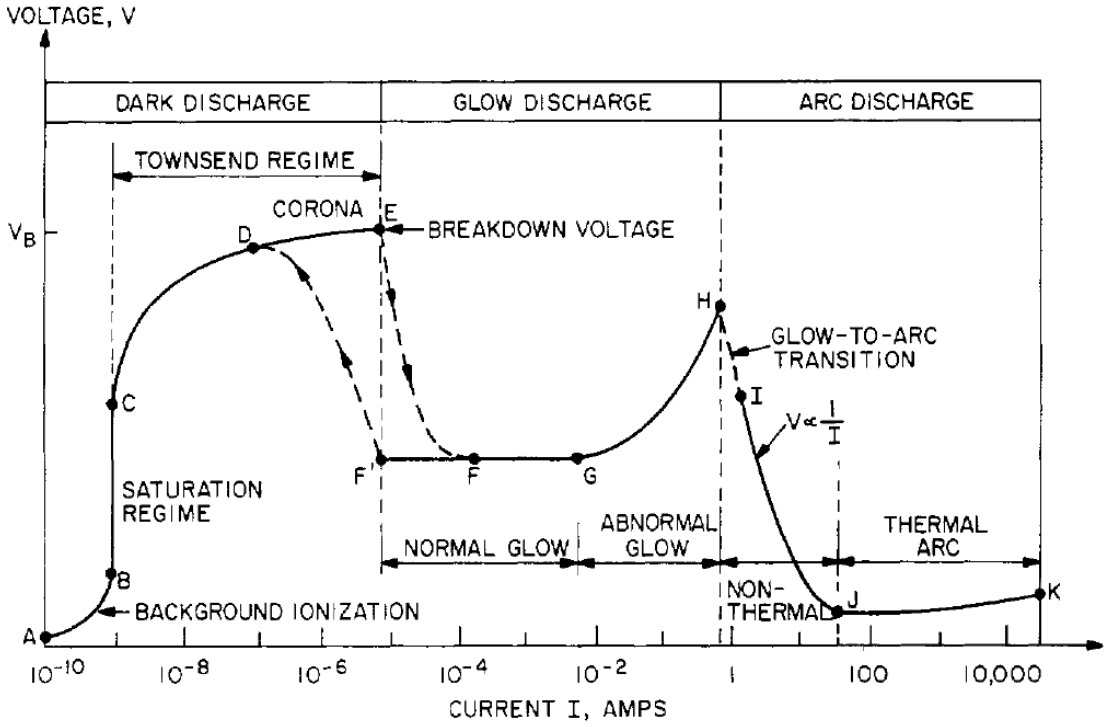

Figure 2.9: Various plasma regimes; figure taken with permission from Roth [228].

Rajzer [224] defined a glow discharge as "a self-sustaining discharge with a cold cathode emitting electrons due to secondary emission mostly due to positive ion bombardment", and the "best

pronounced and most widespread example of a weakly ionized plasma". Already several key terms have been introduced and they will be addressed in turn, but for now it is sufficient to state that glow discharges are weakly ionized with characteristic ionization fractions of $\mathscr{O}(10^{-8} - 10^{-6})$ and thermal nonequilibrium introduced from the high electron temperatures and low ro-translational temperatures due the gas' specific heat and natural cooling [224]. Further characteristic values are included in Table 2.3 from Roth [228].

Parameter	Low	Characteristic	High
Pressure (Torr)	10^{-6}	0.5	760
Electrode Voltage (V)	100	1,000	50,000
Electrode Current (A)	10^{-4}	0.5	20
Number Density $\left(\frac{e}{m^3}\right)$	10^{14}	5×10^{15}	6×10^{18}
Electron Kinetic Temperature (eV)	1	2	5
Plasma Volume (L)	10^{-6}	0.1	100

Table 2.3: Characteristic glow discharge parameters; taken from Roth [228].

2.4.1 Breakdown

It is important to understand the process by which a glow discharge is generated before proceeding into a fully quantitative analysis. This is especially true here as the main region of interest for the plasma employed was dominated by breakdown-like physics. Much of the concepts are physically intuitive, so a series of progressive thought experiments are a helpful approach.

Consider one described by [224] of a characteristic glow discharge setup with two planar electrodes at distance d, an applied voltage V, and a sufficient vacuum P, but of insufficient field strength to produce a glow discharge. Now introduce a lone electron in the electrode gap. The number of ionizing collisions that electron performs per second is captured by the ionization frequency ν_i [224]. If the field is strong enough, each new electron produced will begin ionizing new neutral "targets". Should the ionizing frequency be held constant and there be no loss of electrons, then the number of electrons exponentially increases and a so-called "electron avalanche"

develops; this is described by $n_e = n_e(0)\exp(\nu_i t)$ [224].

In a DC application it is convenient to measure Townsend's ionization coefficient $\alpha = \frac{\nu_i}{v_d}$ as opposed to ν_i directly [224]. Here v_d is the drift velocity and α describes the number of ionizing collisions per unit length. Measurements of α over a variety of conditions are reported in [164], but Townsend provided a useful empirical formula

$$\alpha = AP\exp\left(-\frac{PB}{E}\right) \tag{2.120}$$

A and B are empirical and taken from tabulated experimental observations. Common values for air are, for $\frac{E}{P} = 100 - 800\frac{\text{V}}{\text{cm}\cdot\text{torr}}$, $15\text{cm}^{-1}\cdot\text{torr}^{-1}$ and $365\frac{V}{cm\cdot torr}$ respectively [289]. Despite A and B being empirical constants, under certain assumptions one can ascribe physical meaning to them. Rajzer [224] shows that by assuming every collision is an ionizing event, which is only valid for high $\frac{E}{P}$), given the context of Townsend's empirical formula for α one can write

$$A = (\lambda P)^{-1} = \left(\frac{k_B T}{\sigma}\right)^{-1} \text{ and } B = A\frac{I}{e} \tag{2.121}$$

where λ is the mean free path, I is the ionization energy, and e is unit charge. Thus A and B can be related to the system parameters, though it is noted that the exact agreement can be poor. For example, assuming room temperature, if $A = 15\text{cm}^{-1}\cdot\text{torr}^{-1}$ then $\sigma = 4.554\times10^{-20}\text{m}^2$, which is an order of magnitude away from the $43\times10^{-20}\text{m}^2$ reported in [11]; in this specific case the discrepancy is likely due to different definitions of molecular diameter in addition to the inherent limitation of the empirical model. A and B are dependent on temperature, and this will be explored in a later section.

Returning to Rajzer's thought experiment, imagine now shining an energy source (UV light) onto the cathode for one second, releasing $\mathscr{N}_o$ electrons from the surface. If an electron avalanche forms, the number of electrons in the gap will be a function of space (in the direction of the cathode to the anode) according to $\mathscr{N}(x) = \mathscr{N}_o\exp(\alpha x)$. This effectively provides the anode's electron current $i = i_0\exp(\alpha x)$ for a given cathode current $i_0 = e\mathscr{N}_o$, and if the system is in steady state

this describes the current through the gap. The current is carried almost entirely by the electrons; the slower ions left in between the electrodes produce a positive charge but do not distort the field so $E = \frac{V}{d}$ is trivially known. This type of plasma is known as Townsend's dark discharge because while it is capable of carrying charge, the energies are too low to cause emission via electronic excitation. This type of discharge is not self sustaining because an external ionization source, here a UV lamp, is required to produce electrons from the cathode.

At this point it is natural to ask how electrons are emitted from a solid. In general, strong fields can pull electrons out of a material via tunneling (field electron emission), hot cathodes can, by virtue of statistics, produce electrons with sufficient energy to escape the solid's potential well (thermionic emission), and these two mechanisms can occur in tandem (thermionic field emission) [224]. The most important mechanisms for glow discharges, which do not require strong fields or dramatically heat the cathode, is secondary emission, represented by the coefficient γ. Any number of particles can cause this secondary emission, but Rajzer [224] stated the dominant form is ion-electron emission. In glow discharges the ion kinetic energy is insufficient to liberate electrons from the cathode via bombardment, but in a process first suggested by Penning (1928) as the nucleus approaches the cathode the local field becomes strong enough to pull an electron out of the surface.

Recall from the thought experiment that for a cathode photocurrent i_0 one can expect an anode current of $i = i_0 \exp(\alpha x)$. The effect secondary emission can now be introduced. A single electron produces $\exp(\alpha d) - 1$ ions, all of which migrate, albeit slowly, towards the negatively charged cathode; thus the total cathode current is the sum of both the photocurrent and ionic current $i = i_0 + i_0 [\exp(\alpha d) - 1]$. However, the $\exp(\alpha d) - 1$ ions produced by a single electron liberate γ electrons from the cathode, so the electron portion of the cathode current becomes $i_1 = i_0 + \gamma i_0 [\exp(\alpha d) - 1]$. With this the current at the anode and that recorded in the circuit is

$$i = i_1 \exp(\alpha d) = \frac{i_0 \exp(\alpha d)}{1 - \gamma[\exp(\alpha d) - 1]} \tag{2.122}$$

Such a formula was first suggested by Townsend (1902) and offers a means to explain when a dark discharge will ignite into a glow discharge and become self-sustaining: when the denominator becomes zero. Plotting the natural log of Equation 2.122 against electrode spacing d yields an experimental means of determining γ. Such data is shown in Figure 2.10. The slope of the linear portions of the curves provides α (this is effectively how it was measured by Lozanskiœ and Firsov [164]), and if i is measured than γ can be calculated. The d at which it deviates from the linear regime represents the growing influence of secondary emission. In practice, due to different surface finishes and material selection γ is difficult to measure and characteristic values must be used [224]. Francis [92] reported for N_2 on copper electrodes at $PD = 50\text{Torr}\cdot\text{cm}$ $\mathcal{O}(10^{-6}) < \gamma < \mathcal{O}(10^{-3})$; γ for the current setup is experimentally verified Section 4.4.8.

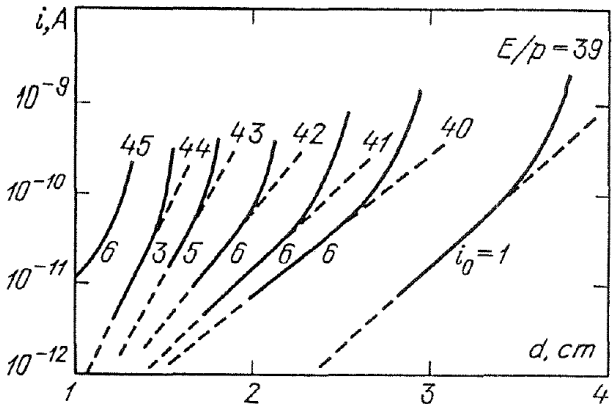

Figure 2.10: Plots of 2.122; data from [129], figure taken with permission from Rajzer [224].

It is at this point appropriate to consider breakdown from a practical perspective. Remove the UV lamp from Raizer's thought experiment [224] and instead imagine standing before a power supply with controllable voltage and a large but finite available current. In the beginning a homogenous electric field is applied, and electrons randomly appearing from the cathode and in the gap move towards the anode. Many of these electrons are lost to the wall or react with charged molecules, but as the voltage, and thus electric field, is steadily increased, more and more electrons do make it to the anode so the recorded current rises. At some voltage, all of the electrons make

it to the anode, and the current is said to be "saturated" [224]; see Region B-C on Figure 2.9. The environment is now current-limited because all of the electrons which are produced already make it to the anode, so any increase in field strength is unnecessary. However, at a certain voltage the electrons have sufficient energy to ionize neutral molecules in their path, which leads to a rise in current and a self-sustaining Townsend dark discharge. Continuing to increase the voltage, secondary emission comes into effect, and the current rises exponentially, asymptotically approaching a "threshold voltage" [224], also known as a "breakdown voltage". At this condition, which corresponds to a null denominator in Equation 2.122, an infinite current is demanded from the power supply as the circuit effectively shorts. A ballast resistor must be included in a glow discharge circuit to prevent damage to the power supply at this condition, as well as to provide some resistive load during normal operation. Rajzer [224] estimated this so-called Townsend breakdown process takes $\mathcal{O}(10^{-5} - 10^{-3})$s and illustrates it in Figure 2.11. As the voltage is increased past V_t, Equation 2.122 becomes invalid and a self-sustaining normal DC glow discharge is established.

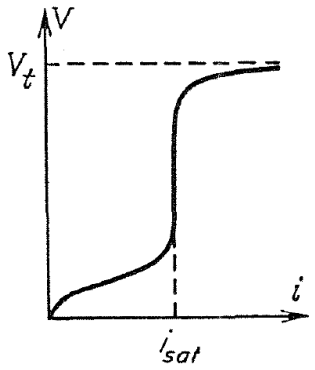

Figure 2.11: The voltage-current relation during a normal gas breakdown; figure taken with permission from Rajzer [224].

This process has been quantized. As was discussed, the critical moment occurs when the denominator of Equation 2.122 becomes zero, or

$$\alpha d = \ln\left(\frac{1}{\gamma} + 1\right) \tag{2.123}$$

Substituting in Equation 2.120 and recalling that $E_t = \frac{V_t}{d}$ one arrives at Paschen's Law

$$V_t = \frac{B(PD)}{\ln\left(A(PD)\right) - \ln\left(\ln\left(1+\frac{1}{\gamma}\right)\right)} \tag{2.124}$$

This provides a way to calculate the threshold voltage as a function of Pd. Plots of this relationship ($\log(V_t)$ *vs.* Pd) are called Paschen curves and are shown for a variety of gases in Figure 2.12. This plot will be produced with the present equipment in Section 4.4.8. For now it is sufficient to note that there exists a minimum point in Equation 2.124 $(Pd, V_t)_{min}$ where for $Pd < (Pd)_{min}$ the curve $V_t(Pd)$ rises steeply and for $Pd > (Pd)_{min}$ it rises more gradually. This is because at large Pd the electrons are unable to reach energies sufficient to sustain an avalanche, either because the gap is too large and the electric field is too weak or because the pressure is too high and the mean free path is too low. On the left hand branch, either the gap is so small the plasma is obstructed and the negative glow cannot form or the pressure is so low that there are not enough neutral molecules in the gap to sustain an avalanche [224].

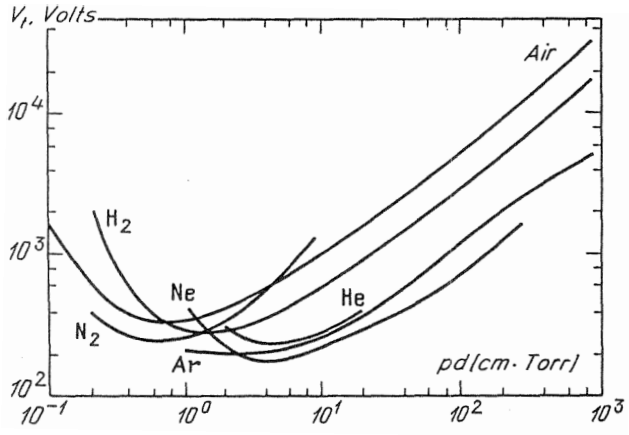

Figure 2.12: Paschen curves for a variety of gases; data from [47, 175], figure taken with permission from Rajzer [224].

And so breakdown is explicitly dependent on pressure, and through the pseudo-constants A and B implicitly dependent on temperature as well. Again, physically the pressure and temperature

simply provide a means of describing the number of particles in between the electrode. Thus breakdown is best described as a function of the electric field and particle density, which is one reason why the reduced electric field $\frac{E}{n}$ (to be formally introduced shortly) is so widely adopted. It combines the two most important parameters in a plasma, the field strength, which is controlled by the circuit and electrode configuration, and number density of the gas, which is controlled by the system's thermodynamics.

2.4.2 Characteristic Regions

DC glow discharges have distinct regions pictorialized in Figure 2.13. It is interesting to describe each of these regions from the perspective of an electron emitted from the cathode. Note that the discussion here is a focused summary, and further detail is provided in [224, 228, 162].

Immediately after emission, the electron enters the Aston dark space wherein it has insufficient energy to cause excitation and by extension illumination. Accelerating into the cathode glow (alternatively called negative glow) region, the electron attains enough kinetic energy to excite the dense cloud of ions attracted to the cathode; sputtered atoms, the large number density of ions, and exceptionally energetic collisions cause this region to have a different color than the bulk plasma [228, 224]. Roth [228] further states the cathode glow can cling to the cathode and cover the Aston dark space. The next region is the Cathode/Crookes/Hittorf dark space, which is also dominated by ions and has a moderate electric field. By this point the electrons are so energetic their collisions do not cause excitation but instead ionization; this is the dominant region of ion, and by extension electron, production [224].

These three regions are cumulatively known as the cathode region and behave together as the cathode sheath. For reasons which will soon become apparent, this region is by far the most important to the current effort and as such it will be analyzed in a separate section. Between the cathode surface and the end of the cathode dark space, a distance d_c, the potential falls V_c, the electric field almost linearly drops to zero, and most of the plasma's power is dissipated. The electrons in the bulk plasma are repelled by the cathode, and so those present in this region are secondary electrons emitted from the cathode itself. Due to their size and weight, the ions are too

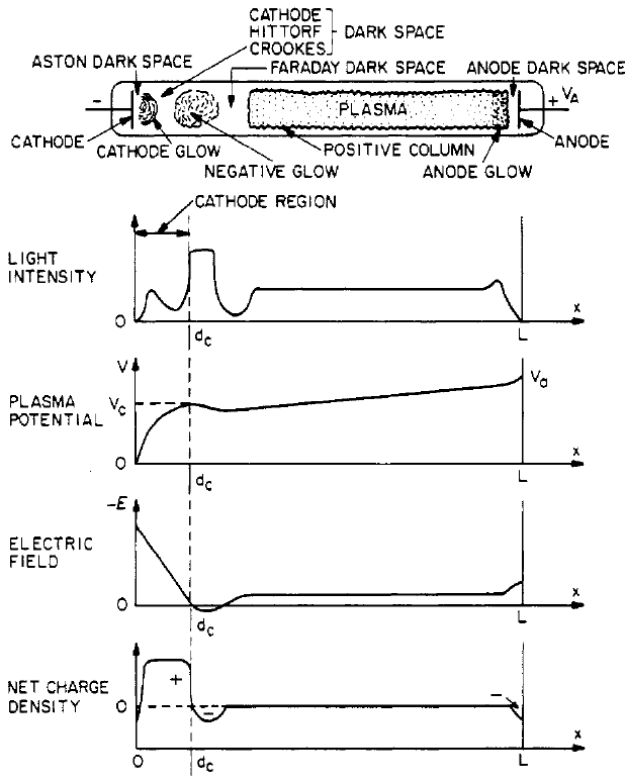

Figure 2.13: Distinct regions in a DC glow discharge and characteristic parameter values along the axial direction; figure taken with permission from Roth [228].

slow to carry the full current required for a sustained discharge, so the secondary electrons are critical in making up this deficit [162]. The plasma will self-regulate such that d_c maintained with changes in the voltage or current, and it is noted that V_c and Pd_c are near the Paschen minimum. Throughout the cathode layer the behavior of the electrons follows that of the breakdown section described above including secondary emission due to ionic behavior in the cathode dark space and an electron avalanche forming in the cathode dark space.

Once an excess of high energy electrons are generated in the cathode dark space, they immediately begin exciting and ionizing molecules in the negative glow region. The large number of electrons and the strength of their collisions produces the brightest region of the plasma, though this intensity drops until one eventually reaches the Faraday dark space. This occurs because the electrons lose significant energy through the collisions in the negative glow and their number

density drops off due to diffusion and recombination [228]. The electron now enters the positive column, which Roth [228] recognized as Irving Langmuir's initial classification of a plasma. While the cathode layer Pd_c is constrained to the Paschen minimum, the positive column expands and contracts as the electrode spacing is altered. Here the field is weak, and the number density of electrons and ions are approximately equal so quasi-neutrality is maintained. In air the positive column is pink, and the expected relevant electronic transitions are nitrogen's so-called second positive system ($N_2(C \rightarrow B)$) and first negative ($N_2^+(A \rightarrow X)$) systems [24]; higher energies in the negative glow region can give it a blue color in air [224]. The electron now passes through the anode glow region and the anode's pre-sheath [162] before entering the sheath proper, the anode dark space, and finally entering the anode and completing the electrical circuit.

Because the plasma studied here was placed in a high-speed wind tunnel, it was worthwhile to compare the velocity scales between the ions, electrons, and bulk flow, at least with a rough approximation. For simplicity, the strong fields in the sheaths were ignored so only a characteristic positive column with $T_e = 2\text{eV} = 23209.05\text{K}$ and negligible electric field [228] in a $u_{bulk} = 850\frac{\text{m}}{\text{s}}$ flow with $T_{bulk} = 60 - 360\text{K}$ at the freestream and wall respectively was considered. In the absence of electric fields and considering only N_2 ions of equivalent mass to neutral N_2, the conservation of energy $\frac{1}{2}mv^2 = k_B T$ [101] was used to obtain $v_e = 8.389 \times 10^5 \frac{\text{m}}{\text{s}}$ and $v_i = 188.7 - 462.3\frac{\text{m}}{\text{s}}$. This result was confirmed by assuming a Maxwellian velocity distribution in the bulk plasma [101] such that the average thermal velocity was $\overline{C} = \sqrt{8R_{specific}T\pi^{-1}}$. This provided $v_e = 9.464 \times 10^5 \frac{\text{m}}{\text{s}}$ and $v_i = 212.9 - 521.6\frac{\text{m}}{\text{s}}$, with $R_e = 1.5156 \times 10^7 \frac{\text{J}}{\text{kg}\cdot\text{K}}$ and $R_i = 296.8\frac{\text{J}}{\text{kg}\cdot\text{K}}$. It was clear that, at least following the simple analysis conducted here, the electrons would be largely unaffected by the bulk velocity while the ions would be more susceptible to it. The main message from these calculations was that hindrance to the ion current needed to be considered when designing the test article.

As a final practical remark, Rajzer [224] noted that of all the structures identified, only the cathode layer is required for a glow discharge to be maintained. Decreasing the electrode gap removes the positive columm, Faraday dark space, negative glow, and then finally the cathode layer, but it is only when the cathode layer is destroyed the plasma is said to be obstructed. This

corresponds to being on the left hand side of the Pashen curve.

2.4.2.1 Classification

There is a relevant phenomena worth introducing at this point, that of a normal *vs.* abnormal glow discharge (see regions F-G and G-H of Figure 2.9 respectively). When breakdown first occurs (region E-F on Figure 2.9, F'-D is due to hysteresis [162]), the plasma is restricted to a small portion of the electrodes, and the cathode layer is constrained to Pd_c near the Paschen minimum. As the voltage is increased, the plasma passes more, often several order of magnitude, current. However, the voltage drop across the cathode layer remains the same, so much of the extra voltage is dropped across the ballast resistor according to Ohm's Law. Furthermore, the current density $j = i/A$ remains constant as the plasma expands to cover the entire cathode. It is only when the entire cathode is finally covered the cathode layer deviates from the stable minimum and begins to extend into the negative glow and positive column. This regime is the abnormal discharge. For this experiment, it is highly desirable for the plasma to be a normal glow discharge as it allows for simplifications in some key equations, but one just strong enough to cover the entire cathode to ensure uniform vibrational excitation across the region of interest. The affect of current on the plasma regime is shown in Figure 2.14.

2.4.2.2 Cathode Layer

The complications of plasma sheaths necessitate a deeper exploration. As was previously stated, the cathode layer is the only structure required to maintain a glow discharge, persists at the smallest possible electrode gaps, has a predictable structure, and dissipates most of the plasma's energy. Furthermore, it remains fixed to the surface of the cathode despite electrode motion or, critically, air flow [224]. The stability, durability, uniformity, and intensity of this region make it the optimal means to deposit vibrational energy into the flow. Furthermore, the notion that the bulk of the plasma's power is dissipated in the cathode layer implies that again, only the cathode layer is strictly needed for the current application of instilling vibrational nonequilibrium.

There are several theoretical parameters useful for characterizing the glow discharge in a hy-

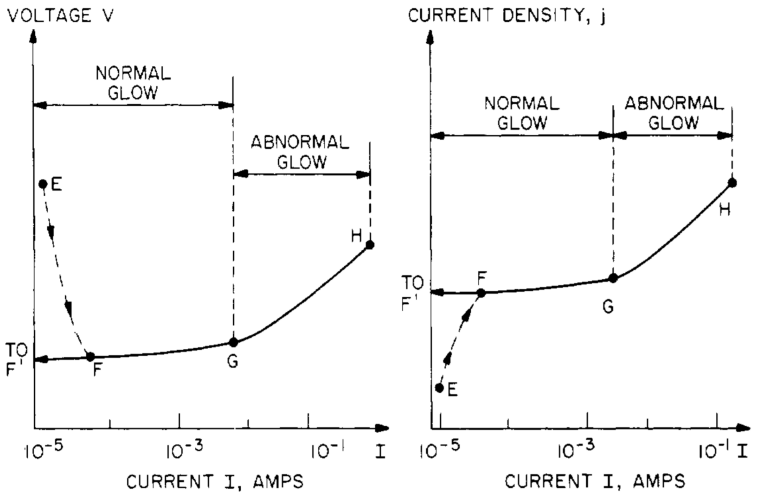

Figure 2.14: The effect of current on plasma voltage and current density. Note that "EF" corresponds to breakdown. Figure taken with permission from Roth [228]

.

personic flow, the reduced electric field and Joule (or Ohmic) volumetric heating [224, 162, 268]. The former is $\frac{E}{n}$ with units of Townsend (Td) where n corresponds to the gas density (it is sometimes alternatively written E/P where P is pressure) while the later is $P_J = jE = eEv_d n_e$ where v_d is the drift velocity, e is unit charge, and the subscript e denotes an electron measurement [224]. Consider here the more nuanced Joule heating. Notice how the replacement of i and V transforms the traditional Ohmic Power Law $P = iV$ into a volume-dependent equation. Also, as a comparison, Lieberman and Lichtenberg [162] defined $j = en_e\mu_e E$, where $\mu_e = v_d/E$ is the electron mobility. Furthermore, some authors [269, 216, 270, 271, 253] included a factor η to account for energy spent heating the flow (ro-translational excitation do to the gas' electrical resistance) as opposed exciting the vibrational and electronic states ($\delta = 1 - \eta$). As η is increased, more energy is deposited into the ro-translational states; a value of $\eta = 0.5$ is in agreement with these author's work for nitrogen plasmas. This effect was generally not considered further due to its inconsistent application in the literature, and a further analysis is beyond the scope of the present report.

The reduced field provides a useful way to classify a plasma based on a normalized parameter; after all, an electric field at atmospheric pressure will have a very different effect on the gas than an equivalent one at a few Torr. Starikovskiy and Aleksandrov [268] provided a relevant and useful

example of such a classification in Figure 2.15. The goal of the plasma in the present application was to excite vibrational modes, so knowing where the setup fell on Starikovsky's plot was useful. Joule heating, meanwhile, provides the energy deposited by the electric field into the gas due to its resistance per unit volume. There are several ways a plasma can affect a flow, especially near the cathode where the field and ion concentration are strongest; these include Joule heating, cathode heating, and electrohydrodynamic "ion wind" forces due to the charged particles and electric field. The first two mechanisms are discussed later, while Macheret et al. [166] wrote that generally Joule heating dominates ion wind effects. It is important to understand that a circuit loses power at the ballast resistor, heating up the electrodes, and heating up the gas (η), so only a fraction of the original energy is actually spent ionizing the gas and exciting its internal modes.

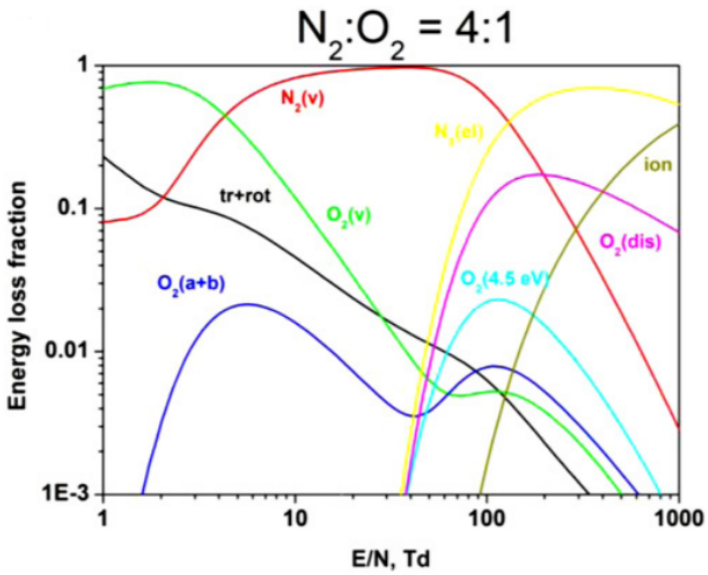

Figure 2.15: Excitation modes in a discharge; figure taken with permission from Starikovskiy and Aleksandrov [268].

Measurement of both of these important parameters requires accurate measurement of E. Figure 2.13 shows that this is not straightforward because in the cathode layer, as in all sheaths, the electric field is not constant. That said, if for preliminary analyses one chooses to assume

$E_c = Const = \frac{V_c}{d_c}$, then V_c and E_c and their corresponding minima as functions of Pd_c follow from Paschen's law [224]:

$$V_c = \frac{B(PD)}{\ln(A(PD)) - \ln\left(\ln\left(1+\frac{1}{\gamma}\right)\right)} \tag{2.125}$$

$$E_c = \frac{B(P)}{\ln(A(PD)) - \ln\left(\ln\left(1+\frac{1}{\gamma}\right)\right)} \tag{2.126}$$

$$\frac{j_c}{P^2} = \frac{(1+\gamma)}{9\times10^{11}}\frac{(\mu_+ P)V_C^2}{4\pi(Pd)_c^3} \tag{2.127}$$

$$(Pd)_{c,min} = \frac{2.72}{A}\ln\left(\frac{1}{\gamma}+1\right) \tag{2.128}$$

$$V_{c,min} = \frac{2.72B}{A}\ln\left(\frac{1}{\gamma}+1\right) \tag{2.129}$$

$$\left(\frac{E}{P}\right)_{c,min} = B \tag{2.130}$$

This Townsend approximation, so named because it follows the same assumptions as the Townsend breakdown process, can yield satisfactory results. von Engel and Steenbeck [288][2] found this Paschen approximation yielded $V_c = 1.1V_{c,min}$, $(Pd)_c = 1.4(Pd)_{c,min}$ and j_c/P^2 is $1.8\times$ Equation 2.127; Kotov et al. [149] wrote Equation 2.127 as $\frac{j_c}{P^2} = 5.92\times10^{-11}\frac{AB^2\mu_+ P(1+\gamma)}{\ln(1+1/\gamma)}$ and found it had strong agreement with data taken at room temperature above $1-2$Torr.

Aston [10] provided the foundation of an improved model for the electric field in the cathode layer, that the electric field is nearly linear.

$$E \approx E_o\left(1-\frac{z}{d_c}\right) \tag{2.131}$$

Cobine [63] noted that this effectively assumed a matrix sheath, a transient, high-voltage sheath where a sudden, large negative voltage temporarily forces all electrons out of the near-wall region leaving behind a region of slower ions at a constant number density [228]. This does indeed loosely describe the behavior in the cathode layer. A diagram of a matrix sheath is shown in Figure 2.16.

[2] A mathematical error in [288] and [47] produced the wrong coefficient for $(Pd)_{c,min}$, but Rajzer [224] corrected the mistake.

Integrating the equation for the electric field with respect to z with the assumed boundary condition $V_c(z = d_c) = V_c$ provided the expected parabolic voltage profile.

$$V_c(z) = \frac{2V_c}{d_c}\left(z - \frac{z^2}{2d_c}\right) \tag{2.132}$$

with $E_o = \frac{2V_c}{d_c}$ such that

$$E_c(z) = \frac{2V_c}{d_c}\left(1 - \frac{z}{d_c}\right) \tag{2.133}$$

With Poisson's equation, one can also find the constant ion number density

$$\frac{d^2V}{dx^2} = -\frac{en_i}{\varepsilon_0}$$

$$-\frac{2V_c}{d_c^2} = -\frac{en_i}{\varepsilon_0}$$

$$\delta n_i = -\frac{2\varepsilon_0 V_c}{ed_c^2} \tag{2.134}$$

where ε_0 is the permittivity of free space. Finally, assuming a collisional sheath [162],

$$v_i(0) = \mu_i E_o = \mu_i \frac{2V_c}{d_c} \tag{2.135}$$

where v_i and μ_i are the ion velocity and mobility respectively.

Recall that the cathode layer behaves like the Townsend breakdown described above. Revisiting Townsend's ionization coefficient, Equation 2.120, and substituting in the newly found electric field yields

$$\frac{\alpha}{P} = A\exp\left(-\frac{BP}{E_0\left(1 - \frac{z}{d}\right)}\right) \tag{2.136}$$

This is applied to the natural log of the self-sustainment criteria [162]

$$\int_0^d \alpha(z)dz = \ln\left(1 + \frac{1}{\gamma}\right)$$

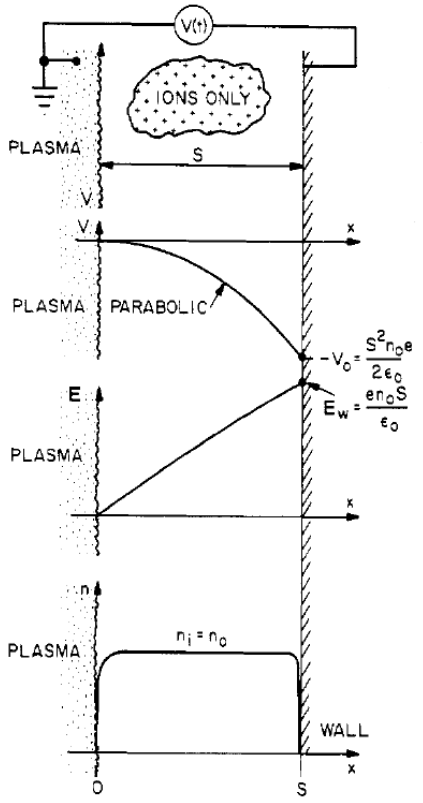

Figure 2.16: A schematic of a matrix sheath with characteristic profiles of key parameters; figure taken with permission from Roth [228].

$$\int_0^d AP \exp\left(-\frac{BP}{E_0\left(1-\frac{z}{d}\right)}\right) dz = \ln\left(1+\frac{1}{\gamma}\right) \tag{2.137}$$

This equation can be integrated to provide a function for V_c as a function of Pd_c [162]

$$\frac{AB(Pd_c)^2}{2V_c} S\left(\frac{2V_c}{BPd_c}\right) = \ln\left(1+\frac{1}{\gamma}\right) \tag{2.138}$$

where $S(\zeta) = \int_0^\zeta e^{-\frac{1}{y}} dy$ has a tabulated solution. A plot of $V_c(Pd_c)$ for a given gas reveals a minimum value near, as expected, the Paschen minimum. Cobine [63] tabulated some experimental data for common gases and electrode materials, but Roth [228] warned that in this older dataset there is a high risk of mercury contamination.

Regardless, it is more useful to remove the parameter d_c, which can be hard to measure, for the

current density described by

$$j(0) = en_i v_i(0)(1+\gamma) \tag{2.139}$$

Substituting in the previously derived expressions for ion number density and velocity

$$j(0) = \frac{4\varepsilon_0 \mu_i V_c^2 (1+\gamma)}{d_c^3} \tag{2.140}$$

One can use this result to replace the dependency of d_c in Equation 2.138. The result has already been plotted by [63]. The left-hand branch of Figure 2.17 is purely theoretical and the plasma will constrict until the normal glow is reached, the normal glow occurs at the stable point when $j = j_{min}$, and the right-hand branch relates to the abnormal glow discharge.

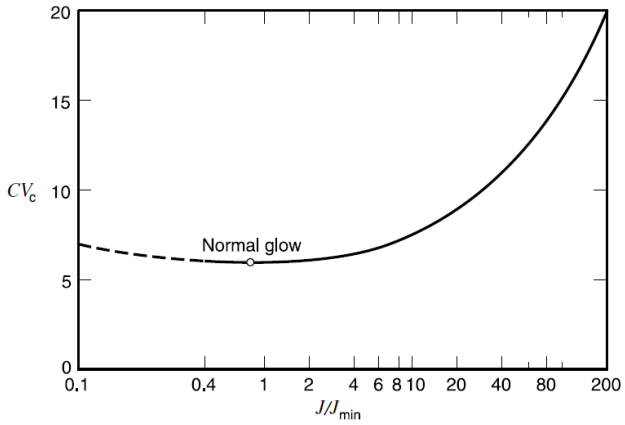

Figure 2.17: Cathode fall as a function of normalized current density, where $C = \frac{2A}{B\ln\left(1+\frac{1}{\gamma}\right)}$; data from Cobine [63], figure taken with permission from Lieberman and Lichtenberg [162].

With this, j_{min} can be approximately measured as the current when the plasma just covers the known cathode area. j can then be recorded at the test condition to provide the normalized current density. With this Figure 2.17 can provide the cathode fall, and the total Joule heating will be

$$P_J = jE = \frac{iV_c}{Ad_c} \tag{2.141}$$

so the bulk of the plasma energy deposition into the flow will be known. This requires estimation of A, B, and γ, and while this will be done, it is useful to check the validity of this approach by simply measuring the voltage drop between the electrodes and assuming most of it occurs in the cathode layer. As a final, alternative approach, Nishihara et al. [203] simply extracted the trendline from a voltage-current plot to find where the line intercepted the V axis (when $i = 0$) and called this value V_c; this is somewhat in disagreement, however, with the theory in Figure 2.14 because it shows a perfectly linear plot is unexpected. These techniques are compared in Section 7.2.1.

2.4.3 Vibrational Nonequilibrium

Here several theoretical and practical aspects of the applicability of a glow discharge in instilling vibrational nonequilibrium are discussed. Surzhikov [270] confirmed the feasibility of glow discharges for fomenting meaningful vibrational nonequilibrium, reasoning that because N_2 relaxation times are high a distinct vibrational mode can exist in a plasma between the electronically excited species and external energy bath. Furthermore, in a hypersonic environment these vibrationally excited molecules can easily convect out of the plasma before they have sufficient time to equilibrate. This effect can only be enhanced as one moves out of the plasma, and all electronically excited molecules and recombining ions relax, distributing themselves across ground electronic state's vibrational levels.

Ideally, the goal of this subsection is the prediction of the concentration of vibrationally excited N_2 generated by the plasma and blown along the test article. However, one cannot neglect the complexity of the proposed test environment, a hot-wall boundary layer downstream of a plasma and trips. Because of the boundary layer, the number density was a function of the wall-normal coordinate. Estimation of $n(y)$ was complicated by the inclusion of the trips, which could create laminar, turbulent, or transitional boundary layers, as well as strong spanwise variation. A traditional glow discharge is difficult to analyze due to variation in the electric field from the sheaths and in some cases low pressures, but with the electrodes mounted in a flush configuration there were both streamwise and spanwise gradients in E. Finally, the system's thermal kinetics needed to be understood as the flow traveled downstream; just leaving the plasma itself caused electrically

excited molecules to relax into a distribution of ro-translational and vibrational levels.

Even under ideal circumstances each individual element of this system presented a significant theoretical challenge. Taken together, the problem became overwhelming. In such cases, the best course is often to conduct the experiment and collect enough data to fill in as many blanks as possible. This approach is risky because without any guidance it is easy to design an experiment which provides insufficient data or obfuscates key physics. To that end, here some relevant past work is reviewed which suggested that a meaningful population of vibrationally excited N_2 could be produced, albeit in a far simpler environment that the final experiment. This was perhaps the best prediction one could make of the proportion of vibrationally excited molecules in the final experiment without performing a dedicated and advanced simulation.

Perhaps the simplest approach was to plot the conditions on Figure 2.15. Starikovskiy and Aleksandrov [268] commented that self-sustaining glow discharges form above $\frac{E}{N} = 120$Td, so the data suggested that for weakly-ionized air plasmas the majority of the energy is stored in the electronic state of N_2, with strong vibrational excitation in certain regions. The realities of operating in a tripped boundary layer, however, made this approach illustrative but only qualitatively accurate. Petrusev et al. [216] performed a simulation of a quiescent, low-density glow discharge with experimental parameters ($V_{PS} = 2000$V, $R_b = 300$kΩ, $P = 5$Torr, $T^{rot-trans} =$ Room temperature) very similar to those listed here and found a mass fraction of $N_2^{v=1} \approx 20\%$. They further estimated that as much as $60-70\%$ of all electron energy was spent collisionally exciting the vibrational modes of N_2 to any of the 50 vibrational states simulated. This number makes sense because vibrational energy levels are so much farther spaced than rotational ones [109], so a small portion of vibrationally excited molecules can store an outsized amount of energy; only the most energetic electrons can electronically excite or ionize molecules. Storozhev and Surzhikov [269] performed further calculations under the same conditions and found that if one were to sum the number densities of all molecules in the first 47 vibrationally excited levels of ground N_2 then the concentration of vibrationally excited molecules was 62%. That said, in the cathode layer they calculated more energy was lost to electronic modes than vibrational modes, which makes sense as

this is where the electrons are the most energetic. Finally, in the proceeding section many authors [269, 216, 270, 271, 253] use $\eta \approx 0.5$ in their simulations of a very similar plasma environment to denote that half of the plasma's power goes into internal excitation, and half to external excitation. Taken together, these results show that a weakly ionized plasma can in fact generate a significant portion of vibrationally excited N_2, even though an exact predication is not offered at this time.

2.4.4 Classic Experiment: AFRL/VA Plasma Channel Flat Plate Campaign

The review papers by Starikovskiy and Aleksandrov [268], Adamovich et al. [1], and Semenov et al. [242] showed that plasmas are applicable to a variety of fields, and within a given discipline there are often multiple applications for them. For example, within hypersonics plasmas are studied for the external aerodynamics of a reentry vehicle, precombustion in high-speed engines, and active flow control. Here only the most relevant environment is considered, a glow discharge on a flat plate in a hypersonic flow.

An excellent facility for such experimentation was built in a collaboration between Wright State University and Wright-Patterson Air Force Base (AFRL/VA). This facility was described by Shang et al. [254]. It is a standard blow-down hypersonic wind tunnel with a 2D planar nozzle designed for $M = 5$ (nominally 5.15) and a free-jet test section. It runs at $Re = 1.15 \times 10^6/m$. Its stagnation conditions are $T_o = 300$K and $P_o = 10.1325 - 101.325$kPa, and for the nominal condition of $P = 300$Torr its freestream velocity, density, and temperature are $698.4\frac{\mathrm{m}}{\mathrm{s}}$, $0.005\frac{\mathrm{kg}}{\mathrm{m}^3}$, and 51.6K respectively; over the full range of stagnation pressures the freestream number density falls between $n = 3 \times 10^{16} - 3 \times 10^{17}/\mathrm{cm}^3$. The test section is $177.8 \times 228.6 \times 73.4\mathrm{mm}^3$ ($L \times H \times W$) and is lined with optical/instrument access ports. The facility can support Langmuir, Pitot, static pressure, schlieren, optical emission spectroscopy, and lift/drag force balance measurements. The tunnel is not preheated as liquefaction was not predicted for the run conditions. Compare all of this to the ACE tunnel, summarized in Table 4.1, and the similarities in both design and flow conditions are clear. What sets the AFRL/VA tunnel apart is its construction from solely plastics and ceramics. This allows for the generation of a variety of plasmas (DC or RF glow discharges, see [176]) and the application of magnetic fields anywhere in the facility to study an

array of electrohydrodynamic and magnetodynamic effects without any accidental ignition or field distortion. Furthermore, the low number density allows for plasma generation at low voltages and realistic flight altitudes, and the test section's small size aids with the uniform and precise application of magnetic fields. The AFRL/VA tunnel was carefully and purposefully designed to provide a testbed for hypersonic electro- and magnetohydrodynamic experimentation, and it has been put to great use.

Of the many problems studied in the AFRL/VA tunnel, those of a spanwise DC glow discharge on a sharp leading edge (half-angle design) were the most pertinent; any work on this geometry including a magnetic field was neglected. As with the facility, the design of the test article was left as generalized as possible so the impact of many different factors could be independently studied. The experimental work was supported by computational efforts. A summary of each of these incremental campaigns is included:

- Menart et al. [180] (2003): Studied the effect of electrode orientation and polarity on surface pressure measurements in between the electrodes. The authors found that the plasma caused a measureable pressure rise in electrode gap, likely due to Joule heating, though the effect of cathode heating could not yet be discounted. Visual observations found spanwise electrodes provided the most predictable results.

- Estevadeordal et al. [87] (2004): Tested different illumination sources for schlieren imaging of a glow discharge in a low-density hypersonic facility. The authors found a continuous LED provided sufficient sensitivity without saturating the camera.

- Shang and Surzhikov [248] (2004): Drift-diffusion simulation of the plasma experiments using $V_{power\,supply} = 1200\text{V}$, $R_b = 12\text{k}\Omega$, and $I = 50 - 100\text{mA}$. This paper provided plots of charged particle number density, current density, electric field, temperature, and Joule heating. For the first time in this series the authors isolated the effect of Joule heating from electrode heating (assumed 600K) and found it was dominant. Heating effects were strongest over the electrodes. This effect was sufficient to cause oblique shocks, especially

over the cathode, and alter the boundary layer thickness, causing deviation from leading edge inviscid-viscous leading edge interaction theory [108] (described in Section 4.4.2).

- Menart et al. [177] (2004): Compared Joule and cathode heating by making a plate with an embedded resistance heater and another with spanwise electrodes and using static pressure, Pitot, and thermocouple (not true temperature) measurements to compare their results; further evidence provided with computations. Both heat sources were run at a constant 60W. No correction was offered for the glow discharge's voltage drop across the ballast resistor, so one needed to assume the plasma itself was set to 60W, not the power supply; this was a recurring issue in the experimental papers reviewed here. The data showed that the plasma approached steady state in approximately $20-40$s while the heater needed 20min; the plasma had a more immediate impact on the flow, and the heater tended to heat up the entire plate as it reached the test condition. Once both heat sources approached their steady state values, they had comparable effects on the flow. As expected, both techniques showed the strongest impact above the cathode/heater. The computations showed the heater was strongly dependent on the plate's thermal properties; this implied cathode heating due to a glow discharge should be similarly affected. In addition to the aforementioned experiments, a Langmuir probe was used to measure the ion number density; as expected [224], the concentration was the highest above the cathode.

- Kimmel et al. [139] (2004): Used Pitot, surface pressure, Langmuir, and total-temperature (uncalibrated) techniques to characterize a 60W (50mA, $1100-1200V$) glow discharge. Note that no ballast resistance was provided, leaving one to assume the 60W was entirely deposited into the flow; this is a recurring issue in the experimental papers reviewed here. The Pitot measurements were able to detect the oblique shock at the cathode, and the static pressure rise scaled roughly linearly with discharge power. The hot plasma thickened the boundary layer, which the authors postulated caused a pressure rise through viscous interaction; the 10% surface pressure rise was equivalent to the jump across an oblique shock from

turning the flow an 0.8°. The authors also studied the return of Pitot pressures to normal values following different plasma ignition durations to study the effect of cathode heating; the recovery time increased from nearly zero seconds for a five-second discharge to over sixty seconds for a forty second discharge, which implied cathode heating was significant and thus could not be discredited as a major source of flow perturbation for lengthy discharges.

- Surzhikov and Shang [271] (2005): A drift-diffusion simulation of the plate. The authors confirmed the model against the theoretical viscous-interaction theory [108]; this theory is described in Section 4.4.2. They then simulated cathode heating on an adiabatic plate and found it produced a strong enough pressure effect to produce a shock, and at excessive heats even separation. Next a glow discharge at $V_{power\,supply} = 1200$V and $R_b = 12$kΩ (the current was left to self-stabilize) was tested and the results were compared to those from the cathode heating; although a modest pressure rise was observed due to heating of the positive column, for the realistic electrode temperatures of 600K cathode heating was the dominant mechanism for flow perturbation. These mechanisms had a stronger affect on viscous-interaction the closer the electrodes were placed to the leading edge.

- Menart et al. [178] (2005): Used load cells to measure effectiveness of plasma for lift and drag control. While there was no effect on drag, a linear relationship was found between plasma power and lift. Due to insufficient information on the circuit, one needed to assume the listed power is spent entirely by the plasma; this is a recurring issue in the experimental papers reviewed here. This result persisted at both positive and negative angles of attack. For a 60W plasma, a 4% change in lift was observed; data was provided up to 230W which yielded a 18% change in lift, but at higher powers the plasma began to constrict.

- Shang et al. [250] (2005): Mostly a review paper, though some new plots such as skin friction and pressure coefficients reinforce the concept that the plasma actuates via pressure, not surface shear. The authors did write that for "a total power supply power" (how this relates to plasma power is unclear) of 60W, the power per unit length of electrode needed to

provide an equivalent angle of surface actuation was 18.90W/cm/degree.

- Kimmel et al. [140] (2006): Journal article which mostly covered magnetohydrodynamics and reviews past findings; it confirmed the importance of uniform discharges to prevent localized pressure differentials as well as the linear relationship between input power and pressure rise. One novelty was the direct measurement of the copper cathode temperature immediately after the plasma was switched off via an embedded thermocouple. The cathode rose over 100K from below room temperature in as little as five seconds and reached temperatures above 500K after forty seconds of operation at 50mA; steady state was not attained. Temperature sensitive paint showed the ceramic model rose 50K and $<$ 10K at the cathode and anode respectively after 40s of plasma operation.

- Menart et al. [179] (2006): Studied the effect of cathode size and placement using laser displacement. It was found moving the cathode closer to the leading edge and making it larger increased its effectiveness. The current and power never exceeded 24mA and 30W (without ballast resistance, one must gain assume this is the discharge power), and it is remarkable so little power had an effect. The authors note because the required voltage increased as the area and current are decreased, the discharge was likely in the abnormal glow regime.

- Stanfield et al. [266] (2006): Performed spatially resolved optical emission spectroscopy to measure the rotational temperature in the glow discharge. They measured the hottest temperature just above the cathode and a decrease at the cathode surface attributed to heat flux into the copper. The effect of spanwise, streamwise, wall-normal, and temporal gradients were discussed and where possible measured or resolved.

- Bennett et al. [25] (2008): A numerical study of the plasma. The simulated cathode was very large in the streamwise direction, but under this condition a plasma power as low as even 1W was enough to measurably alter the pressure distribution over the plate. Still, below 50W thermal gradients and flow modifications were weak. Of particular interest is the comparison

of adiabatic *versus* conducting wall conditions. As expected, the conducting wall had a lower temperature, and thus weaker plasma effects, than the adiabatic case because the energy was being absorbed by the wall and not being directly deposited into the flow.

- Shang et al. [251] (2008): Mostly a review paper; its contents are deferred to the journal article by Shang et al. [252], which will be discussed shortly.

The above works were well-summarized in the journal articles [255, 253, 252]; the lattermost work was the most recent publication, so it was the main source for the present synopsis of the AFRL/VA plasma channel flat plate campaign. The numerical work included the derivation of a drift-diffusion model for DC glow discharges [272, 273]. This was necessary because quasi-neutral and ambipolar models are generally used above 50Torr [255, 253]. These models are known to fail in plasma sheaths [224], but the freestream plasmas generated in [176, 180] validated their use for calculations of the bulk plasma. The viscous-interaction theory of Hayes and Probstein [108] showed how disturbances at the sharp leading edge of a hypersonic flat plate can have an outsized effect on the boundary layer; additional detail is provided in Section 4.4.2. There are two main mechanisms by which a glow discharge can introduce such a perturbation, Joule and cathode heating. The heat lowers the density and increases the size of the boundary layer, especially above the cathode, which can cause enough flow deflection for an oblique shock to form. This shock is strong enough to be captured by both Pitot [139] and schlieren Shang et al. [251, 252] measurements. Between the two heating mechanisms, no conclusive determination of which is more important was offered and one must assume they complement one another; this was evinced both computationally and numerically [253, 255, 180]. That being said, Shang et al. [249] wrote that Joule heating provides actuation in $\mathcal{O}(1\text{ms})$, three orders of magnitude faster than convective heating. Furthermore, the plot in [176, 249] shows that it takes longer for the cathode to approach its steady state temperature (here $>$ 500K [140]). Experimentation and computation [180, 178, 139, 179] showed that glow discharges are capable of significant flow control solely via pressure forcing (lift), not surface shear (drag). A consistent challenge with the above papers was the interpretation of "plasma power". Glow discharges waste power at their ballast resistor, so the power supply's full power

is not delivered to the electrodes; without a complete description of the circuit, assumptions must unfortunately be made in interpreting the data.

In closing, some important points must be made. All of the above experiments were conducted in a laminar boundary layer; none of the listed authors studied the effect of a glow discharge on a turbulent boundary layer. In fact, even after a broader literature search, no publications regarding a DC glow discharge on a hypersonic ZPG TBL were found. The present work endeavored to fill this gap. Also, the leading edge was somewhat blunted, so viscous-inviscid interactions were not considered relevant, justified in Section 4.4.2. Finally, in all of the above experiments, the plasma had a "macroscopic" effect on the flow; its heating was sufficient to engender a weak shock and alter the boundary layer structure. That was not the goal of the present work, which was instead to study the effect of vibrational nonequilibrium on turbulence. This could not be done if the presence of the plasma itself had a direct effect on the flow. Put another way, the plasma was desired only as a source of vibrational excitation, not as a flow actuator. The plasma used needed to be weak enough so as to not conflate any of its heating effects with those due to thermal nonequilibrium.

2.5 Planar Laser-Induced Fluorescence (PLIF) Techniques

At its core, PLIF involves using a laser to excite a specific energy transition of a group of molecules, then recording the fluorescence as they relax back to their original state. The technique is non-intrusive, instantaneous, relatively simple, returns high-signal, and provides excellent spatial and temporal resolution in quantitative measurements of flow structure, velocity, temperature, pressure, and concentration. For these reasons, it is popular for testing in turbulent and/or high-speed flows [241]. In hypersonic environments, NO is a popular target molecule because of its high signal, stability in even high-temperature or reacting environments, natural formation at hypersonic enthalpies, and transition wavelengths easily achievable with tunable dye lasers [84]. In this work, a combination of flow visualization, velocimetry, and thermometry was used, and so each of these processes are analyzed in turn.

2.5.1 General Chemistry

It should by now be well understood that molecules have quantized energy states due to their precise nuclear, electronic, vibrational, rotational, and translational energy (see Section 2.3). This energy is related to wavelengths via Plank's equation $E = h\nu = h\left(\frac{c}{\lambda}\right)$ where h is Plank's constant, ν is the frequency, c is the speed of light, and λ is the wavelength; for a tractable description of these phenomena, readers are referred to Barrow's texts [13, 14]. This means that a Nd:YAG-pumped tunable dye laser can be used to supply the precise energy necessary to foment a specific transition, though one must assume that the laser's bandwith is broader than the transition's so the energy is constant at the desired frequency. A diagram of a generalized LIF event is shown in Figure 2.18.

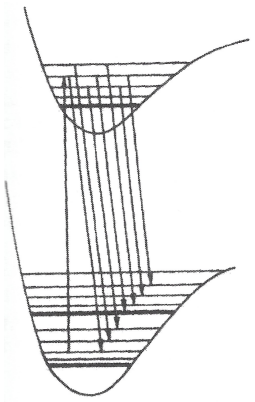

Figure 2.18: A general LIF event between two electronic states covering absorption (excitation) and fluorescence (relaxation). Bold lines represent vibrational energy levels, thin lines rotational levels. Figure taken with permission from Eckbreth [84].

A common transition for NO is $A^2\Sigma \rightarrow X^2\Pi_{1/2}$, and specifically the ground vibrationally state within each electronic state ($(v'' = 0, v' = 0)$); with only four significant figures, this transition corresponds to $\lambda \approx 226.5$nm [84]. For reference, it will be shown in Section 6.8 that for the $(v'' = 1, v' = 1)$ transition $\lambda \approx 223.8$nm. The true precision of the laser is necessary to probe specific rotational (J) transitions, which are far more closely spaced [14]. One unique detail of NO

is that it has non-integer J states. Intuitively this should be impossible, but it occurs because NO is a radical which means it has a free electron. This electron can be spin up or spin down, which contributes to the overall angular momentum of the molecule through a process called spin orbital coupling. Greater spectroscopic detail is provided by Eckbreth [84] and especially Herzberg [109], but Sanchez-Gonzalez [235] gave a summary of the spectroscopy most relevant to this work.

Once a molecule like NO has been excited by a laser, it can do one of five things, illustrated in Figure 2.19: 1) immediately return to the ground state by laser-stimulated emission ($B_{21}I_\nu$) 2) be excited by a second photon into a higher energy level ($B_{2i}I_\nu$) 3) collisionally quench (Q_{elec}, $Q_{rot,vib}$) 4) predissociate Q_{pre} 5) relax through fluorescence (A_{u1}), emitting energy as photons at a distinct wavelength [241]. Of the five processes, only one is desirable for basic PLIF applications.

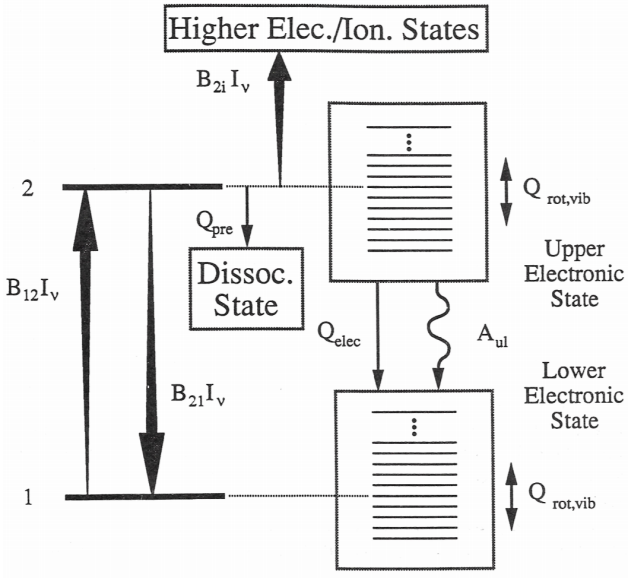

Figure 2.19: Available pathways for excited molecules; figure taken with permission from Seitzman and Hanson [241].

2.5.2 The Rate Equation

Any quantitative analysis of a LIF signal depends on the ability to model the particles' response to excitation. The equations to study this are called rate equations. Seitzman and Hanson [241] provided a generalized walkthrough of the necessary calculations, and it is summarized here. Begin by considering a quasi-control volume. The rate of change of the population of the excited state j equals the sum of the events which populate it minus the sum of the events which depopulate it. Mathematically,

$$\frac{dn_j(t)}{dt} = \sum_{i \neq j} \left[n_i(t) R_{ij} \right] - n_{ji}(t) \sum_{i \neq j} \left[R_{ji} \right] \tag{2.142}$$

where R_{ij} is the total rate coefficient ($\left[s^{-1}\right]$) containing: the collisional transfer coefficient Q_{ij} (captures intermolecular and intramolecular collisions); the Einstein A coefficient A_{ij} (captures spontaneous fluorescence rate); and the coefficient for laser-stimulated processes (single-photon) $B_{ij}I_\nu$, where B_{ij} is the Einstein B coefficient (captures absorption and stimulated emission) and I_ν is the laser spectral intensity $\left(\frac{W*s}{cm^2}\right)$. Seitzman and Hanson [241] noted that spontaneous emission only occurs towards lower energy levels (ex.- $A_{ij} = 0$ if $E_j > E_i$) and that the laser-stimulated rates follow a detailed balance $G_i B_{ij} = G_j B_{ji}$ where G_i is the degeneracy of level i (see also [109]).

Because PLIF only considers the transition between two states, the ground (1) and excited (2), one can economically write the rate equation as

$$\frac{dn_2(t)}{dt} = n_1(t) \left[Q_{12} + B_{12} I_\nu \right] - n_2(t) \sum_{i \neq j} \left[Q_{21} + B_{21} I_\nu + A_{21} \right] \tag{2.143}$$

There are a finite number of electrons in the system, and one can assume as an initial condition that the population of the excited state is negligible relative to the ground state, or mathematically $n_1(t) + n_2(t) = Constant = n_1(t=0)$; this is a decent assumption for experiments in a cold, blow-down hypersonic facility like the one used in this work. This allows the differential equation to be solved providing the population of the excited state as a function of time.

$$n_2(t) = n_1(0) \left[Q_{12} + B_{12} I_\nu \right] \tau \left[1 - e^{-t/\tau} \right] \tag{2.144}$$

Here the time constant, which for reference is $\mathcal{O}(ns)$, is $\tau = \left[Q_{12} + B_{12}I_\nu + \frac{g_1}{g_2}B_{12}I_\nu + Q_{21} + A_{21}\right]^{-1}$, where g is the line shape function (not to be confused with the degeneracy G_i). For many applications, $t > \tau$, so n_2 reaches steady state. Furthermore, Q_{12} can safely be omitted due to the large energy difference between two electronic states; put another way, collisional excitation to elevated electronic states is unlikely for most applications of interest. What remains is an equation for the rate of photon generation per unit volume, where the saturation intensity is $I_\nu^{sat} = \frac{Q_{21}+A_{21}}{B_{12}\left(1+\frac{g_1}{g_2}\right)}$.

$$R_p = n_1(0)B_{12}I_\nu \frac{A_{21}}{A_{21}+Q_{21}} \frac{1}{1+\frac{I_\nu}{I_\nu^{sat}}} \tag{2.145}$$

At this point there is a divergence, the linear fluorescence regime and the saturation limit. In the former, laser intensity is low ($I_\nu \ll I_\nu^{sat} \implies \frac{1}{1+I_\nu/I_\nu^{sat}} \approx 1$) and the fluorescence is a linear function of this intensity. In the latter, the laser energy is beyond what is necessary for maximum photon generation ($I_\nu \gg I_\nu^{sat} \implies \frac{1}{1+I_\nu/I_\nu^{sat}} \approx \frac{I_\nu^{sat}}{I_\nu}$) and thus photon generation is independent of it. In the saturated regime, collisional quenching effects can be neglected [71], which is advantageous. However, it can be difficult to attain sufficient power in a planar configuration, so both equations are listed here and the linear regime equation is used for the remainder of this section.

$$Linear: R_p = n_1(0)B_{12}I_\nu \frac{A_{21}}{A_{21}+Q_{21}} \tag{2.146}$$

$$Saturated: R_p = n_1(0)B_{12}\left(\frac{Q_{21}+A_{21}}{B_{12}\left(1+\frac{g_1}{g_2}\right)}\right)\frac{A_{21}}{A_{21}+Q_{21}} = n_1(0)\frac{A_{21}}{1+\frac{g_1}{g_2}} \tag{2.147}$$

With the rate equations Seitzman and Hanson [241] have provided a way to relate photon generation to laser intensity. By integrating over the pulse duration and accounting for collection efficiencies, this can instead be extended to a practical estimation of signal per pulse. In the steady state, broadband laser profile, and linear fluorescence limits, and assuming emission into

4π steradians, a detector will collect N_p photons from an interrogation volume V_c

$$N_p = \eta \frac{\Omega}{4\pi} f_1(T) \chi_m n V_c B_{12} E_\nu \frac{A_{21}}{A_{21} + Q_{21}} \tag{2.148}$$

where η is the optic's transmission efficiency, Ω is the collection solid angle, $f_1(T)$ is the fractional population of the lower laser-coupled state in the absence of the laser field, χ_m is the mole fraction of NO, n is the total number density, and E_ν is the spectral fluence (energy per unit area $\frac{J}{cm^2 Hz^{-1}}$). The pre-excitation population can be found from the Boltzmann relation (see [6])

$$f_1(T) = g_n \exp\left(-\frac{\varepsilon_{vib}}{kT_{vib}}\right) g_j \exp\left(-\frac{\varepsilon_{rot}}{kT_{rot}}\right) = (1) \exp\left(-\frac{\varepsilon_{vib}}{kT_{vib}}\right) (2J'' + 1) \exp\left(-\frac{\varepsilon_{rot}}{kT_{rot}}\right) \tag{2.149}$$

Here k is the Bolztmann constant, g_x is the dengeneracy of the x state (for the vibrational degeneracy $g_n = 1$; for diatomic molecules and the rotational degeneracy is $g_j = 2J'' + 1$, see [6]), and ε is the molecular energy.

Equation 2.148 allows one to estimate the expected signal from a laser pulse. It was derived from the theoretical rate equations and is therefore exact. It will be seen that this equation is the theoretical foundation of all PLIF applications.

2.5.3 Flow Visualization

The most basic application of NO PLIF is flow field visualization, which can be thought of as a qualitative concentration measurement. Equation 2.148 shows a linear relationship between $\chi_m n$ and N_p, which means the higher the local number density of NO the more photons are emitted from that region of the flow. Simply measuring this light provides immediate flow visualization with excellent spatial and temporal ($\mathcal{O}(ns)$) resolution. This is a clear benefit of PLIF over traditional schlieren imaging, especially in high speed turbulent flows; the temporal resolution provides streamwise clarity, and by only imaging a single plane integration of transverse data is avoided. PLIF also offers strong signal relative to other laser-based optical techniques such as Rayleigh and Mie scattering.

Though beyond the scope of the present work, Seitzman and Hanson [241] outlined a methodology to allow for quantitative measurement of the species concentration during flow imaging. To begin, consider the proportion of fluoresced to absorbed photons in Equation 2.148, $\frac{A_{21}}{A_{21}+Q_{21}}$. Assume that collisional electronic quenching dominates Q_{21} and the pressure is sufficient for $Q_{21} \gg A_{21}$, then model Q_{21} with kinetic theory $Q_{21} = n\sigma_m\langle v\rangle$ where v is the mean molecular speed proportional to $\sqrt{T}$ (see [286]) and σ_m is the mixture-averaged quenching cross-section. Now assume that σ_m is a constant over the range of conditions in the flow; this allows one to write $\frac{A_{21}}{A_{21}+Q_{21}} \sim Const * \frac{1}{n\sqrt{T}}$. By grouping all experimental parameters into a single *Constant* and cancelling the number densities, Equation 2.148 becomes

$$N_p \sim Constant * \chi_m \left[\frac{f_1(T)}{\sqrt{T}}\right] \tag{2.150}$$

With careful *in situ* calibration and known temperature, Equation 2.150 shows how signal can become a function of concentration alone. While many assumptions were made and details were omitted, this illustrates a basic approach to concentration measurement with PLIF.

2.5.4 Two-Line Thermometry

The measurement of off-body, instantaneous temperature is a very useful PLIF application; it provides 2D maps of $\overline{T}$ and T'. The strategy employed here is called two-line thermometry as two separate lasers tuned to excite NO from the same unique ground states to two different rotational or vibrational levels in an excited electronic state; if the same vibrational level is used between images, then rotational temperature is probed, and if the same rotational level is used between images, the vibrational temperature is probed. It is noted that if the concentration is known monochromatic thermometry measurements are possible using Equation 2.150 [156]. This technique was compared to two-line thermometry by Lee et al. [159], who concluded that while it is advantageous to simplify the experiment and only use one laser, monochromatic thermometry is more niche due to its assumptions and prerequisite knowledge of the flow field and has therefore seen less use.

The theory for two-line thermometry follows many of the same assumptions used in deriving Equation 2.150, that Q_{21} is primarily electronic quenching and dominates A_{21} and that all collection coefficients can be grouped into one *Constant*. Additionally, one must assume that both images freeze the flow, and that the flow is steady between the images; for turbulent flows, this can be remedied by taking the average of many frames or taking both images in quick succession. Applying these approximations to the number of the photons generated between Frames A and B, Equation 2.148, yields

$$R = \frac{N_{p,a}}{N_{p,b}} = Constant * \frac{f_1(T)_a Q_{21} T_a}{f_1(T)_b Q_{21} T_b} \tag{2.151}$$

where R is the ratio of the signal between the two images. Seitzman and Hanson [241] suggested using the same upper energy level so that the ratio of the quenching terms becomes unity; alternatively, if the species of interest has quenching rates independent of temperature and species concentration, this term can be grouped into the constant. Similarly, the ratio of the temperatures of the excited states can be called unity as well due to the close spacing between rotational levels. Grouping the non-temperature dependent coefficients in $f_1(T)$ into *Constant* and assuming an equilibrium rotational temperature all that remains is

$$R = \frac{N_{p,a}}{N_{p,b}} = Constant * \exp\left(\frac{-\Delta\varepsilon_{ab}}{kT}\right) \tag{2.152}$$

Because the difference in energy is known for the probed states, and with careful calibration at a known temperature to find *Constant*, one can measure the ratio of the signal R to solve Equation 2.152 for T.

Seitzman and Hanson [241] commented on the uncertainty of Equation 2.152 by taking its derivative.

$$\left|\frac{dR}{R}\right| = \frac{|\Delta\varepsilon_{ab}|}{kT}\left|\frac{dT}{T}\right| \tag{2.153}$$

where $\frac{|\Delta\varepsilon_{ab}|}{kT}$ is the slope sensitivity. Probing states with larger energy separations improves the sensitivity at the cost of reducing signal as higher energy levels are typically less populated. It is also stated that if $\frac{|\Delta\varepsilon_{ab}|}{kT} > 1$, the uncertainty of the temperature measurement $\left|\frac{dT}{T}\right|$ will be less than

that of the ratio of the fluorescence signal $\left|\frac{dR}{R}\right|$.

2.5.5 Molecular-Tagging Velocimetry (MTV)

MTV is effectively a series of flow visualization PLIF applications and can produce $\overline{u}$, u', $\overline{v}$, and v' data, all of great interest to the turbulence research. The technique to gather 1D data is pictorialized in Figure 2.20. Consider shooting a single line perpendicular to a wall, straight through a boundary layer, and capturing the fluorescence as the molecules relax from the excited electronic state. One will be left with an image of a line at a known time, and a "written" line of molecules in some distribution of excited vibration states which have not yet equilibrated. Now wait a known amount of time to allow the line of vibrationally "tagged" molecules to move with the flow before striking the region with a plane of laser light tuned to excite only those molecules in the excited vibration level (here $v = 1$). These molecules will fluoresce for imaging. After collecting the second image, one is left with two images of a line separated by a known length of time. If the images can be overlayed and scaled, a trivial task if the same camera is used for both, then the displacement can be recorded and the velocity calculated. Note that a plane of light is necessary to "read" the vibrationally excited molecules because these molecules can move to an unknown location with the flow thus requiring a broad search area, and that the first excited vibrational state is acceptable for the current application, with temperatures below 400K, because there should be few NO molecules naturally in this state, especially relative to the "written molecules".

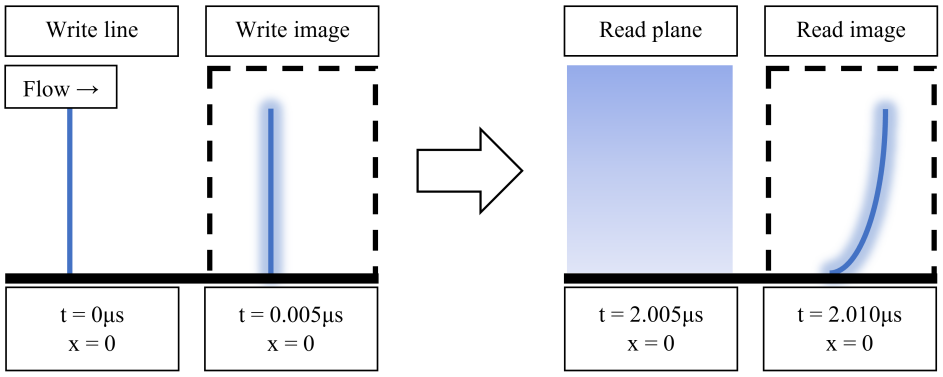

Figure 2.20: The four stages of MTV in a laminar boundary layer with characteristic times.

A complicating but often necessary step for analyzing MTV data was offered by Danehy et al. [77]. NO fluorescence signal is controlled by temperature and temporal decay, so Δt is not simply the delay between the two images. Consider the fluorescence decay equation $\frac{I(t)}{I(t=0)} = \exp(-t/\tau)$ where I is the signal and $\tau = f(Temperature)$ is the fluorescence time constant. If the temperature is already known from CFD or experimentation, τ can be calculated [77]. One can then integrate $\frac{I(t)}{I(t=0)}$ to find where say 50% of the area under the curve is reached t'. This process can be repeated for both the write and read images, and the delay between t'_{write} and t'_{read} becomes a better representation of the gap between the two measurements. Thus the inclusion of a bit of chemistry can make MTV more accurate.

Even with this step, MTV is simpler than laser-Doppler velocimetry, and with injection far upstream of the test domain the gas tracks the flow perfectly compared to particle-imaging velocimetry; the latter point is especially important in low-density hypersonic wind tunnel facilities. That said, MTV is only appropriate in high speed flows where the molecules move a resolvable distance before they quench back into the ground vibrational state.

In order to extend MTV into 2D, instead of writing a single line one can use a beamsplitter and screen to write a grid of vibrationally excited NO. Through cross-correlation one can then track how the "nodes" move in two directions. This allows MTV to be extended to turbulent boundary layers where wall-normal velocity can be significant. Still, optics limit the number and size of nodes that can be positioned inside the boundary layer.

2.5.6 Vibrationally Excited Nitric Oxide Monitoring (VENOM)

VENOM, developed at the NAL by Sanchez-Gonzalez [235], is the simultaneous application of 2D thermometry and MTV. Thus it can provide all of the mean and fluctuating temperature and velocity data previously discussed as well as correlated data like Reynolds stress ($\overline{u'v'}$) and energy flux ($\overline{u'T'}$ and $\overline{v'T'}$). The ability to directly measure such higher-order flow physics is of great interest to the turbulence modeling community, so although VENOM was not conducted for this report due to time constraints, it is worth reviewing here; VENOM campaigns on the present test article are proposed as part of Madeline Smotzer's doctoral research. It is noted that if one assumes

the wall-normal mean and fluctuating velocities are much less than the streamwise components, a reasonable approximation at least in the mean case, then a simplified version of VENOM can be performed using a single line instead of a grid of points. This only produces 1D velocity data, but it greatly reduces the optical and analytical complexity.

As with 2D MTV, a grid of $v = 1$ NO molecules are "written" into the flow and subsequently "read" by a plane tuned to selectively excite $v = 1$ molecules. Now however, a second "read" sheet probes a different rotational transition in the $v = 1$ level; thus all of the measurements are done on the $v = 1$ molecules, as opposed to the ground state probing for traditional PLIF techniques. This is shown in Figure 2.21. In post-processing, one produces the 2D velocity map then uses it to lay the grid nodes from "Image 2" onto their original position in "Image 1" to allow for thermometric calculations. Because all analysis is done between the fluorescence from probing the $v = 1$ state there can be a reduced signal as the state depopulates over time, but this is unavoidable for thermometry. Just as it is necessary to probe the same upper level so the ratio of Q_{21} drops out of Equation 2.152, one must probe rotational states within the same vibrational level to neglect convolution of signal loss from the differing populations of each vibrational level. The loss of signal to quenching and the progression of uncertainty as one relies on velocity maps for thermometry calculations add to the challenge of VENOM, but the resulting 2D, coupled, instantaneous (fluctuating) maps of 2D velocity and temperature are critical to validating turbulence models.

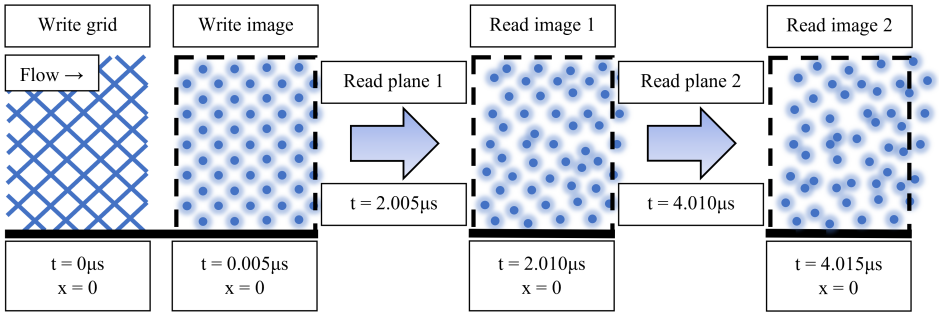

Figure 2.21: The six stages of VENOM in a turbulent boundary layer with characteristic times.

A methodology to perform VENOM with vibrational as opposed to rotational temperature was consideredas part of the present work. The technique was complicated by the theoretical need to use a "read" sheet to probe the line at $v = 0$ without exciting all of the background NO. It is possible through careful selection of isolated rotational states and strong "write" lines the signal-to-noise ratio will be sufficient for analysis despite widespread fluorescence, but further testing is required.

2.5.7 Classic Experiment: NASA Langley PLIF on a Wedge Campaign

Because of the criticality and resolution of the data, and its relative simplicity and strong signal, PLIF has been utilized in a variety of applications in subsonic through hypersonic flow regimes. However, due of the breadth of the available literature, the present discussion is restricted only to hypersonic NO PLIF on a wedge in a blow-down wind tunnel, a relevant experiment.

An excellent body of work was produced at NASA Langley Research Center's 31-Inch Mach 10 Air Tunnel. This facility is described in [27]. It is a standard blow-down hypersonic wind tunnel with a 2D planar nozzle designed for $M = 10$ (nominally $9.68 - 9.96$). It runs at $Re = 1.73 - 6.66 \times 10^6/\text{m}$. Its stagnation conditions are $T_o = 986.1 - 994.4\text{K}$ and $P_o = 2413.17 - 9997.40\text{kPa}$, and for the nominal conditions of $P = 0.517 - 1.820\text{Torr}$ its freestream velocity and temperature are $1400.1 - 1410.0\frac{\text{m}}{\text{s}}$ and $52.04 - 50.14\text{K}$ respectively. The test section is a $78.74\text{cm} \times 78.74\text{cm}$ ($31\text{in} \times 31\text{in}$) square. The test section is lined on three sides with three access ports for windows or diagnostic tools. The fourth side contains a model injection system, which rapidly inserts the model once the tunnel is preheated and started to prevent it from excessive thermal loading. Preheating is necessary before every run to prevent the liquefaction of O_2 in the freestream. The same injection system allows controllable $\pm 45°$ pitch and pre-set $\pm 5°$ yaw angles. Compare all of this to the ACE tunnel, summarized in Table 4.1, and it is clear the ACE facility is analogous, but generally milder.

The test articles used were $10°$ half-angle wedges with sharp leading edges; the models could be pitched to alter the flow deflection against the top test surface and thereby the boundary layer thickness. A unique element of the model design was the direct injection of NO into the boundary layer. For the flat plate experiments described in [77, 208], the tests were conducted in a shock tube facility which naturally produced NO from air due to high-temperature effects (see Section

2.3); this nascent gas was used for PLIF measurements. Blowdown facilities like the ACE or 31-Inch Mach 10 wind tunnels typically are not designed to attain the temperatures necessary for this reaction, so *NO* must be artificially seeded. There are different ways to do this, each with their own pros and cons, but for the campaign covered here the gas was injected through the model directly into the boundary layer. This offered excellent and controllable signal in the boundary layer, but it ran the risk of perturbing the flow and providing non-thermalized *NO* thermometry; these consequences were studied in the proceeding papers. The majority of the papers reviewed here used a 127mm wide and 162.5mm long sharp wedge with a 11mm spanwise slot for *NO* injection. Only Danehy et al. [73] used a previous iteration of the model which was 157.2mm long with four streamwise orifices for *NO* injection. The model was made to allow different test surfaces to be mounted with customizable trips, materials, windows, *etc.*, to be tested. Scatter was controlled through a varying combination of timing data collection long after the pulse, installing a filter on the camera to block the laser's wavelength, and other mounting a window in the test surface. The high signal, control of the angle of attack, and customizability of the test surface allowed a variety of different PLIF techniques, including flow visualization, velocimetry, and thermometry to be studied on laminar, transitional, and turbulent boundary layers. A summary of each of these incremental campaigns is included:

- Danehy et al. [73] (2007): Installed triangular and rectangular trip elements 45° relative to the flow to simulate a gap filler protuberance on the Space Shuttle Orbiter. The pitch controlled the flow turn angles from $0° - 20°$ and thereby the boundary layer height. The trips were sized to be less than, equal to, and greater than the expected boundary layer heights across this range. A laser beam was sent through the boundary layer to determine its state via flow visualization. The beam position could be changed during a run to probe 3D structures. A filter was placed in front of the camera to attenuate scatter. The images were scaled, dewarped, and filtered in post processing. The laminar boundary layer thickness, measured with PLIF flow visualization, matched CFD predictions. It was found that when the trips were smaller, equivalent to, and larger than the boundary layer, the flow was laminar, tran-

sitional, and turbulent respectively. The larger rectangular trips seemed more effective than the triangular trips, but they caused the gas to flow around, not over, themselves; this effect is exacerbated for smaller boundary layers, emphasizing that trips' effects are enhanced for smaller boundary layers.

- Danehy et al. [74] (2009): Installed a hemispherical trip element to study its effect on hypersonic boundary layer transition. The flow turning angle was $5° - 25°$ which controlled the boundary layer thickness. Pure NO was injected between $0.03 - 1.0$slpm corresponding to $2 - 68\frac{\text{m}}{\text{s}}$; the majority of the tests were conducted at 0.3slpm ($20\frac{\text{m}}{\text{s}}$, 2.6% NO by mass). Injection of NO at this rate was not found to perturb the flow, which matches the findings in [28]; this was further confirmed through pressure measurements. Furthermore, at this rate the measured laminar boundary layer thickness matched CFD predictions. The NO was assumed frozen following Olbregts [209]. Both spanwise and wall-normal PLIF visualizations were taken to study the state of the boundary layer. The nonuniformity in the laser intensity was corrected to first order via normalization with the mean image. The hemispherical trip was most effective at fomenting transition at the higher angle of attack as incoming the boundary layer was thinner.

- Bathel et al. [16] (conference, 2010), Bathel et al. [22] (journal, 2011): A detailed look of the analysis necessary to perform PLIF 1D velocimetry using a double-frame camera. The technique allowed analysis of single-shot images with predicted uncertainty. Of particular interest was the correction to the spatial measurement due to the fluorescence decay of the NO during excitation and collection, similar to the correction taken in [77]. These corrections complicated the velocimetry analysis due to the introduction of chemistry effects, but they were shown to have a meaningful impact on the final result and were therefore necessary. The uncertainty analysis was also useful to the present work. It was noted that using a single camera with a double-frame feature helped remove uncertainty due to image correlation and tunnel/camera vibration; this was done at the cost of lower signal. Single-line velocimetry

was performed using light passed through a lens array; this was possible because the flow was fast enough that sufficient displacement was attained for a second collection before the fluorescence fully decayed.

- Bathel et al. [17] (2010): PLIF velocimetry campaign on a laminar and tripped (predominantly cylindrical trip) boundary layer. The flow turning angle was kept at 5°, and NO injection rates were limited to prevent flow perturbation following [28, 74]. Single-laser velocimetry was performed with multiple lines produced with a lens array for simultaneous measurement of several test locations; the data were collected with a single camera with a dual-image feature. The images were filtered, dewarped, binned, and background corrected to improve their clarity. Successive 1D cross-correlation and other work on uncertainty improved the accuracy of and confidence in the data over past work [16]. Possibly due to scatter saturating the camera, model vibration, and the sensitivity of the profiles near the wall, the no-slip condition at the wall appeared violated; also, perhaps due to low signal, there was comparatively high uncertainty at the outer edge of the boundary layer. Furthermore, especially near the NO inlet, one could not assume the NO permeated the entire boundary layer and entered the freestream, so the edge velocity measurements did not necessarily match the freestream values. That being said, excellent mean velocimetry along the plate was provided in both wall-normal and spanwise configurations. In conclusion, the authors recommended wall-normal measurements for improved resolution, but they advised against forgoing spanwise measurements entirely as these measurements illustrated broader flow features. These data were abetted by temperature sensitive paint measurements.

- Jiang et al. [126] (2010): Provided details regarding execution of 1MHz PLIF measurements. The wedge was used as a characteristic test article to integrate this technique into the 31-Inch Mach 10 Tunnel. Flow visualization of a tripped boundary layer revealed the temporal resolution was sufficient to track individual flow structures. More frames could be taken at 500kHz, so longer image sequences ($16-20$ *vs.* $8-10$ frames) were produced.

- Danehy et al. [75] (2010): Used PLIF visualization to study the flow around a rectangular and rounded-rectangle-like protuberance at 45° at varying temporal (10Hz, 500kHz) and spatial resolutions (high, low). The purpose was to compare the flow structure to those experienced in a boundary layer transition experiment on the Space Shuttle Orbiter. The flow was turned 20° to provide the desired boundary layer thickness. The model was rolled 1.5° to remove reflections from the laser passing through the tunnel windows in the viewing area; filters were placed in front of the cameras to further prevent scatter. The data were normalized by the laser intensity and spatial uniformity of the beam, and the process by which this was completed was outlined. Low-speed PLIF (low repetition rate) showed the efficacy of the trips was increased with the Reynolds number, and the sharp rectangle caused transition earlier than the rounded shape. High-speed PLIF visualized how the vortices break down into turbulence. The data were abetted by temperature sensitive paint measurements.

- Danehy et al. [76] (2010): PLIF visualization campaign of flow around a cylindrical trip. The boundary layer thickness was controlled via the test article pitch. Spanwise and streamwise flow visualization measurements were made. A 1MHz PLIF system was employed to produce movies of the flow. Furthermore, anaglyphs were produced in post-processing to create 3D images of the flow. The variations in laser intensity was only employed on the high-speed data; without this correction, and changes in intensity would need to be treated as qualitative. Different trip sizes, boundary layer thicknesses (controlled by pitch), and Reynolds numbers were tested. The data again confirmed that trips were more effective in thinner boundary layers and higher Reynolds numbers, but if the trips became too large the flow would go around, not over them; this last case is supported by oil flow visualization. It is interesting, but surprising to see, that for turbulent flows more NO is transported higher off the plate. By using two cameras and a thick laser sheet, stereoscopic PLIF measurements were taken to allow for 3D visualization of the boundary layer. The high-frequency visualization data showed the development of individual flow structures, and the authors noted that were it extended to velocimetry it would provide temporal resolution sufficient to compare

with high-frequency pressure and hotwire measurements.

- Bathel et al. [18] (2011): Used three-laser velocimetry to extend PLIF to higher stagnation pressures where the shorter fluorescence necessitate two excitation events. Conducted experiments in both laminar and tripped (cylinder) flows. A grid of NO was produced by photodissociating NO_2 with a 355nm beam; the ground vibrational NO was then probed with two sequential read sheets. A single camera with a dual-image feature was used. A UV window was mounted into the model to prevent damaging its surface with the pump beam. The authors described the data processing for this new technique in detail; for example, they showed how longer time delays between the two images and higher signal-to-noise ratios both reduced the uncertainty, and they also explored the effect of pressure on uncertainty. Both mean and single-shot data sets were presented, and fluctuations were demonstrated to increase in tripped boundary layers. It was shown that despite the plate heating from 308 to 350K during a run, there was no loss in signal or accuracy. A discrepancy between the measured and theoretical edge velocities was explored, but not definitively solved. Because of difficulties with non-uniform NO_2 photodissociation, as well as inter-line noise when probing the ground state NO it was recommended the latter problem be fixed by probing the first vibrational state of NO so only the tagged molecules fluoresce following [117].

- Bathel et al. [19] (2012): Used three-laser velocimetry to study the effect of inter-image time delay and gas injection rate on boundary layer perturbation. The PLIF setup was improved over that in [18] by changing camera timing to reduce scatter (at the cost of signal), using efficient UV mirrors to direct beams into the wind tunnel, changing the beam angles, and improving the spatial resolution by moving the camera closer to the test section. Several datasets were taken with no flow in order to quantify the uncertainty of the system and calibration other parameters; for example, it was shown higher signal-to-noise ratios and time delays between measurements reduced uncertainty at the cost of spatial resolution. The pressure uncertainty calculation proved the improvements made to the system reduced the

uncertainty compared to that in [18]. Furthermore, the authors found that increasing the time delay between the images had no effect but to reduce uncertainty so long as good signal could still be collected. Again, they found edge velocities much lower than anticipated attributed possible causes to poor edge condition estimation, flow perturbation due to injection, and insufficient seed penetration through the boundary layer; they wrote the lattermost was the most likely source of error. It was found that higher injection rates created larger flow velocity deficits and increased velocity perturbations, especially near the edge of the boundary layer; that said, higher blowing rates did reach farther through the boundary layer and provided better signal-to-noise, which reduced spatial uncertainty. Thus blowing rates must be fine-tuned as higher rates have both pros and cons. It was noted that either the thermal properties of the quartz window or cooling due to gas injection cause an unexpected thermal perturbation to the boundary layer. Furthermore, the no-slip condition at the wall appeared violated, likely due to scatter.

- Johansen and Danehy [127] (conference, 2012), Arisman et al. [7] (journal, 2015): Performed simulations of the wedge with different common PLIF species (NO, I_2, Kr) and injection rates to study injection's effect on the velocity boundary layer, the convection boundary layer, and the optimal balance between the two. Chemical reactions between NO and O_2 in the air were neglected. Diffusive gas seeding (no jet velocity) was found to deposit some gas into the boundary layer with no noticeable perturbation; under these conditions NO was the first gas with a concentration boundary layer exceeding the velocity boundary layer. For seeded simulations, the flow rate was 150sccm ($\sim 3\frac{\text{mg}}{\text{s}}$), which matched experimental work [22]. This manifested as a slight increase in both the velocity and temperature boundary layer thicknesses due to a weak oblique shock caused by the jet. The calculated velocity deficit was validated against experimental results. As the lightest gas, NO consistently had the largest concentration thickness, but due to the deflection caused by seeding the point at which the concentration boundary layer exceeded the velocity boundary layer moved downstream when the injection mass flow rate was increased. Also, the thermal boundary layer

was thicker than the velocity boundary layer, so it took more time to resolve.

- Arisman et al. [9] (conference, 2013), Arisman and Johansen [8] (journal, 2015): Computational effort of the wedge studying the effect of the exothermic $NO + O_2 \rightarrow 2NO_2$ reaction on laminar hypersonic boundary layers. The reaction occurs preferentially at low temperatures, but because the NO concentration boundary layer was smaller than the thermal boundary layer, most of the gas was kept near the wall and little NO_2 formed; the predicted amount was insufficient to perturb the boundary layer. When the boundary layer thickness changed (by altering the wedge's angle of attack) the reaction became unfrozen in different regions; for example, at a flow turn angle of 5°, NO_2 formation near the injection slot became important where it was not in this region for the 1° case. Indeed, temperature and NO concentration both affect the reaction, not just the former. The formation of N_2O_4 dimers was not considered, but the authors wrote it would negligibly impact the system's thermodynamics.

- Bathel et al. [21] (2013): A review paper of velocimetry techniques, including NO and $NO_2 \rightarrow NO$ photodissociation MTV on the wedge model.

- Bathel et al. [20] (2013): Extended three-laser $NO_2 - NO$ photolysis to tripped (cylinder) boundary layers and provided mean, instantaneous, and fluctuating velocity measurements. The effect of varying the trip height was studied. Image processing was improved over past efforts through new model displacement correction, signal-to-noise calculation, and data rejection procedures. An extensive database was provided in an appendix. The data were compared to computer laminar boundary layer profiles to qualitatively compare the efficacy of the trips at different spanwise locations.

- Bathel et al. [23] (2014): Compared DNS and single-laser MTV measurements around both hemispherical and cylindrical roughness elements in a laminar hypersonic boundary layer. The effect of gas injection on the laminar boundary layer was also studied. Solely comparing DNS data, it was observed gas injection could have a measurable increase on the laminar boundary layer thickness. However, for the cylindrical roughness element far from the trip,

the best agreement was between the DNS simulations without injection and the experiment; this was abetted by the hemispherical roughness element case. The authors concluded the DNS therefore over-predicted the impact gas injection had on the boundary layer. Near the cylindrical trip (scatter prevent near-wall measurements near the hemispherical trip), the simulation consistently under-predicted the measured velocities. An analysis revealed the camera collection window and non-streamwise velocity components were not the cause of this discrepancy. Ultimately no cause, experimental or numerical, was determined. These results were confirmed for the hemispherical roughness element.

- McDougall et al. [172] (2018): Performed PLIF thermometry on a laminar flow turned 5° using a single laser sheet scanned over a spectral range known to contain three isolated transitions; this required 75s to complete. A flush-mounted UV window and filter mounted to the single camera helped reduce scatter. The authors introduced five unique data fitting methods for each pixel's fluorescence *versus* wavelength plot, including two which include saturation corrections. All methods produced results which deviated significantly from a CFD simulation at the wall and above a certain height. The discrepancy in the former region was attributed to laser absorption, laser scatter, and/or a poorly measured wall temperature (especially as the model heats during a lengthy run) while that of the latter region may have been due to reflection obfuscating the signal. The authors recommended only using two transitions in future work, as the third, highest rotational state probed, $J = 17.5$, was sparsely populated. However, error bars produced by an uncertainty analysis showed experimental and CFD data agreed in the bulk of the region of interest.

- McDougall et al. [171] (2018): Used the temperature results in [172] to calculate heat flux and NO mole fraction, both relative and absolute. Because heat flux requires both a velocity measurement and a temperature profile, the former was provided with PLIF from Bathel et al. [22]. The heat flux could help correct the discrepancy in temperature measurement near the wall profile [172]. In general the accuracy of these techniques was limited by the accuracy

of the temperature and velocity profiles used, but here the NO concentration measurements had far better agreement with simulations [7, 8] than the heat flux measurements.

- McDougall et al. [173] (2020): Journal paper offering improvements over the analysis in [172] including eighteen thermometry methods, improved wall temperature estimation, and corrections for the reflection. A benefit of the techniques covered is that they are absolute, meaning they did not need to be calculated "relative" to a known location in the flow; they did, however, require detailed information on the beam such as laser linewidth and spectral resolution and were sensitive to absorbtion and saturation. The analysis included an exploration of these and other features on the results. It was shown two-line method used by Sanchez-Gonzalez [235] could provide good accuracy.

The above body of work covered the development of PLIF flow visualization, velocimetry, and thermometry in hypersonic laminar, transitional, and turbulent boundary layers. These works were largely motivated by the desire to understand transition in a hypersonic boundary layer. There is a natural progression in the complexity of the technique, from single laser spanwise flow visualization to three-laser MTV through a turbulent boundary layer. These experiments injected gas directly into the boundary layer, and while it was shown the effect can be minimal, it nevertheless introduced an point of uncertainty into the results and required dedicated analysis of any potential perturbations. Furthermore, for thermometry, one can only measure the temperature of the NO, not necessarily the bulk gas itself, without assuming the gas thermalizes downstream of injection. While the excellent signal is a benefit of this injection technique, it is clearly not without its drawbacks. The data processing, analysis, and uncertainty techniques employed were advanced and can be used in part or entirely to improve any calculations performed for the present work.

3. MODEL DERIVATION

The gradient diffusion approach for calculating turbulent heat flux q_i^T in a RANS solver was outlined in Section 2.2. Due to its simplicity and reasonable accuracy in the wall-normal direction, this technique is standard [293, 239]. Recall that it assumes one knows a turbulent Prandtl number (Pr_t) that can capture the physics of the turbulent heat flux. For many applications, it is indeed is sufficient to take $Pr_t = Constant = 0.9$. White [293], for example, made this argument by studying experimental data from Blackwell [33] and neglecting the measured deviation in Pr_t near the wall; the reasoning for the latter assumption was that most turbulence is dissipated in the viscous sublayer near the wall, so modest inaccuracies in Pr_t are inconsequential. Bowersox [38] analyzed both experimental and DNS data to show that this approach leads to inaccuracy in the estimation of the temperature profiles for high Mach numbers. A DNS replication of an experiment of a flat plate, cold wall boundary layer at $M = [11, 14]$ by Huang et al. [118] illustrated these discrepancies clearly (Figure 3.1), especially in streamwise predictions. Launder [153] argued the use of eddy viscosity and wall functions to capture the near wall convective heat transfer in high Reynolds number flows is an inferior modeling method to second moment turbulent energy flux closures.

These inaccuracies prompted the derivation of a novel model for the turbulent heat flux. Building on earlier efforts [72, 153], Bowersox provided a more formalized "algebraic energy flux" (AEF) model [38]. These seminal efforts provided the groundwork for the current AEF model and its extension to high speed gaseous shear flows. A key advantage of the algebraic model includes explicit expressions for all three heat flux components. However, the model is explicitly dependent on the Reynolds stress tensor. In their original paper [38], Bowersox used a classical algebraic eddy viscosity model for the Reynolds shear stress with DNS based correlations to recover realistic axial stresses that the Boussinesq approximation cannot directly provide. In early testing, up to 20% improvements in the temperature profile were observed over the constant Pr_t model. The comparisons in [218, 118] abet these findings. Bowersox also examined the relationship between

the AEF and the turbulent Prandtl number, which resulted in a simple near wall correction for the transverse component. However, this model remains beholden to the key issues behind the Boussinesq approximation.

This chapter is intended to expound on Bowersox's [38] paper and subsequent publications [218, 118]. The process will start with the governing equations and proceed all the way to implementation of the model in a 2D compressible boundary layer. Its contents were published in Broslawski et al. [46], and much of the same analysis is included here, but additional detail is provided in the derivation's steps.

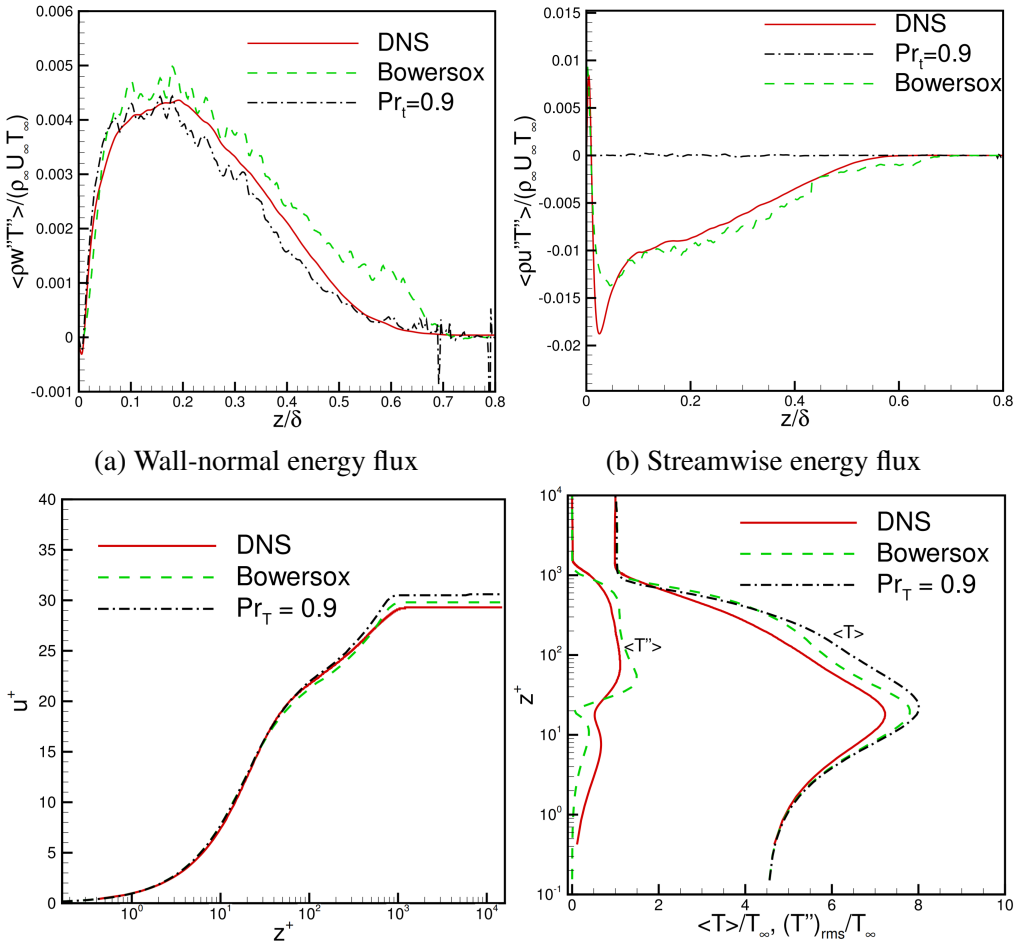

(a) Wall-normal energy flux

(b) Streamwise energy flux

(c) Wall-normal velocity profile

(d) Wall-normal temperature profile

Figure 3.1: Comparison of AEF, constant Pr_t, and DNS replication of a cold-wall, Mach 11 TBL over a flat plate; figures taken with permission from Huang et al. [118]

.

3.1 Governing Equations

The derivation begins by defining the governing equations for mass, momentum, and internal energy for a three-dimensional, compressible, viscous flow. The conservation (Eulerian) form used here is taken from [4]:

$$Mass : \rho_{,t} + (\rho u_k)_{,k} = 0 \tag{3.1}$$

$$Momentum : (\rho u_i)_{,t} + (\rho u_i u_k)_{,k} = -P_{,i} + \tau_{ik,k} \tag{3.2}$$

$$Energy : (\rho e)_{,t} + (\rho e u_k)_{,k} = -q_{k,k} + \tau_{kl} u_{l,k} - P u_{k,k} \tag{3.3}$$

The nonconservative (Lagrangian) form is supplied in the same source:

$$Mass : \rho_{,t} + u_k \rho_{,k} + \rho u_{k,k} = 0 \tag{3.4}$$

$$Momentum : \rho u_{i,t} + \rho u_{i,k} u_k = -P_{,i} + \tau_{ik,k} \tag{3.5}$$

$$Energy : \rho e_{,t} + \rho e_{,k} u_k = -q_{k,k} + \tau_{kl} u_{l,k} - P u_{k,k} \tag{3.6}$$

In these equations, all body forces have been neglected, the heat flux is defined by Fourier's law $q_k = -kT_{,k}$, the shear stress tensor is $\tau_{ij} = \mu\left(u_{i,j} + u_{j,i}\right) + \delta_{ij}\lambda u_{k,k}$, and e represents the fluid element's internal energy.

3.2 Turbulent Transport Equations

One can use the conservation equations to derive the exact turbulent energy transport equations. These equations can then be simplified via progressive assumptions to a form amenable to algebraic modeling. The process to produce such an equation follows a predictable pattern, so while as many as nine different transport equations will be needed, only those for the energy flux $\theta_i^T = \overline{\rho e'' u_i''}$, kinetic energy $k^T = \frac{1}{2}\overline{\rho u_i'' u_i''}$ (the diagonal of the turbulent Reynolds stress $\tau_{ij}^T = -\overline{\rho u_i'' u_j''}$), energy variance $\eta^T = \frac{1}{2}\overline{\rho e''^2}$, Favre-fluctuating velocity $\overline{\rho}\,\overline{u_i''}$ and Favre-fluctuating energy $\overline{\rho}\,\overline{e''}$ will be derived here. The steps are sufficiently generalized to be applicable to any subsequent transport

equation one may need, and enough detail is included to allow for accurate reproduction of the final results shown; as an additional reference, the process for deriving transport equations in the manner shown here was illustrated by Cebeci and Smith [55] and Liou and Shih [163]. Here the most attention is paid to deriving $\frac{D\theta_i^T}{Dt} = \theta_{i,t}^T + (\theta_i^T \tilde{u}_k)_{,k}$, with the goal of expanding on the derivation in [38], as it is the most relevant to the final model. Clarifying the simplifying assumptions and limitations was necessary to allow for further refinement.

3.2.1 Turbulent Energy Flux Transport Equation

Begin by taking the moment of the desired conservation equations; for θ_i^T, one must take the moment of the momentum (3.2) and energy (3.3) conservation equations, $e \cdot Momentum + u \cdot Energy$.

$$e\left[(\rho u_i)_{,t} + (\rho u_i u_k)_{,k} = -P_{,i} + \tau_{ik,k}\right] + u_i\left[(\rho e)_{,t} + (\rho e u_k)_{,k} = -q_{k,k} + \tau_{kl}u_{l,k} - Pu_{k,k}\right] \tag{3.7}$$

$$e(\rho u_i)_{,t} + e(\rho u_i u_k)_{,k} + u_i(\rho e)_{,t} + u_i(\rho e u_k)_{,k} = -eP_{,i} + e\tau_{ik,k} - u_i q_{k,k} + u_i\tau_{kl}u_{l,k} - u_i P u_{k,k} \tag{3.8}$$

The left hand side can be simplified using the Multiplication Rule and mass conservation equation (3.1).

$$(\rho u_i e)_{,t} + (\rho u_i e u_k)_{,k} = -eP_{,i} + e\tau_{ik,k} - u_i q_{k,k} + u_i\tau_{kl}u_{l,k} - u_i P u_{k,k} \tag{3.9}$$

Now expand the velocity and energy terms with Favre [89] averaging ($X = \tilde{X} + X''$) and the shear stress with Reynolds averaging ($Y = \overline{Y} + Y'$). Because $\overline{\rho X''} = 0$ and $\overline{Y'} = 0$ the application of each expansion is strategic; depending on the presence of density in a term's coefficients it can be advantageous to perform one expansion over the other.

$$\begin{aligned}
&(\rho(\tilde{u}_i + u_i'')(\tilde{e} + e''))_{,t} + (\rho(\tilde{u}_i + u_i'')(\tilde{e} + e'')(\tilde{u}_k + u_k''))_{,k} = \\
&-(\tilde{e} + e'')(\overline{P}_{,i} + P'_{,i}) - (\tilde{u}_i + u_i'')(\overline{P} + P')(\tilde{u}_k + u_k'')_{,k} - (\tilde{u}_i + u_i'')q_{k,k} \\
&+(\tilde{e} + e'')(\overline{\tau}_{ik} + \tau'_{ik})_{,k} + (\tilde{u}_i + u_i'')(\overline{\tau}_{kl} + \tau'_{kl})(\tilde{u}_l + u_l'')_{,k}
\end{aligned} \tag{3.10}$$

Perform all distributions, then Reynolds average and simplify the result; the terms which cancel

form the instantaneous equation and those which remain constitute the mean equation.

$$
\begin{aligned}
&(\overline{\rho}\tilde{u}_i\tilde{e} + \tilde{u}_i\cancel{\overline{\rho e''}} + \tilde{e}\cancel{\overline{\rho u_i''}} + \overline{\rho u_i'' e''})_{,t} \\
&+ (\overline{\rho}\tilde{u}_i\tilde{e}\tilde{u}_k + \tilde{u}_i\tilde{u}_k\cancel{\overline{\rho e''}} + \tilde{e}\tilde{u}_k\cancel{\overline{\rho u_i''}} + \tilde{u}_k\overline{\rho u_i'' e''} + \tilde{u}_i\tilde{e}\cancel{\overline{\rho u_k''}} + \tilde{u}_i\overline{\rho e'' u_k''} + \tilde{e}\overline{\rho u_i'' u_k''} + \overline{\rho u_i'' e'' u_k''})_{,k} = \\
&- \tilde{e}\overline{P}_{,i} - \tilde{e}\cancel{\overline{P'}_{,i}} - \overline{e''}\,\overline{P}_{,i} - \overline{e'' P'_{,i}} - \tilde{u}_i\overline{q_{k,k}} - \overline{u_i'' q_{k,k}} + \tilde{e}\,\overline{\tau}_{ik,k} + \tilde{e}\cancel{\overline{\tau'_{ik,k}}} + \overline{\tau}_{ik,k}\overline{e''} + \overline{e''\tau'_{ik,k}} \\
&- \tilde{u}_i\overline{P}\tilde{u}_{k,k} - \tilde{u}_i\cancel{\overline{P'}}\tilde{u}_{k,k} - \overline{u_i''}\,\overline{P}\tilde{u}_{k,k} - \overline{u_i'' P'}\tilde{u}_{k,k} - \tilde{u}_i\overline{P}\,\overline{u_{k,k}''} - \tilde{u}_i\overline{P' u_{k,k}''} - \overline{u_i'' u_{k,k}''}\,\overline{P} - \overline{u_i'' P' u_{k,k}''} \\
&+ \tilde{u}_i\tilde{u}_{l,k}\overline{\tau}_{kl} + \tilde{u}_i\tilde{u}_{l,k}\cancel{\overline{\tau'_{kl}}} + \overline{\tau}_{kl}\tilde{u}_{l,k}\overline{u_i''} + \tilde{u}_{l,k}\overline{u_i''\tau'_{kl}} + \tilde{u}_i\overline{\tau}_{kl}\overline{u''_{l,k}} + \tilde{u}_i\overline{\tau'_{kl}u''_{l,k}} + \overline{\tau}_{kl}\overline{u_i'' u''_{l,k}} + \overline{u_i''\tau'_{kl}u''_{l,k}}
\end{aligned}
\tag{3.11}
$$

$$
\begin{aligned}
&(\overline{\rho}\tilde{u}_i\tilde{e} + \overline{\rho u_i'' e''})_{,t} + (\overline{\rho}\tilde{u}_i\tilde{e}\tilde{u}_k + \tilde{u}_k\overline{\rho u_i'' e''} + \tilde{u}_i\overline{\rho e'' u_k''} + \tilde{e}\overline{\rho u_i'' u_k''} + \overline{\rho u_i'' e'' u_k''})_{,k} = \\
&- \tilde{e}\overline{P}_{,i} - \overline{e''}\,\overline{P}_{,i} - \overline{e'' P'_{,i}} - \tilde{u}_i\overline{q_{k,k}} - \overline{u_i'' q_{k,k}} + \tilde{e}\,\overline{\tau}_{ik,k} + \overline{\tau}_{ik,k}\overline{e''} + \overline{e''\tau'_{ik,k}} \\
&- \tilde{u}_i\overline{P}\tilde{u}_{k,k} - \overline{u_i''}\,\overline{P}\tilde{u}_{k,k} - \overline{u_i'' P'}\tilde{u}_{k,k} - \tilde{u}_i\overline{P}\,\overline{u_{k,k}''} - \tilde{u}_i\overline{P' u_{k,k}''} - \overline{u_i'' u_{k,k}''}\,\overline{P} - \overline{u_i'' P' u_{k,k}''} \\
&+ \tilde{u}_i\tilde{u}_{l,k}\overline{\tau}_{kl} + \overline{\tau}_{kl}\tilde{u}_{l,k}\overline{u_i''} + \tilde{u}_{l,k}\overline{u_i''\tau'_{kl}} + \tilde{u}_i\overline{\tau}_{kl}\overline{u''_{l,k}} + \tilde{u}_i\overline{\tau'_{kl}u''_{l,k}} + \overline{\tau}_{kl}\overline{u_i'' u''_{l,k}} + \overline{u_i''\tau'_{kl}u''_{l,k}}
\end{aligned}
\tag{3.12}
$$

While Equation 3.12 is technically a mean equation, by subtracting its analog derived from the mean conservation equations one is left with a transport equation for the mean energy flux of the fluctuations (adopting the notation of [55]). To get the transport equation of the energy flux of the base flow, as before expand Equations 3.2 and 3.3 and Reynolds average the result to produce the mean momentum and energy equations. Begin with the conservation of momentum:

$$
(\rho(\tilde{u}_i + u_i''))_{,t} + (\rho(\tilde{u}_i + u_i'')(\tilde{u}_k + u_k''))_{,k} = -(\overline{P}_{,i} + P'_{,i}) + (\overline{\tau}_{ik,k} + \tau'_{ik,k}) \tag{3.13}
$$

$$
(\overline{\rho}\tilde{u}_i + \cancel{\overline{\rho u_i''}})_{,t} + (\overline{\rho}\tilde{u}_i\tilde{u}_k + \cancel{\overline{\rho u_i''}}\tilde{u}_k + \cancel{\overline{\rho u_k''}}\tilde{u}_i + \overline{\rho u_i'' u_k''})_{,k} = -(\overline{P}_{,i} + \cancel{\overline{P'}_{,i}}) + (\overline{\tau}_{ik,k} + \cancel{\overline{\tau'_{ik,k}}}) \tag{3.14}
$$

$$
(\overline{\rho}\tilde{u}_i)_{,t} + (\overline{\rho}\tilde{u}_i\tilde{u}_k)_{,k} = -\overline{P}_{,i} + \overline{\tau_{ik,k}} - (\overline{\rho u_i'' u_k''})_{,k} \tag{3.15}
$$

Similarly, for the conservation of energy:

$$
(\rho(\tilde{e} + e''))_{,t} + (\rho(\tilde{e} + e'')(\tilde{u}_k + u_k''))_{,k} = -q_{k,k} + (\overline{\tau}_{kl} + \tau'_{kl})(\tilde{u}_{l,k} + u''_{l,k}) - (\overline{P} + P')(\tilde{u}_{k,k} + u''_{k,k}) \tag{3.16}
$$

$$(\overline{\rho}\tilde{e}+\cancel{\overline{\rho e''}})_{,t}+(\tilde{e}\tilde{u}_k\overline{\rho}+\tilde{u}_k\cancel{\overline{\rho e''}}+\tilde{e}\cancel{\overline{\rho u''_k}}+\overline{\rho e''u''_k})_{,k}=$$
$$-\overline{q}_{k,k}+\overline{\tau}_{kl}\tilde{u}_{l,k}+\overline{\tau}_{kl}\overline{u''_{l,k}}+\cancel{\overline{\tau'_{kl}}\tilde{u}_{l,k}}+\overline{\tau'_{kl}u''_{l,k}}-(\overline{P}\tilde{u}_{k,k}+\tilde{u}_{k,k}\cancel{\overline{P'}}+\overline{P}\,\overline{u''_{k,k}}+\overline{P'u''_{k,k}}) \tag{3.17}$$

$$(\overline{\rho}\tilde{e})_{,t}+(\tilde{e}\tilde{u}_k\overline{\rho}+\overline{\rho e''u''_k})_{,k}=-\overline{q_{k,k}}+\overline{\tau}_{kl}\tilde{u}_{l,k}+\overline{\tau}_{kl}\overline{u''_{l,k}}+\overline{\tau'_{kl}u''_{l,k}}-(\overline{P}\tilde{u}_{k,k}+\overline{P}\,\overline{u''_{k,k}}+\overline{P'u''_{k,k}}) \tag{3.18}$$

Now take the moment of these mean expressions, Equations 3.15 and 3.18. Simplify the left hand side with the Multiplication Rule.

$$\tilde{e}\left[(\overline{\rho}\tilde{u}_i)_{,t}+(\overline{\rho}\tilde{u}_i\tilde{u}_k)_{,k}=-\overline{P}_{,i}+\overline{\tau_{ik,k}}-(\overline{\rho u''_iu''_k})_{,k}\right]$$
$$+\tilde{u}_i\left[(\overline{\rho}\tilde{e})_{,t}+(\tilde{e}\tilde{u}_k\overline{\rho}+\overline{\rho e''u''_k})_{,k}=-\overline{q_{k,k}}+\overline{\tau}_{kl}\tilde{u}_{l,k}+\overline{\tau}_{kl}\overline{u''_{l,k}}+\overline{\tau'_{kl}u''_{l,k}}-(\overline{P}\tilde{u}_{k,k}+\overline{P}\,\overline{u''_{k,k}}+\overline{P'u''_{k,k}})\right] \tag{3.19}$$

$$(\overline{\rho}\tilde{e}\tilde{u}_i)_{,t}+\tilde{u}_i(\overline{\rho e''u''_k})_{,k}+(\overline{\rho}\tilde{u}_i\tilde{u}_k\tilde{e})_{,k}=-\tilde{e}\overline{P}_{,i}+\tilde{e}\,\overline{\tau_{ik,k}}-\tilde{e}(\overline{\rho u''_iu''_k})_{,k}$$
$$-\tilde{u}_i\overline{q_{k,k}}+\tilde{u}_i\overline{\tau}_{kl}\tilde{u}_{l,k}+\tilde{u}_i\overline{\tau}_{kl}\overline{u''_{l,k}}+\tilde{u}_i\overline{\tau'_{kl}u''_{l,k}}-\tilde{u}_i\overline{P}\tilde{u}_{k,k}-\tilde{u}_i\overline{P}\,\overline{u''_{k,k}}-\tilde{u}_i\overline{P'u''_{k,k}} \tag{3.20}$$

In order to derive the mean energy flux of the fluctuations transport equation subtract the mean equation (3.20) from Equation (3.12).

$$\begin{aligned}
&\cancel{(\overline{\rho}\tilde{u}_i\tilde{e}}+\overline{\rho u''_ie''})_{,t}-\cancel{[(\overline{\rho}\tilde{e}\tilde{u}_i)_{,t}]}+\tilde{u}_{i,k}\overline{\rho e''u''_k}+\cancel{\tilde{u}_i(\overline{\rho e''u''_k})_{,k}}-\cancel{\left[\tilde{u}_i(\overline{\rho e''u''_k})_{,k}\right]}\\
&+(\cancel{\overline{\rho}\tilde{u}_i\tilde{e}\tilde{u}_k}+\tilde{u}_k\overline{\rho u''_ie''}+\tilde{e}\overline{\rho u''_iu''_k}+\overline{\rho u''_ie''u''_k})_{,k}-\cancel{\left[(\overline{\rho}\tilde{u}_i\tilde{u}_k\tilde{e})_{,k}\right]}=-\left[-\tilde{e}(\overline{\rho u''_iu''_k})_{,k}\right]\\
&-\cancel{\tilde{e}\overline{P}_{,i}}-\overline{e''}\,\overline{P}_{,i}-\overline{e''P'_{,i}}-\cancel{\left[-\tilde{e}\overline{P}_{,i}\right]}-\cancel{\tilde{u}_i\overline{q_{k,k}}}-\overline{u''_iq_{k,k}}-\cancel{\left[-\tilde{u}_i\overline{q_{k,k}}\right]}\\
&-\cancel{\tilde{u}_i\overline{P}\tilde{u}_{k,k}}-\overline{u''_i}\,P\tilde{u}_{k,k}-\overline{u''_iP'}\tilde{u}_{k,k}-\cancel{\tilde{u}_i\overline{P}\,\overline{u''_{k,k}}}-\cancel{\tilde{u}_i\overline{P'u''_{k,k}}}-\overline{u''_iu''_{k,k}}\,\overline{P}-\overline{u''_iP'u''_{k,k}}\\
&-\cancel{\left[-\tilde{u}_i\overline{P}\tilde{u}_{k,k}-\tilde{u}_i\overline{P}\,\overline{u''_{k,k}}-\tilde{u}_i\overline{P'u''_{k,k}}\right]}+\cancel{\tilde{e}\overline{\tau}_{ik,k}}+\overline{\tau}_{ik,k}\overline{e''}+\overline{e''\tau'_{ik,k}}-\cancel{\left[\tilde{e}\overline{\tau}_{ik,k}\right]}\\
&+\cancel{\tilde{u}_i\tilde{u}_{l,k}\overline{\tau}_{kl}}+\overline{\tau}_{kl}\tilde{u}_{l,k}\overline{u''_i}+\tilde{u}_{l,k}\overline{u''_i\tau'_{kl}}+\cancel{\tilde{u}_i\overline{\tau}_{kl}\overline{u''_{l,k}}}+\cancel{\tilde{u}_i\overline{\tau'_{kl}u''_{l,k}}}+\overline{\tau}_{kl}\overline{u''_iu''_{l,k}}+\overline{u''_i\tau'_{kl}u''_{l,k}}\\
&-\cancel{\left[\tilde{u}_i\overline{\tau}_{kl}\overline{u''_{l,k}}+\tilde{u}_i\overline{\tau}_{kl}\tilde{u}_{l,k}+\tilde{u}_i\overline{\tau'_{kl}u''_{l,k}}\right]}
\end{aligned} \tag{3.21}$$

$$\begin{aligned}
&(\overline{\rho u''_ie''})_{,t}+\tilde{u}_{i,k}\overline{\rho e''u''_k}+(\tilde{u}_k\overline{\rho u''_ie''}+\tilde{e}\overline{\rho u''_iu''_k}+\overline{\rho u''_ie''u''_k})_{,k}=\tilde{e}(\overline{\rho u''_iu''_k})_{,k}\\
&-\overline{e''}\,\overline{P}_{,i}-\overline{e''P'_{,i}}-\overline{u''_iq_{k,k}}-\overline{u''_i}\,\overline{P}\tilde{u}_{k,k}-\overline{u''_iP'}\tilde{u}_{k,k}-\overline{u''_iu''_{k,k}}\,\overline{P}-\overline{u''_iP'u''_{k,k}}\\
&+\overline{\tau}_{kl}\tilde{u}_{l,k}\overline{u''_i}+\overline{\tau}_{ik,k}\overline{e''}+\overline{e''\tau'_{ik,k}}+\tilde{u}_{l,k}\overline{u''_i\tau'_{kl}}+\overline{\tau}_{kl}\overline{u''_iu''_{l,k}}+\overline{u''_i\tau'_{kl}u''_{l,k}}
\end{aligned} \tag{3.22}$$

The left hand side can be simplified by using the material derivative, as well as with the Multipli-

cation Rule $-(\overline{\rho u_i'' u_k''})\tilde{e}_{,k} = -(\tilde{e}\overline{\rho u_i'' u_k''})_{,k} + \tilde{e}(\overline{\rho u_i'' u_k''})_{,k}$. The Multiplication Rule can also be used to write $\overline{e'' P'_{,i}} = \left(\overline{e'' P'}\right)_{,i} - \overline{e''_{,i} P'}$; this step is not intuitive, but it will be seen the result allows for simplification in Section 3.3.

$$\frac{D\theta_i^T}{Dt} = -\tilde{u}_{i,k}\theta_k^T + \tilde{e}_{,k}\tau_{ik}^T - \left(\overline{\rho u_i'' e'' u_k''}\right)_{,k} - \overline{e''}\,\overline{P}_{,i} - \left(\overline{e'' P'}\right)_{,i} + \overline{e''_{,i} P'} - \overline{u_i'' q_{k,k}} - \overline{u_i''}\,\overline{P}\tilde{u}_{k,k} - \overline{u_i'' P'}\tilde{u}_{k,k}$$
$$- \overline{u_i'' u_{k,k}''}\,\overline{P} - \overline{u_i'' P' u_{k,k}''} + \overline{\tau}_{kl}\tilde{u}_{l,k}\overline{u_i''} + \overline{\tau}_{ik,k}\overline{e''} + \overline{e''\tau'_{ik,k}} + \tilde{u}_{l,k}\overline{u_i''\tau'_{kl}} + \overline{\tau}_{kl}\overline{u_i'' u_{l,k}''} + \overline{u_i''\tau'_{kl}u''_{l,k}} \tag{3.23}$$

For now all that remains is to group the transport/diffusion (defined here as $\overline{X_i''}_{,i}$ or $\overline{Y'}_{,i}$), dissipation (τ), triple correlation ($X''Y''Z''$ or $X'Y'Z'$), and molecular (q) terms into a dummy variable $\overline{\rho}\xi_i$. With this, the transport equation is of the form shown by Bowersox [38].

$$\frac{D\theta_i^T}{Dt} = -\tilde{u}_{i,k}\theta_k^T + \tilde{e}_{,k}\tau_{ik}^T - \overline{e''}\,\overline{P}_{,i} + \overline{e''_{,i} P'} - \left[\overline{u_i''}\,\overline{P} + \overline{u_i'' P'}\right]\tilde{u}_{k,k} - \overline{u_i'' u_{k,k}''}\,\overline{P} + \overline{\rho}\xi_i \tag{3.24}$$

3.2.2 Turbulent Kinetic Energy Flux Transport Equation

The mean equation is the result of taking the moment of the conservation of momentum (Equation 3.2) with itself according to $u_i * (Momentum_j) + u_j * (Momentum_i)$, expanding the terms with Reynolds and Favre averaging, then Reynolds averaging the result to remove the instantaneous terms.

$$u_i\left[(\rho u_j)_{,t} + (\rho u_j u_k)_{,k} = -P_{,j} + \tau_{jk,k}\right] + u_j\left[(\rho u_i)_{,t} + (\rho u_i u_k)_{,k} = -P_{,i} + \tau_{ik,k}\right] \tag{3.25}$$

$$u_i(\rho u_j)_{,t} + u_i(\rho u_j u_k)_{,k} + u_j(\rho u_i)_{,t} + u_j(\rho u_i u_k)_{,k} = -u_i P_{,j} + u_i\tau_{jk,k} - u_j P_{,i} + u_j\tau_{ik,k} \tag{3.26}$$

$$(\rho u_i u_j)_{,t} + (\rho u_i u_j u_k)_{,k} = -u_i P_{,j} + u_i\tau_{jk,k} - u_j P_{,i} + u_j\tau_{ik,k} \tag{3.27}$$

$$(\rho(\tilde{u}_i + u_i'')(\tilde{u}_j + u_j''))_{,t} + (\rho(\tilde{u}_i + u_i'')(\tilde{u}_j + u_j'')(\tilde{u}_k + u_k''))_{,k} =$$
$$-(\tilde{u}_i + u_i'')(\overline{P}_{,j} + P'_{,j}) + (\tilde{u}_i + u_i'')(\overline{\tau}_{jk,k} + \tau'_{jk,k}) - (\tilde{u}_j + u_j'')(\overline{P}_{,i} + P'_{,i}) + (\tilde{u}_j + u_j'')(\overline{\tau}_{ik,k} + \tau'_{ik,k}) \tag{3.28}$$

$$
\begin{aligned}
&(\overline{\rho}\tilde{u}_i\tilde{u}_j + \cancel{\overline{\rho u_j''}\tilde{u}_i} + \cancel{\overline{\rho u_i''}\tilde{u}_j} + \overline{\rho u_i'' u_j''})_{,t} + ... \\
&(\overline{\rho}\tilde{u}_i\tilde{u}_j\tilde{u}_k + \cancel{\overline{\rho u_i''}\tilde{u}_j\tilde{u}_k} + \cancel{\overline{\rho u_k''}\tilde{u}_i\tilde{u}_j} + \overline{\rho u_i'' u_k''}\tilde{u}_j + \cancel{\overline{\rho u_j''}\tilde{u}_i\tilde{u}_k} + \overline{\rho u_i'' u_j''}\tilde{u}_k + \overline{\rho u_j'' u_k''}\tilde{u}_i + \overline{\rho u_i'' u_j'' u_k''})_{,k} = \\
&-\tilde{u}_i\overline{P}_{,j} - \tilde{u}_i\cancel{\overline{P'}_{,j}} - \overline{u_i''}\,\overline{P}_{,j} - \overline{u_i'' P'_{,j}} + \tilde{u}_i\overline{\tau}_{jk,k} + \tilde{u}_i\cancel{\overline{\tau'_{jk,k}}} + \overline{u_i''}\,\overline{\tau}_{jk,k} + \overline{u_i''\tau'_{jk,k}} \\
&-\tilde{u}_j\overline{P}_{,i} - \tilde{u}_j\cancel{\overline{P'}_{,i}} - \overline{u_j''}\,\overline{P}_{,i} - \overline{u_j'' P'_{,i}} + \tilde{u}_j\overline{\tau}_{ik,k} + \tilde{u}_j\cancel{\overline{\tau'_{ik,k}}} + \overline{u_j''}\,\overline{\tau}_{ik,k} + \overline{u_j''\tau'_{ik,k}}
\end{aligned}
\tag{3.29}
$$

$$
\begin{aligned}
&(\overline{\rho}\tilde{u}_i\tilde{u}_j + \overline{\rho u_i'' u_j''})_{,t} + (\overline{\rho}\tilde{u}_i\tilde{u}_j\tilde{u}_k + \overline{\rho u_i'' u_k''}\tilde{u}_j + \overline{\rho u_i'' u_j''}\tilde{u}_k + \overline{\rho u_j'' u_k''}\tilde{u}_i + \overline{\rho u_i'' u_j'' u_k''})_{,k} = \\
&-\tilde{u}_i\overline{P}_{,j} - \overline{u_i''}\,\overline{P}_{,j} - \overline{u_i'' P'_{,j}} + \tilde{u}_i\overline{\tau}_{jk,k} + \overline{u_i''}\,\overline{\tau}_{jk,k} + \overline{u_i''\tau'_{jk,k}} \\
&-\tilde{u}_j\overline{P}_{,i} - \overline{u_j''}\,\overline{P}_{,i} - \overline{u_j'' P'_{,i}} + \tilde{u}_j\overline{\tau}_{ik,k} + \overline{u_j''}\,\overline{\tau}_{ik,k} + \overline{u_j''\tau'_{ik,k}}
\end{aligned}
\tag{3.30}
$$

Taking the moment of the mean conservation of momentum equation (3.15) with itself produces

$$
\begin{aligned}
&\tilde{u}_i\left[(\overline{\rho}\tilde{u}_j)_{,t} + (\overline{\rho}\tilde{u}_j\tilde{u}_k)_{,k} = -\overline{P}_{,j} + (\overline{\tau}_{jk} - \overline{\rho u_j'' u_k''})_{,k}\right] \\
&+\tilde{u}_j\left[(\overline{\rho}\tilde{u}_i)_{,t} + (\overline{\rho}\tilde{u}_i\tilde{u}_k)_{,k} = -\overline{P}_{,i} + (\overline{\tau}_{ik} - \overline{\rho u_i'' u_k''})_{,k}\right]
\end{aligned}
\tag{3.31}
$$

$$
(\overline{\rho}\tilde{u}_i\tilde{u}_j)_{,t} + (\overline{\rho}\tilde{u}_i\tilde{u}_j\tilde{u}_k)_{,k} = -\tilde{u}_i\overline{P}_{,j} + \tilde{u}_i\overline{\tau}_{jk,k} - \tilde{u}_i(\overline{\rho u_j'' u_k''})_{,k} - \tilde{u}_j\overline{P}_{,i} + \tilde{u}_j\overline{\tau}_{ik,k} - \tilde{u}_j(\overline{\rho u_i'' u_k''})_{,k} \tag{3.32}
$$

Subtracting Equation 3.32 from Equation 3.30 produces the Reynolds stress transport equation.

$$
\begin{aligned}
&(\cancel{\overline{\rho}\tilde{u}_i\tilde{u}_j} + \overline{\rho u_i'' u_j''})_{,t} + (\cancel{\overline{\rho}\tilde{u}_i\tilde{u}_j\tilde{u}_k} + \overline{\rho u_i'' u_k''}\tilde{u}_j + \overline{\rho u_i'' u_j''}\tilde{u}_k + \overline{\rho u_j'' u_k''}\tilde{u}_i + \overline{\rho u_i'' u_j'' u_k''})_{,k} \\
&-\left[\cancel{(\overline{\rho}\tilde{u}_i\tilde{u}_j)_{,t}} + \cancel{(\overline{\rho}\tilde{u}_i\tilde{u}_j\tilde{u}_k)_{,k}}\right] = \\
&-\cancel{\tilde{u}_i\overline{P}_{,j}} - \overline{u_i''}\,\overline{P}_{,j} - \overline{u_i'' P'_{,j}} + \cancel{\tilde{u}_i\overline{\tau}_{jk,k}} + \overline{u_i''}\,\overline{\tau}_{jk,k} + \overline{u_i''\tau'_{jk,k}} - \left[-\cancel{\tilde{u}_i\overline{P}_{,j}} + \cancel{\tilde{u}_i\overline{\tau}_{jk,k}} - \tilde{u}_i(\overline{\rho u_j'' u_k''})_{,k}\right] \\
&-\cancel{\tilde{u}_j\overline{P}_{,i}} - \overline{u_j''}\,\overline{P}_{,i} - \overline{u_j'' P'_{,i}} + \cancel{\tilde{u}_j\overline{\tau}_{ik,k}} + \overline{u_j''}\,\overline{\tau}_{ik,k} + \overline{u_j''\tau'_{ik,k}} - \left[-\cancel{\tilde{u}_j\overline{P}_{,i}} + \cancel{\tilde{u}_j\overline{\tau}_{ik,k}} - \tilde{u}_j(\overline{\rho u_i'' u_k''})_{,k}\right]
\end{aligned}
\tag{3.33}
$$

$$
\begin{aligned}
&(\overline{\rho u_i'' u_j''})_{,t} + (\overline{\rho u_i'' u_j''}\tilde{u}_k)_{,k} = -(\overline{\rho u_i'' u_j'' u_k''})_{,k} - \overline{u_i''}\,\overline{P}_{,j} - \overline{u_i'' P'_{,j}} - \overline{u_j''}\,\overline{P}_{,i} - \overline{u_j'' P'_{,i}} \\
&+\overline{u_i''}\,\overline{\tau}_{jk,k} + \overline{u_i''\tau'_{jk,k}} + \tilde{u}_i(\overline{\rho u_j'' u_k''})_{,k} - (\overline{\rho u_j'' u_k''}\tilde{u}_i)_{,k} \\
&+\overline{u_j''}\,\overline{\tau}_{ik,k} + \overline{u_j''\tau'_{ik,k}} + \tilde{u}_j(\overline{\rho u_i'' u_k''})_{,k} - (\overline{\rho u_i'' u_k''}\tilde{u}_j)_{,k}
\end{aligned}
\tag{3.34}
$$

$$\begin{aligned}\frac{D\tau_{ij}^T}{Dt} &= (\overline{\rho u_i'' u_j'' u_k''})_{,k} + \overline{u_i''}\,\overline{P}_{,j} + \overline{u_i'' P'_{,j}} + \overline{u_j''}\,\overline{P}_{,i} + \overline{u_j'' P'_{,i}} \\ &- \overline{u_i''}\,\overline{\tau}_{jk,k} - \overline{u_i'' \tau'_{jk,k}} - \tilde{u}_{i,k}\tau_{jk}^T - \overline{u_j''}\,\overline{\tau}_{ik,k} - \overline{u_j'' \tau'_{ik,k}} - \tilde{u}_{j,k}\tau_{ik}^T\end{aligned} \tag{3.35}$$

If i = j, the above equation becomes the mean turbulent kinetic energy transport equation.

$$\frac{Dk^T}{Dt} = -\frac{1}{2}(\overline{\rho u_i'' u_i'' u_k''})_{,k} - \overline{u_i''}\,\overline{P}_{,i} - \overline{u_i'' P'_{,i}} + \overline{u_i''}\,\overline{\tau}_{ik,k} + \overline{u_i'' \tau'_{ik,k}} + \tilde{u}_{i,k}\tau_{ik}^T \tag{3.36}$$

It is noted that if one collapses the pressure term in Equations 3.35 and 3.36 and adds the $\overline{u_i''}\overline{\tau}_{ik,k}$ terms erroneously omitted, the equations match the form of those derived in [55].

3.2.3 Turbulent Energy Variance Transport Equation

The mean equation is the result of taking the moment of the conservation of energy (3.3) with itself according to $e*(Energy)+e*(Energy)$, expanding the terms with Reynolds and Favre averaging, then Reynolds averaging the result to eliminate the instantaneous terms.

$$2e\left[(\rho e)_{,t} + (\rho e u_k)_{,k} = -q_{k,k} + \tau_{kl}u_{l,k} - Pu_{k,k}\right] \tag{3.37}$$

$$e(\rho e)_{,t} + e(\rho e)_{,t} + e(\rho e u_k)_{,k} + e(\rho e u_k)_{,k} = -2eq_{k,k} + 2e\tau_{kl}u_{l,k} - 2ePu_{k,k} \tag{3.38}$$

$$\frac{1}{2}(\rho e^2)_{,t} + \frac{1}{2}(\rho e^2 u_k)_{,k} = -eq_{k,k} + e\tau_{kl}u_{l,k} - ePu_{k,k} \tag{3.39}$$

$$\begin{aligned}&\frac{1}{2}(\rho(\tilde{e}+e'')^2)_{,t} + \frac{1}{2}(\rho(\tilde{e}+e'')^2(\tilde{u}_k+u_k''))_{,k} = ... \\ &-(\tilde{e}+e'')q_{k,k} + (\tilde{e}+e'')(\overline{\tau}_{kl}+\tau'_{kl})(\overline{u}_{l,k}+u''_{l,k}) - (\tilde{e}+e'')(\overline{P}+P')(\tilde{u}_{k,k}+u''_{k,k})\end{aligned} \tag{3.40}$$

$$\begin{aligned}&\frac{1}{2}(\overline{\rho}\tilde{e}^2 + \tilde{e}\cancel{\overline{\rho e''}} + \tilde{e}\cancel{\overline{\rho e''}} + \overline{\rho e''^2})_{,t}... \\ &+\frac{1}{2}(\overline{\rho}\tilde{e}^2\tilde{u}_k + \tilde{e}\tilde{u}_k\cancel{\overline{\rho e''}} + \tilde{e}\tilde{u}_k\cancel{\overline{\rho e''}} + \tilde{u}_k\overline{\rho e''^2} + \tilde{e}^2\cancel{\overline{\rho u_k''}} + \tilde{e}\overline{\rho e'' u_k''} + \tilde{e}\overline{\rho e'' u_k''} + \overline{\rho e''^2 u_k''})_{,k} = ... \\ &-\tilde{e}\,\overline{q}_{k,k} - \overline{e'' q_{k,k}} + \tilde{e}\overline{\tau}_{kl}\overline{u}_{l,k} + \tilde{e}\,\overline{u}_{l,k}\cancel{\overline{\tau'_{kl}}} + \overline{e''\tau}_{kl}\overline{u}_{l,k} + \overline{e''\tau'_{kl}}\overline{u}_{l,k} + ... \\ &\tilde{e}\,\overline{\tau}_{kl}\overline{u''_{l,k}} + \tilde{e}\overline{\tau'_{kl}u''_{l,k}} + \overline{\tau}_{kl}\overline{e''u''_{l,k}} + \overline{e''\tau'_{kl}u''_{l,k}}... \\ &-\tilde{e}\overline{P}\tilde{u}_{k,k} - \tilde{e}\tilde{u}_{k,k}\cancel{\overline{P'}} - \overline{e''}\,\overline{P}\tilde{u}_{k,k} - \tilde{u}_{k,k}\overline{e''P'} - \tilde{e}\overline{P}\,\overline{u''_{k,k}} - \tilde{e}\overline{P'u''_{k,k}} - \overline{P}\,\overline{e''u''_{k,k}} - \overline{e''P'u''_{k,k}}\end{aligned} \tag{3.41}$$

$$\frac{1}{2}(\overline{\rho}\tilde{e}^2+\overline{\rho e''^2})_{,t}+\frac{1}{2}(\overline{\rho}\tilde{e}^2\tilde{u}_k+\tilde{u}_k\overline{\rho e''^2}+\tilde{e}\overline{\rho e''u''_k}+\tilde{e}\overline{\rho e''u''_k}+\overline{\rho e''^2u''_k})_{,k}=...$$
$$-\tilde{e}\,\overline{q}_{k,k}-\overline{e''q_{k,k}}+\tilde{e}\,\overline{\tau}_{kl}\overline{u}_{l,k}+\overline{e''\tau}_{kl}\overline{u}_{l,k}+\overline{e''\tau'_{kl}}\overline{u}_{l,k}+\tilde{e}\,\overline{\tau}_{kl}\overline{u''_{l,k}}+\tilde{e}\overline{\tau'_{kl}u''_{l,k}}+\overline{\tau}_{kl}\overline{e''u''_{l,k}}+\overline{e''\tau'_{kl}u''_{l,k}}...$$
$$-\tilde{e}\overline{P}\tilde{u}_{k,k}-\overline{e''\,P}\tilde{u}_{k,k}-\tilde{u}_{k,k}\overline{e''P'}-\tilde{e}\overline{P}\,\overline{u''_{k,k}}-\tilde{e}\overline{P'u''_{k,k}}-\overline{P}\,\overline{e''u''_{k,k}}-\overline{e''P'u''_{k,k}} \tag{3.42}$$

Taking the moment of the mean conservation of energy equation (Equation 3.18) with itself produces

$$2\tilde{e}\left[(\overline{\rho}\tilde{e})_{,t}+(\tilde{e}\tilde{u}_k\overline{\rho}+\overline{\rho e''u''_k})_{,k}=-\overline{q_{k,k}}+\overline{\tau}_{kl}\tilde{u}_{l,k}+\overline{\tau}_{kl}\overline{u''_{l,k}}+\overline{\tau'_{kl}u''_{l,k}}-(\overline{P}\tilde{u}_{k,k}+\overline{P}\,\overline{u''_{k,k}}+\overline{P'u''_{k,k}})\right] \tag{3.43}$$

$$\frac{1}{2}(\overline{\rho}\tilde{e}^2)_{,t}+\frac{1}{2}(\tilde{e}^2\tilde{u}_k\overline{\rho})_{,k}+\tilde{e}(\overline{\rho e''u''_k})_{,k}=...$$
$$-\tilde{e}\,\overline{q_{k,k}}+\tilde{e}\overline{\tau}_{kl}\tilde{u}_{l,k}+\tilde{e}\overline{\tau}_{kl}\overline{u''_{l,k}}+\tilde{e}\overline{\tau'_{kl}u''_{l,k}}-\tilde{e}\overline{P}\tilde{u}_{k,k}-\tilde{e}\overline{P}\,\overline{u''_{k,k}}-\tilde{e}\overline{P'u''_{k,k}} \tag{3.44}$$

Subtracting Equation 3.44 from Equation 3.42 produces the mean energy variance of the fluctuations transport equation.

$$\frac{1}{2}(\cancel{\overline{\rho}\tilde{e}^2}+\overline{\rho e''^2})_{,t}+\frac{1}{2}(\cancel{\overline{\rho}\tilde{e}^2\tilde{u}_k}+\tilde{u}_k\overline{\rho e''^2}+\tilde{e}\overline{\rho e''u''_k}+\tilde{e}\overline{\rho e''u''_k}+\overline{\rho e''^2u''_k})_{,k}...$$
$$-\left[\frac{1}{2}(\cancel{\overline{\rho}\tilde{e}^2})_{,t}+\frac{1}{2}(\cancel{\tilde{e}^2\tilde{u}_k\overline{\rho}})_{,k}+\tilde{e}(\overline{\rho e''u''_k})_{,k}\right]=...$$
$$-\cancel{\tilde{e}\,\overline{q}_{k,k}}-\overline{e''q_{k,k}}+\cancel{\tilde{e}\overline{\tau}_{kl}\overline{u}_{l,k}}+\overline{e''\tau}_{kl}\overline{u}_{l,k}+\overline{e''\tau'_{kl}}\overline{u}_{l,k}+\cancel{\tilde{e}\,\overline{\tau}_{kl}\overline{u''_{l,k}}}+\cancel{\tilde{e}\overline{\tau'_{kl}u''_{l,k}}}+\overline{\tau}_{kl}\overline{e''u''_{l,k}}+\overline{e''\tau'_{kl}u''_{l,k}}...$$
$$-\cancel{\tilde{e}\overline{P}\tilde{u}_{k,k}}-\overline{e''\,P}\tilde{u}_{k,k}-\tilde{u}_{k,k}\overline{e''P'}-\cancel{\tilde{e}\overline{P}\,\overline{u''_{k,k}}}-\cancel{\tilde{e}\overline{P'u''_{k,k}}}-\overline{P}\,\overline{e''u''_{k,k}}-\overline{e''P'u''_{k,k}}$$
$$-\left[-\cancel{\tilde{e}\,\overline{q}_{k,k}}+\cancel{\tilde{e}\,\overline{\tau}_{kl}\tilde{u}_{l,k}}+\cancel{\tilde{e}\,\overline{\tau}_{kl}\overline{u''_{l,k}}}+\cancel{\tilde{e}\overline{\tau'_{kl}u''_{l,k}}}-\cancel{\tilde{e}\overline{P}\tilde{u}_{k,k}}-\cancel{\tilde{e}\overline{P}\,\overline{u''_{k,k}}}-\cancel{\tilde{e}\overline{P'u''_{k,k}}}\right] \tag{3.45}$$

$$\frac{1}{2}(\overline{\rho e''^2})_{,t}+\frac{1}{2}(\tilde{u}_k\overline{\rho e''^2}+\overline{\rho e''^2u''_k}+\tilde{e}\overline{\rho e''u''_k}+\tilde{e}\overline{\rho e''u''_k})_{,k}-\left[\tilde{e}(\overline{\rho e''u''_k})_{,k}\right]=-\overline{e''q_{k,k}}... \tag{3.46}$$
$$+\overline{e''\tau}_{kl}\overline{u}_{l,k}+\overline{e''\tau'_{kl}}\overline{u}_{l,k}+\overline{\tau}_{kl}\overline{e''u''_{l,k}}+\overline{e''\tau'_{kl}u''_{l,k}}-\overline{e''\,P}\tilde{u}_{k,k}-\tilde{u}_{k,k}\overline{e''P'}-\overline{P}\,\overline{e''u''_{k,k}}-\overline{e''P'u''_{k,k}}$$

$$\frac{D\eta^T}{Dt}=-\tilde{e}_{,k}\theta_i^T-\frac{1}{2}(\overline{\rho e''^2u''_k})_{,k}-\overline{e''q_{k,k}}... \tag{3.47}$$
$$+\overline{e''\tau}_{kl}\overline{u}_{l,k}+\overline{e''\tau'_{kl}}\overline{u}_{l,k}+\overline{\tau}_{kl}\overline{e''u''_{l,k}}+\overline{e''\tau'_{kl}u''_{l,k}}-\overline{e''\,P}\tilde{u}_{k,k}-\tilde{u}_{k,k}\overline{e''P'}-\overline{P}\,\overline{e''u''_{k,k}}-\overline{e''P'u''_{k,k}}$$

3.2.4 Favre-Fluctuating Velocity Transport Equation

Here it is unnecessary to take the moment of any equations. Instead, skip to finding the mean form of the nonconservative conservation of energy by expanding Equation 3.5, Reynolds averaging the result, and removing the instantaneous terms. The challenge in this section is the desire to get the transport of a Favre-fluctuating velocity without letting it cancel with density, which is why the nonconservative form is needed. To begin, divide through by density

$$u_{i,t} + u_k u_{i,k} = \frac{1}{\rho}\left(\tau_{ik,k} - P_{,i}\right) \tag{3.48}$$

When expanding, a linearized Taylor series expansion terms is applied to the density term following Liou and Shih [163]: $\rho^{-1} = (\overline{\rho} + \rho')^{-1} = \overline{\rho}^{-1}\left(1 + \frac{\rho'}{\overline{\rho}}\right)^{-1} \approx \overline{\rho}^{-1}\left(1 - \frac{\rho'}{\overline{\rho}}\right)$. Note this is only acceptable when written in the form in the penultimate step and converges because $\frac{\rho'}{\overline{\rho}} < 1$. With this the conservation equation becomes

$$\tilde{u}_{i,t} + u''_{i,t} + \tilde{u}_k\tilde{u}_{i,k} + \tilde{u}_k u''_{i,k} + u''_k\tilde{u}_{i,k} + u''_k u''_{i,k} = \frac{1}{\overline{\rho}}\left(1 - \frac{\rho'}{\overline{\rho}}\right)\left(\overline{\tau}_{ik,k} + \tau'_{ik,k} - \overline{P}_{,i} - P'_{,i}\right) \tag{3.49}$$

$$\begin{aligned} &\overline{\rho}\tilde{u}_{i,t} + \overline{\rho}\overline{u''_{i,t}} + \overline{\rho}\tilde{u}_k\tilde{u}_{i,k} + \overline{\rho}\tilde{u}_k\overline{u''_{i,k}} + \overline{\rho}\overline{u''_k}\tilde{u}_{i,k} + \overline{\rho}\overline{u''_k u''_{i,k}} = \ldots \\ &\overline{\tau}_{ik,k} + \cancel{\overline{\tau'_{ik,k}}} - \overline{P}_{,i} - \cancel{\overline{P'_{,i}}} - \frac{1}{\overline{\rho}}\left(\cancel{\overline{\rho'}}\overline{\tau}_{ik,k} + \overline{\rho'\tau'_{ik,k}} - \cancel{\overline{\rho'}}\overline{P}_{,i} - \overline{\rho' P'_{,i}}\right) \end{aligned} \tag{3.50}$$

$$\overline{\rho}\tilde{u}_{i,t} + \overline{\rho}\overline{u''_{i,t}} + \overline{\rho}\tilde{u}_k\tilde{u}_{i,k} + \overline{\rho}\tilde{u}_k\overline{u''_{i,k}} + \overline{\rho}\overline{u''_k}\tilde{u}_{i,k} + \overline{\rho}\overline{u''_k u''_{i,k}} = \overline{\tau}_{ik,k} - \overline{P}_{,i} - \frac{1}{\overline{\rho}}\left(\overline{\rho'\tau'_{ik,k}} - \overline{\rho' P'_{,i}}\right) \tag{3.51}$$

Equation 3.51 represents the mean momentum equation in nonconservative form. The mean momentum equation in conservative form was provided in Equation 3.15. One can expand the left hand side of Equation 3.15 with the Multiplication Rule and simplify with the mean conservation of mass $\tilde{u}_{,i}\left(\overline{\rho}_{,t} + (\overline{\rho}\tilde{u}_k)_{,k}\right) = 0$ to produce

$$\overline{\rho}\tilde{u}_{i,t} + \overline{\rho}\tilde{u}_k\tilde{u}_{i,k} = -\overline{P_{,i}} + \overline{\tau_{ik,k}} - (\overline{\rho u''_i u''_k})_{,k} \tag{3.52}$$

Subtracting Equation 3.52 from Equation 3.51 yields a transport equation for the mean Favre-fluctuating velocity.

$$\begin{aligned}&\cancel{\overline{\rho}\tilde{u}_{i,t}} + \overline{\rho}\overline{u''_{i,t}} + \cancel{\overline{\rho}\tilde{u}_k\tilde{u}_{i,k}} + \overline{\rho}\tilde{u}_k\overline{u''_{i,k}} + \overline{\rho}\overline{u''_k}\tilde{u}_{i,k} + \overline{\rho}\overline{u''_k u''_{i,k}} - \left[\cancel{\overline{\rho}\tilde{u}_{i,t}} + \cancel{\overline{\rho}\tilde{u}_k\tilde{u}_{i,k}}\right] = \ldots \\ &+ \cancel{\overline{\tau}_{ik,k}} - \cancel{\overline{P}_{,i}} - \frac{1}{\overline{\rho}}\left(\overline{\rho'\tau'_{ik,k}} - \overline{\rho' P'_{,i}}\right) - \left[-\cancel{\overline{P}_{,i}} + \cancel{\overline{\tau}_{ik,k}} - \left(\rho u''_i u''_k\right)_{,k}\right]\end{aligned} \tag{3.53}$$

$$\overline{\rho}\overline{u''_{i,t}} + \overline{\rho}\tilde{u}_k\overline{u''_{i,k}} + \overline{\rho}\overline{u''_k}\tilde{u}_{i,k} + \overline{\rho}\overline{u''_k u''_{i,k}} = -\frac{1}{\overline{\rho}}\left(\overline{\rho'\tau'_{ik,k}} - \overline{\rho' P'_{,i}}\right) - \tau^T_{ik,k} \tag{3.54}$$

Adding $\overline{u''_i}\left(\overline{\rho}_{,t} + \left(\overline{\rho}\tilde{u}_k\right)_{,k}\right) = 0$ to the left hand side to allows the standard material derivative form.

$$\left(\overline{\rho}\overline{u''_i}\right)_{,t} + \left(\overline{\rho}\tilde{u}_k\overline{u''_i}\right)_{,k} + \overline{\rho}\overline{u''_k}\tilde{u}_{i,k} + \overline{\rho}\overline{u''_k u''_{i,k}} = -\frac{1}{\overline{\rho}}\left(\overline{\rho'\tau'_{ik,k}} - \overline{\rho' P'_{,i}}\right) - \tau^T_{ik,k} \tag{3.55}$$

$$\frac{D\overline{\rho}\overline{u''_i}}{Dt} = -\overline{\rho}\overline{u''_k}\tilde{u}_{i,k} - \overline{\rho}\overline{u''_k u''_{i,k}} - \frac{1}{\overline{\rho}}\left(\overline{\rho'\tau'_{ik,k}} - \overline{\rho' P'_{,i}}\right) - \tau^T_{ik,k} \tag{3.56}$$

The preceding equation can now be simplified. Address the Reynolds stress term by moving diffusion and triple correlation terms into D_{ik}. Expanding yields
$\tau^T_{ik,k} = -\left(\overline{\rho u''_i u''_k}\right)_{,k} = -\left(\overline{\rho}\overline{u''_i u''_k}\right)_{,k} - \left(\overline{\rho' u''_i u''_k}\right)_{,k}$, then from the Chain Rule $\tau^T_{ik,k} = -\overline{\rho}\left(\overline{u''_i u''_k}\right)_{,k} - \overline{\rho}_{,k}\overline{u''_i u''_k} - \left(\overline{\rho' u''_i u''_k}\right)_{,k} = -\overline{\rho}_{,k}\overline{u''_i u''_k} + D_{ik}$. Multiplying by $\frac{\overline{\rho}}{\overline{\rho}}$ this becomes $-\overline{\rho}_{,k}\frac{\overline{\rho}\overline{u''_i u''_k}}{\overline{\rho}} + D_{ik} = -\overline{\rho}_{,k}\frac{\left(\overline{\rho u''_i u''_k} - \overline{\rho' u''_i u''_k}\right)}{\overline{\rho}} + D_{ik} = -\overline{\rho}_{,k}\frac{\left(\overline{\rho u''_i u''_k}\right)}{\overline{\rho}} + D_{ik}$. Therefore

$$\tau^T_{ik,k} = \frac{\overline{\rho}_{,k}\tau^T_{ik}}{\overline{\rho}} + D_{ik} \tag{3.57}$$

Substituting this result

$$\frac{D\overline{\rho}\overline{u''_i}}{Dt} = -\overline{\rho}\overline{u''_k}\tilde{u}_{i,k} - \overline{\rho}\overline{u''_k u''_{i,k}} - \frac{1}{\overline{\rho}}\left(\overline{\rho'\tau'_{ik,k}} - \overline{\rho' P'_{,i}} + \overline{\rho}_{,k}\tau^T_{ik}\right) + D_{ik} \tag{3.58}$$

3.2.5 Favre-Fluctuating Energy Transport Equation

Here it is unnecessary to take the moment of any equations. Instead, skip to finding the mean form of the nonconservative conservation of energy by expanding, Reynolds averaging, and simplifying Equation 3.6. The challenge in this section is the desire to get the transport of Favre-fluctuating energy without letting it cancel with density, which is why the nonconservative form is needed.

$$e_{,t} + u_k e_{,k} = \frac{1}{\rho}\left(\tau_{kl}u_{l,k} - Pu_{k,k} - q_{k,k}\right) \tag{3.59}$$

When expanding, a linearized Taylor series expansion terms is applied to the density term following Liou and Shih [163]: $\rho^{-1} = (\overline{\rho}+\rho')^{-1} = \overline{\rho}^{-1}\left(1+\frac{\rho'}{\overline{\rho}}\right)^{-1} \approx \overline{\rho}^{-1}\left(1-\frac{\rho'}{\overline{\rho}}\right)$. Note this is only acceptable when written in the form in the penultimate step and converges because $\frac{\rho'}{\overline{\rho}} < 1$. With this the conservation equation becomes

$$\begin{aligned}
&\tilde{e}_{,t} + e''_{,t} + \tilde{u}_k\tilde{e}_{,k} + \tilde{u}_k e''_{,k} + u''_k\tilde{e}_{,k} + u''_k e''_{,k} = \ldots \\
&\frac{1}{\overline{\rho}}\left(1-\frac{\rho'}{\overline{\rho}}\right)\left(\overline{\tau}_{kl}\tilde{u}_{l,k} + \overline{\tau}_{kl}u''_{l,k} + \tau'_{kl}\tilde{u}_{l,k} + \tau'_{kl}u''_{l,k} - \overline{P}\tilde{u}_{k,k} - \overline{P}u''_{k,k} - P'\tilde{u}_{k,k} - P'u''_{k,k} - \overline{q}_{k,k} - q'_{k,k}\right)
\end{aligned} \tag{3.60}$$

$$\begin{aligned}
&\overline{\rho}\tilde{e}_{,t} + \overline{\rho}\overline{e''_{,t}} + \overline{\rho}\tilde{u}_k\tilde{e}_{,k} + \overline{\rho}\tilde{u}_k\overline{e''_{,k}} + \overline{\rho}\overline{u''_k}\tilde{e}_{,k} + \overline{\rho}\overline{u''_k e''_{,k}} = -\overline{q}_{k,k} - \cancel{\overline{q'_{k,k}}} - \frac{1}{\overline{\rho}}\left(-\cancel{\overline{\rho'}}\overline{q}_{k,k} - \overline{\rho' q'_{k,k}}\right) \\
&\overline{\tau}_{kl}\tilde{u}_{l,k} + \overline{\tau}_{kl}\overline{u''_{l,k}} + \cancel{\overline{\tau'_{kl}}}\tilde{u}_{l,k} + \overline{\tau'_{kl}u''_{l,k}} - \overline{P}\tilde{u}_{k,k} - \overline{P}\,\overline{u''_{k,k}} - \cancel{\overline{P'}}\tilde{u}_{k,k} - \overline{P'u''_{k,k}} \\
&- \frac{1}{\overline{\rho}}\left(\overline{\tau}_{kl}\tilde{u}_{l,k}\cancel{\overline{\rho'}} + \overline{\tau}_{kl}\overline{\rho' u''_{l,k}} + \overline{\rho'\tau'_{kl}}\tilde{u}_{l,k} + \overline{\rho'\tau'_{kl}u''_{l,k}} - \overline{P}\tilde{u}_{k,k}\cancel{\overline{\rho'}} - \overline{P}\,\overline{\rho' u''_{k,k}} - \overline{\rho' P'}\tilde{u}_{k,k} - \overline{\rho' P' u''_{k,k}}\right)
\end{aligned} \tag{3.61}$$

$$\begin{aligned}
&\overline{\rho}\tilde{e}_{,t} + \overline{\rho}\overline{e''_{,t}} + \overline{\rho}\tilde{u}_k\tilde{e}_{,k} + \overline{\rho}\tilde{u}_k\overline{e''_{,k}} + \overline{\rho}\overline{u''_k}\tilde{e}_{,k} + \overline{\rho}\overline{u''_k e''_{,k}} = -\overline{q}_{k,k} - \frac{1}{\overline{\rho}}\left(-\overline{\rho' q'_{k,k}}\right) \\
&+ \overline{\tau}_{kl}\tilde{u}_{l,k} + \overline{\tau}_{kl}\overline{u''_{l,k}} + \overline{\tau'_{kl}u''_{l,k}} - \overline{P}\tilde{u}_{k,k} - \overline{P}\,\overline{u''_{k,k}} - \overline{P'u''_{k,k}} \\
&- \frac{1}{\overline{\rho}}\left(\overline{\tau}_{kl}\overline{\rho' u''_{l,k}} + \overline{\rho'\tau'_{kl}}\tilde{u}_{l,k} + \overline{\rho'\tau'_{kl}u''_{l,k}} - \overline{P}\,\overline{\rho' u''_{k,k}} - \overline{\rho' P'}\tilde{u}_{k,k} - \overline{\rho' P' u''_{k,k}}\right)
\end{aligned} \tag{3.62}$$

Equation 3.62 represents the mean energy equation in nonconservative form. The mean energy equation in conservative form was provided in Equation 3.18. One can expand the left hand of Equation 3.18 with the Multiplication Rule and simplify with the mean conservation of mass

$\tilde{e}\left(\overline{\rho}_{,t}+\left(\overline{\rho}\tilde{u}_k\right)_{,k}\right)=0$ to produce

$$\overline{\rho}\tilde{e}_{,t}+\overline{\rho}\tilde{u}_k\tilde{e}_{,k}=-\overline{q}_{k,k}-\theta^T_{k,k}+\overline{\tau}_{kl}\tilde{u}_{l,k}+\overline{\tau}_{kl}\overline{u''_{l,k}}+\overline{\tau'_{kl}u''_{l,k}}-\overline{P}\tilde{u}_{k,k}-\overline{P}\,\overline{u''_{k,k}}-\overline{P'u''_{P,k}} \tag{3.63}$$

Subtracting Equation 3.62 from Equation 3.63 yields a transport equation for the mean Favre-fluctuating energy.

$$\begin{aligned}
&\cancel{\overline{\rho}\tilde{e}_{,t}}+\overline{\rho}\overline{e''_{,t}}+\cancel{\overline{\rho}\tilde{u}_k\tilde{e}_{,k}}+\overline{\rho}\tilde{u}_k\overline{e''_{,k}}+\overline{\rho}\overline{u''_k}\tilde{e}_{,k}+\overline{\rho}\overline{u''_ke''_{,k}}-\left[\cancel{\overline{\rho}\tilde{e}_{,t}}+\cancel{\overline{\rho}\tilde{u}_k\tilde{e}_{,k}}\right]=-\cancel{\overline{q}_{k,k}}-\frac{1}{\overline{\rho}}\left(-\overline{\rho'q'_{k,k}}\right)\\
&+\cancel{\overline{\tau}_{kl}\tilde{u}_{l,k}}+\cancel{\overline{\tau}_{kl}\overline{u''_{l,k}}}+\cancel{\overline{\tau'_{kl}u''_{l,k}}}-\cancel{\overline{P}\tilde{u}_{k,k}}-\cancel{\overline{P}\,\overline{u''_{k,k}}}-\cancel{\overline{P'u''_{k,k}}}\\
&-\frac{1}{\overline{\rho}}\left(\overline{\tau}_{kl}\overline{\rho'u''_{l,k}}+\overline{\rho'\tau'_{kl}}\tilde{u}_{l,k}+\overline{\rho'\tau'_{kl}u''_{l,k}}-\overline{P}\,\overline{\rho'u''_{k,k}}-\overline{\rho'P'}\tilde{u}_{k,k}-\overline{\rho'P'u''_{k,k}}\right)\\
&-\left[-\cancel{\overline{q}_{k,k}}-\theta^T_{k,k}+\cancel{\overline{\tau}_{kl}\tilde{u}_{l,k}}+\cancel{\overline{\tau}_{kl}\overline{u''_{l,k}}}+\cancel{\overline{\tau'_{kl}u''_{l,k}}}-\cancel{\overline{P}\tilde{u}_{k,k}}-\cancel{\overline{P}\,\overline{u''_{k,k}}}-\cancel{\overline{P'u''_{P,k}}}\right]
\end{aligned} \tag{3.64}$$

$$\begin{aligned}
&\overline{\rho}\overline{e''_{,t}}+\overline{\rho}\tilde{u}_k\overline{e''_{,k}}+\overline{\rho}\overline{u''_k}\tilde{e}_{,k}+\overline{\rho}\overline{u''_ke''_{,k}}=...\\
&\frac{1}{\overline{\rho}}\left(\overline{\rho'q'_{k,k}}\right)+\theta^T_{k,k}-\frac{1}{\overline{\rho}}\left(\overline{\tau}_{kl}\overline{\rho'u''_{l,k}}+\overline{\rho'\tau'_{kl}}\tilde{u}_{l,k}+\overline{\rho'\tau'_{kl}u''_{l,k}}-\overline{P}\,\overline{\rho'u''_{k,k}}-\overline{\rho'P'}\tilde{u}_{k,k}-\overline{\rho'P'u''_{k,k}}\right)
\end{aligned} \tag{3.65}$$

Adding $\overline{e''}\left(\rho_{,t}+\left(\rho u_k\right)_{,k}\right)=0$ to the left hand side to allows the standard material derivative form.

$$\begin{aligned}
&\left(\overline{\rho}\overline{e''}\right)_{,t}+\left(\overline{\rho}\tilde{u}_k\overline{e''}\right)_{,k}+\overline{\rho}\overline{u''_k}\tilde{e}_{,k}+\overline{\rho}\overline{u''_ke''_{,k}}=...\\
&\frac{1}{\overline{\rho}}\left(\overline{\rho'q'_{k,k}}\right)+\theta^T_{k,k}-\frac{1}{\overline{\rho}}\left(\overline{\tau}_{kl}\overline{\rho'u''_{l,k}}+\overline{\rho'\tau'_{kl}}\tilde{u}_{l,k}+\overline{\rho'\tau'_{kl}u''_{l,k}}-\overline{P}\,\overline{\rho'u''_{k,k}}-\overline{\rho'P'}\tilde{u}_{k,k}-\overline{\rho'P'u''_{k,k}}\right)
\end{aligned} \tag{3.66}$$

$$\begin{aligned}
\frac{D\overline{\rho}\overline{e''}}{Dt}&=\frac{1}{\overline{\rho}}\left(\overline{\rho'q'_{k,k}}\right)+\theta^T_{k,k}-\overline{\rho}\overline{u''_k}\tilde{e}_{,k}-\overline{\rho}\overline{u''_ke''_{,k}}\\
&-\frac{1}{\overline{\rho}}\left(\overline{\tau}_{kl}\overline{\rho'u''_{l,k}}+\overline{\rho'\tau'_{kl}}\tilde{u}_{l,k}+\overline{\rho'\tau'_{kl}u''_{l,k}}-\overline{P}\,\overline{\rho'u''_{k,k}}-\overline{\rho'P'}\tilde{u}_{k,k}-\overline{\rho'P'u''_{k,k}}\right)
\end{aligned} \tag{3.67}$$

The preceding equation can now be simplified. From the Multiplication Rule $\theta^T_{k,k}=\overline{\rho_{,k}e''u''_k}+\overline{\rho e''_{,k}u''_k}+\overline{\rho e''u''_{k,k}}$. To second-order, respectively:

- $\overline{\rho_{,k}e''u''_k}\approx\overline{\rho}_{,k}\overline{e''u''_k}+\cancel{\overline{\rho'_{,k}e''u''_k}}\approx\overline{\rho}_{,k}\overline{e''u''_k}\frac{\overline{\rho}}{\overline{\rho}}\approx\theta^T_k\frac{\overline{\rho}_{,k}}{\overline{\rho}}-\frac{\overline{\rho}_{,k}}{\overline{\rho}}\cancel{\overline{\rho'e''u''_k}}\approx\theta^T_k\frac{\overline{\rho}_{,k}}{\overline{\rho}}$
- $\overline{\rho e''_{,k}u''_k}=\overline{\rho}\overline{e''_{,k}u''_k}+\cancel{\overline{\rho'e''_{,k}u''_k}}\approx\overline{\rho}\overline{e''_{,k}u''_k}$

- $\overline{\rho e'' u''_{k,k}} \approx \overline{\rho}\overline{e'' u''_{k,k}} + \cancel{\overline{\rho' e'' u''_{k,k}}}$

Therefore $\theta^T_{k,k} - \overline{\rho}\overline{e''_{,k} u''_k} = \theta^T_k \frac{\overline{\rho}_{,k}}{\overline{\rho}} + \overline{\rho}\overline{e'' u''_{k,k}}$, so

$$\begin{aligned}\frac{D\overline{\rho}\overline{e''}}{Dt} &= \frac{1}{\overline{\rho}}\left(\overline{\rho' q'_{k,k}}\right) + \theta^T_k \frac{\overline{\rho}_{,k}}{\overline{\rho}} + \overline{\rho}\overline{e'' u''_{k,k}} - \overline{\rho}\overline{u''_k}\tilde{e}_{,k} \\ &- \frac{1}{\overline{\rho}}\left(\overline{\tau}_{kl}\overline{\rho' u''_{l,k}} + \overline{\rho'\tau'_{kl}}\tilde{u}_{l,k} + \overline{\rho'\tau'_{kl}u''_{l,k}} - \overline{P}\,\overline{\rho' u''_{k,k}} - \overline{\rho' P'}\tilde{u}_{k,k} - \overline{\rho' P' u''_{k,k}}\right)\end{aligned} \tag{3.68}$$

Finally, group the third order, molecular ($q_{k,k}$) and viscous (τ_{kl}) terms into the dummy variable M_{kl} to produce the final result.

$$\frac{D\overline{\rho}\overline{e''}}{Dt} = \theta^T_k \frac{\overline{\rho}_{,k}}{\overline{\rho}} + \overline{\rho}\overline{e'' u''_{k,k}} - \overline{\rho}\overline{u''_k}\tilde{e}_{,k} + \frac{1}{\overline{\rho}}\left(\overline{P}\,\overline{\rho' u''_{k,k}} + \overline{\rho' P'}\tilde{u}_{k,k}\right) + M_{kl} \tag{3.69}$$

3.3 Model Simplifications

A combination of dilatation, equation of state, and incompressible pressure scrambling models are derived and applied to Equation 3.24 to allow it to be algebratized and solved numerically. The derivation for each is shown below. The end result is closure, an equation written predominantly in terms of the turbulent energy flux (to be solved for) and Reynolds stress and mean parameters (known). The same simplifications are also applied to Equations 3.58 and 3.69 at this time. Additionally, it is noted that the terms $\overline{e''}\,\overline{P}_{,i}$ and $\overline{\rho}\xi_i$ will be addressed in later sections but will ultimately be removed.

- Turbulent Energy Flux Transport Equation

$$\frac{D\theta^T_i}{Dt} = -\tilde{u}_{i,k}\theta^T_k + \tilde{e}_{,k}\tau^T_{ik} - \overline{e''}\,\overline{P}_{,i} + \overline{e''_{,i}P'} - \left[\overline{u''_i}\,\overline{P} + \overline{u''_i P'}\right]\tilde{u}_{k,k} - \overline{u''_i u''_{k,k}}\,\overline{P} + \overline{\rho}\xi_i$$

The fourth term on the right hand side is removed by Equation 3.106, the bracketed terms modeled by Equation 3.105, and the seventh term modified according to Equation 3.81: $-\overline{u''_i u''_{k,k}}\,\overline{P} = -\overline{P}\frac{\overline{\rho u''_i u''_{k,k}}}{\overline{\rho}} \approx -\overline{P}\frac{\overline{\rho}_{,k}\tau^T_{ik}}{\overline{\rho}^2}$. Again, these relations are derived below. With this the transport equation becomes

$$\frac{D\theta^T_i}{Dt} = -\tilde{u}_{i,k}\theta^T_k + \tau^T_{ik}\left(\tilde{e}_{,k} - \overline{P}\frac{\overline{\rho}_{,k}}{\overline{\rho}^2}\right) - \overline{e''}\,\overline{P}_{,i} - \frac{R}{\overline{C_v}}\theta^T_i\tilde{u}_{k,k} + \overline{\rho}\xi_i \tag{3.70}$$

As a final simplification take the gradient of the specific enthalpy $\tilde{h} = \tilde{e} + \frac{\overline{P}}{\overline{\rho}}$ to define $\tilde{\psi}_{,k} \equiv \tilde{h}_{,k} - \frac{\overline{P}_{,k}}{\overline{\rho}} = \tilde{e}_{,k} - \frac{\overline{P}\overline{\rho}_{,k}}{\overline{\rho}^2}$ such that

$$\frac{D\theta_i^T}{Dt} = -\tilde{u}_{i,k}\theta_k^T + \tau_{ik}^T\tilde{\psi}_{,k} - \overline{e''}\,\overline{P}_{,i} - \frac{R}{\overline{C_v}}\theta_i^T\tilde{u}_{k,k} + \overline{\rho}\xi_i \tag{3.71}$$

- Favre-Fluctuating Velocity Transport Equation

$$\frac{D\overline{\rho}\,\overline{u_i''}}{Dt} = -\overline{\rho}\,\overline{u_k''}\tilde{u}_{i,k} - \overline{\rho}\,\overline{u_k''u_{i,k}''} - \frac{1}{\overline{\rho}}\left(\overline{\rho'\tau_{ik,k}'} - \overline{\rho'P_{,i}'} + \overline{\rho}_{,k}\tau_{ik}^T\right) + D_{ik}$$

The second term on the right hand side can be written $-\overline{\rho}\,\overline{u_k''u_{i,k}''} = \left(\overline{\rho' u_k''u_{i,k}''}\right) - \left(\overline{\rho u_k''u_{i,k}''}\right) = (D_{ik}) + \left(\left[\overline{\rho u_{k,k}''u_i''}\right] - \left[\overline{\rho(u_k''u_i'')_{,k}}\right]\right) = (D_{ik}) + \left(\left[\overline{\rho}\,\overline{u_{k,k}''u_i''} + \overline{\rho' u_{k,k}''u_i''}\right] + [D_{ik}]\right) = \overline{\rho}\,\overline{u_{k,k}''u_i''} + D_{ik}$ in order to cancel with the fifth term according to Equation 3.81; the dummy variable contains triple correlation and diffusion terms and is simply combined with the other such placeholder. Continuing, Equation 3.107 shows the fourth term is negligible. Finally, one can, under the present assumptions, consider the viscous term to be $\mathscr{O}(Diffusion)$ and add it to D_{ik}. With this the transport equation simplifies to

$$\frac{D\overline{\rho}\,\overline{u_i''}}{Dt} \approx -\overline{\rho}\,\overline{u_k''}\tilde{u}_{i,k} + D_u \tag{3.72}$$

- Favre-Fluctuating Energy Transport Equation

$$\frac{D\overline{\rho}\,\overline{e''}}{Dt} = \theta_k^T\frac{\overline{\rho}_{,k}}{\overline{\rho}} + \overline{\rho}\,\overline{e''u_{k,k}''} - \overline{\rho}\,\overline{u_k''}\tilde{e}_{,k} + \frac{1}{\overline{\rho}}\left(\overline{P}\,\overline{\rho' u_{k,k}''} + \overline{\rho'P'}\tilde{u}_{k,k}\right) + M_{kl}$$

The first and second terms on the right hand side cancel according to Equation 3.82. Furthermore, Equation 3.88 modifies the fourth term. With this the transport equation simplifies to

$$\frac{D\overline{\rho}\,\overline{e''}}{Dt} = -\overline{\rho}\tilde{e}_{,k}\,\overline{u_k''} + \frac{\overline{P}\,\overline{\rho}_{,k}\,\overline{u_{k,k}''}}{\overline{\rho}} + \frac{\tilde{u}_{k,k}\overline{\rho'P'}}{\overline{\rho}} + M_{kl} \tag{3.73}$$

3.3.1 Dilatation Models

The processes to derive a velocity ($\overline{\rho u_{k,k}''u_i''}$) and energy ($\overline{\rho u_{k,k}''e''}$) dilatation model are identical and thus both are shown simultaneously in terms of the dummy variable ϕ''. Begin by expanding

the conservation of mass (Equation 3.1) with Favre averaging and the Multiplication Rule; immediately neglect the unsteady term. Next, take a moment with ϕ'' and then Reynolds average the result.

$$\cancel{\rho_{,t}} + (\rho u_k'' + \rho \tilde{u}_k)_{,k} \approx 0 \tag{3.74}$$

$$\rho_{,k} u_k'' + \rho u_{k,k}'' + \rho_{,k} \tilde{u}_k + \rho \tilde{u}_{k,k} \approx 0 \tag{3.75}$$

$$\overline{\phi'' \rho_{,k} u_k''} + \overline{\phi'' \rho u_{k,k}''} + \tilde{u}_k \overline{\phi'' \rho_{,k}} + \tilde{u}_{k,k} \cancel{\overline{\phi'' \rho}} \approx 0 \tag{3.76}$$

By the definition of Favre averaging, $\cancel{\overline{(\rho\phi'')}_{,k}} = \overline{(\rho_{,k}\phi'')} + \overline{(\rho\phi_{,k}'')} \implies \overline{(\rho_{,k}\phi'')} = -\overline{(\rho\phi_{,k}'')}$.

$$\overline{\phi'' \rho_{,k} u_k''} + \overline{\phi'' \rho u_{k,k}''} - \tilde{u}_k \overline{(\rho \phi_{,k}'')} \approx 0 \tag{3.77}$$

Consider the term $\overline{\phi'' \rho_{,k} u_k''}$. Expand the density gradient and then neglect the triple correlation so it becomes $\overline{\phi'' \rho_{,k} u_k''} \approx \overline{\rho}_{,k} \overline{\phi'' u_k''} + \cancel{\overline{\phi'' \rho'_{,k} u_k''}}$. Multiply it by $\overline{\rho}/\overline{\rho}$ to produce $\frac{\overline{\rho}_{,k}}{\overline{\rho}} \overline{\rho} \overline{\phi'' u_k''}$. Because under the second-order assumption triple correlations are considered to be approximately zero, one can write $\frac{\overline{\rho}_{,k}}{\overline{\rho}} \overline{\rho} \overline{\phi'' u_k''} + \frac{\overline{\rho}_{,k}}{\overline{\rho}} \overline{\rho' \phi'' u_k''}$. The mean and fluctuating density terms can now be collapsed into one cumulative term; this is the exact opposite of what was done with $\rho_{,k}$. This last step provides $\frac{\overline{\rho}_{,k}}{\overline{\rho}} \overline{\rho \phi'' u_k''}$. Applying these changes to the above equation and rearranging the terms produces

$$\overline{\phi'' \rho u_{k,k}''} \approx -\frac{\overline{\rho}_{,k}}{\overline{\rho}} \overline{\rho \phi'' u_k''} + \tilde{u}_k \overline{(\rho \phi_{,k}'')} \tag{3.78}$$

Now expand density on the left hand side and cancel the triple correlation. Meanwhile, on the right hand side the $\tilde{u}_k \overline{(\rho \phi_{,k}'')}$ term is assumed to be negligibly small in a shear layer.

$$\overline{\rho} \overline{\phi'' u_{k,k}''} + \cancel{\overline{\phi'' \rho' u_{k,k}''}} \approx -\frac{\overline{\rho}_{,k}}{\overline{\rho}} \overline{\rho \phi'' u_k''} + \cancel{\tilde{u}_k \overline{(\rho \phi_{,k}'')}} \tag{3.79}$$

$$\overline{\rho} \overline{\phi'' u_{k,k}''} \approx -\frac{\overline{\rho}_{,k}}{\overline{\rho}} \overline{\rho \phi'' u_k''} \tag{3.80}$$

All that remains is to substitute in u_i'' for velocity dilatation and e'' for energy dilatation. The

final result is

$$Velocity\,Dilatation: \overline{\rho} \overline{u_i'' u_{k,k}''} \approx \frac{\overline{\rho}_{,k}}{\overline{\rho}} \tau_{ik}^T \tag{3.81}$$

$$Energy\,Dilatation: \overline{\rho} \overline{e'' u_{k,k}''} \approx -\frac{\overline{\rho}_{,k}}{\overline{\rho}} \theta_{ik}^T \tag{3.82}$$

A density dilatation ($\overline{\rho' u_{k,k}''}$) model can be completed following an analogous process. As before, begin by taking a moment of the conservation of mass, here with density fluctuations ρ'; again neglect unsteady and triple correlation terms. This time it is necessary to expand both the velocity and density terms in Equation 3.1 with Favre and Reynolds averaging respectively.

$$\cancel{\rho_{,t}} + (\overline{\rho}\tilde{u}_k + \overline{\rho} u_k'' + \rho' \tilde{u}_k + \rho' u_k'')_{,k} \approx 0 \tag{3.83}$$

$$\overline{\rho_{,k}} \tilde{u}_k + \overline{\rho} \tilde{u}_{k,k} + \overline{\rho_{,k}} u_k'' + \overline{\rho} u_{k,k}'' + \rho'_{,k} \tilde{u}_k + \rho' \tilde{u}_{k,k} + \rho'_{,k} u_k'' + \rho' u_{k,k}'' \approx 0 \tag{3.84}$$

$$\cancel{\overline{\rho'}\,\overline{\rho_{,k}} \tilde{u}_k} + \cancel{\overline{\rho'}\,\overline{\rho} \tilde{u}_{k,k}} + \overline{\rho_{,k}} \overline{\rho' u_k''} + \overline{\rho} \overline{\rho' u_{k,k}''} + \overline{\rho' \rho'_{,k}} \tilde{u}_k + \overline{\rho' \rho'} \tilde{u}_{k,k} + \cancel{\overline{\rho' \rho'_{,k} u_k''}} + \cancel{\overline{\rho' \rho' u_{k,k}''}} \approx 0 \tag{3.85}$$

$$\overline{\rho} \overline{\rho' u_{k,k}''} \approx -\overline{\rho_{,k}} \overline{\rho' u_k''} - \overline{\rho' \rho'_{,k}} \tilde{u}_k - \overline{\rho'^2} \tilde{u}_{k,k} \tag{3.86}$$

From the Multiplication Rule $(\rho'^2)_{,k} = \rho'_{,k}\rho' + \rho'\rho'_{,k} = 2\rho'\rho'_{,k} \implies \rho'\rho'_{,k} = \frac{1}{2}(\rho')^2_{,k}$.
Also, $-\overline{\rho_{,k}} \overline{\rho' u_k''} = -\overline{\rho_{,k}} \overline{(\rho - \overline{\rho}) u_k''} = -\overline{\rho_{,k}} \cancel{\overline{\rho u_k''}} + \overline{\rho_{,k}}\,\overline{u_k''}\,\overline{\rho} = \overline{\rho_{,k}}\,\overline{u_k''}\,\overline{\rho}$.

$$\overline{\rho} \overline{\rho' u_{k,k}''} \approx \overline{\rho_{,k}}\,\overline{u_k''}\,\overline{\rho} - \frac{1}{2}\overline{(\rho')^2_{,k}} \tilde{u}_k - \overline{\rho'^2} \tilde{u}_{k,k} \tag{3.87}$$

Divide both sides by $\overline{\rho}$. Also, the second and third terms on the right-hand side are assumed to be small. What remains is the model.

$$Density\,Dilatation: \overline{\rho' u_{k,k}''} \approx \overline{\rho_{,k}}\,\overline{u_k''} \tag{3.88}$$

Bowersox [38] used the DNS data from [217] to show these dilatation models are reasonably accurate.

3.3.2 Equation of State Model

Both the caloric and thermal equations of state can be used to write the bracketed term in Equation 3.24 in terms of the energy flux θ_i^T. Here one makes the important assumption that the gas is thermally perfect, but caloric imperfections are permissible. That said, it is also necessary to assume $\frac{C_v'}{\overline{C_v}} \ll \frac{e''}{\tilde{e}}$, or by corollary $C_v' \approx 0$.

Both the mean and fluctuating forms of the caloric and thermal equations of state must be derived. While the former will be substituted into the latter, in both cases the fluctuating equation will be derived by expanding the equation with Reynolds and Favre fluctuations and Reynolds averaging to get the mean equation, then subtracting this result from the expanded form. For the caloric equation of state $e = C_v T$ there is a unique substitution step before Reynolds averaging, to multiply both sides of the equation by density, which allows for greater simplification.

$$(\tilde{e} + e'') \approx (\overline{C_v} + \cancel{C_v'})(\tilde{T} + T'') \tag{3.89}$$

$$\rho\tilde{e} + \rho e'' \approx \overline{C_v}\rho\tilde{T} + \overline{C_v}\rho T'' \tag{3.90}$$

$$\overline{\rho}\tilde{e} + \cancel{\overline{\rho e''}} \approx \overline{C_v}\overline{\rho}\tilde{T} + \cancel{\overline{C_v \rho T''}} \tag{3.91}$$

$$\tilde{e} \approx \overline{C_v}\tilde{T} \tag{3.92}$$

Subtracting Equation 3.92 from Equation 3.90 and dropping the distributed density produces the fluctuating equation form.

$$e'' \approx \overline{C_v} T'' \tag{3.93}$$

The mean and fluctuating forms of the thermal equation of state $P = \rho RT$ are derived following the steps outlined above, but the results from Equations 3.92 and 3.93 are used to replace the temperature dependence with the gas constant and constant volume specific heat.

$$(\overline{P} + P') \approx \rho R \left(\frac{\tilde{e}}{\overline{C_v}} + \frac{e''}{\overline{C_v}} \right) \tag{3.94}$$

$$(\overline{P}+\cancel{\overline{P'}}) \approx \frac{R}{\overline{\overline{C_v}}}(\overline{\rho}\tilde{e}+\cancel{\overline{\rho e''}}) \tag{3.95}$$

$$\overline{P} \approx \frac{R}{\overline{\overline{C_v}}}\overline{\rho}\tilde{e} \tag{3.96}$$

Subtracting Equation 3.96 from Equation 3.94 produces the fluctuating thermal state equation, though additional steps are needed to put it into the desired form.

$$(\cancel{\overline{P}}+P') - [\cancel{\overline{P}}] \approx \rho R\left(\frac{\tilde{e}}{\overline{\overline{C_v}}}+\frac{e''}{\overline{\overline{C_v}}}\right) - \left[\frac{R}{\overline{\overline{C_v}}}\overline{\rho}\tilde{e}\right] \tag{3.97}$$

$$P' \approx \frac{R}{\overline{\overline{C_v}}}\left(\rho\tilde{e}+\rho e''-\overline{\rho}\tilde{e}\right) \tag{3.98}$$

$$P' \approx \frac{R}{\overline{\overline{C_v}}}\left(\cancel{\overline{\rho}\tilde{e}}+\rho'\tilde{e}+\rho e''-\cancel{\overline{\rho}\tilde{e}}\right) \tag{3.99}$$

$$P' \approx \frac{R}{\overline{\overline{C_v}}}\left(\rho'\tilde{e}+\rho e''\right) \tag{3.100}$$

Now use Equations 3.96 and 3.100 to simplify Equation 3.24.

$$\overline{P'u_i''}+\overline{u_i''}\,\overline{P} \approx \overline{\frac{R}{\overline{\overline{C_v}}}\left(\rho'\tilde{e}+\rho e''\right)u_i''}+\overline{u_i''}\frac{R}{\overline{\overline{C_v}}}\overline{\rho}\tilde{e} \tag{3.101}$$

$$\overline{P'u_i''}+\overline{u_i''}\,\overline{P} \approx \frac{R}{\overline{\overline{C_v}}}\left(\overline{\rho'u_i''}\tilde{e}+\overline{\rho e''u_i''}+\overline{u_i''}\overline{\rho}\tilde{e}\right) \tag{3.102}$$

Combine two of the terms by collapsing the density with $\rho = \overline{\rho}+\rho'$.

$$\overline{P'u_i''}+\overline{u_i''}\,\overline{P} \approx \frac{R}{\overline{\overline{C_v}}}\left(\overline{\rho'u_i''}\tilde{e}+\overline{u_i''}\overline{\rho}\tilde{e}+\overline{\rho e''u_i''}\right) \tag{3.103}$$

$$\overline{P'u_i''}+\overline{u_i''}\,\overline{P} \approx \frac{R}{\overline{\overline{C_v}}}\left(\cancel{\overline{\rho u_i''}}\tilde{e}+\overline{\rho e''u_i''}\right) \tag{3.104}$$

$$\overline{P'u_i''}+\overline{u_i''}\,\overline{P} \approx \frac{R}{\overline{\overline{C_v}}}\theta_i^T \tag{3.105}$$

3.3.3 Incompressible Pressure Scrambling Model

The incompressible pressure scrambling effect $\overline{P'e''_{,i}}$ can be removed from Equation 3.24. Begin by expanding P' according to Equation 3.100, producing $\overline{P'e''_{,i}} = \frac{R}{\overline{C_v}}\left(\tilde{e}\overline{\rho'e''_{,i}} + \overline{\rho}\overline{e''e''_{,i}}\right)$. The Multiplication Rule shows $e''e''_{,i} = \frac{1}{2}(e''^2)_{,i}$, so assuming the gradient of the energy variance is negligible then $\overline{\rho}\overline{e''e''_{,i}} \approx D$, where D symbolizes terms on the order of diffusion. For $\tilde{e}\overline{\rho'e''_{,i}}$, assume statistical moments are homogeneous $P' \ll \rho', T' \implies \frac{\rho'}{\overline{\rho}} \sim \frac{T'}{\overline{T}}$; this is extended to the internal energy with the caloric equation of state such that $\frac{\rho'}{\overline{\rho}} \approx \frac{e''}{\tilde{e}}$. This allows $\tilde{e}\overline{\rho'e''_{,i}} \approx \tilde{e}\overline{\left(\frac{\overline{\rho}e''}{\tilde{e}}\right)e''_{,i}} \approx \overline{\rho}\tilde{e}\overline{e''e''_{,i}}$; as before, apply the Multiplication Rule and the same assumption to the gradient of the energy variance, $\tilde{e}\overline{\rho'e''_{,i}} \approx \frac{\overline{\rho}}{2}\overline{(e'')^2_{,i}} \approx D$. Taken together,

$$\overline{P'e''_{,i}} \approx D \tag{3.106}$$

The same process can also be used to simplify $\overline{P'\rho'_{,i}}$ in Equation 3.58. Expanding P' with the fluctuating equation of state produces $\overline{P'\rho''_{,i}} = \frac{R}{\overline{C_v}}\left(\tilde{e}\overline{\rho'\rho'_{,i}} + \overline{\rho}\overline{e''\rho'_{,i}}\right)$. As before, through the Multiplication Rule the first term can be expressed as the gradient of a fluctuating quantity and can therefore be assumed to be negligible. For the second term, again use $\frac{\rho'}{\overline{\rho}} \approx \frac{e''}{\tilde{e}}$ to write $\overline{\rho}\overline{e''\rho'_{,i}} \approx \overline{\rho}\overline{\frac{\rho'\tilde{e}}{\overline{\rho}}\rho'_{,i}} \approx \tilde{e}\overline{\rho'\rho'_{,i}}$, which once again becomes the gradient of a fluctuating term and can therefore be grouped with diffusion. And so

$$\overline{P'\rho''_{,i}} \approx D \tag{3.107}$$

These assumptions, in particular, require additional study, which is now readily available via companion DNS works (ex.- [218, 118, 201]).

3.4 Algebratization

The above transport equation has been heavily simplified, but it remains a partial differential equation. In order to solve this equation numerically, an algebratization technique proposed by Girimaji and Balachandar [99] is implemented. The Favre-fluctuating velocity and energy equations are also algebratized to allow for later simplification of the algebraic energy flux equation.

3.4.1 Algebraic Turbulent Energy Flux Transport

The simplified transport equation (3.71) is repeated for convenience.

$$\frac{D\theta_i^T}{Dt} = -\tilde{u}_{i,k}\theta_k^T + \tau_{ik}^T\tilde{\psi}_{,k} - \overline{e''}\overline{P}_{,i} - \frac{R}{\overline{C_v}}\theta_i^T\tilde{u}_{k,k} + \overline{\rho}\xi_i$$

Now define the correlation coefficient and differentiate it following the Quotient and Multiplication Rules.

$$F_i = \frac{\theta_i^T}{\sqrt{k^T}\sqrt{\eta^T}} \tag{3.108}$$

$$\frac{DF_i}{Dt} = \frac{\sqrt{k^T}\sqrt{\eta^T}\frac{D\theta_i^T}{Dt} - \theta_i^T\frac{D\sqrt{k^T}\sqrt{\eta^T}}{Dt}}{k^T\eta^T} \tag{3.109}$$

$$\frac{DF_i}{Dt} = \frac{1}{\sqrt{k^T}\sqrt{\eta^T}}\frac{D\theta_i^T}{Dt} - \frac{\theta_i^T}{k^T\eta^T}\left(\frac{\sqrt{k^T}}{2\sqrt{\eta^T}}\frac{\eta^T}{Dt} + \frac{\sqrt{\eta^T}}{2\sqrt{k^T}}\frac{Dk^T}{Dt}\right) \tag{3.110}$$

$$\frac{DF_i}{Dt} = \frac{1}{\sqrt{k^T}\sqrt{\eta^T}}\frac{D\theta_i^T}{Dt} - \frac{\theta_i^T}{2\sqrt{k^T}\sqrt{\eta^T}}\left(\frac{1}{\eta^T}\frac{\eta^T}{Dt} + \frac{1}{k^T}\frac{Dk^T}{Dt}\right) \tag{3.111}$$

Apply the weak equilibrium assumption, that $\frac{DF_i}{Dt} \approx 0$; described verbally, this states that F_i is constant along a streamline.

$$0 \approx \frac{D\theta_i^T}{Dt} - \frac{\theta_i^T}{2}\left(\frac{1}{\eta^T}\frac{\eta^T}{Dt} + \frac{1}{k^T}\frac{Dk^T}{Dt}\right) \tag{3.112}$$

Now substitute in the transport equations for $\frac{D\theta_i^T}{Dt}$ (3.71), $\frac{Dk^T}{Dt}$ (3.36), and $\frac{D\eta^T}{Dt}$ (3.47), though it will be seen shortly the latter two need not be fully defined. It is useful to adopt the generalized notation $\frac{DX^T}{Dt} = P^X + D^X + A^X$ where P^X denotes production terms, D^X denotes diffusion terms, and A^X is the aggregate of the remaining terms such as dissipation, molecular terms, pressure-strain, *etc*. Equation 3.71 has already been grouped such that $D^{\theta_i^T} + A^{\theta_i^T} = \overline{\rho}\xi_i$ and every remaining term is production $P^{\theta_i^T}$.

$$0 \approx \left[P^{\theta_i^T} + D^{\theta_i^T} + A^{\theta_i^T}\right] - \frac{\theta_i^T}{2}\left(\frac{1}{\eta^T}\left[P^{\eta^T} + D^{\eta^T} + A^{\eta^T}\right] + \frac{1}{k^T}\left[P^{k^T} + D^{k^T} + A^{k^T}\right]\right) \tag{3.113}$$

Here, one assumes that $\overline{\rho}\xi_i \approx 0$, or at least $P^{\theta_i^T} \gg \overline{\rho}\xi_i$. For some terms, there is some justification for this step. For example, in their model for turbulent kinetic energy Launder et al. [155] wrote dissipation as $\frac{2}{3}\delta_{ij}\varepsilon$ (see Section 2.2), which implies dissipation is negligible for cross-correlation ($i \neq j$) terms; if one treats $\theta_i^T = \overline{\rho e'' u_i''}$ as a cross-correlation between energy and velocity, than one can assume its dissipation terms are also negligible.

For a more general justification, one could invoke Launder's so-called WET hypothesis [152, 153], which states "Wealth" is proportional to "Earnings" multiplied by "Time". Philosophically, it means that the amount of something is equal to the rate at which it is produced multiplied by the time that rate has been applied. Laudner admits it is an oversimplification, but intuitively there is some logic to it. In the present context, the amount of energy flux θ_i^T is equal to its production terms $P^{\theta_i^T}$ multiplied by a time constant to be defined shortly, and $P^{\theta_i^T}$ dominates all other terms such as dissipation and diffusion.

So while there is some reason to this step, in the end it remains a modeling necessity as it allows one to write

$$P^{\theta_i^T} \approx \frac{\theta_i^T}{2}\left(\frac{1}{\eta^T}\left[P^{\eta^T} + D^{\eta^T} + A^{\eta^T}\right] + \frac{1}{k^T}\left[P^{k^T} + D^{k^T} + A^{k^T}\right]\right) \tag{3.114}$$

where the right hand side lends itself naturally to the time constant

$$\tau_\theta^{-1} = \frac{1}{2}\left(\frac{1}{\eta^T}\left[P^{\eta^T} + D^{\eta^T} + A^{\eta^T}\right] + \frac{1}{k^T}\left[P^{k^T} + D^{k^T} + A^{k^T}\right]\right) \tag{3.115}$$

This is in and of itself too complex for feasible calculation, so it is modeled in Section 3.5. For now it is sufficient to consider the term closed.

What remains is at last an algebraic expression for turbulent energy flux

$$-\tilde{u}_{i,k}\theta_k^T + \tau_{ik}^T\tilde{\psi}_{,k} - \overline{e''}\,\overline{P}_{,i} - \frac{R}{\overline{\overline{C_v}}}\theta_i^T\tilde{u}_{k,k} \approx \frac{\theta_i^T}{\tau_\theta} \tag{3.116}$$

Or, written in the standard matrix notation,

$$a_{ik}\theta_k^T = b_i \tag{3.117}$$

where $a_{ik} = \left[\tau_\theta^{-1} + \frac{R}{\overline{C}_v}\tilde{u}_{m,m}\right]\delta_{ik} + \tilde{u}_{i,k}$ and $b_i = \tau_{ik}^T\tilde{\psi}_{,k} - \overline{e''}\,\overline{P}_{,i}$. The Kronecker delta is needed to align the indices between θ_i^T and θ_k^T. b_i can be further simplified by algebratizing the Favre-fluctuating velocity and energy transport equations.

3.4.2 Algebraic Favre-Fluctuating Velocity Transport

The simplified transport equation (3.72) is repeated for convenience.

$$\frac{D\overline{\rho}\,\overline{u_i''}}{Dt} \approx -\overline{\rho}\,\overline{u_k''}\tilde{u}_{i,k} + D_u$$

Using Favre-averaging, $\overline{\rho}\,\overline{u_i''} = \overline{\rho u_i''} - \overline{\rho' u_i''} = -\overline{\rho' u_i''}$, which allows the definition of a correlation coefficient

$$F_i = \frac{-\overline{\rho' u_i''}}{\sqrt{\overline{\rho'^2}}\sqrt{\overline{u_i''^2}}} \tag{3.118}$$

The terms in the denominator are squared to prevent division by zero due to a $\overline{\rho'}$ term. Differentiate this expression following the Quotient Rule.

$$\frac{DF_i}{Dt} = \frac{-\sqrt{\overline{\rho'^2}}\sqrt{\overline{u_i''^2}}\frac{D\overline{\rho' u_i''}}{Dt} + \overline{\rho' u_i''}\frac{D\sqrt{\overline{\rho'^2}}\sqrt{\overline{u_i''^2}}}{Dt}}{\overline{\rho'^2}\,\overline{u_i''^2}} \tag{3.119}$$

$$\frac{DF_i}{Dt} = -\frac{1}{\sqrt{\overline{\rho'^2}}\sqrt{\overline{u_i''^2}}}\frac{D\overline{\rho' u_i''}}{Dt} + \frac{\overline{\rho' u_i''}}{\overline{\rho'^2}\,\overline{u_i''^2}}\left(\frac{\sqrt{\overline{\rho'^2}}}{2\sqrt{\overline{u_i''^2}}}\frac{D\sqrt{\overline{u_i''^2}}}{Dt} + \frac{\sqrt{\overline{u_i''^2}}}{2\sqrt{\overline{\rho'^2}}}\frac{D\sqrt{\overline{\rho'^2}}}{Dt}\right) \tag{3.120}$$

$$\frac{DF_i}{Dt} = -\frac{1}{\sqrt{\overline{\rho'^2}}\sqrt{\overline{u_i''^2}}}\frac{D\overline{\rho' u_i''}}{Dt} + \frac{\overline{\rho' u_i''}}{\overline{\rho'^2}\,\overline{u_i''^2}}\left(\frac{\sqrt{\overline{\rho'^2}}\sqrt{\overline{u_i''^2}}}{2\overline{u_i''^2}}\frac{D\sqrt{\overline{u_i''^2}}}{Dt} + \frac{\sqrt{\overline{\rho'^2}}\sqrt{\overline{u_i''^2}}}{2\overline{\rho'^2}}\frac{D\sqrt{\overline{\rho'^2}}}{Dt}\right) \tag{3.121}$$

$$\frac{DF_i}{Dt} = -\frac{1}{\sqrt{\overline{\rho'^2}}\sqrt{\overline{u_i''^2}}}\frac{D\overline{\rho' u_i''}}{Dt} + \frac{\overline{\rho' u_i''}}{2\sqrt{\overline{\rho'^2}}\sqrt{\overline{u_i''^2}}}\left(\frac{1}{\overline{u_i''^2}}\frac{D\sqrt{\overline{u_i''^2}}}{Dt} + \frac{1}{\overline{\rho'^2}}\frac{D\sqrt{\overline{\rho'^2}}}{Dt}\right) \tag{3.122}$$

Apply the weak equilibrium assumption, that $\frac{DF_i}{Dt} \approx 0$; described verbally, this states that F_i is constant along a streamline.

$$0 \approx -\frac{D\overline{\rho' u_i''}}{Dt} + \frac{\overline{\rho' u_i''}}{2}\left(\frac{1}{\overline{u_i''^2}}\frac{D\sqrt{\overline{u_i''^2}}}{Dt} + \frac{1}{\overline{\rho'^2}}\frac{D\sqrt{\overline{\rho'^2}}}{Dt}\right) \tag{3.123}$$

Now substitute in the transport equations for $-\frac{D\overline{\rho' u_i''}}{Dt}(=\frac{D\overline{\rho}\,\overline{u_i''}}{Dt})$ (3.72), $\frac{D\sqrt{\overline{u_i''^2}}}{Dt}$, and $\frac{D\sqrt{\overline{\rho'^2}}}{Dt}$. Because this equation never needs to be solved and only serves to simply Equation 3.117 in the theory, generalized notation and formal transport equations for $\frac{D\sqrt{\overline{u_i''^2}}}{Dt}$ and $\frac{D\sqrt{\overline{\rho'^2}}}{Dt}$ are unnecessary.

$$0 \approx -\overline{\rho}\,\overline{u_k''}\tilde{u}_{i,k} + D_u + \frac{\overline{\rho' u_i''}}{2}\left(\frac{1}{\overline{u_i''^2}}\frac{D\sqrt{\overline{u_i''^2}}}{Dt} + \frac{1}{\overline{\rho'^2}}\frac{D\sqrt{\overline{\rho'^2}}}{Dt}\right) \tag{3.124}$$

This time do not neglect the diffusion-order terms; because the goal here is not to model the above equation, there is less motivation to isolate P^u. Introduce a time constant

$$\tau_u^{-1} = \frac{1}{2}\left(\frac{1}{\overline{u_i''^2}}\frac{D\sqrt{\overline{u_i''^2}}}{Dt} + \frac{1}{\overline{\rho'^2}}\frac{D\sqrt{\overline{\rho'^2}}}{Dt}\right) \tag{3.125}$$

With this the algebratized equation becomes

$$0 \approx -\overline{\rho}\,\overline{u_k''}\tilde{u}_{i,k} + D_u + \frac{\overline{\rho' u_i''}}{\tau_u} \tag{3.126}$$

Re-writing $\overline{\rho' u_i''}$ as $-\overline{\rho}\,\overline{u_i''}$, absorbing $\frac{1}{\overline{\rho}}$ into D_u, and aligning indices with a Kronecker delta produces

$$\left(\tilde{u}_{i,k}\delta_{ik} + \tau_u^{-1}\right)\overline{u_k''} \approx D_u \tag{3.127}$$

Equation 3.127 suggests $\overline{u_k''} = \mathscr{O}(D_u)$ and therefore is negligible under the assumptions throughout

this work.

3.4.3 Algebraic Favre-Fluctuating Energy Transport

The simplified transport equation (3.73) is repeated for convenience.

$$\frac{D\overline{\rho}\overline{e''}}{Dt} = -\overline{\rho}\tilde{e}_{,k}\overline{u''_k} + \frac{\overline{P}\,\overline{\rho}_{,k}\overline{u''_{k,k}}}{\overline{\rho}} + \frac{\tilde{u}_{k,k}\overline{\rho' P'}}{\overline{\rho}} + M_{kl}$$

Using Favre-averaging, $\overline{\rho}\overline{e''} = \cancel{\overline{\rho e''}} - \overline{\rho' e''} = -\overline{\rho' e''}$, which allows the definition of a correlation coefficient

$$F_i = \frac{-\overline{\rho' e''}}{\sqrt{\overline{\rho'^2}}\sqrt{\overline{e''^2}}} \tag{3.128}$$

The terms in the denominator are squared to prevent division by zero due to a $\overline{\rho'}$ term. Differentiate this expression following the Quotient Rule

$$\frac{DF_i}{Dt} = \frac{-\sqrt{\overline{\rho'^2}}\sqrt{\overline{e''^2}}\frac{D\overline{\rho' e''_i}}{Dt} + \overline{\rho' e''}\frac{D\sqrt{\overline{\rho'^2}}\sqrt{\overline{e''^2}}}{Dt}}{\overline{\rho'^2}\,\overline{e''^2}} \tag{3.129}$$

$$\frac{DF_i}{Dt} = -\frac{1}{\sqrt{\overline{\rho'^2}}\sqrt{\overline{e''^2}}}\frac{D\overline{\rho' e''}}{Dt} + \frac{\overline{\rho' e''}}{\overline{\rho'^2}\,\overline{e''^2}}\left(\frac{\sqrt{\overline{\rho'^2}}}{2\sqrt{\overline{e''^2}}}\frac{D\sqrt{\overline{e''^2}}}{Dt} + \frac{\sqrt{\overline{e''^2}}}{2\sqrt{\overline{\rho'^2}}}\frac{D\sqrt{\overline{\rho'^2}}}{Dt}\right) \tag{3.130}$$

$$\frac{DF_i}{Dt} = -\frac{1}{\sqrt{\overline{\rho'^2}}\sqrt{\overline{e''^2}}}\frac{D\overline{\rho' e''}}{Dt} + \frac{\overline{\rho' e''}}{\overline{\rho'^2}\,\overline{e''^2}}\left(\frac{\sqrt{\overline{\rho'^2}}\sqrt{\overline{e''^2}}}{2\overline{e''^2}}\frac{D\sqrt{\overline{e''^2}}}{Dt} + \frac{\sqrt{\overline{\rho'^2}}\sqrt{\overline{e''^2}}}{2\overline{\rho'^2}}\frac{D\sqrt{\overline{\rho'^2}}}{Dt}\right) \tag{3.131}$$

$$\frac{DF_i}{Dt} = -\frac{1}{\sqrt{\overline{\rho'^2}}\sqrt{\overline{e''^2}}}\frac{D\overline{\rho' e''}}{Dt} + \frac{\overline{\rho' e''}}{2\sqrt{\overline{\rho'^2}}\sqrt{\overline{e''^2}}}\left(\frac{1}{\overline{e''^2}}\frac{D\sqrt{\overline{e''^2}}}{Dt} + \frac{1}{\overline{\rho'^2}}\frac{D\sqrt{\overline{\rho'^2}}}{Dt}\right) \tag{3.132}$$

Apply the weak equilibrium assumption, that $\frac{DF_i}{Dt} \approx 0$; described verbally, this states that F_i is constant along a streamline.

$$0 \approx -\frac{D\overline{\rho' e''}}{Dt} + \frac{\overline{\rho' e''}}{2}\left(\frac{1}{\overline{e''^2}}\frac{D\sqrt{\overline{e''^2}}}{Dt} + \frac{1}{\overline{\rho'^2}}\frac{D\sqrt{\overline{\rho'^2}}}{Dt}\right) \tag{3.133}$$

Now substitute in the transport equations for $-\frac{D\overline{\rho' e''}}{Dt}(=\frac{D\overline{\rho}\,\overline{u''}}{Dt})$ (3.73), $\frac{D\sqrt{\overline{e''^2}}}{Dt}$, and $\frac{D\sqrt{\overline{\rho'^2}}}{Dt}$. Because this equation never needs to be solved and only serves to simply Equation 3.117 in the theory, generalized notation and formal transport equations for $\frac{D\sqrt{\overline{e''^2}}}{Dt}$ and $\frac{D\sqrt{\overline{\rho'^2}}}{Dt}$ are unnecessary.

$$0 \approx \left(-\overline{\rho}\tilde{e}_{,k}\overline{u''_k} + \frac{\overline{P}\,\overline{\rho}_{,k}\overline{u''_{k,k}}}{\overline{\rho}} + \frac{\tilde{u}_{k,k}\overline{\rho' P'}}{\overline{\rho}} + M_{kl} \right) + \frac{\overline{\rho' e''}}{2} \left(\frac{1}{\overline{u''^2_i}} \frac{D\sqrt{\overline{u''^2_i}}}{Dt} + \frac{1}{\overline{\rho'^2}} \frac{D\sqrt{\overline{\rho'^2}}}{Dt} \right) \tag{3.134}$$

Now neglect the molecular term M_{kl}; because the goal here is not to model the above equation, there is less motivation to isolate P^e. Introduce a time constant

$$\tau_e^{-1} = \frac{1}{2} \left(\frac{1}{\overline{e''^2}} \frac{D\sqrt{\overline{e''^2}}}{Dt} + \frac{1}{\overline{\rho'^2}} \frac{D\sqrt{\overline{\rho'^2}}}{Dt} \right) \tag{3.135}$$

With this the algebratized equation becomes

$$0 \approx \left(-\overline{\rho}\tilde{e}_{,k}\overline{u''_k} + \frac{\overline{P}\,\overline{\rho}_{,k}\overline{u''_{k,k}}}{\overline{\rho}} + \frac{\tilde{u}_{k,k}\overline{\rho' P'}}{\overline{\rho}} \right) + \frac{\overline{\rho' e''}}{\tau_e} \tag{3.136}$$

Re-writing $\overline{\rho' e''}$ as $-\overline{\rho}\overline{e''}$ and re-arranging produces

$$\overline{\rho}\overline{e''} \approx \left(-\overline{\rho}\tilde{e}_{,k}\overline{u''_k} + \frac{\overline{P}\,\overline{\rho}_{,k}\overline{u''_{k,k}}}{\overline{\rho}} + \frac{\tilde{u}_{k,k}\overline{\rho' P'}}{\overline{\rho}} \right) \tau_e \tag{3.137}$$

Now recall Equation 3.127; by assuming diffusion-order terms are negligible, one can write $\overline{u''_k} \approx D_u$. Further assuming that the third term on the right hand side is negligible because it is a dilitation and second-order compressibility effect which both tend to be small, one is left with

$$\overline{e''} \approx D_e \tag{3.138}$$

Again, it is emphasized this result is only usable under the assumptions of the preceding derivation.

3.5 Implementation

Using Equation 3.138 in Equation 3.117 one is left with the final, simplified form of the algebraic energy flux model:

$$a_{ik}\theta_k^T = b_i \tag{3.139}$$

where $a_{ik} = \left[\tau_\theta^{-1} + \frac{R}{\bar{C}_v}\tilde{u}_{m,m}\right]\delta_{ik} + \tilde{u}_{i,k}$ and $b_i = \tau_{ik}^T\tilde{\psi}_{,k}$. This approach has been successfully compared to a range of equilibrium flows [153, 38, 218, 118], including homogenous shear flows, wakes, and wall boundary layers (Mach $0-14$); recently, it was extended to high speed flows with both adverse and favorable pressure gradients [46]. However, because diffusion and dissipation are neglected, the current model is limited to the outer region of wall boundary layers and free shear layers until near wall corrections are produced. The purpose of this subsection is to provide some guidance on the application of the above theory to practical hypersonic, ZPG, RANS turbulent boundary layer modeling. A procedure to implement the model in an industry-level CFD package is provided in [46], but it provides detail beyond the scope of this report.

As the model is being actively researched, some parameters have changed with each publication (in order, [38], [218], [118]). Bowersox's original paper [38] remains both the theoretical and practical foundation for many of the concepts described below, but ultimately [118] is taken as the main reference regarding the implementation. The parameters discussed below were used in the boundary layer solver described in Chapter 5. Additionally, note that in the model's recent publications [38, 218, 118] there is an extra term, placed either in a_{ik} or b_i, that is not present here; the derivation in [46] and the additional detail provided above show this term is indeed a simple typing error originating in [38] and carried through subsequent works. The authors of the affected sections confirmed in private communications it was never actually coded into any of the programs used to generate the data in these publications.

Equation 3.139 can be solved explicitly using Cramer's Rule. Bowersox [38] recommended using $|a_{ik}| \approx \tau_\theta^{-3}$ for stability; Broslawski et al. [46] wrote that numerical instabilities grew in the determinant as greater pressure gradients were applied, and so this approximation should hold for

ZPG flows. Hereafter x_1 is the streamwise coordinate, x_2 is the wall normal coordinate, and x_3 is the spanwise coordinate.

$$\begin{aligned}
\theta_1^T &= \left(\frac{1}{\tau_\theta^{-3}}\right)\left[b_1\left(a_{22}a_{33}-a_{32}a_{23}\right)-b_2\left(a_{12}a_{33}-a_{32}a_{13}\right)+b_3\left(a_{12}a_{23}-a_{22}a_{13}\right)\right] \\
\theta_2^T &= \left(\frac{1}{\tau_\theta^{-3}}\right)\left[-b_1\left(a_{21}a_{33}-a_{31}a_{23}\right)+b_2\left(a_{11}a_{33}-a_{31}a_{13}\right)-b_3\left(a_{11}a_{23}-a_{21}a_{13}\right)\right] \\
\theta_3^T &= \left(\frac{1}{\tau_\theta^{-3}}\right)\left[b_1\left(a_{21}a_{32}-a_{31}a_{22}\right)-b_2\left(a_{11}a_{32}-a_{31}a_{12}\right)+b_3\left(a_{11}a_{22}-a_{21}a_{12}\right)\right]
\end{aligned} \tag{3.140}$$

For 2D thin shear layers, these equations reduce to, as written in [118],

$$\begin{aligned}
\theta_1^T &= \left(\tau_{12}^T-\tau_{22}^T\tilde{u}_{1,2}\tau_\theta\right)\tau_\theta\tilde{\psi}_{,2}/d_1 \\
\theta_2^T &= \tau_{22}^T\tilde{\psi}_{,2}\tau_\theta
\end{aligned} \tag{3.141}$$

where d_1 is a wall damping correction $d_1 = 1-\exp(-x_2^*/C_1^*)$ with semi-local scaling on the wall coordinate and the model constant C_1^*; x_2^+ and 12 are recommended, respectively [38]. In the absence of a pressure gradient $\tilde{\psi}_{,2} = \tilde{h}_{,2}$. The time constant τ_θ was calculated from $\tau_\theta \approx \sigma_\theta\tau_u$, where σ_θ was a tunable parameter set for all known implementations [38, 218, 118, 46] to $\sigma_\theta = 0.28/\gamma$; note that this assumed that the turbulent energy flux timescale was on the same order as that of the turbulent timescale. From the dimensional analysis of Jones and Launder [130], $\tau_u = \frac{k^T}{\varepsilon}$. The approximation ultimately used here was first written in [218] as $\tau_u \approx \frac{a_1}{C_\mu\tilde{u}_{1,2}}$ where $a_1 = 0.28$ and $C_\mu = 0.09$; as a numerical tip, add a small constant (ex.- 10^{-9}) to the derivative $\tilde{u}_{1,2}$ to prevent division by zero at all points throughout the domain. Additional explanation for the origin of the constants is found in [38].

For the flat plate case the Reynolds stress is solved with the Boussinesq approximation $\tau_{12}^T = \mu^T u_{1,2}$ and the streamwise stress with

$$\frac{\tau_{12}^T}{\tau_{22}^T} = -\frac{C}{1-\exp(-x_2^+/A^+)} \tag{3.142}$$

where $C = 0.68$ and $A^+ = 26.0$ [218], though here d_1 was used all the wall scaling coefficient. This formula was purpose-built for a flat plate boundary layer, limiting its application. The use of μ^T does imply the Boussinesq approximation, even though it was not extended to the heat flux calcuulation. While this is acceptable for the flat plate case, in general it limits the application of the AEF approach under high speed conditions. In the proceeding section, it will be seen that DNS can be used to provide the Reynolds stresses, but as these remain highly specialized and expensive techniques improved RANS models for the Reynolds stresses under general hypersonic conditions are needed.

Finally, in order to relate the energy flux to heat flux for thermally perfect and calorically imperfect gases, begin with the enthalpy equation $\rho h = \rho e + P$. Expand it with Reynolds and Favre terms, multiply through by u_i'', then Reynolds average the result.

$$\tilde{h}\cancel{\overline{\rho u_i''}} + \overline{\rho h'' u_i''} = \tilde{e}\cancel{\overline{\rho u_i''}} + \overline{\rho e'' u_i''} + \overline{P}\,\overline{u_i''} + \overline{P' u_i''} \tag{3.143}$$

$$q_i^T = \theta_i^T + \overline{P}\,\overline{u_i''} + \overline{P' u_i''} \tag{3.144}$$

Using Equation 3.105 and $R = C_p - C_v$ yields

$$q_i^T = \gamma \theta_i^T \tag{3.145}$$

With this the AEF model supplies the turbulent heat flux.

To summarize, for the numerical boundary layer solver described in Chapter 5, it was sufficient to calculate $q_2^T = \gamma \theta_2^T$ where $\theta_2^T = \frac{b_2 a_{11} a_{33}}{\tau_\theta^{-3}}$ with $a_{11} = a_{33} = \tau_\theta^{-1}$ and $b_2 = \tau_{22}^T \tilde{\psi}_{,2}$.

3.6 Extension to Flows with Pressure Gradients

The relevant work of Broslawski et al. [46] is summarized here as it extended the above theory to a real flow with pressure gradients. It used an in-house RANS code (not the one described in Chapter 5) to model a 2D turbulent boundary layer in a wind tunnel at $M = 4.9$ and $Re = 45 \times 10^6/\text{m}$. Particle imaging velocimetry (PIV) provided the Reynolds stresses for both favorable

[278] and adverse [195] pressure gradient cases. These data validated DNS for the favorable [200] and adverse [199] cases. These simulations in turn provided the wall normal and streamwise components of the turbulent heat flux q_y^T and q_x^T. Due to the pressure gradients, the authors used the Reynolds stresses provided by the DNS to calculate the turbulent heat flux using the AEF approach, completely removing all uses of the Boussinesq approximation.

The Reynolds stresses from the experiments and simulations for the adverse (APG), weak favorable (FPG-WPG), and strong favorable (FPG-SPG) cases are compared in Figure 3.2. The under prediction of the experimental data was attributed a known phenomena of the PIV technique [45, 50, 299], and the agreement was considered satisfactory for the DNS to be used. The data suggested the favorable pressure gradient was re-laminarizing the flow, as evinced by the sign change in the Reynolds stress. This is noteworthy, because, by their very formulation, Boussinesq turbulence models cannot predict negative Reynolds stresses. As expected, the adverse pressure gradient tended to increase the production of the Reynolds stresses.

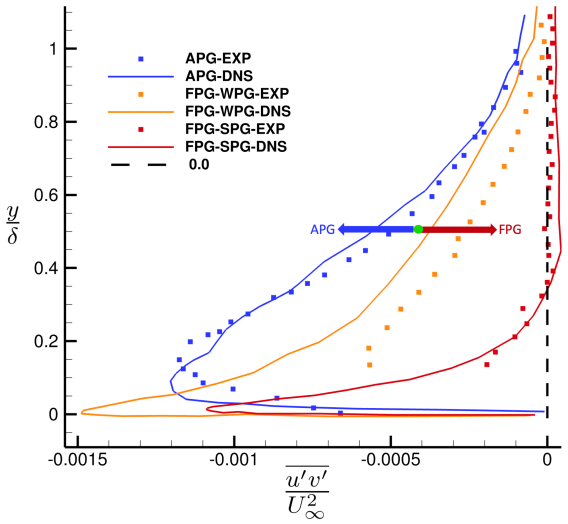

Figure 3.2: Reynolds stresses for AEF model study; figure taken with permission from Broslawski et al. [46].

Nicholson et al. [200] observed that, given a large enough streamwise domain (beyond that

shown in Figure 3.3) and for the case of the strong favorable pressure gradient, the wall normal component of the turbulent heat flux q_y^T had a similar sign change. Broslawski et al. [46] identified two reasons these physics challenged the AEF model. The first was that they called into question the central weak equilibrum assumption, that the correlation coefficients F_i were constant along streamlines; in the case of pressure gradients, this appears to be violated, requiring direct investigation going forward. They also note the dominant dependence/scaling q_y^T had on $\overline{v'v'}$, an inherently positive parameter. These two factors were deemed problematic and may motivate further development of the AEF model for the generalized case of pressure gradients.

Figure 3.3 compares the wall normal and streamwise components of the the turbulent heat flux as calculated with the AEF data (Reynolds stresses from DNS) and standard Boussinesq approach (constant Pr_t). The results were from the same test location as the Reynolds stresses in Figure 3.2.

Beginning with q_x^T, it was immediately clear that the Boussinesq approach was completely incapable of predicting the streamwise component of the turbulent heat flux (Figure 3.3(a)). The AEF approach (Figure 3.3(b)) yielded improved agreement with the DNS for all three cases, though further development was needed to address an under prediction of the results in the case of the adverse pressure gradient. What was especially surprising was how well the AEF model performed near the wall, accurately capturing the spike in this region. Here diffusion, and especially dissipation, dominate the physics, and these were effectively omitted in the AEF model's derivation as part of the WET hypothesis. For q_y^T the Boussinesq approach (Figure 3.3(c)) did a better job matching the DNS, which made sense as it was specifically tuned to capture this component of the turbulent heat flux. However, the results were still inferior when compared to the agreement seen for the AEF approach (Figure 3.3(d)). Here it was noted again that there was a slight sign reversal in the case of the strong favorable pressure gradient, but the AEF model could not capture it. Finally, that $|q_x^T| \gg |q_x^T|$ underscored the importance of predicting all three components of turbulent heat flux and the gravity of Boussinesq models' inability to do so.

In summary, the work of Broslawski et al. [46] extended the AEF model to mechanically strained flows and showed it was able to outperform standard RANS techniques. The improve-

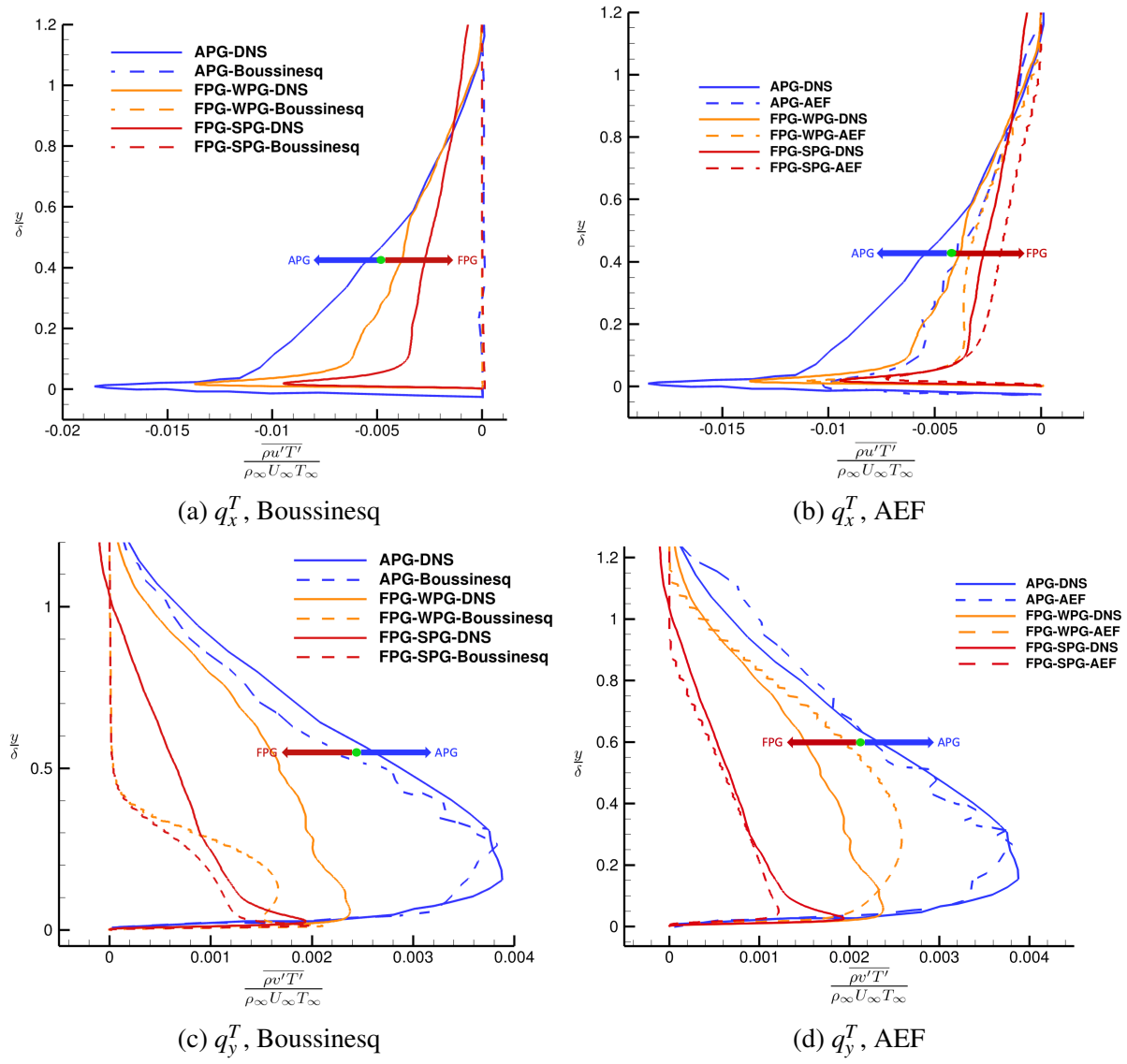

(a) q_x^T, Boussinesq

(b) q_x^T, AEF

(c) q_y^T, Boussinesq

(d) q_y^T, AEF

Figure 3.3: Comparisons of streamwise and wall normal turbulent heat flux as predicted by the Boussinesq and AEF models; figures taken with permission from Broslawski et al. [46].

ment was most profound in the case of q_x^T. This success motivated further development of the model, for example in the case of adverse pressure gradients. The derivation clarified the necessity and justification for the assumptions used throughout the process, which allowed each one to be studied individually. For example, the assumed dominance of production throughout the boundary layer, especially in the near wall region, and the weak equilibrium assumption could both benefit from an analysis like that by Nicholson et al. [201], which used DNS to individually plot each com-

ponent of various transport equations and thereby study their individual behavior and importance. Such detailed work was invaluable in understanding the complex physics entrained in turbulence transport equations and deciding how each term should be treated in a model; for example, the authors found production was in fact important in the near wall transport of q_x^T in the case of favorable pressure gradients and recommended these physics be included in models of such flows. Overall the current state of the AEF model as derived above has been shown to be effective in a variety of flows, improving the prediction of turbulent heat flux within a RANS framework. Further work, aided by ever-advancing computational resources, will only continue to drive it forward.

4. EXPERIMENTAL FACILITIES

This chapter covers all of the main facilities and hardware used throughout the campaign. This includes the wind tunnel, along with its support infrastructure and any modifications made for the present work (specifically NO injection), a vacuum chamber for plasma development, the equipment for generating the glow discharge, and the test article. The design of the test article is covered with the most detail, with justification provided for each of its main features and special attention given to its critical elements such as the leading edge, trips, and electrodes.

4.1 Actively Controlled Expansion (ACE) Tunnel

All wind tunnel data included in this report were taken in the blowdown ACE tunnel at the NAL first introduced in [244]. Indeed, the entire campaign was designed to be conducted in this facility. Here the lab infrastructure is described in the sequential order it is used, starting with the air delivery system to the data acquisition system. Characteristic tunnel conditions are summarized in Table 4.1. Note that these values are a combination of theoretical calculations, personal experience, and published data and are intended only to provide a frame of reference. Modifications to the tunnel and the optimization of conditions may produce data outside the characteristic ranges shown here. Also included in Table 4.1 are the test conditions for the present campaign. Transience during a run and imperfect repeatability may cause slight deviation from these test conditions; tolerable experimental uncertainties are included in the table.

Parameter	Characteristic	Test Condition
M	$5-8$	5.70 ± 0.05
Duration (s)	$30-50$	40
$Re\,(\times 10^6/\mathrm{m})$	$0.5-8$	6.00 ± 0.25
$P_o\,(\mathrm{kPa})$	$48.26-689.48$	496.42 ± 20.68
$T_o\,(\mathrm{K})$	$300-533$	430 ± 15
$P\,(\mathrm{Torr})$	$0.05-10$	3.23 ± 0.13
$T\,(\mathrm{K})$	$40-70$	57.35 ± 2.00
$\rho\left(\frac{\mathrm{kg}}{\mathrm{m}^3}\right)$	$5.81\times10^{-4}-6.63\times10^{-2}$	$2.61 \pm 0.2 \times 10^{-2}$
$n\left(/\mathrm{cm}^3\right)$	$1.21\times10^{16}-1.38\times10^{18}$	$5.43 \pm 0.41 \times 10^{17}$
$\frac{P'_{RMS}}{P}\,(\%)$	$0.1-2.0$	1.5 ± 0.25

Table 4.1: ACE tunnel conditions.

4.1.1 Support Infrastructure

As a blowdown facility, the ACE tunnel requires a large pressure differential to achieve hypersonic conditions. To reach high pressures on the supply side, air is compressed at 3.7 standard cubic meters per minute by two CompAir Reavell 5442 compressors before passing through a cyclone separator, two 99% efficient filters, a regenerative desiccant dryer and then finally being stored at 17.24MPa in an A.O. Smith 23.2m^3 tank. The conditioning process removes oil and particulates greater than 1μm and enough moisture reach a dew point of 233.15K. It takes $\sim$ 2.5hr for the tank to be fully recharged after a run, nominally from 10.34MPa, and this represents the largest limitation on the number of achievable runs in a campaign. To further increase the pressure differential through the tunnel, a 530Pa vacuum is supplied by a Fox Venturi Products two-stage air ejector pictured in Figure 4.1. This equipment operates on the Venturi principal and thus requires a motive air supply; here $\sim 25\frac{\mathrm{kg}}{\mathrm{s}}$ of air at 1MPa is supplied via a 10.16cm pipe (4 inch line) to drive the system. The mass flow through the ACE tunnel is $\mathscr{O}\left(1\frac{kg}{s}\right)$, making it clear that the limiting factor on run time, and thus on the facility's duty cycle, is the ejector.

Air is supplied to the tunnel via a 5.08cm pipe (2 inch line). In doing so, it passes through a 0.5MW electrical resistance heater capable of temperatures of 530K; to prevent accidental overheat and improve repeatability, the heater is only used during the tunnel's preheat and not during a

Figure 4.1: The two-stage air ejector.

run. Blowdown hypersonic tunnels must be preheated to elevated stagnation temperatures in order to prevent liquefaction of oxygen during the expansion process [168]. A dome-loaded Stra-Val regulator upstream of the heater protects it from being over-pressurized. After passing through the heater, the air is passed through a second Stra-Val regulator followed by a final 1μm filter before finally entering the settling chamber. A US Hose Corporation UFBX stainless steel braided hose formed the final connection between the support infrastructure and the tunnel as it provides flexibility during tunnel modifications. The use of two regulators in series prevents pressure oscillations in the line, and also provides better control of the tunnel's stagnation pressure. All infrastructure inside the laboratory space is covered with custom fiberglass insulation from the Advanced Thermal Corp. in order to prevent heat loss after preheat, and also for safety. It is noted that several redundant safety mechanisms are located throughout the air delivery system including fail-closed actuators, pop-off valves, and burst disks. An excellent description of the entire air delivery system is provided by Tichenor [279].

4.1.2 Design and Characterization

As was previously stated, the ACE tunnel is a blowdown facility; its flow path is shown in Figure 4.2. All materials were constructed in the Texas A&M Oran W. Nicks Low Speed Wind Tunnel's machine shop from stainless steel, which allows the use of *NO* for PLIF without risk

of excessive corrosion. A full description of the tunnel design can be found in [244, 279, 168], though the reader is again cautioned that progressive upgrades to the facility may alter the values reported therein. Air is delivered into the settling chamber via a four 3.81cm flexible hoses split between ports on the top and bottom surfaces in order seed the flow throughout the entire plenum. Two 250W Omegalux HCS-080-240V heaters on the sides and a 1000W Omegalux HCS-120-240V on the top of the settling chamber help prevent heat loss after preheat and in between runs; these surfaces are covered with Advanced Thermal Corp. insulation for safety and to prevent heat loss. The uniformity is further improved by two aerogrids consisting of 0.32cm hole patterns in stainless steel plates [279]; if the flow is non-uniform some of the holes will choke and the flow will redistribute itself to become more even across the entire array [168]. The hole patterns between the two grids are offset to enhance this effect. Downstream of the aerogrids are three stainless steel screens of progressive refinement, from 7.87. then 23.62, and finally 59.06 grids per cm [279]. The meshes break up turbulent structures to pass laminar flow into the nozzle [168].

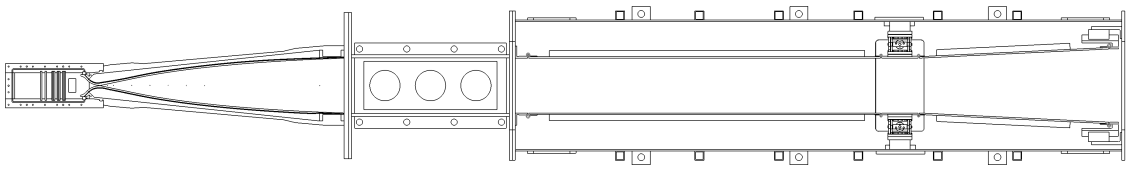

Figure 4.2: The Actively Controlled Expansion tunnel.

The contours for the 2D, planar, de Laval nozzle were designed using an in-house method of characteristics code following Shapiro [256] with a correction for the effect of the viscous boundary layer on the area ratio [282]. Simulations over the predicted experimental range were conducted with Aerosoft Inc.'s GASP CFD program. Semper et al. [244] provided a detailed explanation of the nozzle design. As with all supersonic flows, the Mach number is controlled by

the ratio between the nozzle's throat and exit via the following expression [128]

$$\left(\frac{A}{A^*}\right)^2 = \frac{1}{M^2}\left[\frac{2}{\gamma+1}\left(1+\frac{\gamma-1}{2}M^2\right)\right]^{\left(\frac{\gamma+1}{\gamma-1}\right)} \tag{4.1}$$

A unique design of the ACE tunnel's nozzle is the adjustable throat. The top and bottom surfaces of the nozzle are free floating, rigidly attached to the test section but otherwise held in place by pressure due to brackets along the two sidewalls and by resting on silicone O-rings inside the settling chamber. This allows operators to insert and remove shims at the throat to control the area ratio and thereby the Mach number. For the proposed test condition, $M = 5.7$, and for an exit area of $A = 831.70\text{cm}^2$ (including a 0.32cm step between the nozzle and test section), the theoretical throat area is $A^* = 19.43\text{cm}^2$. The actual throat height deviates from the theory, and indeed even changes at different Reynolds numbers, due to the presence and state (laminar/turbulent) of the nozzle's boundary layer.

Mai [168] and Semper [243] provided Mach number and freestream acoustic noise calibrations of the freestream over a range of Reynolds numbers and for $M = [5,6,7]$. Using these results, for the current campaign $\frac{P'_{RMS}}{\langle P \rangle} = 1.0 - 1.5\%$ and the Mach number varied $0.5 - 1.5\%$ across the test section. There is a considerable jump in freestream noise at $Re \approx 3.0 \times 10^{-6}/\text{m}$ attributed to transition of the nozzle's sidewalls [245], so it was desirable to pick a test condition far from this Reynolds number to guarantee the nozzle's boundary layer had completely transitioned and was fully and consistently turbulent.

The test section is 35.88cm wide, 23.18cm tall, and 66.04cm long. All internal surfaces are painted black to prevent reflection when performing optical measurements. A series of three 12.70cm ports on both the top and bottom surfaces allow for optical access or custom test article supports and probe mounts. One port on the top surface is reserved for a 101.325kPa pop-off valve in the event of accidental pressurization of the test section. $20.19 \times 55.75\text{cm}^2$ removable doors on both sides of the test section allow for further customization, be it for model support, further optical access, *etc*. A stainless steel table was constructed beneath the test section to form the

base of an XT-95 optical rail cage that surrounded the entire test section. This is used to position equipment around the entire test section without being affected by the tunnel's vibration.

The final stage of the tunnel's flowpath is the adjustable diffuser. It was originally designed following Bertram [30] and Wegener and Lobb [291], but because diffuser design is somewhat left to intuition [220] liberties were taken with the final design reported by Semper et al. [244]. The main goal of a diffuser is to decelerate the flow to a normal shock at the throat, maintaining an advantageous pressure differential and mass flux over a broad range of pressure differentials. Leidy [160] redesigned the ACE tunnel's diffuser to make it easier to adjust the throat height, provide an overall better construction based off the initial success of the first iteration, and use only stainless steel in the flow path. The first two points had the cumulative effect of increasing the Reynolds number range of the facility for a wide range of test article, while the last allowed for *NO* to be used in the flow with without the risk of excessive corrosion. The diffuser's outlet connects to the ejector system discussed above.

4.1.3 *NO* Injection

Under true hypersonic conditions, *NO* is naturally produced from dissociated nitrogen and oxygen atoms [6]. However, the enthalpy in the ACE tunnel was too low to cause such thermochemical effects. For this reason, aside from shock-type facilities capable of simulating flight conditions, *NO* needed to be artificially seeded into the flow; Danehy et al. [77] provided an example of *NO* PLIF MTV in such a facility. On smaller-scale and pulse burst facilities, *NO* PLIF has been successfully conducted by pre-mixing *NO* into the N_2 supply [174, 235, 116]. In the PLIF campaign reviewed in Section 2.5.7, the gas was blown directly into the boundary layer through the model; the serious implications of this approach on boundary layer stability and thermographic measurements are discussed in that section.

Here a different approach was used. It was desirable to accelerate the *NO* through the nozzle like [174, 235, 116] not only to ensure homogenous mixing, but also to allow adequate time for thermalization between the injected gas and the main air supply; this was especially important for PLIF thermometry as it was assumed the *NO* was of the same temperature as the surrounding gas.

This meant the ideal location for *NO* injection was the tunnel's settling chamber, pictured in Figure 4.3. The settling chamber was originally designed with replaceable plugs on all four sides of the box downstream of the flow conditioners; it is through one of these ports that 3.18mm total temperature and pressure probes are inserted into the flow. Because past tunnel characterizations had not found and effect on flow quality from to these probes [168] and due to the ease of machining new plugs for different configurations, this was the primary candidate location for an *NO* seeder.

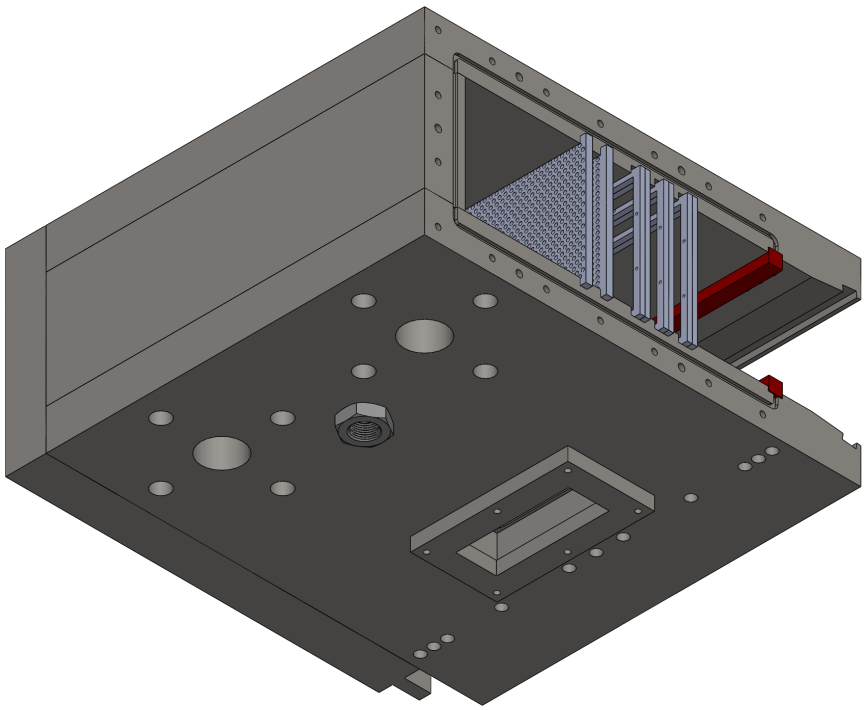

Figure 4.3: CAD model of the ACE tunnel's settling chamber; bottom corner view.

Many different seeder geometries were tested before the final design was selected. Design parameters included: the openings' geometry (slit or holes); the open area (length of slit or number/size of holes); the diameter of the pipe; the orientation of the pipe (straight from bottom or bent 90° to inject in the streamwise direction); the position of the slit/holes (before/after flow conditioners as well as vertical distance from the floor); and the injection pressure. All pipe designs

were crimped to a roughly elliptical shape to simulate a symmetric airfoil and help reduce wakes. A characteristic seeder is shown in Figure 4.4. Many of the aforementioned design choices were answered in preliminary testing; for example, a water visualization test revealed in slit designs the momentum of the fluid travelling up the seeder caused non-streamwise injection.

Figure 4.4: A characteristic *NO* seeder.

An analysis of the independent impact of each parameter is included in [49], but a representative summary is provided in [48]. Three tests were conducted where a 9.53mm seeder, crushed roughly 2:1 for a final width of 4.77mm to reduce its cross-sectional area, was placed upstream and downstream of the flow conditioners, as well as removed completely such that the *NO* was injected as a plume from the floor of the settling chamber. The results are shown in Figure 4.5. The intricacy of the eddies Figure 4.5(a), which did not use a physical seeder inserted into the flow, suggest that even the act of injecting the gas itself could greatly impact the quality of the flow; this phenomenon was enhanced by the cross-flow direction of the injection. The physical seeder of 4.5(b) performed better. The streamwise injection of the gas removed many of the ed-

dies, but a wake structure formed; even reducing the side of the seeder to a crushed 3.18mm pipe, the same size as the settling chamber's stagnation pressure and temperature ports created a wake [49]. Therefore it was necessary to inject the gas upstream of the settling chamber's flow conditioners. It was modified to allow for a pipe to be inserted ~ 2.54cm upstream of the first aerogrid, as far upstream as space would allow. The resulting flow shown in Figure 4.5(c) was absent of any wake or injection artifact, so this injection location was used all subsequent experiments. It is noted that subtle streaks were present in the *NO* cloud in Figure 4.5(c), which Buen [49] attributed to be the result nonuniform *NO* seeding being passed through the aerogrids; these streaks tended to dissipate when a set of images were averaged.

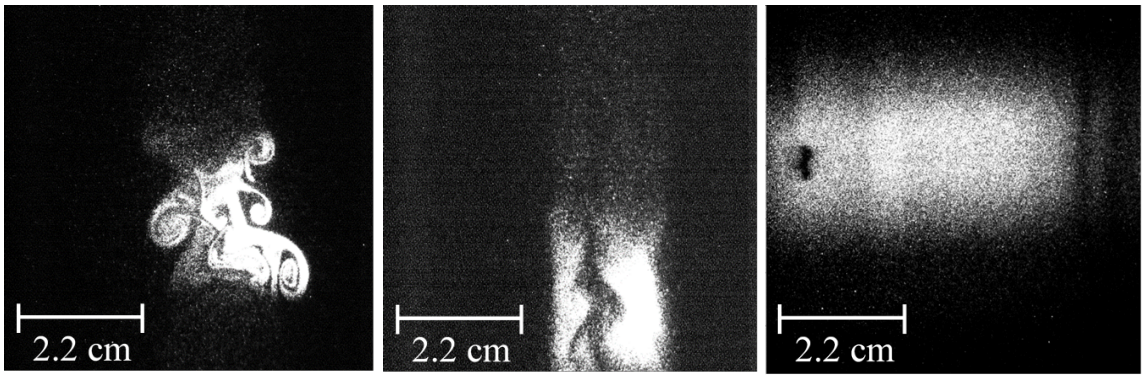

(a) (b) (c)

Figure 4.5: Effect of seeder body and placement. (a) No seeder, injection downstream of flow conditioners, (b) seeder dowstream of flow conditioners, (c) seeder upstream of flow conditioners. It is noted there is a burn spot in the camera visible in the fluorescing region in (c). The flow direction was bottom-to-top. Figures taken with permission from Buen et al. [48].

Figure 4.5 also shows how PLIF flow visualization can be used to approximate the size and location of the *NO* cloud in the settling chamber. This was important because such visualization tests revealed the top-to-bottom location of the cloud was dependent on the location of the seeder's holes; the wedge, which effectively cut the test section into two regions, exacerbated this effect and made it very important to select a hole placement which puts the bulk of the cloud on the top

of test article in the core flow. Note that when the test article was not used the tunnel could not be run at $Re = 6 \times 10^6/\text{m}$ without risking unstart, so a slightly lower Reynolds number was used. The height of the seeder's hole was adjusted until the bulk of the gas was place above the plate in the region of interest; this success of the final placement, the dimensions of which will be quantified shortly, is demonstrated in Figures 4.6(a)-(d). The approximate placement of the test article was included via the red outline in Figures 4.6(c) and (d). The strong increase in signal directly above the plate in Figure 4.6(c) was due to the temperature and pressure increase across the bow shock.

It was surprising to see the gas spread nearly twice as far in the top-down direction than in the spanwise direction, but the compression and expansion of the ACE tunnel's nozzle occured in this only, which could help explain this distribution. At the extrema of the spanwise images, Figures 4.6(e) and (f), one can see evidence of two wake structures. It was believed these were the wakes cast by the 3.18mm tubes (these tubes were uncrimped) for the settling chamber's stagnation pressure and temperature probes. The probes' 50.8mm separation across the centerline matches the results. An analysis of the fluorescence in Figures 4.6(a) and (b) is reserved for Section 6.8.

The size of the NO cloud could approximate the NO's concentration. From Figure 4.6 one could assume the gas had an elliptical shape with a major axis of 120mm and a minor axis of 60mm and uniform concentration. Estimating the the amount of NO in the region of interest required: the tunnel conditions (T_o, P_o, T, P, and M); cloud size (width and height); and the NO injection parameters (orifice diameter, number of orifices, NO concentration, and injected NO reservoir temperature and pressure). Note here the naming convention for gas injection was taken from John and Keith [128] where the "reservoir" pressure referred to the stagnation conditions of the injected gas (here NO), the "exit" conditions referred to those of the injected gas at the nozzle exit plane, and the "backing" conditions referred to those of the recipient gas (here the settling chamber) at the nozzle exit plane. A Microsoft Excel spreadsheet was produced to calculate injection conditions for a variety of cases. The user must input values for the parameters listed above, and then the spreadsheet performed the following steps:

1. Check to see if the orifices are choked; a choked nozzle has the sonic velocity at the throat

and therefore cannot propagate information regarding the state of the "backing" conditions to the "reservoir", so it behaves independent of the backing conditions [128]. A nozzle is choked if [128]

$$P_b < P_r \left(1 + \frac{\gamma - 1}{2}\right)^{-\frac{\gamma}{\gamma - 1}} \tag{4.2}$$

Note that, for the accuracy needed here, $\gamma = 1.4$ and $R_{specific} = 287 \frac{\mathrm{J}}{\mathrm{kg} * \mathrm{K}}$ for both air and NO.

2. Use isentropic flow relations to find the conditions at the orifice exit. If the orifice is not choked the flow is subsonic so $P_e = P_b$ and $\frac{P_e}{P_r}$ can be used in isentropic flow relations to find M_e and $\frac{T_e}{T_r}$ [128]. Analogously, if the flow is choked, $M_e = 1$ (again, this is not a converging-diverging nozzle so there is no acceleration beyond the sonic condition) and the isentropic flow relations can be used to calculate $\frac{P_e}{P_r}$ and $\frac{T_e}{T_r}$. These ratios are used with the reservoir conditions to provide T_e and P_e.

3. The Ideal Gas Law ($P = \rho R_{specific} T$) provides ρ_e.

4. The definition of Mach number, M_e, and T_e provides the exit velocity u_e.

5. The conservation of mass ($\dot{m} = \rho_e A_e u_e$) provides the mass flow through each orifice. Further multiplying by the total number of orifices and NO concentration provides $\dot{m}_{NO}$. Analogous calculations using the test section area and flow conditions provide $\dot{m}_{ACE}$.

6. Dividing the NO by the ACE mass flow rates provides the mass percentage of NO in the test section; this result is multiplied by the area ratio of the NO cloud and test section, which provides the "concentrated" mass percentage.

7. An alternate form of the Ideal Gas Law ($P = n k_B T$) provides the number density of NO in the cloud, n_{NO}.

The NO mix delivery system is described in [49]. In short, a LabVIEW Proportional-Integral-Derivative (PID) algorithm was used to provide customized mixtures of NO (99.95%, Praxair) and N_2 (99.999%, Brazos Valley Welding Supply). The gas concentration was set by MKS Mass-Flo

1179A mass flow controllers running of an MKS 247 power supply. The mixture was stored in a series of two Swagelok 304L-HDF4-1GAL 304L stainless steel ballast tanks with a total capacity of 7570cm^3; these tanks, as well as lines delivering the mixture, were evacuated with a Leybold D65Bvacuum pump prior to running to remove any humid air. An Omega Type PX309-200A5V pressure transducer reported the pressure in the ballast tanks, and an Omegadyne PX5500C0-250G5T pressure transducer (serial no. 47235; $0-1723.69$kPa range) connected to a static pressure tap just before the seeder entered the settling chamber provided the effective reservoir pressure. These measurements were necessary to record the NO delivery pressure drop during a tunnel run, which affected the NO concentration but not the size or shape of the NO cloud [49]. Several redundant shutoff, vacuum, vent, and purge valves were built into the NO delivery system for safety, and stainless steel was used exclusively for all components exposed to NO. Also for safety the NO was only introduced once the tunnel started, and it was shut off a few seconds before unstart to let the tunnel clear itself.

Through extensive testing, the final design was a 0.9525cm crimped pipe analogous to that in Figure 4.4; the top was sealed by completely crimping and then silver soldering it to prevent leaks. A single 0.1588cm hole was drilled into it and positioned approximately 6.668cm from the settling chamber floor. During a nominal run (Table 4.1) the nozzle is choked if $P_r > 939.693$kPa; the NO pressure typically falls from $1241.06 \rightarrow 551.581$kPa during a run, so it operates in both the choked and unchoked regimes. In testing any drop in NO number density during a run was not detectable. The ACE tunnel's mass flow rate was $\dot{m}_{ACE} = 1.8766$kg/s, and the NO mass flow rate fell from $\dot{m}_{inj} = 4.5858 \rightarrow 2.0381 \times 10^{-3}$kg/s.

For the assumed elliptical NO cloud of uniform density and with NO mix percentages of 75% (velocimetry) and 0.5% (ro-translational thermometry) the approximate NO number densities throughout a run were $n_{NO(75\%)} = 4.568 \rightarrow 1.253 \times 10^{15}/\text{cm}^3$ and $n_{NO(0.5\%)} = 30.46 \rightarrow 8.354 \times 10^{12}/\text{cm}^3$. Using $n_{ACE} = 5.43 \times 10^{17}/\text{cm}^3$ from Table 4.1, then the flow by percentage would be $0.841 \rightarrow 0.231\%$ and $0.00561 \rightarrow 0.00154\%$ for the velocimetry and ro-translational thermometry runs respectively; note that $1\% = 10,000$ppm. The vibrational thermometry was

conducted with an injection of 15% *NO*, which fell within the bounds of the other two campaigns. Using this technique, the local concentrations scale linearly based on the percentage at injection, so the local concentration in this case can be readily calculated from the listed data if so desired.

Buen [49] estimated the local *NO* density by measuring the fluorescent lifetime of *NO* and modelings its decay through different pathways. They found that there was an approximately 100:1 reduction in the seeded *NO* concentration and the measured value in the test section; for example, if 75% *NO* was injected for a velocimetry measurement, the local concentration in the test section would be 0.75%. Thus the approximate method based off the choked flow relations agrees with Buen's independent measurement to within an order of magnitude. This means such an *a priori* estimation of the local *NO* number density can be used to check the feasibility of a proposed gas injection setup in the future.

An additional consideration was the presence of the test article's hot wall (relative to the freestream temperature). A boundary layer assumption is that $\frac{\delta P}{\delta y} = 0$ [293], so $P_e = P_w$. However, here $T_e \ll T_w$ so from the Ideal Gas Law $n_e \ll n_w$; because the relationship is linear, for $T_e \approx 60$K and $T_w \approx 360$K, there should be approximately a $\frac{1}{6}$ drop in the number density near the wall. Thus there was a considerable and unavoidable drop in PLIF signal in the critical region near the wall. Through intentional selection of the transitions to probe (see Section 6.8.2) and rigorous data processing [49], measurements could be made near the wall, but as will be seen in all of the PLIF results in Chapter 7, the uncertainty approaching the wall increased considerably due to fewer acceptable results; the statistical methodology by which results were filtered was described by Buen [49]. These physics set the bottom limit for the injection *NO* concentration, as data near the wall was critically important.

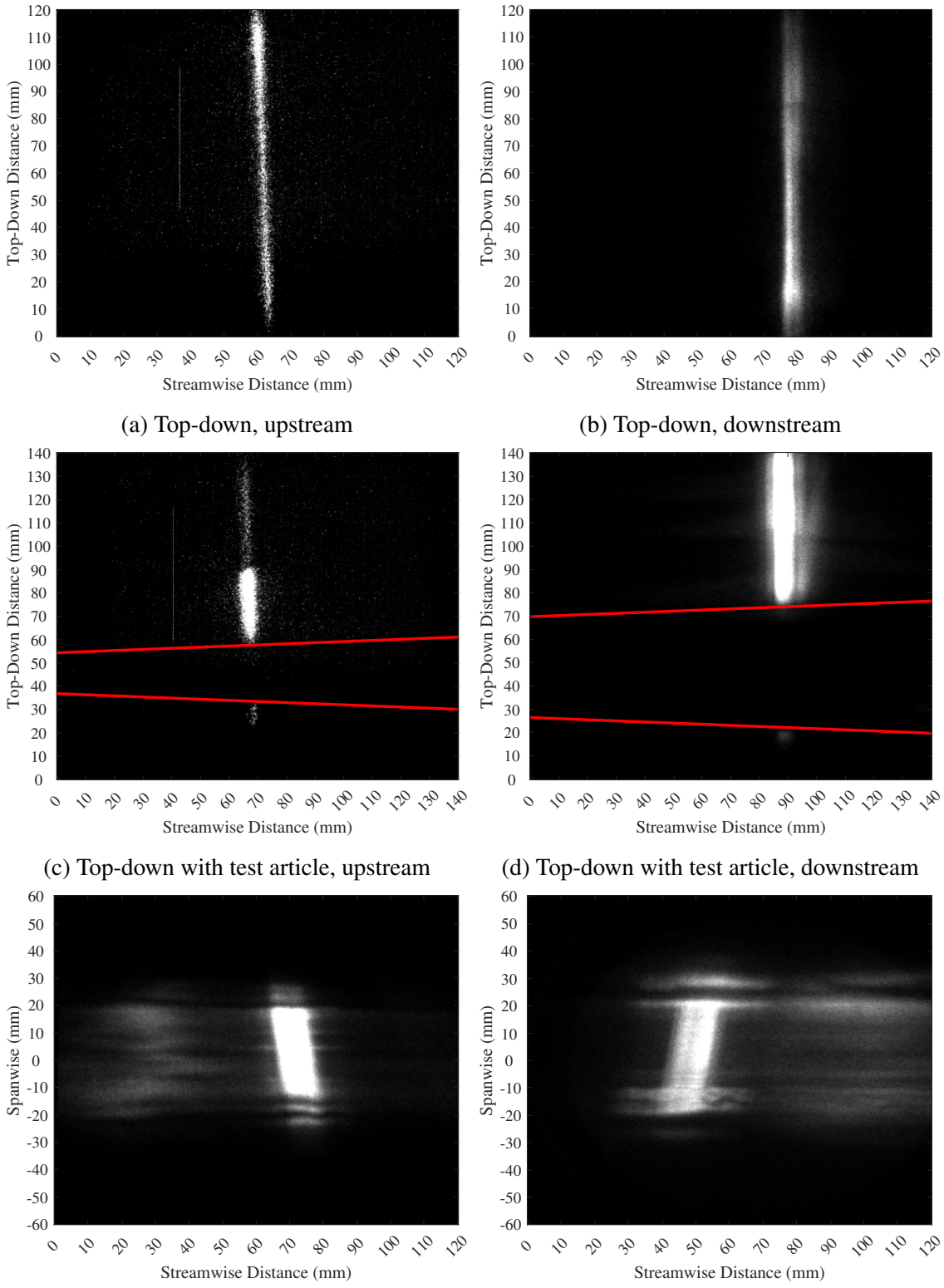

(a) Top-down, upstream

(b) Top-down, downstream

(c) Top-down with test article, upstream

(d) Top-down with test article, downstream

(e) Spanwise, upstream

(f) Spanwise, downstream

Figure 4.6: Visualization of *NO* cloud in test section. All positions are relative, except for the spanwise position in (e) and (f); all beam positions approximately match final test locations, 125 and 405mm from the LE roughly along the test section's centerline. Flow was left to right.

4.1.4 Instrumentation & Data Acquisition

The NAL's standard in-house LabVIEW VI "NALDAQ" was used to record tunnel conditions during a run. Data is read in through a 16-bit NI USB-6255 M-Series DAQ capable of recording at $1.25 \times 10^6 \frac{\text{samples}}{\text{sec}}$, though in practice most data is read at 100Hz and then averaged and recorded at 10Hz in a comma-separated variable file. Data from the entire system line is read through this system, including the air delivery system, the tunnel, and the ejector. A rise in pressure in a leg of the ejector tells the VI the tunnel is being run and that data should be saved; otherwise, data is simply printed out on a display. Two eight-channel NI USB-6366 X series "FASTDAQ"s provided a total of sixteen additional channels for experimental measurement. These DAQs could sample up to 2MHz, be synced to the NALDAQ by triggering from the same ejector condition, and could be linked together or run separately. Finally, a NI 9213 DAQ card mounted in a NI 9171 chassis to forms a "TCDAQ" for reading thermocouple data. Like the FASTDAQ it can be triggered off the same pulse as the NALDAQ and thus linked to it, and although its maximum repetition rate is lower it is capable of matching the 100Hz of the other DAQs.

The stagnation pressure in the ACE tunnel is read from an Endevco 8540-200 pressure transducer connected to a Pitot tube located just before the settling chamber exit, and downstream of the flow conditioners. The sensor was located on the settling chamber at the end of the tube. Error introduced due to sensor heating was not corrected here, nor in [160, 194], though Mai [168] took this step. The Endecvo's properties are listed in Table 4.2. The Endevco was re-calibrated just before the work in this campaign began, and the validity of the new calibration was tested in Section 7.3.5.3. The stagnation temperature data comes from an Omega type K thermocouple with an exposed junction positioned alongside the Pitot probe; nominal error for such a thermocouple is the greater of 2.2K or 0.75% of the reading, so for the nominal condition of 430K the expected error is $\pm$3.23K. Mai [168] estimated that the response time of the pressure transducer was negligible, but that of the thermocouple was $\mathcal{O}(1\text{s})$. To correct for this lag, Mai [168] used an average of 250ms worth of stagnation temperature data instead of the 100ms the rest of the sensors use, but this practice was not repeated here, nor in [160, 194]. The test section static pressure is recorded through

Property	Endevco 8540-200
Measurement Range	1378.95kPa (200psia)
Housing Diameter	3.86mm
Resolution	N/A
Sensitivity (typical)	0.218mV/kPa
Full-Scale Output (nominal)	0.3V at 10V
Resonant Frequency	450kHz
Temperature Range	$239-533$K
Temperature Sensitivity Shift	$\pm 4\%$ max
Temperature Zero Shift	$\pm 3\%$ FSO max
Combined Error (non-linearity, hysteresis, and repeatability)	$\pm 0.75\%$ FSO RSS max

Table 4.2: ACE tunnel settling chamber pressure sensor properties.

a static pressure tap 11.4cm upstream of the nozzle exit and downstream of the last characteristic. The pressure is fed into a MKS Baratron 631C-10 capacitance manometer thermally stabilized at 423K to provide an accuracy of $\pm 0.5\%$. While other sensors are employed to provide a detailed view of the health of the system, through isentropic flow relations and classic flow equations [128] these three values were sufficient to provide freestream values for:

- Mach number: $\frac{P}{P_t} = \left(1 + \frac{\gamma-1}{2}M^2\right)^{\frac{-\gamma}{\gamma-1}}$
- Static temperature: $\frac{T}{T_t} = \left(1 + \frac{\gamma-1}{2}M^2\right)^{-1}$
- Density (Ideal Gas Law): $P = \rho R_{air} T$
- Viscosity (Sutherland's Law [274], with constants for air from [110]): $\frac{\mu}{\mu_o} \approx \left(\frac{T}{T_o}\right)^{\frac{3}{2}} \frac{T_o+S}{T+S}$ where $\mu_o = 1.716 * 10^{-5} \frac{N*s}{m^2}$, $T_o = 273K$, and $S = 111K$
- Velocity: $U = M\sqrt{\gamma R_{air} T}$
- Unit Reynolds number: $Re = \frac{\rho U}{\mu}$

4.1.5 Standard Operating Procedure

Due to the hazards of performing tests in the ACE facility (high temperatures, high pressures, harmful noise, and for PLIF toxic gas and laser exposure), it was necessary to have a strict set of

operating procedures to ensure all equipment had been initialized properly and was used in the correct order. It is a lab practice to have a second operator in the room when the tunnel is run in case of emergency. All personnel in the room must wear ear and eye protection during both the tunnel preheat and run. Due to the excessive noise produced by the ejector, nearby buildings are alerted of tunnel operation, and runs are avoided when pedestrians are in the vicinity.

- Prepare
  - Check NALDAQ VI is functioning properly, and that there are no error messages from the compressors
  - Ensure ejector regulators are properly pressurized
  - Check that test section is secure and there are no tools left inside the tunnel
  - Warn lab personnel (verbal) and surrounding buildings (email) of incipient run
  - Insert key to activate tunnel control system
  - Open knife gate separating diffuser from ejector
  - Open manual ball valve supplying air to ACE tunnel, check that supply valves for other facilities are closed
  - Ensure manual ball valve on the 5.08cm line is open, and that all actuators are turned on and operational
  - Set regulators controlling the pressure in heater and settling chamber to nominal values
  - Ensure proper backing pressures are being delivered to ejector's regulators
  - Set desired test temperature and pressure in NALDAQ VI
  - Turn on yellow warning light outside of building to warn people in the vicinity of the run. Use cameras to check for pedestrians
- Preheat
  - Use actuator to pressurize 5.08cm line up to the heater

  - Turn on heating element. Allow temperature to rise to a nominal value
  - Give final verbal warning for lab personnel to put on ear and eye protection
  - Use actuator to send air through heater and tunnel
  - Monitor heater temperature and settling chamber temperature and pressure. Cycle heater and adjust pressure as necessary
  - Once the proper conditions have been reached, turn off heater (if not already done), set tunnel stagnation pressure to desired condition for the run, and use heater room actuator to cease flow of air into facility
  - If access to the test section is needed (test article installation, laser alignment, *etc.*), wait for air drain through the diffuser, then close manual ACE tunnel supply ball valve

- Pre-run
  - Ensure test section is secure, no tools left in tunnel, personnel wearing PPE
  - Open the manual ACE tunnel supply ball valve if closed
  - Switch the warning light from yellow to red. Sound a warning horn as a final signal to passersby
  - Set the ejector regulators to proper setting, and check that their requisite backing pressure has been maintained
  - Check that heater is turned off
  - Check that data acquisition systems and assisting personnel are prepared
  - Use cameras to check there are no pedestrians

- Run
  - Use actuators to send air through the ejector via the 10.16cm line
  - When test section pressure drops below 10Torr, use heater room actuator to send air through the ACE tunnel

- Conduct test
    - For safety during PLIF tests, manually turn NO after tunnel has successfully started, and turn it off before unstart
    - For safety during plasma tests, manually turn plasma on after tunnel has successfully started, and turn it off before unstart
- When test is complete, tunnel unstarts, or the tank pressure drops below 10.34MPa close 4 inch line actuators, then close upstream 5.08cm line actuator
- Wait for 5.08cm line to depressurize, then close heater room actuator, followed by manual supply ball valve, and finally knife gate
- Remove key to deactivate tunnel control system

4.2 Quiescent Air Vacuum Chamber

Although the main experiment was conducted in the ACE tunnel, it is a difficult environment to work in: all materials must be securely fastened and rated to above the stagnation temperature; conditions are somewhat transient and difficult to replicate precisely; runs are brief and limited; and electrical and optical access is challenging. For these reasons prototypes and experiments critical to the development of the glow discharge and optical emission spectroscopy technique were done in a traditional quiescent air vacuum chamber.

The vacuum was produced by a Leybold Trivac D8B rotary vane pump capable of an ultimate pressure of 1×10^{-4}Torr and a nominal volumetric flowrate of $11.6\frac{\mathrm{m}^3}{\mathrm{hr}}$. The vacuum chamber was made from stainless steel components purchased predominantly from the Kurt J. Lesker Company. The bell jar was mounted to an automatic lift to allow for easy access to the test volume during setup, and it had a maximum height of 74.9cm and an inner diameter of 61.0cm. Its inner walls were wrapped in neoprene to help insulate against accidental ignition during plasma testing. Three 15.24cm CF flange windows, also purchased from the Kurt J. Lesker Company, allowed for optical access into the chamber; two of the windows were Kodial (Corning 7056 alkali borosilicate) windows with 8.99cm viewing diameters, while the third was high-purity fused silica (Corning 7980

HPFS) with a viewing diameter of 9.86cm. The HPFS window was used for all spectroscopic measurements because it was rated to maintain over 90% transmissivity above 250nm. The bell chamber sealed with Viton O-ring against a 20.3cm tall feedthrough collar, which itself sealed against a final end plate with another Viton O-ring. The feedthrough collar was ringed by eighteen 6.99cm CF blind flanges which could be easily modified to accommodate passing sensors or hardware into the chamber; such equipment included the manual pressure relief valve, wire throughputs, and pressure sensor. All CF flanges were sealed with annealed copper gaskets.

A Duniway Stockroom Corporation CVT-275-101 pressure sensor, rated to 10% accuracy between $1 \times 10^{-3} - 4 \times 10^{2}$Torr, provided pressure data. It was connected to a Terranova 906A Convection Gauge Controller with its own 1% accuracy, so the Euclidean norm of the total error of pressure readings was 10.05%. The controller was calibrated per the manufacturer's instructions, by recording a point at atmosphere and another at a pressure an order of magnitude below the sensor's minimum readout of 1×10^{-3}Torr. Raw voltage from the controller was input into a custom LabVIEW "PlasmaDAQ" VI via the FASTDAQ and was calibrated such that the pressure matched what was displayed on the Terranova 906A's display. All flanges were sealed with annealed copper gaskets. The entire quiescent air vacuum chamber is shown in Figure 4.7.

During testing, the electrodes were affixed in a channel cut into a custom ceramic holder and were polished and flush-mounted just as they would be in the ACE tunnel (see Section 4.4.8). The channel helped support the electrodes and allowed varying electrode widths to be tested. The wires were affixed by screws on the backside of the electrodes, which also held the electrodes in place. This approach ensured all hardware was securely fixed and centered, the electrodes were flat and flush with the channel, the test surface was clean, and, as best was possible, no breakdown occurred between the screws. For measurements across a gap (the electrodes facing each other), two ceramic mounts were used, and an aluminum extrusion was used during setup to guarantee planarity.

Figure 4.7: The quiescent air vacuum chamber, bell jar open.

4.3 Plasma Hardware

The simple circuitry required for glow discharges is shown in Figure 4.8. A Spellman SL300 power supply provided up to 300W at 100mA and 3000V to the system. It had manual dials for current and voltage control as well as analog outputs so these values could be read into a custom "PlasmaDAQ" LabVIEW VI. When in the ACE tunnel for the main testing campaign, this "Switching" power supply always settled in a "Voltage Limited" configuration, which meant the delivered current was limited by the setting from the "Voltage" dial. For example, if the "Current" dial was maxed out, but the "Voltage" dial was low, the power supply could not provide the requested current and the amount delivered would depend on the "Voltage" setting.

A chassis mount Ohmite $10 \pm 5\%$kΩ resistor on the high-voltage side of the circuit acted as a ballast resistor. The logic behind the resistor sizing is covered in Section 7.2.1, but here it is sufficient to say the maximum tolerable load was 100W and the total resistance, measured *in situ* to within 10Ω with a Fluke 117 multimeter (0.9% accuracy), was $R_b = 10.03$kΩ. For electrical and thermal protection the resistor rested on ceramic bricks and was stored in a plastic enclosure

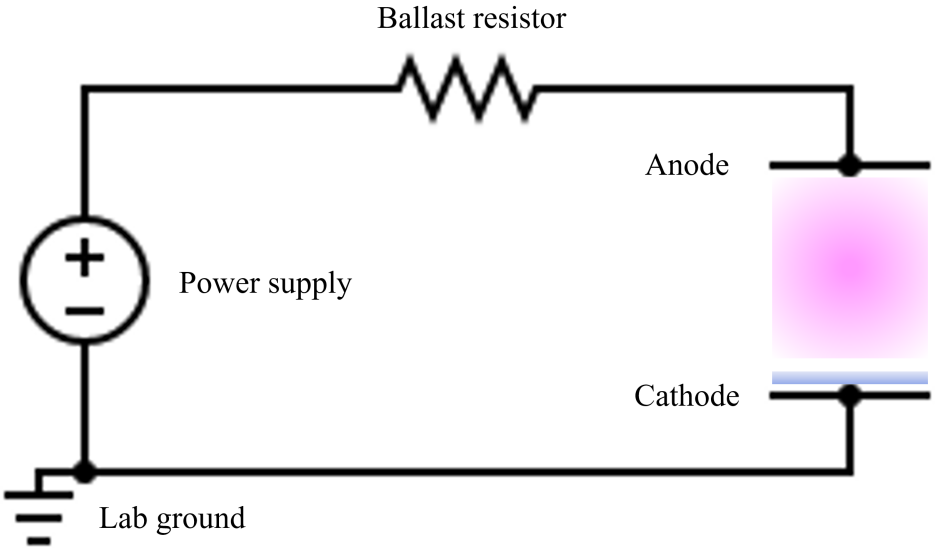

Figure 4.8: DC glow discharge wiring diagram.

with a cooling fan.

Alpha Wire 22AWG rated for 5000V at 473.15°K was selected to carry the power to the electrodes. For the ACE experiments, the wire simply passed through two small holes in a window plug which were sealed with tape on both the inside and outside of the test section. For the vacuum chamber, where leaks were a more serious concern, the high voltage wire was passed into the chamber with a custom high voltage throughput recommended by Dr. David Staack[1]. A length of high voltage wire had its braided core removed and replaced with a solid core lightly covered in vacuum grease. The modified wire was fed through one of the chamber's blind flanges tapped to accept a compression fitting which sealed against the silicone wire insulation. This approach provided a workable seal and electrical insulation. From here the wire was attached to the anode. The cathode was wired through a Kurt J. Lesker power throughput; while this throughput was rated for 5000V at 15A, it was designed for ultra-high vacuum applications and therefore offered no electrical insulation, so it was appropriate only for the ground side of the circuit. On the outside of the chamber, the ground wire was attached to the chamber itself and the building's ground before finally connecting back to the power supply, completing the circuit. The cathode wire for the ACE

[1]Texas A&M University's Plasma Engineering and Diagnostics Laboratory

tunnel was grounded to the wind tunnel itself in a similar fashion.

The power supply had analog outputs for the voltage and current which could be connected to the NI USB-6366 "FASTDAQ". A "PlasmaDAQ" VI was built which mimicked the design of the NALDAQ in that had the same sampling rate and trigger so the tunnel and plasma data were automatically synced to within 10Hz. The user needed to input the ballast resistance manually. With the power supply voltage V_{PS}, current I, and ballast resistance R_b known, one could use Ohm's law to calculate the voltage drop across the ballast resistor V_b (see [115]). Thus the voltage across the plasma was known from $V_{pl} = V_{PS} - V_b$. The total plasma power was then provided by Ohm's Law $P_{pl} = IV_{pl}$. The VI calculated, recorded, and displayed this information in real time, and these data were sufficient to find the Joule heating described in Section 2.4.

4.4 Test Article

The design of the test article was a direct result of its application, the study of vibrational nonequilibrium on hypersonic, ZPG TBLs in the ACE tunnel. All of the features and compromises to be discussed were intentionally chosen to provide a successful test environment for the planned experiments. Individual aspects of the design are discussed in their own subsections. The test article's final design is shown here in Figure 4.9 to provide a visual reference for subsequent discussions; measurements will be provided as they become relevant. Also, for reference, the test area/volume will hereafter refer to $\pm$25.4mm along the model's centerline and the flow above it as this was the core flow.

4.4.1 Past Work

The general design of the test article evolved from the recommendations in the doctoral works of Semper [243] and Leidy [160]. Both of these authors studied hypersonic, ZPG boundary layers in the ACE tunnel, and the former even focused on TBLs as well.

Semper [243] used a true flat plate in their work, and designed it to span the entire test section. This successfully prevented edge effects due to the pressure differential between the top and bottom surfaces, but oil flow results showed channeling of the streamlines due to tunnel sidewall

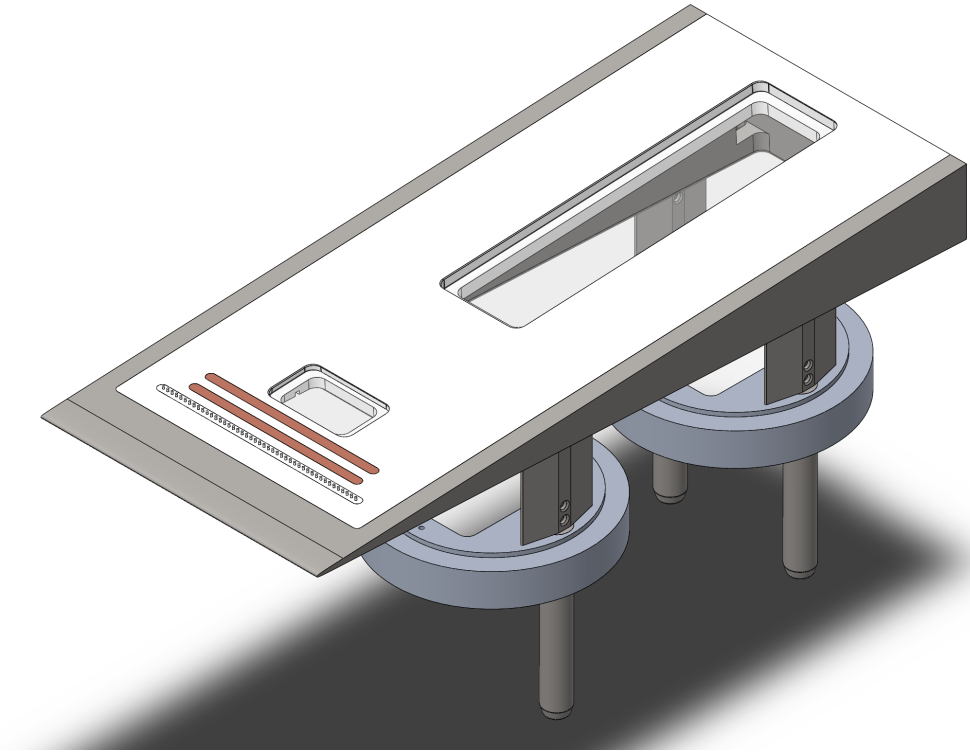

Figure 4.9: CAD model of the test article.

interference. Notably, the model had a nonsymmetrical leading edge with 1.59mm bluntness and was mounted at a -2° angle of attack to reliably produce stagnation on the top surface of the wedge. Finally, this model was constructed entirely out of aluminum, painted black for better contrast during oil flow studies, and was left in the tunnel during preheat as it mounted with four struts to the test section's floor.

Leidy [160] made several attempts avoid sidewall interference before ultimately deciding to reduce the span of the model to 25.4cm, which left 5.24cm between the sides of the test article and the tunnel walls. Another notable feature was the use of a polyether ether ketone (PEEK) insert on the test surface, which allowed the use of infrared (IR) thermography as a diagnostic technique. Mounting fast response pressure transducers in a nonconductive material also reduced the data's noise. These properties, coupled with PEEK's high glass transition temperature and machinability, led Leidy [160] to attempt to make a test article entirely out of the material, but this resulted in

warping in the thin section near the leading edge during manufacturing, so the plastic was instead mounted inside a larger stainless steel frame. The final model was mounted onto a sting attached to a door so the model could be quickly installed inside the tunnel after preheat; oil flow visualization showed the effect of the sting tangibly manifested on the test surface, but its effects never reached the core flow [160]. A long threaded rod connecting the test article to the floor of the test section allowed the model to be leveled before each run and helped prevent vibration.

In moving the model away from the test section's walls to reduce interference, Leidy [160] introduced the possibility of three dimensionality due to the pressure differential between the top and bottom surface of the test article. Early iterations of Leidy's model used a flat plate, leading edge, and angle of attack analogous to Semper [243], but it was found that without the aid of the tunnel sidewalls the effect of the pressure differential on the streamlines was severe [160]. In order to remove this effect, Leidy ultimately switched to a slender wedge mounted without any angle of attack and with a symmetric leading edge. The final design had a 1.3° half-angle, which according to the theoretical work of Cohen and Reshotko [64] should have only deviated slightly from true ZPG results.

4.4.2 Leading Edge

Because of the impact it has on the flow, special attention must be paid to the design of the leading edge. For example, failing to match the curvature of the leading edge with that of the wedge will produce a pressure spike and receptivity source [107]. Furthermore, if the leading edge is not sufficiently blunt the stagnation point may vacillate between the top and bottom surfaces, separating the flow and causing noise [236]. Neither of these effects were desirable even for the present study of TBLs because of their lack of predictability and uniformity; turbulence should come from uniform tunnel background noise or controllable trips, not design imperfections. Finally, slight bluntness should remove the viscous-inviscid interation which arises at sharp hypersonic leading edges (see [108, 293, 239]); this will be discussed in detail shortly. Leidy [160] used a mathematics-driven approach to design the polynomial $P(x)$ for the leading edge to account for these effects, and it was adopted here and programmed in Matlab.

To begin, the user inputs a wedge half-angle δ and a polynomial-to-wedge transition point (x_{trans}, P_{trans}), where $P_{trans} \equiv P(x_{trans})$ is its distance from the leading edge and x_{trans} is its height from the centerline; this puts the streamwise direction along the vertical axis. In these coordinates, with the wedge angle now a known constant the slope of the polynomial at the transition point must be $P'_{trans} = \frac{1}{\tan(\delta)}$. The radius of curvature of a polynomial is $R = \left| \frac{\left(1+P'^2\right)^{\frac{3}{2}}}{P''} \right|$ and the curvature κ is its reciprocal, so for the constant-slope wedge the curvature must be zero. Therefore P''_{trans} must also be zero to match this condition at the transition point. With this there are three conditions for the polynomial, so it is possible to solve for three coefficients. The program will attempt to find suitable polynomials of the order $n = 2-10$, but for $n \neq 2$ only the highest order-terms are solved. For example, for a polynomial of order $n = 6$, the program solves

$$\begin{bmatrix} x_{trans}^6 & x_{trans}^5 & x_{trans}^4 \\ 6x_{trans}^5 & 5x_{trans}^4 & 4x_{trans}^3 \\ 30x_{trans}^4 & 20x_{trans}^3 & 12x_{trans}^2 \end{bmatrix} \begin{Bmatrix} A \\ B \\ C \end{Bmatrix} = \begin{Bmatrix} P_{trans} \\ P'_{trans} \\ P''_{trans} \end{Bmatrix} \tag{4.3}$$

to produce $P(x) = Ax^6 + Bx^5 + Cx^4$. In order to check the validity of the solution for each n, κ is calculated over the polynomial's domain, and if it becomes negative the solution is discarded. Using this technique, for a half-angle of $\delta = 2.75°$ and $(x_{trans}, P_{trans}) = (0.082, 0.813)$in, a sixth-order polynomial was produced in inches

$$P(x) = 4.2809 \times 10^6 x^6 - 1.1188 \times 10^6 x^5 + 8.0936 \times 10^4 x^4 \tag{4.4}$$

As was previously stated, sufficient leading edge bluntness is necessary to prevent flow separation [236]. It can be difficult to describe a polynomial with a single value of radius of curvature, especially for higher order polynomials which adopt a box-like shape (which in turn produces blunter profiles). It was therefore useful to adopt a new term, the "effective radius of curvature" R_{eff}, the x-coordinate where the traditional radius of curvature was minimized. Figure 4.10 visualizes the challenge of selecting a single radius of curvature for Equation 4.4, and shows the most

pronounced feature is κ_{max} or R_{min}. The final result for Equation 4.4 was $R_{eff} = 1.25 \times 10^{-2}$in. This is sharper than the result in [160], $R_{eff} = 1.44 \times 10^{-2}$in, but it is blunter than the profile used for the $\delta = 2°$ wedge also studied in the ACE tunnel in [83], $R_{eff} = 5.51 \times 10^{-3}$in. Schlieren imaging of the leading edge in these studies did not show any separation, and the same technique was used to verify this claim for the current work (see Section 7.2).

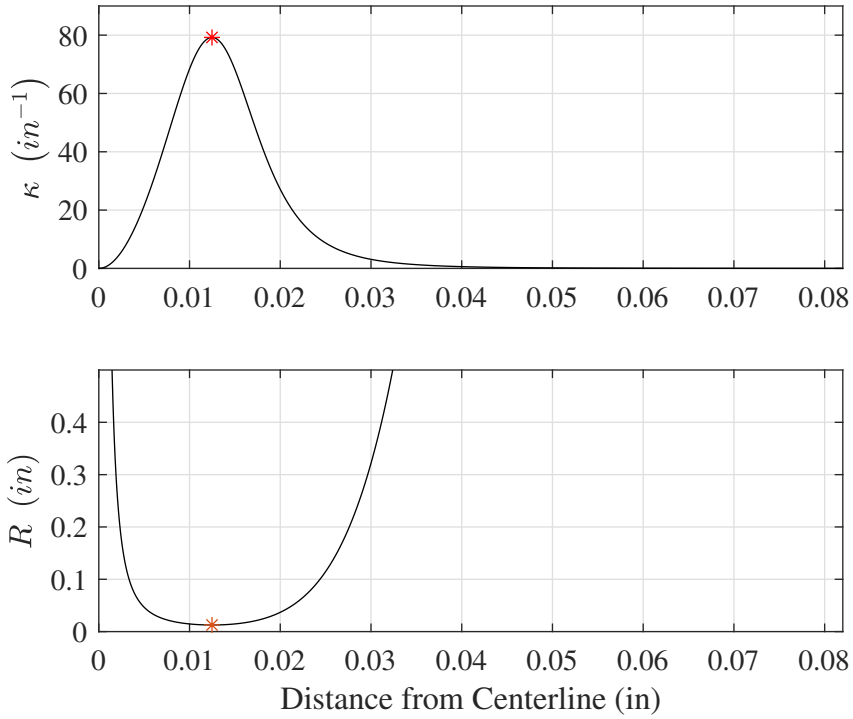

Figure 4.10: The curvature κ and radius of curvature R over the domain of the leading edge polynomial (Equation 4.4).

An additional consideration was the viscous interaction theory for hypersonic flows over flat plates with sharp leading edges, well described in [108, 239, 293, 6]. Due to the high Mach number and low density (Reynolds numbers) associated with hypersonic flows, a laminar boundary layer can grow rapidly at $\delta \propto \frac{xM_e^2}{\sqrt{Re_x}}$ [6]. So sudden is the growth at the leading edge it can create a shock and cause an "induced pressure" $\frac{P_e}{P_\infty}$ which decays along the length of the plate. An idealized flat plate with a sharp leading edge and no angle of attach would otherwise not generate a shock

as the streamlines would not deflect and $P_e = P_\infty$; even should a shock form due to real-world considerations, at the very least the pressure should be constant along the surface following the discrete jump across the shock [6].

This phenomena is governed by $\overline{\chi} = \frac{M_\infty^2}{\sqrt{Re_x}}\sqrt{C}$, where $C = \frac{\rho_w \mu_w}{\rho_w \mu_e}$. For $\overline{\chi} \gtrsim 3$, usually near the leading edge because of the $x^{-\frac{1}{2}}$ dependence, the flow is in a "strong interaction" regime. The flow "sees" the rapidly growing displacement boundary layer $\frac{d\delta^*}{dx}$, the streamlines turn, and a shock is formed which affects, most importantly, the boundary layer growth (decreased), skin friction (increased), and heat transfer (increased); these effects become negligible in the "weak interaction" region. In the strong interaction regime, Anderson [6] shows $\delta^* \propto x^{\frac{3}{4}}$, $\frac{d\delta^*}{dx} \propto x^{-\frac{1}{4}}$, and $\frac{P_e}{P_\infty} \propto x^{\frac{1}{2}}$, or $\frac{P_e}{P_\infty} = 1 + a_1\overline{\chi}$ where a_1 is a constant. In the weak interaction regime, $\delta^* \propto x^{\frac{1}{2}}$, $\frac{d\delta^*}{dx} \propto x^{-\frac{1}{2}}$, and $\frac{P_e}{P_\infty} = 1 + b_1\overline{\chi} + b_2\overline{\chi}^2$ where b_1 and b_2 are constants. Hayes and Probstein [108] ascribed values to these constants for the cases of adiabatic and cold-wall ($\frac{T_w}{T_{aw}} \ll 1$) flat plates.

The point here is that even idealized, perfectly sharp leading edges are not without their own unique complexities which can manifest in practical environments, as was seen in the experiments in Section 2.4. Because the test article was modeled after a flat plate in such an environment, the theory was worth reviewing. However, the bluntness of the leading edge and wedge's turning angle meant that a bow shock would form independent of any viscous effects. Furthermore, it was assumed the strength and curvature of the bow shock, the length of the plate, and the presence of the trips, would dominate a these leading edge effects. Indeed, a rough calculation showed the flow would enter the "weak interaction" regime $\lesssim$ 1cm from the leading edge, well ahead of the trips.

4.4.3 Half-Angle

If flow physics necessitated the design of a slightly blunted, symmetric leading edge then the electrodes, and to a lesser extent optical access, motivated the half-angle. As was shown in Section 2.5, in order to provide the greatest effect the electrodes should be placed as near the leading edge as possible. However, they must be insulated in order to prevent accidental ignition with the tunnel or test article. PEEK had suitable properties for this application, in addition to those for IR thermography and fast-response pressure measurement discussed above. Therefore a single,

seamless PEEK insert was fit into the stainless steel wedge frame, following Leidy's [160] final model; an internal O-ring ensured there was no suction or blowing onto the test surface through the seam. As in the quiescent air vacuum chamber, the wires were attached to the electrodes with screws, which meant the electrodes needed a significant thickness. Additionally, they needed to mount flush inside a PEEK pocket, which itself needed to be attached to the metal wedge far enough upstream to prevent accidental ignition.

All of these design requirements required a certain thickness, enough material for each feature to be machined, and the only way to provide it was to increase the wedge's half-angle. Ultimately a 2.75° half-angle yielded the thinnest realizable wedge. While $\delta = 2.75°$ should still behave like a flat plate [64], the increased cross-sectional area drove up tunnel blockage. This problem was exacerbated by the desire to keep the wedge as long as possible to provide testing locations at large Re_x. Taken together, it was necessary to reduce the test article's span to prevent tunnel unstart at the test condition due to excessive blockage. This makes the core flow more susceptible to edge effects, but the oil flow in [160, 83] assuaged these early design concerns and suggested a sufficient test area would be maintained. In the final design, the conservative tunnel blockage was approximately 13.2% without and 16.1% with the stands. If the total tunnel blockage, including probes, was to be kept below the empirical upper limit of 20% then the wedge could not be made significantly longer or wider.

4.4.4 Translating Stands

In an effort to prevent interference due to the sting on the test surface seen by [160], and to minimize vibration during a run, the model was mounted in the test section with three stands. The stands were 1.27cm wide with angular leading and trailing edges to prevent the additional blockage produced by strong bow shocks and to prevent vortex-induced vibration. The stands could be attached via pins at one of three locations covering 7.62cm in the streamwise direction, allowing the test article to be translated in between runs. This was useful as optical access in the test section is somewhat limited. The stands themselves were connected to rods which extended through custom tunnel plugs. Outside of the tunnel three Mitutoyo 7850 Micrometer Jacks could be used

to precisely raise or lower the test article while maintaining flatness in both the streamwise and spanwise directions; silicone O-rings ensured a hermetic dynamic seal between the rods and the tunnel. The ability to translate the model up and down was useful for laser diagnostic measurements of the boundary layer where it could be difficult to move the beams and maintain proper alignment. Only three stand/rod pairs were required to translate the model because adding a fourth would have over-constrained the test article and led to binding (a plane is defined by three points, not four). Note that wires could be passed into the test section through small holes in the custom plugs and then sealed with high temperature polymide (Kapton) tape or Permatex High Temperature Gasket Maker (room temperature vulcanizing (RTV) rubber). A $\pm 0.1^\circ$ tolerance in pitch and roll was maintained throughout the campaign, confirmed using a SPI-TRONIC Pro 3600 digital angle indicator ($\pm 0.05^\circ$ though $0 - 10^\circ$, overall accuracy $\pm 0.2^\circ$).

Keeping the entire model support system constrained to custom plugs prevented permanent modification to the ACE tunnel's test section and restricted the design of the stands to a small area away from the test article's sides, where their influence may have affected the test surface. While this approach prevented all model vibration and guaranteed a level test surface, leaving the model in the tunnel during preheat meant all materials and sensors needed to be rated to above the tunnel stagnation temperature, especially those in contact with the test article's thermally conductive metal components.

4.4.5 Mounted Optics

The PLIF techniques require shooting a laser through the boundary layer at the wall. Directed exposure to a focused laser beam would degrade the test article, and the scatter thrown as the beam reflects off the model would be so strong it could damage the ICCD. Therefore it is necessary to have a means for the beam to pass through the model, as was done with the test articles covered in Section 2.5.7.

To prevent these issues, custom fused silica windows were purchased from Technical Glass Products Inc. which should maintain $> 90\%$ transmission at the wavelengths of interest. These windows were mounted on both the top and bottom surfaces of the test article, as well as the

mounting plugs to allow the beam to pass completely though the model and out of the tunnel. They were specifically sized to maximize access to the test volume. This is illustrated in the model section view in Figure 4.11. The windows were hermetically sealed using Permatex High Temperature Gasket Maker RTV and were mounted flush with the test surface. This PEEK insert was only used for PLIF applications; a seamless PEEK insert was used for all other diagnostics.

Small channels were left on the underside of the test article to allow pressure relief in the space between windows as the model was thermally and barometrically cycled during a tunnel run. While a window blowout was unlikely, this approach should also help prevent any suction or blowing out through the top window's seam, which would directly affect the results. Figure 4.11 should communicate the effect wedge angle had on window placement. Neither the upstream nor downstream windows could be shifted farther upstream or made considerably thicker without making the test article too delicate to produce; this again shows why increasing the half-angle was the only way to increase the test area in the streamwise direction. Also, note how in the upstream location, the PEEK is directly exposed on both the top and bottom surfaces. The width of the windows was somewhat arbitrary and was selected to keep cost down and provide enough distance to collect off-centerline data without running into edge effects due to the windows' seams. In preliminary testing it was revealed that despite the high transmissivity, the reflections off of the windows were strong enough to conflate the results, so the glassware was sent to Newport Thin Film Laboratories where the top surface of each of the four windows was coated to reflect $< 0.5\%$ of the wavelengths of interest. The mounting plugs were also painted black to help prevent any scatter due to beam misalignment at the tunnel exit.

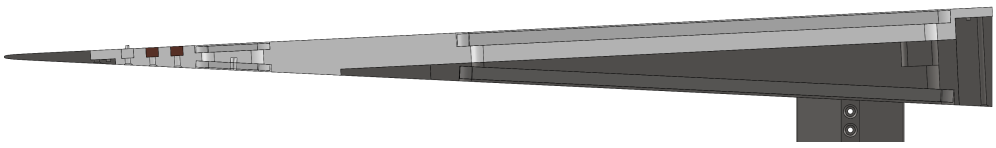

Figure 4.11: A section view of the test article.

4.4.6 Materials and Manufacturing

Most of the test article's components, most importantly the metal wedge frame, were made by Quicksilver Manufacturing, Inc. Wherever possible, SAE 304 stainless steel was used to add durability during handling, especially in thin sections like the leading edge. The wedge frame was heat treated to prevent warping of the leading edge during machining and was ground to a 0.813μm finish. A notable exception to the material restriction was the mounting plugs, which were made from 6061 aluminum due to an ultimately abandoned idea to surface treat them with an anti-reflective coating. The PEEK used for the insert was made from Victrex 450G granules extruded into a "Ketron 1000" sheet by Mitsubishi Chemical Advanced Materials and sold by Professional Plastics, Inc. Victrex supplied material properties, specifically the thermal conductivity and specific heat capacity, over a the range of temperatures expected in the ACE tunnel, which is critical for accurate heat flux calculation. Because of the need to use a known plastic source, the PEEK inserts were made in the Texas A&M Department of Chemistry's machine shop from stock purchased from the known supplier, Professional Plastics, Inc. Other versions of the PEEK insert without any window mounts were produced for testing with non-optical techniques without the risk of interference of any Mach waves produced by the windows' seams (ex.- one with static pressure taps for Pitot measurements, one with holes for Kulite pressure transducers, *etc.*). Finally, the electrodes and trips were made in the Texas A&M Oran W. Nicks Low Speed Wind Tunnel due to its wire electric discharge machining capabilities. All materials used are either inert in the presence of NO, or could be easily replaced (ex.- the 3D printed trips). The full assembly's final dimensions are shown in Figure 4.12; the design and placement of the trips and electrodes is to be discussed. Each set of trips and electrodes were sanded to sit flush within their specific PEEK insert.

4.4.7 Trips

In this study discrete trips were used to foment turbulence. The design selected are known colloquially as "pizza box" trips [243], but are more formally described as diamond trips. The width

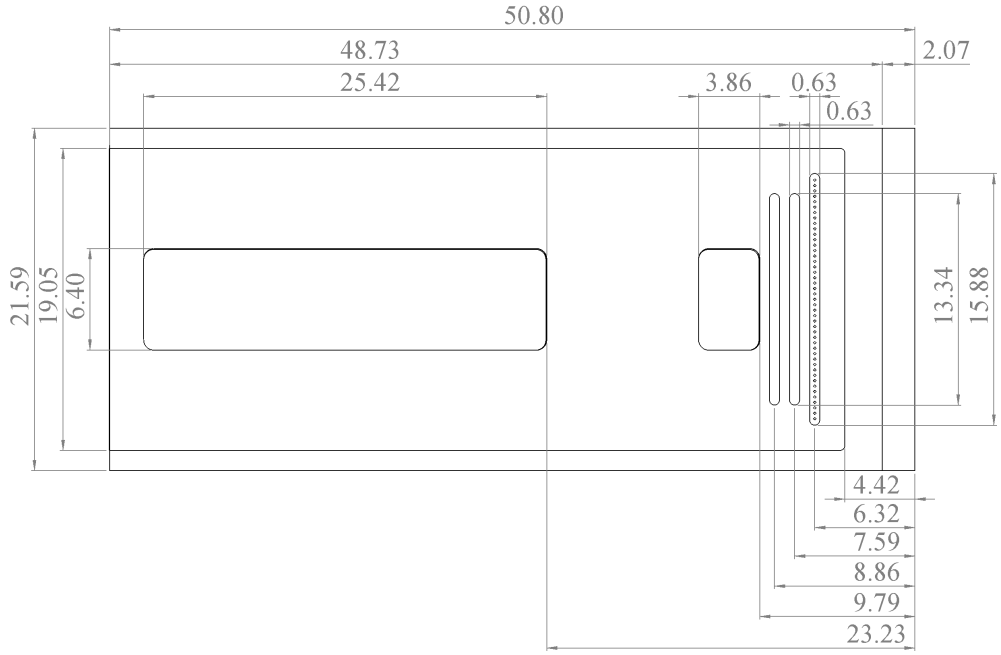

Figure 4.12: Drawing of the final test article. All dimensions are in centimeters.

("diameter", d), height (h), and spacing (w) of the diamonds are variable and impact the efficacy of the trips as a whole; these parameters are shown in Figure 4.13. Berry et al. [29] performed a comparative study of the diamond trips to other geometries typical for supersonic and hypersonic applications; this included a campaign at freestream Mach and Reynolds numbers attainable by the ACE tunnel, 6 and $7.22 \times 10^6/\text{m}$ respectively. Furthermore, the test article they used, the inlet to the Hyper-X scramjet, could be simplified without much loss to a slender wedge like the one used here. The authors scaled the trip geometry by the total enthalpy boundary thickness $\left(\delta_{H_o,99.5\%}\right)$, which was itself calculated from a laminar CFD simulation. The diamond diagonal and center-to-center spacing were $d_{trip} = \delta_{H_o,99.5\%}$ and $w_{trip} = 2\delta_{H_o,99.5\%}$ respectively, while element heights ranging from $\frac{h_{trip}}{\delta_{H_o,99.5\%}} = 0.185 - 1.48$ were tested. Berry et al. [29] concluded that with the previously described size and spacing, the minimum "effective" diamond trip height was $\frac{h_{trip}}{\delta_{H_o,99.5\%}} = 0.74$, where "effective" meant turbulence was initiated immediately downstream of the trips.

While Berry et al. [29] ultimately recommended a different trip design for their specific ap-

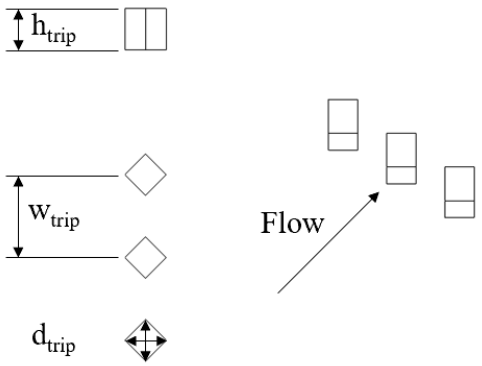

Figure 4.13: Diamond trip parameters; figure adapted with permission from Berry et al. [29]

.

plication, the diamond trips have been used repeatedly on slender wedge geometries in the ACE tunnel. Semper and Bowersox [246] used said trips to study low Reynolds number $\left(4.4\times10^6/\mathrm{m}\right)$ turbulent boundary layers on a true flat plate at $M=5.92$ at a slight (2°), negative angle of attack. This study used the same $\delta_{H_o,99.5\%}$ and $2\delta_{H_o,99.5\%}$ width and spacing as Berry et al. [29], and used $\frac{h_{trip}}{\delta_{Ho,99.5\%}}=1.48$, where $\delta_{H_o,99.5\%}$ was again determined from a laminar CFD simulation. The careful boundary layer surveys conducted by Semper and Bowersox [246] showed the trips were indeed effective at producing classical, fully-developed turbulent boundary layers in the ACE tunnel; it is noted that this effort included numerical and experimental studies of the flow physics around each trip. Semper and Bowersox [246] did remark, however, that optimal disturbance spacing should be $\sim 3\delta_{H_o,99.5\%}$ according to the work by Reshotko and Tumin [225].

In their work on transitional boundary layers tripped using the diamond elements over a 1.3° half-angle wedge at $M=6$ in the ACE tunnel, Leidy [160] explored the effect of center-to-center spacing on the trip performance; trips in the range of $w_{trip}=(2-5)\delta$ were tested. Here it was assumed δ was where the velocity profile recovered 99% of its freestream value, which the Leidy [160] predicted with the self-similarity solutions of van Driest [283] and validated with schlieren imaging. Using oil flow visualization, Leidy [160] found that only $w_{trip}=2\delta$ was able to produce a turbulent boundary layer for the trip heights studied; again, as the focus of that work involved transitional boundary layers, ultimately $h_{trip,max}/\delta_{H_o,99.5\%}=0.6$ and $d_{trip}=\delta$ so laminar, transitional,

and turbulent boundary layers could be achieved. Also, in a previous paper on the same subject, Leidy et al. [161] commented that trips placed nearer to the leading edge were more effective than those placed further downstream.

These works provided a clear path for trip sizing to produce TBLs in the ACE tunnel. Diamond trips were produced using Formlabs stereolithography 3D printing equipment in the Texas A&M Oran W. Nicks Low Speed Wind Tunnel's machine shop. A Form 3 "UltraHerbivore" model printer made the trips with 100μm layers from Gray Pro resin. The parts were washed in isopropyl alcohol in a FormWash "EbonyServal" part washer and cured in a FormCure "CoffeeTonkinese" UV chamber. The parts were lightly sanded to ensure they fit in the test article and all support material was removed, and they were manually tapped so they could be screwed into a pocket on the PEEK insert; these screws were covered with polymide tape to prevent suction or blowing onto the test surface through the holes.

δ was determined from the boundary layer solver described Chapter 5. The full boundary layer code was not run, just the self-similar solution as at the time it was the validated portion (van Driest's [283] results provided the comparison). The current wedge was slender enough to be handled by and compared to such a flat plate, 0° angle of attack technique. Eventually, schlieren imaging of the trips interacting with the boundary layer validated the choice of their height. It was desirable to use the smallest trips possible so as to reduce the effect of the trip itself on the flowfield. For this reason, four different trip heights were considered, $\frac{h_{trip}}{\delta} = [1, 1.25, 1.5, 1.75]$. Similarly, the spacings tested were $\frac{d_{trip}}{\delta} = [1, 1.5, 2]$ and $\frac{w_{trip}}{\delta} = [2, 3, 4]$. Analogous to the phosphor thermography in [29], IR imaging was used to determine the state of the boundary layer for each trip height over an array of Reynolds numbers.

The laminar boundary layer profile was solved for the 2.75° half-angle wedge used in the present study 63.5mm from the leading edge, which was where the trips were centered; note that this was as far upstream as the geometry of the test article would allow and was similar to that used by Leidy [160] (64mm) and significantly farther upstream than Semper and Bowersox [246] (95.2mm). The flow conditions conditions were $M = 5.75$, $P_o = 517.11$kPa, $T_o = 430$K, which

yielded a pre-shock Reynolds number[2] of $6.01 \times 10^6/\text{m}$. Following [246], who also left their model in the tunnel during preheat, an adiabatic wall condition was used; IR testing will show this assumption is in general not appropriate, but for a laminar boundary layer and for the fidelity needed at this point, the results remained usable. The simulation was conducted on an equally spaced grid with 250 points in the wall-normal direction simulating up to 10mm from the wall. The simulation was repeated with 1000 points and showed no meaningful change, implying the grid was converged. The resulting boundary layer thicknesses were: $\delta_{H_o,99.5\%} = 1.71\text{mm}$; $\delta_{u,99.5\%} = 1.64\text{mm}$; $\delta_{T,99.5\%} = 1.83\text{mm}$. There was little to choose, but for the sake of consistency with the work of Berry et al. [29] and Semper and Bowersox [246], the total enthalpy definition was used for trip sizing. This meant that $h_{trip} = [1.71, 2.14, 2.57, 2.99]\text{mm}$, $d_{trip} = [1.71, 2.57, 3.42]\text{mm}$, and $w_{trip} = [3.42, 5.13, 6.84]\text{mm}$. The results of the trip sizing are included in Section 7.2.2.

4.4.8 Electrodes

Thermal NEQ was seeded into to the flow via a DC glow discharge. In true hypersonic conditions, thermochemical NEQ naturally occurs [6], but the enthalpies in the ACE tunnel are too low for this condition to happen to a meaningful degree. Here electrical energy was used to create a plasma, which ionized the nitrogen molecules in the air and excited their electronic and vibrational states [268]; the broadband OES in [116] suggested molecular nitrogen would be preferentially excited, especially with respect to molecular oxygen. As the plasma recombined and relaxes from excited electronic states, energy was stored in elevated vibrational modes in the neutral nitrogen's ground electronic state. This process was central to the overall experiment, so extra attention was paid to the design of this element of the test article.

4.4.8.1 Orientation

The plasma's primary role is to provide a uniform test area, perturbing nothing but thermal equilibrium. For this reason, flush electrodes spanning the width of the test article like those in

[2]The viscosity model used here in the calculation of Reynolds number matched that of the NALDAQ, even though the most recent version of the boundary layer solver discussed in Chapter 5 used a slightly different model; these and other small discrepancies revealed as the code was refined were acceptable as the final trips performed well.

[140] were selected. This configuration produced a manageably-sized, predictable, and uniform glow discharge. There are several practical considerations one must consider in regard to electrode placement such as plasma stability, efficacy, and shielding. As a starting point, the electrodes were placed as near the leading edge as possible, but downstream of the trips. This is because the space necessary for trips could act as insulation to prevent plasma formation between the anode and metal wedge frame. Following Kimmel et al. [140], the cathode was placed upstream of the anode. This made sense because it put the larger flow perturbation nearer to the leading edge to increase its effect, the negative glow was less likely to be distorted by the trip wakes, and it moved the high-voltage anode farther away from the metallic wedge body.

Unfortunately, during preliminary testing streaks began to form on the PEEK between the two electrodes, their location corresponding with individual trip structures. It was unclear if these formed due to copper sputtering off the cathode or the PEEK degrading, but in either case there was a risk that over time they could allow breakdown across the surface of the PEEK. For this reason, the position of the cathode and anode were flipped. Streaks on the PEEK downstream of the cathode were formed throughout the remainder of the test campaign, but the risk of permanent damage to the test article was removed.

Two physical phenomena related to this change should be mentioned. It was shown in Section 2.4 that the ion velocity is of the same order as the flow velocity. It is not unreasonable to expect some ions clustered above the cathode may be blown into the test domain. Furthermore, the ions traveling towards the cathode were now sped along by the flow, increasing the ion current. It will be seen in Section 7.2.1 that this manifested in a $\sim 150\%$ increase in plasma power from the original electrode configuration and the formation of a positive column. The concern about a nonuniform positive column was assuaged by a visual inspection of the plasma and minor role the region plays in the first place, and accidental ignition was prevented by providing ample space on all sides of the electrodes and only supplying high voltage when the wind tunnel was started and stable.

4.4.8.2 *Paschen's Curve to Determine Inter-Electrode Gap*

A classic experiment for glow discharge facilities is the manifestation of Paschen's Law (Equation 2.124). Understanding this theory is important because it can be used to help set the electrode gap D. There is a delicate balance in selecting the electrode spacing, and getting it wrong risks either producing a nonuniform plasma, an abnormal glow discharge, or failing to even produce a glow discharge.

As was discussed in Section 2.4, breakdown is controlled by γ as well as A and B (Equation 2.121). γ is difficult to predict for a given setup, while the latter two were shown to be quasi-dependent on the system's temperature. Thus the presence of a strong thermal boundary layer further complicated the estimation of V_t because the exact temperature at which breakdown will occur (or, put another way, where in the boundary layer) was unknown. Here γ was determined experimentally and the result was used in Equation 2.124; this equation was then solved over the range of A's and B's corresponding to the temperatures expected in the ACE tunnel. This ensured the electrode gap selected would produce an attainable V_t wherever in the boundary layer the gas ultimately broke down.

Paschen's Law was experimentally replicated in the quiescent air vacuum chamber because it provided a relatively controllable pressure and temperature environment. Data was recorded at each pressure condition with the "PlasmaDAQ" VI for 30s at 100Hz averaged into 10Hz intervals; this was conservatively several orders of magnitude slower than characteristic breakdown times [224]. The electrodes used were rounded rectangles using 7.62cm long tip-to-tip and 1.27cm wide designed after the experiments in Kimmel et al. [140] (see Section 2.4.4). They were sanded down to P400 roughness and then polished with 800grit (10μm) lapping paste. Thus the electrodes were analogous to those ultimately mounted in the test article, but in order to remove all the ambiguity in measuring D for a flush electrode configuration, center-to-center or edge-to-edge, here the electrodes faced one another 2.54cm apart.

During a data collection period, the current was maximized and the voltage was slowly ramped; because there was no current, no voltage was lost to the ballast resistor so $V_{PS} = V_t$ and $E = V_{PS}/D$.

The time at which the current first exceeded 0.4mA for three consecutive samples determined V_t. Visual observations of the plasma confirmed this was an appropriate benchmark. Data was collected at a number of pressures and ceased when the plasma started being produced at the metal walls of the bell jar.

The results are shown in Figure 4.14, with error bars due to the 10.05% uncertainty in the pressure reading. The experimental data were fit with Equation 2.124 using A and B calculated from Equation 2.121 at $T_{room} = 294.82\text{K}$ with σ and $\frac{I}{e}$ found from von Engel's measurements of $A = 15\text{cm}^{-1}\text{Torr}^{-1}$ and $B = 365\frac{\text{V}}{\text{cm}\cdot\text{Torr}}$ [289]. This approach was valid because the experiment was conducted at room temperature and $\frac{E}{P}$ was mostly within the listed $100-800\frac{\text{V}}{\text{cm}\cdot\text{Torr}}$. With this the only free parameter left was γ. Different values were used until a curve was produced which matched the data. In the end, $\gamma = 2.5\times10^{-4}$ provided reasonable agreement at both $V_{t,min}$ and on the right hand branch; the discrepancy in the left hand side of the branch was likely due to having $\frac{E}{P} > 800\frac{\text{V}}{\text{cm}\cdot\text{Torr}}$. This value for the secondary emission coefficient fell well within the bounds $\mathcal{O}(10^{-6}) < \gamma < \mathcal{O}(10^{-3})$ set by Francis [92] for N_2 on copper electrodes at $PD = 50\text{torr}\cdot\text{cm}$.

With γ known, the effect of temperature on Pachen's Law could be explored. Here $\sigma = 4.554\times10^{-20}\text{m}^2$ and $\frac{I}{e} = 24.333\text{V}$, calculated from von Engel's measurements at room temperature [289], were used. Again, comparing with direct measurements like those by Atkins and Paula [11], these parameters are off, and the conditions under which they were found may not match the present experiment in the ACE tunnel, but they are sufficient to illustrate the effect of temperature on Paschen's Law and provide some approximation of V_t over the expected temperature range. Remember, the goal here is to ensure D is reasonably chosen, not precisely predict V_t as it is far easier to just measure it in the tunnel.

To that end, temperatures between 50 and 450K were simulated and results are shown on Figure 4.15. The results suggest increasing the temperature decreases V_t on the right hand side of Paschen's curve, has no effect on $V_{t,min}$, and increases V_t on the left hand side of the curve. The 3000V power supply should be capable of providing breakdown up to $Pd \sim \mathcal{O}(10-100)\text{cm}\cdot\text{Torr}$, but in practice V_t should be limited to $< 1000\text{V}$ to ensure there is enough range to fully cover the

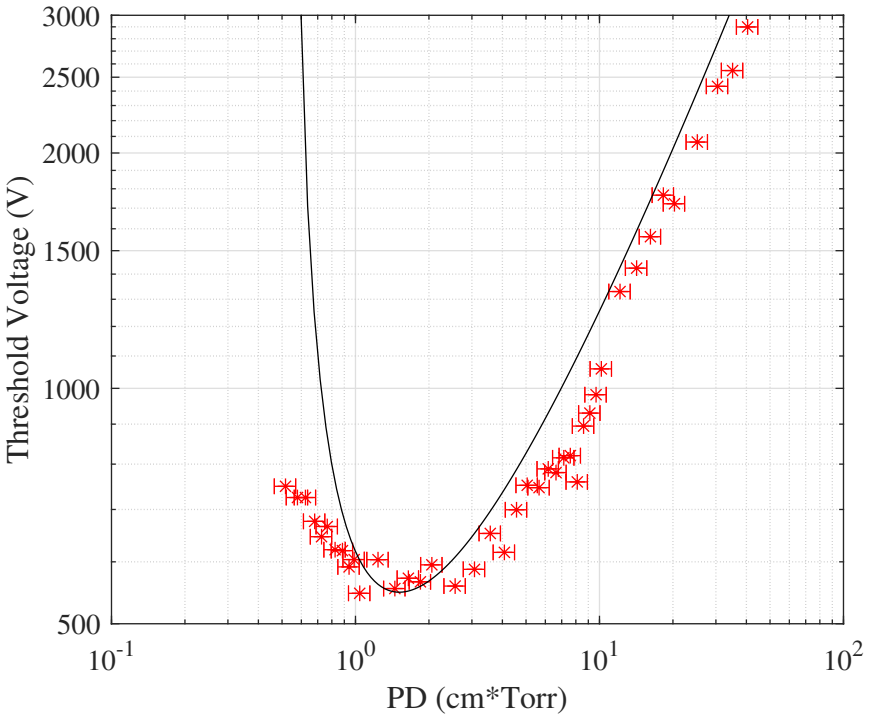

Figure 4.14: Paschen's curve in a the quiscient air vacuum chamber; $\gamma = 2.5 \times 10^{-4}$

cathode in plasma. This puts $PD \sim 1 - 10\text{cm} \cdot \text{Torr}$. Because the a nominal post-shock pressure was $\sim$ 5Torr, the electrode gap was fixed at $D = 1.27\text{cm}$. This was the center-to-center distance, following the convention of Kimmel et al. [140], and although additional testing in the quiescent air vacuum chamber found that using the edge-to-edge distance had better agreement with Paschen's Law, it will continue to be used here. Finally, note that keeping the gap small had the additional benefit of helping to prevent accidental ignition between the electrodes and metal wedge frame.

There was some concern that making the inter-electrode gap too small could cause the PEEK insulation between the electrodes to short, especially at higher temperatures or near the electrodes' rounded sides. Remember, D was a center-to-center measurement, and for the final design the PEEK thickness between the electrodes was only 0.635cm. Lacking applicable data from the manufacturer, this dielectric strength was tested with a leftover piece of PEEK with channels cut into it and an overpowered power supply.

Electrodes matching the surface treatment and size of the final design were mounted into the

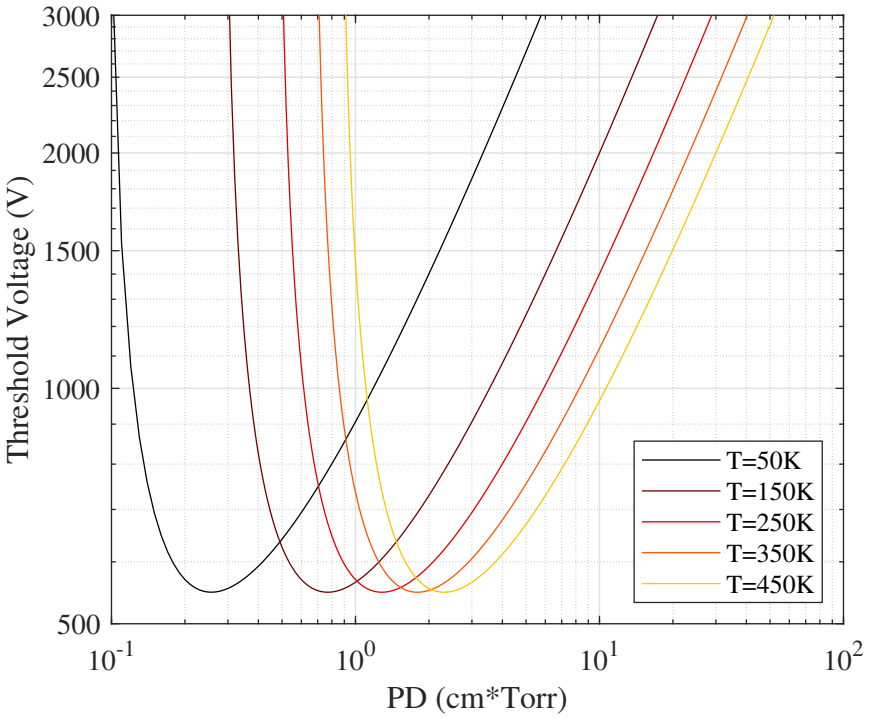

Figure 4.15: Theoretical Paschen's curves illustrating the effect of temperature on breakdown.

PEEK. A 600W (10kV at 60mA) Glassman PS/EJ10R60.0 (serial no. N629111-01-NR190624) DC power supply provided the voltage. Three 50Ω and one 20Ω Ohmite chassis mount ballast resistors in series provided a total resistance of $R_b = 170\Omega$ and total power dissipation of 400W (the resistors were briefly overloaded during breakdown). To account for thermal effects, before testing the setup was heated face-down on a hot plate to $\sim 373.15K$, as measured with a Extech Inst. 42510A IR Thermometer; it is noted this setup did not provide uniform heating through the PEEK, but this was not a priority. The power supply was put into a "voltage limited" mode and the requested current maximized. The voltage was then increased until breakdown occurred. The experiment was conducted in open air, save for a cover for safety.

The PEEK eventually shorted at $\sim$ 8kV, so the chosen gap was safe for the lower temperatures and 3kV power supply used throughout the campaign. Nevertheless, the power supply was only ever briefly turned on at low voltages before a run when the plate was cold and was shut off before tunnel unstart during a run to minimize the PEEK having to insulate the electrodes.

4.4.8.3 Size

It was discussed in Section 2.4 that a normal glow discharge was desirable because of its simplicity, uniformity, and stability. Recall that normal glow discharges grow on the electrode surface as the current is increased. Therefore in order to produce a glow discharge which completely covered the electrodes, a necessity for providing a constant test environment, one could either increase the power supply's current or decrease the size of the electrode. In practice, it was far easier to control the current than design multiple different electrodes of different size, so the approach taken here was to reduce the electrode area as much as reasonably possible and rely on current control thereafter. Following Kimmel et al. [140], the end result was a rounded rectangle 13.34cm long (tip-to-tip) and 0.635cm wide and with a total area of 8.381cm^2. The width was smaller than the trip insert to conserve area, but still large enough to prevent any plasma edge effects in the region of interest. The final width left 2.858cm on either side of the electrodes to prevent ignition between the the metal wedge frame; this distance is 4.5$\times$ the edge-to-edge electrode distance, 0.635cm, and was a minimum maintained around all sides of the electrodes. The thickness was set to provide ample material to tap support and conducting screws into and to provide sufficient rigidity for handling and polishing despite being made of soft copper.

Preliminary testing showed that this size became fully covered around $I \approx 90$mA, so it was an excellent match for the 100mA power supply. Remember from Section 2.4, putting additional current through the electrodes once they are fully covered by plasma will lead one into the less well-characterized abnormal regime, where any power benefits are paid for with the necessity of more complex theory.

4.4.8.4 Construction, Wiring, and Support

The electrodes were made from a 0.476cm-thick 110 copper bar and machined with a wire electric discharge machine at the Oran W. Nicks Low Speed Wind Tunnel's machine shop; the thickness provided rigidity during production, sufficient thread length for fasteners, and, with proper tolerancing, provided some extra material to be sanded and polished away for a secure and flush

fit. They were sanded down to P400 and polished with 800grit (10μm) lapping paste, just as those for the Paschen characterization. The electrodes were fit into pockets in the PEEK and fastened from below by three screws; the screws were covered in Permatex High temperature Gasket maker RTV to prevent plasma ignition and also sucking/blowing along the sides of the electrodes. Two screws were made from electrically insulative, thermally safe PTFE and one screw on each electrode was made from metal and acted to carry the current from the wire into the electrodes. The cathode's wire was connected to the center of the electrode to ensure a uniform glow discharge in the centerline, while for space the anode's wire was attached on one of the side screws; although a non-uniform positive column focused around the connection point would not be too problematic due to its relative lack of importance, it was nevertheless evenly distributed along the gap.

5. NUMERICAL METHODS

The ultimate goal of this chapter is to provide all the information necessary to write a compressible boundary layer solver, and in doing so produce a tool which could abet the current experimental campaign. The theory behind each section of the code is described in the order in which it becomes relevant. At the end of the section, a language-agnostic pseudocode is included which summarizes all of the theory into detailed programming steps. For readers in search of immediate access to simple viscous flow solvers or those who would like to explore approaches or flow types other than that over a compressible flat plate, the JAVA applets of Devenport and Shetz are recommended [79, 80][1].

5.1 Problem Statement & Assumptions

As work was conducted in the ACE tunnel, the need for quantitative predictive tools for key variables through the boundary layer became apparent. For example, knowing the density drop through the hot-wall boundary layer would help predict the expected NO number density, a parameter critical for early PLIF feasibility analyses. Numerical techniques lent themselves well to this problem. Order-of-magnitude estimates of the parameters were deemed sufficient for these first-order predictions as the added complexity and cost of commercial codes, both temporal and financial, were not justified. Furthermore, there is always a benefit of writing one's own codes as an educational exercise. For these reasons an in-house code was written to provide low-fidelity estimations of both laminar and turbulent boundary layers in the compressible flow regime with adiabatic and isothermal wall conditions. It is worth mentioning that analytical solutions to the laminar problem exist, perhaps the most famous of which being van Driest's self-similar solutions [283]. van Driest's plots may be useful references the laminar case, or for code validation.

The laminar, steady, 2D, planar boundary layer form of the conservation equations to be solved

[1] https://www.engapplets.vt.edu/fluids/bls2/

were provided by White [293]:

$$\frac{\partial}{\partial x}(\rho u)+\frac{\partial}{\partial y}(\rho v)=0 \tag{5.1}$$

$$\rho u\frac{\partial u}{\partial x}+\rho v\frac{\partial u}{\partial y}\approx -\frac{dP_e}{dx}+\frac{\partial}{\partial y}\left(\mu\frac{\partial u}{\partial y}\right) \tag{5.2}$$

$$\frac{\partial P}{\partial y}\approx 0 \tag{5.3}$$

$$\rho u C_p\frac{\partial T}{\partial x}+\rho v C_p\frac{\partial T}{\partial y}\approx u\frac{dP_e}{dx}+\frac{\partial}{\partial y}\left(k\frac{\partial T}{\partial y}\right)+\mu\left(\frac{\partial u}{\partial y}\right)^2 \tag{5.4}$$

Again, the Prandtl number is defined as $Pr=\mu C_p/k$.

There were several key assumptions integral to the code, the most reasonable of which was the restriction to steady, 2D planar flows of perfect gases; this was all acceptable for simulating flows in the ACE tunnel, albeit without the thermal nonequilbrium introduced by the glow discharge. More general programs which considered thermochemical nonequilibrium were provided by Anderson and Lewis [3] and Blottner [34]. Leading edge complications like the Hayes-Probstein viscous-inviscid interaction [108] and shock curvature (and thereby entropy layers) were not considered.

A bolder simplification was the approximation of the 2.75° half-angle wedge used throughout the experimental campaign as a flat plate with zero pressure gradient. This was necessary as it greatly simplifies the code, and for the relatively slender 2D test article it was deemed acceptable. As a compromise, to accommodate the wedge's half-angle the program calculated the flow conditions across the oblique shock at the leading edge using isentropic flow relations [128]. It then used the results after the shock as the inputs to the flat plate solution. The simplification was further justified using the theoretical work on self-similar methods for flows with pressure gradients (wedges) by Cohen and Reshotko [64]. If one defines a parameter $\beta=\frac{\delta}{180\,\mathrm{deg}}$ then for the current wedge $\beta=0.015$, which according to their data was sufficiently close enough to $\beta=0$ for pressure effects to be neglected.

5.2 Grid Generation with Clustered Spacing

A tacit requirement of turbulence modeling of any kind is clustered spacing [275]. When doing turbulent simulations, it is highly inefficient to use a uniform wall-normal grid because the resolution necessary to capture the sublayer is overly refined for the remainder of the boundary layer and especially the freestream [275], wasting computational effort is in these regions. Instead, a clustered wall-normal coordinate is used, which means extra nodes are added near regions of interest and the remainder of the domain is more sparsely discretized. Of the many ways achieve this, a popular technique for hypersonic flows is provided by Malik [170] which was adopted in this work; an alternative was described by Cebeci and Smith [55].

The central tenant of Malik's technique is to map a clustered, dimensional wall-normal coordinate ($y = [0, y_{max}]$) onto an equally-spaced domain ($\eta = [0, 1]$) for numerical differentiation and integration, then bring it back to the dimensional frame for final processing. Here the clustering used was

$$y = \frac{a\eta}{(b - \eta)} \tag{5.5}$$

where $a = \frac{y_{max} y_{crit}}{(y_{max} - 2y_{crit})}$ and $b = 1 + \frac{a}{y_{max}}$. This puts half of the nodes below y_{crit} and the other half above it [170].

The complication of using a mapping is that when differentiating or integrating with respect to y, one must use the Chain Rule. When doing this for higher derivatives, it is helpful to use Faá di Bruno's formula [88], written here for the current application up to the fourth derivative

- $\frac{D^1 f(g(x))}{1!} = f_g g_x$
- $\frac{D^2 f(g(x))}{2!} = f_g \frac{g_{xx}}{2!} + f_{gg} \frac{(g_x)^2}{2!}$
- $\frac{D^3 f(g(x))}{3!} = f_g \frac{g_{xxx}}{3!} + f_{gg} g_x \frac{g_{xx}}{2!} + f_{ggg} \frac{(g_x)^3}{3!}$
- $\frac{D^4 f(g(x))}{4!} = f_g \frac{g_{xxxx}}{4!} + f_{gg} \left(g_x \frac{g_{xxx}}{3!} + \frac{(g_{xx})^2}{2!2!2!} \right) + f_{ggg} \frac{(g_x)^2 g_{xx}}{2!2!} + f_{gggg} \frac{(g_x)^4}{4!}$

In the above formulas, $D^n = \frac{\partial^n}{\partial y^n}$, $g(x) = \eta(y) = \frac{by}{(y+a)}$, and f is what is being differentiated with respect to η. Thus

- $g_x = \frac{\partial \eta}{\partial y} = \frac{ab}{(a+y)^2}$
- $g_{xx} = \frac{-2ab}{(a+y)^3}$
- $g_{xxx} = \frac{6ab}{(a+y)^4}$
- $g_{xxxx} = \frac{-24ab}{(a+y)^5}$

With this, the differentiation becomes

- $D^1 = \left(\frac{ab}{(a+y)^2}\right)\frac{\partial}{\partial \eta}$
- $D^2 = \left(\frac{-2ab}{(a+y)^3}\right)\frac{\partial}{\partial \eta} + \left(\frac{ab}{(a+y)^2}\right)^2 \frac{\partial^2}{\partial \eta^2}$
- $D^3 = \left(\frac{6ab}{(a+y)^4}\right)\frac{\partial}{\partial \eta} + (3)\left(\frac{ab}{(a+y)^2}\right)\left(\frac{-2ab}{(a+y)^3}\right)\frac{\partial^2}{\partial \eta^2} + \left(\frac{ab}{(a+y)^2}\right)^3 \frac{\partial^3}{\partial \eta^3}$
- $D^4 = \left(\frac{-24ab}{(a+y)^5}\right)\frac{\partial}{\partial \eta} + \left((4)\left(\frac{ab}{(a+y)^2}\right)\left(\frac{6ab}{(a+y)^4}\right) + (3)\left(\frac{-2ab}{(a+y)^3}\right)^2\right)\frac{\partial^2}{\partial \eta^2} + \left((6)\left(\frac{ab}{(a+y)^2}\right)^2\left(\frac{-2ab}{(a+y)^3}\right)\right)\frac{\partial^3}{\partial \eta^3} + \left(\frac{ab}{(a+y)^2}\right)^4 \frac{\partial^4}{\partial \eta^4}$

The equations rapidly become complex, but fortunately the current problem only required second-order differentiation.

The key is to remember what was physically happening. When using the Malik transformation, the program generated a clustered grid in physical coordinates and then mapped each point onto an equally spaced grid, which was necessary for finite difference differentiation and integration. Now everywhere there was differentiation or integration with respect to y in the finite difference equations, such as in the calculation of shear stress or momentum thickness, the Chain Rule as outlined by the equations of D^X needed to be used. However, if y was used by itself in a formula, say in the calculation of y^+, it did not need to be replaced by η. Similarly, when the results for u, T, v, *etc.* were output for all points through the boundary layer at a given streamwise location, no mapping was necessary to convert from η to y or *vice versa*. Because this was a $1:1$ mapping, when indexing a wall-normal coordinate the program did not need to know if it was referring to a clustered grid or equally spaced grid. The n^{th} node in a column of data referred to the same

value, and whether it corresponded to $y(n)$ or $\eta(n)$ did not numerically matter. As a final example to emphasize that once the operation was complete parameters were independent of the grid used, the formula for the kinematic displacement thickness is shown in both physical and equally spaced coordinates.

$$\delta_k^* = \int_0^{y_{max}} \left(1 - \frac{u}{u_e}\right) dy = \int_{\eta(y=0)}^{\eta(y_{max})} \left(1 - \frac{u}{u_e}\frac{dy}{d\eta}\right) \partial\eta = \int_0^{\frac{by_{max}}{y_{max}+a}} \left(1 - \frac{u}{u_e}\right) \frac{ab}{(b-\eta)^2} d\eta \quad (5.6)$$

Throughout the remainder of this section, all formulas will be provided with the Malik coefficients included to ensure the more complicated forms of the equations are clearly shown.

5.3 Finite Difference Scheme

With the grid established, the boundary layer equations could be discretized. The following derivation follows White [293], though it was modified to include the Malik clustering; in the final implementation, Malik clustering could be turned off and the simplified equations solved. Here m represents the streamwise coordinate, and n represents the wall-normal coordinate.

It will be seen that the current AEF model was only amenable to an explicit scheme, but the stability limitations on these equations made a solely explicit code overly restrictive. As a compromise, both explicit and implicit discretizations of Equations 5.2 and 5.4 were derived and coded to solve for u and T respectively. Equation 5.1, which provided v, was only ever solved explicitly; this was acceptable as the final equation is stable [293]. The implicit equations could be solved with any tridiagonal matrix algorithm such as the Thomas Aglorithm [275] or prebuilt, language-specific functions. Comparing the explicit and implicit discretizations, usually it was only the treatment of one term which distinguished the two.

All derivations are shown below and follow White [293]. Streamwise derivatives were solved using first-order methods while wall-normal derivatives were solved with second-order methods, making all of the schemes $\mathcal{O}(\Delta x) + \mathcal{O}(\Delta y^2)$ accurate. While higher-order schemes could be used to make the code entirely second-order, for basic solvers first-order methods were sufficient [275].

When discretizing the boundary layer equations, it was important to maintain linearity of the

$m+1$ variables. For example, consider Equation 5.2; the coefficients in front of each derivative on the left-hand side make the equation nonlinear at each streamwise step $m+1$. Tannehill et al. [275] discussed various techniques for addressing this complication, but the one adopted here was "lagging", wherein the coefficients were evaluated at the m location under the boundary layer assumption that streamwise gradients were small. This is not the most accurate approach, but Tannehill et al. [275] suggested it is typically sufficient for low-fidelity codes. Also, because this is a flat plate, perfect gas solver, C_p, ρ_e, and u_e were all constants and thus did not need to be discretized. That being said, wherever they could be removed entirely from the equations they were kept in for generality.

Finally, some non-dimensional parameters to simplify the algebra are provided:

$$Let \quad \alpha = \frac{\mu_{m,n}\Delta x}{\rho_{m,n}u_{m,n}\Delta\eta^2}\left(\frac{ab}{(a+y)^2}\right)^2 \tag{5.7}$$

$$\beta = \frac{\nu_{m,n}\Delta x}{2u_{m,n}\Delta\eta^2}\left(\frac{ab}{(a+y)^2}\right) \tag{5.8}$$

$$\zeta = \frac{(\mu_{m,n+1}-\mu_{m,n-1})\Delta x}{4\rho_{m,n}u_{m,n}}\left(\frac{ab}{(a+y)^2}\right)^2 \tag{5.9}$$

5.3.1 x-Component Conservation of Momentum: Implicit

Using Bernoulli's theorem in the freestream $\left(\frac{dP}{dx} = -\rho u_e \frac{du_e}{dx}\right)$, the Multiplication Rule on the appropriate terms, and lagging the coefficients, Equation 5.2 becomes

$$\rho_{m,n}u_{m,n}\frac{\partial u}{\partial x} + \rho_{m,n}v_{m,n}\frac{\partial u}{\partial y} \approx \rho_e U_e\frac{dU_e}{dx} + \frac{\partial \mu}{\partial y}\frac{\partial u}{\partial y} + \mu_{m,n}\frac{\partial^2 u}{\partial y^2} \tag{5.10}$$

$$\begin{aligned}
&\rho_{m,n}u_{m,n}\frac{u_{m+1,n}-u_{m,n}}{\Delta x} + \rho_{m,n}v_{m,n}\left(\frac{ab}{(a+y)^2}\right)\frac{u_{m,n+1}-u_{m,n-1}}{2\Delta\eta} \approx \\
&\rho_{e(m,n)}\frac{U^2_{e(m+1,n)}-U^2_{e(m,n)}}{2\Delta x} + \left(\frac{ab}{(a+y)^2}\right)^2\frac{(\mu_{m,n+1}-\mu_{m,n-1})(u_{m,n+1}-u_{m,n-1})}{(2\Delta\eta)^2} \\
&+ \mu_{m,n}\left(\left(\frac{-2ab}{(a+y)^3}\right)\frac{u_{m,n+1}-u_{m,n-1}}{2\Delta\eta} + \left(\frac{ab}{(a+y)^2}\right)^2\frac{u_{m+1,n+1}-2u_{m+1,n}+u_{m+1,n-1}}{\Delta\eta^2}\right)
\end{aligned} \tag{5.11}$$

Multiplying through by $\frac{\Delta x}{\rho_{m,n}u_{m,n}}$,

$$
\begin{aligned}
&-\alpha u_{m+1,n+1}+(1+2\alpha)u_{m+1,n}-\alpha u_{m+1,n-1}\approx \\
&\frac{\rho_{e(m)}(U_{e(m+1)}^2-U_{e(m)}^2)}{2\rho_{m,n}u_{m,n}}+u_{m,n}-\left((\beta-\zeta)-\frac{\Delta x\mu_{m,n}}{2\Delta\eta\rho_{m,n}u_{m,n}}\left(\frac{-2ab}{(a+y)^3}\right)\right)(u_{m,n+1}-u_{m,n-1})
\end{aligned}
\tag{5.12}
$$

5.3.2 x-Component Conservation of Momentum: Explicit

Using Bernoulli's theorem in the freestream $\left(\frac{dP}{dx}=-\rho u_e\frac{du_e}{dx}\right)$, the Multiplication Rule on the appropriate terms, and lagging the coefficients, Equation 5.2 becomes

$$
\rho_{m,n}u_{m,n}\frac{\partial u}{\partial x}+\rho_{m,n}v_{m,n}\frac{\partial u}{\partial y}\approx\rho_e U_e\frac{dU_e}{dx}+\frac{\partial\mu}{\partial y}\frac{\partial u}{\partial y}+\mu_{m,n}\frac{\partial^2 u}{\partial y^2} \tag{5.13}
$$

$$
\begin{aligned}
&\rho_{m,n}u_{m,n}\frac{u_{m+1,n}-u_{m,n}}{\Delta x}+\rho_{m,n}v_{m,n}\left(\frac{ab}{(a+y)^2}\right)\frac{u_{m,n+1}-u_{m,n-1}}{2\Delta\eta}\approx \\
&\rho_{e(m)}\frac{U_{e(m+1)}^2-U_{e(m)}^2}{2\Delta x}+\left(\frac{ab}{(a+y)^2}\right)^2\frac{(\mu_{m,n+1}-\mu_{m,n-1})(u_{m,n+1}-u_{m,n-1})}{(2\Delta\eta)^2} \\
&+\mu_{m,n}\left[\left(\frac{-2ab}{(a+y)^3}\right)\frac{u_{m,n+1}-u_{m,n-1}}{2\Delta\eta}+\left(\frac{ab}{(a+y)^2}\right)^2\frac{u_{m,n+1}-2u_{m,n}+u_{m,n-1}}{\Delta\eta^2}\right]
\end{aligned}
\tag{5.14}
$$

Multiplying through by $\frac{\Delta x}{\rho_{m,n}u_{m,n}}$,

$$
\begin{aligned}
&u_{m+1,n}\approx \\
&\frac{\rho_{e(m)}(U_{e(m+1)}^2-U_{e(m)}^2)}{2\rho_{m,n}u_{m,n}}+\frac{\mu_{m,n}\Delta x}{\rho_{m,n}u_{m,n}}\left(\frac{-2ab}{(a+y)^3}\right)\left(\frac{u_{m,n+1}-u_{m,n-1}}{2\Delta\eta}\right) \\
&+u_{m,n+1}\left[-\beta+\zeta+\alpha\right]+u_{m,n}\left[1-2\alpha\right]+u_{m,n-1}\left[\beta-\zeta+\alpha\right]
\end{aligned}
\tag{5.15}
$$

5.3.3 Conservation of Energy: Implicit

Using Bernoulli's theorem in the freestream $\left(\frac{dP}{dx} = -\rho u_e \frac{du_e}{dx}\right)$, the Multiplication Rule on the appropriate terms, and lagging the coefficients, Equation 5.4 becomes

$$\rho_{m,n} u_{m,n} C_{p(m,n)} \frac{\partial T}{\partial x} + \rho_{m,n} v_{m,n} C_{p(m,n)} \frac{\partial T}{\partial y} \approx -u_{m,n} \rho_e U_e \frac{dU_e}{dx} + \mu_{m,n} \left(\frac{\partial u}{\partial y}\right)^2 + \frac{\partial k}{\partial y}\frac{\partial T}{\partial y} + k_{m,n}\frac{\partial^2 T}{\partial y^2} \tag{5.16}$$

$$\begin{aligned}
&\rho_{m,n} u_{m,n} C_{p(m,n)} \frac{T_{m+1,n} - T_{m,n}}{\Delta x} + \rho_{m,n} v_{m,n} C_{p(m,n)} \left(\frac{ab}{(a+y)^2}\right) \frac{T_{m,n+1} - T_{m,n-1}}{2\Delta\eta} \approx \\
&- u_{m,n} \rho_{e(m,n)} \frac{U^2_{e(m+1,n)} - U^2_{e(m,n)}}{2\Delta x} + \mu_{m,n} \left(\frac{ab}{(a+y)^2}\right)^2 \left(\frac{u_{m,n} - u_{m,n-1}}{\Delta\eta}\right)^2 + \\
&\left(\frac{ab}{(a+y)^2}\right)^2 \frac{(k_{m,n+1} - k_{m,n-1})(T_{m,n+1} - T_{m,n-1})}{(2\Delta\eta)^2} \\
&+ k_{m,n} \left[\left(\frac{-2ab}{(a+y)^3}\right) \frac{T_{m,n+1} - T_{m,n-1}}{2\Delta\eta} + \left(\frac{ab}{(a+y)^2}\right)^2 \frac{T_{m+1,n+1} - 2T_{m+1,n} + T_{m+1,n-1}}{\Delta\eta^2}\right]
\end{aligned} \tag{5.17}$$

Multiplying through by $\frac{\Delta x}{\rho_{m,n} u_{m,n} C_{p(m,n)}}$,

$$\begin{aligned}
&- \frac{k_{m,n}\alpha}{\mu_{m,n} C_{p(m,n)}} T_{m+1,n+1} + \left(1 + \frac{2k_{m,n}\alpha}{\mu_{m,n} C_{p(m,n)}}\right) T_{m+1,n} - \frac{k_{m,n}\alpha}{\mu_{m,n} C_{p(m,n)}} T_{m+1,n-1} \approx \\
&T_{m,n} - \frac{\rho_{e(m,n)}(U^2_{e(m+1,n)} - U^2_{e(m,n)})}{2\rho_{m,n} C_{p(m,n)}} + \frac{\alpha}{C_{p(m,n)}} (u_{m,n} - u_{m,n-1})^2 \\
&- \left[\beta + \left(\frac{ab}{(a+y)^2}\right)^2 \left(\frac{\Delta x (k_{m,n+1} - k_{m,n-1})}{4\Delta\eta^2 \rho_{m,n} u_{m,n} C_{p(m,n)}}\right)\right] (T_{m,n+1} - T_{m,n-1}) \\
&+ k_{m,n} \left(\frac{-2ab}{(a+y)^3}\right) \left(\frac{T_{m,n+1} - T_{m,n-1}}{2\Delta\eta}\right) \left(\frac{\Delta x}{\rho_{m,n} u_{m,n} C_{p(m,n)}}\right)
\end{aligned} \tag{5.18}$$

5.3.4 Conservation of Energy: Explicit

Using Bernoulli's theorem in the freestream $\left(\frac{dP}{dx} = -\rho u_e \frac{du_e}{dx}\right)$, the Multiplication Rule on the appropriate terms, and lagging the coefficients, Equation 5.4 becomes

$$\rho_{m,n} u_{m,n} C_{p(m,n)} \frac{\partial T}{\partial x} + \rho_{m,n} v_{m,n} C_{p(m,n)} \frac{\partial T}{\partial y} \approx -u_{m,n} \rho_e U_e \frac{dU_e}{dx} + \mu_{m,n} \left(\frac{\partial u}{\partial y}\right)^2 + \frac{\partial k}{\partial y}\frac{\partial T}{\partial y} + k_{m,n}\frac{\partial^2 T}{\partial y^2} \tag{5.19}$$

$$\rho_{m,n}u_{m,n}C_{p(m,n)}\frac{T_{m+1,n}-T_{m,n}}{\Delta x}+\rho_{m,n}v_{m,n}C_{p(m,n)}\left(\frac{ab}{(a+y)^2}\right)\frac{T_{m,n+1}-T_{m,n-1}}{2\Delta\eta}\approx$$
$$-u_{m,n}\rho_{e(m,n)}\frac{U^2_{e(m+1,n)}-U^2_{e(m,n)}}{2\Delta x}+\mu_{m,n}\left(\frac{ab}{(a+y)^2}\right)^2\left(\frac{u_{m,n}-u_{m,n-1}}{\Delta\eta}\right)^2+$$
$$\left(\frac{ab}{(a+y)^2}\right)^2\frac{(k_{m,n+1}-k_{m,n-1})(T_{m,n+1}-T_{m,n-1})}{(2\Delta\eta)^2} \tag{5.20}$$
$$+k_{m,n}\left[\left(\frac{-2ab}{(a+y)^3}\right)\frac{T_{m,n+1}-T_{m,n-1}}{2\Delta\eta}+\left(\frac{ab}{(a+y)^2}\right)^2\frac{T_{m,n+1}-2T_{m,n}+T_{m,n-1}}{\Delta\eta^2}\right]$$

Multiplying through by $\frac{\Delta x}{\rho_{m,n}u_{m,n}C_{p(m,n)}}$,

$$T_{m+1,n}\approx-\frac{\rho_{(e)m}(U^2_{e(m+1,n)}-U^2_{em,n})}{2\rho_{m,n}C_{p(m,n)}}+\left(\frac{\alpha}{C_{p(m,n)}}\right)(u_{m,n}-u_{m,n-1})^2+T_{m,n}$$
$$-\left[\beta-\left(\frac{ab}{(a+y)^2}\right)^2\left(\frac{\Delta x(k_{m,n+1}-k_{m,n-1})}{4\Delta\eta^2\rho_{m,n}u_{m,n}C_{p(m,n)}}\right)\right](T_{m,n+1}-T_{m,n-1})$$
$$\left(\frac{\Delta xk_{m,n}}{\rho_{m,n}u_{m,n}C_{p(m,n)}}\right)\left[\left(\frac{-2ab}{(a+y)^3}\right)\frac{T_{m,n+1}-T_{m,n-1}}{2\Delta\eta}+\left(\frac{ab}{(a+y)^2}\right)^2\frac{T_{m,n+1}-2T_{m,n}+T_{m,n-1}}{\Delta\eta^2}\right] \tag{5.21}$$

When using the AEF model for turbulent heat flux, one must add $\frac{\partial q_y^T}{\partial y}$ to the right hand side, discretize it with second-order central differencing, and then multiply it by $\frac{\Delta x}{\rho_{m,n}u_{m,n}C_{p(m,n)}}$. Ultimately

$$\frac{\Delta x}{\rho_{m,n}u_{m,n}C_{p(m,n)}}\left(\frac{ab}{(a+y)^2}\right)\frac{q^T_{y(m,n+1)}-q^T_{y(m,n-1)}}{2\eta} \tag{5.22}$$

must be added to the right hand side. Again, if the traditional gradient diffusion approach is taken for turbulent heat flux, this term can be omitted.

5.3.5 Conservation of Mass: Explicit

Again, Equation 5.1 was solved explicitly, but care must be taken in the selection of the nodes used. For example, White [293] showed that if the following scheme was used,

$$\frac{\partial}{\partial x}(\rho u)+\frac{\partial}{\partial y}(\rho v)=0 \tag{5.23}$$

$$\frac{\rho_{m+1,n}u_{m+1,n}-\rho_{m,n}u_{m,n}}{\Delta x}+\left(\frac{ab}{(a+y)^2}\right)\frac{\rho_{m+1,n}v_{m+1,n}-\rho_{m,n}v_{m,n}}{\Delta\eta}\approx 0 \tag{5.24}$$

then the streamwise differentiation was at the n node while the wall-normal differentiation was evaluated at the $n-\frac{1}{2}$ node, which a detriment to the numerical accuracy. Wu [302] offered a solutions by calculating

$$\left(\frac{\partial u}{\partial x}\right)_{avg}\approx\frac{1}{2}\left(\frac{u_{m+1,n}-u_{m,n}}{\Delta x}+\frac{u_{m+1,n-1}-u_{m,n-1}}{\Delta x}\right) \tag{5.25}$$

and thereby moving the streamwise differentiation down to the $n-\frac{1}{2}$ node. With this, 5.1 becomes

$$\begin{aligned} v_{m+1,n}\approx&\frac{\rho_{m+1,n-1}v_{m+1,n-1}}{\rho_{m+1,n}}-\\ &\frac{\Delta\eta}{2\rho_{m+1,n}\Delta x}\left(\frac{(a+y)^2}{ab}\right)\left(\rho_{m+1,n}u_{m+1,n}-\rho_{m,n}u_{m,n}+\rho_{m+1,n-1}u_{m+1,n-1}-\rho_{m,n-1}u_{m,n-1}\right)\end{aligned} \tag{5.26}$$

5.3.6 Adding Turbulence

Using RANS turbulence modeling with the Boussinesq approximation, in order to add turbulence to the code one need only solve for μ_t using the models described in Section 2.2.1 and then add it to μ in the above equations. Analogously, using gradient diffusion one can use the turbulent Prandtl number and eddy viscosity to calculate k_t and then add it to k in the above equations. Thus no structural changes needed to be made to the finite difference scheme or derived equations to toggle between laminar or turbulent flow, the code only had to check and see if it was solving downstream of a user-specified trip.

The problem was complicated by the introduction of the AEF model for turbulent heat flux derived in Chapter 3. The model still used the Boussinesq approximation to calculate μ_t, but it completely ignored k_t and solved for q_y^T directly. This was an issue for the implicit discretization of the conservation of energy. Recall that on the right hand side one takes the gradient of the heat flux $q_{,y}=\left(-kT_{,y}\right)_{,y}$. Under an implicit scheme, the $\frac{\partial^2 T}{\partial y^2}$ portion was evaluated at T_{m+1}, which was ultimately brought to the left hand side. If one wanted to add a distinct q_y^T term, technically it must

also be evaluated at $m+1$. To avoid adding an entire new unknown to the left hand side, the AEF model would need to be re-derived to be entirely in terms of temperature so the appropriate T_{m+1} terms could be moved to the proper place. For now, the simpler solution was to only apply the AEF model to explicit schemes where both the laminar and turbulent $q_{,y}$ were evaluated at m and thus remained on the right hand side.

From a practical perspective, the introduction of eddy viscosity and either gradient diffusion or AEF heat flux required a careful series of conditional statements. The user had to decide whether they wanted to run and implicit or explicit scheme, where they wanted to trip the boundary layer, and what turbulence models to use; the code would return an error if the implicit scheme was used with the AEF model. When $x < x_{transition}$, $\mu_t = k_t/q_y^T = 0$. If the flow was turbulent and a gradient diffusion model was requested, eddy viscosity was calculated from the specified model, eddy thermal conductivity was calculated with the turbulent Prandtl number, and both values were simply added to their laminar counter parts before the conservation equations were solved; $q_y^T = 0$ so the explicit energy equation could be solved without modification. In the AEF case, $k_t = 0$ and q_y^T was solved which "turned on" the extra term in the explicit energy equation.

5.4 Initial and Boundary Conditions

All finite difference schemes require initial and boundary conditions; recall that in every case above the solution began at the $(m+1)^{th}$ step but required data at m. Detailed instructions for the necessary starting conditions are provided below, and a summary of the process is as follows: The user specified the Mach number and upstream stagnation conditions. The code then used isentropic flow relations to calculate the conditions downstream of the bow shock. These results provided the initial conditions and freestream values for the finite difference solution, effectively simulating the wedge flow as a flat plate. The program used the shooting method to solve the self-similar equations, taking the freestream velocity and temperature (and if the flow is isothermal, wall temperature) as inputs. Once converged, the self-similar results were interpolated onto the user's dimensional grid, and standard equations were used to calculate some secondary variables through the boundary layer. With this boundary layer at a specific streamwise location was calculated and

the code was ready to proceed to the finite difference scheme.

5.4.1 Initial Condition

The initial conditions required more effort to produce than the boundary conditions. Again, this code solved isentropic shock relations to simulate flow over a wedge as flow over a flat plate. Therefore one could start every simulation at the leading edge and assume the $(m-1,n)$ values are simply the freestream parameters, but it was found that doing so introduces a sharp numerical spike in the results as the code rapidly attempted to correct for the presence of a boundary layer. This was most apparent in v, which instantly went from being identically zero to being non-zero, causing a ripple effect through the rest of the variables that took $\mathscr{O}(10)$ steps to damp out. Furthermore, being forced to start at the leading edge could be a waste of numerical effort if one was only interested in the boundary layer far downstream. A better method was to solve the boundary layer equations at a given streamwise coordinate, then use this value as an input to the finite difference scheme. Because the code only considered laminar, 2D planar flows over flat plates as inputs, self-similar techniques were applicable; note that this was the technique used by van Driest [283] to generate exact compressible boundary layer solutions.

A self-similar solution typically uses a coordinate transformation to reduce the number of independent variables; in boundary layers, the characteristic length scale is removed such that the solutions at one point on a plate are "similar" to the solution everywhere, effectively allowing for rapid scaling to the desired location [293]. Central to the self-similar solution of the boundary layer equations is the transformation used; the one used here was adopted from Illingworth [121].

$$Let \quad \xi = \int_0^x \rho_e(x) U_e(x) \mu_e(x) dx \tag{5.27}$$

$$\eta = \frac{U_e}{\sqrt{2\xi}} \int_0^y \rho dy \tag{5.28}$$

In the present application, the freestream conditions were constant, so $\xi = \rho_e U_e \mu_e x$. Palmer [211] defined two further variables, a nondimensional stream function $f = \frac{\Psi}{\sqrt{2\xi}}$ and the enthalpy ratio $g = \frac{h}{h_e}$. By definition, $u = \frac{\partial \Psi}{\partial y}$ and $v = -\frac{\partial \Psi}{\partial x}$; substituting in Ψ and η yields $u(\eta) = u_e f'$ and

$v(\eta) = \sqrt{\frac{\rho_e u_e \mu_e}{2x}}(f'\eta - f)$. Furthermore, for perfect gases g can be written solely in terms of temperature as $T(\eta) = T_e * g$.

Using these parameters the boundary layer equations for a flat plate were reduced from three equations to two (excluding y-momentum conservation, Equation 5.3)

$$\textit{Self-Similar Cons. of X-Momentum} \quad (Cf'')' + ff'' = 0 \tag{5.29}$$

$$\textit{Self-Similar Cons. of Energy}: \quad \left(\frac{C}{Pr}g'\right)' + fg' + C\frac{U_e^2}{h_e}(f'')^2 \tag{5.30}$$

where $C = \frac{\rho\mu}{\rho_e\mu_e}$. Solving these equations for f and g provided both components of the flow velocity as well as the temperature. To solve the system using a Runge-Kutta ordinary differential equation (ODE) solver, the two equations needed be split into first-order ODEs, so one ended up with five equations to be integrated

$$(Cf'')' = -ff'' \tag{5.31}$$

$$(f')' = f'' \tag{5.32}$$

$$(f)' = f' \tag{5.33}$$

$$\left(\tfrac{C}{Pr}g'\right)' = -fg' - C\frac{U_e^2}{h_e}f''^2 \tag{5.34}$$

$$(g)' = g' \tag{5.35}$$

The boundary conditions for these equations are provided in Table 5.1

Variable	$\eta = 0$		$\eta = \eta_e$	
	Value	Interpretation	Value	Interpretation
f	0	$v = 0$	N/A	N/A
f'	0	$u = 0$	1	$u = U_e$
f''	N/A	N/A	0	$\frac{du}{dy} = 0$
g	(N/A, $\frac{h_w}{h_e}$)	(Adiabatic, Isothermal)	N/A	N/A
g'	(0, N/A)	(Adiabatic, Isothermal)	0	$\frac{dh}{dy} = 0$

Table 5.1: Boundary conditions for the self-similar solution

For both the adiabatic and isothermal cases there were five ODEs to be solved, but only three boundary conditions; put another way, this was a two-point boundary problem with two free variables [211]. The technique used to solve this system is called the Shooting Method and was described by Palmer [211], who solved the compressible boundary layer problem as an example. The philosophy of the shooting method is to guess values for the missing initial conditions, solve the system, and then compare the results at the farfield boundary to the known values. If the results match to within some tolerance, then the proper solution has been found, but if they do not new guesses are made and the process repeats. The challenge is therefore to find an efficient way to generate new guesses; following Palmer [211], the multi-dimensional, globally convergent Newton-Raphson technique was used.

Let $[V]$ be an array of the guesses, and $[E]$ be the array of the corresponding errors; for the current application, both were two-by-two arrays as there were two free variables. The problem is to find some perturbation $[\delta V]$ that will drive $[E]$ to zero. This can be done by solving the following expression, written in the classic $Ax = B$ form,

$$\frac{dE}{dV}\delta V = -E \tag{5.36}$$

Once $[V]$ has been calculated, the new values for each free variable can be found from,

$$V^{n+1} = V^n + \delta V \tag{5.37}$$

Palmer [211] suggested a finite difference approach to the calculation of $\frac{dE}{dV}$, namely $\frac{\Delta E}{\Delta V}$, admitting that it was not straightforward. Note that $\frac{\Delta E}{\Delta V}$ was a two-by-two array because, again, this is a multidimensional problem: there were two free variables to optimize at once, and changing one will affect the error of both. Therefore the code needed to study the effect of perturbing each free variables separately. The code was run with an initial guess for $[V]$, the system of ODEs was solved, and the errors were calculated. Next, one of the free variables was incremented by a small amount, say 1×10^{-4}, the system of ODEs was re-solved, and the errors were re-calculated.

The first column of $\frac{\Delta E}{\Delta V}$ was the latest error array divided by the perturbation on the free variable (1×10^{-4}); in this way the effect of perturbing one variable on both errors was stored. This process was repeated once more by perturbing the second free variable, and the $\frac{\Delta E}{\Delta V}$ matrix was complete. With this done, Equation 5.36 could be solved and the $[V]$ array updated. Note that it is recommended to under relax the solution by multiplying δV by a value ω between 0 and 1 before adding it to $[V]$. A formal review of so-called relaxation schemes was provided by Tannehill et al. [275], but here Palmer [211] used $\omega = 0.5$, which drove the error in both free variables below 1×10^{-6} in $\mathscr{O}(10)$ iterations. This process will be reviewed sequentially in the pseudocode.

Once the program converged, its results needed to be converted to physical coordinates and scaled before they could be used to set the initial and boundary conditions for the entire domain. The conversion between f and g and the physical variables was covered above. The edge conditions were provided by isentropic flow relations [293]. From these, the following critical variables could be calculated:

- Viscosity blended between Keyes' (air) and Sutherland's [274] Laws, as reported in [231]
  - Keyes: $\mu_K = 1.488 \times 10^{-6} \left(\frac{T^{1/2}}{1+122.1T_1/T} \right)$ where $T_1 = 10^{-5.0/T}$
  - Sutherland: $\mu_S = 1.458 \times 10^{-6} \left(\frac{T^{3/2}}{T+110.4} \right)$
  - Blending at $T_{switch} = 200\text{K}$: $\mu = f_{switch}\mu_K + (1 - f_{switch})\mu_S$ where $f_{switch} = \frac{1}{1+(T/T_{switch})^3}$
- Mach number by definition $M(\eta) = \frac{\sqrt{\gamma R_{specific} T(\eta)}}{u(\eta)}$, where for air $\gamma = 1.4$ and $R_{specific} = 287.058 \frac{J}{kg*K}$ [128]
- Density from the Ideal Gas Law $\rho(\eta) = \frac{P_e}{R_{specific} T(\eta)}$
- Thermal conductivity from the Prandtl number $k(\eta) = \frac{\mu(\eta) C_p}{Pr}$, where $C_p = 1004.5 \frac{J}{kg*K}$ and $Pr = 0.71$ [293]

Note the use of the boundary layer approximation $P(y) = P_e$ from $\frac{\partial P}{\partial y} = 0$.

Now there was the matter of scaling the wall-normal coordinate. The self-similar solution used an arbitrary equally-spaced grid $\eta = [0, 10]$, where the upper value was deemed large enough

to simulate infinity. This parameter needed to be converted back into dimensional "$y_{similarity}$"-coordinates. This required numerical integration of Equation 5.28; the Trapezoid Rule approximation is shown below, where $y_{j=0} = 0$:

$$y_j = (\eta_j - \eta_{j-1})\sqrt{\frac{2x\mu_e}{U_e\rho_e}}\left(\frac{2\rho_e}{\rho_j + \rho_{j-1}}\right) + y_{j-1} \tag{5.38}$$

Just as with the Malik mapping, because this was a $1:1$ mapping any variable X could be called either with respect to η or $y_{similarity}$ provided the index of the wall-normal coordinate stayed the same; for example, if the code called $X(10)$, it did not matter what $\eta(10)$ or $y_{similarity}(10)$ are. This meant that once $y_{similarity}$ was known, linear interpolation could be used to map nearly all of the flow parameters onto the user-defined grid. The values of all parameters at locations above $y_{similarity,max}$ were simply set to the freestream value. With this, the initial condition was solved and the boundary conditions could be addressed.

Before concluding, it is worth repeating that for laminar boundary layers the self-similar approach could be applied at all streamwise locations, completely ignoring the finite difference solution. Indeed, van Driest [283] used such an "exact" (without the inaccuracies of finite differencing) approach to great success. If information is only required at a few streamwise locations, this may be advisable. However, the iterative technique outlined here typically required $\mathcal{O}(10)$ iterations for each solution while the implicit finite difference scheme only required $\mathcal{O}(1)$. Thus for well-refined grids, the former was more efficient.

5.4.2 Boundary Conditions

As was previously mentioned, the freestream conditions were solved from isentropic flow conditions through the bow shock. Note again that this allowed the approximation of the thin wedge flows as flat plate flows. The oblique shock relations were provided in [128]:

- Assume γ, M_1, P_{o1}, T_{o1}, and δ (wedge half-angle) were provided by the user
- $P_1 = \frac{P_{o1}}{(1+\frac{\gamma-1}{2}*M_1^2)^{\frac{\gamma}{\gamma-1}}}$

- $T_1 = \frac{T_{o1}}{(1+\frac{\gamma-1}{2}*M_1^2)}$
- θ was found approximately to within 1×10^{-6} using a brute force search between $\theta = \left[\sin^{-1}\frac{1}{M_1}, 30^\circ\right]$. When $\left[\cot\theta\left(\frac{M_1^2\sin^2\theta-1}{\frac{\gamma+1}{2}M_1^2-(M_1^2\sin^2\theta-1)}\right)\right]$ was within 1×10^{-7} of $\tan\delta$ than θ had been found.
- $M_2 = \sqrt{\frac{1+\frac{1}{2}(\gamma-1)M_1^2}{\gamma M_1^2\sin^2\theta-\frac{1}{2}(\gamma-1)} + \frac{M_1^2\cos^2(\theta)}{1+\frac{1}{2}(\gamma-1)M_1^2\sin^2\theta}}$
- $T_2 = T_1\left(\frac{\left(1+\frac{\gamma-1}{2}M_1^2\sin^2\theta\right)\left(\frac{2\gamma}{\gamma-1}M_1^2\sin^2\theta-1\right)}{\left(\frac{(\gamma+1)^2}{2(\gamma-1)}\right)M_1^2\sin^2\theta}\right)$
- $P_2 = P_1\left(\frac{2\gamma M_1^2\sin^2\theta}{\gamma+1} - \frac{\gamma-1}{\gamma+1}\right)$
- $u_2 = M_2\sqrt{\gamma R T_2}$
- $P_{o2} = P_{o1}\left(\left(\frac{P_2}{P_1}\right)\left(\frac{T_2}{T_1}\right)^{\frac{\gamma}{1-\gamma}}\right)$

The freestream conditions along the entire domain could now be taken from the results after the shock because $\frac{\partial P}{\partial x} = 0$. This also meant that the pressure was known at all points as $\frac{\partial P}{\partial x} \approx 0$.

Meanwhile, at the wall, both components of the velocity were zero along the entire domain, in accordance with the no-slip condition. If the wall was isothermal, then the user could input the known wall temperature to be applied along the entire wall. For adiabatic flows the wall temperature was set to the adiabatic wall temperature T_{aw}. For laminar flows T_{aw} was calculated by the self-similar solver, and for the turbulent portion of adiabatic-wall flows it was calculated from Equation 2.23 using $r = Pr^{\frac{1}{3}}$ [82]. It was found in testing that for laminar flows using the self-similar solver's result outperformed Equation 2.23 with $r = Pr^{\frac{1}{2}}$, yielding q_w closer to zero. For this reason the self-similar solver's results were used for T_{aw}, though Equation 2.23's prediction was output for consistency when comparing with other diagnostics. Similarly, even for laminar flows the turbulent adiabatic wall temperature was output for reference.

5.4.3 Convergence

When solving the finite difference equations at $m+1$ with lagged coefficients, the viscosity was taken at m. With viscosity known, one could calculate the thermal conductivity, solve the

conservation equations, calculate density from the Ideal Gas Law, and so on. It was already stated that although lagging the coefficients is theoretically simple, it clearly introduces error throughout the entire code. However, if one could recalculate the coefficients once u_{m+1} and T_{m+1} were known, a more accurate result could be produced. The effect was exacerbated when implementing a RANS turbulence model, as even more coupled variables like δ_k^* were introduced.

The solution taken here was a Predictor-Corrector-like iterative process (see [97]) and was applied in both laminar and turbulent cases. For the first iteration at a $m+1$ step, the previous μ_m value was used to solve for the thermal conductivity, eddy viscosity, conservation variables, *etc.* and values for u_{prev}, T_{prev}, and v_{prev} were taken from the results from the previous spatial step m. For all subsequent iterations, X_{prev} was the result from the previous iteration and μ was calculated from T_{prev}. The error for the three conservation equations was calculated from

$$X_{Error} = \frac{1}{n_{pts}} \sum_{n=1}^{n_{pts}} \left(X_{m+1,n} - X_{prev,n}\right)^2 \tag{5.39}$$

The three errors were then combined via a Euclidean norm

$$Error = \sqrt{\left(\frac{u_{error}}{u_e}\right)^2 + \left(\frac{T_{error}}{T_e}\right)^2 + \left(\frac{v_{error}}{u_e}\right)^2} \tag{5.40}$$

Note that v was normalized with u_e because theoretically $v_e = 0$.

This process was repeated until a convergence tolerance was met. For $Tolerance = 1 \times 10^{-6}$ nominally < 5 and < 10 iterations were needed for laminar and turbulent cases respectively, though more iterations were typically needed exactly at the tripping point due to the sudden changes there.

5.4.4 Secondary Variables & Post Processing

The code produced a number of secondary results that, while not necessary to the solution of the conservation equations, provided useful data throughout the entire domain. These included:

- Mach number (neglect v): $M = \sqrt{\gamma R_{air} T}$
- Specific enthalpy (perfect gas): $h = C_p T$

- Total enthalpy (perfect gas): $H_o = h + \frac{1}{2}u^2$
- Number density: $n = \frac{P}{k_B T}$

The velocities, temperature, density, viscosity, and thermal conductivity were also returned throughout the entire domain. In the streamwise direction, the code calculated the wall shear stress and heat flux with a $\mathcal{O}(\Delta y)$ and $\mathcal{O}(\Delta y^2)$ forward difference scheme respectively

$$\tau_w = \mu_{n=wall} \frac{u_{(n=2)} - u_{(n=wall)}}{\Delta\eta} \left(\frac{ab}{(a+y)^2} \right) \tag{5.41}$$

$$q_{y(w)} = k \frac{-T_{(n=3)}/2 + 2T_{(n=2)} - 3T_{(n=wall)}/2}{\Delta\eta} \left(\frac{ab}{(a+y)^2} \right) \tag{5.42}$$

as well as the 99.5% boundary layer thickness by linearly interpolating the u, T, and H_o data; note that in the case temperature and/or total enthalpy fall through the boundary layer ($X_w > X_e$), δ was taken at 1.005% the freestream value. The lower order scheme was used for τ_w for simplicity, though in the future a higher order scheme could be used.

2D plots were made of the velocities, temperature, and Mach number, and the wall shear stress, wall heat flux, and boundary layer thicknesses were plotted along the streamwise coordinate as well. A ".csv" file was generated containing the run inputs, for repeatability, as well as the values of the primary and secondary variables at the final streamwise location. If the flow was turbulent at this last position, then the velocity and temperature were reported in inner law coordinates and u^+_{eq} was plotted against y^+: $y^+ = \frac{y v^*}{\nu_w}$ (with $v^* = \sqrt{\frac{\tau_w}{\rho_w}}$); $u^+ = \frac{u_{eq}}{v^*}$; u^+_{eq} (Equation 2.36); and $T^+ = \frac{T_w - \overline{T}}{T^*}$ (with $T^* = \frac{q_w}{\rho C_p v^*}$ for heat transfer case, $T^* = (v^*)^2$ for adiabatic case to avoid division by zero).

5.5 Summary of Workflow: Pseudocode

It would be cumbersome to include the entire boundary layer solver code in this report, even as an appendix. Furthermore, readers unfamiliar with the chosen programming language, Matlab, may find such a section unnecessarily restrictive. Instead, the steps necessary to understand how the finite difference solver are written below, the goal being to include enough detail for a faithful reproduction of the original code. Some recommendations and comments are included here:

- It is critical to be clear with the units used throughout the program. It is recommended to used dimensional, SI units wherever possible.
- Writing individual functions (Matlab) wherever possible helps keep the main program sequential and organized.
- The code produced allowed the user to solve on either an equally-spaced or Malik-clustered grid by setting a binary flag in the input section. When necessary, this flag caused the code to solve either the "clustered" or "standard" form of an equation.
- It will become clear that the actual solution of the boundary layer was a relatively small, straightforward portion of the code. Converting the user's inputs into the format necessary for the scheme "under the hood" was by far the bulk of the code. This is typical for finite difference schemes in general as they tend to be relatively simple, which is a large part of their appeal [275].

5.5.1 User Inputs

This is the only place for user inputs in the code.

1. Define the scheme
    - State whether to use "Implicit" or "Explicit" finite difference scheme
2. Define the grid
    - X grid: Define where to begin the simulation with the self-similar solution, where to end the simulation, and the step size
    - Y grid: State the number of points to use, the upper limit of the simulation, whether or not to use Malik clustering, and if so where the critical Malik point lies.
3. Define the gas
    - Input γ, Pr, C_p, and $R_{specific}$

4. Define the system

    - State wall condition (isothermal or adiabatic) as well as wall temperature (only used for isothermal simulations)
    - Input pre-shock flow conditions (P_o, T_o, and M)
    - State the wedge half-angle

5. Define the turbulence parameters

    - State the turbulence model to use. For eddy viscosity, the "Prandtl" or "Cebeci-Smith" models are included. For turbulent heat flux, the "Gradient Diffusion" or "AEF" models are included.
        - Ensure the AEF model is not used with the implicit scheme with a conditional "Error" return
    - Set the flow transition point; if no turbulence is desired, the transition point should be beyond the x domain.
    - Define the maximum number of corrector steps to use in the Predictor-Corrector method, as well as the convergence tolerance

5.5.2 Calculate Grid

- Define the nondimensional Malik wall-normal coordinate η and ancillary parameters (number of points, spacing, *etc.*)
- Calculate the Malik parameters a and b, then use them to generate the clustered dimensional grid from Equation 5.5
- Generate a dimensional grid from the results and the user's streamwise spacing

5.5.3 Calculate the Pre-and Post-Shock Flow Conditions (Boundary Conditions)

- Use the user's stagnation conditions, Mach number, and wedge half-angle in the isentropic flow relations to calculate P_1, T_1, and θ. Use Keyes' and Sutherland's Laws and the Ideal Gas Law to calculate μ_1 and ρ_1 respectively, and with them find the unit Reynolds number
- Analogously, use the same technique to find the u_2, T_2, μ_2, M_2, P_2, ρ_2, and Re_2.
- Use the Prandtl number, Ideal Gas Law, and caloric equation of state to find k_2, n_2, and h_2 respectively. Calculate H_o from u_2 and h_2.
  - Because this is a ZPG flow, these values are constant in the freestream and thus form the edge condition. Note that v does not have an edge condition.

5.5.4 Generate the Initial Conditions

This entails solving the self-similar boundary layer equations via the shooting method, scaling the results onto a dimensional grid, then interpolating those points back onto the user's grid.

1. Initialize the problem
   - Take u_e, T_e, P_e, μ_e from the post-shock conditions. The wall temperature is either input (isothermal) or calculated (adiabatic)
   - Define uniform the nondimensional grid; be sure it is sufficiently large and refined to capture all the the relevant physics (here $\eta = [0, 10]$ and $\Delta\eta = 0.01$).
   - Set Runge-Kutta tolerances (Matlab)
   - Set guess step size ΔV and under-relaxation parameter ω. Here 1×10^{-4} and 0.5 were used respectively.
   - Set the initial conditions for the $[(Cf'')', (f')', (f)', (Cg')', (g)']$ equations. The initial guesses listed here worked well over a range of flow and wall conditions.
     - Adiabatic case: $[V_1, 0, 0, 0, V_2]$ where $V = [0.33, 25]$

- Isothermal case: $[V_1, 0, 0, V_2, T_w/T_w]$ where $V = [0.25, 5]$

- Solve the system once to initialize the error matrix $E = [f'_e - 1, g_e - 1]$

2. Use multi-dimensional, globally convergent Newton-Raphson technique

   - Enter a "while" loop (Matlab) until the solution converges. Here both errors must be below 1×10^{-6}

   - Fill in the δV array. Perturb each guess by ΔV separately, which is necessary for multi-dimensional problems. This is shown below, where each column represents a case:

$$V = \begin{bmatrix} V_1 + \Delta V & V_1 \\ \underbrace{V_2}_{Case\,A} & \underbrace{V_2 + \Delta V}_{Case\,B} \end{bmatrix}$$

   - Calculate the error array. For both sets of V, solve the system of ODEs and determine how the each individual error changes as the guess is perturbed.

$$E = \begin{bmatrix} f'_e - 1 & f'_e - 1 \\ \underbrace{g_e - 1}_{Case\,A} & \underbrace{g_e - 1}_{Case\,B} \end{bmatrix}$$

   - Calculate $\frac{dE}{dV} = \frac{([E] - [E]_{prev})}{\Delta V}$

   - Solve Equations 5.36 for δV

   - Update guesses using 5.37. Remember to under-relax δV with ω to aid convergence

   - Use the new guesses to solve the system again and calculate the errors. Check convergence; if converged, output $[(Cf''), (f'), (f), (Cg'), (g)]$, otherwise store V and E and iterate

3. Apply the results

   - By definition, $u(\eta) = u(y_{similar}) = f' * u_e$, $v(\eta) = v(y_{similar}) = \sqrt{\frac{\rho_e u_e \mu_e}{2x}}(f'\eta - f)$ and

(for perfect gases) $T(\eta) = T(y_{similar}) = g * T_e$. With this information, $\mu(y_{similar})$, $M(y_{similar})$, $\rho(y_{similar})$, and $k(y_{similar})$ are calculable, though $\mu(y_{similar})$ and $k(y_{similar})$ do not need to be calculated because they are solved within the finite difference loop. Note that due to the boundary layer assumptions, at all points in the domain $P(y_{similar}) = P_e = Constant$

- Store the wall conditions for $u_w(=0)$, T_w, and $v_w(=0)$. Because this is a flat plate (ZPG), the wall conditions do not change and can now be set along the entire domain. Note that for the adiabatic case, $T_w = T_{aw}$, calculated either from the self-similar (where laminar) or recovery temperature (where turbulent) methods.
- Map the nondimensional self-similar grid onto a dimensional grid using Equation 5.38. Now that the physical coordinates of the self-similar results are known, use linear interpolation to map the results for u, v, T, P, ρ, and M from the self-similar grid onto the user's grid. Should the user's grid exceed the self-similar grid's upper limit, set any higher nodes to the edge condition.
- Initialize the output matrices for α, β, ζ, u, T, P, ρ, v, μ, μ_t, k, k_t, M, h, H_o, q_y^T, q_w, and τ_w for speed. For the present code, the arrays are organized as

$$\begin{bmatrix} (m_{start}, n_w) & \rightarrow & (m_{end}, n_w) \\ \downarrow & \searrow & \downarrow \\ (m_{start}, n_e) & \rightarrow & (m_{end}, n_e) \end{bmatrix}$$

5.5.5 Prepare Arrays

Initialize arrays for α, β, ζ, u, T, P, ρ, v, μ, μ_t, k, k_t, M, h, H_o, q_y^T, q_w, and τ_w and apply initial and boundary conditions.

- The entire first row is set to the wall condition, the entire last row is set to the edge condition (except v, which has no edge condition), and the entire first column is set to the initial condition interpolated from the self-similar solution or is calculated from these "primary"

variables (ex.- M from T).

- Save the calculation of the initial condition for α, β, ζ, μ, μ_t, k, and k_t until inside the finite difference structure because these parameters will be solved as the first part of every finite difference calculation at every streamwise location in the domain.

5.5.6 Solve the Finite Difference Equations

The case considered here will be turbulent to illustrate the full functionality of the code. Laminar solutions will simply skip over the turbulent steps.

1. Enter a "for" loop (Matlab) from the first to the final streamwise locations

2. Calculate the fluid properties through the boundary layer. For μ use Keyes' and Sutherland's Laws, and use this result to calculate k using the definition of the Prandtl number

3. Begin the Predictor-Corrector iteration

   - Initialize by setting the "Count" to zero and the "Error" to infinity
   - Enter a "while" loop (Matlab) for be completed while $Error > Tolerance$ and $Count \leq 1 + n_{Corrector\,steps}$
   - Increment the count
   - Calculate the fluid properties μ and k using Keyes' and Sutherland's Laws and the Prandtl number. If this is the first iteration ($Count = 1$), then use the temperature from the previous streamwise step; otherwise, use T_{m+1}.
     - This means that during "corrector" iterations technically μ and k are no longer lagged coefficients. However, updating the fluid properties in step with the fundamental variables is necessary to drive convergence. In fact, in the laminar case using $T_{m+1(prev)}$ to update μ is the only way to implement the previous iteration as a guess; if μ does not update, nothing else can because μ is used in all subsequent calculations. Thus it is necessary to assume the temperature does not change

enough between each streamwise step to cause appreciable nonlinearity with the μ_{m+1} and k_{m+1} terms, or mismatch with any other properties which use these terms at the m location. With a small enough step, this is a reasonable assumption.

  - In implementation, even though T_{m+1} is being used in Keyes' and Sutherland's Laws, continue to store the results in the μ_m location in order to keep the indexing straight.

- Store the results for the previous iteration of u, T, v, μ, and ρ as guesses for the basic state values, and to be used for error calculation. If this is the first iteration ($Count = 1$), then use the results from the previous streamwise step as the initial guess.
- If the streamwise coordinate exceeds the user-defined transition location, enter the turbulence function (Matlab)
  - Use linear interpolation to determine $\delta_{99.5\%}$
  - Set the coefficients/constants for the turbulence model specified by the user
  - Calculate the kinematic displacement thickness using Equation 5.6
  - Set the wall conditions for μ_t, τ_w (use Chain Rule), and v^*
  - Calculate y_{switch} according to the model used
  - For the internal points (not the wall or the edge) use the desired turbulence model (Equation 2.41 or 2.46) to calculate μ_t. Again, the reason to only do this for the internal nodes only is the central differencing scheme used to calculate $\left|\frac{\partial u}{\partial y}\right|$ requires one "buffer" point on either side of the current node.
  - Set $\mu_{t(edge)}$ to the lower node's value. This is acceptable provided the domain is sufficiently large
  - Calculate k_t using the turbulent Prandtl number for the gradient diffusion model (set $q_y^T = 0$) or q_y^T for the AEF model (set $k_t = 0$).
- Add the flow properties (μ_t and k_t) to their respective fluid properties and proceed

- Because $k_t = 0$ when q_y^T is being used, and *vice versa*, both can be used in the same equation at the same time. This simplifies the code.

4. Calculate α, β, and ζ from Equations 5.7, 5.8, and 5.9

5. Solve the conservation of X-momentum equation for u_{m+1}

   - Implicit:
     - Initialize the LHS and RHS and proceed to fill them in a "for" loop (Matlab)
     - If at the wall, set the diagonal element of the LHS to one and the RHS to u_w
     - If at an internal node, set the LHS and RHS according to Equation 5.12
     - If at the edge, set the diagonal element of the LHS to one and the RHS to u_e
     - Solve the system with the preferred tridiagonal matrix algorithm
   - Explicit
     - Begin a "for" loop (Matlab) for all wall-normal nodes
     - If at the wall, set $u(m+1)$ to the known boundary value
     - If at an internal node, solve for u_{m+1} according to Equation 5.15
     - It at the edge, set $u(m+1)$ to the known edge value

6. Set all values of the pressure to the edge condition in accordance with the boundary layer assumptions

7. Solve the conservation of energy equation for T_{m+1}. Follow the same procedure as for the Conservation of X-Momentum equation, except use Equation 5.18 or 5.21

8. Use the Ideal Gas Law to solve for ρ through the boundary layer

9. Solve the continuity equation for v_{m+1}

   - Begin a for loop (Matlab) for all wall-normal nodes
   - If at the wall, set v_{m+1} to the known boundary value

- If not at the wall, solve for v_{m+1} according to 5.26

10. If the streamwise coordinate exceeds the user-defined transition location, check for convergence

    - For u, T, and v, calculate the magnitude of the difference for all nodes in the boundary layer between the previous iteration and current iteration. Find the mean of the results, normalize by the freestream value (again, for v use U_e), and calculate the Euclidean norm. Use this as the error for the convergence check.
    - If the solution has not converged and has not expended all "corrector" loops, return to the start of the "while" loop and iterate

11. Once converged, calculate the secondary variables M, h, H_o, n, τ_w, and q_w

5.5.7 Post-process results

- Plot the wall shear stress τ_w against the streamwise location
- Plot the wall heat flux q_w against the streamwise location
- Calculate $\delta_{99.5\%}$ using linear interpolation of the u, T, and H_o data at each streamwise location. Plot the results
  - Should T_o or H_o fall through the boundary layer ($X_w > X_e$) use $\delta_{1.005\%}$
- Generate 2D plots of u, v, T, and M
- Save all plots
- If the simulation ends in the turbulence regime, calculate
  - Velocity in wall coordinates (y^+ and u^+_{eq} with v^*) using the compressible modification, the effective velocity u_{eq} from Equation 2.36
  - Temperature in wall coordinates (T^+ with T^*)
- Write out the inputs (for repeatability) and outputs to a spreadsheet

6. EXPERIMENTAL METHODS

The theory and practice behind each of the techniques employed by the current work are covered herein. Each experiment was justified by the data it could yield and the questions it could answer. An effort was made to provide enough detail for the results to be independently replicated.

6.1 Surface Profilometry

Past work on similar geometries [160] has shown the susceptibility of wedge models to deformation during manufacturing. This is especially important at the leading edge, where the flow is the most sensitive. In order to verify there were no machining errors, measurements were made of the leading edge using a surface profilometer.

This work was conducted using a Keyence LK-H022 contactless laser distance sensor mounted to a custom traverse and resting on a vibration damping table. The system was described in [69], but the critical parameters are listed here. It offered an interrogation volume of $x \times y \times z = 950\text{mm} \times 75\text{mm} \times 6\text{mm}$ with a maximum resolution of $\Delta x = 2\mu\text{m}$, $\Delta z = 0.02\mu\text{m}$, and a user-defined Δy, here $250\mu\text{m}$. The on-target laser spot size was $25\mu\text{m}$ and data was recorded at 10kHz.

It was advantageous to keep the laser in center of the z range in order keep the laser spot size small and maximize its sensitivity. This posed a problem for the test article which had a half-angle of 2.75°, so when rested on a flat surface it had a slope of $\tan(5.5°) = 0.096\frac{\text{mm}}{\text{mm}}$. Therefore a custom aluminum block was made with a 5.5° cutout which would allow the wedge to lie flat. Screws and washers along the ends of the block ensured the test article was square with the block, and similarly screws in the breadboard tabletop ensured the block was square with the profilometer. The height of the profilometer could then be adjusted such that all measurements were $|z| < 1\text{mm}$.

The profilometer supports were leveled by resting against two Stanridge Granite Corp. certified flat calibration blocks (Grade B, maximum deviation of $\pm 5\mu\text{m}$) and were squared by being screwed into the table's breadboard working surface. Even with these precautions, it was still necessary to zero the instrument relative to the test article. This was accomplished by fine-tuning the

supports until the readings at four corners of a flat region $200 \times 20\text{mm}^2$ (starting 23mm from the leading edge, downstream of the polynomial profile) were all within 25μm of one another. The experimental setup is shown in Figure 6.1.

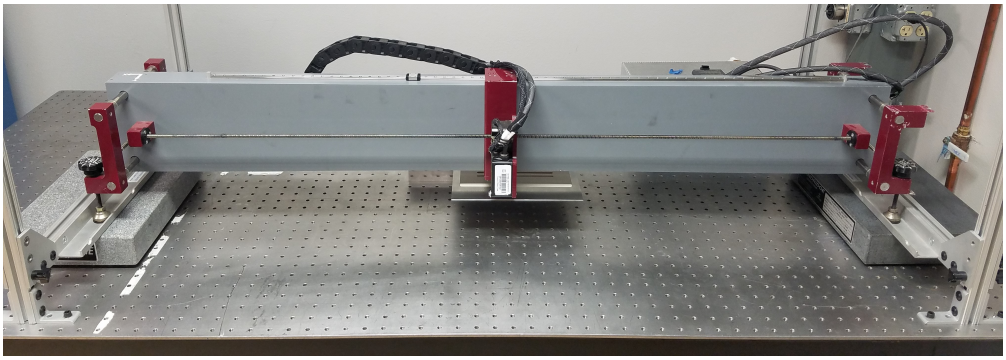

Figure 6.1: The laser profilometer during testing.

Once level, measurements were taken across the entire span of the test article over a total streamwise distance of $0-43$mm from the leading edge, which was just upstream of the pocket for the PEEK insert; again, the spanwise scans were conducted at $\Delta y = 0.25$mm, which gave 172 lines of data per scan. The process was conducted three times for repeatability.

Processing the profilometery data was a multi-step process conducted in a custom Matlab script which followed Leidy [160] and Neel [194]. Upon first visualizing the profilometer's ASCII data, it was observed that the results for the two opposite directions of laser travel were $\mathcal{O}(50\mu\text{m})$ apart. This was a relatively small misalignment most likely due to a loose bearing or gear, but the results in a given direction remained valid. Thus the data were split into "even" and "odd" data sets each with $\Delta y = 0.5$mm; again no detail was lost during this process as the roughness parameters from each set should be identical and any deformations were still captured. Continuing with the data reduction, the results were median filtered to account for the width of the laser spot size. Erroneous data was smoothed out by linearly interpolating the results from the adjacent streamwise coordinates.

Now each spanwise scan could be treated as its own independent signal. A second-order polynomial was fit to the data and then subtracted in order to remove any bulk trends and leave only the model's waviness. In order to separate the roughness from the wavy profile, the result was fit by a Zero-Order Gaussian Regression Filter provided in [191]; the filter was applied in sections of $\lambda_c = 0.3$mm, which was sufficiently small to separate the roughness from the broader waviness. Once the filtered noise was subtracted, all that remained from the wavy profile was the true roughness. This process was depicted graphically in Figure 6.2.

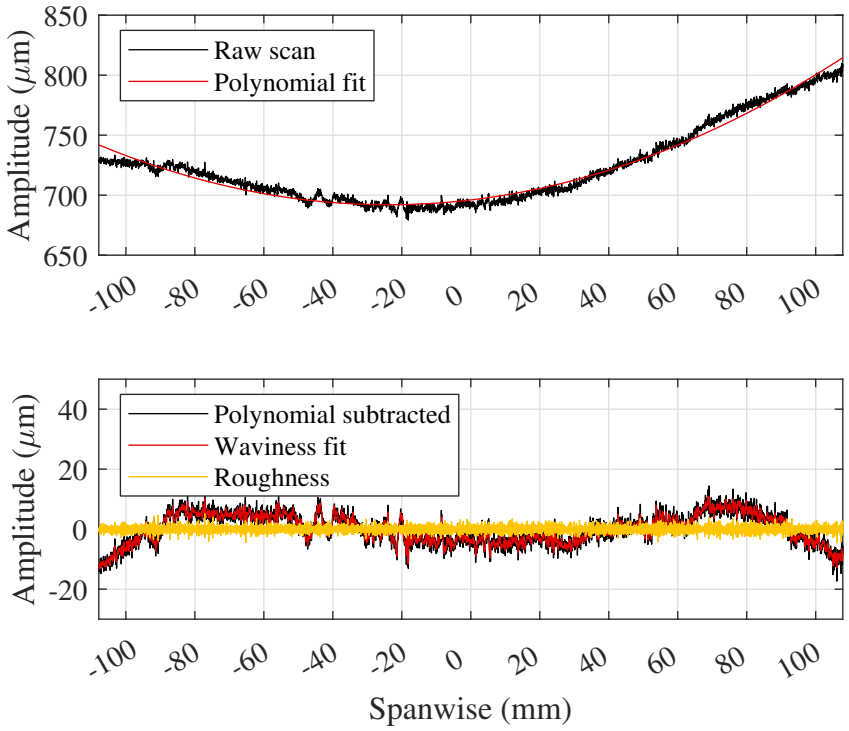

Figure 6.2: Reduction of the roughness data.

There are multiple ways to define roughness [191], and here the center-line average R_{avg}, root-mean square R_{RMS}, and peak-to-peak R_{ptp} values were calculated. R_{avg} is the average of the absolute value of the difference between the data and the mean value for that scan. R_{ptp} is the maximum difference between the roughness values in a λ_c window; the average value was then taken as the

average for all the windows in the scan. R_{RMS} is the root-mean square value for the scan. Roughness was measured in the flat region $23-43$mm from the leading edge across the entire span of the test article except for 1mm on either side to remove erroneous edge data. This meant that at the current resolution, there were 80 quasi-independent scans for each test, so for all three tests there were 240 scans. Each of the three roughness parameters was calculated for each of the 240 scans. For each set of 40 "even" or "odd" scans the 3σ outliers were removed; there were only a few outliers for a given scan. The results from all 240 scans were combined to provide a single value for each of the three parameters.

6.2 Oil Flow Visualization

Oil flow visualization is a simple technique which communicates even weak pressure gradients on test articles. It was used to ensure there were no unforseen pressure gradients on the test surface like those seen in [160], and to study the behavior of the trips; for example, would their wakes persist after the flow became turbulent? Here a UV-phosphorescent pigment, Day-Glo Color Corporation "Blaze Orange" was used to provide enhanced contrast on the model. A mix of 1.5g of pigment in 100mL of Esco E200 Silicone Fluid (100CS) provided good results. Increasing the viscosity of the oil reduces its sensitivity, but can help prevent excessive motion and a loss of signal as oil blows off the model.

A foam brush was used to apply the oil across the model's PEEK insert after preheat. For laminar runs, the oil was applied in a thick strip just upstream of the camera's field of view so individual beads would roll across the test area, while for turbulent runs it was applied in an even coat over the entire PEEK insert and show the trips' structures. For safety, the plasma was never turned on during the oil flow tests, and the electrodes were completely removed from the PEEK and cleaned upon completion of the campaign as Leidy [160] found oil seeped into seams in the model during testing; this was another reason a single, seamless PEEK insert was designed for the present study.

Once the model was preheated and coated with oil, data was recorded with a Nikon D5000 camera above the test section at 30fps with a manually adjusted, near-focus Nikkon Micro Nikkor

(60mm, $f/2.8D$) lens which afforded 1280×720 pixels at a spatial resolution of $\sim 200 \frac{\mu\text{m}}{\text{pixel}}$. The camera angle was adjusted to the wedge's 2.75° to help keep the image focused and uniformly scaled across the entire test area. The camera's controls were tuned to maximize the contrast of the orange pigment; the shutter speed was $1/30$s, the f-number was 3.2, the ISO was 1000, and a fluorescent (high temperature mercury vapor) white balance further tuned to maximize the blue color ($A6$) were used. The lens' barrel distortion was removed using the same procedure to be described in Section 6.4.

Two Feit Electric 13W BPESL15T/BLB UV lights were directed onto the surface of the model from the sides of the test section to cause the oil to phosphoresce. UV-transmissible fused silica windows were used to pass the light into the tunnel, and to observe the phosphorescence as well. To maximize contrast, the lamps used nearly covered the entire window port and all other room lighting was switched off; it was found that despite manually specifying the camera's settings, for some as of yet unknown reason starting the recording before shutting off all the lights provided the best results. All windows on the test section not involved in data collection were replaced with blank plugs to prevent excess light from causing uneven illumination. The tunnel was typically only run for $10-15$s as this was sufficient to allow any structures to develop and after this time most of the oil had blown off the test article.

All data was processed in a custom Matlab script. The data was imported, de-warped (discussed in Section 6.4), rotated to account for camera misalignment, scaled, and then cropped. Under the current setup, attempts to identify tunnel start and unstart based off changes in the oil were unsuccessful, so all times were relative. The code saved data at user-specified times, and provided spanwise traces of the signal at a user-defined streamwise location. Both mean (5 frames, 0.167s) and instantaneous images and traces were saved.

6.3 Schlieren Imaging

Schlieren imaging is a ubiquitous technique for visualizing structures in fluids [247]. Here it was employed to interrogate the test article's boundary layer and shock structure. It provided a measurement on the state and size of the boundary layer, and ensured the test environment was

clean (no impinging shocks, vacillating separation at the leading edge, *etc.*). It also provided information regarding the complex shock structure at the trips, and probed any pressure effects due to the plasma. Schlieren imaging's core concept is that light travels differently through media of different density, so by sending a collimated beam through the wind tunnel the intensity should change near the hot wall and across shocks as density gradients unevenly bend the light. Here a Z-type schlieren setup was used; it is outlined in Figure 6.3 and described in detail by Settles [247].

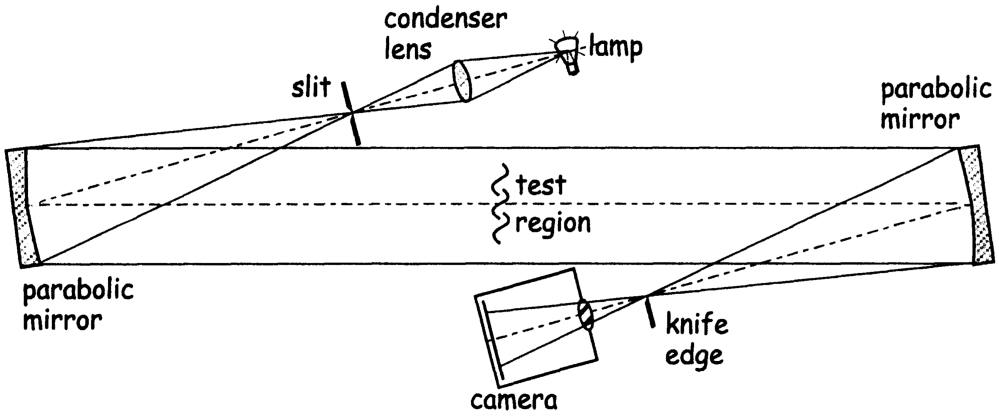

Figure 6.3: A characteristic Z-type schlieren setup; figure taken with permission from Settles [247].

Light was produced by a Luminus Devices, Inc. PT-120-RAX-L15-MPK red-amber (613nm) continuous LED which was nominally powered with a Extech Instruments 382275 power supply at 3.4V and 21.5A for a total power of 73.1W; the LED was water-cooled with an external chiller, and red-amber was selected as the manufacturer's documentation stated the camera was most sensitive to this wavelength range. The light was condensed by a 55mm Nikon camera lens, which focused it onto a ThorLabs VA100 adjustable slit, which meant it effectively behaved as a point source. The slit was positioned at the focal point of a 152mm Edmunds Optics parabolic mirror with a 914mm focal length (f-number f/6), which directed the light through the test section. Because the slit was positioned exactly at the mirror's focal point, the light sent through the test section was collimated. On the opposite side of the test section, an identical mirror focused the light onto an adjustable horizontal knife edge. Because the knife edge was horizontal, just like the slit, the knife

edge provided intensity gradients in the vertical direction by separating the light deflecting up from that deflecting down. The light was then collimated by a planoconvex lens and passed directly onto the camera's imaging plane; in addition to collimating the light, this lens also focused the image at the model's centerline. The camera used in this study was a Photron FASTCAM SA-Z CMOS with a full resolution of $1024 \times 1024 \text{pixels}^2$, a maximum frame rate of 2.1×10^6fps (with fewer active pixels), and a minimum exposure time of 159ns. The camera had 32GB of RAM, which was sufficient storage to record high-speed data over an entire tunnel run before it was downloaded through the control software Photron FASTCAM Viewer (PFV).

It is noted that PFV can be used to adjust the shutter, frame rate, and active sensor area; the last two are also somewhat coupled, because for higher frame rates the camera reduced the number of active pixels. Furthermore, increasing the frame rate reduced the time the could camera record because its RAM filled more quickly. These parameters were adjusted in order to provide optimal conditions for the present application, boundary layer visualization. The frame rate was the highest amount possible to still have enough active pixels to record the flow across the entire width of one of the test section's windows (the orientation of the active pixels was customized to meet this requirement) and also allow recording for the entire duration of the run. Using a faster shutter could make the boundary layer more difficult to see, though using too slow of a shutter could blur turbulent structures. Ultimately a shutter of 1000fps, a gate of 1.25μs, and 1024×640 active pixels were selected. This provided a spatial resolution of $\sim 120 \frac{\mu \text{m}}{\text{pixel}}$, as measured with a gridcard placed along the model's centerline. It is noted that in this gridcard image a plumb bob was hung, the weight suspended in viscous oil, to provide a true vertical measurement which could be used to estimate the camera's roll, though in post-processing it was decided this step was not necessary.

Schlieren data was processed using a custom Matlab script. All images were rotated to negate the wedge slope and scaled in this "flat" orientation. The streamwise scale was set from the known placement of the gridcard, but vertical scale was set manually by identifying the wall after the flow was starts and the test article shifted into its final position; similarly, the rotation was set from the data after the tunnel had started. The NALDAQ recorded conditions at 10Hz, so for each tunnel

condition there were 100 frames of schlieren data. The code therefore used every hundredth frame to determine when unstart occured by checking when the signal in a region of interest suddenly changed; this was then used to link the DAQ data timeline to the camera timeline. The maximum temporal uncertainty using this approach was 0.1s which was tolerable, especially for runs when the tunnel was held on a single condition. Once the timelines were set, the user could select specific run times at which to save schlieren images. The code also averaged together the 100 frames adjacent to that image (50 on each side) to provide a mean image.

6.4 Infrared Thermography

Infrared (IR) thermography is a popular technique for quantifying transition to turbulence in compressible flows. As the flow transitions, the increase in skin friction drag causes increased heating which signifies a turbulent front. The advent of laboratory-ready IR cameras provided a new way to quantify this thermal loading in high resolution and reasonable response time. Its main benefit is over surface-mounted thermocouples, which offer only pointwise readings and may perturb the flow.

6.4.1 Camera and Calibration

The present work used a FLIR SC8100 mid-wavelength IR camera with a indium antimonide sensitive to $3-5\mu$m wavelengths. The camera's thermal resolution was 25mK, its 1024×1024 active pixel array offered for the current testing configuration a nominal spatial resolution of approximately $\sim 250\frac{\mu\text{m}}{\text{pixel}}$, and its maximum temporal resolution was 132fps though this required storing the data on a specialized FLIR high speed data recorded [68]; for this study, the camera wrote directly to a computer at 15Hz, which offered better temporal resolution than the NALDAQ and generally did not produce skipped or corrupt frames. Nevertheless, a catch was included in the code to account for any skipped frames by looking for gaps the camera's frame timeline, and should one exist, linearly interpolating to generate a new image to fill it. For this study the camera was mounted 21.6cm above the test article and tilted 2.75° ($\pm 0.1°$)to account for the wedge's slope. It has been shown that excessive angles can effect perceived emissivity enough to affect tem-

perature calculation [305, 233], though according to Running et al. [233] even if the camera was not normal to the surface for this study the angles were modest enough that any discrepancy would have a negligible effect. The camera collected data through a 11.43cm wide, 0.95cm thick II-VI Incorporated zinc-selenide window with a thin film, dual-band anti-reflective (DBAR) coating on both sides transmissible to $3-5$ and $8-9\mu$m; further reflections were reduced by exclusively conducting IR measurement with no other windows on the test-section and shrouding the gap between the lens and window with a lint-free shop rag.

Two calibrations were necessary to get accurate IR images. The first was a temperature calibration to convert the sensor's counts into temperature readings. This was conducted *in situ* by Leidy [160], and because the same lens and window used here the results were used for the present application. Note that a central assumption of the calibration of the camera was that FLIR's black-coated aluminum calibration plate had the same emissivity as PEEK; the emissivity of PEEK is $0.91-0.95$ [105, 111, 56], which matches typical values for coated metal. In calibrating Leidy [160] noticed that the 2^{14}bit sensor was saturating for certain integration times, called "Presets" in FLIR's control software ResearchIR. This effectively provided an upper limit on the temperature that could be detected, and as the current test article was left in the tunnel during preheat, camera saturation was a real concern. For example, Leidy [160] reported that for an 8ms integration window, the camera saturated at $\sim$ 325K, while for a 1ms integration window it would saturate at $\sim$ 415K; both of these are well below the tunnel's stagnation temperature. It was desirable to use the preset which would provide the best sensitivity (the broadest span of bits), but would not saturate. Success was found using, in general, the 1ms preset near the leading edge and a 2ms preset everywhere else (this should provide data up to $\sim$ 380K [160]). It is noted a 4ms preset with a maximum operational temperature of $\sim$ 350K was also available [160].

The second calibration conducted was of the intrinsic camera properties. It was desirable to use the SC8100's 17mm lens as it had a slight fisheye effect which enabled it to see a span of approximately 20.32cm through the 11.43cm window. However, this introduced barrel/fisheye distortion in the final image, warping straight lines noticeably at the edges of the frame. MathWorks

(Matlab) provides a detailed tutorial for performing a camera calibration[1] to remove this distortion, and it was closely followed here using the technique established by Neel [194]. In short, a precise, vinyl 1.27cm checkerboard was made into a custom $17.78 \times 20.32\text{cm}^2$ sticker by FastSigns; the final product then adhered to a 0.95cm thick piece of aluminum. This provided the Matlab tool a precise, easily identifiable (even in IR) grid of points which could be used to determine the distortion parameters. These parameters could then be applied to all subsequent images read into Matlab where a pre-defined function could be applied to reduce the distortion to a tolerable limit. As an added complication, it was expected that the internal parameters would change as the lens was focused. The procedure was conducted with the calibration plate focused 15.24, 17.78, 20.32, 22.86, and 25.40cm from the lens to provide an array of corrections from which users could pull the most applicable case; here the 20.32cm case was used exclusively.

6.4.2 Material and Boundary Conditions

PEEK was selected as the material for the test article's insert for its electrical insulation, machinability, and high service temperature, but what distinguishes it from other materials used for hypersonic wind tunnel testing are its advantageous thermal properties for IR measurement. The first is its low thermal conductivity, which means thermal events leave a lasting "fingerprint" on the material before becoming diffuse as the heat conducts throughout the material. PEEK's high emissivity is also critical because it makes it easily visible to IR cameras; it also lowers the material's reflectivity. Finally, because of its popularity in other applications, PEEK has been well-characterized over a range of conditions; the applicable examples are the thermal conductivity and specific heat capacity, both of which are shown in Figure 6.4. These data were supplied by Victrex, who supplied the raw PEEK granules eventually extruded into the sheets used here. Note that the jump observed in the plot of thermal conductivity was due to the room temperature value being reported separately from the main temperature sweep data and was otherwise unexplained by the manufacturer; for the present application, the room temperature value should never be needed and is only shown for completeness.

[1] https://www.mathworks.com/help/vision/ug/single-camera-calibrator-app.html

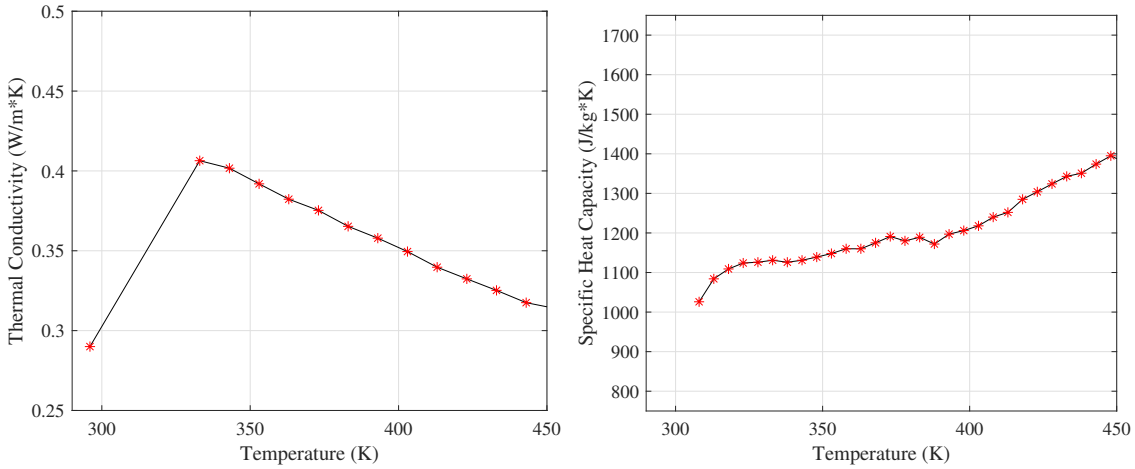

Figure 6.4: The PEEK (a) thermal conductivity and (b) specific heat capacity as functions of temperature. All data available upon request from the manufacturer Victrex.

It will be seen that a critical part of heat flux calculation was the measurement of an internal temperature because it provided a boundary condition to the heat equation. An effort was made to measure this parameter directly as opposed to approximating it based on the surface temperature measured by the IR camera. To do so, custom East Coast Sensors Type K thermocouples were purchased. The TF1-KDTGC060A-05 design put the junction at the tip of a screw which could be threaded a specific amount into the material; here Techspray 1978-DP Heat Sink Compound was applied to improve the thermal connection. An analogous design, TE2-KF1C060A, had a flat junction covered by a piece of polymide tape to allow measurement of the surface temperature. This sensor was placed on the underside of the PEEK insert to provide a temperature reading at a third and final location; the surface thermocouple data was collected, but ultimately not used during the present analyses. During IR testing, a series of TF1 and TE2 thermocouples were mounted along the centerline article within the IR camera's field of view to provide the required internal temperatures. A linear polynomial fit provided the boundary condition in between the thermocouples, and data beyond the first and last thermocouple was neglected to prevent extrapolation; the streamwise temperature profile was assumed to be constant across the span of the test area. The manufacturer stated the accuracy of their thermocouples were the Type K standards of the greater of 2.2K or

0.75%. The thermocouples were connected to the TCDAQ and used its built-in cold junction for temperature calculation. The thermocouples were read with the same custom PlasmaDAQ VI as the plasma conditions, so they had the same read rate and triggering as the rest of the tunnel variables. The response time of the thermocouples was unknown, but rapid changes in the internal temperature were not expected.

This technique removed the assumption that the internal temperature boundary condition was constant and equal to some initial condition at the surface necessary in [194, 160]. That said, one still needed to assume that the internal temperature was uniform throughout the insert despite some areas being in direct contact with the metal wedge and others, including where the thermocouples were, being free or even exposed to the flow; when exposed, the thermocouple's bodies were insulated with Permatex High-Temperature RTV gasket maker. This was a reasonable assumption because the portion in contact with metal is 15.62mm thick and the thermocouple is at a depth of 6.09mm from the top surface, well over halfway through the material. Nevertheless, to avoid all confusion, the test area was selected to be free of any metal on the underside, removing any interference in the final data. Still, the effect is checked in Section 7.3.3.

6.4.3 Data Reduction

Boyd and Howell [39] illustrated how one could use a 1D assumption to calculate heat transfer from thermocouples on a wind tunnel model. This was adopted to more modern IR measurements in [132, 35] and then introduced to the NAL by Neel et al. [196]. The core functionality of Neel's code, best described in [194], was adopted into a new Matlab program for IR data reduction custom-built for the current experiment. This program, whose outputs have been validated against Neel's, will be described here to enough detail to permit its replication. Following Neel [194], atmospheric interference with IR signal was neglected due to the short distance between the test surface and camera, as were reflections off of the PEEK due to its high emissivity. The fundamental assumption was that the heat flux was 1D which greatly simplified the required calculation. In the context of IR thermography, this essentially allowed the code to consider each pixel as its own independent heat transfer problem. Boyd and Howell [39] and Running et al. [233] compared

1D results to 2D results and for the simple geometry, relatively low gradients, and high frame rate used here the 1D assumption was appropriate. The present code used interpolation to add in any dropped frames, so the time between frames was a constant $1/15\text{Hz} = 0.067\text{s}$.

The code began an analysis with standard bookkeeping, allowing the user to specify paths to the data, the region of interest, frame averaging. The raw .ats files from ResearchIR were read into Matlab arrays by a processing code provided by FLIR for Matlab. The thermal calibration was then performed for the user-specified preset, followed by rotation and distortion corrections before the final pixel-to-millimeter scale was set. Because the camera was triggered manually a few seconds before the 10.16cm line was opened and recorded at a different frame rate than the NALDAQ and PlasmaDAQ VI, it was necessary to unite the camera and tunnel's timelines. This is done using unstart, a dramatic even clearly visible in both data sets; in IR, it manifested as a sudden and uniform rise in temperature across the model. The code identified where the mean temperature on the whole plate suddenly rose, setting the IR camera's unstart, and where the Mach number suddenly fell, setting the NALDAQ's unstart. With a shared event marked in both timelines, the code then stepped backwards in time at the camera's known framerate and linearly interpolated tunnel conditions from the slower DAQ data, producing a "united" dataset between the IR camera and tunnel's DAQ.

With this the code could proceed to the heat transfer calculation. The first step was to define the PEEK thermal properties, all of which were collected directly from the manufacturer Victrex. The density ρ of the Ketron 1000 PEEK was a constant $1300\frac{\text{kg}}{\text{m}^3}$, but the thermal conductivity k and specific heat capacity c_p were more complicated due to the temperature dependence illustrated in Figure 6.4. Every node in every pixel of every frame had its own unique temperature, so each node should then be able to interpolate from Victrex's data to determine the thermal properties. However, in practice this was unacceptably slow with any Matlab function attempted, standard or otherwise. As a compromise, a single characteristic temperature for a user-defined region of interest in each frame was used for the properties of that frame. The characteristic temperature was the average of the mean of the temperature of the top and inner surfaces. While the loss of

fidelity was unfortunate, in testing it was discovered the temperature seldom rose more than 10K in the test area during a run, so from the data presented in Section 6.4 there was little justification for the excessive computational expense of performing the ideal calculation. The thermal properties were used to calculate the thermal diffusivity $\alpha = \frac{k}{\rho c_p}$, which played an important role in the finite difference scheme.

The 1D equation for transient heat conduction through a wire is

$$\frac{\partial T}{\partial t} = \alpha \frac{\partial^2 T}{\partial \zeta^2} \tag{6.1}$$

This equation can be approximated with the following explicit, forward-time, central-space (FTCS) scheme [275]

$$\frac{T_j^{i+1} - T_j^i}{\Delta t} = \alpha \frac{\left(T_{j-1}^i - 2T_j^i + T_{j+1}^i\right)}{\left(\Delta\zeta\right)^2} + \mathscr{O}\left(\Delta t, \Delta\zeta^2\right) \tag{6.2}$$

This represented a means to calculate the temperature at an internal node j at a future time step i provided the entire heating distribution was currently known through the wire. The variable ζ represented the spatial coordinate into the PEEK (with the origin at the surface). Its selection required care: more points improve fidelity, but the FTCS scheme was only stable if $\zeta \geq \sqrt{2\alpha\Delta t}$ [275]. Remember that α was now a function of temperature and changed with each frame, but ζ needed to be constant and amenable to all frames. To balance these concerns, ζ was calculated with the frame with the largest α, guaranteeing stability. Finally, both the surface and internal boundary conditions were "background corrected" by subtracting the data corresponding to $t = 0$s (or however many frames the user averaged together to temporally smooth the result) so as to help remove any artifacts like reflections, edge effects from the test article's walls or thermocouples, preheat gradients, *etc*.

With the PEEK's properties set and the boundary conditions known at all times from the IR camera and thermocouples, the temperature through the PEEK for every pixel of every frame could be calculated. For the initial condition, the plate was assumed to be isothermal everywhere but the surface, with the temperatures measured from the thermocouples and IR camera respectively. The

boundary conditions for each pixel were applied for each frame with the data from the thermocouple and IR camera for that frame. Once the temperature distribution within the model was known, the heat flux could be calculated from a second-order forward differencing approximation of Fourier's Law

$$q \approx -\frac{k\left(-\frac{3}{2}T_0^i + 2T_1^i - \frac{1}{2}T_2^i\right)}{\Delta\zeta} \tag{6.3}$$

Once the heat flux had been calculated all that remained was post processing. For the current work, this included averaging several frames (typically no more than five) together in order to smooth the final result; the images were median filtered for the same reason. It was also common [194, 160] to report the Stanton number, or the nondimensionalized form of the film coefficient h, to report the heating [293]. Doing so helped account for discrepancies in heat flux due to test article and tunnel heating as well as run-to-run variability. The Stanton number was

$$St = \frac{h}{\rho_e u_e c_p} = \frac{q}{\rho_e u_e c_p (T_{aw} - T_w)} \tag{6.4}$$

Here the density, velocity, and specific heat are for the fluid outside of the boundary layer, T_w was the wall temperature, and T_{aw} was the adiabatic wall temperature where, as was done throughout this report, T_{aw} could be found from $T_{aw} = T_e * (1 + \frac{1}{2}r(\gamma - 1) * M^2)$, where for laminar flows $r = Pr^{\frac{1}{2}}$ and for turbulent flows $r = Pr^{\frac{1}{3}}$. This procedure fails, however, if the state of the boundary layer was unknown. Thus for the trip sizing study in Section 7.2.2, where quantitative results were unnecessary, the Stanton number was calculated with T_o instead of T_{aw}. Otherwise, for consistency if trips were installed, the flow was considered turbulent, which meant the Stanton number results just downstream of the trips were unreliable.

Temperature, heat flux, and Stanton number images were produced either at fixed Reynolds numbers or run times specified by the used. Spanwise traces of the variables at a user-specified location were also plotted. All heat flux and Stanton number figures were restricted by the domain of the internal thermocouples, the space between the first and last thermocouples in the streamwise direction. The effect of wall condition (metal contact, enclosed chamber, exposed to flow) is

discussed in Section 7.3.3

6.5 High Frequency Pressure Transducers

Studying the pressure frequency content of a boundary layer can provide information regarding its condition (laminar, transitional, or turbulent), spatial and temporal growth, and spanwise uniformity. Past work on a similar geometry in the ACE tunnel [160] found meaningful content up to 300kHz. This work utilized Kulite XCE-062-15A Type A (screenless) ultra miniature, high temperature sensors for content below 80kHz, and then PCB 132B38 sensors for content up to 300kHz; these ranges were limited by the estimated flat-frequency response of each sensor (see [26] and [58] respectively). The sensors are compared in Table 6.1.

Property	**Kulite XCE-062-15A Type A**	**PCB 132B38**
Measurement Range	103kPa	345kPa
Housing Diameter	1.70mm	3.18mm
Resolution	Infinitesimal	7Pa
Sensitivity (typical)	N/A	$20.3\text{mV}/\text{kPa}$
Full-Scale Output (nominal)	0.1V	7V
Resonant Frequency	$200-250$kHz (empirical)	>1MHz
Temperature Range	$298-508$K (compensated)	$248-352$K
Temperature Sensitivity Shift	$\pm 1\%/100$K	N/A
Temperature Zero Shift	$\pm 1\%/100$K	N/A
Combined Error (non-linearity, hysteresis, and repeatability)	$\pm 0.1\%$ FSO BFSL (typical)	N/A

Table 6.1: High frequency pressure sensor properties.

The current test article was designed to stay in the tunnel during preheat, and so it reached temperatures considerably hotter than that in [160]; preliminary IR thermography data showed run temperatures of ~ 350K were nominal, and the temperature was known to rise even higher during unstart. According to the manufacturer's specification sheet, the PCBs used by Leidy [160] had a maximum operating temperature of 352K. Thus the PCBs would likely be damaged during the present application or, perhaps worse, provide misleading, inaccurate results. For this reason,

PCBs were not used in this campaign.

Kulite XCE-062-15A sensors (S/N 8534-3-79, -80, -81, -83) were fixed into the PEEK with Permatex high-temperature RTV as the cosmetic nail polish used by Leidy [160] and Neel [194] would fail at the temperatures seen by the current model; RTV was recommended by the manufacturer to safely mount the sensors for repeated removal and reuse. Four Kulites were used at a time as limited by the available channels on the signal conditioning boxes to be introduced. They were placed in the three test locations used throughout this work, 130, 260, and 405mm from the leading edge; the 130mm location was slightly farther downstream than the PLIF measurements, but this was done to reduce the risk of the plasma damaging the sensors. In order to remove any chance of the 1.78mm holes for the upstream test locations interfering with the downstream test results, data was collected moving from the rear to the front of the test article, with each test location's holes only being drilled when that region was being studied.

The sensors were placed 0 (K4, Kulite -80/-83), -3.42 (K3, -83), -6.84 (K2, -81), and -10.26mm (K1, -79/-81) from the centerline following a wake-trough pattern from the trips; their off-centerline locations were on the same side as all other measurements. This was done to study the behavior of being in the trips' wakes or troughs (especially relevant near the leading edge) and look for more generalized spanwise nonuniformity (especially relevant near the rear of the plate). As best as possible, the same sensors were kept in the same spanwise location across all tests, but by the time the "Front" test location was reached failed sensors necessitated moving the "inner" Kulites to "outer" locations in order to fill gaps in the data. Ideally, oil flow and IR thermography could have informed the placement of the sensors to ensure they were indeed in wakes or troughs, but the growth and movement of the structures along the plate, as well as the potential for misalignment, led to the more rigid approach.

It was desirable to be just at the edge of a wake because it was the vortices cast by the corners of the trips which fomented turbulence and Neel [194] found the most distinct frequencies in these locations. Thus either the middle two sensors would validate the outermost sensor's results, or they would provide information on this third region. IR thermography was conducted concurrently

with the Kulites to document exactly where each sensor was with respect to the flow structures; only temperature data was collected, a 2ms integration time was used for all cases, and all other specifications matched those in Section 6.4. The Kulites were used to add extra fidelity to the scale of the IR images, as they provided exact coordinates on the test article with the flow on.

6.5.1 Extension of Kulite Operating Frequency Range and Current Setup

A Kulite's flat frequency response range is limited by the presence of a strong peak at its resonant frequency f_r [120]; this strong excitation can "bleed back" into lower frequencies, masking subtler effects and thereby defining the upper edge of the flat frequency response regime. Beresh et al. [26] showed that for the Type A variant, the flat response of Kulite XCE-062 sensors was $30-40\%$ of f_r and as low as 20% for the screened Type B. On the product specification sheet for the XCE-062-15A the manufacturer listed $f_r = 200$kHz, though in the NAL's facilites Neel [194] found the actual natural frequency to be $250-270$kHz; while such variability in piezoresistive Kulite sensors is not uncommon, the temperature and speed of sound effects of testing in a hypersonic environment also likely played a role [120]. Taking the manufacturer's value of f_r, one is left with a usable range of $0-80$kHz. In their PCB data Leidy [160] found meaningful results up to 300kHz, so there became a desire to increase the Kulites' usable bandwidth for the present work.

The solution was the employment of a Kulite KSC-2 signal conditioning box with resonance frequency compensation (REZCOMP™). This signal conditioning box could provide the Kulites a clean 10V source, and, more importantly, filter the output signal to remove the natural frequency spike as shown in Figure 6.5. According to the manufacturer, doing so allowed flat frequency responses up to 80% of f_r, and in some cases reliable data could be obtained above f_r. Hurst et al. [120] show improvements of the usable bandwidth of $200-300\%$, with varying results and temperature effects for different classes of sensors (the XCE class was not tested). The ability to measure up to 200kHz would cover most of the key features observed in Leidy's [160] analogous experiments and thereby negate the loss of the PCBs. The efficacy of the new REZCOMP was directly compared to a Kron-Hite Corporation Active Filter Module 8-pole Bessel 200kHz low-pass filter with unity gain housed in a Krohn-Hite FMB3002 chassis in the corresponding results

section, Section 7.3.4.

As an input for the REZCOMP™ filter, the KSC-2's control software required an accurate measurement of the sensor's natural frequency and quality factor $Q = \frac{f_r}{\Delta f_{FWHM}}$. These quantities were determined experimentally *in situ* following Hurst et al. [120]. Performing a tunnel run with the REZCOMP™ feature turned off allowed one to identify f_r in the spectra, and from that an approximate Q; the results were clearer with the trips in as the turbulence better excited resonance in the sensor. This *in situ* calibration of tunnel data is preferable as the sensors had the same thermal loading as during a data collection run. Although resonant frequency is a function of the sensor construction, this procedure was repeated for every Kulite configuration, confirming only slight changes in each individual sensor's results.

Following Leidy [160], the data were reduced using Matlab's implementation of Welch's power spectral density method. The number of samples per window was an input to Matlab's "pwelch" function, so a quasi-grid convergence study was performed where $2 \times 10^{8-16}$samples were used, in 10^2sample increments, until f_r changed by less than 1kHz, the resolution of the KSC-2's control software. Typically convergence occurred at 2×10^{12}samples, and 2×10^{10}samples were used for actual data reduction following Leidy [160]. The resonant frequencies fell between $225 - 246$kHz, with most above 240kHz. While the resonant frequency could be input into the KSC-2's software, Q was problematic. In its current form, the KSC-2 was not optimized to work with such high frequency sensors, and so the maximum programmable quality factor was $Q \leq 50$. However, nominal results yielded $Q = 50 - 100$ for window sizes of 2×10^{10}samples. Fortunately, Hurst et al. [120] showed that while accurate measurement of f_r is critical, that for Q was somewhat forgiving, even up to 25% from the correct value. Thus the filters were left at $Q = Q_{max} = 50$.

The KSC-2 signal conditioning box provided two sensor channels which could be individually controlled by the affiliated software. Two boxes were generously loaned to the NAL for this work, one from Mr. Steve Carter at Kulite Semiconductor Products, Inc. (S/N 200469-014, calibrated 4/11/2021-5/18/2022) and another from Dr. Jerrod Hofferth at the Air Force Research Laboratory at the Arnold Engineering Development Complex (S/N 200469-015, calibrated 4/11/2018-

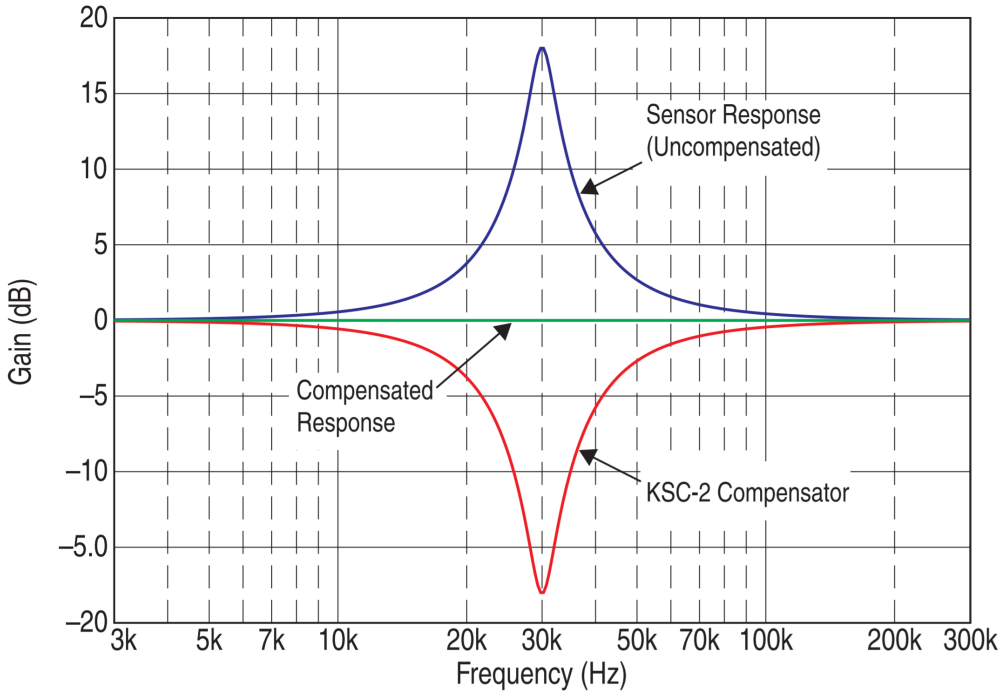

Figure 6.5: An example of the resonant frequency compensation with the KSC-2's REZCOMP™ filter; figure taken with permission from Hurst et al. [120].

9/12/2019). As best as possible, the same channels and wires were used for each spanwise test location throughout the entire campaign, and new cables were used throughout the system. Both boxes were powered through a Furman M-8x^2 surge protector for uniformity. The boxes were set to use their "Chassis Ground", and the sensors were connected to this chassis ground at the DB-9 connection to the box; thus in the affiliated software the "Shield" field was set to "Ground". While using new cables, common power, and the current grounding scheme did yield a tolerably low-noise environment, it was found to be critically important that USB control cable for each box be unplugged during testing; failure to do so introduced so much white noise the data were rendered nearly unusable.

The KSC-2 boxes were programmed to provide 10V of bipolar excitation, which is required for the XCE class Kulites. The "Sense" field was set to "Local", another such requirement for this hardware. These Kulites return $0-100$mV from $0-103.421$kPa, and so for DC operation they could be amplified up to $100\times$ before saturating the NI USB-6366 DAQ's 10V limit. The boxes

could output either DC- or AC-coupled data, and the former was chosen as it was more intuitive in noise reduction, data interpretation, and in checking sensor health. That being said, the Kulites were not calibrated or balanced as the temperatures experienced during a run would be challenging to replicate on a bench and pressure values were not needed to meet the experimental objectives, only voltage fluctuations.

Because the KSC-2 box's control software only provides set amplification values, a pregain of $16\times$ and postgain of either $6\times$ or $5\times$ were used for a total of $96\times$ or $80\times$ amplification. This value allowed the full resolution of the DAQ to be used, but did not saturate the sensors at atmospheric pressure, which was necessary to determine the sensors' statuses; the lower amplification was used when daily temperature and humidity fluctuations led to slightly higher outputs to the DAQ. Common practice was to maximize the pregain as opposed to the postgain so any noise introduced by amplification can be filtered out. The KSC-2 boxes have programmable, custom 6-pole "flat" low-pass filters recommended for the current application, but their maximum cutoff of 127.5kHz was too low. Therefore the filter was switched off in the software and the boxes' inherent 3-pole Butterworth wideband amplifier frequency response was used to low-pass filter by -3dB frequency at 500kHz. Because the data were sampled at 2MHz the Nyquist frequency should be 1MHz, so low-pass filtering at 500kHz was sufficient to prevent aliasing.

The data were processed with a LabVIEW VI developed by Neel [194] and the power spectral density plots produced using Welch's method in a Matlab script following Leidy [160] and Neel [194]. The VI was modified to read in the plasma conditions. It was manually triggered before the air ejector was started, and then turned off after unstart, providing full context for the sensors' performances. During this time, the sensors were sampled at 2MHz in 100ms intervals, yielding 2×10^5samples at the NALDAQ's frequency of 10Hz. Matlab's "pwelch" method used 2×10^{10}samples in Hamming windows with the default 50% overlap, which yielded a resolution of approximately 2kHz.

6.6 Pitot Pressure

Pitot surveys were an integral part of the experimental campaign as they provided direct measurements of the Mach number, and by extension velocity and temperature, through the boundary layer. These data communicated the state of the boundary layer, which was especially important in transitioning/tripped flows, compared the flow in the trips' wakes as opposed to their troughs, and probed any effect of the plasma. They also provided a measurement of the wall shear stress, as well as validation for other experiments, including PLIF. This work was conducted alongside Joel White, another graduate student at the NAL who led the design and operation of the traverse system as part of their doctoral research. The resulting system had sufficient complexity to warrant a detailed description here; for clarity, this section is organized into discussions of the design of the traverse mechanism, the Pitot probes, the sensors, the measurement of the probes' positions, the data reduction, and an ancillary freestream measurement.

6.6.1 Traverse Motion and Sealing

A universal probe mount was designed to provide a platform for the present and future diagnostics. Motion was provided by two Aerotech PRO165 Mechanical-Bearing Ball Screw Linear Stage tables orthogonally mounted to afford 400mm of motion in the vertical and 200mm in either the streamwise or spanwise direction; the rig was mounted to the optical rail surrounding the ACE test section. Each stage had a factory High Accuracy Linear and Rotary calibration which provided a precision of $< \pm 5\mu$m at room temperature. These stages were controlled by Aerotech Ensemble HLe Controllers and linear drivers. Aerotech's Ensemble Motion Composer control software interfaced with LabVIEW to allow for control within a custom-built DAQ VI. This system was originally selected as it provided low electronic noise which could interfere with hot wire measurements [112], but due to the success and universality of the Aerotech platform subsequent students [243, 168, 160, 194] adapted it for use with both hot wire and Pitot probes.

Any sting mounted to the traverse should capitalize on its two degrees of freedom. To do so necessitated a dynamic seal in both the vertical and horizontal plane, where the latter referred to

motion in either the streamwise or spanwise direction. Mai [168] offered a solution which allowed for vertical and streamwise motion, and Neel [194] later simplified it, but due to the presence of sharp corners required to prevent excessive blockage and separation around the sting, both designs suffered from leaks at its interface with the O-ring. It was for this reason the Pitot mount was redesigned, with the final result included in Figure 6.6.

Again, any sting required an aerodynamic shape to reduce blockage and vortex shedding, but such geometries are challenging to dynamically seal. Ultimately, all efforts to design such a seal were abandoned and instead the sting was divided into two distinct sections. The top half was a "piston" which had two standard Buna-A Durometer 70A 2-326 O-rings set inside a shaft; the shaft provided 55.8mm of vertical motion before the top O-ring would become exposed. Note that Dow Corning Vacuum Grease was applied to all O-rings for lubrication and to aid with the seals. The second half of the sting was a traditional blunted diamond shape 9.5mm wide and 25.4mm long; it extended a total length of 127mm, which was set to insert the Pitot probe into the region of interest with maximum protection. This component was made with the Oran W. Nicks Low Speed Wind Tunnel's FormLabs Form 3L SLA 3D printer from Rigid 10K as this material was shown to be mechanically and thermally durable enough to survive wind tunnel testing and made it trivial to produce complex parts [301].

The piston's shaft, shown in Figure 6.6(b), statically sealed against an adapter plate with a Buna-N Durometer 70A 2-141 O-ring. This adapter plate then dynamically sealed to the modified window plug with a custom $3/32$in fractional (0.103in actual) silicon O-ring. In order to translate in either the streamwise or spanwise direction, one must loosen the screws sealing the adapter plate to the window plug, actuate the traverse, then fasten all of the screws. The same procedure applied to the second plate on the inside of the tunnel as well, which prevented re-circulation inside the modified window plug's cavity. This system allowed the traverse to move 92.1mm in the spanwise direction, or, should the entire traverse be re-mounted 90°, 76.2mm in the streamwise direction. The reason the modified window plug needed to be so tall was to allow the adapter plate to slide over the other plugs on the top of the test section when the traverse was moving in the streamwise

direction. It is noted that the system needed to be square with the tunnel to prevent binding when moving in the spanwise or streamwise directions. While this design was limited to moving the probe in the vertical direction while the tunnel was running, it provided sufficient functionality to precisely align the probe with test location on the test article, and sealed well.

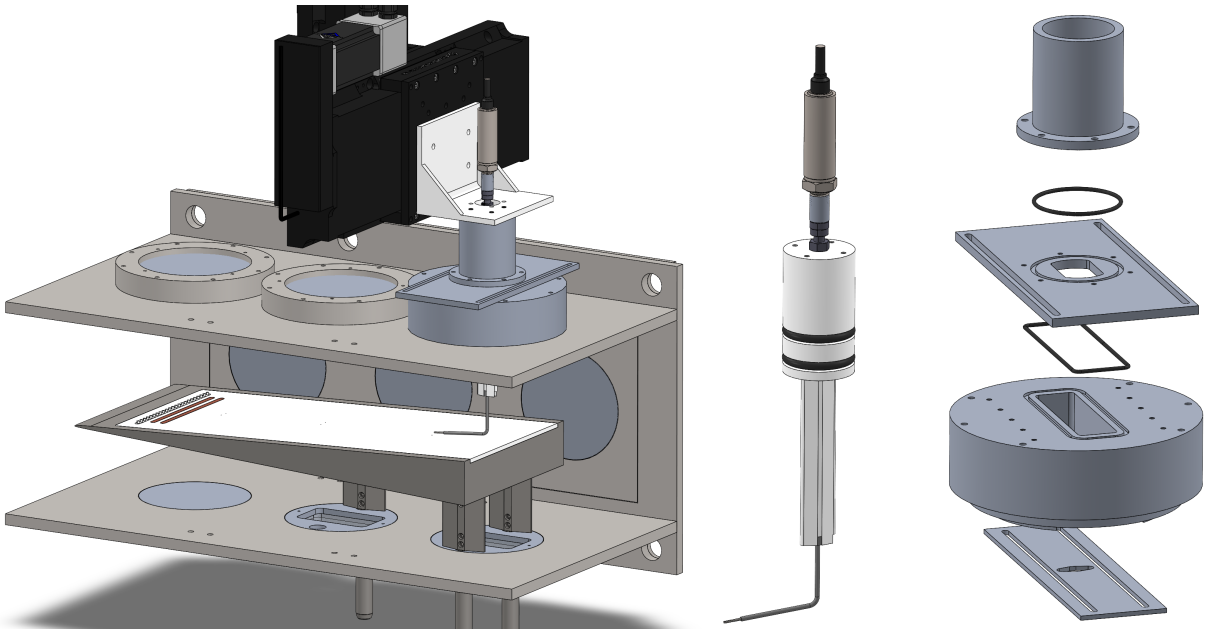

(a) Full view (b) Exploded view

Figure 6.6: CAD of 2D traverse.

6.6.2 Pitot Probe Construction, Alignment, and Test Locations

The Pitot probe was constructed from two concentric stainless steel tubes joined with JB Weld Kwikweld Epoxy; the outer tube dynamically sealed through the piston head with a Swagelok Ultra-Torr vacuum fitting following [243]. This outer support tube had an outer diameter of 3.175mm, a wall thickness of 0.711mm, and an inner diameter of 1.753mm. The inner tube, meanwhile, had an outer diameter of 1.651mm, a wall thickness of 0.127mm, and an inner diameter of 1.397mm; the tip of this tube was crushed to an elliptic ratio with outer dimensions of nominally $2:1$mm to compensate for the large internal diameter. Semper [243] used an equally sized, crushed

inner tube and collected data in the ACE tunnel, though their wall thickness was larger than that used here. The tubing used here was chosen to balance rigidity with near-wall measurements and venting; a thicker tube would be sturdier, but it would not be able to get as effectively close to the wall. Furthermore, its smaller hole would take longer to settle on the tunnel's near-vacuum conditions; near the wall Semper [243] noted it took 2s for the Pitot pressure to settle, as compared to 0.5s in the freestream. Because many different test locations were to be interrogated, the ability to quickly reach the stagnation conditions was a top priority if a decent density of test points were to be used. Crushing the tube had the added benefit of reducing the size in the direction with the strongest gradients, which helped reduce the sensed probe displacement [287, 104].

The probe's yaw was confirmed to be zero before each run by measuring the tip's distance from the side of the test article with a ruler and a camera positioned directly above the probe, and then by moving the camera to the leading edge, centering it relative to the probe using a ruler, and checking the angle with a camera looking head-on at the probe. A shaft collar "JB Welded" into the sting fixed the probe in place, and while the alignment was checked before every run, the probe seldom drifted. The probe's pitch was determined through careful trigonometry, as one needed to limit the angle between the test article and the probe, but also let the crushed tip of the inner tube touch the surface before the thicker outer tube. It was found that an angle of 7.5° relative to the centerline (4.75° relative to the test article) worked well, with no more than 25.4mm of the inner tube ever needing to be exposed to the flow. It is shown in [287] that this angle offset it expected to have only a minimal effect on the results. The tubing was manually bent with a 12.7mm radius following a stencil traced on paper.

There were six test locations for this campaign, three streamwise locations and two spanwise locations; the test locations were selected to match those of other diagnostics, especially the PLIF data. The spanwise locations corresponded to the trips' theoretical wakes (0mm off-centerline) and troughs (-10.26mm off-centerline), though the IR thermography data taken for Sections 6.4 and 6.5 show that these structures do move somewhat along the length of the test article. Streamwise data were collected at "Forward", "Middle", and "Back" test locations 140, 261, and 406.5mm

from the leading edge respectively. The static pressure ports were positioned -6.84 and 3.42mm for the "Wake" and "Trough" measurements, respectively, taking advantage of the symmetry of the flow to maximize the distance between the holes and the probes to minimize interference. The static ports were 130, 260, and 405mm from the leading edge; the discrepancy between the Pitot probe and static ports in the "Forward" location was due to poor optical access at this point, a necessity which will be discussed shortly.

For the "Rear" test location, the traverse was moved in the spanwise direction such that the same probe could take the "Wake" and "Trough" data. For the "Middle" and "Forward" locations, the traverse and test article (on its struts) were moved in the streamwise direction so one probe could make the "Wake" measurements in both positions, and another could take the "Trough" data. In order to access the "Trough" without the ability to move the traverse in the spanwise direction, a Pitot tube was bent into position using screws drilled to trace out the proper horizontal "Z-shaped" displacement before the tube was turned in the streamwise direction as usual; this probe is shown in Figure 6.7.

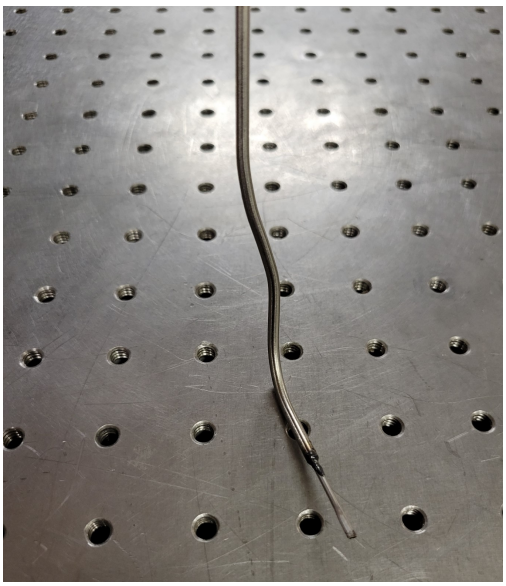

Figure 6.7: Trough Pitot probe.

The static pressure taps were drilled with a 0.508mm bit to provide minimal flow disturbance, though it was later seen they still produced shocks. On the underside of the wedge, NPT-to-barb adapters connected the hole to Teflon PTFE tubing with an outer diameter of 3.175mm and an inner diameter of 1.588mm. This tubing was rated to above the temperatures of the ACE tunnel, was strong enough to endure the crushing effect of the vacuum, was flexible and workable, and had a small internal volume to reduce the settling time. It was passed out of the tunnel and into a series of adapters which connected it to the barometer. To ensure a hermetic seal, at the joint inside the tunnel JB Weld epoxy or Permatex RTV was applied, while outside the tunnel Dow Corning vacuum grease covered the barb adapter. When not in use, the underside of the static taps were covered in Kapton polymide tape, but the top remained uncovered as the holes were so small and effort to plug or cover them was likely to have a greater impact than the cavity itself.

6.6.3 Sensors, Data Collection, and Uncertainty

The Pitot probe was connected to an Omega PX409-005A10V pressure transducer (serial no. 528724) which provided $0-10$V from $0-258.6$Torr. It was connected and sealed to the Pitot tube through a Swagelok Ultra Torr fitting and adapter set. The transducer came pre-calibrated from the manufacturer, and had a cumulative accuracy of 0.08% the full-scale voltage output. This sensor had an operating range of $-45-115$°C and a compensated temperature range of $-17-85$°C, but as the transducer was mounted outside of the tunnel it was not expected to deviate from room temperature, a convenience Semper [243] confirmed. This device was powered to 24V and 5mA with a BK Precision 9110 100W Multi Range 60V/5A DC Power Supply. The static pressure was recorded with a Baratron 631C capacitance manometer (model no. 631C12TDFP, serial no. 07XX09 016522584) which had a range of $0-100$Torr and an accuracy of 0.5% of the reading. The Baratron 631C was thermally regulated to 200°C to provide thermal stability, though again, as it sat outside of the tunnel any such affect was likely to be minimal.

Data was collected at 1000Hz while the probe was parked at a test location. This was chosen to provide an ample number of points, and to match the frequency of the schlieren images to be discussed. It was expected that there would be some settling time for both the Pitot and static

pressure tubing owing to their small diameter. Preliminary testing showed that the Pitot tube settled within quarter of a second for any point in the boundary layer, showing the efficacy of the wider internal diameter than that in [243]. However, because stagnation pressure grew as the probe moved up from the hot surface, it was found starting each set of points near the surface and moving away from it produced quicker settling times; the effect was minor, but it was found vacuuming out the probe was less efficient then blowing into it, so taking full advantage of the hard vacuum achieved during the tunnel's startup was recommended. The static pressure probe took far longer to settle, perhaps due to the large internal volume of the Baratron 631C or small size of the static ports, but it ultimately converged within 0.5Torr by the final data point in a run. And so it was decided for each test point data would be collected for the conservative duration of one second, then in post processing stagnation pressures would be the average of the last half second of data and the static pressure would be the average of the full second of data for the last point.

Collecting data for one second per point meant that, including the time to ramp up the plasma and move between points, only as many as fourteen points could be collected per run. Wile this was sufficient resolution for the laminar boundary layers, for thicker, turbulent boundary layers this meant two runs would need to be combined to complete a survey. Initial efforts involved moving the probe in a staggered, "even/odd" pattern between two runs to prevent a step at the junction between the points from each run, but the concern was that due to inconsistent tunnel flexure it would be easy to either miss or repeat the critical points very near the wall. Instead, an "inner" and "outer" sweep was conducted for each sweep, where small steps as small as $\frac{1}{3}$mm were taken in the inner survey and as large as 5mm were taken in the outer survey; such large steps were susceptible to increased settling times, but none more than a quarter of a second were observed. In practice, no significant shift in Mach numbers was recorded at the junction between "inner" and "outer" runs at the same location.

Both of these sensors were selected to be as accurate as possible. It is noted that the dynamic range of both sensors exceeded the predicted values of $\mathcal{O}(10)$ (including the probe's normal shock) and $\mathcal{O}(1)$Torr for the stagnation and static pressures, sensors which returned errors which scaled

with the reading and not the full-scale output were preferred. The data reduction process will be reviewed shortly, but put simply the ratio of the stagnation to the static pressure provided the Mach number, which then yielded the temperature profile through the modified Crocco-Busemann correlation, and then the Mach number and temperature gave the velocity. Thus all of the variables of interest related to the pressure ratio, and both pressures had a conservative affiliated uncertainty from the sensors of $\frac{P_o \pm X}{P \pm Y}$. So, an upper bound for the cumulative error of the pressure ratio would be $\frac{P_o+X}{P-Y}$ and the lower bound would be $\frac{P_o-X}{P+Y}$. This then tracked through all subsequent calculations; for example, the Mach number was calculated three times, once with the measured pressure ratio and again with both the upper and lower pressure ratio bounds. Repeating this process, the original sensor uncertainty could then follow all the way to the velocity. This approach yields large uncertainties, but it will be seen that even these were negligible.

6.6.4 Probe Positioning

During normal operation, the wind tunnel flexed, and while it was never more than a few millimeters, it was enough to throw off any pre-run calibration. The effect was exacerbated by the flexure of the Pitot probe itself. Therefore to accurately measure the position of the probe, it was necessary to record its position in real time. Here schlieren imaging was used alongside each Pitot run. It was triggered by the DAQ using the FASTDAQ's analog output channel and the Photron PFV4's "Random Reset" triggering feature at the start of each point's collection. With careful scaling using a dotcard before the run (see Section 6.3), the probe's position in pixels could be converted into millimeters with a nominal resolution of $103\frac{\mu\text{m}}{\text{pixel}}$. Just as in Section 6.3, a framerate of 1000fps was used at a shutter speed of 1.25μs, though the image resolution remained the default $1024 \times 1024\text{pixels}^2$ as PFV4 did not have the same customizability as Fastcam.

A Matlab script was written which identified the wall and corner. Matlab's in-built image processing tools were key to this process. The code grayed then binarized the mean schlieren image such that all dark pixels became ones and all other pixels became zeros; the result was filtered, the edges were detected, and finally it was diagonally smoothed. The code identified the top corner of the probe by checking, for all pixels in the user-defined region of interest, if there

were: no pixels in the twenty-five above it which were one (shocks could be erroneously labeled edges); no pixels upstream which were one; the neighboring pixels downstream and below were one. Should there be any issues identifying the corner, the code would prompt the user to manually select one. The wall identification was simpler, the code simply looked for the last nonzero pixel in the first and last column of the binary image; it then considered the wall to be the mean of those pixel locations, though with careful image rotation the identified points were never more than three pixels apart.

The top corner of the probe was identified because the ACE tunnel and floor were not perfectly level, so seeing the precise pixel the probe touched the surface at was impossible without perfect alignment. While great care was taken when aligning to see as much of the probe as possible when it was touching the surface, only the top corner was ever definitively visible. For this reason, it was necessary to identify the offset between when the bottom of the probe was physically touching the surface and the observable, faux surface in the schlieren image. To do so, an image was taken with the bottom of the probe touching the surface. The top of the probe was identified, and its known thickness and angle were used to calculate the bottom pixel. Using the scale calculated from the gridcard, the height in millimeters between the bottom of the probe and the surface was calculated. The offset to be added to all subsequent calculated heights was the theoretical height minus the measured value. For mean run images at each position, an analogous process was carried out; the top corner and wall pixels were identified, scaled, and the offset was added, but here the center of the probe was output.

The spatial uncertainty of the probe was taken to be 2pixels plus the scale uncertainty multiplied by the number of pixels between the measured probe position and the wall. The $mm/pixel$ uncertainty was half of the difference between the x- and y-scales as measured from the dotcard; this was acceptable as approximately the same number of x- and y-points went into the mean "total" scale. No account of the effective probe centerline displacement was considered. This error came from the transverse velocity gradient over the probe and the unequal contribution the higher velocities have on the overall pressure reading, and it was especially relevant in the near-wall mea-

surements of the turbulent boundary layer. Its effect could have been lessened experimentally by reducing the side of the probe, but that step was not taken here for fear of creating an unsustainable settling time in the Pitot probe. There exist empirical corrections [287, 104, 223], but none were found for hypersonic boundary layers. For this reason, no compensation could be applied, but in general it would seem the probe's effective reading would be for a position higher than it was actually placed.

6.6.5 Calculations

The process to bring the measured stagnation and static pressures into a scaled velocity profile was as follows. The Mach number can be calculated from the following [128]

$$M < 1: \quad M = \sqrt{\left(\frac{2}{\gamma-1}\right)\left(\left[\frac{P_o}{P}\right]^{\frac{\gamma-1}{\gamma}} - 1\right)} \tag{6.5}$$

$$M \geq 1: \quad \frac{P_o}{P} = \left[\frac{(\gamma+1)^2 M^2}{4\gamma M^2 - 2(\gamma-1)}\right]^{\frac{\gamma}{\gamma-1}} \frac{1-\gamma+2\gamma M^2}{\gamma+1} \tag{6.6}$$

The first equation is the isentropic flow relation, and is valid for shock-free flows. For supersonic flows, the second equation must be used, the Rayleigh-Pitot formula; this equation solves for the supersonic Mach number upstream of the Pitot probe by working backwards from the subsonic flow in the tube and then across the probe's normal bow shock. The Rayleigh-Pitot formula must be solved iteratively, and here a Newton-Raphson method (see [97]) with a tolerance of 1×10^{-4} and the isentropic Mach number as a first guess was used.

In order to convert from the Mach number to a velocity, the temperature must be known. While PLIF thermometry results could be used, the second Crocco-Busemann relation for non-adiabatic flows (Equation 2.24) flows was more easily integrated into the process. This equation relied on the velocity, but it could be re-written in terms of solely the temperature, edge velocity, and Mach number using $u = M\sqrt{\gamma R_{air} T}$

$$T = T_w + (T_{aw} - T_w)\frac{M\sqrt{\gamma R_{air} T}}{u_e} + (T_e - T_{aw})\frac{M^2 \gamma R_{air} T}{u_e^2} \tag{6.7}$$

Recall from Section 2.1.2.2 that the recovery factor is $r_{lam} = Pr^{\frac{1}{2}}$ or $r_{turb} = Pr^{\frac{1}{3}}$ and the adiabatic wall temperature is $T_{aw} = T_e\left(1 + \frac{r}{2}(\gamma - 1)M_e^2\right)$; note that in the "Turbulent/Front" case, where the flow was likely to be transitional and not fully turbulent, using r_{turb} was an unwanted but necessary approximation. The edge conditions were calculated using the measured tunnel conditions from the NALDAQ and oblique shock relations as was done in Section 5.4.2; this does introduce an inaccuracy in that this is not an ideal oblique shock due to the leading edge's bluntness, but it was deemed acceptable as the measured edge Mach number agreed with the theory satisfactorily well, even with the trips installed. From the results of the IR thermography campaign in Section 7.3.3, the wall conditions were set with the values in Table 6.2. It was clear from the results in Section 7.3.3 there was a high degree of variation between runs and exact placement in the heat flux, but here an effort was made to choose an intermediate value agnostic of the presence of a wake or trough. Similarly, in the "Front/Turbulent" case, the flow was transitional, not fully turbulent, yet the turbulent T_{aw} was used in calculating St, so the wall shear stresses calculated using this parameter at this location were somewhat unreliable. A Newton-Raphson iteration scheme with a tolerance of 1×10^{-4} and T_w as a first guess was used to solve the Crocco-Busemann relation.

Location	**Laminar**			**Turbulent**		
	T_w (K)	q_w (W/m^2)	St $(\times 10^{-3})$	T_w (K)	q_w (W/m^2)	St $(\times 10^{-3})$
Front	365	700	2.5	365	1150	1.75*
Middle	355	300	0.6	355	1100	1.25
Back	345	300	0.5	345	975	1

Table 6.2: Wall thermal conditions for Pitot campaign calculations. *Calculated assuming turbulent T_{aw}, though flow was transitional.

With the temperature known, the velocity could be calculated as $u = M\sqrt{\gamma R_{air} T}$. For turbulent flows, it was desirable to scale the velocity with inner variables. This could be accomplished with

the theory in Section 2.1.4.2. Summarizing, for $v^* = \sqrt{\frac{\tau_w}{\rho_w}}$, $u^+ = \frac{\bar{u}}{v^*}$, and $y^+ = \frac{yv^*}{\nu_w}$ one can calculate

$$u_{eq} = \frac{U_e}{a}\left(\sin^{-1}\left(\frac{2a^2\frac{\bar{u}}{U_e} - b}{Q}\right) + \sin^{-1}\left(\frac{b}{Q}\right)\right)$$

such that in the viscous sublayer layer $u^+_{eq} = y^+$ and in the log layer $u^+_{eq} = \frac{1}{\kappa}\ln y^+ + C$ with $\kappa = 0.41$ and $C = 4.9$, following [61, 239]. As is customary, these theoretical results were plotted alongside the data. As was done in Chapter 5, the viscosity used throughout these calculations was derived from the temperature, blending Keyes' and Sutherland's Laws in the cold and hot regions respectively.

6.6.5.1 Estimation of Wall Shear Stress

Critical to the calculation of u^+_{eq} is the wall shear stress τ_w. There are many ways to approach this parameter both theoretically and experimentally, and several are reviewed here. Perhaps the first choice would be to calculate it from $\tau_w = \mu\frac{du}{dy}$, and indeed using the results from the numerical boundary layer solver this was tractable; it did, however, rely on an idealized model of the boundary layer, which was not desireable. To better anchor the result to the data, one could use a modified definition of the Reynolds Analogy from White's derivation of the Crocco-Busemann relations, Equation 2.26. In this equation the skin friction coefficient is $C_f = \frac{\tau_w}{\frac{1}{2}\rho_e U_e^2}$. Also from Section 2.1.2 is the van Driest II approach, Equation 2.29, which White [293] says is the superior model, but this is limited to adiabatic flows. Thus only the Reynolds analogy could be solved entirely from the tunnel's conditions, which made it at the very least a useful validation for the boundary layer solver's result. The Reynolds Analogy and van Driest II (for comparison) approaches were performed using the IR data available in Table 6.2 and the NALDAQ's run data as edge conditions were not measured for the "Inner" turbulent runs. P was taken from the NALDAQ's run data and not the static pressure port for consistency, though this did remove any "Wake/Trough" dependence in the results, as well as any parameter changes across the trips' shock structure.

To capture such effects, it was preferable to directly measure the wall shear stress. A serious effort was made using a new IC2 DirectShear Optical Shear Stress Sensor OS-210 (serial no.

102107) with an IC2 Differential Optical Sensor Unit OSU-1011-H2U (serial no. 103602), but the signal did not clearly rise above the noise floor, likely due to the low-density nature of the ACE tunnel and the large range of the sensor used. Nevertheless, there were other, somewhat more circuitous ways to measure the wall shear stress that stemmed from Pitot data.

One such approach is the Clauser chart method [61], a simple method well-summarized in [292]. The conceit is to try different values of τ_w until a good fit of the slope of the log layer on an inner variable plot is achieved. For compressible flows, mathematically this means

$$\frac{u_{eq}(y)}{v^*} = \frac{1}{\kappa}\ln\left(\frac{yv^*}{\nu_w}\right) + C \tag{6.8}$$

Multiplying by $\frac{v^*}{u_e}$ yields

$$\frac{u_{eq}(y)}{u_e} = \left[\frac{1}{\kappa}\frac{v^*}{u_e}\right]\ln\left(\frac{yu_e}{\nu_w}\right) + \left[\frac{1}{\kappa}\frac{v^*}{u_e}\ln\left(\frac{v^*}{u_e}\right) + C\frac{v^*}{u_e}\right] \tag{6.9}$$

Because the skin friction coefficient can be written $C_f = 2\left(\frac{v^*}{u_e}\right)$ then one can write

$$\frac{u_{eq}(y)}{u_e} = \left[\frac{1}{\kappa}\sqrt{\frac{C_f}{2}}\right]\ln\left(\frac{yu_e}{\nu_w}\right) + \left[\frac{1}{\kappa}\sqrt{\frac{C_f}{2}}\ln\left(\frac{v^*}{u_e}\right) + C\sqrt{\frac{C_f}{2}}\right] \tag{6.10}$$

While this equation could be solved for the log layer points, in practice, it was far simpler and tolerably accurate to allow the user to guess different values of τ_w until the results lined up with the theoretical line $u^+_{eq} = \frac{1}{\kappa}\ln y^+ + C$. Wei et al. [292] noted this method is susceptible to variability in the constants κ and C, as well as Reynolds number effects, but here the flow was simple and at a constant Reynolds number, so it was deemed worth investigation. Neeb et al. [193] added Coles' [65] Law of the Wake to the equation to get more points to fit, but here this step was not taken. It is noted, however, in their comparison of different means of finding τ_w in a turbulent, Mach 6 boundary layer this fitting method performed well.

The final experimental approach attempted used a Preston tube to measure τ_w. A Preston tube is just a small Pitot tube placed directly on the surface, so here the first data point from every

laminar and turbulent "inner" sweep was used to calculate a wall shear stress. Preston [223] used a functional analysis to relate this measurement to τ_w through the incompressible, pipe flow formula[2]

$$\log \frac{\tau_w d^2}{4\overline{\rho}\overline{v}^2} = -1.396 + \frac{7}{8}\log \frac{(\overline{P}-\overline{P}_o)d^2}{4\overline{\rho}\overline{v}^2} \tag{6.11}$$

Here d refers to the outer diameter of the tube and an overline $\overline{X}$ denotes a variable at a constant property/incompressible condition. Hopkins and Keener [114, 137] would extend this theory to compressible boundary layers. They used $\frac{\tau_w d^2}{4\overline{\rho}\overline{v}^2} = \overline{R}_d \frac{\overline{C}_f}{8}$ and $\frac{(\overline{P}-\overline{P}_o)d^2}{4\overline{\rho}\overline{v}^2} = \overline{R}_d \frac{\overline{C}_p}{8}$ in Preston's equation to produce

$$\log R_d C_f = -1.283 + \frac{7}{8}\log R_d C_p \tag{6.12}$$

They also showed $R_d C_p \approx 1.4 R_{air} T_w \left(\frac{M_w d}{\nu_w}\right)^2$ such that only P, P_o, and T_w would be needed to calculate τ_w, where the pressures would be used to calculate the Mach number at the wall. The authors tuned this relation in non-adiabatic hypersonic flow and thus it was adopted here. There was some concern that the crimped tubing used here may have been problematic owing to the sensitivity probe size can have on the results, but Semper [243] successfully used a similarly crimped and sized tube for their work in the ACE tunnel and recovered a satisfactory value for τ_w. Furthermore, Preston recommended an internal-to-external diameter ratio of 0.6, though the authors in [91, 265] successfully used probes with ratios from $0.55-0.75$; again considering the minor axis of the probe to be d, then the probe used here had $d \approx 0.75$.

Finally, it is noted that from the work in Section 2.4.4 (ex.-[252]) that there was no expectation the skin friction would be altered downstream of the plasma, though the above techniques were repeated for both the plasma "On" and "Off" cases regardless.

6.6.6 Freestream Mach Number

At the beginning of this cumulative research effort, the settling chamber's Endevco 8540-200 High Temperature Pressure Sensor was re-calibrated, but not *in situ* due to the complexities of calibrating at an elevated temperature. Mai [168] took the additional step of manually adding

[2] In the original publication, the constant -1.396 was written with the convention $-1.396 = -2 + .604 = \overline{2}.604$.

temperature compensation factor into the sensor's results in post-processing, but from personal communication it seems this effort was generally not taken by other experimentalists at the NAL. Futhermore, in installing the *NO*'s injection pipe, the nozzle and settling chamber were disassembled several times. For these reasons, with a Pitot system installed in the tunnel, a test was conducted to confirm the freestream Mach number.

For this test the probe was centered in the vertical and spanwise direction, and it was roughly centered in the streamwise direction as well. The probe was constructed from the 3.175mm tube bent to be parallel with the flow; there was no need to crimp the opening or use the smaller inner tube as they would only reduce the probe's response time. After preliminary testing revealed no probe motion during the run, no further schlieren data was taken. The tunnel was ramped to $Re = [2,4,6] \times 10^6/\text{m}$, with a few seconds of delay at each Reynolds number to ensure the probe would settle at each condition.

Mach number from $P_{o,SC}/P_{o,TS}$ (SC-settling chamber, TS-test section) was calculated from isentropic flow relations, and $P_{o,TS}/P_{TS}$ from the Rayleigh-Pitot formula. The $P_{o,TS}/P_{o,SC}$ Mach number was calculated from normal shock relations [128]

$$\frac{P_{o2}}{P_{o1}} = \left[\frac{\frac{\gamma+1}{2}M^2}{1+\frac{\gamma-1}{2}M^2}\right]^{\frac{\gamma}{\gamma-1}} \left[\frac{1}{\frac{2\gamma}{\gamma+1}M^2 - \frac{\gamma-1}{\gamma+1}}\right]^{\frac{1}{\gamma-1}} \tag{6.13}$$

This equation was solved using the bisection method (see [97]) to a tolerance of 10^{-4} using $M = [5,8]$ as the initial guesses. It is noted that the equation monotonically decreases, at least in the relevant range of Mach numbers, which was useful for the bisection method. These results were compared to freestream PLIF measurements made by Buen [49], which included measurements of the ACE tunnel's freestream velocity and temperature fluctuations.

6.7 Optical Emission Spectroscopy (OES)

OES is a useful tool for determining the ro-translational, vibrational, and in some cases electronic, temperature of a plasma. It can communicate key chemical data such as species' formation and excitation; for example, Hsu [116] noted *NO* mixed into their flow for PLIF measurements

was electronically excited by their RF glow discharge. The emission is passed into a spectrograph which contains gratings that diffract the light into its constituent wavelengths. An entrance slit controls the amount of light passed into the instrument and controls resolution by ensuring a portion of the source is perfectly aligned with the instrument's internal optics. Mirrors focus and redirect the light, increasing the optical path to allow for more divergence and thereby better resolution. The light is eventually directed onto a charge-coupled device (CCD), where, because of the physical width of the detector and divergent nature of the beam, after careful calibration with a known source each pixel can be correlated different wavelength. Through this technique discrete lines in the spectra from specific ro-translation, vibrational, and electronic transitions can be isolated. A detector's resolution is inversely proportional to pixel width, and its total width sets the device's bandwidth. Fine resolution is required to resolve certain features like ro-translational transitions as they are very closely spaced.

It has been shown that the dominant spectroscopic peak in an air plasma was the second positive $N_2\left(C^3\Pi_u \rightarrow B^3\Pi_g\right)$ which manifests predominantly between $300-400$nm [116, 24]. In certain setups [192, 24] it was possible to see some electronic excitation of the first positive system of the nitrogen ions $N_2^+\left(B^2\Sigma \rightarrow X^2\Sigma\right)$ above ~ 390nm, and while this was unexpected for the low power glow discharge utilized here, it was worth avoiding quantitative analysis within this region. Indeed, one of the objectives of the broadband spectroscopic measurements was the determination of other excited species the N_2 ions or NO. Note that because of the fine spacing between vibrational levels in a given electronic state, the OES employed here was unable to directly measure vibrational temperature of the molecules in the ground electronic state.

6.7.1 Slit Function and Calibration

In order to infer temperature from a spectra, a fitting code is required. N2SPECFIT [300, 266] is one such program specifically written for N_2 plasmas by Dr. Charles DeJoseph and graciously provided to the NAL; further explanation of the code is provided in [267], and it was previously used at the NAL by Hsu [116]. In general, it works by comparing an experimental spectra to a theoretical result calculated using tabulated constants. By running successive iterations at different

temperatures and reducing the difference between the observed and synthetic spectra, the program can converge on a specific temperature. Several peaks must be fit as the ratio of their signal provides the temperature. Although N2SPECFIT must fit both vibrational and rotational peaks, it does not report vibrational temperatures; for such information, Specair [157, 158] is recommended. Pursuing vibrational temperatures was unnecessary here because they would only represent those of the elevated electronic state, not the desired ground state temperature.

An important input parameter for any fitting code is the spectrograph's resolution as it allows the program to not only simulate the plasma physics, but the effect of the actual instrument itself. Even an idealized, Dirac delta-like signal will be broadened as it passes through a spectrograph's slits, mirrors, and gratings; accurately measuring how this perfect signal distorts and passing it as an input allows the program to add in a proportional amount of experimental realism to its theoretical results via the so-called slit function. While it is calculable, here the resolution was measured as the full width at half maximum (FWHM) of a discrete peak. In order to measure this peak, four hollow cathode lamps (HCL) from Westinghouse Electric Corp. and Photron Pty. Ltd. were used; they are summarized in Table 6.3. All of the lamps were powered Photron Pty. Ltd. HCL power supply (P209). Each of these lamps produced at least one strong line in slightly different locations of the expected range of interest, so no matter where the spectrometer looked, a peak would be present. Assuming this peak was an ideal emitter and providing sufficient time to warm up ($5-10$min), the lamps allowed one to record a custom, experimental resolution measurement. It was important to change nothing about the spectrograph or CCD once the slit function was recorded unless another measurement was taken with the new settings. Using the HCLs was easier and safer, for both the detector and operator, than performing this measurement with a laser.

Additionally, the HCL's other strong lines were used to calibrate the detector by using tabulated data such as the National Institute of Standards and Technology Handbook of Basic Spectroscopic Data[3]; one needed to be careful to correctly attribute the lines from either the metal or the inert gas contained within each HCL. While this technique allowed a calibration, from pixel to wavelength,

[3]https://www.nist.gov/pml/handbook-basic-atomic-spectroscopic-data

Element	Manufacturer	Part No.	Dominant Wavelength (nm)	Current (mA)	Inert Gas
Hg	Westinghouse	N/A	228.47	15	Ar
Rh	Photron	P844	343.5	6	Ne
Ti	Photron	P861	364.3	18	Ne
Cu	Photron	P814	324.8	4	Ne

Table 6.3: Summary of HCLs.

to be performed before a run and wavelength data to be directly exported, in practice it could be difficult to find exactly what lines appeared as compared to those listed on standard tables; furthermore, for the most resolved data sets the bandwidth did not always include multiple lines across the entire detector. Because N_2 plasmas are so well characterized it was in these cases better to use the plasma's known vibrational peaks calibrate the spectra. Gilmore et al. [98] provided the requisite wavelengths for each transition; this is one of the sources used for the constants in N2SPECFIT's libraries and was therefore deemed reliable. In applications such as the present project where the plasma was turned off faster than one could feasibly perform a calibration, one had to perform the calibration during post processing and apply it to the existing data. Note that it was important to read the CCD's manual in order to make sure the proper polynomial fit was used; the one used here will be discussed shortly. As in [116], no intensity calibration was completed, though Stanfield et al. [266] took this step.

6.7.2 Technique for Broadband Measurements

Broadband spectroscopy probed three main questions. First, was the injected NO being electronically excited by the plasma, and would there be any other excited species like N_2^+? Next, would the trips affect the plasma's intensity? Finally, would there be any difference in the spectra between the negative glow and positive column regions? For example, Rajzer [224] stated that because of the high energy of the electrons emitted by the cathode, higher energy transitions should be visible in the negative glow than in the positive column, explaining the visible color difference between the two. It is sufficient to answer these questions qualitatively using spectroscopy, and the

enhanced bandwidth of an OceanOptics USB2000+ spectrometer was desired.

This spectrometer (CCD integrated into the spectrograph; serial no. USB2K10117) is sketched in Figure 6.8. The characteristics of the build used for the present experiments are included here. The usable bandwidth was approximately $175-875$nm and the theoretical resolution estimated by the manufacturer was 1.42nm. A fiber optic cable could be directly coupled via an SMA 905 connector, and the installed entrance slit was 25μm. It used OceanOptics' "Grating 01", which had: 600grooves/mm; a spectral range of 650nm; a blaze wavelength of 300nm; offered $> 30\%$ efficiency between $200-575$nm. There were no internal filters or lenses, but the detector had OceanOptics' "Mfg B" coating, an "Array Wavelength" of 4, a capacity (WC) of $62500e^{-}$, and 2048 pixels. When controlled by Ocean Optics SpectraSuite software, the spectrometer had a integration time range of $1ms-65s$ and a maximum acquisition rate of 30Hz under normal settings with the option to sample at $50-500$Hz using the program's high-speed mode.

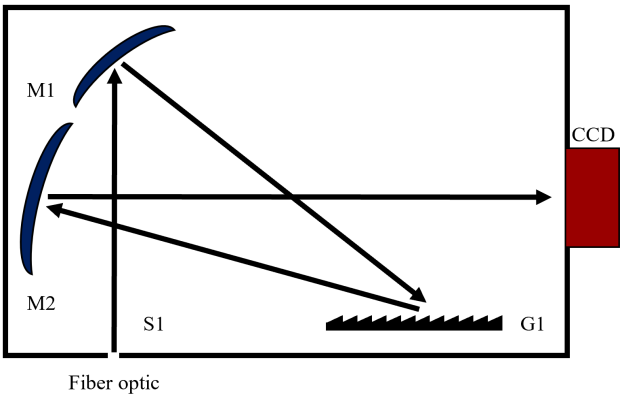

Figure 6.8: Diagram of the OceanOptics USB2000+ Spectrometer (S-Slit, M-Mirror, G-Grating).

The OceanOptics spectrometer was calibrated using the $Hg-Ar$ HCL; this same calibration was used for all subsequent data taken with the instrument. Once it was calibrated, the spectrometer was used to record the spectra from the remainder of the HCLs, yielding a database of reliable lines. Note that for each HCL, spectra were taken such that the strong gas lines and then weaker metal lines each took up the full range of the spectrometer; this was accomplished by adjusting

the integration time. While the gas lines saturated during the latter set of measurements, this provided the clearest picture of the metal lines, which overlapped better with the plasma's spectra. For all HCL measurements, a single frame of background-subtracted data was recorded for both conditions for each HCL.

With the spectrometer calibrated, the focus was shifted to recording spectra in the ACE tunnel. A series dummy runs were performed to optimize the placement of the fiber optic, as well as ensure the proper integration time to maximize the amplitude of the data and thereby improve the signal-to-noise ratio. Ultimately 15ms collections were taken for 15s of plasma-on run time, providing ample data to average out any imperfections; attempting to take more data caused problems with file corruption and was largely unnecessary. Background data was taken under the settings for each run to be subtracted from the full data; it was chosen to do this step manually, though SpectraSuite could do it automatically, to remain consistent between this spectrometer and the Andor EMCCD. All negative glow and positive column data were taken consecutively, so there was no variation in the signal due to minor adjustments from re-positioning the collimator; such physical considerations will be discussed shortly. When NO was introduced to study its behavior in the plasma, a 10% $NO-N_2$ mix was injected at 1378.95kPa. The moderate concentration (between that needed for PLIF thermometry and velocimetry) was selected for safety and conservation, and the higher pressure helped ensure better signal throughout the duration of the run. An image of the experimental setup for the broadband measurements is shown in Figure 6.9.

6.7.3 Technique for Rotationally-Resolved Measurements

In order to determine the rotational temperature of the bulk plasma, better resolution was required. To meet this objective, a Spex Industries 1877E Triple-Monochromator (serial no. 6768) was employed; this instruments is sketched in Figure 6.10. This device was donated to the NAL and brought into service with custom modifications by Dr. Andrea Hsu for the temperature measurements in [116]. The repairs mostly consisted of new stepper motors to control the wavelength selector mirrors. This spectrograph used a series of three gratings, three slits, and a 0.6m optical path to achieve excellent resolution. In the first "bandpass" stage, two gratings were mounted on

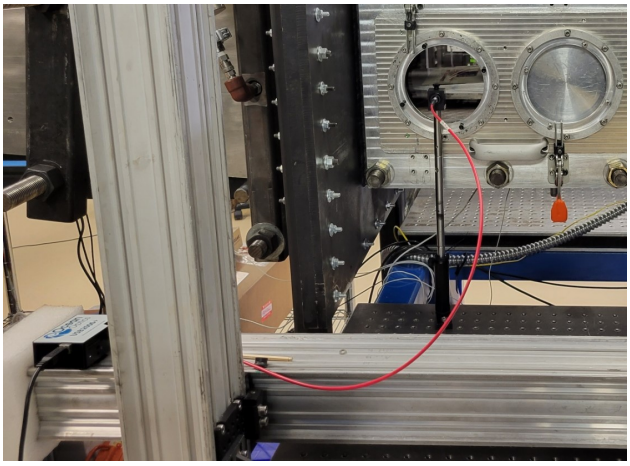

Figure 6.9: Picture of broadband OES setup. Note that for clarity in this picture the blackout sheet covering the window and fiber optic to block stray light was removed.

adjustable mounts controlled by two Anaheim Automation DPE25601 stepper motors, themselves controlled with the company's SMC60WIN program. Within this stage, empirically the first slit was found to reduce the intensity of the incoming light and the second reduced the bandwidth of the spectra; for the current application, best results were obtained when both were left entirely open. The second stage was a more standard layout. The inlet was controlled by a final slit which tuned the final resolution; here it was set to 40μm. There were three separate gratings on a carousel available for use: 600; 1200; and 1800lines/mm. Due to the instrument's age and background, little information was available regarding its gratings, bandwidth, theoretical resolution, *etc*.

An Andor Newton DU970N-BV EMCCD (serial no. CCD-8652) was coupled with the Spex spectrograph. This camera was back illuminated, water cooled, and electron multiplying to provide sufficient sensitivity for even single-photon events. The detector had 1600×200 square 16μm pixels for a total $25.6 \times 3.2\text{mm}^2$ image area. In electron-multiplying mode, it had an output node WC of $1.3 \times 10^6 \text{e}^-$ and a readout noise (RN) of $< 1\text{e}^-$ for a total dynamic range of $WC/RN > 1.3 \times 10^6$; in the conventional mode, these numbers were $3 \times 10^5 \text{e}^-$, 2.8e^-, and 1.07×10^5 respectively. The detector's spectral range at 298.15K was $200 - 1050$nm though it had a precipitous drop in quantum efficiency between $300 - 400$nm; regardless, in a similar glow discharge application with water cooling to the optimal 183.15K, Hsu [116] was able to get usable results for thermographic

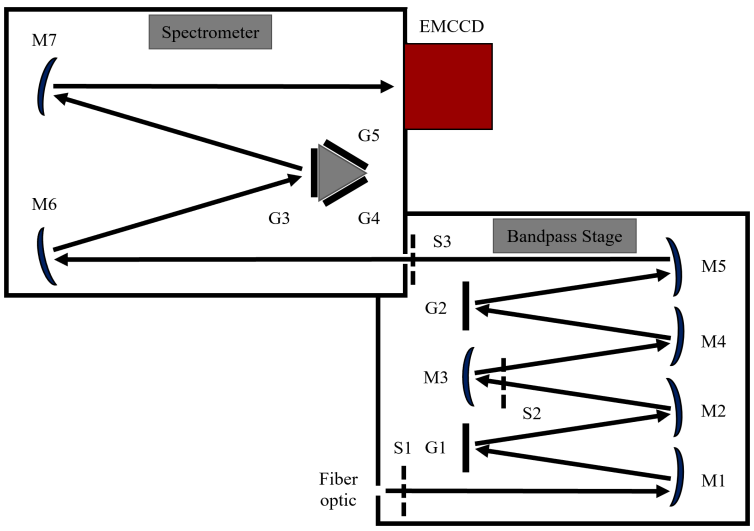

Figure 6.10: Diagram of the Spex 1877E Triple-Monochrometer (S-Slit, M-Mirror, G-Grating).

analyses. The EMCCD was controlled with Andor's Solis program.

Resolved measurements were conducted in an analogous fashion to the broadband collections. Alignment at the tunnel matched the broadband measurements due to markings on the table and a shaft collar on the optical post, and alignment at the spectrograph was set by adjusting the positioning of the fiber optic until the recorded signal from an HCL was maximized. Due to the complexity of this setup, the majority of the optimization was conducted in the quiescent air vacuum chamber as it allowed unlimited plasma-on time. Again, it was found that leaving the first and second slits fully open yielded the best results while the final slit reached a balance of resolution and signal at 40μm. Efforts to improve the resolution by closing the slit and compensating for the lower signal with increased intensification and/or integration times were ineffective. Setting the spectrograph to probe in the 380nm region with a 1800line/mm grating produced the clearest rotational lines. It is known that the transitions in this region are relatively weak [24], but the dropoff in intensity due to the fiber optic, Newton EMCCD, and potentially gratings below this value were significant and observable, and to go any higher would risk convolution with the first negative system. The Newton EMCCD was water cooled to -183.15K.

Solis, the control software for the Newton EMCCD, suffered from several bugs of which Andor

was made aware. Ideally, an "Accumulation" of background subtracted "Reference Data" frames would be collected, but this caused the program to crash. As a workaround, a "Kinetic" series of frames were taken; by selecting only one frame per series, and then repeating twenty times per acquisition, twenty separate frames could be taken and then summed in post-processing, mirroring the "Accumulation" mode. Background-subtracted data could not be collected due to another bug, so plasma-off data were recorded separately and then removed from the full spectra in post-processing. By taking twenty collections per run, not only was there enough data to reduce the noise via averaging, but the error for each pixel, represented by standard deviation, could be passed as an input into N2SPECFIT. To further improve signal-to-noise and to reduce the 2D image into a 1D trace as one would get from a linear pixel array, in Solis each frame was vertically binned, averaging all 200 pixels in the vertical direction. Solis' cosmic ray removal feature was also used to reduce noise. In both the vacuum chamber and in the ACE tunnel, a one second integration time with $4\times$ preamplifier gain and $100\times$ electron multiplication fully filled the range of the detector. Again, the integration time and intensification factors could have been fine-tuned, but these settings produced excellent results, yielded enough frames for averaging and statistical analyses, and with such a short duration of plasma-on time in the tunnel the amount of optimization that could feasible be performed was limited.

With these settings, the bandwidth of the high-resolution setup was empirically known to be $\sim$ 24nm. Even combining multiple spectra, the HCLs had insufficient strong lines across the range to provide a reasonable calibration. Thus the tunnel was first run and the data was recorded uncalibrated. In this region the second positive N_2 transition had vibrational bands at $(v', v'') = (0,2)$, $(1,3)$, and $(2,4)$ spanning $\sim$ 10nm. With the inclusion of a strong Hg line, the total spread was $\sim$ 15nm, so enough of the detector was covered to perform a calibration. It was found Solis' "Parabolic" calibration, recommended for when the control points are located near the center of the detector, outperformed the "Linear" and "Cubic" fits and thus was exclusively used. Once the calibrated pixel $\rightarrow$ nm data was saved, it could be applied to every dataset for each run: the plasma; the background; and the HCL. The added benefit of this approach is the strong Hg line could double

as an isolated, slender peak for measurement of the spectrograph's resolution, a required input for N2SPECFIT. The Newton EMCCD was re-calibrated for every run, as it was found to drift slightly and more than the OceanOptics spectrometer.

6.7.4 Experimental Considerations

There were several additional details worth discussing here. Perhaps the most important was the materials used for the transmission and measurement of UV light. As was mentioned previously, the Newton EMCCD begins to lose sensitivity below 400nm. While this was remedied by taking data at as high of a wavelength as possible and using a small bandwidth, the issue of optical losses persists in other equipment. For the tunnel window, the same UV transmissible fused silica window used for the *NO* PLIF was used for OES measurements. The light was collected by an Newport 77644 collimator which used an 11mm fused silica planoconvex lens to collimate the light; this ensured optimal transmission of light onto the fiber optic. Two separate Newport fiber optics were used, 78277 and 78303. The former "UV-VIS" cable was 1m long, had a 1mm diameter core, and was rated to transmit $280-1150$nm; because of its superior performance in the deep UV region, this cable was used for the broadband measurements with the OceanOptics spectrometer. The other "VIS-NIR" cable was 2m long, had a 1mm diameter core, and was rated to transmit $400-2200$nm; this longer cable was necessary to couple the larger Spex spectrograph to the wind tunnel, but its dropoff below 400nm was concerning. However, in reviewing the data listed by Newport, both cables performed identically $\gtrsim 350$nm, and the desired transition would be near 400nm due to the Newton EMCCD's limitations, so the cable's losses were deemed acceptable. All of this underscores the materials challenge of collecting UV spectra.

Background light was removed at the tunnel side of the fiber optic by using blank plugs in every window port except the one used for data collection and then wrapping the assembly, from the test section around the collimator, in an opaque, black, and anti-reflective plastic sheet. For collecting HCL data, a custom housing was built to entirely encapsulate the HCL and place a collimator directly above the cathode, ensuring optimal alignment and reducing all stray light. For the OceanOptics spectrometer, the fiber optic's SMA connector mounted directly to the instrument's

inlet, so no stray light was possible. For the Spex spectrograph, the cable's SMA was mounted into a Newport 77670 ferrule adapter, itself installed in another adapter and then positioned using a Newport 77612 mount such that the output from the fiber optic was as close to the slit as possible. The large openings into the spectrograph were covered with either aluminum tape or the same plastic sheeting.

Alignment at the tunnel interface was set visually. The collimator was positioned so the center of the lens was just above the plate's surface, where the plasma was known to be brightest; this put a portion of the lens below the test surface. The height was fixed using a shaft collar on the optical post supporting the mount, and the apparatus was itself screwed into the laser table beneath the ACE tunnel. The streamwise position and planarity were visually set, but the data collected had strong signal so the placement was accepted. While it was positioned as close to the window as possible, the collimator did not touch the test section to prevent any vibrations from being transferred to the optic. For consistency, for each spectrometer all measurements at each streamwise location were taken consecutively and when moving between spectrometers the exact placement of the mount on the breadboard tabletop was clearly marked so it could be returned to that position as accurately as possible. The inlet into the Spex spectrograph showed remarkable sensitivity to alignment, so to optimize it the stable output from an HCL was passed into the spectrograph as both the fiber optic was moved vertically and rotated about the vertical axis until the signal was maximized; once set, the position did not change throughout the entire campaign. Again, the alignment at the HCL and into the OceanOptics spectrometer were automatically set.

Finally, it is noted that the diameter of the collimator, 11mm, was larger than both the width of the electrodes and interelectrode gap, 6.35mm; it was also taller than the plasma. Unfortunately, this removed the ability to take spatially-resolved species and temperature measurements as was done by Stanfield et al. [266]. It was decided that aligning a custom focusing lens during a comparatively brief ACE tunnel run would be infeasible and the improved data would be beyond the needs of the present work; the same sentiment precluded the use of a 2D spectroscopy setup. Indeed, de-resolved bulk temperatures would be sufficient, despite the expected thermal gradients in

the plasma and the boundary layer because the goal was to provide an order of magnitude estimate of the plasma temperature. This in turn would allow the determination of the significance of any thermal perturbation and the likelihood of any species generation and excitation.

6.8 PLIF

The theory and general approach for the varying PLIF techniques described here are provided in Section 2.5. To review, flow visualization uses a single sheet of fluorescing NO to provide a spatially and temporally resolved snapshot of the flow and is useful for studying the state of the boundary layer as well as identifying any large flow features. Thermometry uses the ratio of signal between two sheets exciting specific transitions to return a map of both the mean and fluctuating the ro-translational temperatures; vibrational temeratures can also be measured by changing the transitions probed. It is noted that flow visualization is a natural consequence of PLIF thermometry. Molecular tagging velocimetry writes a line or grid of NO into an excited state, captures its fluorescence, then uses a plane to repeat the process for only those molecules "tagged" by the first beam; the displacement between the structures and the known time delay provides one (line) or two (grid) components of the mean and fluctuating velocity. Note the 2D approach would also provide the Reynolds stress.

To summarize, laser diagnostics allow temporally and spatially resolved measurements of off-body flow parameters without any interference from a physical probe body. This makes them ideally suited for high speed, turbulent flows, and their data can validate theory and other experimental results.

The laser diagnostic measurements were the purview of Zachary Buen's doctoral research and as such specifics on the hardware, calibration, experimental setup, and data analysis are best explained in their dissertation [48]. All data reduction was done by Buen with custom LabVIEW VIs. Only a comparatively brief overview is included here.

Note that all "Trough" measurements were conducted in the first trough off centerline, -3.42mm, as opposed to the second trough off-centerline at -10.26mm due to the complexity of moving the beams a full centimeter. When aligning the beams, the measured location was ~ -4.95mm, but it

was confirmed the beams fell precisely between the first and second trips at every streamwise test location; the source of the measurement discrepancy is unknown, but was likely due to the poor access to the test section during PLIF campaigns.

6.8.1 Infrastructure

Two injection seeded Spectra Physics PRO-290-10 Nd:YAG pump lasers provided 532 and 355nm beams, corresponding to the second and third harmonics, respectively. The injection seeder provided a linewidth of 0.003cm^{-1} [174] and the flashlamps could provide a maximum repetition rate of 10Hz. In order to get the proper wavelengths for the desired NO transitions (~ 226.5 and ~ 223.8nm) the beams were each sent into a Sirah Cobra Stretch dye laser. The YAG's second harmonic passed through a methanol-Rhodamine 610/640 dye solution and tunable grading optics to produce a beam in the range of $600-630$nm; this was then combined with the YAG's third harmonic in the Sirah's with a sum frequency mixing unit to provide the final desired output. Note that the methanol-Rhodamine 610/640 dye provided better performance for wavelengths necessary to probe excited vibrational states for applications like velocimetry, while a Rhodamine 640 in ethanol dye had better performance when probing ground vibrational states like those for thermometry. The linewidth was 0.08cm^{-1} [174] and the energy delivered to the tunnel was estimated to be $\sim 8\text{mJ}/\text{pulse}$. The lasers were controlled by interfacing the manufacturer's software with a custom LabVIEW VI.

The lasers were calibrated by scanning across a bandwidth with the beam in a small cell containing NO; this process was described well by McManamen [174]. As the laser passed through a transition, the fluorescence was recorded with a photo-multiplier tube. The signal was normalized against the beam power, captured by a photo diode with the portion of the beam reflected off a fused silica optic. The fluorescence *versus* wavelength was compared to theoretical spectra generated with SRI International's LIFBase. In order to calibrate an excited vibrational state, NO_2 was generated by mixing chilled NO and air, photodissociated with a YAG's third harmonic into a mixture containing excited NO [116, 235], and then probed with the beam being calibrated. Relevant theoretical spectra are shown in Figure 6.11; note the sub-Angstrom precision, and that no

$v' = 1 \leftarrow v'' = 1$ transitions were predicted for a "Cold" (60K) flow.

The beams were directed into the tunnel using 225nm dichroic mirrors, and they were shaped (focused into lines, planes, grids, etc.) using fused silica optics for high UV transmission. The tunnel's test section windows, both for passing the beam and observing the fluorescence, were fused silica as well. The beams were directed out of the test section through windows whenever feasible, but often the geometry of the problem made this impossible, and they reflected around the test section beneath the test surface.

Fluorescence was detected with up to two Princeton Instrument PI-Max4 1024i ICCD cameras. The cameras could be intensified up to $100\times$, had lens extenders to improve their resolution, and were liquid-cooled to $-20\text{deg}\,\text{C}$ to reduce noise. The cameras' $1024 \times 1024\text{pixel}^2$ active area was 2×2 binned to improve their repetition rate to 10Hz. This trade-off, of resolution for faster cycles, was necessary as the ACE tunnel only provides $\sim 30 - 50$s of run time, whereas the pulse systems used by Sanchez-Gonzalez [235] and McManamen [174] could run indefinitely. The spatial resolution was determined before a run by taking an image of a "grid card", a translucent piece of glass with a uniform grid, here $1 \times 1\text{mm}^2$, printed on it.

The cameras were controlled either with Princeton Instrument's LightField program, or by interfacing with LightField through a custom LabVIEW VI. All camera and laser timing was set with a BNC Model 575 Pulse/Delay generator. Data acquisition was automatically triggered by the same pressure drop which starts the NALDAQ, syncing the two programs to within a tenth of a second, a tolerable amount for this constant Reynolds number study.

In addition to the fluorescence, the NO tank pressure throughout the run was recorded, as well as the relative laser power. The latter was collected with a photodiode measuring the fluorescence of a 50mg Rhodamine 610/20mL dye when exposed to a portion of the output beam, split using a $92\% - 8\%$ transmission-reflection fused silica window. This was useful in isolating the effect of laser power fluctuations.

It is important to note the size of the laser beams and sheets as these dimensions limited the resolution of the laser diagnostics. The sizes were set to optimize power and signal and were

often constrained by optical access and interference; for example, single beams were nominally "waisted" (focused to a minimum size) just above the camera's frame and then allowed to expand towards the surface of the test article to limit reflection, scatter, and damage to the windows. Each of the diagnostics will be introduced in the proceeding subsections, but for ease of comparison the sizes are discussed here. For rotational thermometry measurements, the 2D sheets were $\sim$ 2cm wide and $\sim 800\mu$m thick; for vibrational thermometry measurements, the dimensions were $\sim$ 1.5cm and $\sim 800\mu$m respectively. The wide sheets maximized the amount of data provided by each test. For the velocimetry measurements, the "Write" beams varied in diameter from $\sim 0.5-1.25$mm and the "Read" sheets were $\sim$ 1cm wide and $\sim 800\mu$m thick; the reduced width of the "Read" sheet relative to the thermometry measurements improved signal as the laser power was more concentrated. The spanwise thermometry "Write" beams were a thicker $\sim 0.85-1.5$mm due to the divergence of the beam along the larger test domain, but the "Read" sheets were the same size as they were for the wall normal campaign.

It will be seen shortly that given the resolution of the cameras, the most experimental blurring in the thermometry measurements would be due to the thickness of the sheets. Still, the resolution in this spanwise dimension was excellent, and this coordinate was unimportant relative to the wall normal and streamwise directions. In both velocimetry campaigns, the streamwise measurement was the most directly affected by the beams' thicknesses. While this was of little consequence to the mean velocity measurements, it could impact the fluctuation measurements by effectively averaging all perturbations within the beam. This was addressed as best as possible by allowing a large degree of displacement between velocimetry "Write" and "Read" measurements so fluctuations could better manifest, using high resolution cameras, and careful estimation of the beams' centerlines during image analysis.

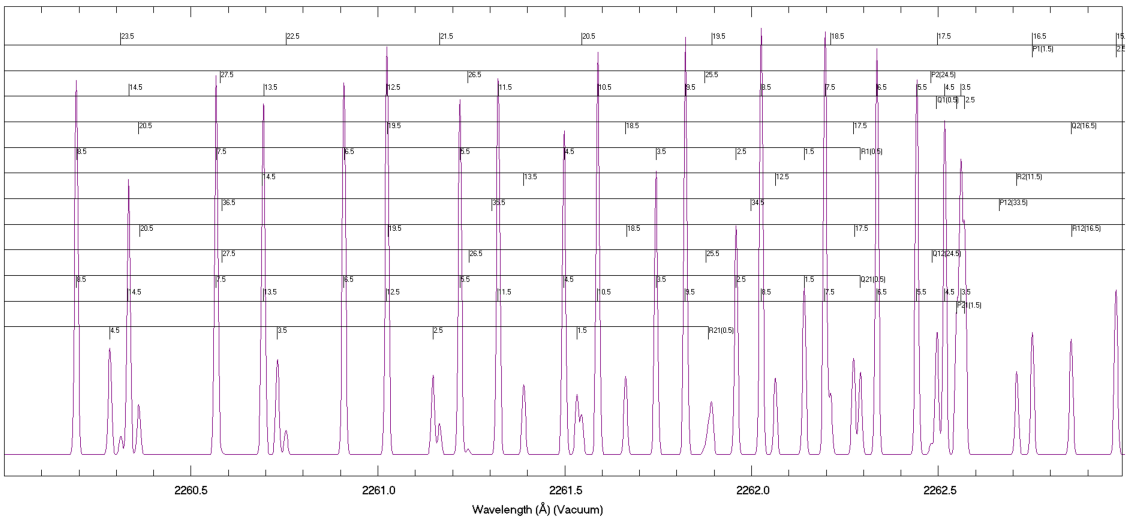

(a) "Hot" $v' = 0 \leftarrow v'' = 0$ spectra (thermal equilibrium at 350K)

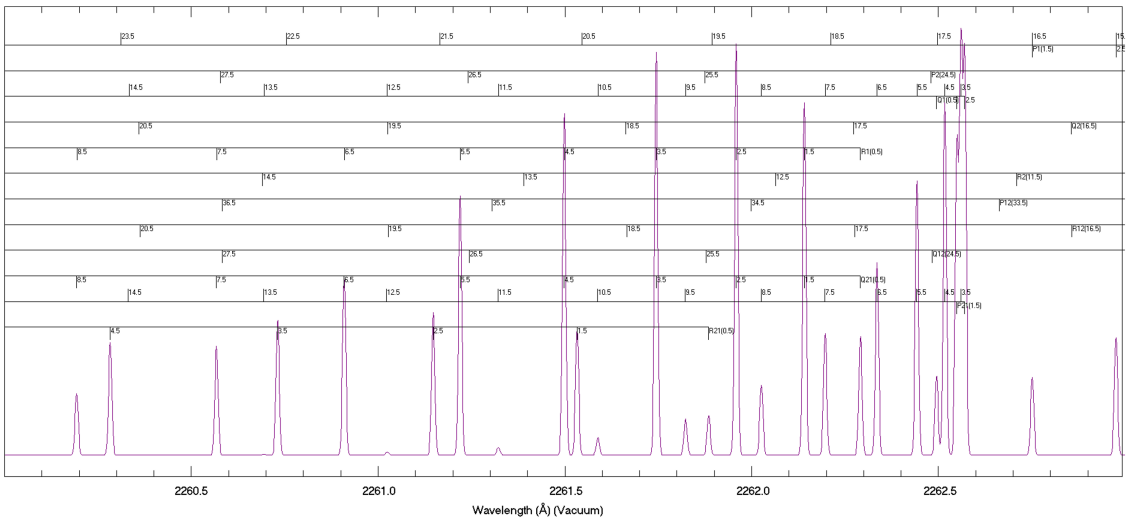

(b) "Cold" $v' = 0 \leftarrow v'' = 0$ spectra (thermal equilibrium at 60K)

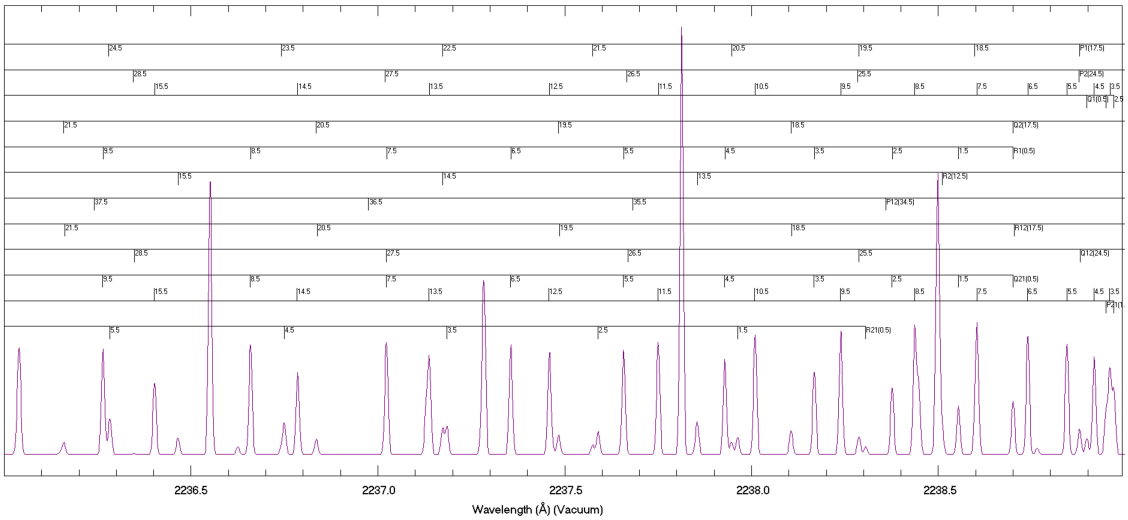

(c) "Hot" $v' = 1 \leftarrow v'' = 1$ spectra (thermal equilibrium at 350K)

Figure 6.11: Simulated *NO* spectra for two vibrational transitions using LIFBase. Rotational transitions are labeled.

6.8.2 Thermometry

The nominal conditions for ro-translational and vibrational thermometry are summarized in Tables 6.4 and 6.5 respectively. The "Cold" and "Hot" labels owe to the fact the lower J and v states are more populated at lower temperatures. For rotational thermometry, isolated J states were selected to provide high signal in the freestream and low signal near the wall ("Cold"), and *vice versa* for the "Hot" measurement. To visualize the effect, refer to the data in Figure 6.11(a) and (b) simulated at 350 and 60K, roughly showing the behavior near the test article's wall and freestream respectively. This effect was lessened in vibrational thermometry due to the high spacing between vibrational levels, and a relatively temperature invariant J state was used to prevent convolution with rotational heating as one moved towards the wall. For both thermometry campaigns, the time between the images was $\sim$ 500ns, which allowed sufficient time for thermalization any only allowed a displacement of ~ 4.25pix in the freestream (assuming $850\frac{\mathrm{m}}{\mathrm{s}}$ flow.)

Stage	**Transition**	**Intensifier**	**Gate (ns)**	**Resolution (μm/pixel)**
Cold	$J = 1.5\, Q_{21}/R_1$ $A^2\Sigma^+(v'=0) \leftarrow X^2\Pi_{\frac{1}{2}}(v''=0)$	100×	20	$100\frac{\mu\mathrm{m}}{\mathrm{pix}}$
Hot	$J = 8.5\, Q_{21}/R_1$ $A^2\Sigma^+(v'=0) \leftarrow X^2\Pi_{\frac{1}{2}}(v''=0)$	100×	40	$100\frac{\mu\mathrm{m}}{\mathrm{pix}}$

Table 6.4: Nominal laser and camera settings for PLIF ro-translational thermometry

To collect these data, two cameras we placed at opposite sides of the test section to collect data in the same region of interest. The "Cold" and "Hot" beams were passed through a 300mm spherical plano-concave lens to tighten the beam, then a 500mm planar plano-convex lens to sheet it; because the beams were separated by a time delay, they could be passed through the same optics to conserve space. The sheets were overlapped in the wind tunnel covering the region of interest. One camera collected the fluorescence from the "Cold" beam, and the other collected the signal

Stage	Transition	Intensifier	Gate (ns)	Resolution (μm/pixel)
Cold	$J = 4.5\, Q_{21}/R_1$ $A^2\Sigma^+(v'=0) \leftarrow X^2\Pi_{\frac{1}{2}}(v''=0)$	100×	3	$100\frac{\mu\text{m}}{\text{pix}}$
Hot	$J = 4.5\, Q_{21}/R_1$ $A^2\Sigma^+(v'=1) \leftarrow X^2\Pi_{\frac{1}{2}}(v''=1)$	100×	100	$100\frac{\mu\text{m}}{\text{pix}}$

Table 6.5: Nominal laser and camera settings for PLIF vibrational thermometry

from the "Hot" beam. In post-processing, a grid card image was used to ensure both cameras were aligned. This setup is shown in Figure 6.12.

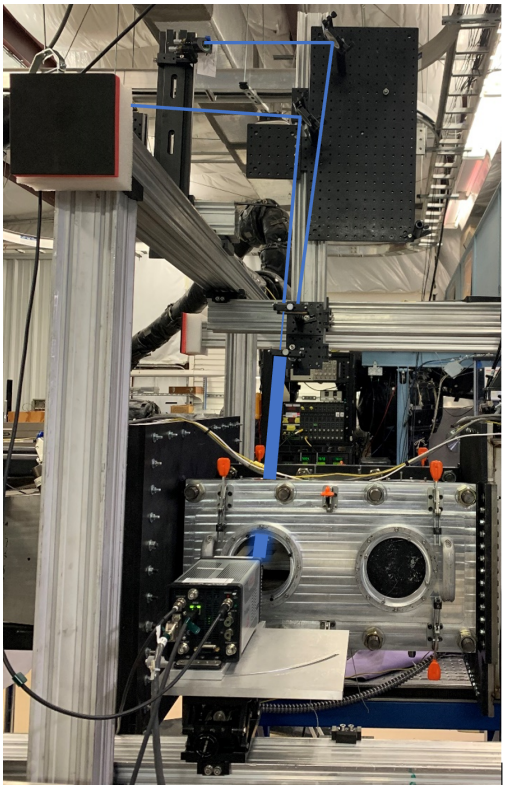

Figure 6.12: PLIF thermometry setup. Only one beam shown beyond focusing optic for clarity.

6.8.2.1 Additional Considerations

There were several interesting but complicating factors to take into account when performing the rotational and vibrational thermometry measurements. They are reviewed here.

Begin with the rotational thermometry measurements. Recall Figures 4.6(a) and (b), top-down freestream visualization experiments. These data showed a decrease in signal at the centerline of the NO cloud. Buen [49] hypothesized that this drop in signal was due to the formation of N_xO_y species as well as higher order clusters of the NO and these nascent species. The idea was the concentration of NO would be the highest along the centerline, and so it would be most susceptible to losses due to the formation of new species. To test this theory, Buen conducted simulations for a set of the most probable reactions and were carried out both in the settling chamber and at the variable temperature and pressure along the nozzle; they noted that the reaction rate constants were used outside of the temperature ranges for which they were found in the literature, owing to the ACE tunnel's low temperature. The injected concentrations tested were the limiting cases of 100 and 0.5%. The results suggested in the upper concentration limit N_2O_3 was the dominant nascent species, and in the lower concentration limit the concentrations of N_2O_3 and NO_2 converged. In both cases, however, there was little appreciable drop in the NO concentration, so Buen concluded the drop in signal was more probably due to the collisional quenching of the vibrationally excited NO by the nascent species, a process less covered by the literature.

It was soon discovered, however, these nascent N_xO_y species would have a critical impact on the PLIF thermometry technique. When seeding in gas above $\geq 1\%$ NO, Buen [49] calculated nonphysical wall and freestream temperatures. They attributed this error to either collisional quenching of the vibrationally excited NO or the photodissociation of the N_xO_y species due to the lasers. A calculation found that collisional quenching, while likely not insignificant, would be unable to generate the unrealistic temperatures. Buen surveyed the literature to study the photodissociation of the most likely N_xO_y species, as well as NO dimers, and found it was reasonable to attribute the higher-than-expected temperatures to these species. This effect would be enhanced as one increased the NO concentration, be it due to injection or moving closer to the centerline.

One of the benefits of injecting NO into the settling chamber instead of the boundary layer like the authors in Section 2.5.7 was that it allowed the assumption that the NO and air were fully thermalized. This meant the NO used was taken as a proxy for the bath temperature, so any uncertainty in T_{NO} had strong implications. Testing found a 0.5% NO mix injected at 1241.06kPa produced a uniform fluorescence signal and reasonable thermometric results. For vibrational thermometry, 15% NO was injected. This was necessary due to the lower signal of the vibrational readings. The photodissociation effects were more limited owing to the more invariant nature of the vibrational state (see the experiment in [205]), and the results were reasonable; still, ideally the experiments would have been conducted at lower NO concentrations.

Pragmatically, having such a low gas concentration limits the types of experiments one can perform because in order to obtain sufficient signal, on must open the gate for a long period of time. This is unacceptable for linear or point measurements like the VENOM measurements seen in [235] because the written structures can blur as they moved. It is noted that the pulsed facilities used by Sanchez-Gonzalez [235] and McManamen [174] were run with only an NO and N_2 mix, so no N_xO_y species or NO dimers could form. Here the data collection was restricted to planar images which could provide 2D average and fluctuating temperature maps and be relatively unaffected by blurring, especially in the slow-moving boundary layer. These data were collected for the laminar and turbulent cases, with the plasma on and off, at the upstream and downstream location, and in the turbulent wakes and troughs.

In order to scale PLIF thermometry data, one requires a known temperature. Ideally one could use the wall, but because the laser passed through glass, not PEEK, the wall temperature was not reliably known. Instead, for rotational thermometry measurements at the "Front" test location included data both above and below the bow shock. It was decided that $T_{pre-shock}$, as measured by the NALDAQ from compressible flow theory, would provide the anchor temperature; this was nominally $\sim$ 58K. As will be discussed in detail in Section 7.4.2.1, this approach yielded reasonable wall temperatures, but provided an unexpected measurement of $T_{post-shock}$. In the "Back" test location, the same $T_{post-shock}$ used in the "Front" was used, with no correction for the Mach waves

or trip shocks.

Finding an anchor temperature for the vibrational thermometry was uniquely challenging and required a degree of temperature modeling. It was discussed in Section 2.5 the temperature in a portion of the flow must be known in order scale the remainder of the image. A natural choice would be the wall, thanks to the no-slip conditions, but as was seen in Section 2.3.1.1 an unknown degree of vibrational slip was possible, and even likely. This left the edge as the only available choice, but estimation of the vibrational temperatures here was more complex than the case for the rotational thermometry; there were no isentropic flow relations on which one could rely.

To produce an answer, Buen [49] performed a simulation of the vibrational decay of the N_2, O_2, and NO mixture from the ACE tunnel's throat all the way to its test section. The process is summarized here, but details are provided in [49] and in Chapter 8. At the throat, it was assumed the mix was at thermal equilibrium at 358K, taken from the same set of conditions as the previous species formation simulation. The rate constants were calculated from

$$k_{VT,v=1} = \frac{k_B T}{pt(T)\left(1 - e^{-\theta_v/T}\right)} \tag{6.14}$$

where θ_v was the vibrational characteristic temperature and $pt(T)$ were constants taken from [53], following Hsu [116]; it was noted these rate constants fell precipitously with the decreasing temperature along the length of the nozzle. Candler et al. [53] provided equations for $k_{VV,v=1}$ as well. The change in the relative $NO^{v=1}$ due to collisions was

$$Rate_{VT,v=1} = \sum_i \left[n_{NO,v=1} n_i k_{VT} - \exp\left(-\frac{\Delta E_v}{k_B T}\right) n_{NO,v=0} n_i k_{VT,v} \right] \tag{6.15}$$

where $n_{NO^{v=1}}$ was the total number density of the vibrationally excited NO, n_i was the total number density of the collisional partner, and ΔE was the energy difference between the $v = 1$ and 0 states of NO. These equations were also used to consider VV collisions. Finally, the Boltzmann equation

(as reported in [49]) provided the vibrational temperature

$$N_{v=1} = N_{v=0} e^{-\frac{\Delta E}{k_B T}} \tag{6.16}$$

Note that a slightly different form, and the one actually coded, is provided in Chapter 8. For the three species, Buen considered twelve reactions, the same shown in Table 2.2. Each of the vibrationally excited molecules $N_2^{v=1}$, $O_2^{v=1}$, and $NO^{v=1}$ could relax through collision with an other ground state molecule, for a total of nine reactions. The three VV reactions considered involved $N_2^{v=1} + O_2$, $N_2^{v=1} + NO$, and $NO^{v=1} + O_2$.

The results showed the $NO\ VT$ and $NO - O_2\ VV$ reactions dominated the relaxation process, and of these the former was the most important; these data will be displayed and discussed in detail in Chapter 8. The N_2 and O_2 were vibrationally frozen at the nozzle's throat temperature of 358K, but $T_{NO^{v=1}} = 230$K; this established the inherent NEQ of the ACE facility and was shown in Figure 6.13. The vibrational temperature decay ceased as the expansion rapidly reduced the bath temperature, highlighting the temperature dependence of the rate constants. It was shown in Section 2.3.6 in the experiments of Nishihara et al. [205] that there was little change in vibrational temperature across a normal bow shock in an analogous wind tunnel environment, so here the effect of the weaker oblique bow shock, Mach waves, trip shocks, *etc.* could be discounted and the edge condition of $T_{NO^{v=1}} = 230$K was used in the subsequent calculations. It is noted Buen [49] did attempt to provide an upper limit on the calculations by assuming vibrational equilibrium such that $T_{NO^{v=1}} = 358$K. The results using $T_{NO^{v=1}} = 230$K were shown in Section 7.4.2.2 to follow the format in [49], but those for 358K were included in Appendix A.

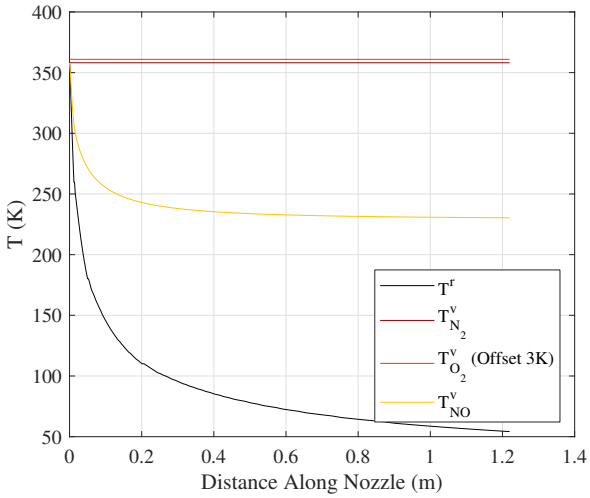

Figure 6.13: Simulated nozzle temperatures; note that $T^v_{O_2}$ was offset 3K to distinguish it from $T^v_{N_2}$.

6.8.3 Velocimetry

Velocitmetry relies in probing the *NO*'s rotational states within an excited vibrational state. Because of the relatively low number of *NO* molecules which can be "written" into this vibrational state as well as the low gas number density near the test article's hot wall, preliminary testing revealed a high gas concentration must be used to achieve usable signal. Even turning the YAG lasers to a power level which risked damaging the plate's glass was not a workable solution. In the end, a 75% *NO* injection at 1241.06kPa was selected; a higher concentration was not used because a noticeable pattern of diminishing returns made it not worth the safety risk and cost. Unfortunately, this meant one had to assume the nascent *NO* dimers and N_xO_y species did not effect the bath gas temperature and thereby the turbulence statistics excessively.

Traditional PLIF MTV offered useful insight into the environment's fluid dynamics without the complexity of coupled velocity and temperature measurements (VENOM). A single-line experiment provided the streamwise velocity profile; in reality, two lines from two YAGs were used simultaneously write two parallel lines and double the data collected. This technique provided both the mean and fluctuating velocity profiles. The cameras were placed on opposite sides of the test section to probe the same region of interest, and their overlap was confirmed using a grid card

image. One camera was used to collect "Write" images, and the other to collect "Read" images. A spherical plano-convex lens was used to focus the single-line "Write" beam for the 1D measurement (to save space, the same optic is used for both beams), but for the 2D measurements two micro-cylindrical lens arrays could be used to provide a focused grid of nodes. For both the 1D and 2D measurements, the lasers would probe the same transition, so only the optical setup would change. The "Read" beam was sheeted through the same planar focusing and sheeting lenses as was done for the thermometry measurement. The experimental setup is summarized in Table 6.6 and shown in Figure 6.14; note that these measurements were the only ones collected on the P_{21}/Q_1 branch as it was determined the Q_{21}/R_1 yielded better results. In order to include chemistry effects in the calculation of the true time delay between the images, a temperature profile must be known at the measurement location; this had the added benefit of allowing longer integration times on the weak read signal. While this step was taken in the final analysis, for now it is sufficient to say $\sim 2\mu$s passed between each image.

Stage	**Transition**	**Intensifier**	**Gate (ns)**	**Resolution (μm/pixel)**
Write	$J = 8.5\, P_{21}/Q_1$ $A^2\Sigma^+(v'=0) \leftarrow X^2\Pi_{\frac{1}{2}}(v''=0)$	100×	$3-15$	$50\frac{\mu\text{m}}{\text{pix}}$
Read	$J = 8.5\, P_{21}/Q_1$ $A^2\Sigma^+(v'=1) \leftarrow X^2\Pi_{\frac{1}{2}}(v''=1)$	100×	150	$50\frac{\mu\text{m}}{\text{pix}}$

Table 6.6: Nominal laser and camera settings for PLIF velocimetry

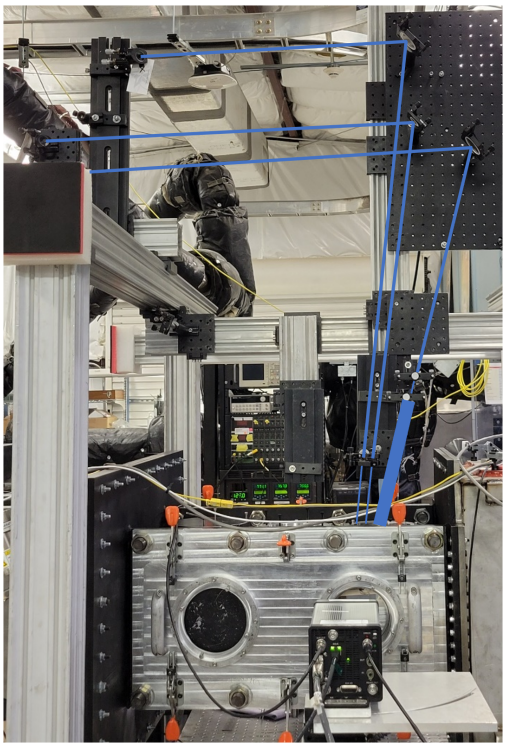

Figure 6.14: PLIF MTV setup. Two "Write" lines are used to double the usable data

6.8.4 Spanwise Velocimetry

As part of the broader velocimetry campaign, tests were conducted where the beam was passed horizontally across the span of the test article. These tests were carried out for both laminar and turbulent profiles at both the upstream and downstream test locations. The purpose of these tests was to look for any gradients across the test article, as well as to check the spanwise uniformity of the boundary layer. The effect of the plasma was not tested due to time constraints. For the laminar cases, the beam was positioned 2mm across the span of the test article, and for the turbulent cases, because the boundary layer was thicker, the beam was positioned 3mm above the surface. For these tests a 25% mix of NO was used as the beams were far enough from the wall so as to avoid the worst of the low density effects and to conserve the gas. A single camera was used to record both the "Write" and "Read" images through the use of the dual image feature, a special setting which allowed the camera to capture two images in rapid succession up to 2.5Hz, the frequency used here;

more information on this setting is available in [49, 174]. This camera was tilted 2.75° to match the slope of the test article. A $\sim 4\mu$s delay was used between the "Write" and "Read" beams. The rotational states probed were relatively temperature invariant. The optics used generally matched those from the boundary layer MTV campaign; a single spherical plano-convex lens focused the "Write" beam, and a set of two planar optics were used to sheet and focus the beam. The "Read" beam was not pitched 2.75° as it only needed to overlap with the "Write" line, which had little streamwise component. Further experimental conditions are included in Table 6.7, and the setup is shown in Figure 6.15; again, these measurements were taken on the Q_{21}/R_1 branch and not the P_{21}/Q_1 branch used for the wall normal measurements as it was found the former performed better. Note that additional data, spanwise flow visualization images originally taken as part of the model characterization discussed in Section 4.1.3, are included in the corresponding results section for this campaign, Section 7.4.2.4; whatever additional information regarding the simple setup for these few images that was not covered in Section 4.1.3 is included alongside their analysis.

Stage	**Transition**	**Intensifier**	**Gate (ns)**	**Resolution (μm/pixel)**
Write	$J = 4.5\, Q_{21}/R_1$ $A^2\Sigma^+(v'=0) \leftarrow X^2\Pi_{\frac{1}{2}}(v''=0)$	100×	3	$43\frac{\mu\text{m}}{\text{pix}}$
Read	$J = 4.5\, Q_{21}/R_1$ $A^2\Sigma^+(v'=1) \leftarrow X^2\Pi_{\frac{1}{2}}(v''=1)$	100×	150	See above

Table 6.7: Nominal laser and camera settings for spanwise PLIF velocimetry

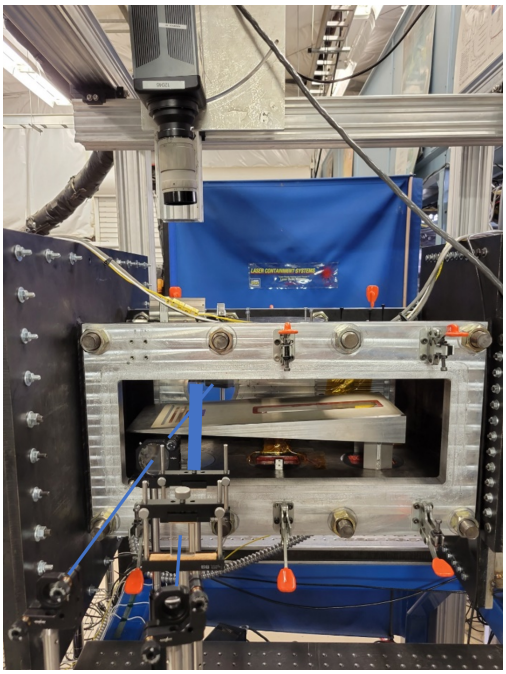

Figure 6.15: PLIF spanwise MTV setup.

7. RESULTS

All available data are presented below. When possible, patterns between the experiments are identified, but a full comparison is saved for the final section. Each diagnostic is introduced by its purpose in the broader study and the test matrix used to meet these goals; when relevant, the plasma's performance for each run in the campaign is also included via a figure and table. Due to the breadth of the techniques used and to help identify correlations, for each diagnostic the data and motivation are summarized below. The purpose is to provide a key by which this lengthy chapter can be better navigated. The final section of this chapter is reserved to compare results obtained from different techniques in order to identify patterns or discrepancies.

- Boundary Layer Solver: Numerical results from the boundary layer solver described in Chapter 5.
  - Boundary Layer Solver
    * Motivation: Build turbulence modeling intuition through experience; provide values for all relevant flow parameters throughout the test domain; study effect of AEF model as compared to gradient diffusion approach
    * Data: 2D plots of velocity, temperature, and Mach number; streamwise plots of wall heat flux, boundary layer thickness, and wall shear stress; boundary layer plots of velocity, temperature, Mach number, total enthalpy, and number density; inner variable plot of velocity; grid convergence study and validation test
- Test Article Characterization: Preliminary experiments studying specific features which informed decisions for the main campaign, examples being the polarity of the electrodes and the size of the trips.
  - Plasma Characterization

    - Motivation: Maximize plasma power; study effects of system parameters (polarity, Reynolds number, trips, ballast resistance, *etc.*); determine if normal or abnormal glow; observe any features, nonuniformities, or trends; measure breakdown voltage
    - Data: Traces of current, voltage, and power while varying system parameters; images of the plasma; table of breakdown voltages
  - Trip Sizing Study
    - Motivation: Determine efficacy of different trip designs
    - Data: Stanton number traces at "Back" test location as functions of Reynolds number and time
  - Leading Edge Uniformity and Roughness
    - Motivation: Check for any nonuniformities in the test article; determine roughness at critical leading edge
    - Data: Map of leading edge surface; table of leading edge roughness (various techniques)

- Flow Physics Data: Classic diagnostics and physical probes which studied the development of the boundary layer as a whole and specific elements, such as trips' wakes.
  - Oil Flow
    - Motivation: Ensure streamlines were straight in test area (no impinging shocks, edge effects, pressure gradients, suction/blowing, etc); study evolution of streamlines and flow structures, especially turbulent wakes; study trip behavior and breakdown process
    - Data: Oil flow images at all test locations and flow conditions; normalized spanwise intensity traces to show temporal evolution; turbulent images at "Front" test location to show temporal evolution

- Schlieren Imaging
  - Motivation: Determine the state of the boundary layer; measure boundary layer thickness for comparison with other techniques (ex.- boundary layer solver, PLIF, *etc.*); study complex behavior at trips, including transition if possible; confirm stable stagnation point at leading edge; confirm quality of test environment (no impinging shocks, strong Mach waves, suction/blowing, *etc.*); look for pressure bubble due to plasma
  - Data: Instantaneous and mean images at all test locations; instantaneous and mean images at leading edge
- IR Thermography
  - Motivation: Measure wall condition (temperature, adiabatic/isothermal) for other techniques (numerical boundary layer solver, PLIF, wall shear stress, *etc.*); observe behavior and location of flow structures, especially wakes; determine degree of plasma heating
  - Data: Temperature, heat flux, and Stanton number traces at all test locations and flow conditions; full view temperature images to show effect of internal wall boundary condition (thermocouple, flow, metal, *etc.*); streamwise temperature traces to study plasma heating
- High Frequency Pressure Transducer
  - Motivation: Determine flow condition at each test location; look for any dominant frequencies which could inform transition process; compare spectra in wake *versus* trough; test novel hardware in ACE wind tunnel
  - Data: Temperature images and traces with Kulites installed; spectral content at all test locations and flow conditions, but without plasma
- Pitot Probe
  - Motivation: Directly measure Mach number, use it to calculate temperature and

velocity profiles for comparision with other off-body techniques (numerical boundary layer solver and PLIF); measure, calculate, or estimate wall shear stress to scale inner variable plots; use inner variable plots to compare with turbulent boundary layer theory; look for effect of plasma or wake *versus* trough; confirm wind tunnel performance

    * Data: Plots of Mach number, temperature, velocity, and inner variable velocity at all test locations and flow conditions; wall shear stress from various techniques; freestream Mach number from various techniques

- Advanced Optical Techniques: Nonobtrusive diagnostics which used techniques novel to the ACE tunnel to study the plasma and boundary layer.

  - Optical Emission Spectroscopy

    * Motivation: Study effect of laminar *versus* turbulent flow; study effect of negative glow *versus* positive column on plasma; look for NO excitation in the plasma; estimate the bulk temperature to ensure no large thermal perturbations

    * Data: Broadband and resolved spectra of negative glow and positive column; estimations of bulk ro-translational temperature in negative glow and positive column; measurement of HCL spectra

  - PLIF

    * Motivation: Non-obtrusive, spatially and temporally resolved techniques provide excellent measurement opportunities for off-body parameters, informing the effect of the trips and plasma; measurement of turbulent statistics and analysis of system's thermochemistry to look for effect of vibrational nonequilibrium on the flow; produce a detailed dataset for turbulence model development

    * Data: Ro-translational and vibrational temperature maps; wall normal and spanwise velocity profiles; fluctuations for turbulence statistics; raw frames for flow visualization; combined temperature and velocity data for Mach number and in-

ner variable plots (comparison to numerical boundary layer solver and Pitot probe results)

7.1 Boundary Layer Solver Results

The results of the boundary layer solver covered in Chapter 5 are shown below, along with a discussion of their implications. But first, the requisite grid convergence and validation study is reviewed.

7.1.1 Grid Convergence Study and Validation

With any CFD, it is necessary to ensure the grid itself is not introducing error; here this was accomplished by showing there was little change in the results calculated using a "Medium" and "Fine" grid, meaning the former was acceptably resolved. For new codes, the results should be compared to either experimental data or well-established theroy to validate the code. These checks are now discussed.

The simulations were run for both "Laminar" and "Turbulent" boundary layers, with the "Cebeci-Smith" and "Gradient Diffusion" models used for the latter. The domain covered $25-125$mm in the streamwise direction and $0-25$mm in the wall-normal direction with transition forced at the test article's trip location, 63.5mm. The "Turbulent" grid used Malik clustering with half of the points placed below the critical value of 3mm; this was selected after preliminary testing with the laminar boundary layer. Standard air at the test conditions was used (which will be explicitly tabulated in a later subsection), as was the final wedge half-angle of 2.75°. The Predictor-Corrector tolerance was set to 1×10^{-6}.

A total of three different grids were produced for both the "Implicit" and "Explicit" schemes, "Coarse", "Medium", and "Fine"; thus there were six in total. The stability requirements of the "Explicit" scheme required far finer streamwise steps than the "Implicit" scheme, and limited the wall-normal resolution. These grids are defined in Table 7.1. Note that in the streamwise direction, the streamwise step within the domain was the controllable parameter, not the number of streamwise points. This choice made it easy to add resolution as needed. Meanwhile, in the wall-

normal direction the number of wall-normal points was used as the controllable parameter because clustered spacing made the wall-normal step a variable.

Grid	**Implicit**		**Explicit**	
	$X \times Y$	ΔX (mm)	$X \times Y$	ΔX (m)
Coarse	51×50	2	10001×50	1×10^{-2}
Medium	251×250	0.4	20001×75	5×10^{-3}
Fine	1251×1250	0.08	40001×100	2.5×10^{-3}

Table 7.1: Grids for convergence study; here X denotes the streamwise coordinate, and Y denotes the wall-normal coordinate.

The results of the grid convergence study are shown in Table 7.2. The fidelity of a grid was quantified by comparing its results to those of the finest mesh, which was assumed to be the most accurate. For example, for the "Coarse/Turbulent/Implicit" grid the u, v, and T data from the finest turbulent, implicit run were interpolated to match the coordinates of the test grid, then the Euclidean norm of the absolute value of the difference was calculated. The data were taken from the ends of the domains to allow errors to accumulate and were normalized by the edge values. This process mirrored the Predictor-Corrector convergence procedure in the boundary layer solver itself (see Chapter 5), and these three variables were chosen as they were the primary variables calculated directly from the conservation equations; again, v was normalized by u_e as v_e could be near zero. From the results in Table 7.2, it seemed that in order to keep the cumulative error below 1% the computational effort required for the "Medium" grid was necessary. This grid performed well for all four combinations tested, and should be used for future simulations. A more thorough grid convergence study, one to test if fewer points could be used or the error had become asymptotic, was deemed unnecessary for the efficiency and fidelity required here.

Validation was conducted analogously to the grid convergence tests. The exact data was the self-similar solution for laminar boundary layers described in Chapter 5, calculated at the end of the test grid's domain. From here the treatment was the same as for the grid convergence study,

Scheme	Coarse		Medium	
	Laminar	Turbulent	Laminar	Turbulent
Implicit	0.81%	1.57%	0.12%	0.08%
Explicit	0.37%	1.00%	0.12%	0.24%

Table 7.2: Grid convergence study results.

with the self-similar data taking the place of the "Fine" grid. Unfortunately, this approach was applicable only to laminar data, so the turbulent case was ignored; these results would need to be compared against the experimental data (schlieren, IR thermography, Pitot pressure, *etc.*), and this was periodically done throughout this chapter. The results are shown in Table 7.3.

Initially the data suggested, unexpectedly, that the finer the grid the worse the code's performance. A more careful inspection, however, revealed that instead the inherent differences between the finite difference and self-similar approaches were becoming apparent. Consider the implicit, laminar case. Table 7.2 reports a difference between the "Medium" and "Fine" grids of 0.12%. Now, in Table 7.3 the differences between the "Medium" and "Fine" grids and the self-similar solution were 1.1% and 1.23% respectively; thus the "Fine" grid was 0.13% more inaccurate than the "Medium" grid, nearly identical to the 0.12% difference between the two grids themselves. The same pattern was repeated throughout the data; for example, the "Medium/Laminar/Explicit" case was 0.12% off from the "Fine/Laminar/Explicit" grid, and was 0.10% more accurate than the Fine grid as compared to the self-similar solution. This suggested there was some baseline discrepancy between the self-similar and finite difference calculations; in the proceeding section v was identified as the likely source. Such a systematic error may be exacerbated by finite differencing with finer and finer grids, which somewhat diminished the efficacy of the studies at hand; interpolation between the self-similar and fine grids was another potential source of error. Looking at the overall objective and balancing the comparisons between the "Fine" and self-similar grids, it was sufficient to say the "Medium" grid provided a good trade off between speed, resolution, and fidelity to both optimized finite difference and self-similar solutions.

Grid	Coarse	Medium	Fine
Implicit	0.55%	1.10%	1.23%
Explicit	0.67%	0.83%	0.93%

Table 7.3: Validation study results.

7.1.2 Full Boundary Layer Simulations

Simulations were run studying the effect of the boundary layer, numerical scheme, and heat flux method. The domain covered $25-405$mm in the streamwise direction and $0-25$mm in the wall normal direction. For turbulent simulations, transition was forced at 63.5mm, matching the trip location on the physical test article. For all tests, the "Medium" grid was used (see Table 7.2); though the streamwise step size stayed the same, now there were 951 and 76001 streamwise grid points due to the larger domain. For turbulent codes, the "Cebeci-Smith" eddy viscosity model was exclusively used, though the heat flux model varied between the gradient diffusion and AEF approaches. The Predictor-Corrector tolerance was set at 1×10^{-6}.

The simulated flow matched the test conditions shown in Table 4.1: $M=5.7$; $P_o=496.4$kPa; and $T_o=430$K. These provided a flow Reynolds number of $Re_\infty=5.51\times10^6/$m. The discrepancy between this Reynolds number and that calculated by the NALDAQ was due to the low-temperature correction for viscosity in the boundary layer solver which was absent from the NALDAQ; it was acceptable because it only meant the code better matched the actual flow physics, not the tunnel's estimation thereof. The test article's 2.75° half-angle was included, and the calculated shock angle was 11.95°. The pre- and post-shock conditions are summarized in Table 7.4. Preliminary IR thermography data showed an isothermal wall condition at 350K was an appropriate boundary condition.

The results are shown in Figures 7.1 through 7.4. The 2D plots show the expected behavior, that the boundary layer grew with $\sqrt{x}$. The v data required some analysis because there was a jump at the leading edge and then decay along the plate, as well as nonphysical results exactly at the numerical trip.

Location	M	P (Pa)	T (K)
Pre-shock	5.7	430.07	57.35
Post-shock	5.35	626.89	63.97

Table 7.4: Simulation pre- and post-shock conditions.

The discontinuity at the start of the domain was due to a discrepancy between the self-similar prediction for v at the inlet plane and the finite difference result at the next location; Figure 7.1 shows it mostly dissipated within a few iterations. The streamwise decay in the freestream and noise at the trip location were both attributed to a lack of a freestream boundary condition for the conservation of mass equation. Consider the laminar case. As the boundary layer grew, the mass flow at a single plane decreased. In order to prevent violating the conservation of mass, less mass could be ejected out of the vertical domain by v. Again, v was the only conservation variable which could perform such a task because it was not constrained by a freestream boundary condition. Thus v_e could change along the domain. This effect was exacerbated at the trip location, where the boundary layer instantly, artificially, and dramatically grew. However, while the total boundary layer thickness increased, the slowest portion suddenly shrunk, forcing v_e to "suck in" mass from the upper boundary and providing nonphysical negative velocities. Eventually, the code corrected, v_e was effectively re-initialized for a turbulent boundary layer, and the streamwise decay occurred once again, this time more rapidly due to the faster-growing turbulent boundary layer. A numerical transition process would help smooth the streamwise v component, but because $v \ll u$ and the error in v was normalized by the much larger u_e, v was not very impactful and convergence was achieved even with some error.

The plots of heat flux (7.1(e) through 7.4(e)) show several interesting trends. To begin, it was immediately clear that the laminar boundary layer provided less heating than the turbulent one. This was entirely in line with theory and owed to the increase in dissipation due to the presence of eddy viscosity. The general decay in both laminar and turbulent cases owed to the growth of the boundary layer; as the thermal boundary layer thickened, the gradients near the

wall became less severe and thereby reduced the heat flux. For the velocity profiles of laminar boundary layers, $\delta(x) \propto \sqrt{x}$ [6], so the expected trend for the thermal boundary layer was fastest growth near the leading edge followed by a leveling off along the plate. Therefore heat flux should decay rapidly near the leading edge before reaching a "steady state" towards the end of the plate, which was exactly what the data show. The discontinuities and bumps in heat flux at the transition point were due to the harmonic nature of the conservation equations and needed to be corrected with numerics too advanced for the present code. The heat flux data could be used to check the state of the boundary layer. IR thermography could provide the heat flux along the plate, and if the value better matched the turbulent prediction, then one could expect the flow to be turbulent and *vice versa* for the laminar prediction; where the heat flux quickly jumped between the two lines denoted transition. As was expected from the DNS [118] covered in Chapter 3, "AEF" and "Gradient Diffusion" approaches for this ZPG environment predicted similar results for the wall normal component of the heat flux, as well as for the off body variables; studying the streamwise component of heat flux would have shown a larger discrepancy.

The plots of boundary layer thickness (7.1(f) through 7.4(f)) were useful for sizing the boundary layer before schlieren, PLIF, and Pitot measurements. It was useful to have an estimate of the boundary layer size before setting up these techniques to ensure they captured the entire region; once the measurements were complete, they could be used to validate the code. For the laminar case, the $\delta_{99.5\%}$ boundary layer thickness was calculated from u, T, and H_o; for the turbulent cases, the latter was omitted due to its esoteric nature and the complex shape of the total enthalpy profile.

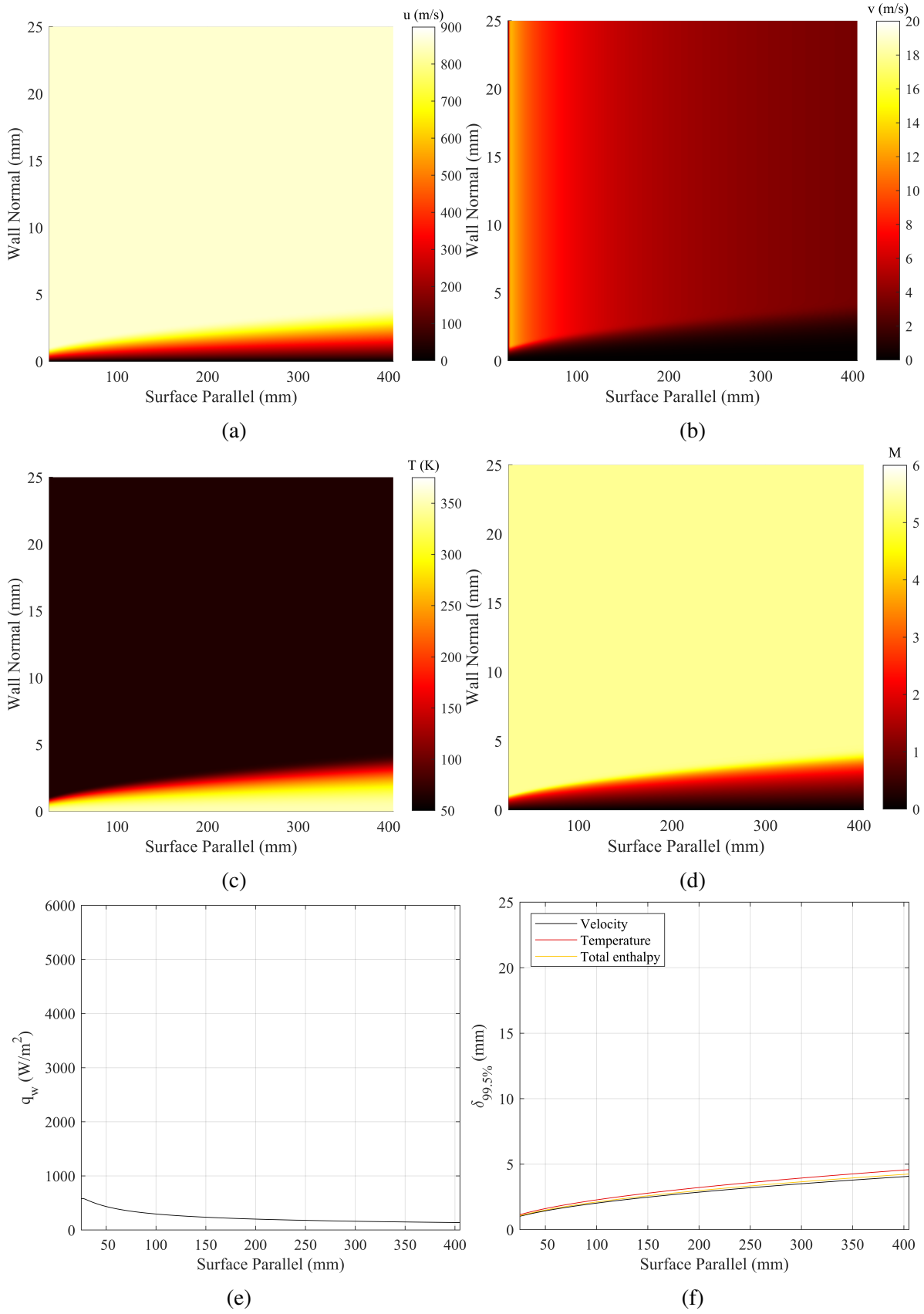

Figure 7.1: Laminar boundary layer implicit simulation results.

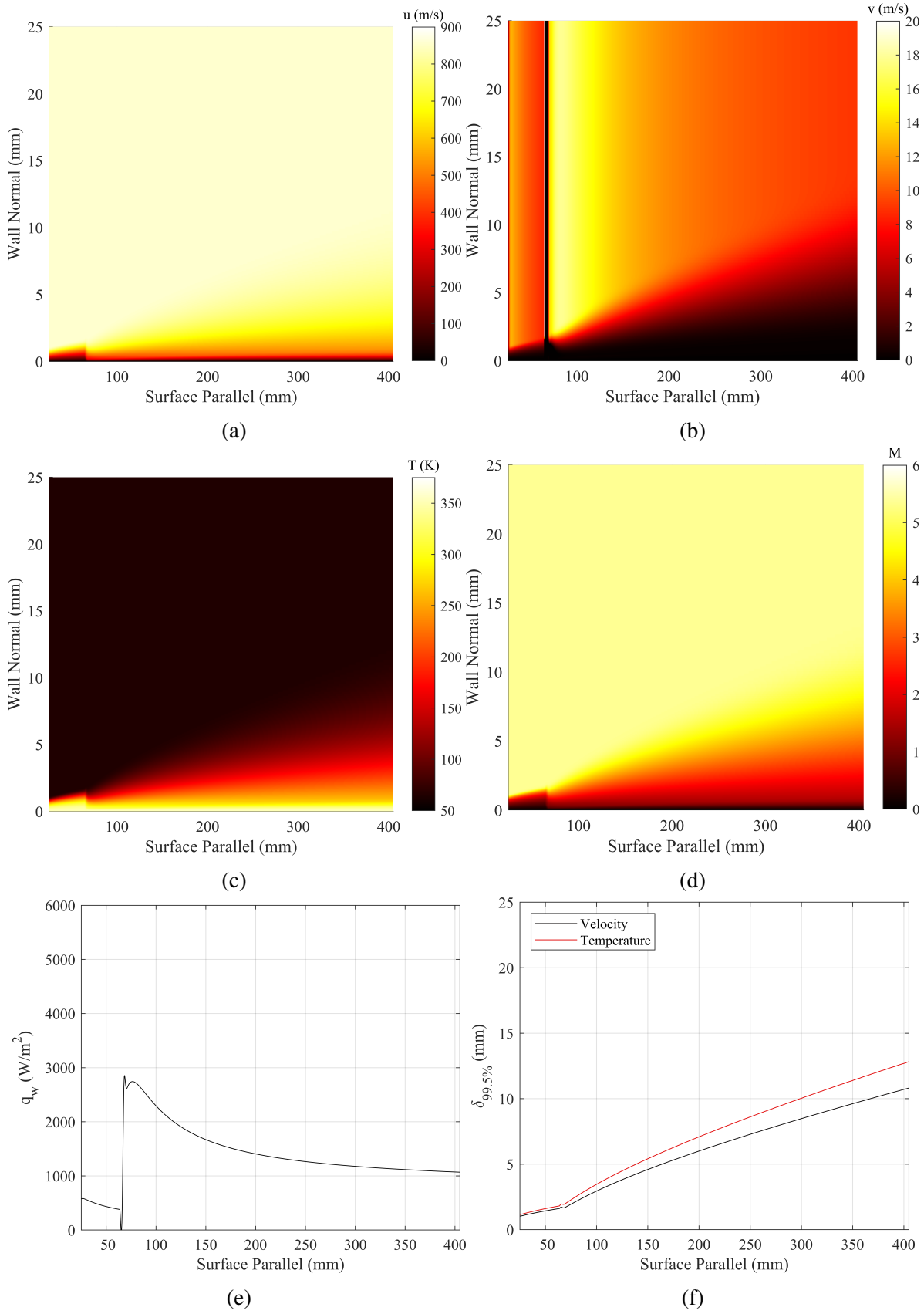

Figure 7.2: Turbulent boundary layer implicit simulation results.

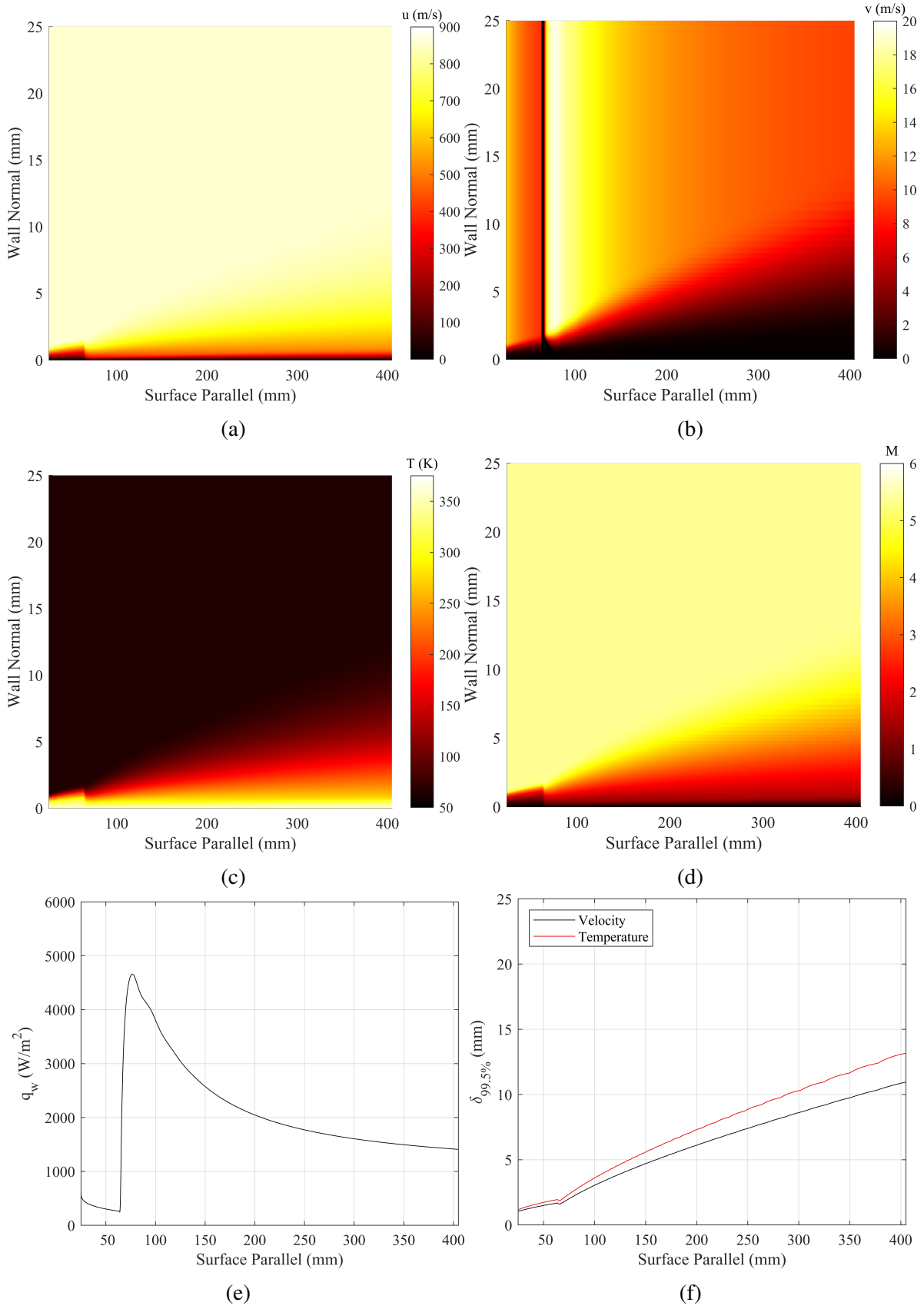

Figure 7.3: Turbulent boundary layer explicit simulation with gradient diffusion heat flux model results.

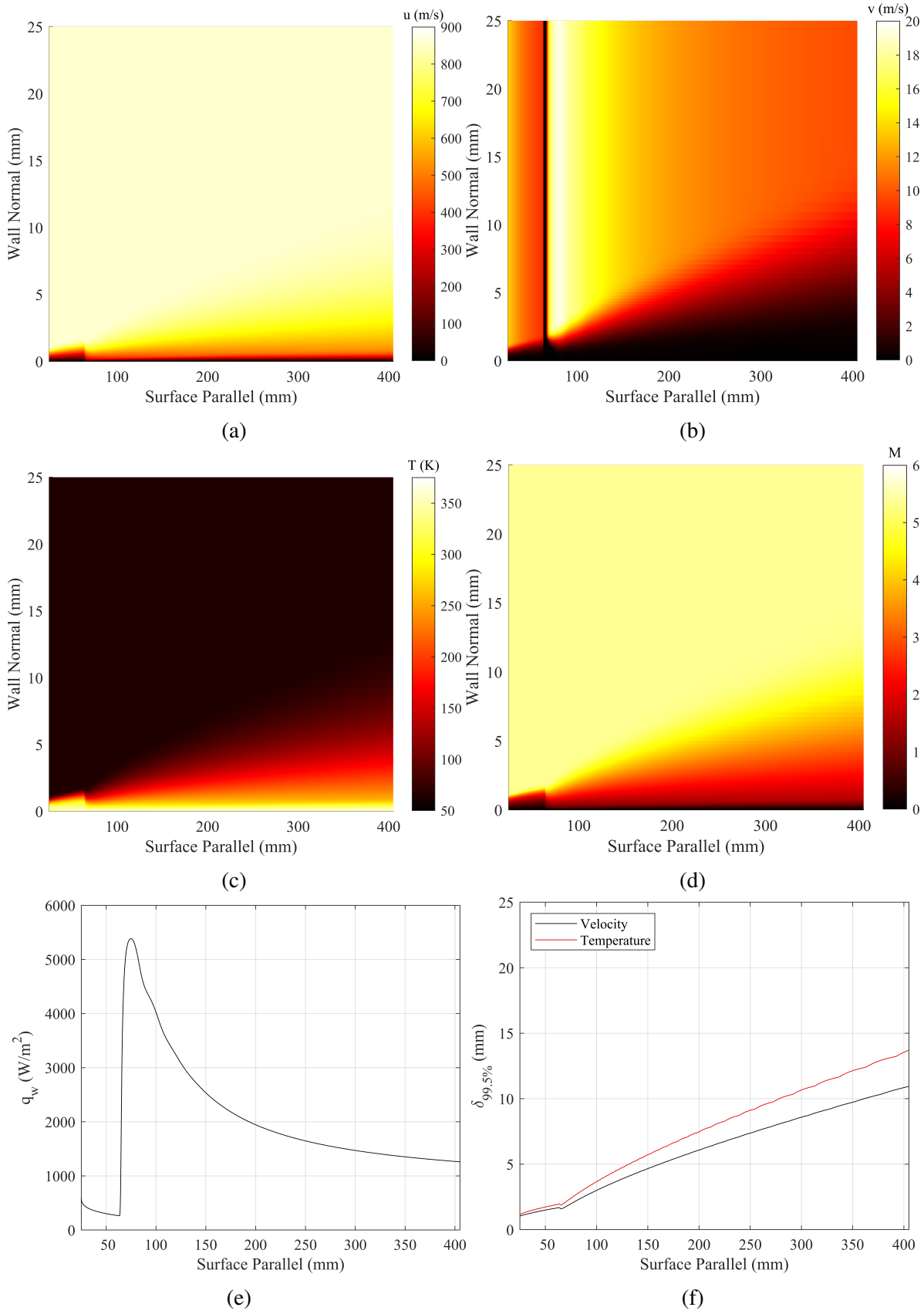

Figure 7.4: Turbulent boundary layer explicit simulation with AEF heat flux model results.

The boundary layer profiles 405mm from the leading edge for several key variables are provided and compared in Figures 7.5 and 7.6. The former shows that in practice there was little to choose between the implicit and explicit turbulence schemes, and that the AEF model did provide some alteration to the profiles, most notably the one using the total enthalpy. The discrepancy in v_e would be unexpected if not for the preceding analysis of the sensitivity of this parameter to any change in boundary layer thickness and its loose convergence criteria. The expected trends such as thicker turbulent boundary layers and thin near-wall regions were correctly manifested. Figures 7.5(c) and (f) show how the Ideal Gas Law, with a constant pressure, causes n to exactly mirror T; this had implications for PLIF, where the signal was dependent on the number density of the gas.

By using the van Driest effective velocity, Figure 7.6 shows the distinct regions of the turbulent boundary layer 405mm from the leading edge. The viscous sublayer existed below $y^+ \lesssim 10$ ($y \lesssim$ 0.59mm), the buffer layer between $10 \lesssim y^+ \lesssim 30$ ($0.59 \lesssim y \lesssim 1.8$mm), the log layer between $30 \lesssim y^+ \lesssim 100$ ($1.8 \lesssim y \lesssim 5.9$mm), and the wake beyond that; the wake was weak for the low-Reynolds number boundary layer simulated, though in the experiment it would be strong due to the presence of the trips. These data were useful for guiding subsequent analyses, especially Pitot experiments, and showed just how thin critical regions fo turbulent boundary layers truly are.

Despite having the proper shape and slope, the data appear to under predict velocity in the log layer. Possible reasons for this include poor simulation of the transition process, improperly accounting for the low densities in the ACE tunnel, or overprediction of τ_w. Of these challenges, the lattermost seemed to be the most likely cause for the disagreement. It will be shown in the Pitot pressure and PLIF velocimetry results (Sections 7.3.5 and 7.4.2.3, respectively) that by the "Back" test location referenced in Figure 7.6 $\tau_w \approx 18$Pa to get the boundary layer profile to sit on the theoretical line for the log layer. However, the simulation's results, shown in Figure 7.7(a), put $\tau_w \approx 19.6$Pa. This increased the friction velocity, which in turn decreased u_{eq}^+. Increasing the order of the differentiation in calculating $\tau_w = \mu_w \frac{du}{dy}$ and checking the numerics by differentiating without Malik mapping did not resolve the issue. Hard-coding $\tau_w = 18$Pa did yield better agreement with the theory, though it was still imperfect. Ultimately it was decided that for the fidelity expected

and required of this in-house boundary layer solver, and remembering program's main goals were to provide order-of-magnitude estimates of flow properties through the boundary layer and to work as an educational tool for turbulence modeling, the agreement was deemed sufficient. The Stanton number is also shown in Figure 7.7(b) for completeness, as Stanton number was the main heat flux parameter discussed in subsequent sections. The wall and off body data are directly compared to the experimentally measured values in Section 7.5.

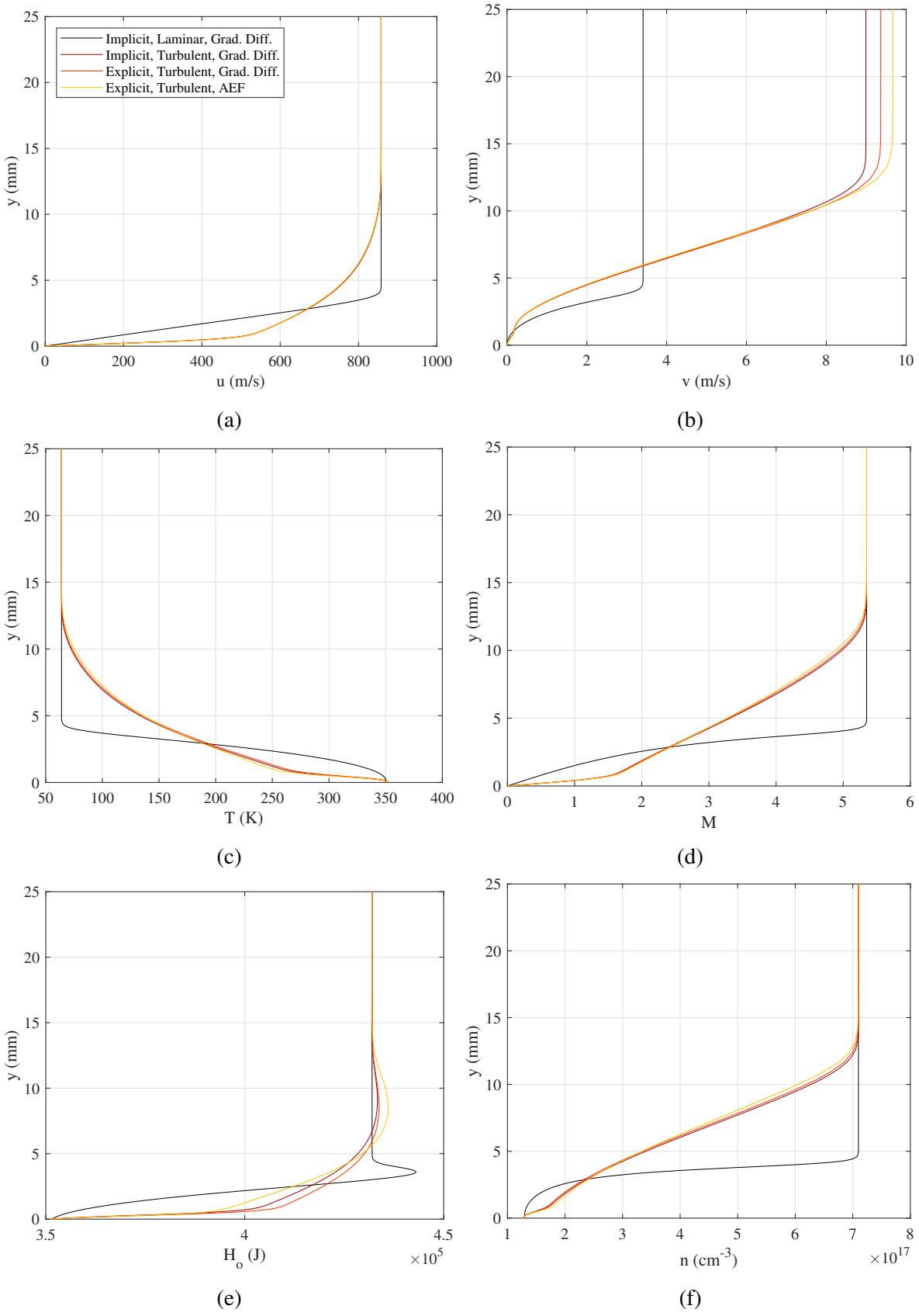

Figure 7.5: Simulation boundary layer profiles at 405mm; same legend applied to all figures.

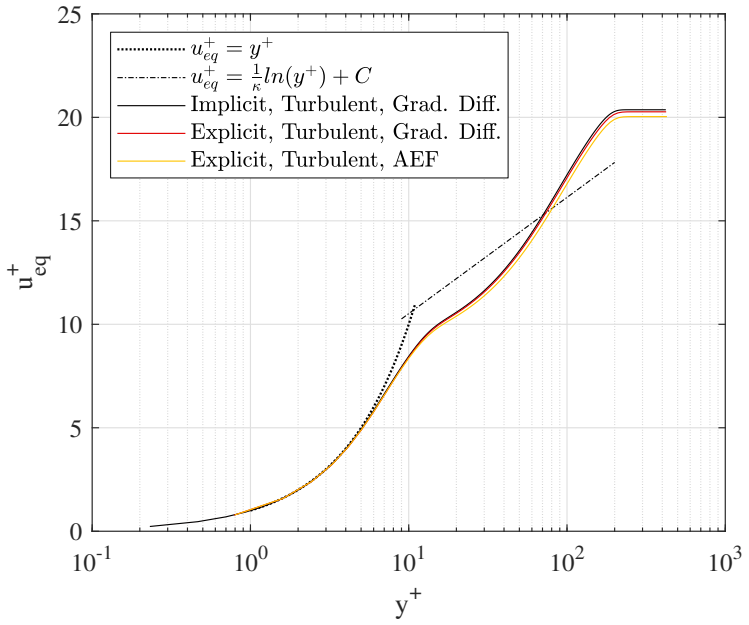

Figure 7.6: Simulated velocity boundary layer profiles at 405mm with inner variable scaling. Following Clauser [61], $\kappa = 0.41$ and $C = 4.9$.

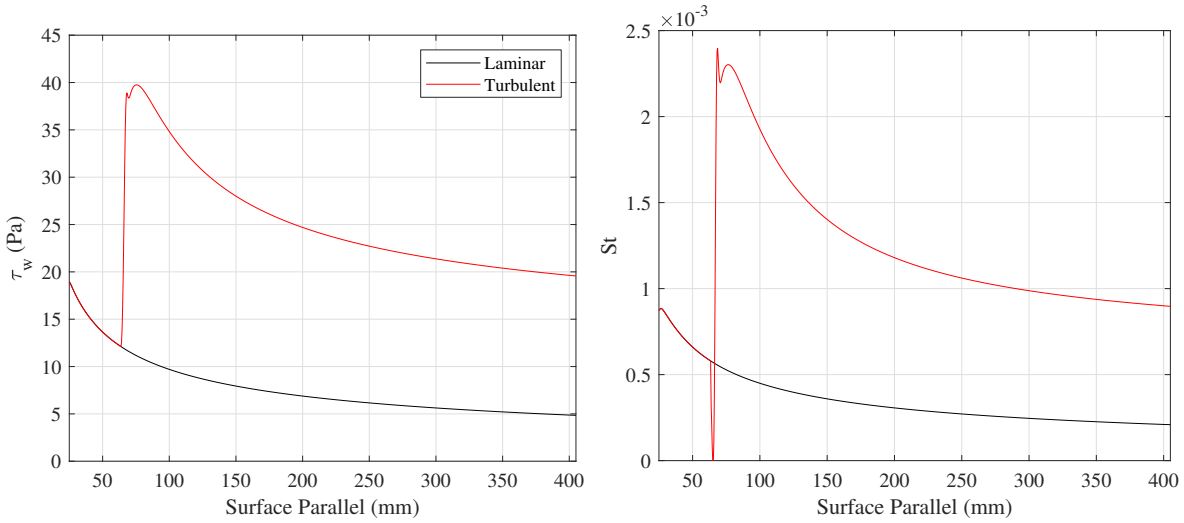

(a) (b)

Figure 7.7: Plot of wall shear stress and Stanton number from simulations; same legend applies to both figures.

7.2 Test Article Characterization

Before beginning with the main experimental campaigns, several tests were conducted to aid with the development of the test article, characterize its behavior, and study its baseline performance. While these tests were preliminary, the data play a crucial role in the broader research objectives. The experiments described here include plasma characterization via its power performance, trip sizing with IR thermography, and leading edge uniformity checks using surface profilometry.

7.2.1 Plasma Characterization

This section covers the development of the glow discharge used for the remainder of the tunnel runs in this report. The test matrix is provided in Table 7.5 and includes four different experiments. The first five "Power characterization" runs studied the effect of varying system parameters like Reynolds number, the power supply voltage, the power supply current, and the Reynolds number. The next five runs studied the breakdown voltage ("Breakdown characterization") and the appearance of the plasma from both the top ("Visualization") and side ("Cathode layer") to identify interesting features, attempt to measure the thickness of the cathode layer, determine if the glow discharge was normal or abnormal, and to test the effect of Reynolds number on these parameters; these experiments were repeated for the turbulent boundary layer in the final three runs to study the effect of the trips.

Additionally, the polarity of the electrodes (cathode upstream of anode and *vice versa*) was also varied. Runs 4469-4475, 4483, and 4476 all had the cathode upstream of the anode; indeed all the runs were initially performed in this configuration, but those not just listed (after Run 4483) were repeated with the final "cathode downstream" orientation. This change was unplanned and a direct result of the preliminary testing reviewed here, so while it was not included in the test matrix its effects are discussed below.

The only circuit data collected was the power supply's current and voltage, both of which were linked to the NALDAQ by a synchronous trigger. However, because the ballast resistance

No.	Experiment	Trip	Power Supply	Reynolds ($\times 10^6/m$)	Run/Date
1	Power characterization	Laminar	I_{Max}, V_{Sweep}, $R_b = 10\text{k}\Omega$	6	4470, 9/15/2020
2	Power characterization	Laminar	I_{Max}, V_{Sweep}, $R_b = 20\text{k}\Omega$	6	4469, 9/15/2020
3	Power characterization	Laminar	I_{Max}, V_{Sweep}, $R_b = 30\text{k}\Omega$	6	4474, 9/16/2020
4	Power characterization	Laminar	I_{Sweep}, V_{Max}, $R_b = 10\text{k}\Omega$	6	4472, 9/15/2020
5	Power characterization	Laminar	I_{Max}, V_{Max}, $R_b = 10\text{k}\Omega$	$4.75 - 6.5$	4475, 9/16/2020
6	Breakdown measurement	Laminar	I_{Max}, V_t, $R_b = 10\text{k}\Omega$	6	4542, 10/7/2020
7	Cathode layer visualization	Laminar	I_{Max}, V_{Sweep}, $R_b = 10\text{k}\Omega$	6	4547, 10/8/2020
8	Cathode layer visualization	Laminar	I_{Max}, V_{Max}, $R_b = 10\text{k}\Omega$	$4.75 - 6.5$	4483, 9/17/2020
9	Visualization to determine normal or abnormal glow	Laminar	I_{Max}, V_{Sweep}, $R_b = 10\text{k}\Omega$	6	4544, 10/8/2020
10	Visualization to determine normal or abnormal glow	Laminar	I_{Max}, V_{Max}, $R_b = 10\text{k}\Omega$	$4.75 - 6.5$	4476, 9/16/2020
11	Breakdown measurement	Turbulent	I_{Max}, V_t, $R_b = 10\text{k}\Omega$	6	4541, 10/7/2020
12	Cathode layer visualization	Turbulent	I_{Max}, V_{Max}, $R_b = 10\text{k}\Omega$	6	4549, 10/9/2020
13	Visualization to determine normal or abnormal glow	Turbulent	I_{Max}, V_{Sweep}, $R_b = 10\text{k}\Omega$	6	4545, 9/17/2020

Table 7.5: Plasma characterization test matrix.

was measurable and it was the only other load besides the plasma, one could use Ohm's Law to determine the plasma's voltage and then $P = IV$ to calculate its power. It is important to be clear, this power represented the rate of all energy loss across the electrodes. It could not differentiate between Joule and cathode heating, nor energy deposited into internal *versus* external modes (η). An effort to approximately differentiate the degrees of Joule and cathode heating is included below.

Here it is noted that the visual data taken in Runs 4547, 4483, and 4549 to attempt to measure

the size of the cathode layer and the effect of Reynolds number on it were largely inconclusive due to the challenging orientation of the camera (looking directly at the side of the plate) and diffuse nature of the plasma. The information lost could be partially recovered via other runs and the theory provided in Section 2.4, but no attempt was made to do so as it was of secondary importance.

The analysis begins with a study of the effect of the ballast resistance R_b captured in Runs 4470, 4469, and 4474. For these tests the voltage was slowly increased until the plasma was ignited, then increased until the current approached the power supply's upper limit of 100mA; this meant the supply was "voltage limited". Here the data were truncated to only include the "plasma on" results. Following the convention in literature [224, 228, 162], it was illuminating to plot the variables against current; this acted almost as a normalization because it removed the temporal dependence and related everything to a fundamental circuit parameter. The results are shown in Figure 7.8.

These data revealed several interesting trends. Consider Figure 7.8(a). For the 30kΩ resistor, the slope was high enough that the power supply's 3000V limit was reached before the current hit the 100mA limit. Decreasing the ballast resistance to 10kΩ reduced this slope to the point that the current's limit was reached before even half of the available voltage was requested. As one would expect and Figure 7.8(b) confirmed, the case with highest voltage at a set current had the highest power supply power; the exponential shape of the curves, however, was surprising and must be somehow due to the plasma. Figures 7.8(c) and (d) reveal the plasma was completely unaffected by the ballast resistance. This implied the plasma was the driving factor for the circuit's behavior, and was itself a function of the flow. It seemed that for the configuration used, the original "cathode upstream" polarity, the present flow could only sustain a voltage drop of $350-380$V regardless of the current used; recall from Figure 2.14 the slight rise in voltage was not unexpected, even for normal glow discharges. Now, because the plasma voltage was effectively a constant and the current was increasing, it made sense Figure 7.8(d) displays a linear dependence between power and current. Synthesizing the results, if one wanted to increase the plasma power, one would need a higher current power supply. Current could then be increased until the power supply's voltage limit

was reach, at which time a smaller ballast resistance could be used; this could continue until either the ballast resistor became impractically small or the plasma constricted into an arc discharge.

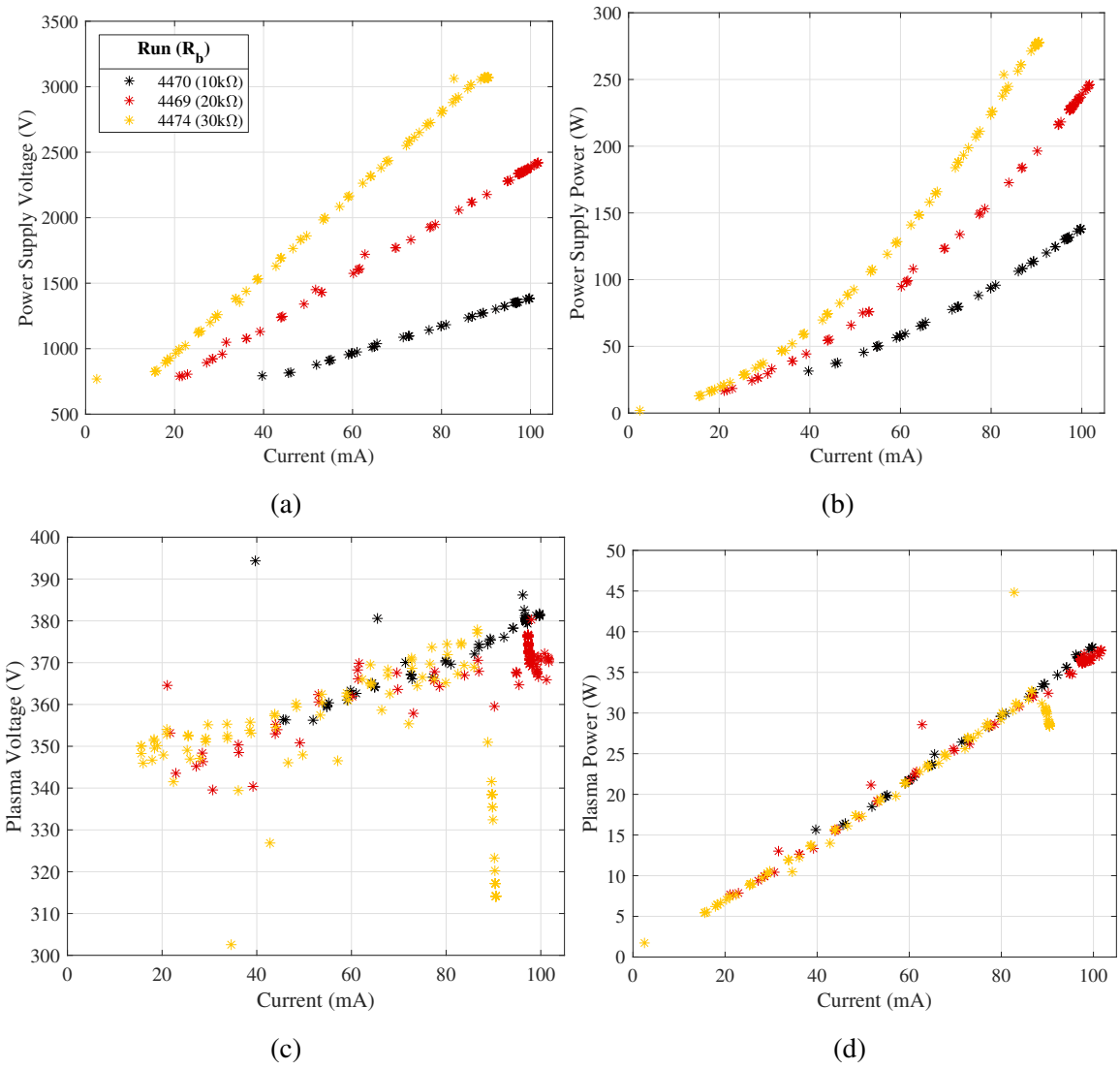

Figure 7.8: Effect of ballast resistance on plasma.

The preceding analysis is for a switching power supply and the runs covered were "voltage limited"; while the behavior with a current- or voltage-fixed power supply was not studied, the effect of running in a "current limited" capacity was. Ultimately it exactly followed the same relationships seen above. This further abetted the claim that it was the flow, not the circuit, that

defined the plasma behavior.

If that was the case, then what effect would the Reynolds number have on the plasma? Run 4475 directly addressed this question. Both the current and voltage were held just below the safe maximum value for the 10kΩ resistor, $\sim$ 95mA and 1350V respectively, then once the plasma was on condition, the Reynolds number was ramped from $4.75 \rightarrow 6.5\times10^{6}/\text{m}$. The condensed results are shown in Figure 7.9 and revealed the plasma's weak dependence on Reynolds number. As the Reynolds number rose, more current was passed through the electrodes; this meant more energy was lost to the ballast resistor, so the plasma voltage dropped. The increased current and dropped voltage somewhat offset one another to maintain a mostly constant plasma power. Visually inspecting the plasma, as the Reynolds number increased, the plasma appeared to dim and even ceased to cover the cathode at the uppermost Reynolds number. This implied the plasma was constricting, which may explain the rise in current. The effect of cathode heating on the plasma performance was deemed negligible because past studies at constant conditions did not show the same behavior. The findings for Run 4475 held for Runs 4483 and 4476, which also used the preliminary "cathode upstream" configuration; because preliminary tests did not reveal dramatic trends, these runs were not repeated with the final "cathode downstream" configuration.

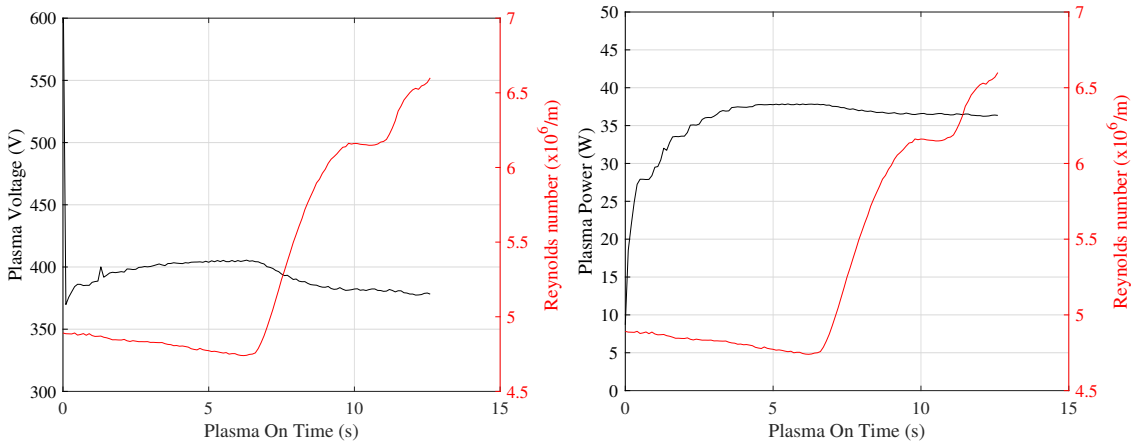

(a) (b)

Figure 7.9: Effect of Reynolds number on plasma.

Another important element of plasma characterization was the determination of the threshold voltage. The parameter was measured by recording the voltage when the current spiked to 1mA, signifying electrical conduction due to the ignition of the plasma; the plasma was cycled three times in a given run to provide extra data points and to check for any effect of plate heating. It was important that the measurement was made with the electrodes in the proper polarity, because, as will be seen shortly, polarity greatly affected electrical performance. Thus for both Runs 4542 and 4541 the cathode was placed downstream of the anode, which was the final test orientation. Qualitative results are shown in Figure 7.10 while quantitative values are provided in Table 7.6. While the turbulent flow did appear to have a slightly lower breakdown voltage, the sensitivity of the measurement apparent in Figure 7.10 made a definitive conclusion elusive. Similarly, there seemed to be little effect of plate and electrode heating, which made sense because the plasma was only briefly ignited, and due to their placement so near the leading edge the electrodes should be thermally saturated from the preheat. It is worth noting that the mean breakdown voltage from the six plasma cases from the IR/schlieren diagnostic campaign to be discussed was 843V. The theoretical pressure behind the bow shock was 4.70Torr (626.89Pa) and the edge-to-edge electrode spacing is 0.635cm, so $PD = 2.98\text{Torr}\cdot\text{cm}$. From Figure 4.15 depicting Paschen curves over a range of temperatures, it appeared the "effective breakdown temperature" was somewhere between $150-250\text{K}$. This number was highly qualitative for the reasons discussed in Section 4.4.8 (i.e.-temperature-dependent conditions and unreliable constants), but it was feasible for the boundary layer and underscored the challenge of a traditional Paschen prediction of V_t. Finally, if the breakdown voltage was $\sim 800\text{V}$ and the power supply's maximum current was 100mA, then the ballast resistor must dissipate 80W during breakdown. The resistors purchased were rated to 100W, so the $10\text{k}\Omega$ resistor was the weakest that could handle breakdown with a reasonable factor of safety.

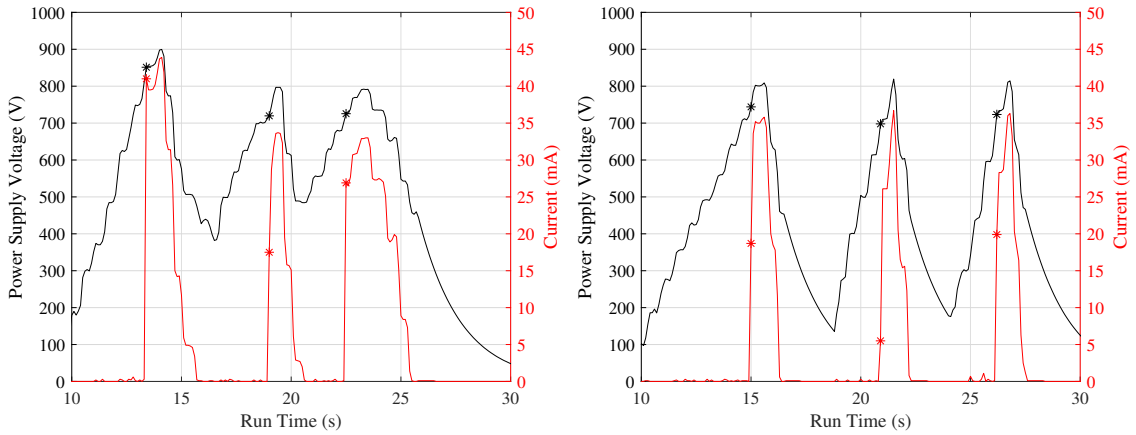

(a) Laminar (Run 6)

(b) Turbulent (Run 11)

Figure 7.10: Measured breakdown voltage (Run 6, laminar flow).

Point	**Laminar (Run 6)**	**Turbulent (Run 11)**
1	851	744
2	720	698
3	725	723
	Average	
	765	722

Table 7.6: Comparison of breakdown voltages over time and with different boundary layers

Runs 4544 and 4545 were the best representation of true run conditions because the plasma and tunnel were both run as they would be for the experimental test campaign, though the plasma voltage was ramped slowly to improve the data's temporal resolution. In addition to the aforementioned circuit data, the same camera in Section 6.2 recorded the plasma from above to study breakdown, stability, and the effect trips had on the plasma's structure. The data are shown in Figures 7.11 and 7.12; the plasma images were true color.

In both cases, the edges of the electrodes ignited first. The cathode's wire was connected in the center of each electrode, and the anode's wire was connected on the side nearer the top of the images. That the breakdown was symmetric meant this was not due to the wiring; another explanation would be slight bowing at the edges of the electrodes, causing them to protrude slightly from

their pockets in the PEEK at the edges. Continuing in time, it was clear that the cathode became fully covered well before the maximum current was applied. This would imply the plasma was just above the normal glow discharge regime. However, the current was not orders of magnitude larger than the normal limit (Figure 2.14), nor was there a large rise in voltage, so it was likely safe to say the plasma was still within the upper limit of the normal regime. This was useful, because many of the formulas and theory covered in Section 2.4 were for normal glow discharges. It was surprising to see how suddenly the plasma grew to cover the cathode between (b) and (c) in both Figures. Also, the plasma did seem to become slightly brighter between (c), when it first covered the cathode and (d), when the power was maximized. Finally, the plasma was indeed uniform across the span, which was a critical design goal for the test article.

When comparing the effect of the trips, there was no noticeable effect on plasma power; it was $\sim$ 47W for both configurations. That being said, it did take slightly more current to fully cover the cathode in the turbulent case, $\sim$ 75mA *versus* the laminar case's $\sim$ 65mA. This could imply the presence of the trips and their complex shock structure affected the flow enough to alter the plasma's performance, but then the breakdown voltage remained at $\sim$ 800V for both cases so this argument was assailable. Ultimately the important parameter was the plasma power, which was indeed identical between the two cases, so for the purpose of this report it was safe to say the two cases were functionally identical.

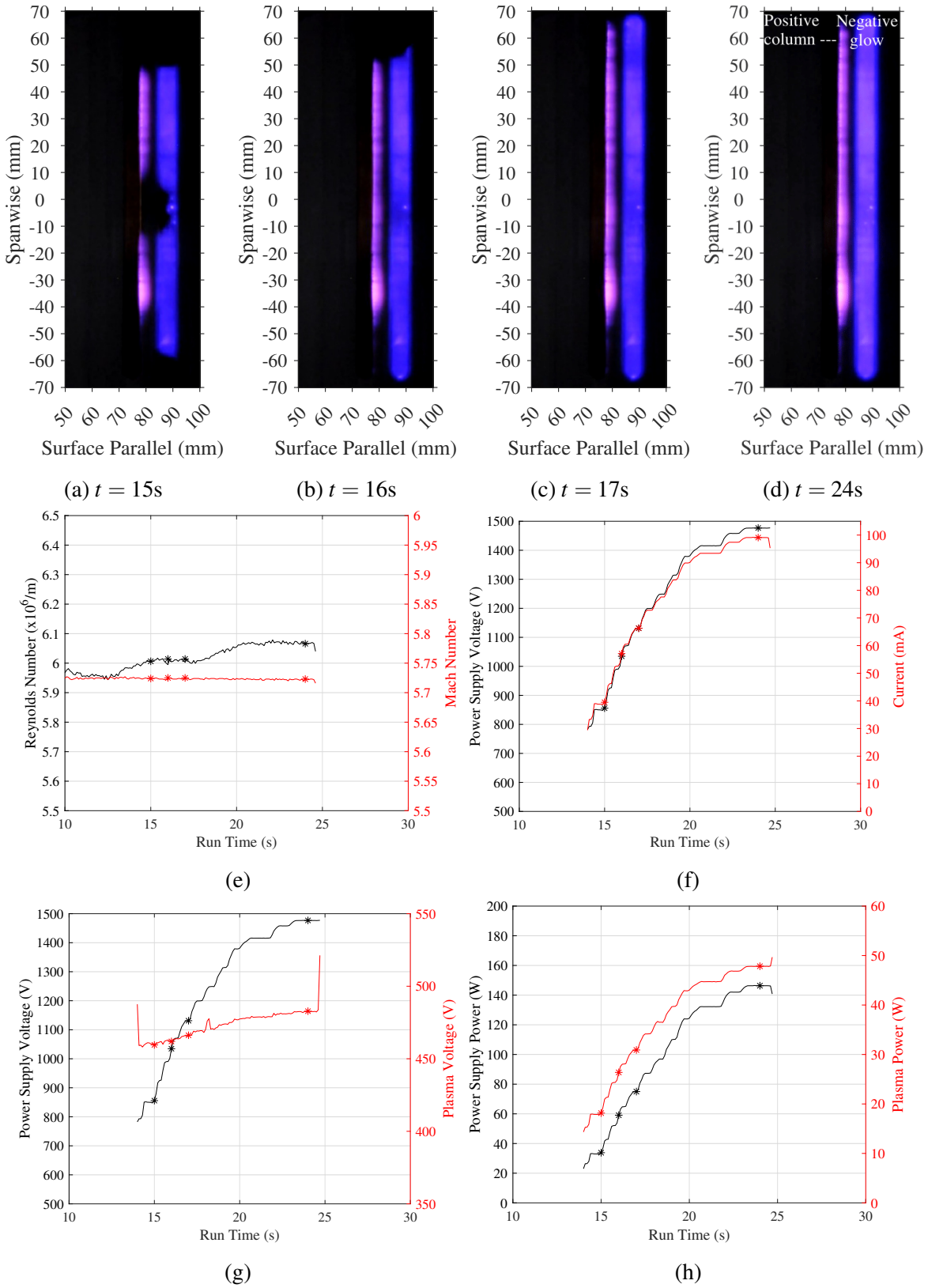

Figure 7.11: Plasma performance in a laminar boundary layer (Run 9).

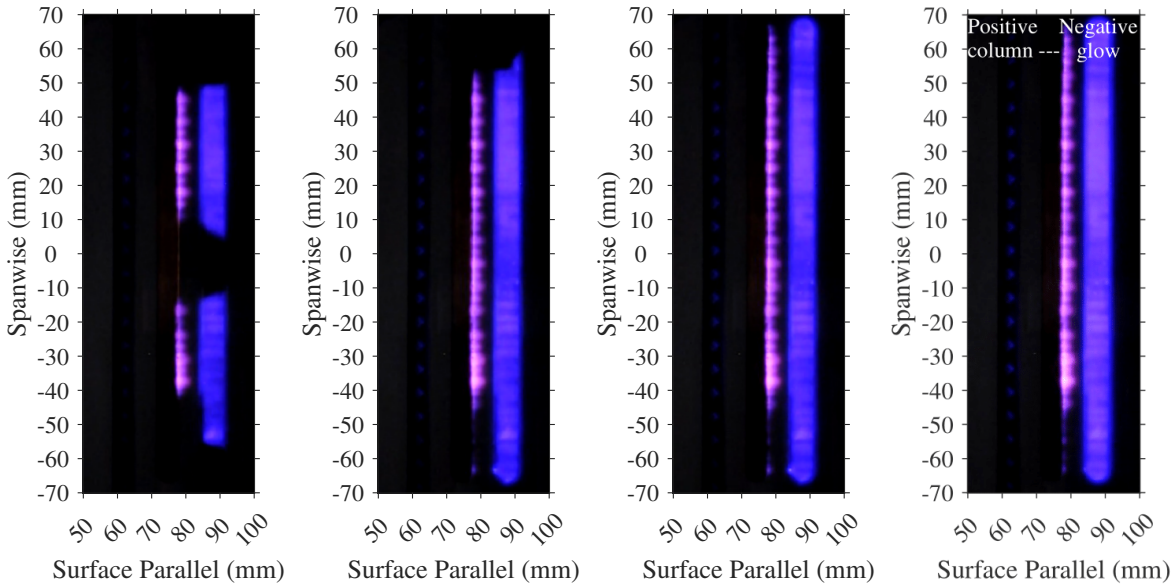

(a) $t = 16$s (b) $t = 19$s (c) $t = 20$s (d) $t = 25$s

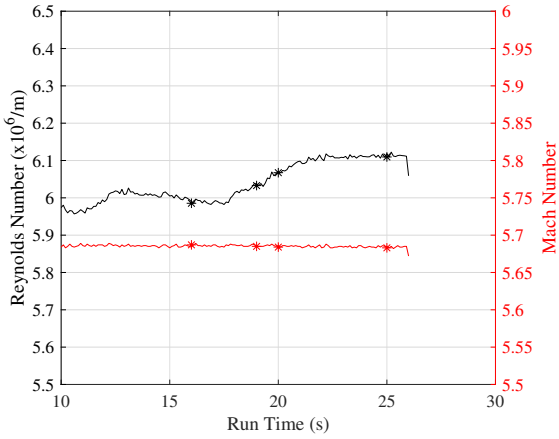

(e)

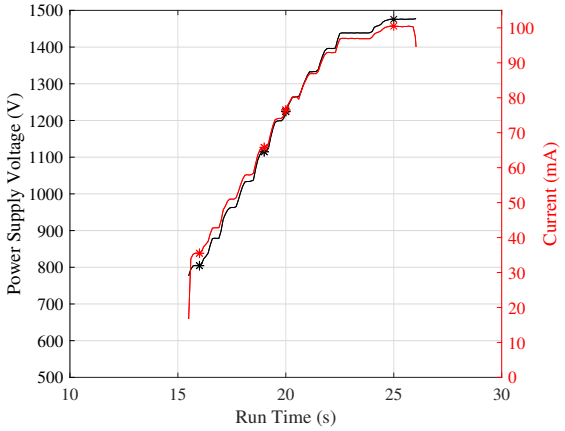

(f)

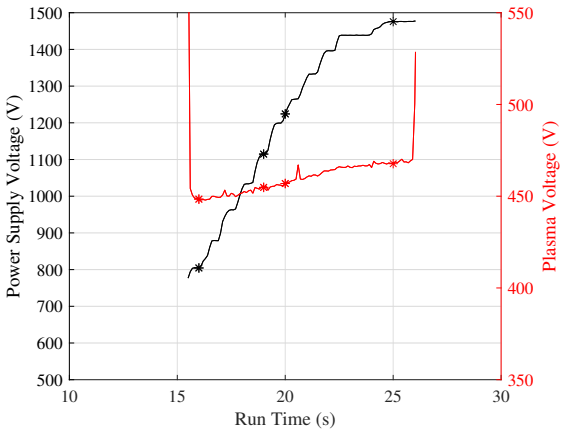

(g)

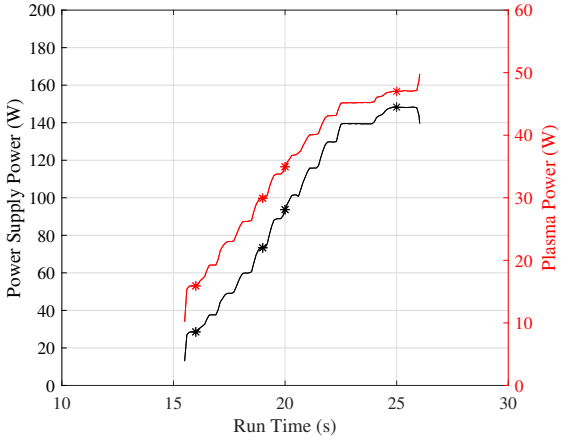

(h)

Figure 7.12: Plasma performance in a turbulent boundary layer (Run 13).

The flow structures present in the turbulent plasma case in Figure 7.12 were worth discussion. Corner vortices were present as pinkish streaks in the negative glow. Meanwhile, in the positive column, the troughs in between the trips had the highest signal, followed by the wakes; the corner vortices seemed to fully suppress the positive column. It was possible that the pressure differential or temperature [122] in the corner vortices was indeed changing the negative glow analogously to the positive column, but the exact mechanism was not determined. The latter explanation seemed more likely, as evinced by Figure 7.13. This image was taken near the end of the PLIF campaign. It shows different degrees of electrode "burning" on the cathode in the corner vortex, wake, and trough regions. The PEEK was most damaged downstream of the corner vortices, which implied these regions were hotter than the rest of the flow; IR thermography was later used to confirm this was a thermal effect and not a result of copper sputtering. It was difficult to say how many runs it took to achieve this degree of burning, but likely dozens.

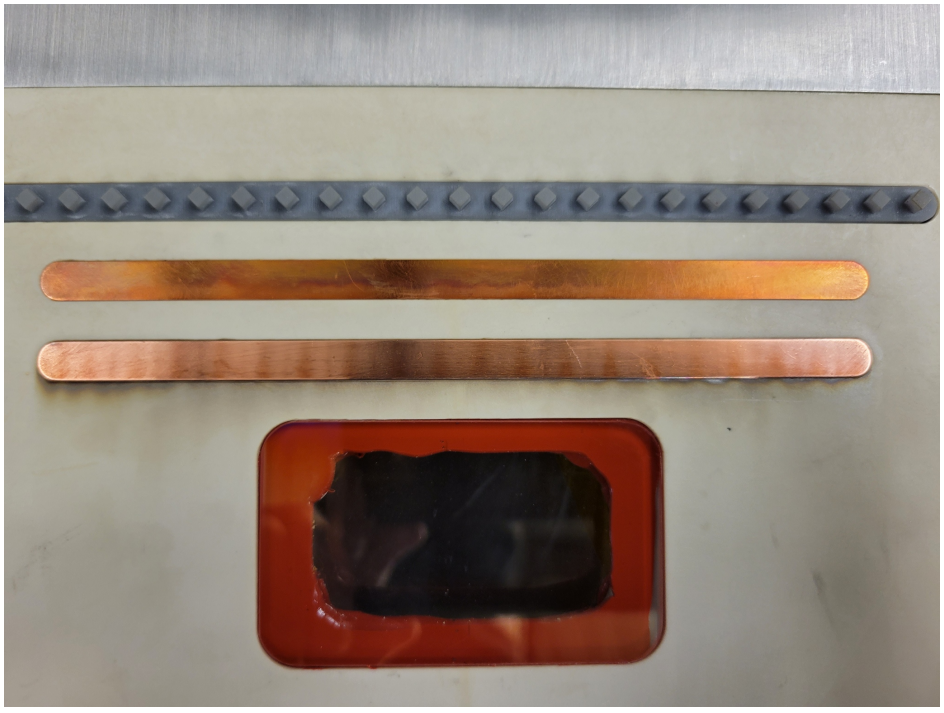

Figure 7.13: Burned electrodes; flow is top to bottom.

The authors covered in Section 2.4.4 placed the cathode upstream of the anode, largely to maximize its impact near the viscous-inviscid interaction region at the leading edge. While they did mention similar degradation around the test article, their orientation was preserved and thus was initially adopted here; note that these authors used a ceramic insert, which should be impervious to burning at the plasma temperatures experienced and thus lending credence to the sputtering hypothesis. Still, even after about ten runs of preliminary testing with the cathode upstream of the anode, here Runs 4469-4475, 4483, and 4476 in Table 7.5, some degradation became noticeable. The concern was that over time, whatever its cause, it would provide a conductive path between the electrodes and form a short circuit. This would destroy the PEEK insert, and so the cathode was moved downstream of the anode.

A surprising consequence of this decision was the improvement in plasma performance. Comparing Figure 7.8(d) and 7.11(h), the plasma power rose from ~ 37W to ~ 47W. Furthermore, the positive column was established only with the latter polarity. This was potentially a manifestation of the velocity analysis conducted in Section 2.4. Recall that absent of the flow the ion and electron velocities were roughly predicted to be $\mathcal{O}(10^2 \frac{m}{s})$ and $\mathcal{O}(10^6 \frac{m}{s})$ respectively. This implied the ions, which traveled towards the cathode, could be largely impeded by the hypersonic flow through most of the boundary layer. A reduction in ion current would lower the overall current, and thus drop the plasma power. The opposite effect was possible if the ions traveled with the flow towards the cathode.

Finally it is worthwhile to return to the theory in Section 2.4 to try and determine the total amount of Joule heating. From Figure 2.17 with $CV_c \approx 6$ for a normal glow discharge and $A = 15\text{cm}^{-1}\text{Torr}^{-1}$, $B = 365 \frac{\text{V}}{\text{cmTorr}}$, and $\gamma = 2.5 \times 10^{-4}$ (constants from Section 4.4.8), then the cathode fall voltage was $V_c = 605$V. This exceeded the entire voltage drop across the electrodes; the discrepancy was most likely due to the failure of the constants at the temperatures experienced in the boundary layer. Meanwhile, taking the approach of Nishihara et al. [203] and extrapolating the data yielded $V_c = 438.5$V ($V = 438.5 + 0.374i$, $R^2 = 0.56$), a much more reasonable result. However, the data (excluding outliers) shown in Figure 7.14 was not perfectly linear, nor would

one expect it to be (see Figure 2.14). Thus all that could be said was that one could assume most of the voltage drop, ~ 475V from Figures 7.11 and 7.12, did indeed occur in the cathode layer. If one did take $d_c \approx 0.1$cm from the pseudo-qualitative data in Runs 4544 and 4549, a maximum current of $i = 0.095$A, and a cathode area of $A = 8.31\text{cm}^2$ then from Equation 2.141 $P_J = 54.3\frac{\text{W}}{\text{m}^3}$. Again, this was simply the plasma power as discussed above (here ~ 45W) divided by the approximate volume of the cathode sheath.

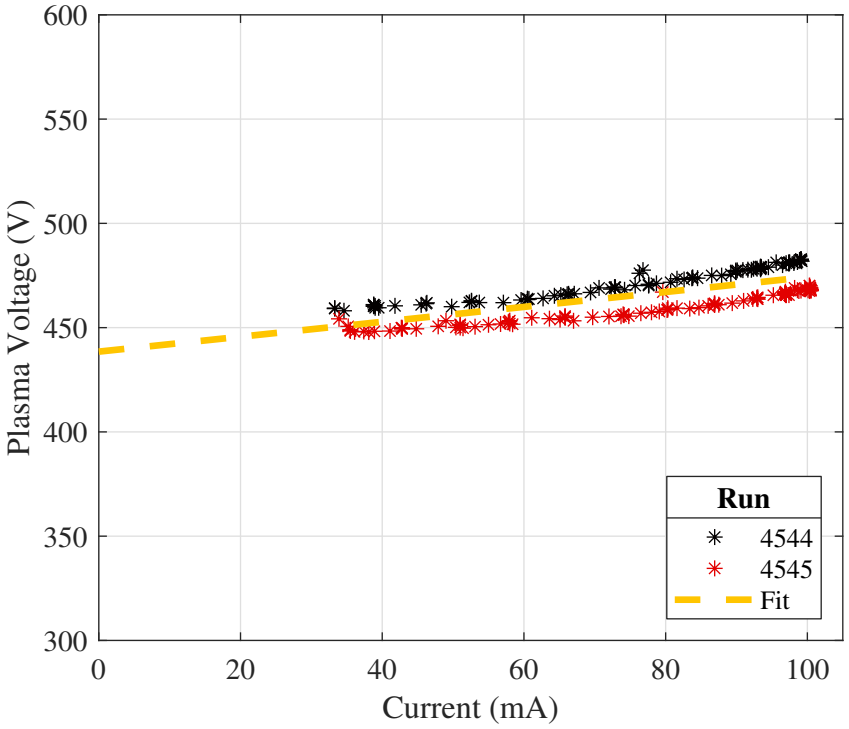

Figure 7.14: Cathode voltage drop following the method of Nishihara et al. [203].

7.2.2 Trip Sizing Study

IR thermography was used to determine the efficacy of different trip heights (h), widths (d, "diameters"), and spacings (w). The goal was to determine if the trips could produce a uniform TBL by the back of the test article at Reynolds numbers attainable in the ACE tunnel. The temperature data was used to calculate a spanwise Stanton number 405mm from the leading edge over a range

of Reynolds numbers for each trip. Recall here that following [160, 194] the Stanton number was calculated with T_o and not T_{aw} as the state of the boundary layer would change as the Reynolds number and trips were varied, so the results cannot be compared to those elsewhere in report. Nevertheless, due to the normalization, turbulence was achieved when the Stanton numbers collapsed on one another, and this approach afforded sufficient fidelity to show that effect. An example of the data is provided in Figure 7.15, which also shows the result for the control "untripped" case; all traces were taken at $x = 405$mm from the leading edge. An analysis of the plate's thermal response and its implications is provided in the dedicated IR thermography section (Section 7.3.3).

The test matrix for the trip sizing campaign is provided in Table 7.7. See that the runs were generally grouped into three sets, where the four h's were tested for a set (d, w) combination. The data are presented in this manner in Figures 7.16, 7.17, and 7.18. The wedge was mounted as far back on the struts as possible to maximize the visible area and check for shock impingement (discussed alongside the schlieren results, Section 7.3.2).

No.	**Location**	**Re** $(\times 10^6/m)$	**Trip** $(\delta_{H_o,99.5\%} * (h,\, d,\, w))$	**Run/Date**
1	Back	$2-6$	*None*	4442, 9/2/2020
2	Back	$2-7$	$(1,\, 1,\, 2)$	4436, 9/1/2020
3	Back	$2-7$	$(1.25,\, 1,\, 2)$	4434, 9/1/2020
4	Back	$2-7$	$(1.5,\, 1,\, 2)$	4435, 9/1/2020
5	Back	$2-7$	$(1.75,\, 1,\, 2)$	4429, 8/31/2020
6	Back	$2-7$	$(1,\, 1.5,\, 3)$	4441, 9/2/2020
7	Back	$2-7$	$(1.25,\, 1.5,\, 3)$	4439, 9/2/2020
8	Back	$2-7$	$(1.5,\, 1.5,\, 3)$	4433, 9/1/2020
9	Back	$2-7$	$(1.75,\, 1.5,\, 3)$	4428, 8/31/2020
10	Back	$2-7$	$(1,\, 2,\, 4)$	4438, 9/2/2020
11	Back	$2-7$	$(1.25,\, 2,\, 4)$	4437, 9/2/2020
12	Back	$2-7$	$(1.5,\, 2,\, 4)$	4432, 9/1/2020
13	Back	$2-7$	$(1.75,\, 2,\, 4)$	4427, 8/31/2020
14	Back	3	$(1.5,\, 2,\, 4)$	4443, 9/3/2020
15	Back	6	$(1.5,\, 2,\, 4)$	4444, 9/3/2020

Table 7.7: Trip sizing study IR thermography test matrix.

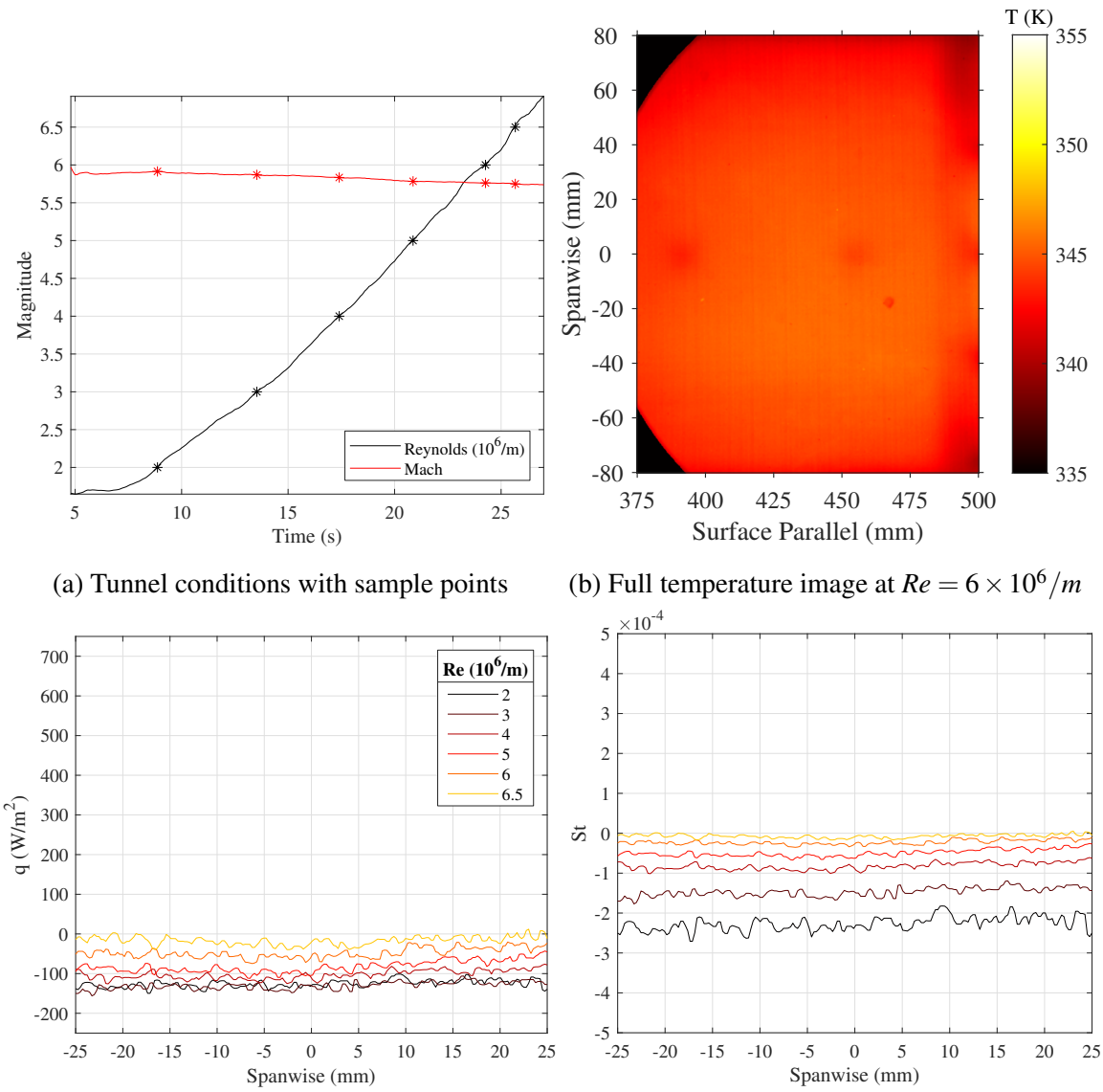

(a) Tunnel conditions with sample points

(b) Full temperature image at $Re = 6 \times 10^6/m$

(c) Heat flux traces

(d) Stanton number traces

Figure 7.15: Sample of IR data for trip sizing from control case. Traces taken at $x = 405$mm from the leading edge; same legend applies to (c) and (d).

Apart from the most modest trips (Figure 7.16a), all of the geometries were successful at fomenting transition. In Figure 7.16, the Stanton numbers collapsed for both the $h = 1.5$ and $h = 1.75$ orientations. Increasing the size and spacing (Figure 7.17), full turbulence was achieved by $Re = 6 \times 10^6/m$ for all of the heights tested. This suggested larger, more independent vortices were more effective at transitioning a flow than those from the smaller, clustered trips. This could

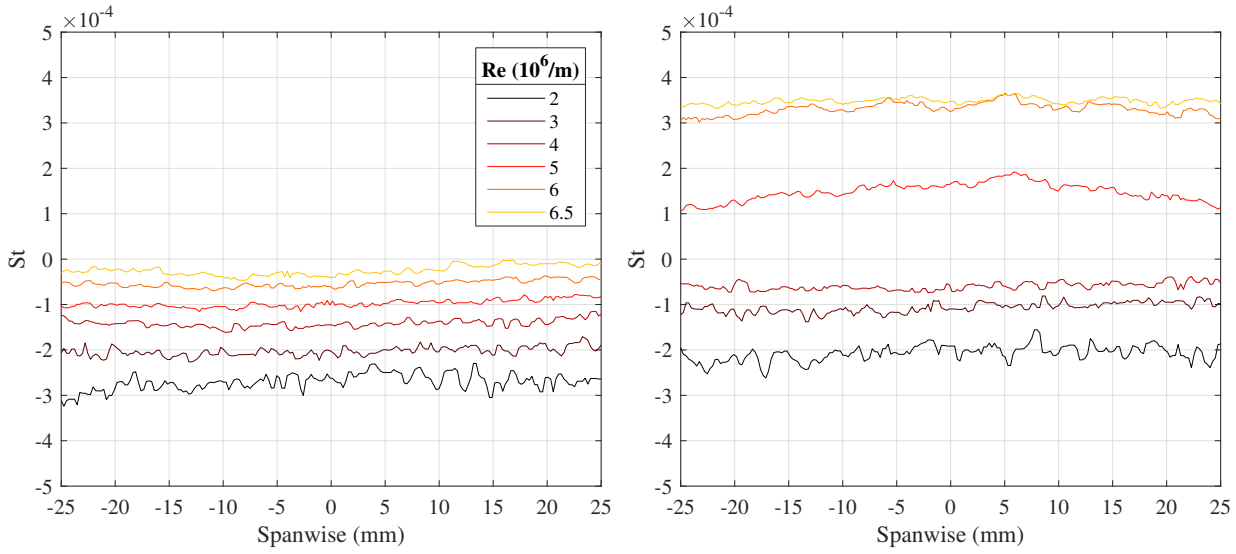

(a) $\delta_{H_o,99.5\%} * (h = 1, d = 1, w = 2)$

(b) $\delta_{H_o,99.5\%} * (h = 1.25, d = 1, w = 2)$

(c) $\delta_{H_o,99.5\%} * (h = 1.5, d = 1, w = 2)$

(d) $\delta_{H_o,99.5\%} * (h = 1.75, d = 1, w = 2)$

Figure 7.16: IR studying sweep of trip heights for ($d = 1$, $w = 2$) family. Same legend applies for all figures.

be because the sets of smaller trips acted more like a blockage than a vortex generator, or because turbulent production occurs in large scales [221]; additional credence was lent to the former theory as there was little evidence of individual trip wakes in the data for the smallest trip cases, just sudden and uneven rises. Either way, the largest trips (Figure 7.18) performed the best, with all heights achieving turbulent flow by $Re = 5 \times 10^6/m$. This provided a factor of safety to ensure the flow is

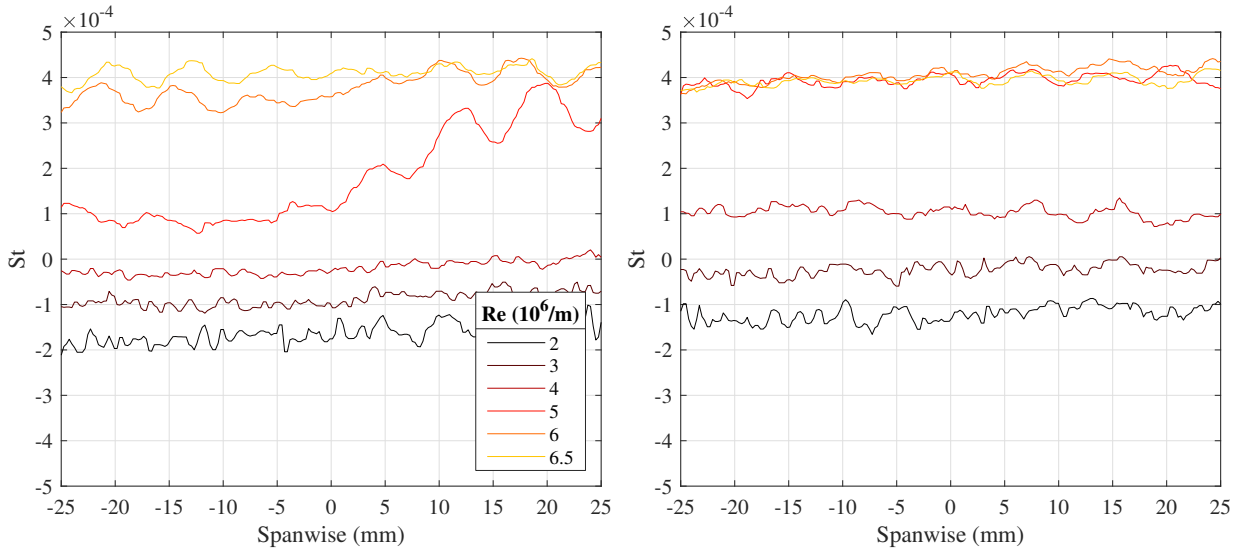

(a) $\delta_{H_o,99.5\%} * (h = 1, d = 1.5, w = 3)$

(b) $\delta_{H_o,99.5\%} * (h = 1.25, d = 1.5, w = 3)$

(c) $\delta_{H_o,99.5\%} * (h = 1.5, d = 1.5, w = 3)$

(d) $\delta_{H_o,99.5\%} * (h = 1.75, d = 1.5, w = 3)$

Figure 7.17: IR studying sweep of trip heights for ($d = 1.5$, $w = 3$) family. Same legend applies for all figures.

turbulent at the test condition. Furthermore, the heating was uniform over the region of interest, which was not always the case for the smallest trips (Figure 7.16). Finally, at higher Reynolds numbers, say above $5 \times 10^6/m$, the waviness of the profiles due to the trip wakes and vortices was diminished. These effects were tolerable ([243, 160]), but it was preferable to avoid them if possible. Finally, it was understood that the consistent rise in heating above $Re = 3 \times 10^6/m$ was

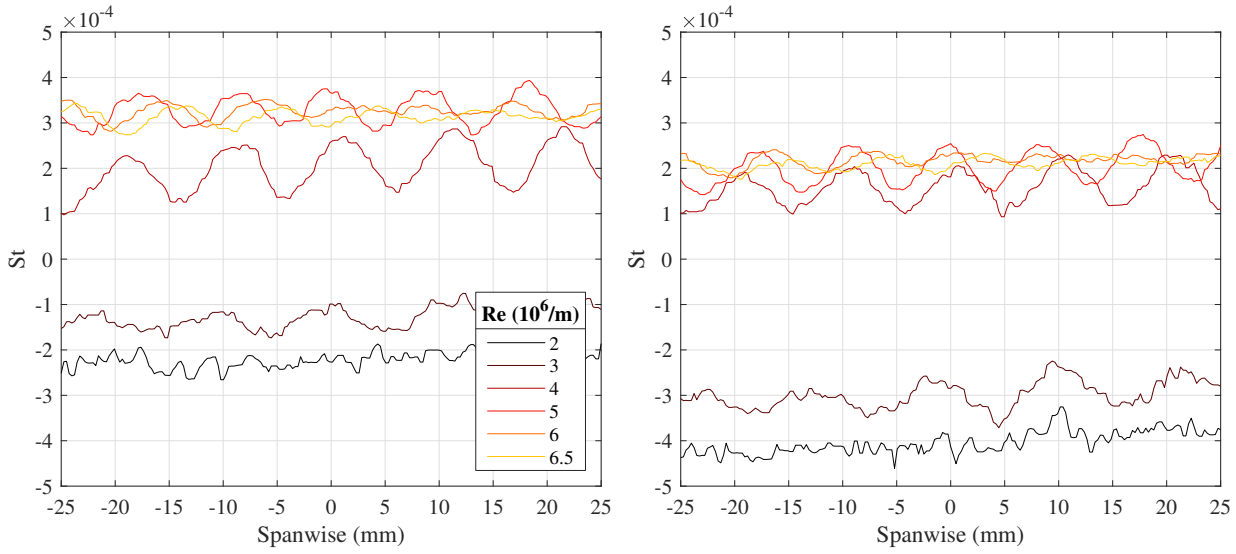

(a) $\delta_{H_o,99.5\%} * (h = 1, d = 2, w = 4)$

(b) $\delta_{H_o,99.5\%} * (h = 1.25, d = 2, w = 4)$

(c) $\delta_{H_o,99.5\%} * (h = 1.5, d = 2, w = 4)$

(d) $\delta_{H_o,99.5\%} * (h = 1.75, d = 2, w = 4)$

Figure 7.18: IR studying sweep of trip heights for $(d = 2, w = 4)$ family. Same legend applies for all figures.

due to the tunnel nozzle's sidewalls transitioning and increasing the freestream noise environment.

Of all the trips tested, the best performing, as defined by the earliest collapse and most spanwise uniformity, were the $\delta_{H_o,99.5\%} * (1.5, 2, 4)$ trips. It was surprising they outperformed the $h = 1.75$ trips in the same family, but perhaps the largest trips produced oversized wakes and not clean vortices. A few preliminary MTV runs were conducted with the trips to further confirm their

efficacy, but any quantitative analysis was reserved for the more careful studies in the dedicated PLIF review. For all subsequent tests hereafter the $\delta_{H_o,99.5\%} * (1.5, 2, 4)$ trips were used.

As an addendum to this study, the degree of plate heating was briefly studied. The IR thermography tunnel runs typically lasted just under 30s, during which time the plate heated up under 5K, even for turbulent flows. This implied an isothermal wall condition, but not necessarily an adiabatic one, so there was a risk the Stanton number would change as a function of time. To study this effect on both a laminar/transitional and turbulent boundary layers, the $\delta_{H_o,99.5\%} * (1.5, 2, 4)$ trips were run at a constant $Re = 3$ and $6 \times 10^6/m$. The results are shown in Figure 7.19. The data suggested that there was very little temporal dependency on the results, validating the use of long tunnel runs.

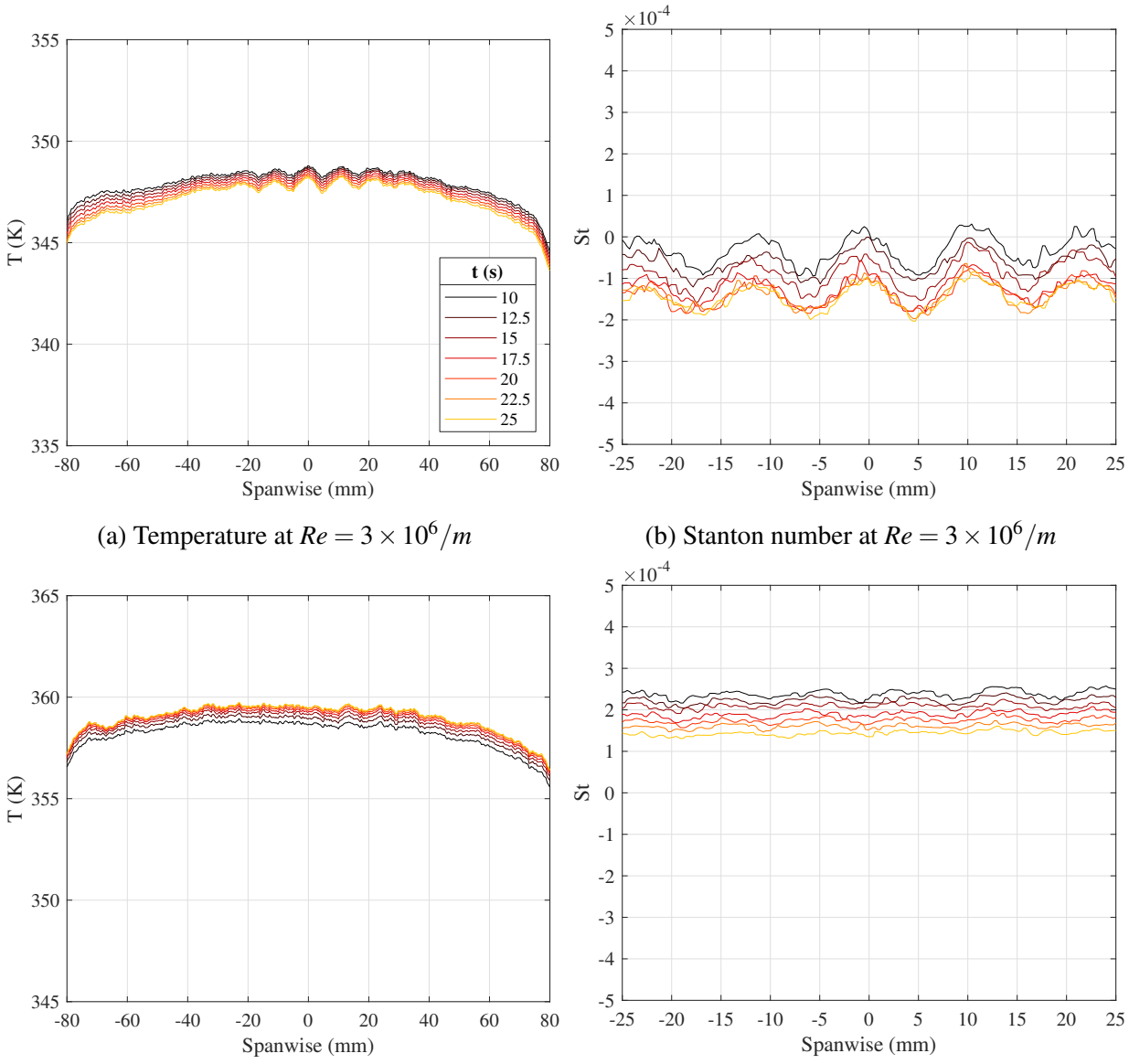

(a) Temperature at $Re = 3 \times 10^6/m$

(b) Stanton number at $Re = 3 \times 10^6/m$

(c) Temperature at $Re = 6 \times 10^6/m$

(d) Stanton number at $Re = 6 \times 10^6/m$

Figure 7.19: IR studying temporal effect on heating. Same legend applies for all figures, but note the change in axis between (a) and (c).

7.2.3 Leading Edge Uniformity and Roughness

Surface profilometry revealed the leading edge was well-machined and uniform across the model span. Characteristic results for one of the tests are shown in Figure 7.20. A dashed line at 20.65mm separated the leading edge polynomial from the flat wedge geometry. The leading edge

was approximately merged with the wedge slope within $\sim$ 5mm of the leading edge, which underscored the need for the definition of the geometry's effective radius of curvature. Data upstream of this point was somewhat noisy, which was expected as this section was less finely ground. That being said, while some machine chatter exactly at the leading edge was visible, it did not appear to have been captured by the surface profilometer beyond the noise floor. The data also suggested the leading edge polynomial did indeed merge smoothly with the wedge slope, which was the entire reason for its inclusion in the design. With regard to the spanwise uniformity of the leading edge, there did seem to be a slight depression in the center of the span; it was $\mathcal{O}(100)\mu$m; this value, which was consistent among all three tests, was acceptable over the $\sim$ 200mm test article. The depression deepened as one moved downstream, but it remained tolerable; this may be due to minor misalignment of the profilometer in the Y-direction.

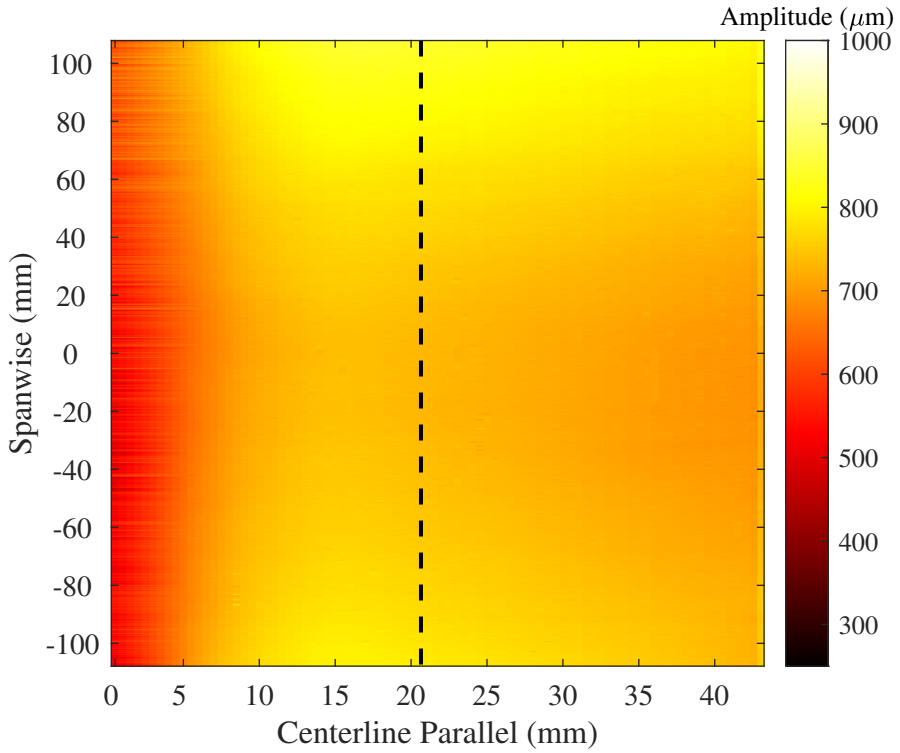

Figure 7.20: Characteristic result of a full profilometer scan. A dashed line at 20.65mm separates the leading edge polynomial from the flat wedge region.

The roughnesses for the "even" and "odd" scans from the three tests were included in Table 7.8 to the resolution of the profilometer. The repeatability between all six data sets was encouraging. Furthermore, the model was specified to be ground to $R_{avg} = 32\mu\text{in} = 0.81\mu\text{m}$, which strongly agrees with the experimental result.

	R_{avg}	R_{ptp}	R_{rms}
Test 1			
Even	0.73	3.12	0.95
Odd	0.74	3.14	0.97
Test 2			
Even	0.73	3.14	0.96
Odd	0.74	3.16	0.97
Test 3			
Even	0.74	3.18	0.98
Odd	0.74	3.18	0.98
Average			
	0.74	3.15	0.97

Table 7.8: Results of three redundant roughness tests; all data are in microns.

7.3 Flow Physics Data

These data used classical diagnostic techniques to gather as much information about the test environment as was feasible. Data was collected at the wall from oil flow and IR thermometry, off-body from schlieren and Pitot probe surveys, and in spectral space using high frequency pressure transducers. These results paint a detailed picture of the test environment, the hypersonic turbulent boundary layer with zero pressure gradient, and they provide further information on specific features such as the flow near the leading edge or just downstream of the trips.

7.3.1 Oil Flow Results

The primary purpose of oil flow visualization was to ensure the quality of the flow within the test area; through their own oil flow campaigns Semper [243] and Leidy [160] showed sting effects, edge effects, pressure gradients, separation, shocks, *etc.* could all effect hypersonic boundary

layers in the ACE tunnel. Additionally, oil flow communicates the presence and longevity of flow features like trip wakes, which could inform the placement of later sensors and measurements. Both full images and spanwise traces of the test area are provided at different stations along the plate and over a range of times to study how the flow evolved both spatially and temporally. For all runs, the test Reynolds number of $6 \times 10^6/m$ was used. Because the oil behaved unpredictably during unstart and is electrically conducting, for safety the plasma was never ignited during these runs. The test matrix is shown in Table 7.9.

No.	Location	Trip	Run/Date
1	Back	Laminar	4508, 9/28/2020
2	Back	Turbulent	4507, 9/28/2020
3	Middle	Laminar	4509, 9/28/2020
4	Middle	Turbulent	4510, 9/29/2020
5	Forward	Laminar	4513, 9/29/2020
6	Forward	Turbulent	4511, 9/29/2020

Table 7.9: Oil flow test matrix.

Figure 7.21 compares laminar and turbulent results at each of the three test locations. The clearest observation was a slight outward motion of the streaks, especially in downstream images. This was present in both the laminar and turbulent images, so it was not due to trip blockage, and the images were dewarped and rotated, so it was not a camera effect. This suggested the top surface of the wedge was at a slightly higher pressure than the underside, causing streamlines to "wrap around" the sides of the model. This was not surprising given the challenges outlined by Leidy [160]; it may be caused by a very slight angle of attack (recall the model was constrained to $\pm 0.1°$) or the fact the model was mounted 2.54cm below the test section's centerline (a necessity discussed in Section 7.3.2). Nevertheless, the streamlines remained relatively straight in a core region roughly $\pm$25mm from the centerline.

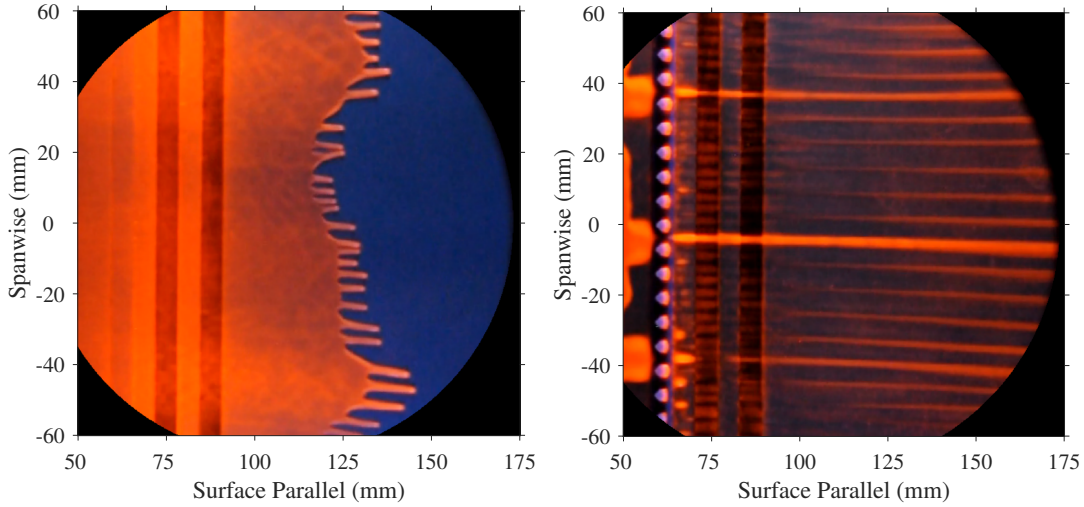

(a) Forward/Laminar

(b) Forward/Turbulent

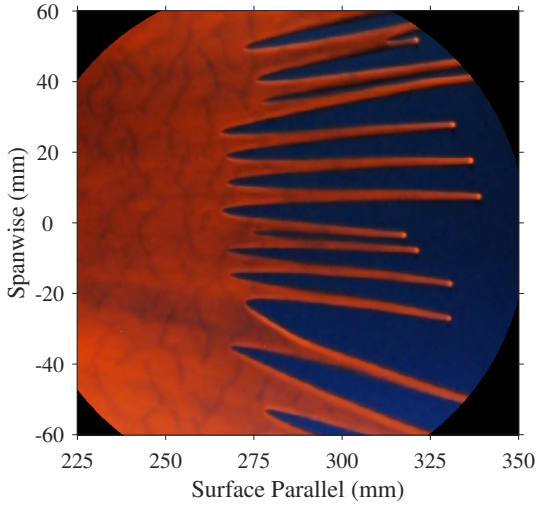

(c) Middle/Laminar

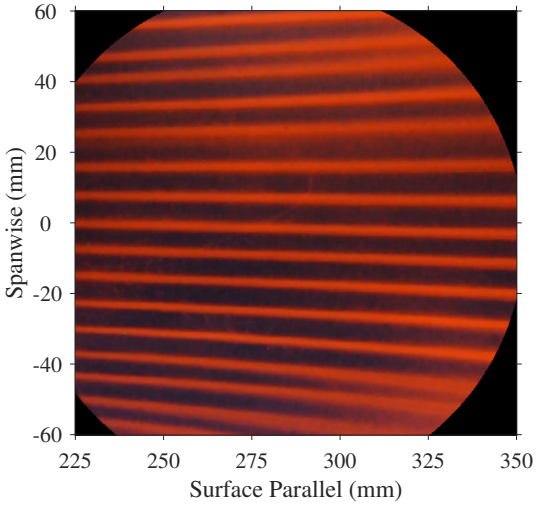

(d) Middle/Turbulent

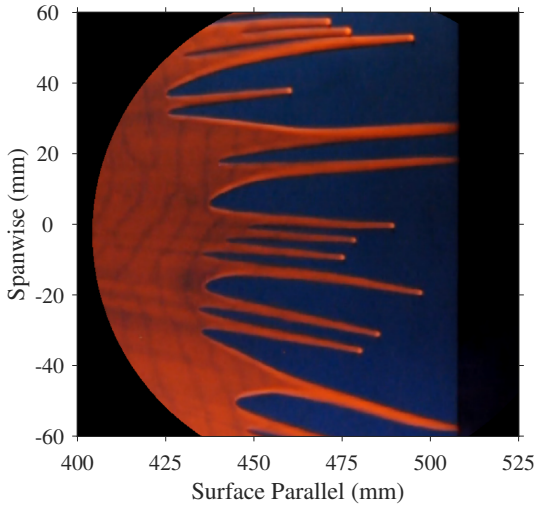

(e) Back/Laminar

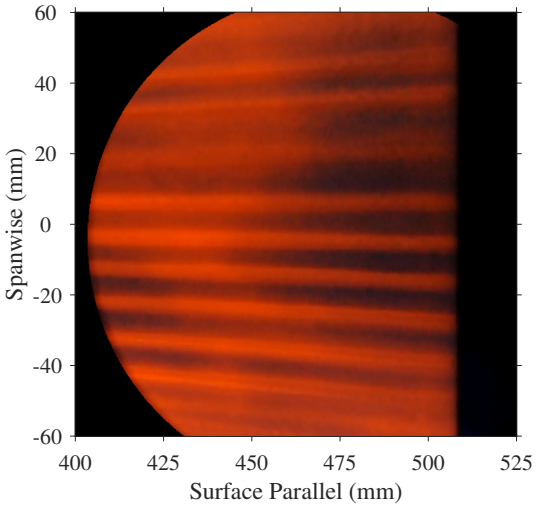

(f) Back/Turbulent

Figure 7.21: Raw color oil flow images along the plate with and without trips.

Another feature present in Figure 7.21 was the thickening of the streaks as one moved downstream. This was likely due to the streamlines merging, and was described by Semper [243]. This was explored in Figure 7.22. Note that due to inherent difficulties with analyzing oil flow data the times displayed count the seconds from a manually identified tunnel start. They were therefore somewhat arbitrary and disconnected from the ACE tunnel's DAQ, but were nevertheless sufficient for the current discussion. Similarly, the "Normalized Intensity" axis was relative only to the camera; the data were normalized to account for the drop in signal as the oil was blown out of frame. The data showed that as one moved downstream, the flow became more unstructured and the periodic trip effects broke down. The regularity of the streaks decreased while their wavelength increased, with an expected drop in their frequency. The location of the streaks changed slightly as one moved downstream, which was understandable due to the aforementioned divergence. At a given location, however, the locations of the structures were fairly constant. The progressive clarity of the waves over time at the "Back" location (Figure 7.22(c)) may be explained by the time it took for weak (compared to the trip effects) flow structures to manifest in the slow-moving oil. The large spikes in signal at the "Forward" location (Figure 7.22a) were due to the pooling seen in 7.21(b), the cause of which was unclear but may have been due to waviness in the plastic trip insert or the thin portion of the PEEK used for attachment to the metal wedge frame; for example, screwing the trip insert into the model produced slight valleys at the attachment points, though their locations were at -63.5, 0, and 63.5mm. Fortunately this effect seemed to dissipate as one moved away from the leading edge. Note that upstream trip effects were studied by Semper [243].

Figure 7.22(a) was of specific interest. By $t \approx 12-15$s the majority of the oil had blown into the troughs and then off of the plate; the low velocity in the wakes and high velocity in the troughs led to this spanwise pressure differential. Once the bulk of the oil was removed, however, new peaks in the data appeared in the traces. These new peaks formed exactly in between the "trough" peaks and corresponded well to the location of the trips.

This dynamism in the data was unexpected and motivated deeper investigation. Greater detail on streamline merging and the transition process was provided in Figure 7.23. Just after the run

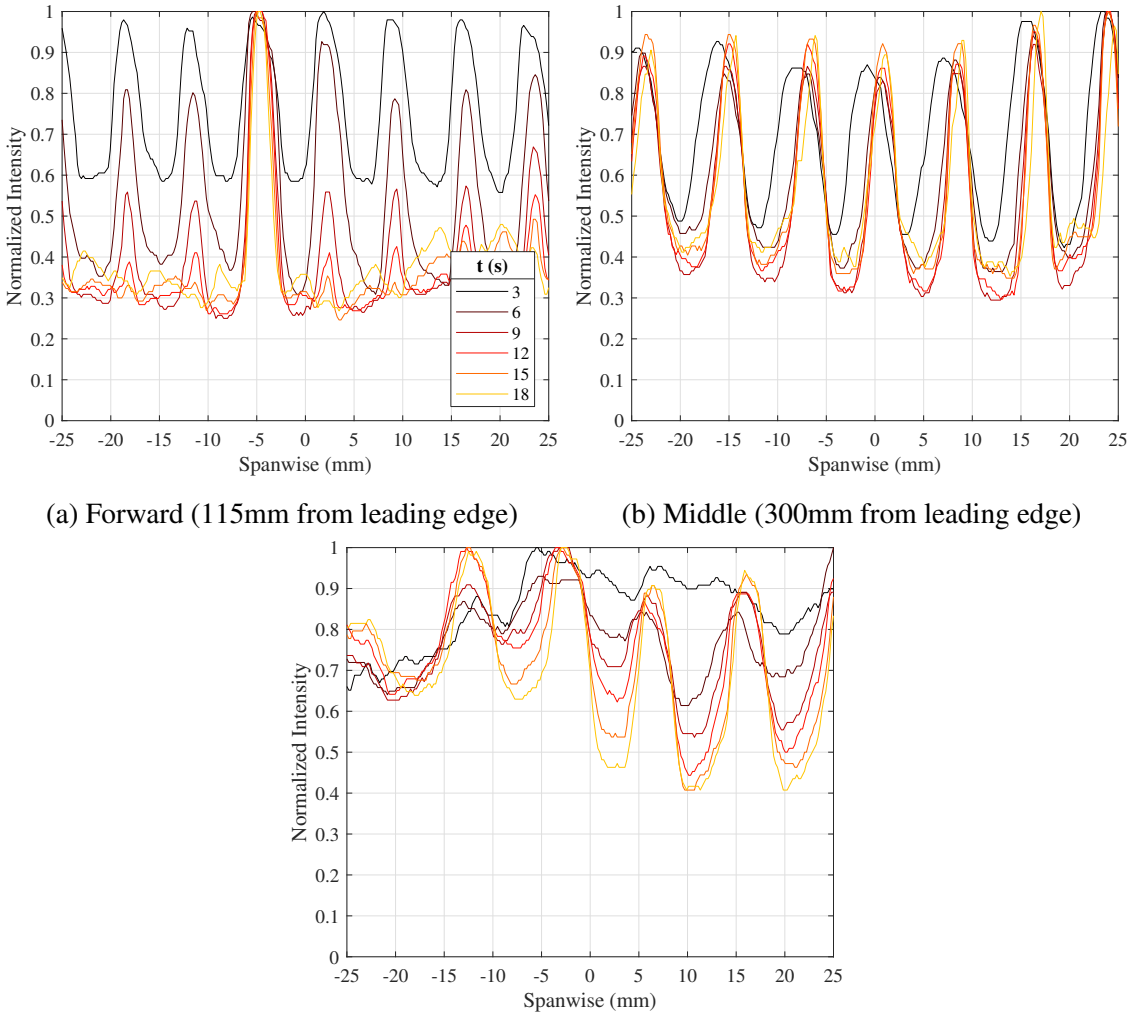

(a) Forward (115mm from leading edge)

(b) Middle (300mm from leading edge)

(c) Back (425mm from leading edge)

Figure 7.22: Spanwise traces of oil flow intensity with temporal evolution. Same legend applies for all figures.

began, at $t = 3$s, there was high signal in between the trips, no signal at the corner vortices, and then some signal in the centerline of the trip wakes. This may have been due to counter-rotating corner vortices pushing oil into the channels, a velocity deficit in the wake, low speeds in the channels due to shock-shock interaction (Semper [243] explored the near-trip shock behavior), or some combination of the three. Whatever the cause, just three seconds later, the channel structures were all that remained. However, evidence of the corner vortices appeared on the upstream electrode; this was a complete reversal of the signal at this location from just three seconds prior. It was

possible that it was not until only a thin coat of oil remained weak flow effects have sufficient force to manifest in the oil. This may have been the case, because another three seconds later at $t = 9$s the bulk of the oil had traveled past the second electrode. At $\sim$ 100mm from the leading edge in Figure 7.23(c), there appeared to be the corner vortices from two adjacent trips merging across a channel. It was possible this was the initiation of the breakdown process. Studying the subsequent images, Figure 7.23(d-f), where a trip's two corner vortices bifurcated, there was a faint rise in signal in the now free wake region. It was possible this was simply residual oil left on the plate, so one could ask if the wakes were breaking down, causing a pressure rise which splits the vortices apart like a wedge, or were the vortices constructively interfering once they reached a critical size? The location of the new vortex structures matched what was seen at downstream locations in Figure 7.21, and Figure 7.21(f) even seemed to have two "sub-streaks" in some of its features. Furthermore, in reviewing the video the streaks at the downstream locations formed immediately and with no obvious difference in streamwise oil velocity, which implied oil was being blown laterally by strong vortices. All of this implied the trip vortices evolved, but remained the dominant flow mechanism along the entire length of the test article. Ultimately, to better explore the space in between other techniques were required. Such a comparison to the features identified with IR thermography is provided in Section 7.5.

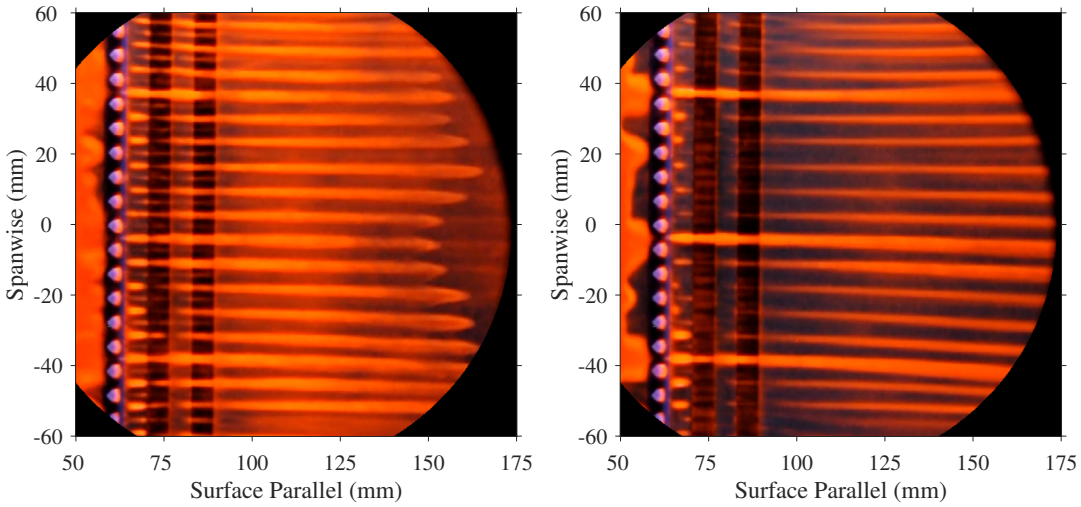

(a) $t = 3$s

(b) $t = 6$s

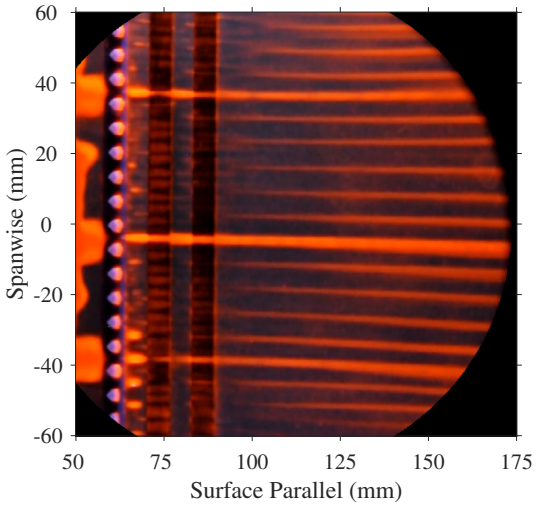

(c) $t = 9$s

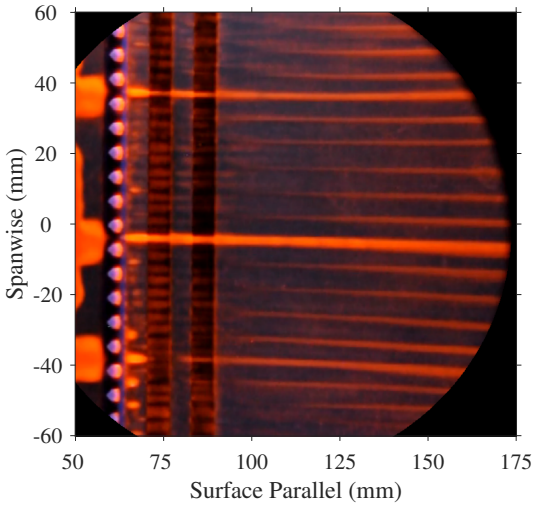

(d) $t = 12$s

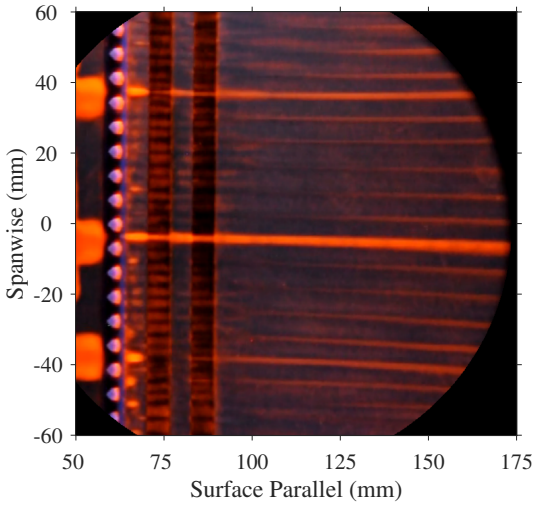

(e) $t = 15$s

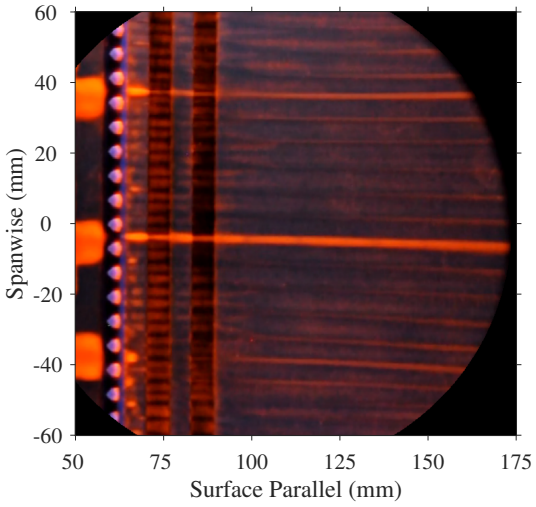

(f) $t = 18$s

Figure 7.23: Temporal evolution at the Forward location.

7.3.2 Schlieren Results

Schlieren imaging serves many useful roles. It visualizes shock structures, boundary layers, and separation/reattachment zones. Seeing shocks is necessary to study the leading edge, as well as identify any issues with the quality of the test volume such as Mach waves or impinging shocks; it is even possible to view the shock produced by a glow discharge [252, 251, 87]. Measuring the boundary layer height is helpful for CFD validation, offers an excellent comparison point for other diagnostics like PLIF or Pitot surveys, and can help scale test article features like the trips; simply showing the boundary layer also describes its state: laminar; transitional; or turbulent. Checking that separation is prevented at the leading edge is an additional application because such a result would adversely affect the flow's temporal stability, and even fatigue the model's sting; it is interesting to study the separation and reattachment structures near the trips as well, as was done by Semper [243].

The schlieren campaign is summarized in Table 7.10; note that IR data was collected concurrently, so the test matrices overlap. Runs were conducted at four test locations, with the test article and test section windows adjusted to maximized the amount of boundary layer seen. The plasma was run on and off and the trips were installed and omitted for four runs at each location. Two additional runs (Runs 4551 and 4550) visualized the shocks at the leading edge with the trips and a blank insert installed; no plasma was ignited as the view was entirely upstream of the electrodes, and the entire wedge itself was moved backwards on the struts to allow visualization of the leading edge. It was helpful to reiterate some elements of the data processing. For all runs data was collected at 1000fps with a 1.25μs gate to capture high-speed effects without restricting the field of view or sacrificing too much signal. The tunnel started at and was left on the test condition of $Re = 6 \times 10^6/\text{m}$. A large area was left above the boundary layer to show the development of shocks in the freestream; this was helpful for comparing to the PLIF data. Finally, the mean images were the average of 100 frames surrounding an instant, so the frame rate of mean images effectively matched the NALDAQ's 10Hz collection frequency. The plasma properties for these runs are summarized in Table 7.11. These data represented each run's average once the plasma reached

it's operational condition. As was shown in Figure 7.24, the plasma was nominally switched on at $\sim$ 10s, reached its operational condition by $\sim$ 15s, and was switched off at $\sim$ 27s, so $\sim$ 10s of data were averaged.

No.	Location	Trip	Plasma	Run/Date
1	Back	Laminar	Off	4518, 10/1/2020
2	Back	Turbulent	Off	4522, 10/2/2020
3	Back	Laminar	On	4533, 10/5/2020
4	Back	Turbulent	On	4532, 10/5/2020
5	Middle	Laminar	Off	4527, 10/3/2020
6	Middle	Turbulent	Off	4524, 10/2/2020
7	Middle	Laminar	On	4529, 10/4/2020
8	Middle	Turbulent	On	4530, 10/4/2020
9	Forward	Laminar	Off	4538, 10/7/2020
10	Forward	Turbulent	Off	4539, 10/7/2020
11	Forward	Laminar	On	4537, 10/6/2020
12	Forward	Turbulent	On	4540, 10/7/2020
13	Forward (LE)	Laminar	Off	4551, 10/9/2020
14	Forward (LE)	Turbulent	Off	4550, 10/9/2020

Table 7.10: Schlieren test matrix.

No.	Current (mA)	Power Supply Voltage (V)	Power Supply Power (W)	Plasma Voltage (V)	Plasma Power (W)
3	93.9	1406	132.1	463.8	43.6
4	94.8	1399	132.7	447.9	42.5
7	88.4	1341	118.5	454.4	40.2
8	89.5	1342	120.1	444.1	39.7
11	93.6	1409	131.9	470.1	44.0
12	93.4	1402	130.9	465.5	43.5
			Average		
	92.3	1383	127.7	457.6	42.2

Table 7.11: Plasma conditions for schlieren campaign.

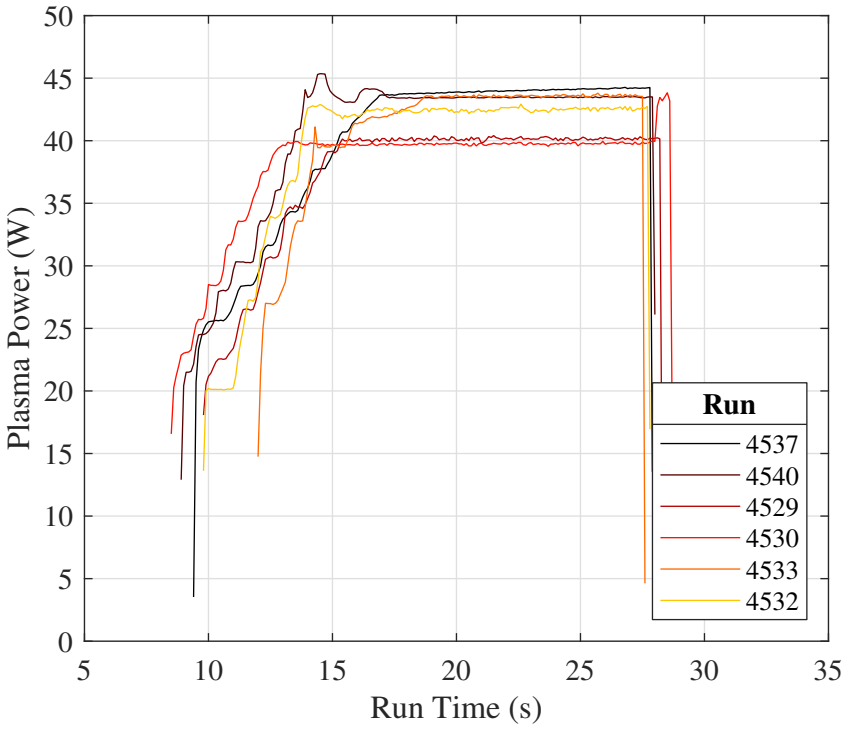

Figure 7.24: Plasma power traces for schlieren and IR thermography runs.

Figure 7.25 shows the leading edge behavior. It is noted the images were rotated such that the top surface was flat to allow better comparison with subsequent images, and that the vertical scale started at the wedge centerline, not the top surface. In reviewing the high speed footage, there was no evidence of separation at the leading edge, and the test article was relatively free of vibration. There was no clear evidence of the trips in this view to distinguish the turbulent run from the laminar run, so the data from the latter was not shown. The characteristic curvature of the hypersonic shock [6], especially near the intentionally blunted leading edge, was present. The thickness of the shock and perceived deformity of the leading edge were a consequence of imperfect alignment between the 3D object (a 2D extrusion) and the schlieren system. The measured shock angle between the shock and the top surface was $\sim 15.25°$, so considering the 2.75° wedge half-angle the total shock angle is $\sim 18°$. This deviated strongly from the 11.95° predicted by the theory in the boundary layer solver (see 7.1, [128]) but it was potentially explained by the bluntness of the leading edge polynomial, the thickness perceived by the technique, the curvature of the shock, and

viscous effects like those described by Hayes and Probstein [108]. In the next downstream view (Figure 7.27), the shock was straighter and the measured shock angle was $\sim 12°$ for a cumulative angle of ~ 14.75, which aligned more reasonably with the theory.

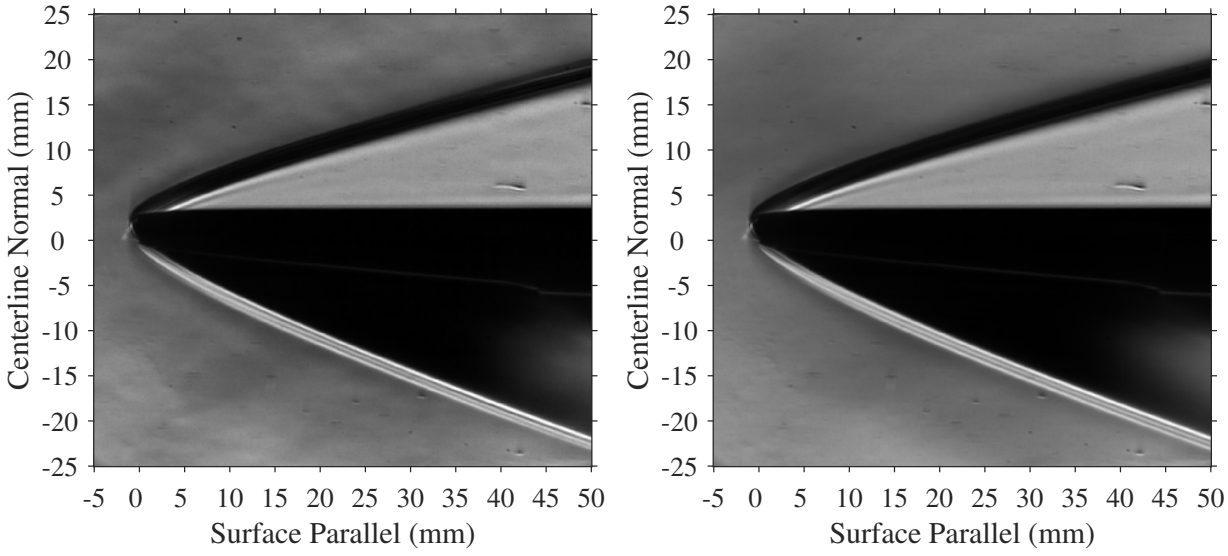

(a) Instantaneous

(b) Mean

Figure 7.25: Instantaneous and mean schlieren images of the leading edge. Trips are installed, but out of view.

There bulk of the data are presented in Figures 7.26, 7.27, 7.28, and 7.29. The former two figures are instantaneous and mean images from runs without the plasma while for the latter two the plasma was ignited. The mean images generally provided clearer trends as it seemed the 1.25μs camera gate was, unsurprisingly, too large to freeze the flow; it will become clear in Section 7.4.2 PLIF remedied this issue.

Comparing the data, it seemed the plasma had no effect on the boundary layer height, and any shocks formed above the cathode were too weak to see. This was not surprising, as the plasma was sized not to be a direct flow perturbation like the studies in Section 2.4.4 but to seed in vibrational nonequilibrium. Any boundary layer thickening due to cathode or Joule heating would convoluted any effects of vibrational relaxation, which were the focus of this report.

For simplicity, the remainder of the analysis was conducted on Figure 7.27. Consider the laminar images first. The Mach waves introduced by the electrodes and PEEK insert were clearly visible. Evidence of the latter was arguably present beyond 45mm in Figure 7.25 as the seam was approximately 44mm from the leading edge. Of greater interest was the boundary layer height. It appeared that the boundary layer was nearly a constant 5mm. This defied the expected growth with the streamwise coordinate [6]. Looking more closely at Figure 7.25, it seemed this feature was faintly present within 20mm of the leading edge, which was further evidence it was not a boundary layer. A likely explanation was that this was the entropy layer. The true boundary layer appeared to be the thin streak entrained within this larger structure. If this was the case, the laminar boundary layer appeared to be $1-2$mm in 7.27(a), $2-3$mm in 7.27(c), and $3-4$mm in 7.27(e); these values were much closer in agreement to the theory of van Driest [283] and predicted by the boundary layer solver in Section 7.1.

Interestingly, in the instantaneous Figures 7.26(e) and 7.28(e), and impinging shock appeared to be causing the boundary layer to transition at 455mm. The shocks presented in the "Back" view were known wind tunnel imperfections caused by the 22.86cm nozzle merging abruptly with the 23.18cm test section. These were so strong that in preliminary IR testing they caused a sudden rise in surface heating. To avoid them, the entire test article was lowered 2.54cm in the test section by machining shorter struts. All runs were conducted with these shorter struts and usually with the wedge in a "Forward" position, and the present schlieren showed these efforts were mostly successful in preventing or delaying the impingement of the strongest shock. For safety, all tests were be conducted upstream of the shock impingement.

The turbulent images contained a wealth of information. Figure 7.27 showed the turbulent boundary layer to be $4-6$mm in 7.27(b), $8-10$mm in 7.27(d), and $10-12$mm in 7.27(f). As expected, the turbulent boundary layer was much thicker than the laminar analog, and while it was not frozen Figure 7.26 does show the chaotic eddies characteristic of turbulence. The laminar boundary layer appeared to be impinging two-thirds of the way up the trips, which was exactly how they were designed.

Furthermore, Figure 7.27(b) shows the upstream recirculation, oblique shock, and shear layer produced by the trips and described by Semper [243]. To be clear, the shear layer produced by the trips was present between $70-90$mm in Figure 7.27(b). Semper directly attributed this behavior to the corner vortices. It was interesting to note that this was roughly the range in which the corner vortices were visible in the oil flow data (Figure 7.23). An inspection of the instantaneous schlieren image Figure 7.26(b) revealed the boundary layer was transitional after this point, perhaps becoming turbulent between $130-150$mm. This supported the theory introduced in Section 7.3.1, that the merging of the streamlines in Figure 7.23 approximately 100mm from the leading edge was indeed transition to turbulence. Further experimentation was warranted, but an important finding has been introduced and corroborated between two independent techniques. Again, the presence of the glow discharge did not have any apparent effect on this transition process (Figure 7.28(b)), but this was not a concern for meeting the project's goals.

It can be difficult to ascribe uncertainty to a schlieren image, but as will be seen in the discussion of the Pitot probe's results, Section 7.3.5, accurate measurement of the wall, and ensuring the Pitot system was level with the plate, were critical. Again, the wall was manually rotated and translated out of frame from "flow on" data to account for any shift and pitch once the tunnel started, but upon reviewing the data it seemed better alignment with the plate, specifically leveling the mirrors to account for the test article's roll, could have been achieved. The effect is most clear in Figure 7.27(b). Just upstream of the trips, one can see the step from their insert just above the wall, which was indicative of excellent alignment. However, the trips themselves seem to fall off towards the horizon, implying the plate was rolled clockwise relative to the mirrors. The same effect likely cause the lack of clarity of the leading edge in Figure 7.25.

From the gridcard images, it was estimated that by the center of the plate $\sim 0.5-1$mm had been cut off due to the roll, so as much as $\sim 1-2$mm could have been lost across the entire plate. With a total span of 215.9mm, this would imply a span of $0.27-0.53°$; recall that when it was installed in the tunnel, the plate was leveled with $\pm 0.1°$. Now, schlieren is a path integrating technique, so even if the boundary layer was obfuscated on one side of the wedge, the full view would be

clear on the other. Thus this uncertainty, while not ideal, would not affect the measured height of the boundary layer, but it could cause vertical blurring in features $\sim 1-2$mm. This explained the perceived thickness of the shocks. It is recommended for any future schlieren work more attention be payed to aligning the schlieren system with the test article, especially if the geometry is as wide as the one studied here.

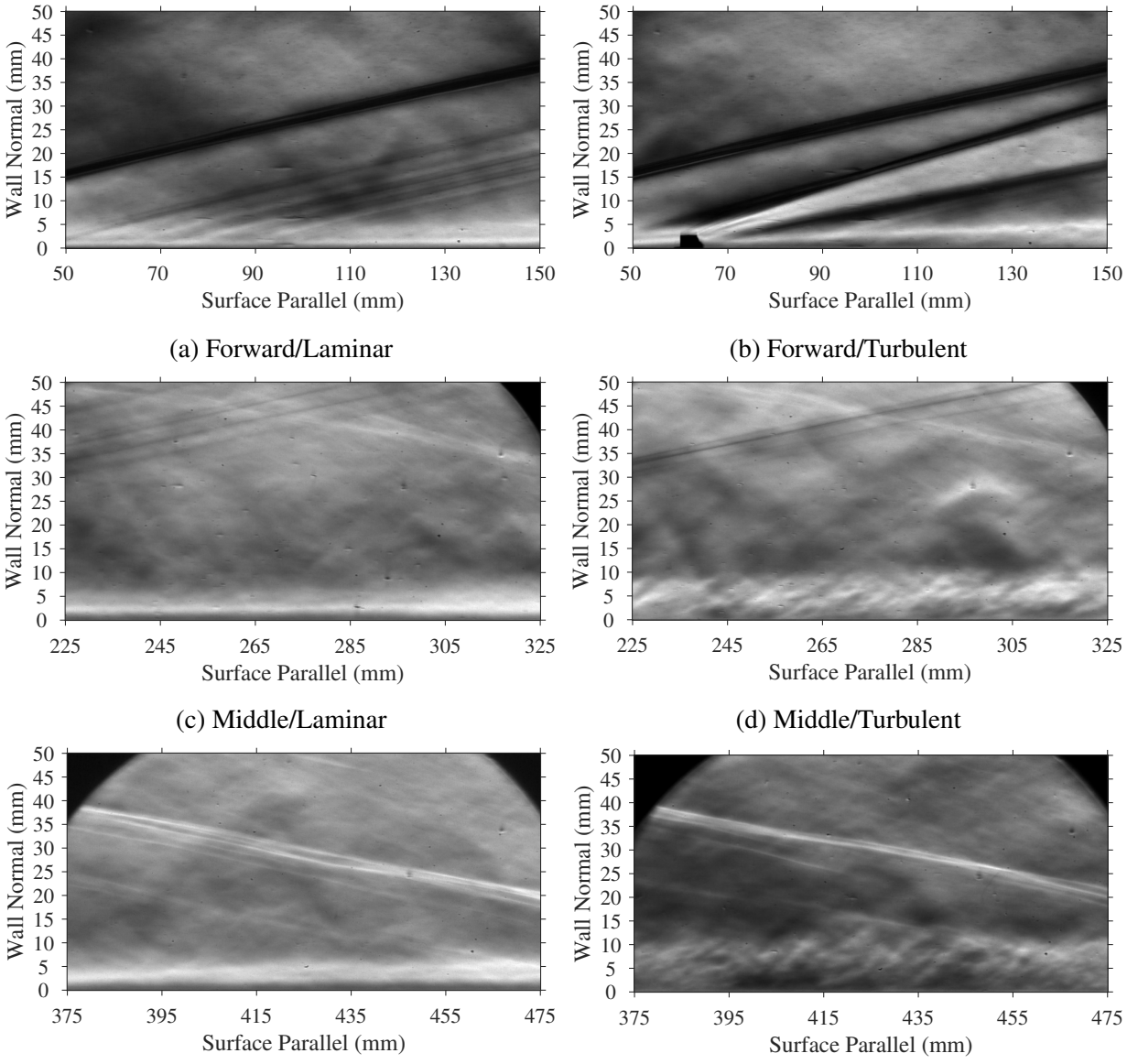

(a) Forward/Laminar

(b) Forward/Turbulent

(c) Middle/Laminar

(d) Middle/Turbulent

(e) Back/Laminar

(f) Back/Turbulent

Figure 7.26: Instantaneous schlieren images with the plasma off.

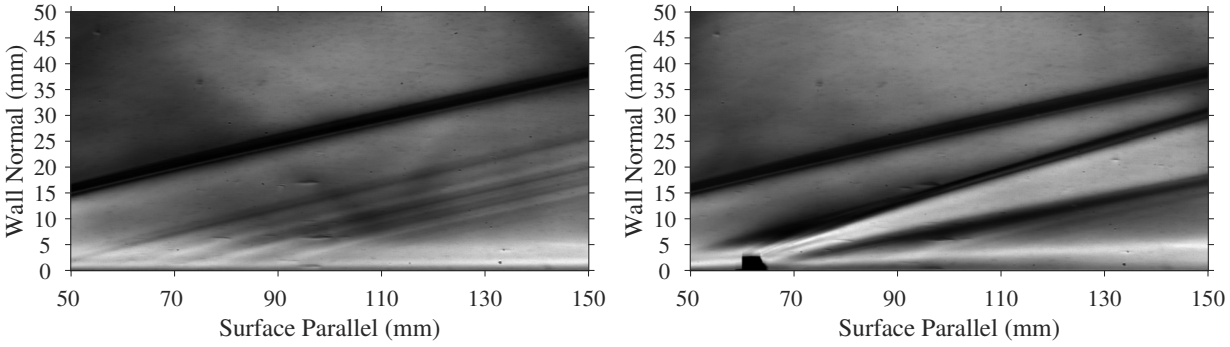

(a) Forward/Laminar

(b) Forward/Turbulent

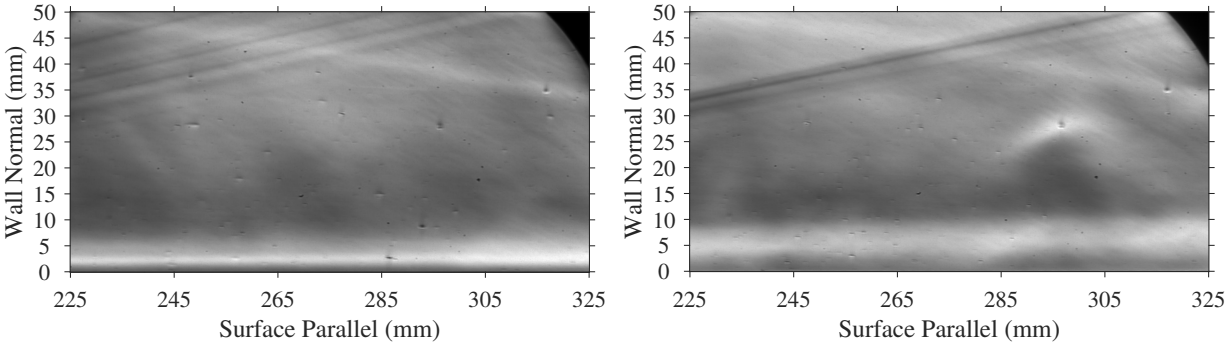

(c) Middle/Laminar

(d) Middle/Turbulent

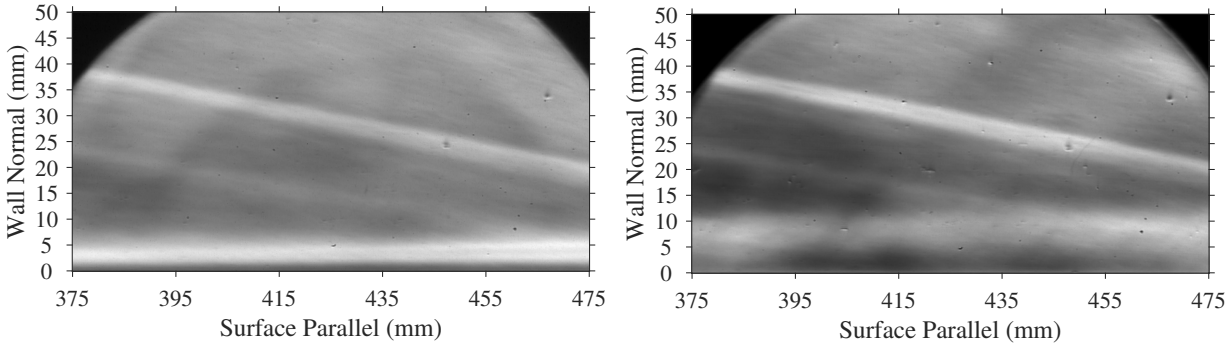

(e) Back/Laminar

(f) Back/Turbulent

Figure 7.27: Mean schlieren images with the plasma off.

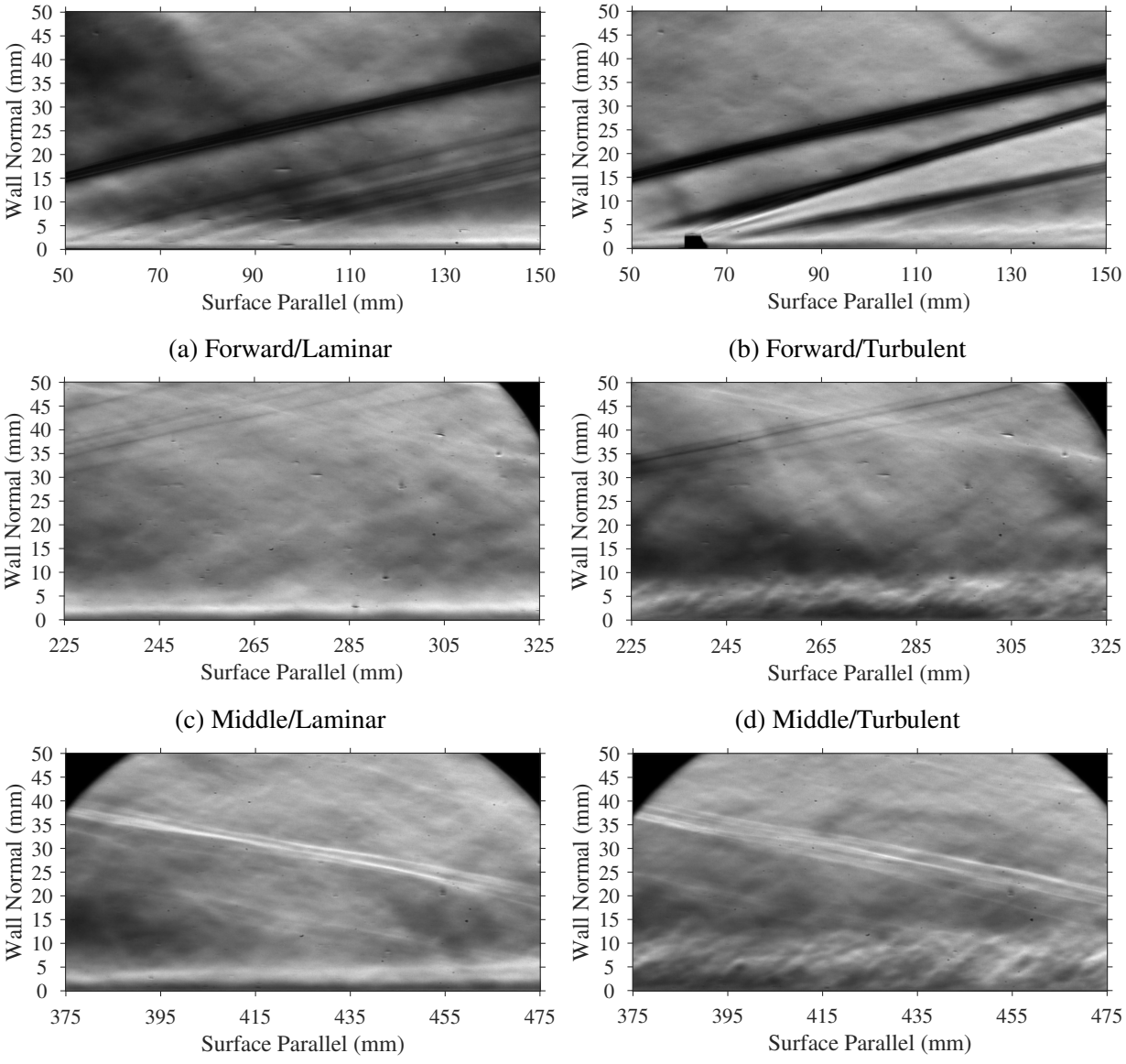

(a) Forward/Laminar

(b) Forward/Turbulent

(c) Middle/Laminar

(d) Middle/Turbulent

(e) Back/Laminar

(f) Back/Turbulent

Figure 7.28: Instantaneous schlieren images with the plasma on.

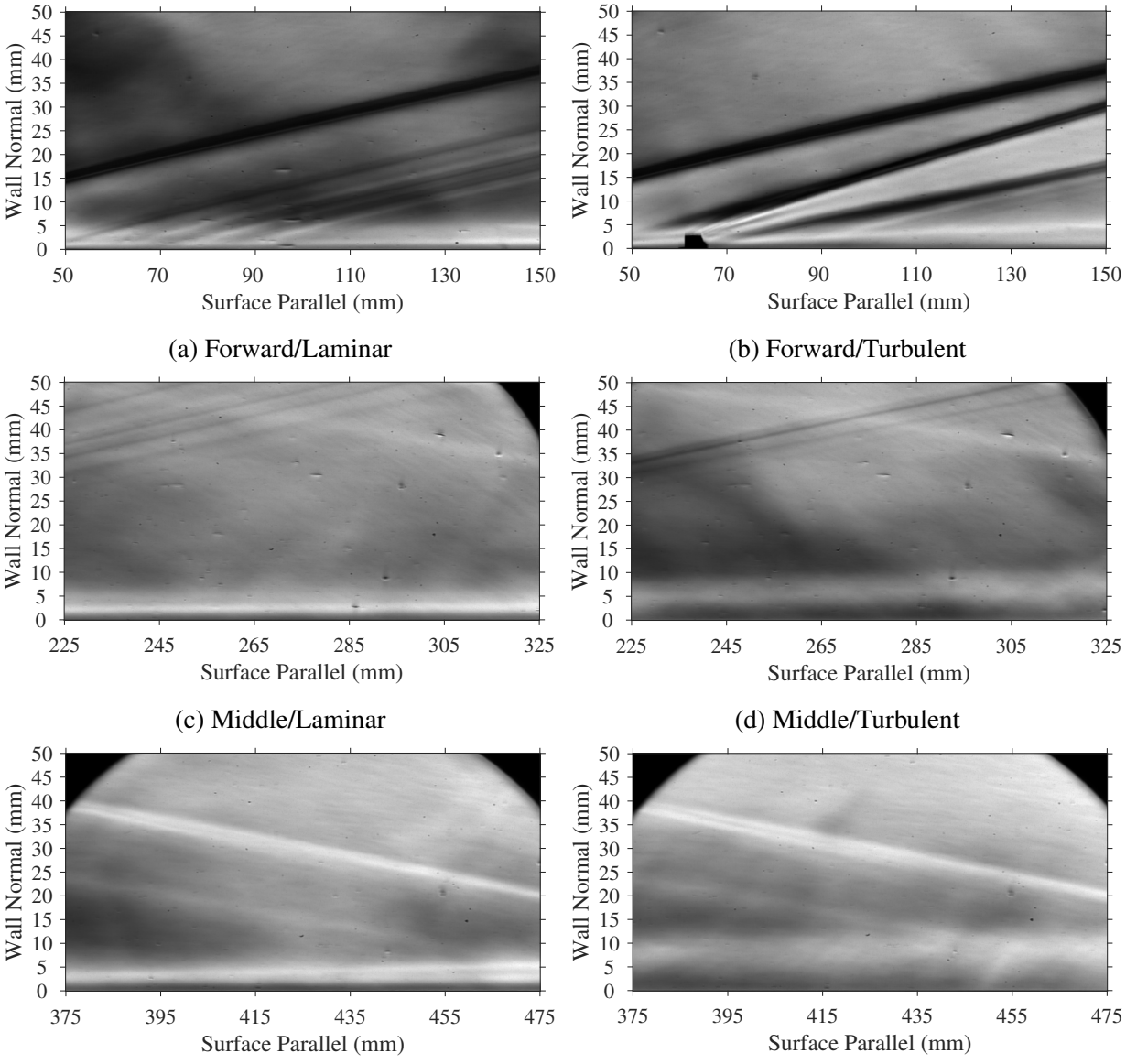

(a) Forward/Laminar

(b) Forward/Turbulent

(c) Middle/Laminar

(d) Middle/Turbulent

(e) Back/Laminar

(f) Back/Turbulent

Figure 7.29: Mean schlieren images with the plasma on.

7.3.3 IR Results

IR thermography measures the wall's thermal conditions. This can be used to set the thermal boundary condition needed for both CFD and PLIF, provide validation data for CFD, inform the state of the boundary layer, and reveal some flow structures like wakes or impinging shocks. Here temperatures were converted into heat flux, and then nondimensionalized into Stanton number. The heat flux, and thereby the Stanton number, both required an internal wall boundary condition to be known for calculation, so data was only provided within the bounds of the embedded thermocouples (with a few millimeters' exception to provide traces at 260mm); enough data was shown in the spanwise direction to study any effect of a free PEEK or metal-supported PEEK wall condition may have. Recall from Section 4.4 that the test article was hollow to allow for laser diagnostics, but outside of the ± 25.4mm span along the centerline the PEEK was in contact with the metal wedge frame. To prevent any contamination from these differing wall conditions, heat flux and Stanton number data is not provided beyond ± 25.4mm. The temperature measurements had no such limitations, and thus were provided over a larger domain. Again, the schlieren and IR runs were conducted concurrently, so the test matrix and plasma conditions are included in Tables 7.10 and 7.11 respectively. All still images were provided after the plasma had reached its operating condition and at the same time as the above schlieren images. Finally, it is noted that the glass used for laser diagnostics likely behaved differently from the PEEK measurements here; no correction is offered here, though Buen [49] used a thermocouple to measure the glass wall temperature for their PLIF work. Similarly, heating of the thermocouple by conduction through its mounting must be ignored. Note that thermocouples were mounted $[104.6, 122.1, 139.5, 157.0, 263.5, 327.0, 390.5, 454.0]$mm from the leading edge in the surface parallel coordinate.

The results are shown below. It is noted that they are compared to the numerical boundary layer solver's predictions and the oil flow's features in Section 7.5. Figure 7.30 provides the PEEK temperature under the maximum domain attainable. The forward views, 7.30(a) and (b) show slight heating near the electrodes; this was explored directly in a later figure. Figure 7.30(b) was especially important because it studied the streak behavior seen in the oil flow data. In Figure 7.23,

the trip vortices merged just downstream of the electrodes. In IR, the corner vortices were apparent just downstream of the trip, and they seemed to blur together into a wake structure downstream of the electrodes. This may have implied that the same mechanism which drove the corner vortices apart in the oil flow data was the main turbulent structure, that the combined "wake" was the true breakdown mechanism and it pushed the oil into the troughs. It was noted that the strong thermal perturbations produced by the trips and enhanced by the plasma were likely to be the source of the degredation of the cathode and evident structures in the glow discharge discussed in Section 7.2.1. The middle and downstream views in Figure 7.30(c-f) show how the cutout beneath the PEEK did produce some spanwise nonuniformity, as did the thermocouples. The effects were small and were mostly corrected via heat flux calculation; this "heat flux normalization" allowed Leidy [160], who used a 6.35mm PEEK insert instead of the present 15.62mm, to produce workable data. Nevertheless, to be conservative it was best to focus on data from the core area where the thermocouples directly measured the internal conditions, and to take spanwise traces away from the location of the thermocouples.

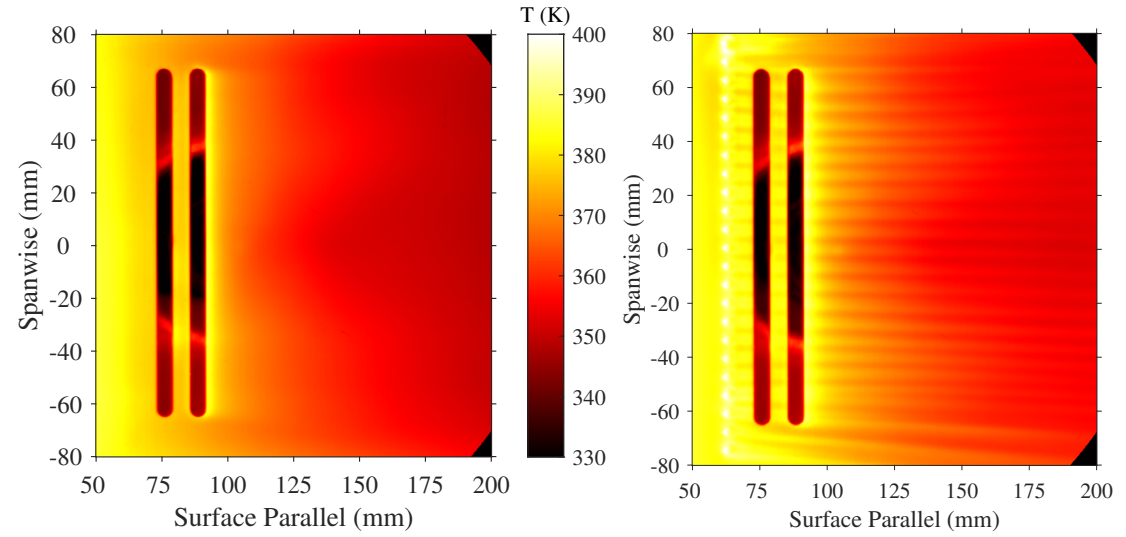

(a) Forward/Laminar

(b) Forward/Turbulent

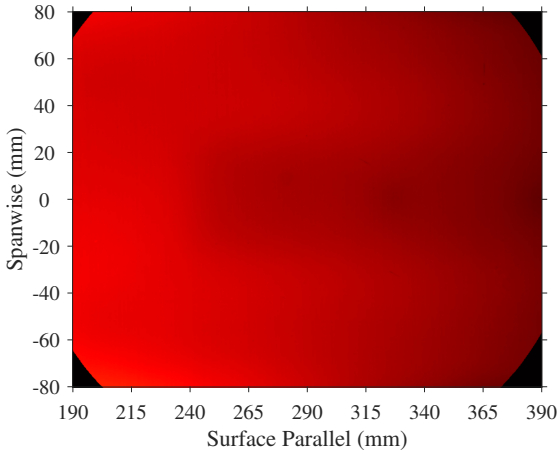

(c) Middle/Laminar

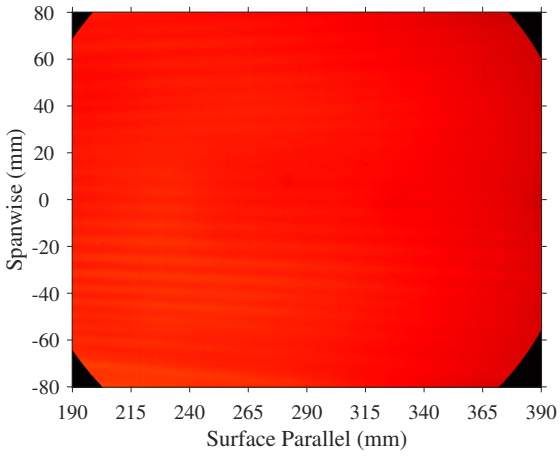

(d) Middle/Turbulent

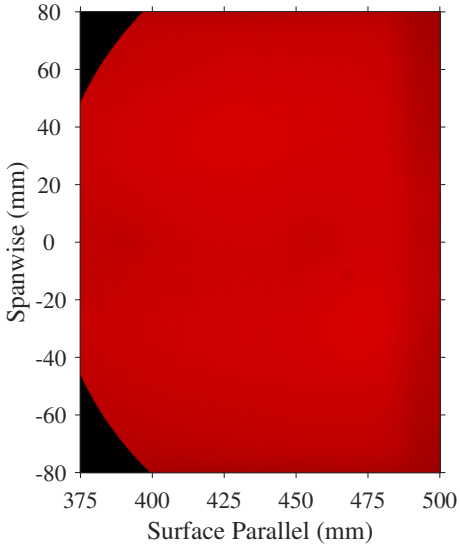

(e) Back/Laminar

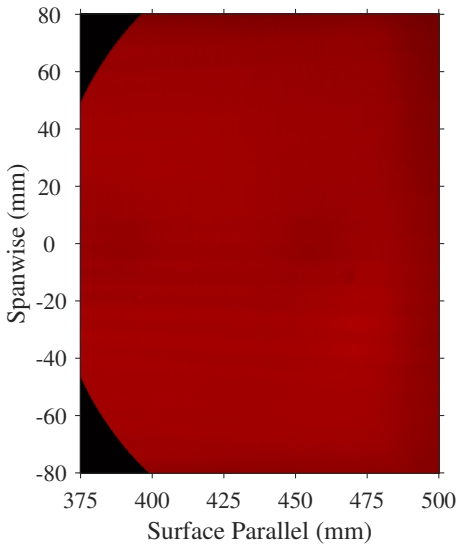

(f) Back/Turbulent

Figure 7.30: IR temperature maps with the plasma on. Same legend applies for all figures.

Figures 7.31 through 7.36 show the effect turbulence and plasma had on temperature, heat flux, and Stanton number. First considering the temperature data, Figures 7.31 and 7.32, there seemed to be little change over time, which suggested an isothermal wall condition of $\sim$ 350K was roughly appropriate throughout the majority of the domain in the core flow. It was surprising that the temperature was not significantly higher for the turbulent case than the laminar case, but this was likely a consequence of leaving the test article in the test section during preheat, which "set" the wall temperature near the adiabatic wall temperature. For the laminar and turbulent cases, the boundary layer solver calculated the adiabatic wall temperature to be 372.4K and 390.5K respectively. It was in this detail that the laminar and turbulent flows differentiated themselves as the turbulent case, being much farther from the adiabatic condition, had much higher heat flux (Figures 7.33 and 7.34). Naturally, the effects of the trips were strongest in the "Forward" location and smoothed out as one moved downstream; this suggested that the boundary layer became more uniform as the turbulence became fully developed, which was important in describing the quality of the test environment. To that end, by the "Back" location, the heat flux agreed reasonably well with the boundary layer solver's turbulent prediction (Figure 7.2(e)), both validating the code and the state of the turbulent boundary layer; the agreement in the laminar case (Figure 7.1(e)) was not as strong, the consequence of which will be discussed in Section 7.3.5. The collapse of heat flux traces over time was due to the internal PEEK becoming hotter. Any evidence of the free space or metal contact on the back of the model was not present in the heat flux data, which meant not only that the temperature difference was locally normalized, but that the thermocouples provided reasonable boundary conditions throughout the domain.

Any trends noticed in heat flux extend to Stanton number, but because the latter was normalized by tunnel and wall conditions it allowed for run-to-run comparisons. Recall that when the trips were installed, the flow was considered "Turbulent" and the T_{aw} in the Stanton number was calculated with $Pr^{\frac{1}{3}}$, so the results in the "Forward" location (Figures 7.33 and 7.34) were suspect as the flow was likely transitional. Also at this location, the "Laminar" results were considerably higher than one might expect, and they varied largely from run-to-run with q_w. This was because

$T_w \rightarrow T_{aw}$, but q_w did not approach 0; again, T_{aw} is considerably lower for laminar flows than for turbulent flows. This was likely a result of the thin PEEK at the leading edge, exposed on both the top and bottom surfaces. Here perhaps the temperature could change more rapidly, faster than the internal condition, as measured by the thermocouples, could. This would explain why the *St* fell so sharply as the flow started. Background subtracting the data may have helped account for the effect of being so near the leading edge during preheat, but it could not help if these elevated temperatures changed the test article's response to the flow.

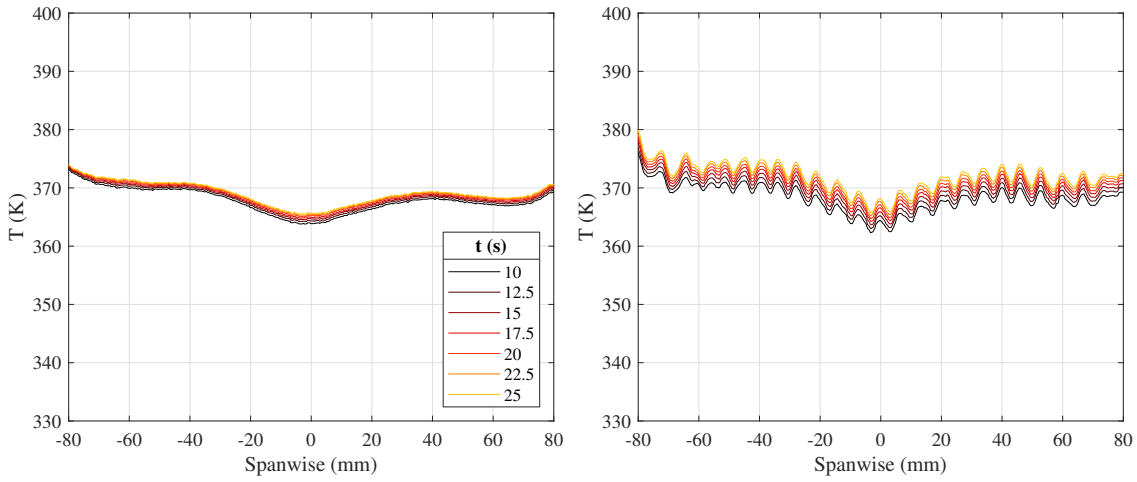

(a) Forward/Laminar

(b) Forward/Turbulent

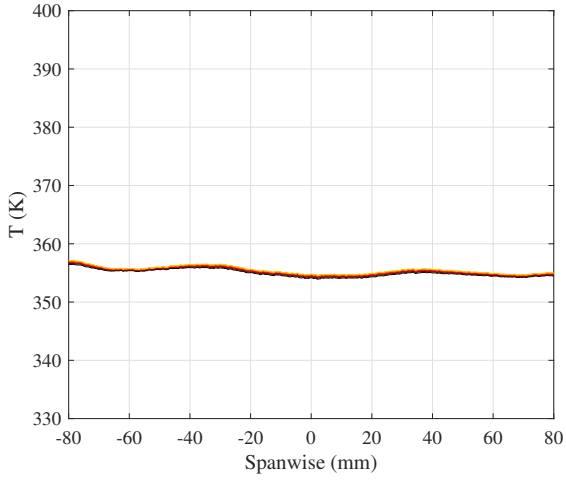

(c) Middle/Laminar

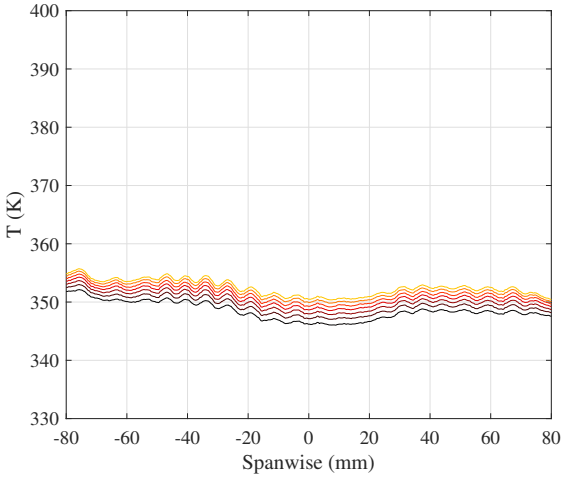

(d) Middle/Turbulent

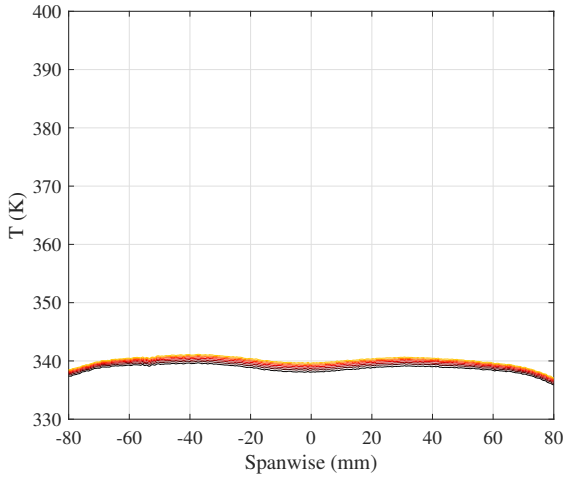

(e) Back/Laminar

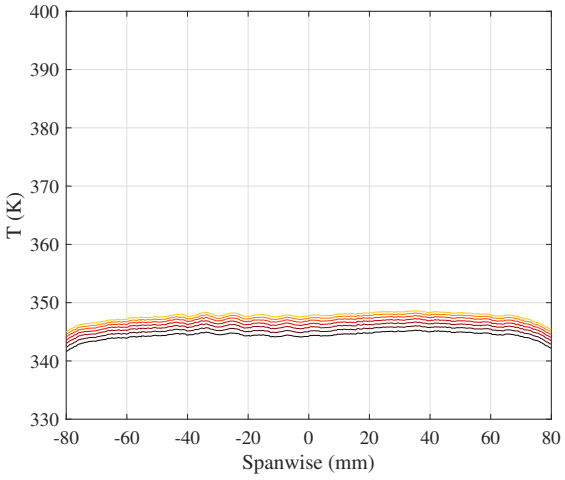

(f) Back/Turbulent

Figure 7.31: IR temperature spanwise traces with the plasma off. Traces are 115 ("Forward"), 260 ("Middle"), and 405mm ("Back") from the leading edge. Same legend applies for all figures.

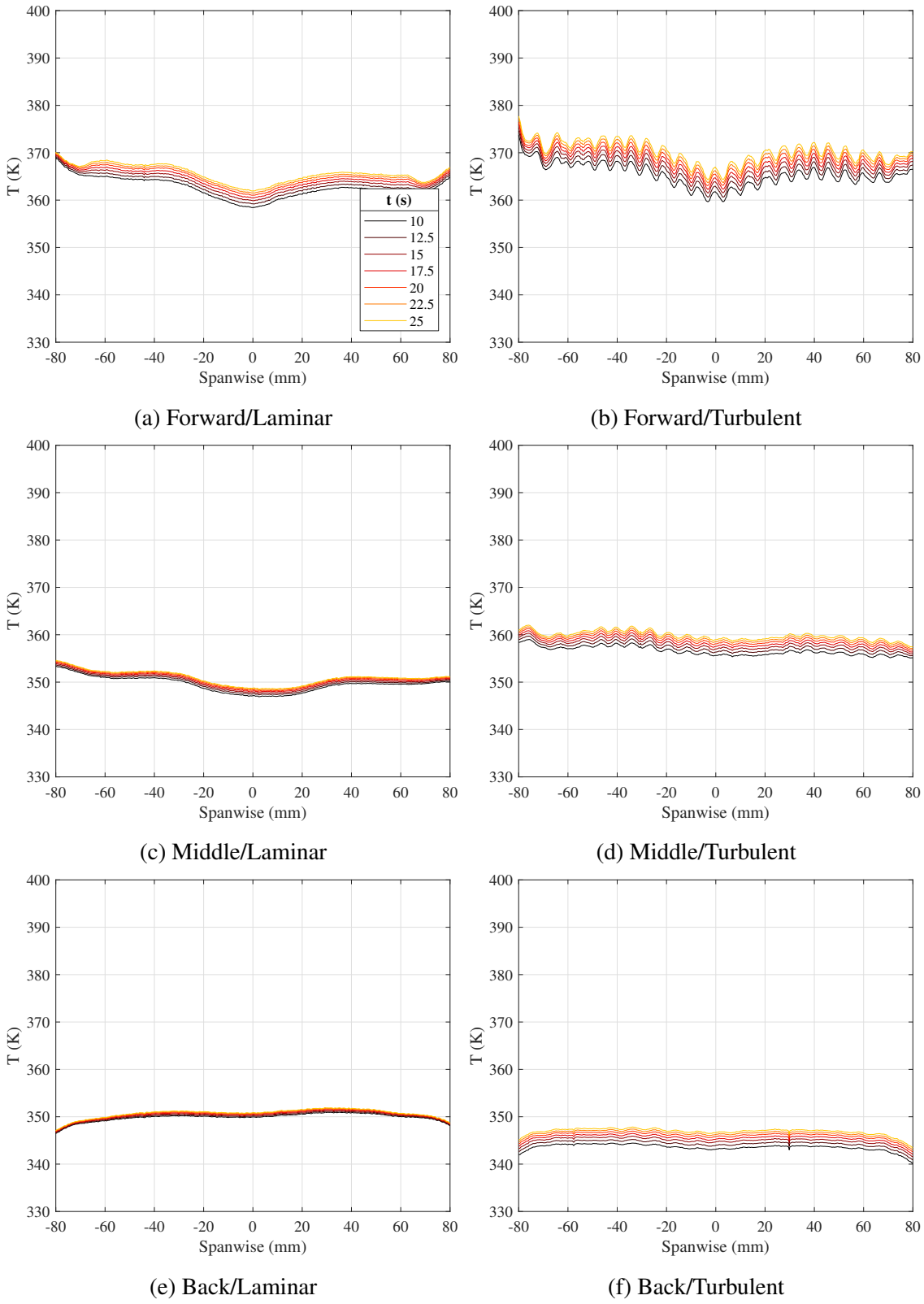

(a) Forward/Laminar

(b) Forward/Turbulent

(c) Middle/Laminar

(d) Middle/Turbulent

(e) Back/Laminar

(f) Back/Turbulent

Figure 7.32: IR temperature spanwise traces with the plasma on. Traces are 115 ("Forward"), 260 ("Middle"), and 405mm ("Back") from the leading edge. Same legend applies for all figures.

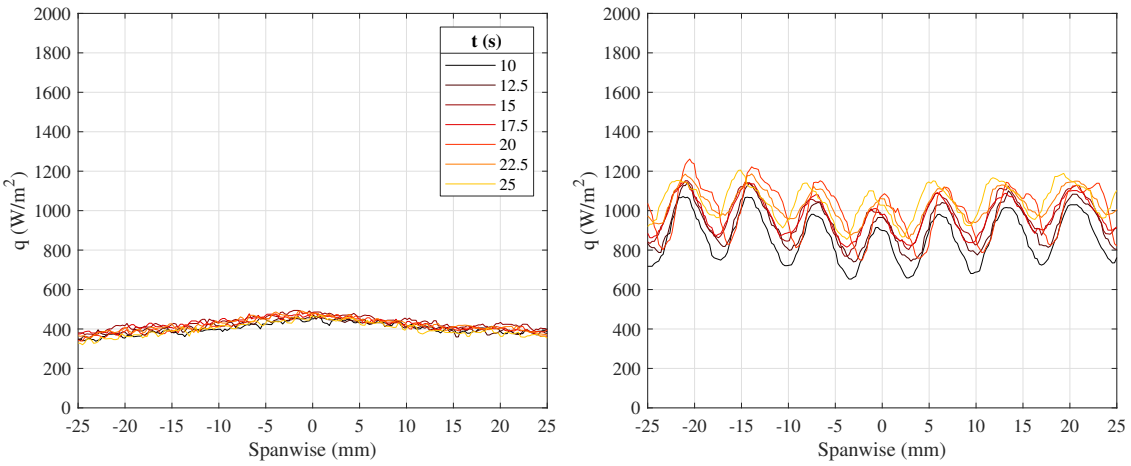

(a) Forward/Laminar

(b) Forward/Turbulent

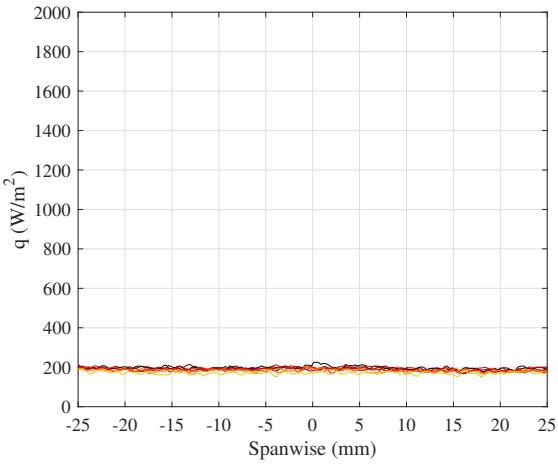

(c) Middle/Laminar

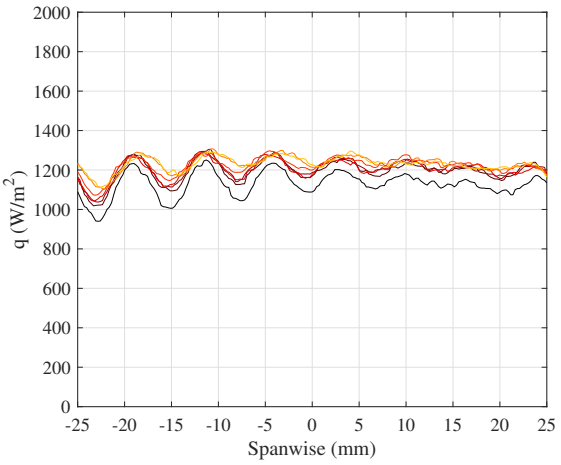

(d) Middle/Turbulent

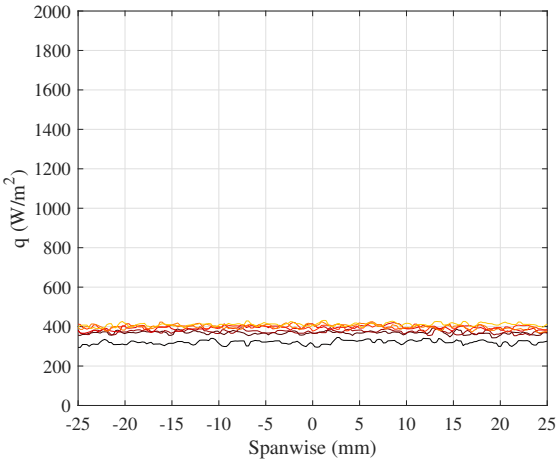

(e) Back/Laminar

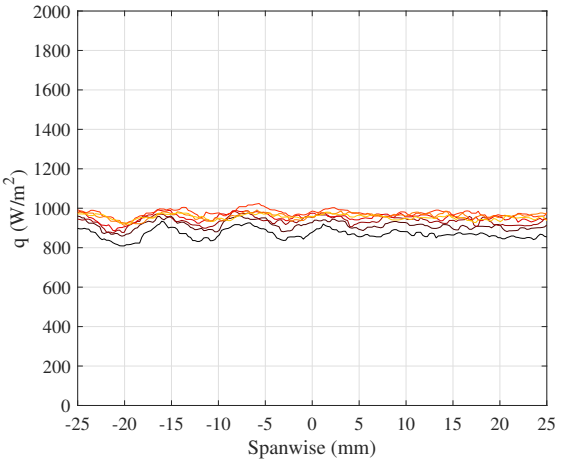

(f) Back/Turbulent

Figure 7.33: IR heat flux spanwise traces with the plasma off. Traces are 115 ("Forward"), 260 ("Middle"), and 405mm ("Back") from the leading edge. Same legend applies for all figures.

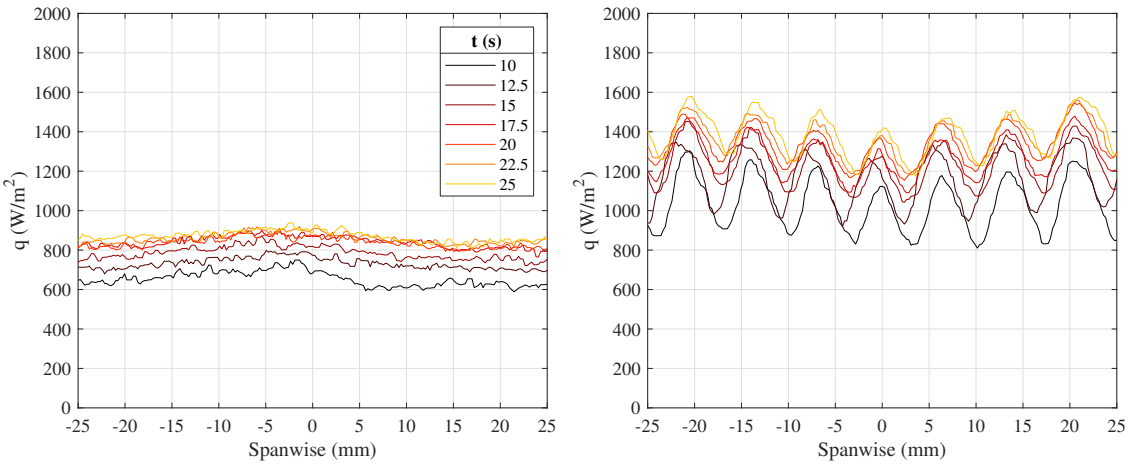

(a) Forward/Laminar

(b) Forward/Turbulent

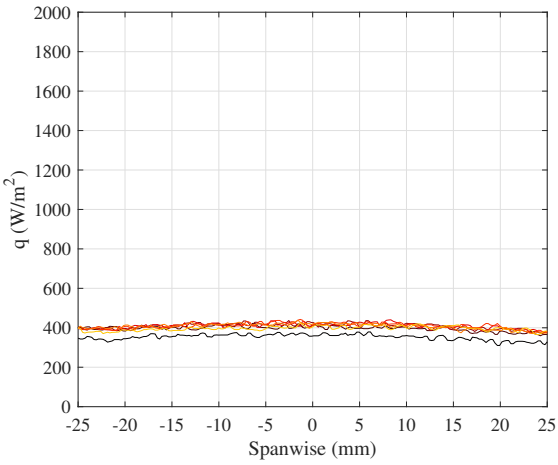

(c) Middle/Laminar

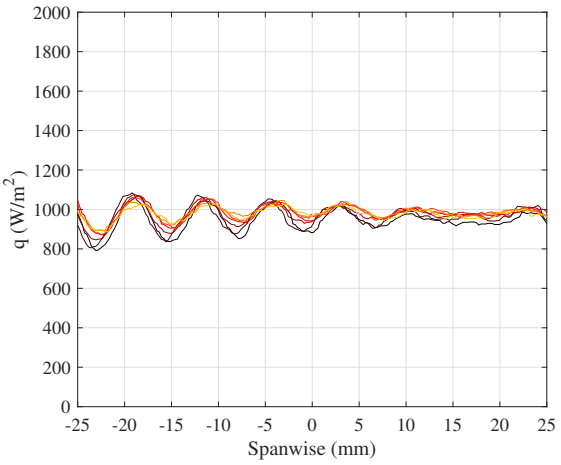

(d) Middle/Turbulent

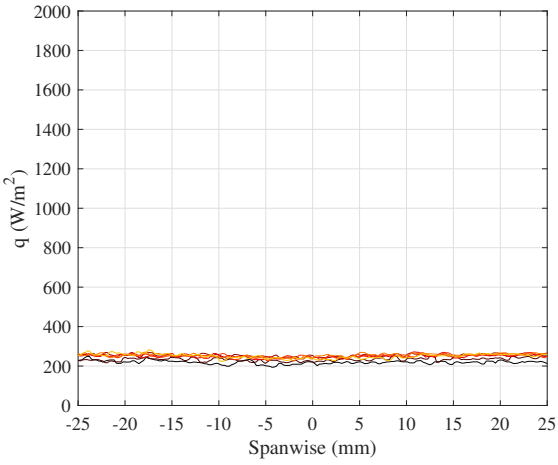

(e) Back/Laminar

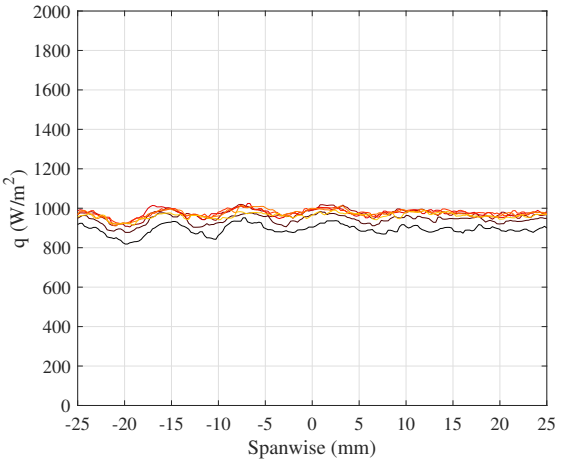

(f) Back/Turbulent

Figure 7.34: IR heat flux spanwise traces with the plasma on. Traces are 115 ("Forward"), 260 ("Middle"), and 405mm ("Back") from the leading edge. Same legend applies for all figures.

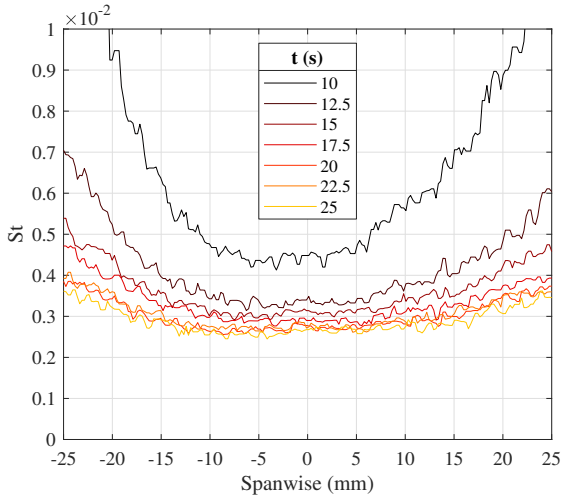

(a) Forward/Laminar. Note unique y-axis

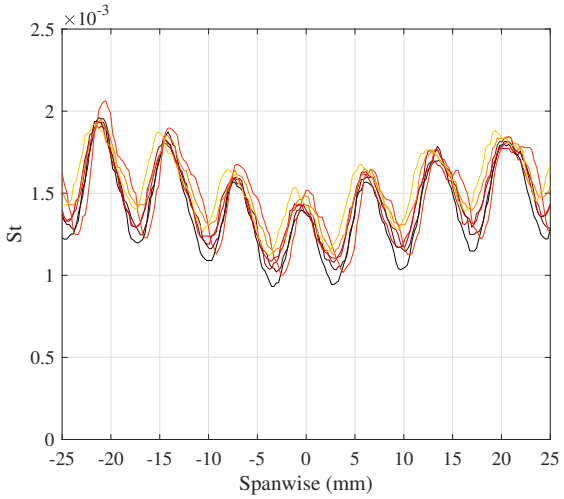

(b) Forward (115mm from LE)/Turbulent

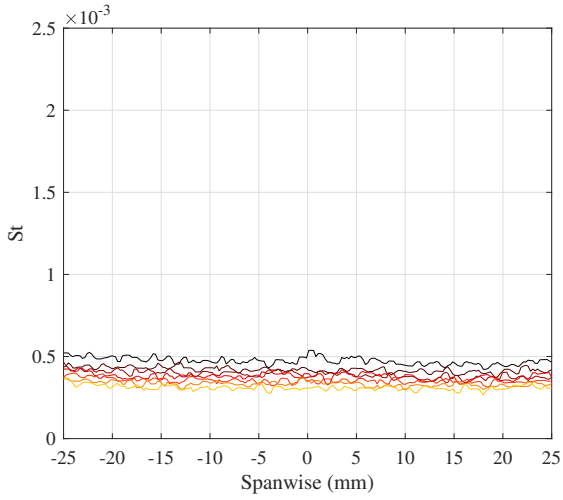

(c) Middle (260mm from LE)/Laminar

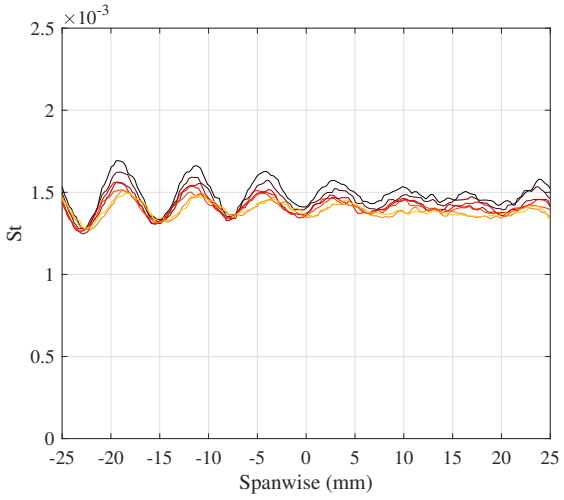

(d) Middle (260mm from LE)/Turbulent

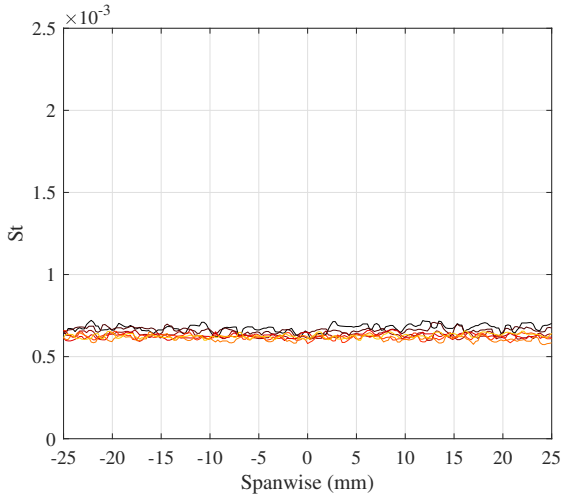

(e) Back (405mm from LE)/Laminar

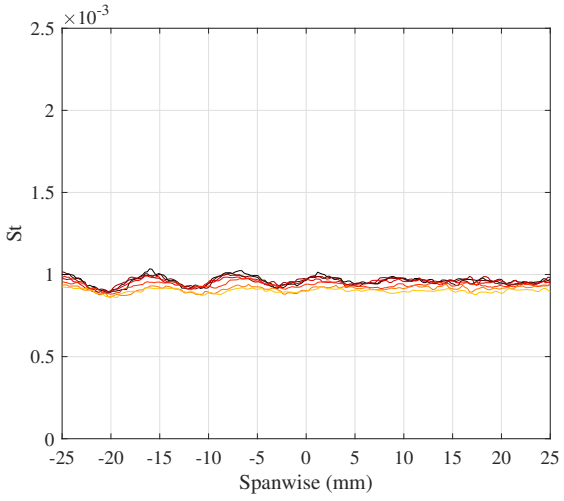

(f) Back (405mm from LE)/Turbulent

Figure 7.35: IR Stanton number spanwise traces with the plasma off. Traces are 115 ("Forward"), 260 ("Middle"), and 405mm ("Back") from the leading edge. Same legend applies for all figures.

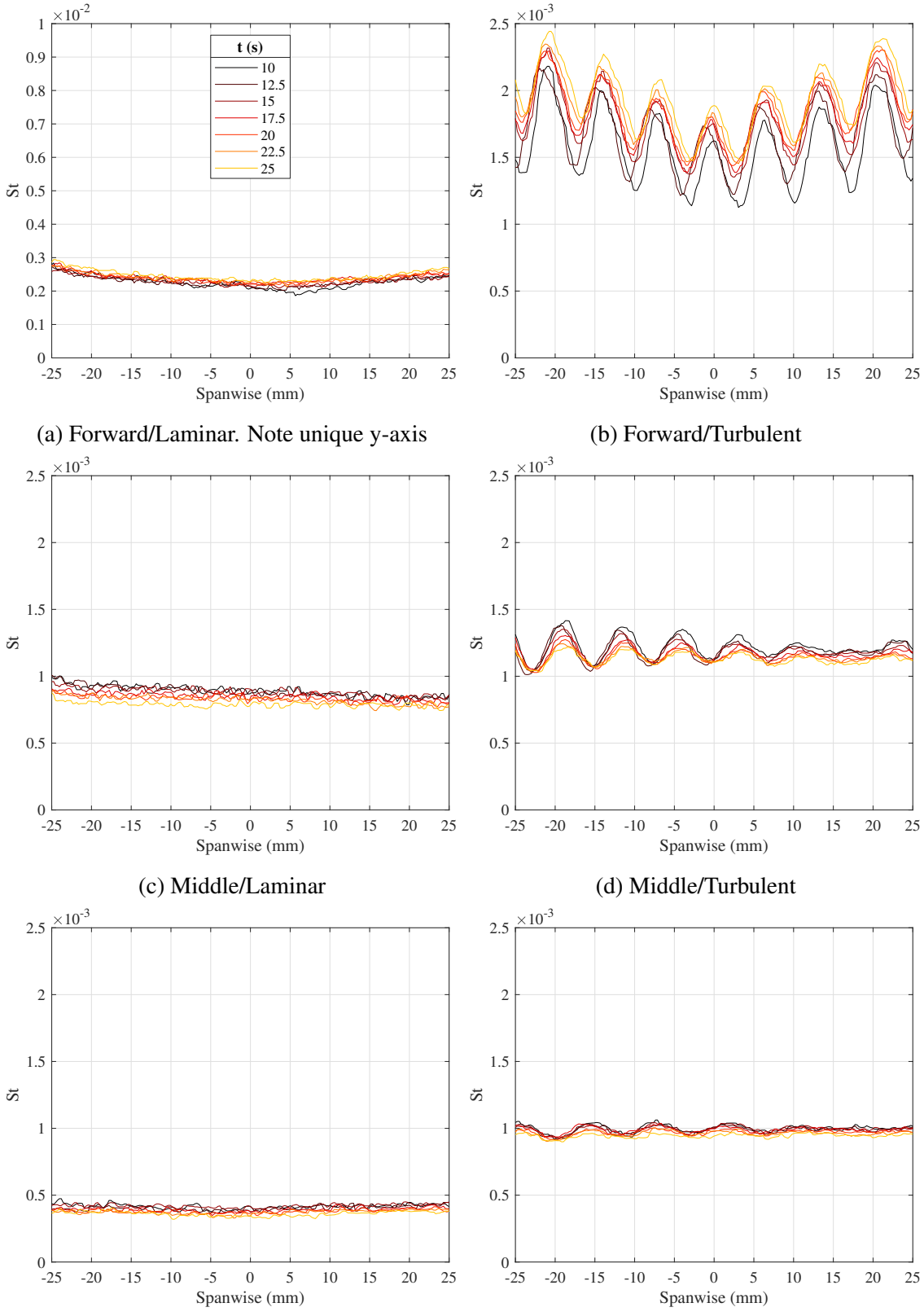

(a) Forward/Laminar. Note unique y-axis

(b) Forward/Turbulent

(c) Middle/Laminar

(d) Middle/Turbulent

(e) Back/Laminar

(f) Back/Turbulent

Figure 7.36: IR Stanton number spanwise traces with the plasma on. Traces are 115 ("Forward"), 260 ("Middle"), and 405mm ("Back") from the leading edge. Same legend applies for all figures.

Otherwise, the run-to-run normalization afforded by the Stanton number was useful when comparing the plasma on and off cases. The plasma had no obvious effect on the data, and despite normalization most of the variation between runs at the same location seemed to be from tolerable wall or tunnel differences. This meant that the plasma did not have a noticeable impact on the state of the boundary layer and thermal boundary condition, at least to within the fidelity of the IR thermography employed here. This was not problematic because the goal was always to seed in nonequilibrium, not modify the boundary layer. Furthermore, this was not to say the plasma had no thermal impact whatsoever. Figure 7.37 shows how the cathode heated up over time. In under 20s of total operation, it heated the PEEK immediately downstream $\sim$ 15K, a considerable amount given the short duration. This underscored the real impact cathode heating could have. The downstream side of the cathode was more greatly affected which implied the heat was convected off the surface as well as conducted through the PEEK.

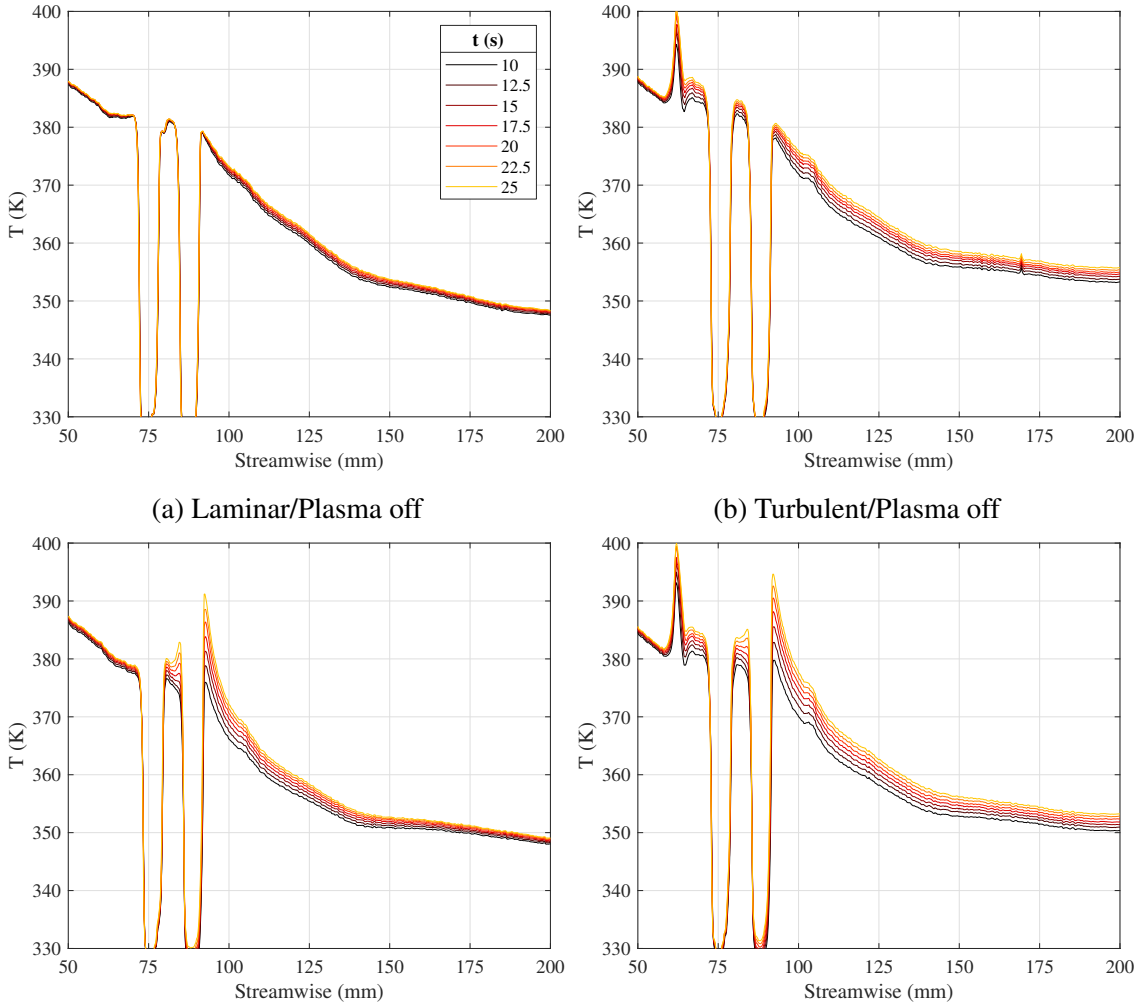

(a) Laminar/Plasma off

(b) Turbulent/Plasma off

(c) Laminar/Plasma on

(d) Turbulent/Plasma on

Figure 7.37: IR Stanton number streamwise traces at the model centerline. Same legend applies for all figures.

7.3.4 High Frequency Pressure Transducer Results

High frequency pressure measurements provide the spectral content in the boundary layer, from which one can infer its state: laminar; transitional; or turbulent. By varying their placement along the plate, these sensors can track the breakdown process; analogously, moving them to different positions along the span can provide detail on specific physics such as the effect of wakes, corner vortices, and troughs. As was discussed in Section 6.5, uncalibrated Kulite XCE-062A pressure transducers with a Kulite KSC2-C3 signal conditioning box were used for all of these measure-

ments which should provide voltage fluctuations from $f = 0 \sim f_r \approx 250$kHz. Because all analyses were done in the frequency space and these Kulites scaled linearly between voltage and pressure, it was sufficient to measure voltage fluctuations alone. The Kulites were placed 130, 260, and 405mm from the leading edge to match, as best as possible, the measurements from other techniques; extra space was added near the electrodes to attempt to prevent electrical interference. The sensors were placed 0 (wake), -3.42 (trough), -6.84 (wake), and -10.26mm (trough) along the span to again match previous off-centerline measurements, and to attempt to make measurements in wakes, troughs, and corner vortices. IR measurements were taken alongside the Kulite data for the express purpose of recording the placement of flow features with respect to the sensors. The test matrix and plasma conditions from what ended up being the few successful plasma runs are shown in Tables 7.12 and 7.13 respectively; Figure 7.38 shows the plasma power traces for the corresponding runs.

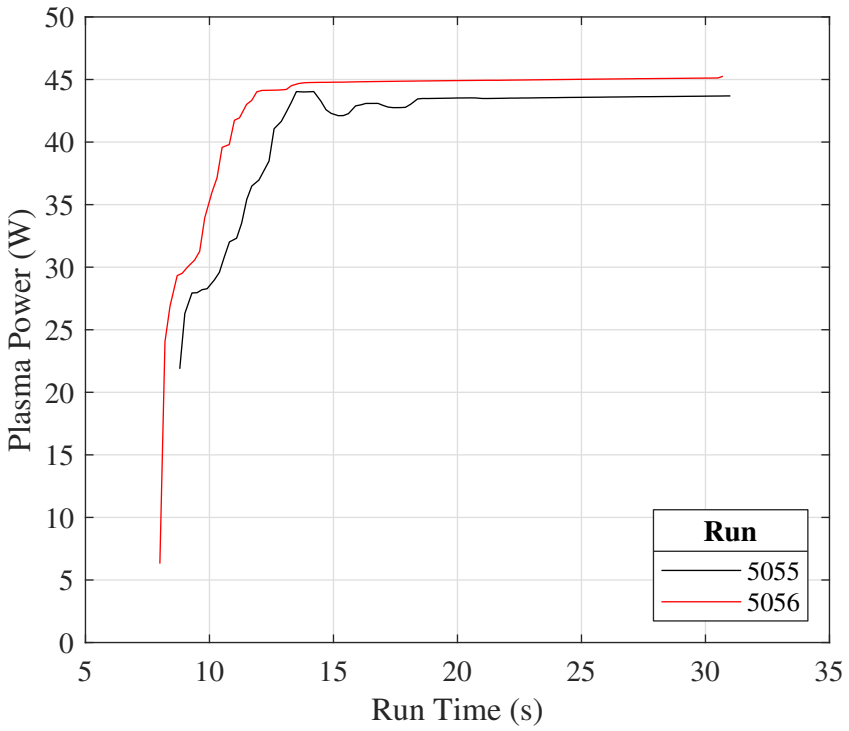

Figure 7.38: Plasma power traces for high frequency pressure runs.

No.	Location	Trip	Plasma	Filter	Run/Date
1	Back	Turbulent	Off	Low-pass filter	5053, 11/9/2021
2	Back	Turbulent	Off	None	5052, 11/9/2021
3	Back	Turbulent	Off	REZCOMP™	5054, 11/9/2021
4	Back	Turbulent	On	REZCOMP™	5055, 11/9/2021
5	Back	Laminar	Off	REZCOMP™	5057, 11/9/2021
6	Back	Laminar	On	REZCOMP™	5056, 11/9/2021
7	Middle	Turbulent	Off	None	5058, 11/11/2021
8	Middle	Turbulent	Off	REZCOMP™	5064, 11/11/2021
9	Middle	Laminar	Off	REZCOMP™	5065, 11/15/2021
10	Front (K3, K2, K1)	Turbulent	Off	None	5068, 11/16/2021
11	Front (K3, K2, K1)	Turbulent	Off	REZCOMP™	5069, 11/16/2021
12	Front (K3, K2)	Laminar	Off	REZCOMP™	5070, 11/16/2021
13	Front (K4)	Turbulent	Off	None	5075, 11/18/21
14	Front (K4)	Turbulent	Off	REZCOMP™	5076, 11/18/2021
15	Front (K4)	Laminar	Off	REZCOMP™	5077, 11/18/2021

Table 7.12: High frequency pressure transducer test matrix.

No.	Current (mA)	Power Supply Voltage (V)	Power Supply Power (W)	Plasma Voltage (V)	Plasma Power (W)
4	95.2	1409	134.1	455.7	43.4
6	95.0	1425	135.3	473.5	45.0
			Average		
	95.1	1417	134.7	464.6	44.2

Table 7.13: Plasma conditions for high frequency pressure campaign.

Before and test data could be taken, the efficacy of the new REZCOMP™ technology needed to be verified. To do so, the tunnel was run three times with the trips installed and the Kulites in the downstream location as it was desirable to pass as noisy of a signal as possible into the signal conditioning boxes. For the first run the signals were passed through a 200kHz Krohn-Hite

low-pass filter (this is the "lab standard" approach), then for the next run through the Kulite KSC-2 with the REZCOMP™ feature turned off, and finally for the last run passed through the Kulite KSC-2 box with REZCOMP™ turned on and optimized. The results from the centerline Kulite, shown in Figure 7.39, show the clear superiority of the REZCOMP™ technology. As expected, the 200kHz low-pass filter did at least partially remove the resonant frequency spike at $\sim$ 250kHz, but it still mostly remained and bled back into the otherwise flat-frequency response regime. The REZCOMP™ filter, however, reduced the resonant frequency to the amplitude of electrical noise like the spikes above 250kHz and extended the desired flat-frequency regime. It is noted that the data were cut off at 500kHz as this is where the Kulite KSC-2 boxes natural roll-off was reported.

There were additional details regarding the optimization of the REZCOMP™ filter worth including here. As was discussed in Section 6.5, the maximum allowable quality factor Q in the control software was lower than what would ideally be set, $Q \leq 50$ when it should have been between $50 - 100$. Again, according to [120], this was not critical as they produced decent results with Q up to 25% off its known value. Here it was believed the inaccuracy of Q led to a depression in the signal $\sim$ 100kHz wide in the vicinity of the resonant frequency evident in Figure 7.39 and all subsequent plots. While this was unavoidable with the current state of REZCOMP™ technology, it still meant REZCOMP™ had effectively doubled the usable range of the XCE-062 Kulites. Furthermore, the results approaching the f_r remained far more intelligible than those cases without REZCOMP™. For this specific case, however, the placement was unfortunate as in turbulent boundary layers one would expect to see a roll-off in the PSD as the turbulent energy dissipates at higher frequencies [221]; here it was hard to tell if the expected roll-off was occurring, if the reduction at $\sim$ 200kHz was entirely due to the REZCOMP™ filter, or if there was some combination thereof. Still, in summation, the results show REZCOMP™ extended the usable range of the Kulites by at least 200% and so this was a viable approach in hypersonic environments.

It is also worthwhile here to quickly address the effect of the plasma on the boundary layer's spectra. In short, there was no meaningful effect, as evinced by Figure 7.40. These data were taken from the centerline Kulite both with and without the trips installed; the "No plasma" case was the

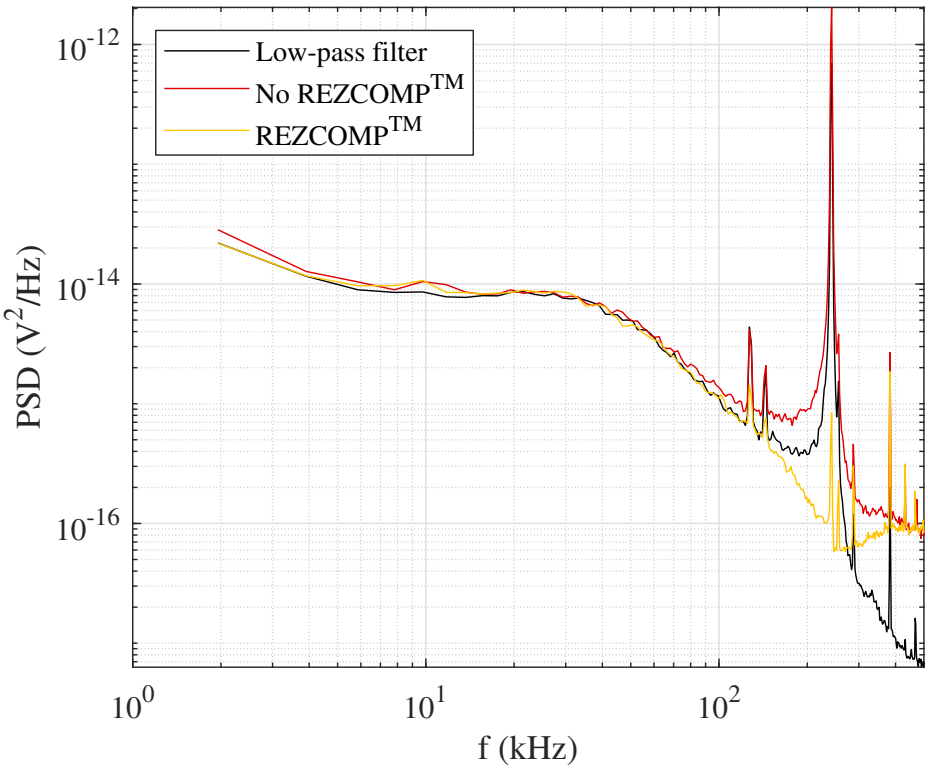

Figure 7.39: Effect of REZCOMP™ on Kulite data.

instantaneous trace when the tunnel reached $Re = 6 \times 10^6/\text{m}$ and the "Plasma" case represented the average of 15s of data when the tunnel was parked at $Re = 6 \times 10^6/\text{m}$ and the plasma was on-condition. In both cases, the traces were almost identical, with some discrepancy likely owing to run-to-run variation and smoothing due to averaging the plasma traces. Specifically, the offset between the traces in Figure 7.40(a) was not consistent, or even present, for the other three Kulites when comparing these runs. These plasma traces were only available for the "Back" test location 405mm from the leading edge; efforts to take data at the stations nearer to the electrodes were foiled by electromagnetic interference, even with the Kulites 168.7mm from the cathode. Thus there remained some tangible consequence of the plasma, but it was too weak to manifest in the boundary layer's spectra; this heavily implied the plasma was not affecting the turbulence as described in Section 2.3.5.

One of the objectives of this campaign was to identify any spanwise variation in the flow,

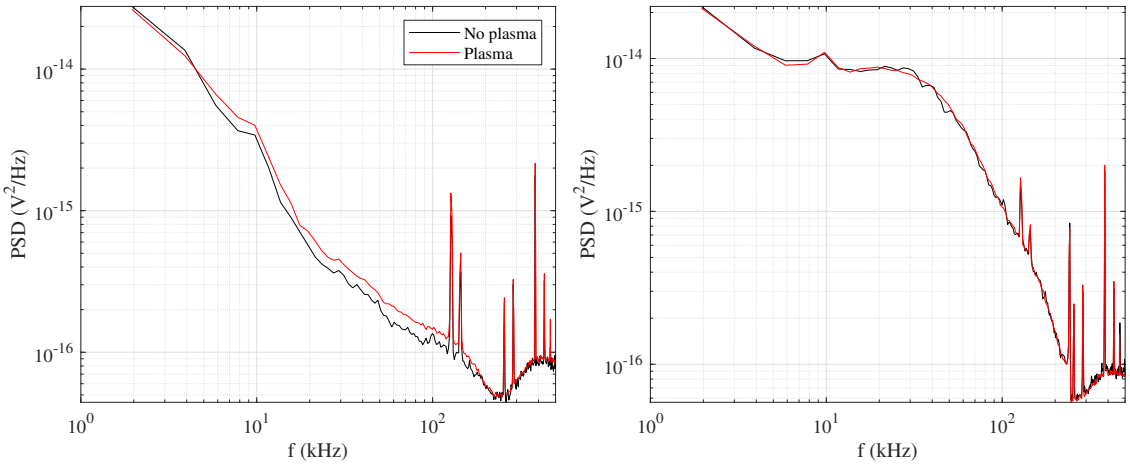

(a) Laminar (b) Turbulent

Figure 7.40: Effect of plasma on fluctuation frequency.

especially as it pertained to wakes and troughs from the boundary layer trips. In order to understand exactly where the Kulites were with respect to flow features, IR thermography was conducted in conjunction with the pressure data collection. The results for characteristic runs at each location and for the laminar and turbulent flows are included in Figures 7.41 and 7.42 respectively. Each figure contains an IR temperature reading from the region of interest at the test condition $Re = 6 \times 10^6/\text{m}$ and a corresponding temperature trace, with the Kulite locations included on the bottom axis. Because the PEEK needed to be pocketed to allow the short Kulites to be installed, the results near the actual sensors were unclear, and so the temperature traces were taken 30mm downstream of the Kulites. As the flow developed downstream there was some movement of the wakes and troughs, but it was observed to be minor and thus this separation was tolerable.

In regards to Figure 7.42, in the "Front" location Kulites 4 and 2 (recall these were 0 and -6.84mm from the centerline respectively) were solidly in the wakes while Kulites 3 and 1 were solidly in the troughs, which followed from their placement with respect to the trips. By the downstream locations, however, the placement became more ambiguous. For example, in the "Rear" location Kulites 4 and 3 were solidly in a wake and trough respectively, but Kulites 2 and 1 were on the boundary between the two; should they still exist so far into the fully turbulent environ-

ment, these sensors may have been in corner vortices. This again shows the development of the boundary layer, movement of the flow features, and physical size of the Kulites complicated their precise placement, and it also underscored the importance of taking real-time IR measurements. Additional results from IR thermography are provided in Section 7.3.3

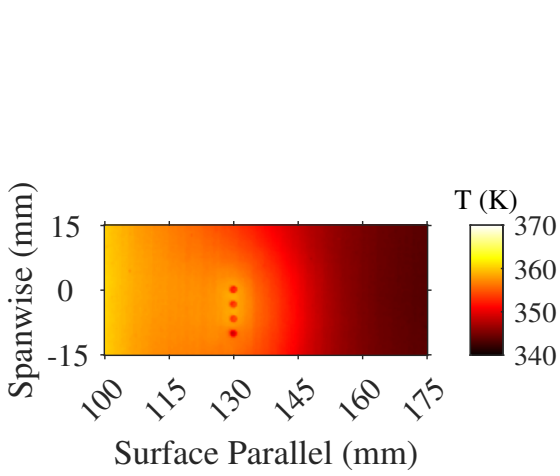

(a) Run 5070 (Forward)

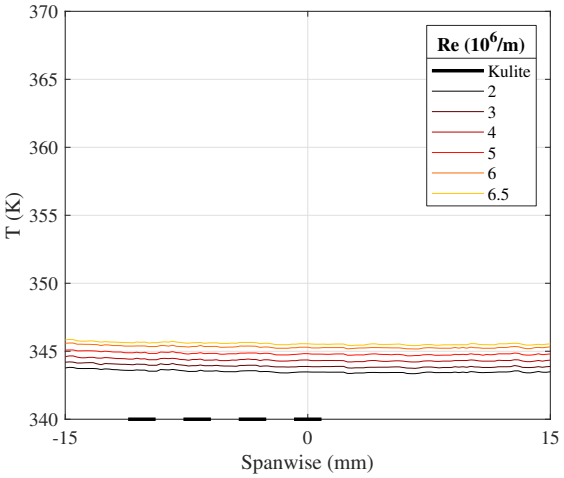

(b) Run 5070: Spanwise trace 160mm from LE

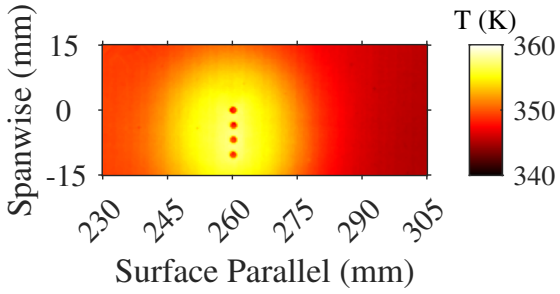

(c) Run 5065 (Middle)

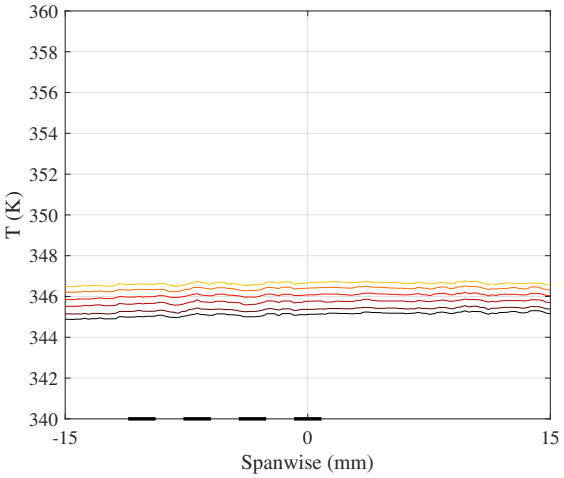

(d) Run 5065: Spanwise trace 290mm from LE

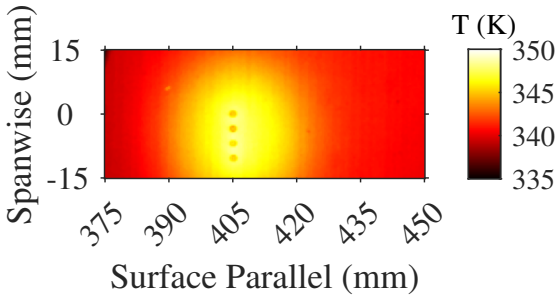

(e) Run 5057 (Back)

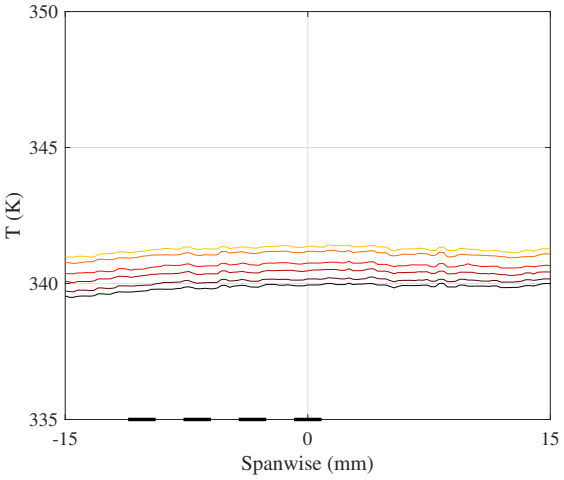

(f) Run 5057: Spanwise trace 435mm from LE

Figure 7.41: IR temperature data for laminar Kulite runs. Same legend applies to all trace figures.

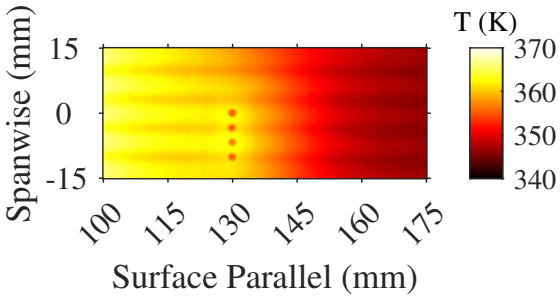

(a) Run 5069 (Forward)

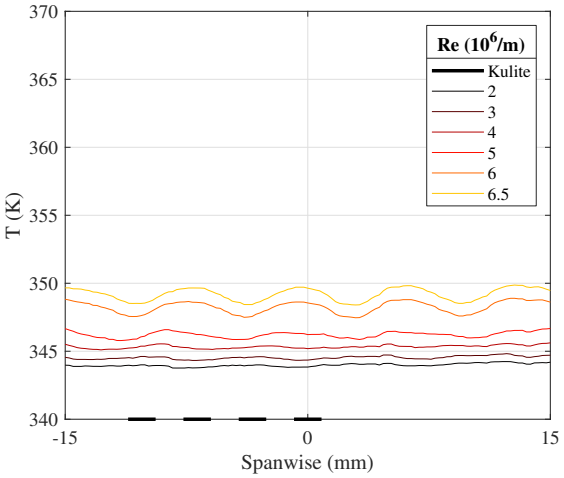

(b) Run 5069: Spanwise trace 160mm from LE

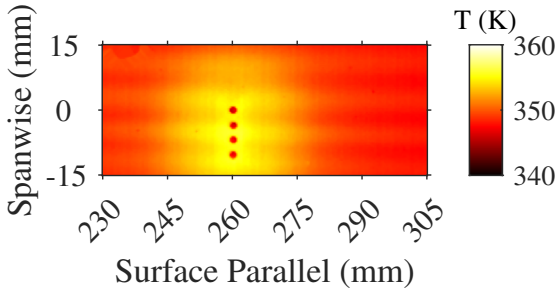

(c) Run 5064 (Middle)

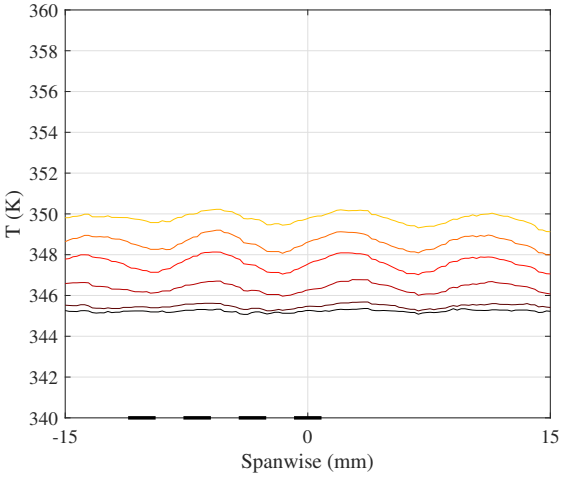

(d) Run 5064: Spanwise trace 290mm from LE

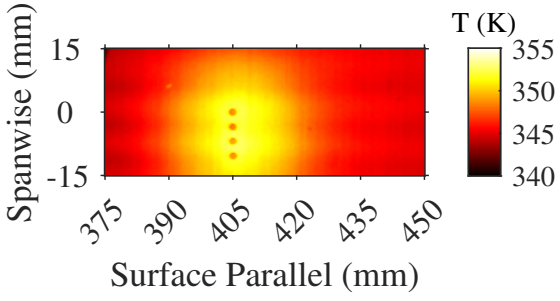

(e) Run 5054 (Back)

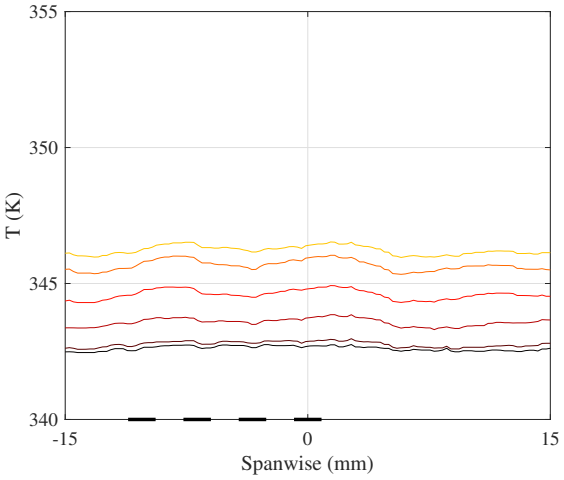

(f) Run 5054: Spanwise trace 435mm from LE

Figure 7.42: IR temperature data for turbulent Kulite runs. Same legend applies to all trace figures.

The bulk of the results are included in Figures 7.43 through 7.48, grouped by location and the boundary layer's state. Every plot contains mean "Pre-run" data from each Kulite, collected over a few seconds before the tunnel started; this allowed the identification of the noise floor as well as any inherent frequencies in the circuit, though in general the signal was clean. Each figure shows the spectra from each of the four Kulites at that streamwise location, with the exception of Figure 7.43 owing to the failure of Kulite 1 during this run; due to the uniformity of the laminar data from the other spanwise and streamwise locations, this run was not repeated to fill this gap in the data.

To that end, in general the laminar data showed little variation between spanwise locations and even streamwise locations. The former was important as it confirmed the spanwise uniformity of the test article, at least between the "Wake" (0mm) and "Trough" (10.26mm) test locations used throughout this project. It was interesting to see that the signal intensified significantly between $Re = 3$ and $3.5 \times 10^6/\text{m}$ owing to the transitioning nozzle sidewalls increasing the freestream noise at this Reynolds number [194, 243]. Beyond this transitory point, the laminar data tended to collapse for the remainder of the Reynolds numbers in the run, with any variation more likely due to the different sensors than true flow physics. In their laminar wedge experiments in the ACE tunnel, Leidy [160] was able to borrow from low speed theory and observe the frequency of the Type-I secondary instability at $f_I = U_e/(2\delta)$ Craig and Saric [67], but here no such frequency was clear. There may be some content at $\sim$ 40kHz at the "Middle" and "Back" locations owing to the slope change in the frequency decay, but the evidence was weak.

The turbulent boundary layer results contained more interesting physics. Begin with the data from the "Front" of the plate, Figure 7.44. For those sensors in the trip wake, K4 and K2, there appeared to be two distinct frequencies at $\sim$ 20 and $\sim$ 50kHz. The latter was established as soon as the freestream became noisy at $Re = 3.5 \times 10^6/\text{m}$, but the former only became defined at $Re = 5 \times 10^6/\text{m}$. In the troughs, only the $\sim$ 50kHz frequency was apparent. This suggested the corner vortices in the wake fomented turbulence through, in part, this higher frequency. Also, in general, that the frequency of a disturbance tended to grow with the Reynolds number likely stemmed from the thinning of the boundary layer (see [257]).

Plotted on all tripped figures is a line with a slope of $-5/3$. This is taken from Kolmogorov's theory [145, 146] that the turbulent kinetic energy $E = f(k, \varepsilon, \nu)$, where k is the wavenumber, ε is the dissipation, and ν is the viscosity. In the so-called inertial subrange, viscosity can be neglected and one can write $E(k) = \alpha\varepsilon^{2/3}k^{-5/3}$. Thus when plotted on a logarithmic wavenumber axis or, here, the frequency (Semper [243] compared the two using $f = \frac{ku_\infty}{2\pi}$), one would expect the kinetic energy of isotropic turbulence to cascade with a slope of $-5/3$. This is Kolmogorov's $-5/3$ Law, which is well described in [221, 277, 210]. Although boundary layers cannot be considered isotropic, here the theory was used to check if flow was turbulent by qualitatively comparing the slope of the cascade portion of the spectrum with the $-5/3$ line. At this upstream location, the agreement was poor, especially in the wakes. This implied the boundary layer was still at least partially transitioning, which followed from the measurements in Sections 7.3.1 and 7.3.2.

As one moved downstream to 260mm from the leading edge, the data better agree with the theory. In Figure 7.46, it seemed the two frequencies had merged to create one production [221, 277] frequency at $\sim$ 30kHz; again, these results only turned on with the presence of freestream noise above $Re = 3.5 \times 10^6/\text{m}$. This energy was passed into progressively higher frequencies until it decayed into the noise floor near the sensors' f_r; again, due to the inability to perfectly predict Q, the depression around f_r made it challenging to definitively say if the turbulent structures had fully dissipated by this point, though the relatively high energy levels at higher Reynolds numbers made this seem unlikely. Moving downstream to 405mm from the leading edge, the boundary layer continued to develop and grow, meaning there was still better agreement with the $-5/3$ Law and the production frequency fell to $\sim$ 20kHz respectively. At both of these turbulent locations, there was no clear difference in the response from any of the sensors, so while Figure 7.42 showed their placement in wakes and troughs may be imperfect, there was a strong case the more turbulent boundary layer become homogenized in the spanwise direction.

In summation, these results demonstrated the efficacy of the Kulite KSC-2 signal conditioning box, the stability and homogeneity of the laminar boundary layer, and the development of the turbulent boundary layer and its maturity by the "Back" test location.

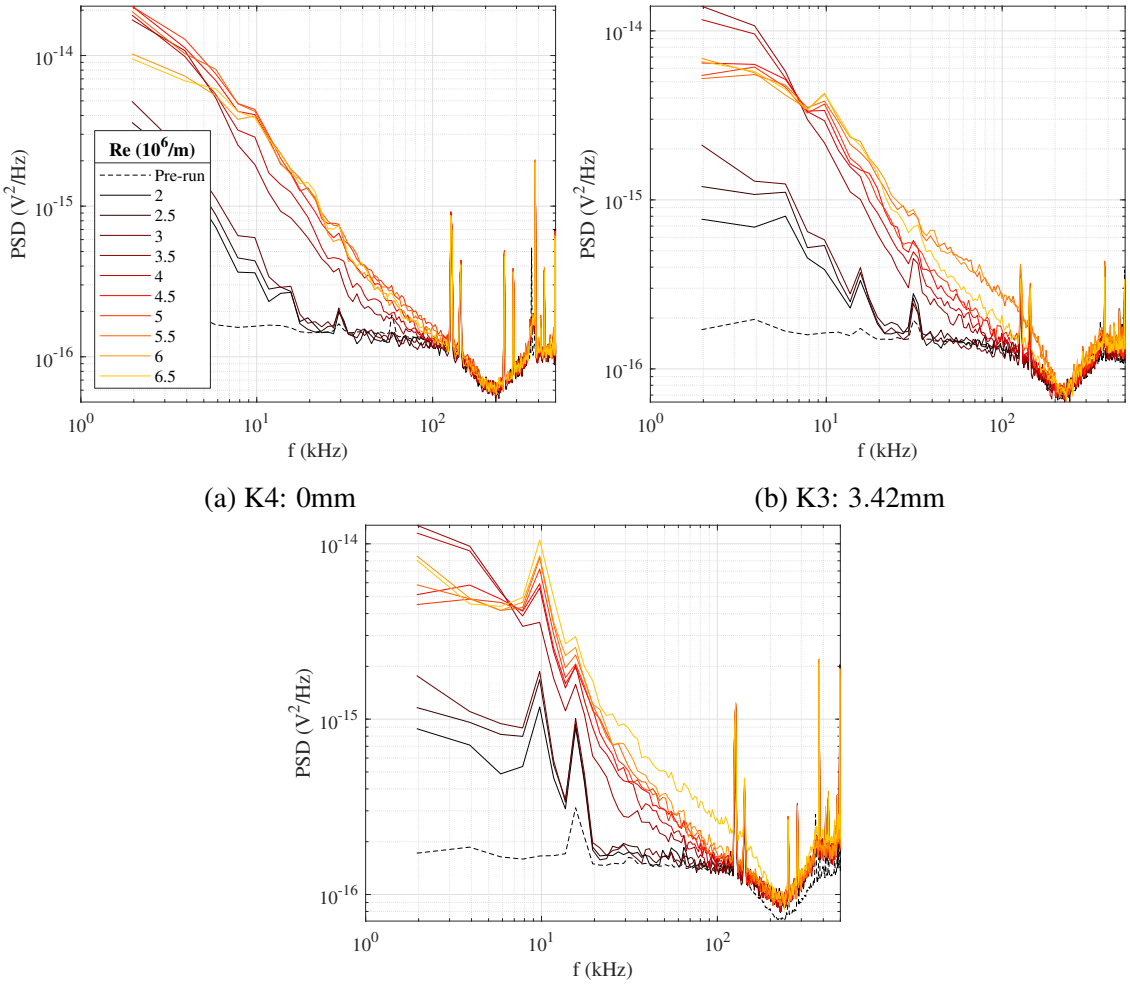

(a) K4: 0mm

(b) K3: 3.42mm

(c) K2: 6.84mm

Figure 7.43: Laminar Kulite pressure fluctuation data, 130mm from the LE.

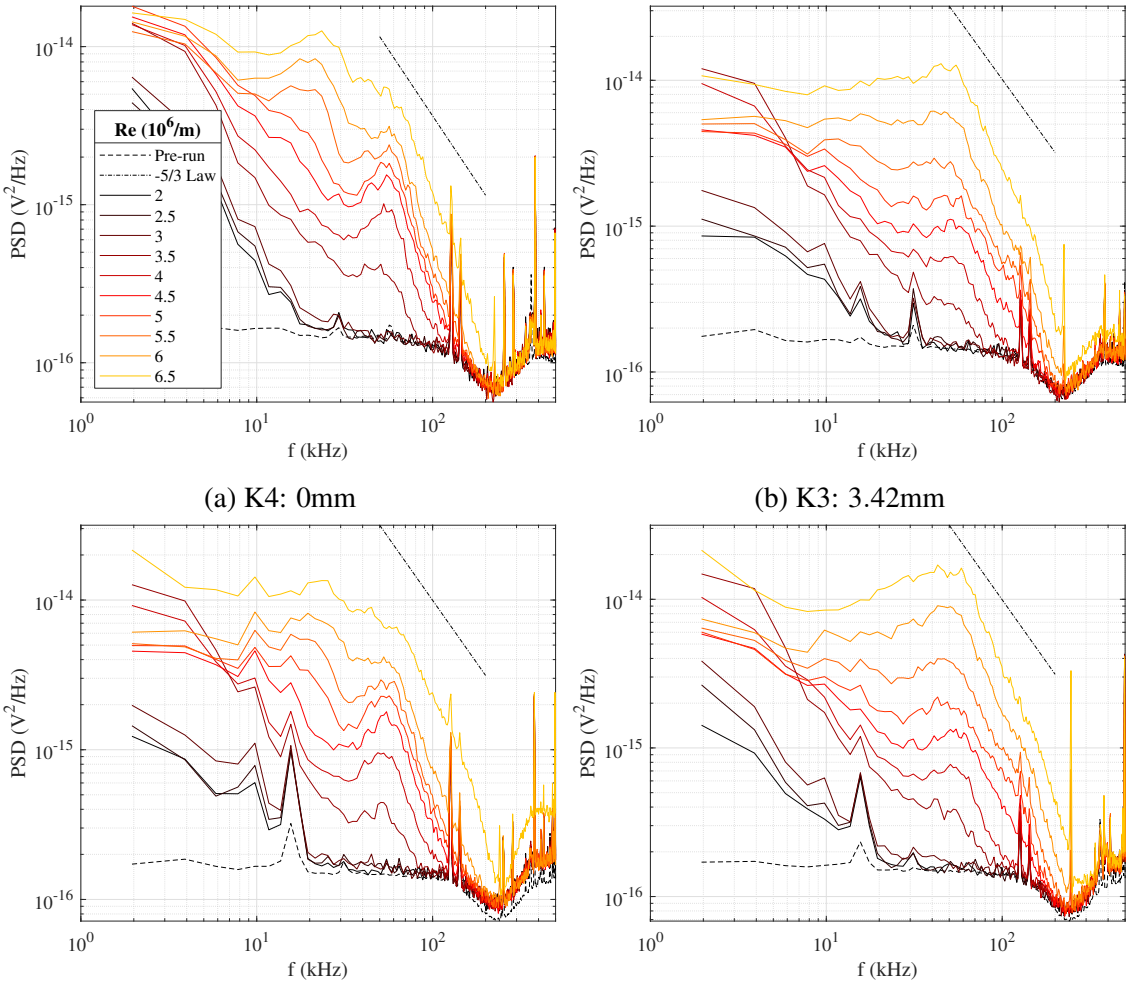

(a) K4: 0mm

(b) K3: 3.42mm

(c) K2: 6.84mm

(d) K1: 10.26mm

Figure 7.44: Turbulent Kulite pressure fluctuation data, 130mm from the LE.

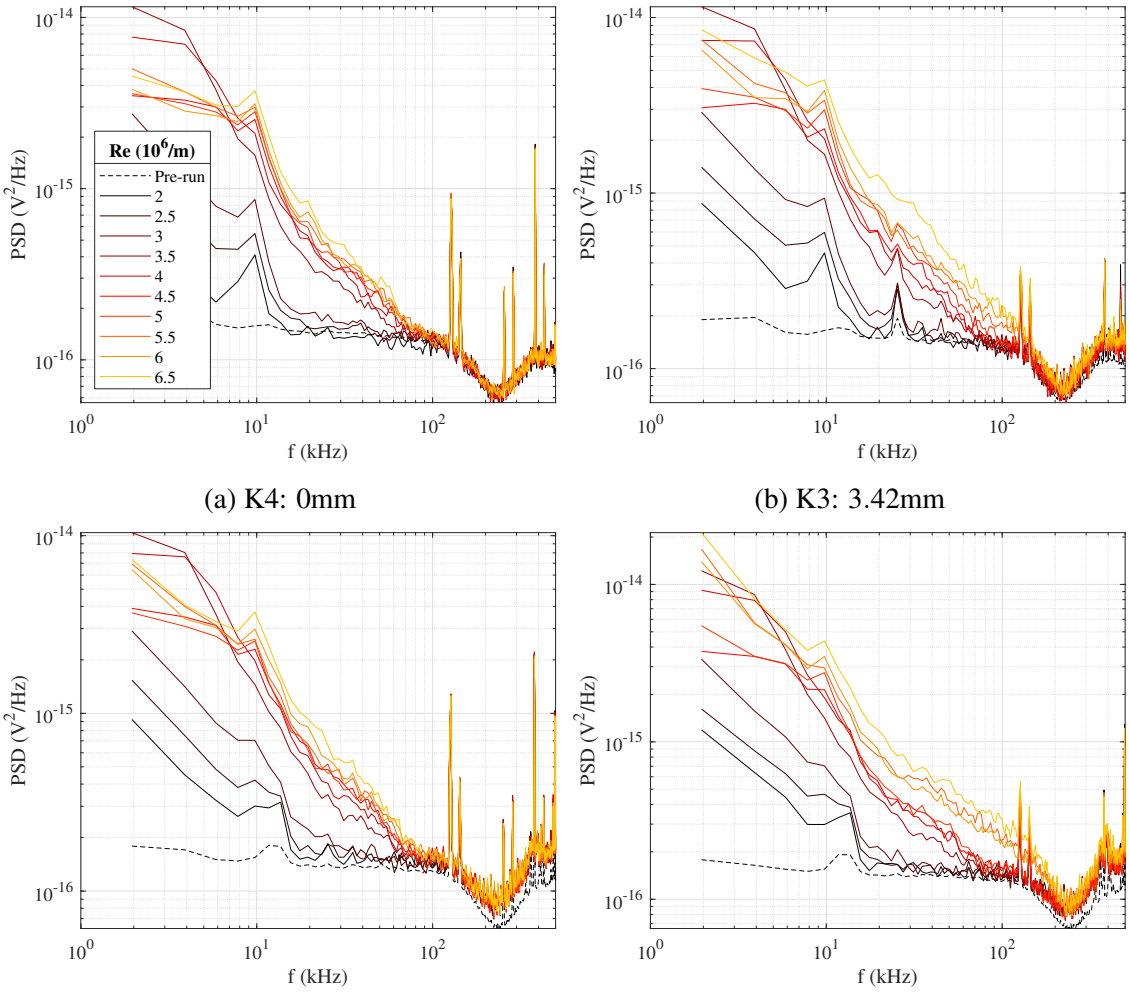

(a) K4: 0mm

(b) K3: 3.42mm

(c) K2: 6.84mm

(d) K1: 10.26mm

Figure 7.45: Laminar Kulite pressure fluctuation data, 260mm from the LE.

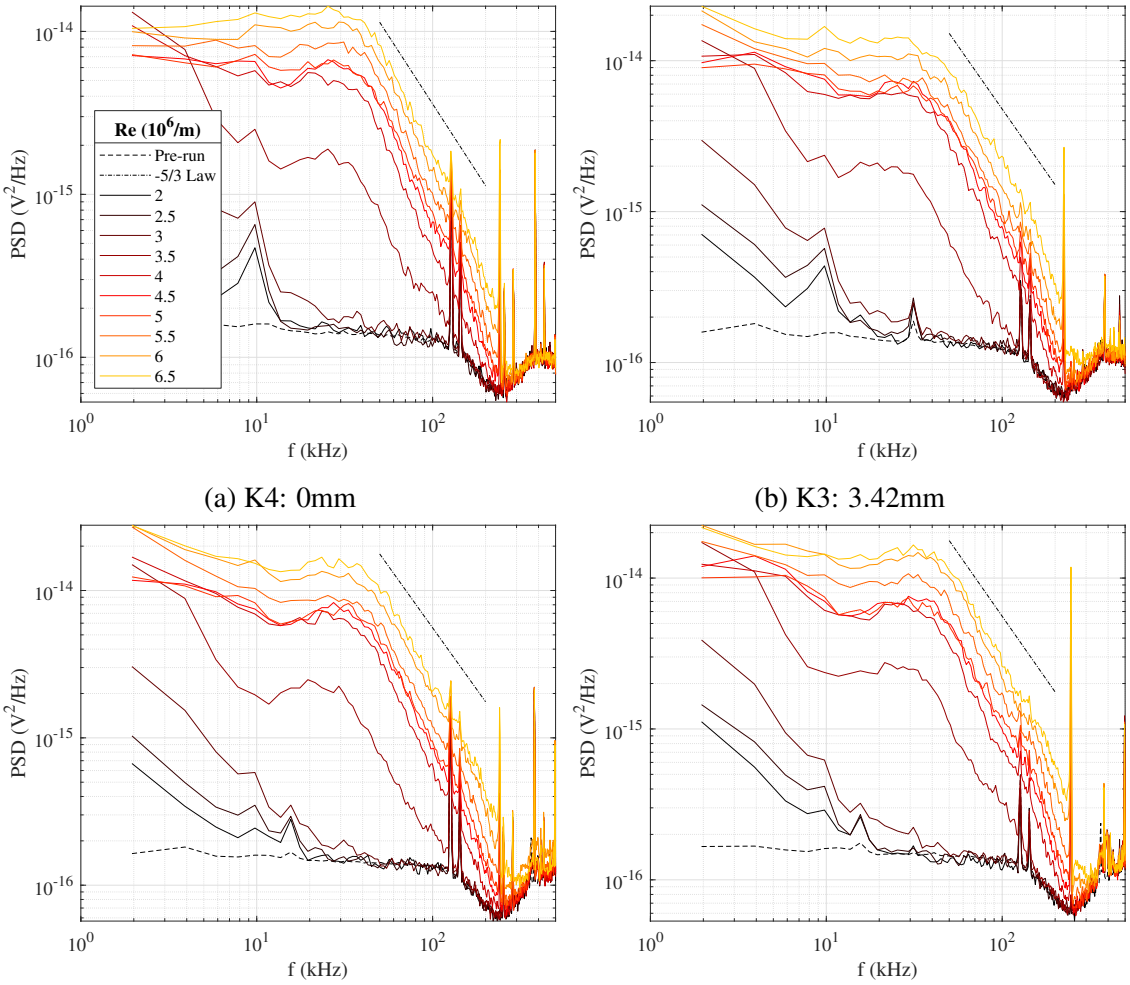

(a) K4: 0mm

(b) K3: 3.42mm

(c) K2: 6.84mm

(d) K1: 10.26mm

Figure 7.46: Turbulent Kulite pressure fluctuation data, 260mm from the LE.

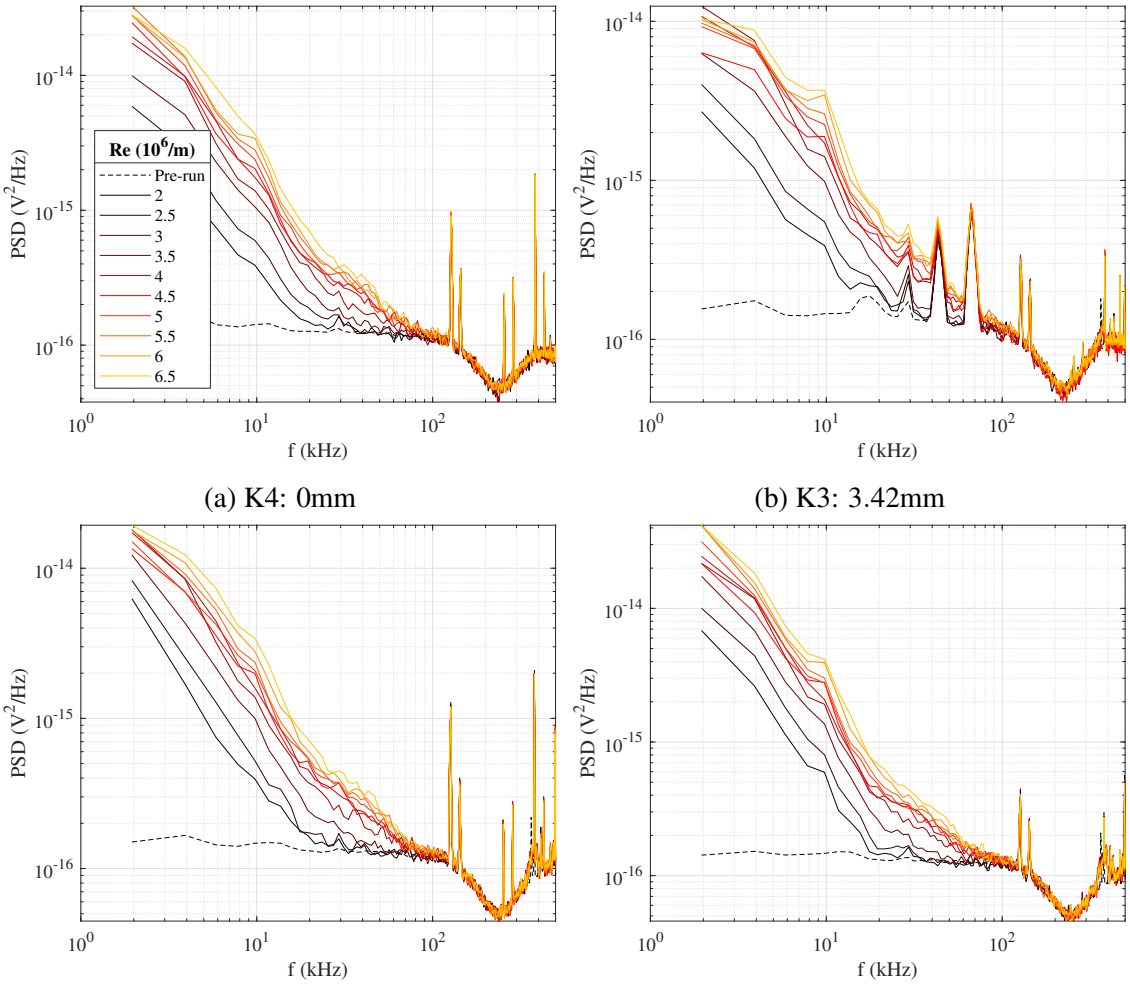

(a) K4: 0mm

(b) K3: 3.42mm

(c) K2: 6.84mm

(d) K1: 10.26mm

Figure 7.47: Laminar Kulite pressure fluctuation data, 405mm from the LE.

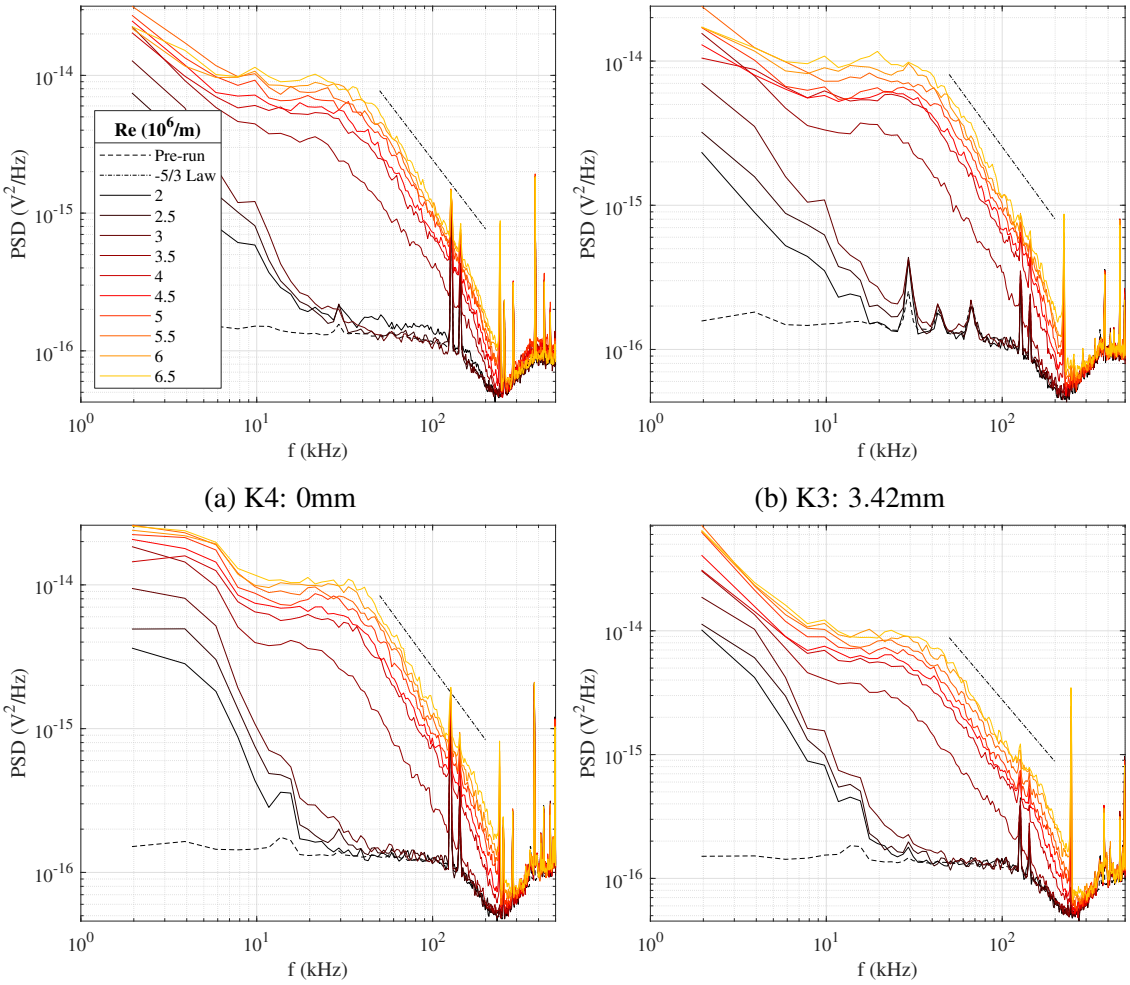

(a) K4: 0mm

(b) K3: 3.42mm

(c) K2: 6.84mm

(d) K1: 10.26mm

Figure 7.48: Turbulent Kulite pressure fluctuation data, 405mm from the LE.

7.3.5 Pitot Probe Results

Pitot probes are classic fluid dynamics tools because they provide a wealth of data with only two simple measurements. Here the Mach number was directly measured, and through well-established theory [293, 239, 55] velocity profiles were calculated. These profiles allowed for classical boundary layer theory like inner variable plots to be produced, the inference of key physics such as transition and wall shear stress, and the validation of other data like that from the numerical boundary layer solver or PLIF. A detailed Pitot campaign was conducted in the ACE tunnel, with the test matrix included in Table 7.14. The plasma conditions and powers for each run are provided in Table 7.15 and Figure 7.49 respectively. Due to an experimental inconsistency, the results for the plasma runs in the "Middle" location were not included in this report; because the plasma was shown to have little to no effect in the "Front" test location and due to the tertiary importance of the "Middle" test location, this was deemed an unfortunate but acceptable loss.

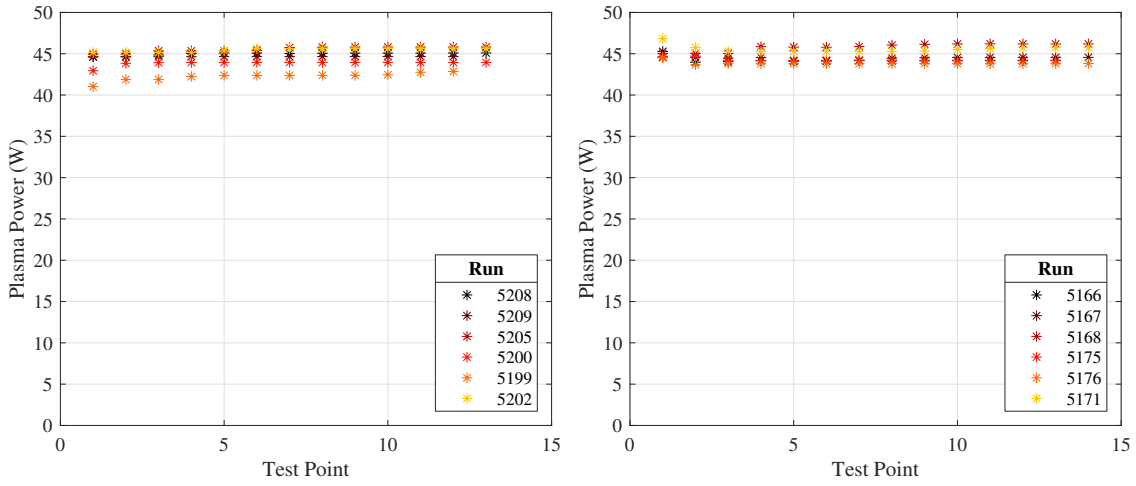

(a) Front run (b) Back runs

Figure 7.49: Plasma power traces for Pitot runs.

Figure 7.50 shows two representative schlieren images taken with the probe in the "Front" test location. Of the hundreds of available images from the entire campaign, these were selected for

No.	Location	Trip	Plasma	Sweep	Run/Date
1	Back, wake	Turbulent	Off	Inner	5163, 1/20/2022
2	Back, wake	Turbulent	Off	Outer	5165, 1/21/2022
3	Back, wake	Turbulent	On	Inner	5166, 1/21/2022
4	Back, wake	Turbulent	On	Outer	5167, 1/21/2022
5	Back, wake	Laminar	Off	Full	5169, 1/22/2022
6	Back, wake	Laminar	On	Full	5168, 1/21/2022
7	Back, trough	Turbulent	Off	Inner	5173, 1/23/2022
8	Back, trough	Turbulent	Off	Outer	5174, 1/23/2022
9	Back, trough	Turbulent	On	Inner	5175, 1/23/2022
10	Back, trough	Turbulent	On	Outer	5176, 1/23/2022
11	Back, trough	Laminar	Off	Full	5172, 1/22/2022
12	Back, trough	Laminar	On	Full	5171, 1/22/2022
13	Middle, wake	Turbulent	Off	Inner	5179, 1/26/2022
14	Middle, wake	Turbulent	Off	Outer	5182, 1/27/2022
15	Middle, wake	Laminar	Off	Full	5184, 1/27/2022
16	Middle, trough	Turbulent	Off	Inner	5187, 1/29/2022
17	Middle, trough	Turbulent	Off	Outer	5188, 1/29/2022
18	Middle, trough	Laminar	Off	Full	5185, 1/28/2022
19	Forward, wake	Turbulent	Off	Inner	5206, 2/4/2022
20	Forward, wake	Turbulent	Off	Outer	5207, 2/4/2022
21	Forward, wake	Turbulent	On	Inner	5208, 2/4/2022
22	Forward, wake	Turbulent	On	Outer	5209, 2/4/2022
23	Forward, wake	Laminar	Off	Full	5204, 2/3/2022
24	Forward, wake	Laminar	On	Full	5205, 2/3/2022
25	Forward, trough	Turbulent	Off	Inner	5195, 2/1/2022
26	Forward, trough	Turbulent	Off	Outer	5198, 2/1/2022
27	Forward, trough	Turbulent	On	Inner	5200, 2/2/2022
28	Forward, trough	Turbulent	On	Outer	5199, 2/2/2022
29	Forward, trough	Laminar	Off	Full	5201, 2/2/2022
30	Forward, trough	Laminar	On	Full	5202, 2/2/2022
31	Probe in center of test section	$Re = 2 - 6 \times 10^6/\text{m}$	N/A	N/A	5212, 2/5/2022

Table 7.14: Pitot probe test matrix.

the unique physics they capture. Note that schlieren images with better contrast are available in Section 7.3.2; those included here were intentionally brightened to increase the contrast between the probe and the flow for better edge detection, not to necessarily describe flow physics.

To begin, the entropy layer is visible in Figure 7.50(a), which served as a reminder that its

No.	Current (mA)	Power Supply Voltage (V)	Power Supply Power (W)	Plasma Voltage (V)	Plasma Power (W)
3	95.4	1418	135.2	463.7	44.2
4	94.8	1418	134.4	469.0	44.5
6	95.1	1434	136.3	482.0	45.8
9	95.2	1418	135.0	465.2	44.3
10	95.1	1413	134.4	461.0	43.8
12	94.9	1430	135.8	480.0	45.6
21	95.2	1426	135.7	472.5	45.0
22	95.0	1421	135.0	470.0	44.6
24	94.5	1428	134.9	482.1	45.5
27	95.0	1412	134.1	461.8	43.9
28	94.0	1391	130.8	449.4	42.3
30	95.4	1431	136.5	476.8	45.5
Average					
	95.0	1420	134.8	469.4	44.6

Table 7.15: Plasma conditions for Pitot probe campaign.

effect may be visible in the Pitot data. Next, 0mm fell a couple pixels below the observed wall. This underscored the importance of measuring the wall offset, and trying to align the schlieren system with the roll of the plate. Similarly, in both images, there is a faint shock passing just below the probe; it was believed that this was the oblique shock generated by the static pressure taps at 130mm; this theory seemed more likely than blowing from the port as preliminary schlieren imaging showed the static ports mostly vented even before the flow was started. This was remarkable because despite their small diameter (0.508mm) and 3.42mm spanwise displacement from the probe, it will be seen shortly that they still interfered with the results. While there was no choice but to offset the probe from the holes in this "Front" location, this result stood as a lesson for future work, and as a warning that the stronger shocks from the electrodes and trips may have had a more pronounced impact. To address that concern, it would have been beneficial to measure the pressure jump across, say, the trip shocks, but due to their complex nature it was not expected they would follow any simple theory. Furthermore, this measurement was already done with the PLIF results, and could be replicated here by comparing any freestream reading at any point along the plate with the trips installed to one without them; this approach was discussed below. Finally, in the "Front"

test location it was more important to add points in the boundary layer to improve its resolution due to its thin size.

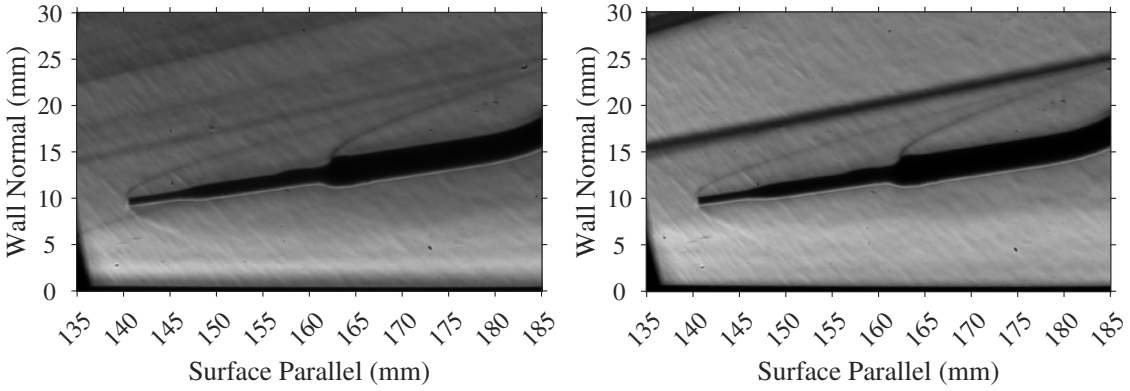

(a) Laminar (b) Turbulent

Figure 7.50: Schlieren images for Pitot probe placement, "Front" location.

7.3.5.1 Wall Shear Stress Results

The wall shear stress for each of the six main test cases (three locations, laminar and turbulent flow) is provided in Tables 7.16-7.21. The results from the numerical boundary layer solver for generalized laminar and turbulent flow ("Implicit" scheme, "Gradient Diffusion" heat flux, same inputs as Section 7.1) are also shown in Figure 7.7(a), and the results for each specific location are provided in the caption of the corresponding table. The van Driest II skin friction model ($\tau_{w,VD}$) was solved for the turbulent cases using Matlab's inbuilt "fsolve" function, but because it is restricted to only adiabatic flows its results were meant to used for reference only; that being said, based on the actual flow conditions, $T_{aw} \approx [375, 395\text{K}]$ for the laminar and turbulent flows respectively, so for example if for the intermediary "Middle" case $T_w = 355\text{K}$ then $\frac{T_w}{T_{aw}} = [0.947, 0.899]$ and the plate was reasonably close to adiabatic conditions, especially near the leading edge and at least to within the other approximations used throughout these calculations.

The Preston tube results were, in general, a factor of two below the expected value for all turbulent cases and near the correct answer for the laminar cases, though the latter was likely

coincidental. There were several possible explanations for this error. Preston [223] recommended $\log \frac{(P-P_o)d^2}{4\rho\nu^2} > 5$, which, if one follows Semper [243] and considers d to be the height of the tube in the wall-normal direction, the data did not satisfy. Similarly, the $R_d^2 C_p$ and $R_d^2 C_f$ results did not fall onto the linear portion of the scaled plots in [137]. The reasons for these discrepancies were unknown, but likely stemmed from the probe itself. The Preston approach was attempted for convenience as the data was already being taken; a more intentional effort would have included a range of truly circular probes of varying diameter precisely fixed to the wall. Even if this was done, the approach was fundamentally imperfect; in their review of several calibrations, Allen [2] said the approach of Keener and Hopkins [137] could have errors up to 50%. The finding here was not to disregard Preston tube for measurement of wall shear stress, but that a dedicated study should be conducted before it is insouciantly attempted.

The laminar data are now specifically discussed. Of the available experimental methods, the Preston tube seemed to perform the best, but given how similar its results were in laminar and turbulent flows, this was likely coincidental. While the Reynolds Analogy method did yield a monotonically decaying profile along the plate, at the "Front" test location it overpredicted the numerical estimation by $\sim 5\times$ and for the downstream locations it overpredicted it by $\sim 2\times$. A possible explanation for this trend owes to the estimation or measurement of heat flux; recall the Reynolds Analogy approach relies on $St = \frac{q_w}{\rho_e u_e c_p (T_{aw} - T_w)}$. In the boundary layer solver, $T_w = 350$K and, $[140, 260, 405]$mm from the leading edge, $q_w = [245.7, 174.9, 137.7] \frac{\text{W}}{\text{m}^2}$. Comparing these results to those in Table 6.2 one can see the temperatures were closer to T_{aw} and the heat flux was $\sim 2-3\times$ higher than the simulated value, both of which would increase St and thereby $\tau_{w,RA}$. The cause for this discrepancy was unknown, but for now one must assume the experimental results were more accurate, at least downstream of the dynamic "Front" test location, as they directly measured the actual physics.

In general, in all cases except the Preston tube, the agreement between the experimental and numerical for the "Turbulent" flows was much better than in the "Laminar" cases. The numerical, Reynolds Analogy, van Driest II approaches never differed by more than 25%, even at the

"Front" test location. At least for the Reynolds Analogy approach, the higher adiabatic wall temperature and better agreement in the heat flux values ($q_w = [1752.7, 1243.9, 1069.0]\frac{\mathrm{W}}{\mathrm{m}^2}$ for the "Implicit/Gradient Diffusion" scheme), especially in the "Back" test location, explained this result. Indeed, by this point all of the techniques except the Preston tube yielded results within 20 ± 3Pa.

The Clauser approach warranted special attention. As described in Section 7.1, the τ_w predicted by the boundary layer solver will cause the inner variable scaled plot of u^+_{eq} *versus* y^+ to fall below the theoretical lines. Clauser's method allowed one to manually alter τ_w until the experimental and theoretical results agreed. Ignoring the transitional flow at the "Front" test location, this did allow for the production of classical inner variable plots at the "Middle" and "Back" test location, indicating fully turbulent flow. However, one must ask, especially given that the Reynolds Analogy and van Driest II wall shear stresses also overpredicted $\tau_{w,Clauser}$, if this approach was not fitting the data? Put another way, theory should explain data, not the other way around. While the Clauser method was helpful because it allowed direct manipulation of the data when there were five competing techniques, one must appreciate its implication.

Looking at the data holistically, it seemed that the numerical, Reynolds Analogy, and Clauser approaches were converging on the same result as the flow moved from the "Middle" to the "Back" test locations, with the van Driest II approach lagging only slightly behind, perhaps due to its adiabatic assumption. What would happen if the test article was 1m long? Inserted into the tunnel after preheat? Its leading edge sharpened? Its material entirely PEEK? Its trips altered; and in the CFD, what if the trips were themselves modeled? At least numerically, increasing the streamwise domain did seem to yield results tending towards better agreement with the theory. The point here was that in experimentation theory should be used to interpret data, and data should be taken only as far as their real-world limitations will allow. These wall shear stress data suggested that the boundary layer was becoming fully developed, and the agreement with classical theory was milquetoast; to that end, perhaps increasing the length of the plate would allow for better interpretation of the observed trends, as the turbulence may become more fully developed.

In summation, the Reynolds Analogy, van Driest II, Clauser, and numerical approaches to

the estimation of the skin friction were all reliable for the turbulent flow, provided it had enough time to fully develop. There were significant issues in "Laminar" cases, likely stemming from the thermal response of the test article. Finally, the Preston tube method warrants further investigation, especially because it could offer a useful validation of the Reynolds Analogy approach for laminar boundary layers. A comparison of the wall shear stress results measured with the Pitot probe with other techniques is included in Section 7.5.

7.3.5.2 Boundary Layer Profiles

The wall shear stress for each of the six main test cases (three locations, laminar and turbulent flow) is provided in Tables 7.51-7.56. For each case, the Mach number, temperature, and velocity profiles are shown, as well as the inner variable velocity profile for the turbulent runs. The data are grouped such that all tests that a given location (plasma "On/Off" and "Wake/Trough") were plotted on the same figure to elucidate any effect.

In general, the uncertainties for the Mach number and displacement were so small that including error bars only served to clutter the figures. The error in the Mach number was $\sim 1\%$ at the wall and $\sim 0.5\%$ in the freestream, values so small the error was not carried into the calculations for temperature or velocity. The displacement error went from $y \approx [0.3, 0.8]$mm at the wall and freestream, respectively. While more significant, the error bars still tended to obfuscate the results. Instead, when the measured height of a point was below half the probe diameter plus the base two pixels of uncertainty, it was called a "wall point" and plotted with an open circle. This denoted a proportionally high degree of uncertainty in the position of the probe, but also in the data itself; recall that no correction was available for the probe's effective center near the wall, and the Preston tube results were relatively inaccurate. Indeed, when plotted using inner variables, these wall points followed unrealistic trends.

The "Front" plots were perhaps the most dynamic. All cases showed a distinct bump at ~ 7mm owing to the weak shock produced by the static pressure holes. And it was indeed weak, as the final points in the "Laminar" and "Turbulent" plots were nearly identical; this implied that the complex shock/separation/reattachment feature produced by the trips was weak enough to not significantly

manifest in the Pitot results, so the far weaker static port shock should have had no effect. The lent credence to the decision to not measure the Mach number on both sides of the trips' shocks and to instead add resolution to the thin boundary layer. That being said, the Mach number did not fully reach the expected freestream value by 10mm above the surface, a factor several times δ. Again, that this occurred in both the "Laminar" and "Turbulent" cases meant that it could not be attributed to the trips' shocks. The more likely explanation would be a prolonged leading edge effect, though this did extend even above the entropy layer.

To that end, the decision to add resolution to the boundary layer instead of the freestream proved fortuitous in that one can see a slight change in the slope of the profiles in Figure 7.51 at $\sim$ 3mm. Taken with the results in Section 7.3.2 it was probable this was the entropy layer. It was interesting to see it represented in the Pitot data.

The added resolution was helpful for the "Turbulent" case as well, though evidently that was a misnomer. As far back as 140mm from the leading edge, downstream of the PLIF measurements, there remained clear evidence of the trips in the "Wake" plots. Indeed, between $3-6$mm, well below the trips' shear layer identified both in the shlieren data in Section 7.3.2 and in the images taken concurrently with the Pitot data, the velocity in the "Wake" lagged behind that in the "Trough". This implied there was some lingering velocity deficit in the boundary layer owing to the wake. The run-to-run repeatability of the feature confirmed it was not likely due to any probe misalignment, and there were no known issues with the probe used as such physics were not measured at the the "Middle", where it was also used. That the "Troughs" remained relatively unaffected and even collapsed onto the inner variable log layer added further evidence of the longevity of the trips' wakes, even in the transitional environment. Cumulatively, therefore, this location must be considered transitional, not fully turbulent. This implied that the use of r_{turb} in T_{aw} in the Crocco-Busemann's equation inaccurate, though it was the best approximation available.

It is noted that the discrepancy between the plasma "Off" (Runs 5206, 5207) and "On" (Runs 5208, 5209) in Figure 7.52 was not attributed to the plasma as there was no similar behavior in the "Trough" case or any of the laminar data. The cause remained unclear at the time of publication

but run-to-run variability, the affect of the bend in the "Trough" probe, the slightly larger (almost 0.1mm) height of the "Trough" probe), elastic rotational deflection of the probe in the presence of the flow, and slight probe misalignment remained possible culprits.

In the "Middle" test location, the boundary layer seemed to follow a more classical path. Near the wall, the "Laminar" data curled downwards at an expedited rate. This was most likely a physical probe effect and could be improved by the inclusion of an effective probe center or a smaller probe. The "Turbulent" data also follow the theoretical trend, and indeed the flow appeared fully turbulent.

There was again disagreement between "Wake" and "Trough" data in this "Middle" location. Here, however, the most likely culprit was the physical probe itself as the data maintained a near-constant offset in the Mach number between all of the runs considered in Figures 7.53 and 7.54. It was interesting to see that as the Mach number was high, the temperature calculated by the Crocco-Busemann relation was low, so when combined the competing effects partially canceled in the calculation of the velocity.

Fortunately, in the "Back" location only one probe was used, and the data collapse closely together. Again, both laminar and turbulent theoretical shapes were recovered; for example, it was encouraging to see the "bent knee" shape in Figure 7.56(c). There was the same downward curl in the points near the wall, but this was again attributed to probe-wall effects.

Taken together, the Pitot campaign was successful in that it provided insight on the laminar, transitional, and turbulent nature of the boundary layer, recovered classical theory, and provided off-body measurements of the flow; this is best shown in Figure 7.57, which compares the evolution of the Mach number, temperature, and velocity profiles along the test article for the "Wake/Plasma off" case. Additionally, it confirmed that, again, there was no tangible impact of the plasma on the flow, and provided a means to study various techniques for the calculation and measurement of wall shear stress. Its data are compared to that of other techniques in Section 7.5. In the future, the results could be improved with more time spent testing the effect of different probes and trying to use the same one for all tests.

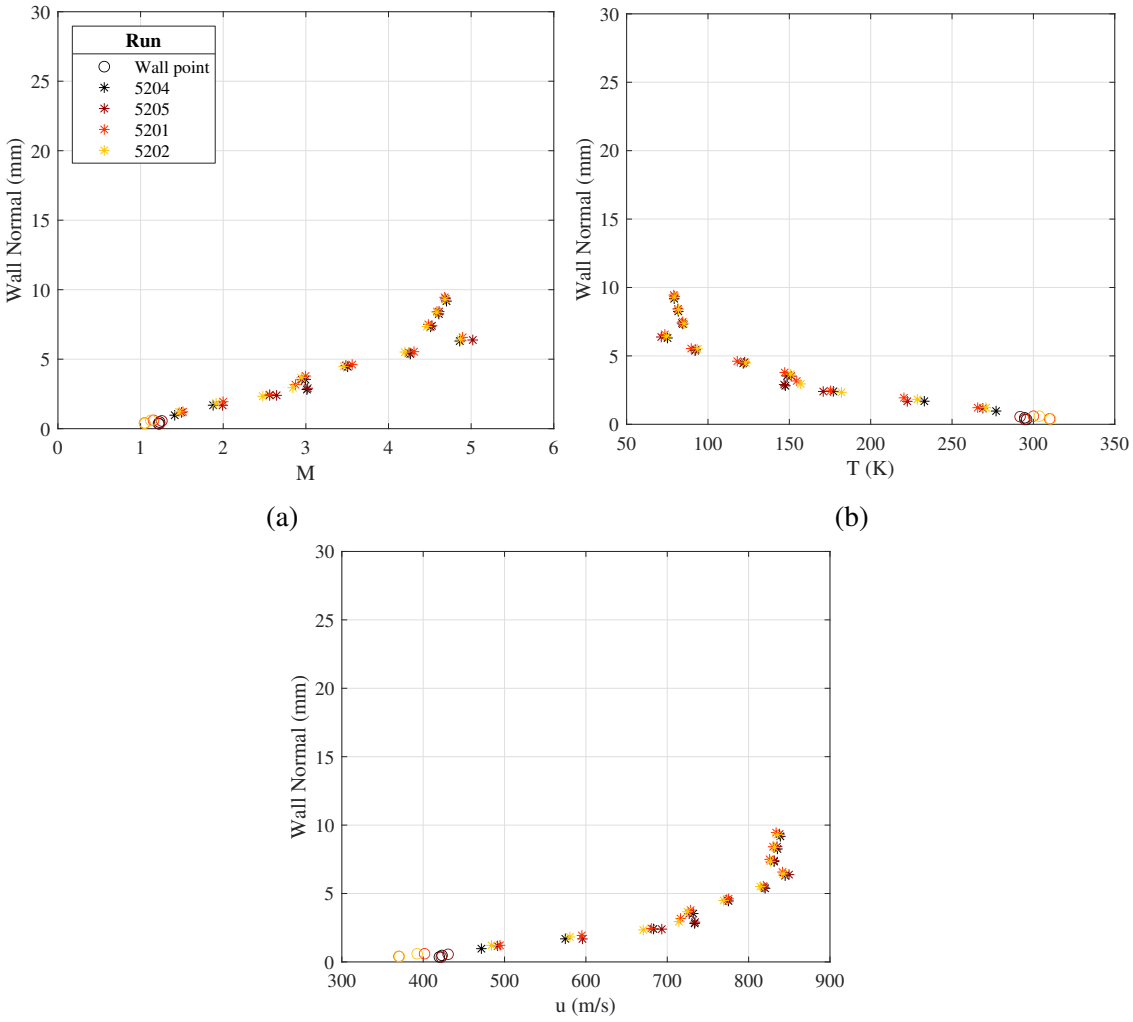

Figure 7.51: Laminar Pitot data, 140mm from the LE. Same legend applies for all figures.

Run	$\tau_{w,RA}$	$\tau_{w,Preston}$
5204	49.6	10.1
5205	49.7	10.3
5201	49.7	7.7
5202	49.9	7.8

Table 7.16: Pitot campaign wall shear stress, laminar flow, 140mm from the LE. $\tau_{w,CFD} = 8.2$. All values are in Pa.

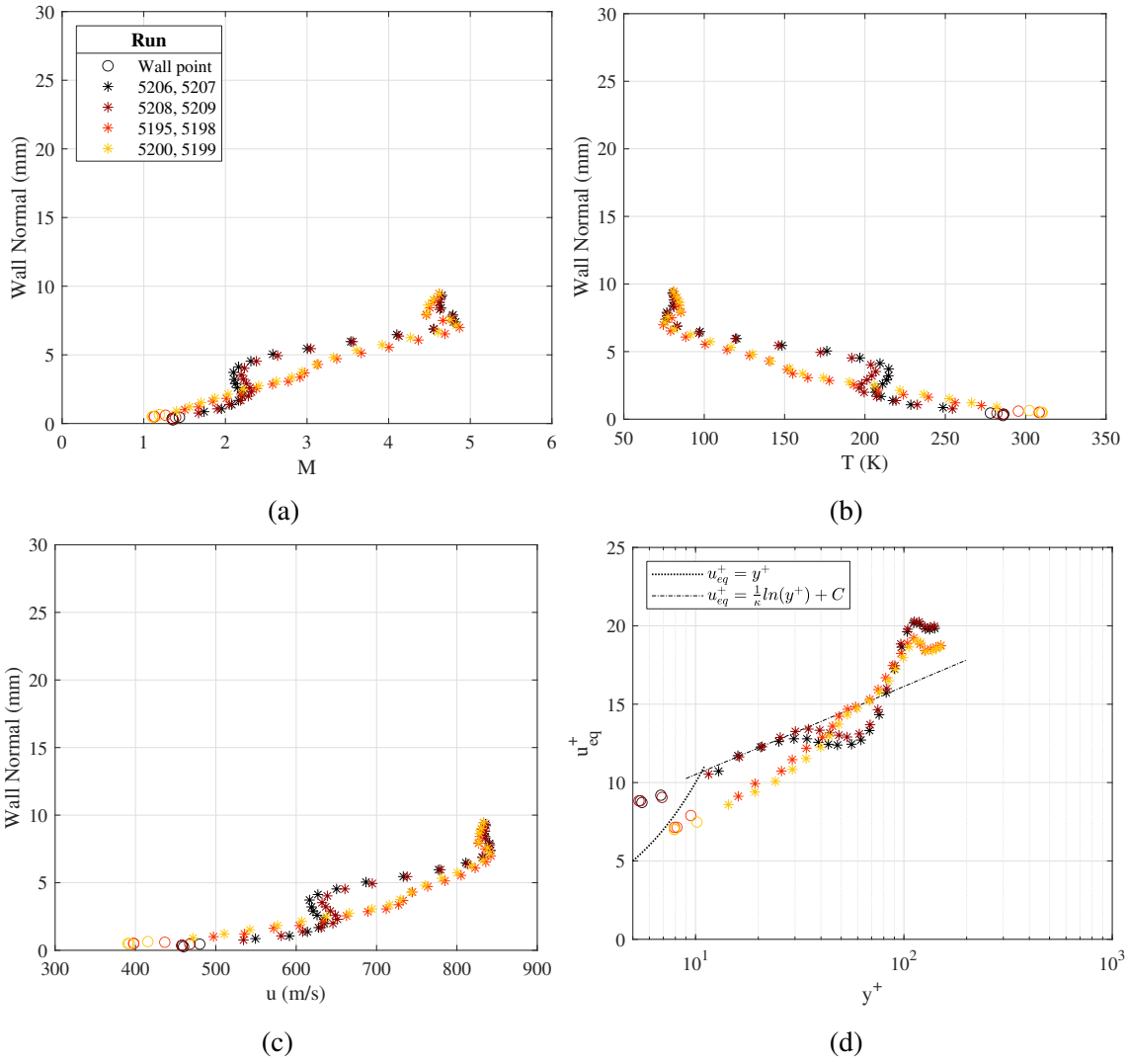

Figure 7.52: Turbulent Pitot data, 140mm from the LE. Same legend applies for all figures.

Run	$\tau_{w,VD}$	$\tau_{w,RA}$	$\tau_{w,Preston}$	$\tau_{w,Clauser}$
5206, 5207	27.7	34.7	12.2	17.5
5208, 5209	28.1	35.2	12.3	17.5
5195, 5198	27.9	34.8	8.8	19.5
5200, 5199	27.8	34.6	8.5	19.5

Table 7.17: Pitot campaign wall shear stress, turbulent flow, 140mm from the LE. $\tau_{w,CFD} = 29.0$. All values are in Pa.

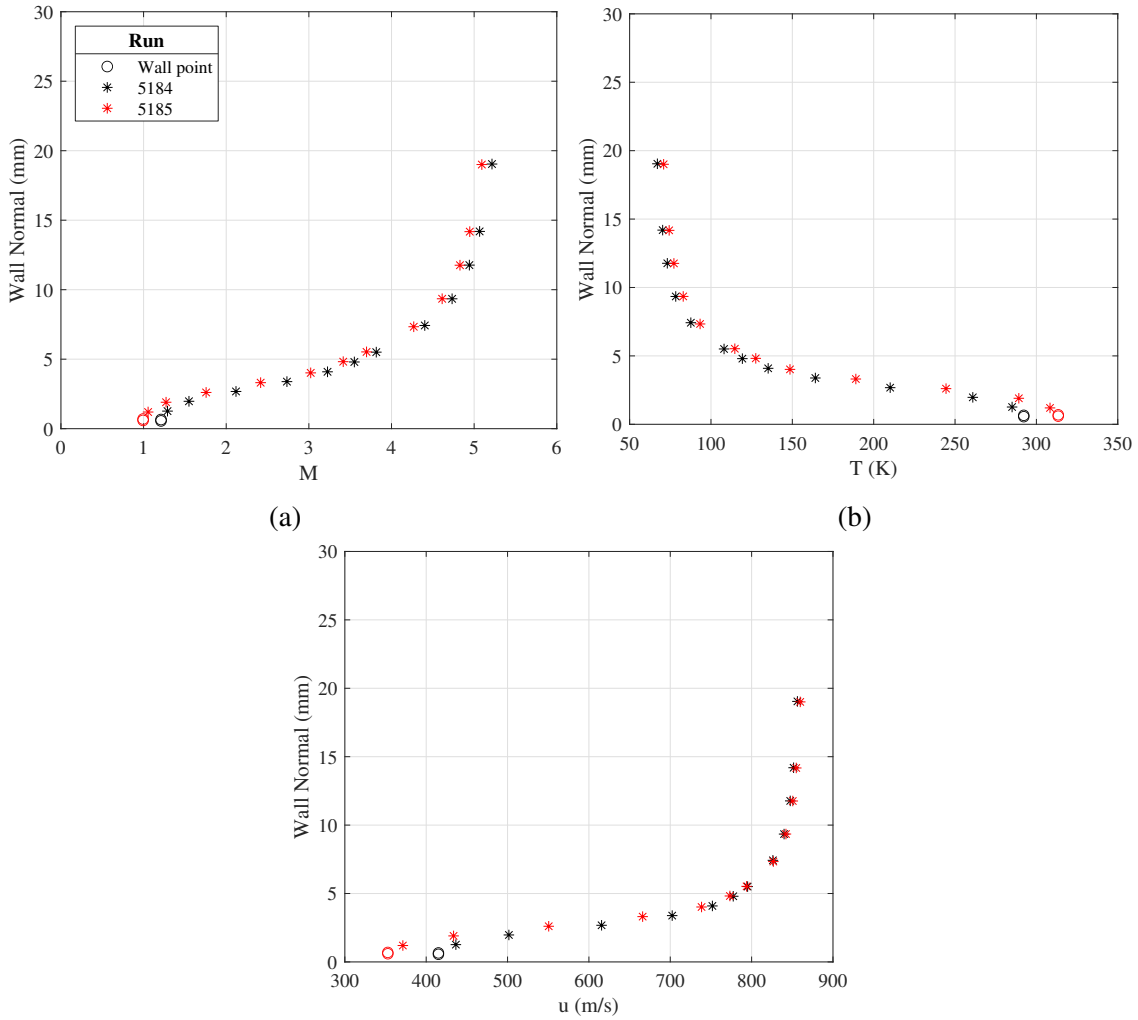

Figure 7.53: Laminar Pitot data, 260mm from the LE. Same legend applies for all figures.

Run	$\tau_{w,RA}$	$\tau_{w,Preston}$
5184	12.1	10.1
5185	12.2	7.1

Table 7.18: Pitot campaign wall shear stress, laminar flow, 260mm from the LE. $\tau_{w,CFD} = 6.0$. All values are in Pa.

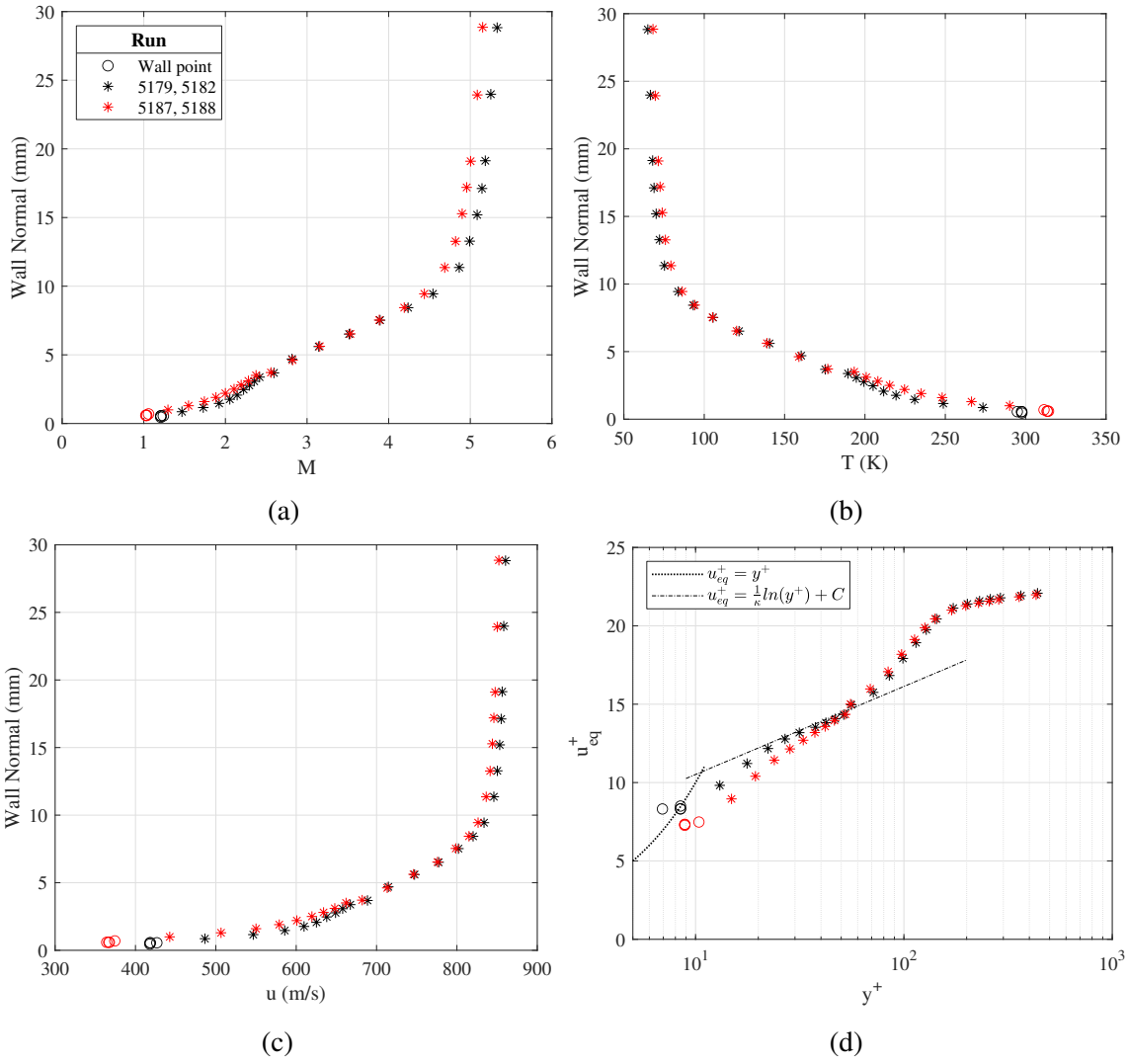

Figure 7.54: Turbulent Pitot data, 260mm from the LE. Same legend applies for all figures.

Run	$\tau_{w,VD}$	$\tau_{w,RA}$	$\tau_{w,Preston}$	$\tau_{w,Clauser}$
5179, 5182	24.9	25.2	10.1	16.5
5187, 5188	24.8	25.1	7.5	16

Table 7.19: Pitot campaign wall shear stress, turbulent flow, 260mm from the LE. $\tau_{w,CFD} = 22.4$. All values are in Pa.

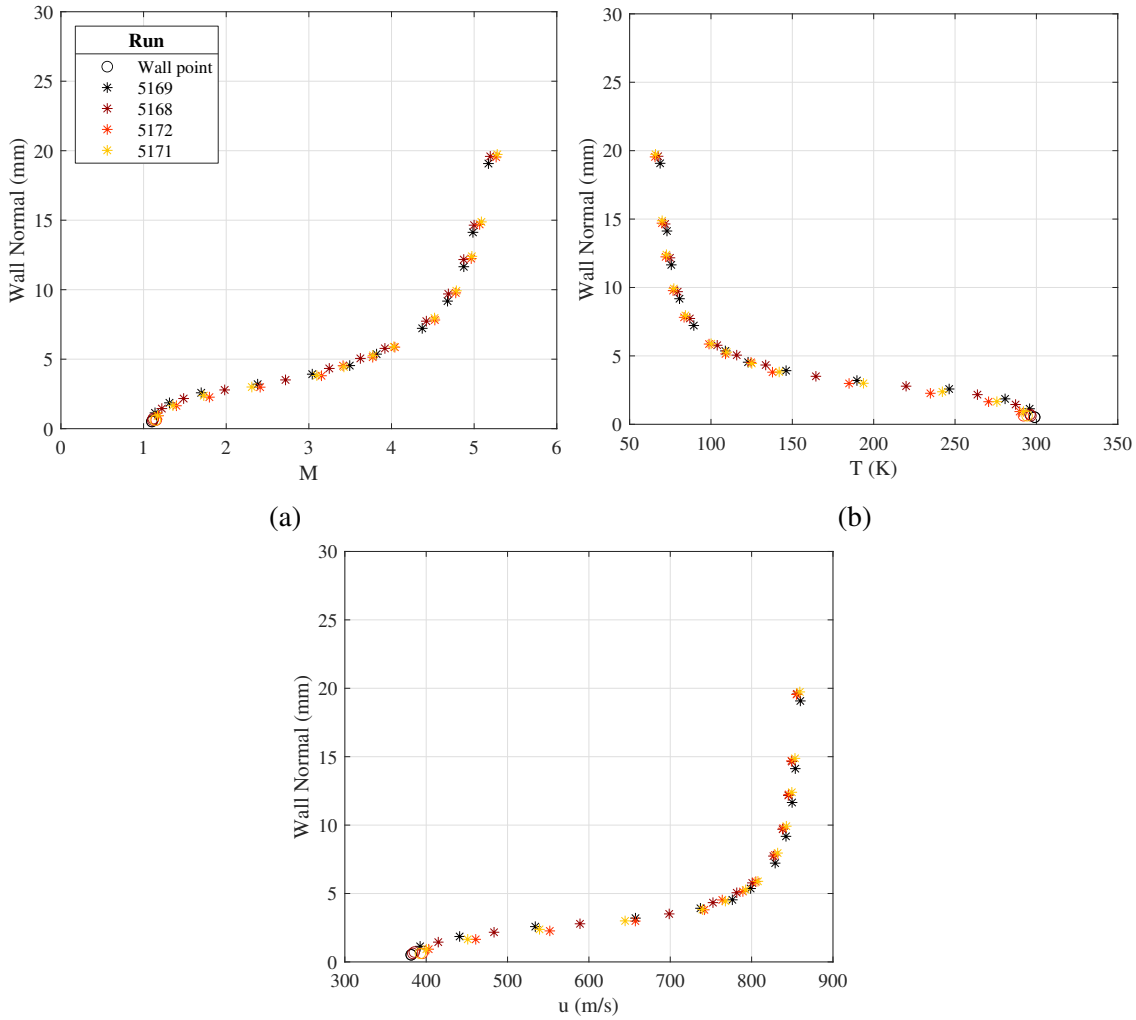

Figure 7.55: Laminar Pitot data, 405mm from the LE. Same legend applies for all figures.

Run	$\tau_{w,RA}$	$\tau_{w,Preston}$
5169	10.2	8.2
5168	10.0	8.4
5172	10.0	8.9
5171	10.1	8.8

Table 7.20: Pitot campaign wall shear stress, laminar flow, 405mm from the LE. $\tau_{w,CFD} = 4.8$. All values are in Pa.

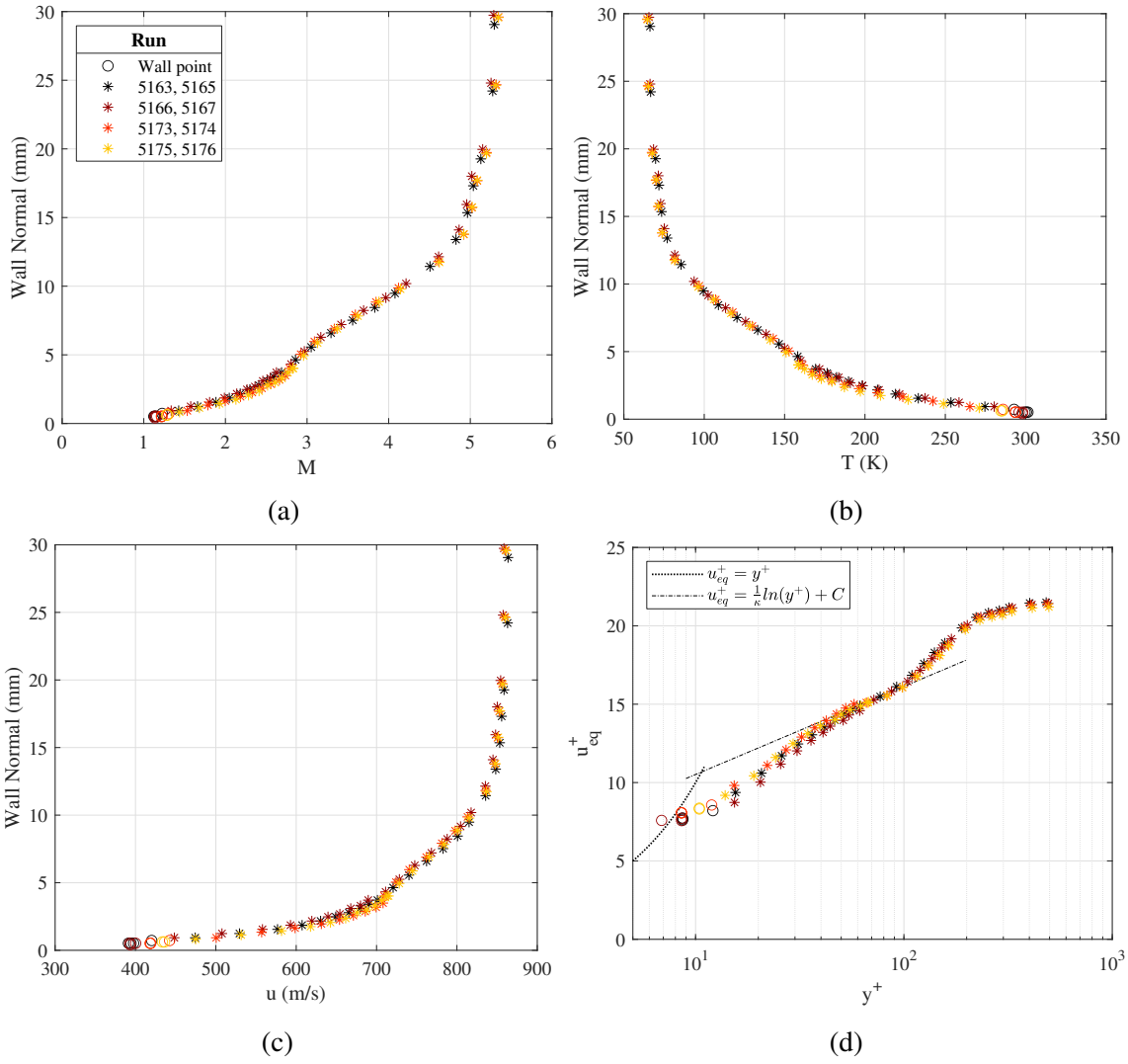

Figure 7.56: Turbulent Pitot data, 405mm from the LE. Same legend applies for all figures.

Run	$\tau_{w,VD}$	$\tau_{w,RA}$	$\tau_{w,Preston}$	$\tau_{w,Clauser}$
5163, 5165	23.4	20.6	8.7	18.0
5166, 5167	22.9	20.2	8.7	18.0
5173, 5174	23.0	20.2	9.8	18.0
5175, 5176	22.9	20.2	10.7	18.5

Table 7.21: Pitot campaign wall shear stress, turbulent flow, 405mm from the LE. $\tau_{w,CFD} = 19.6$. All values are in Pa.

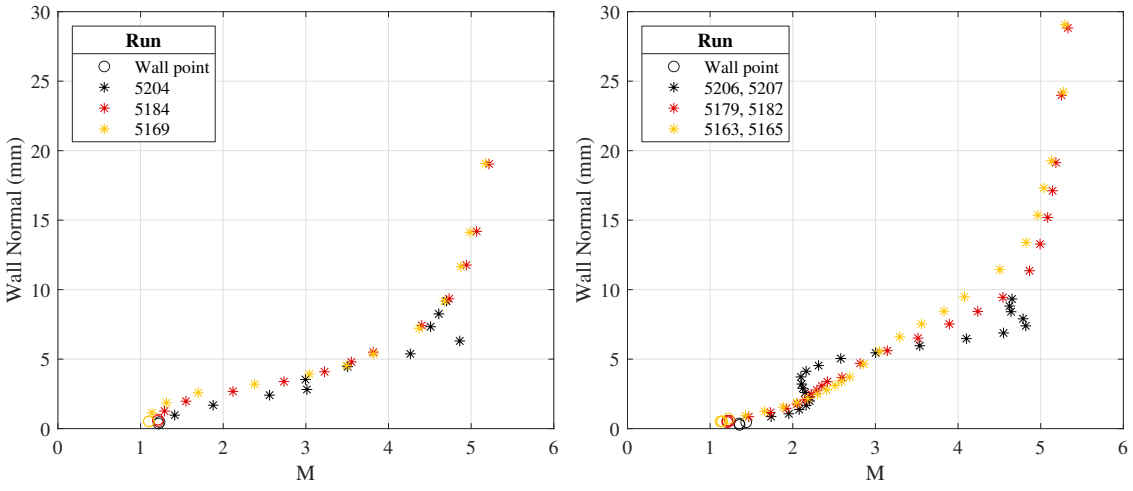

(a) Laminar, Mach number

(b) Turbulent, Mach number

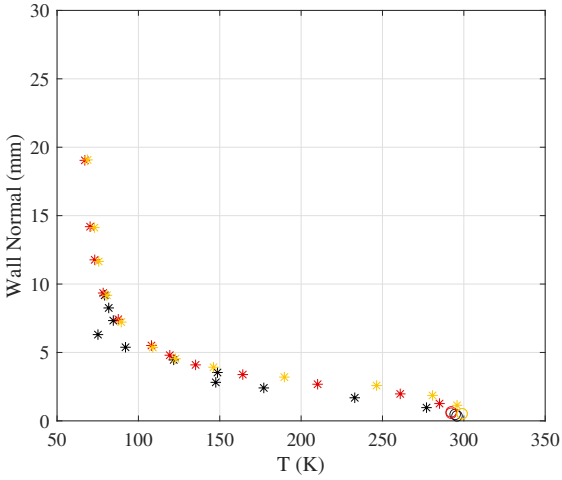

(c) Laminar, temperature

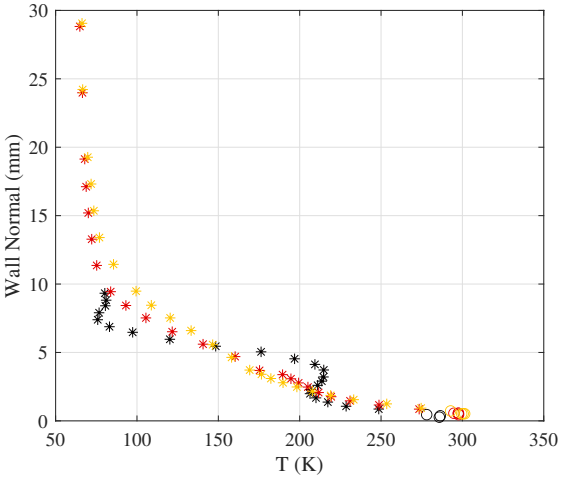

(d) Turbulent, temperature

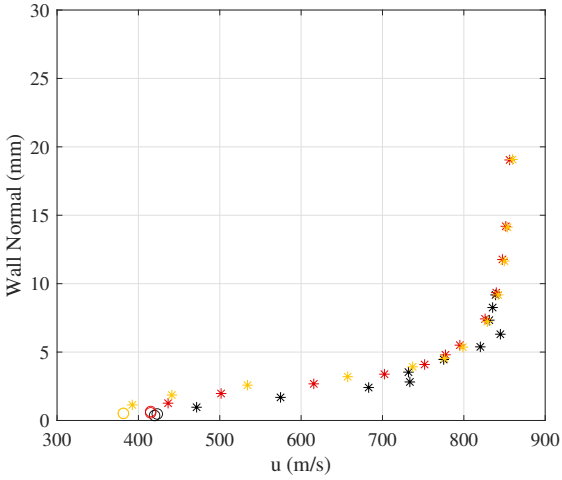

(e) Laminar, velocity

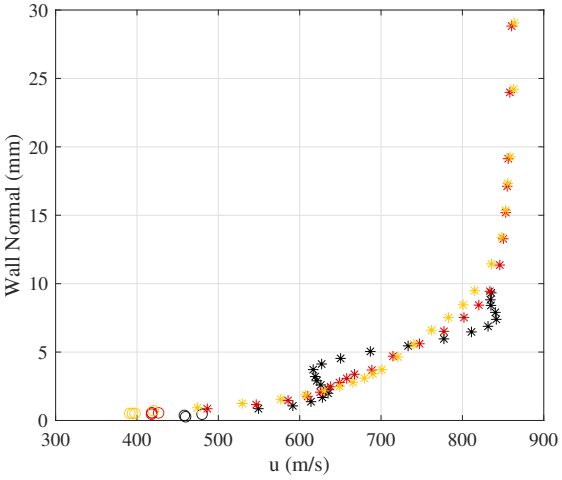

(f) Turbulent, velocity

Figure 7.57: Streamwise plots of Pitot data. All figures in the "Wake" with the plasma "Off". Same legend applies for all figures in column.

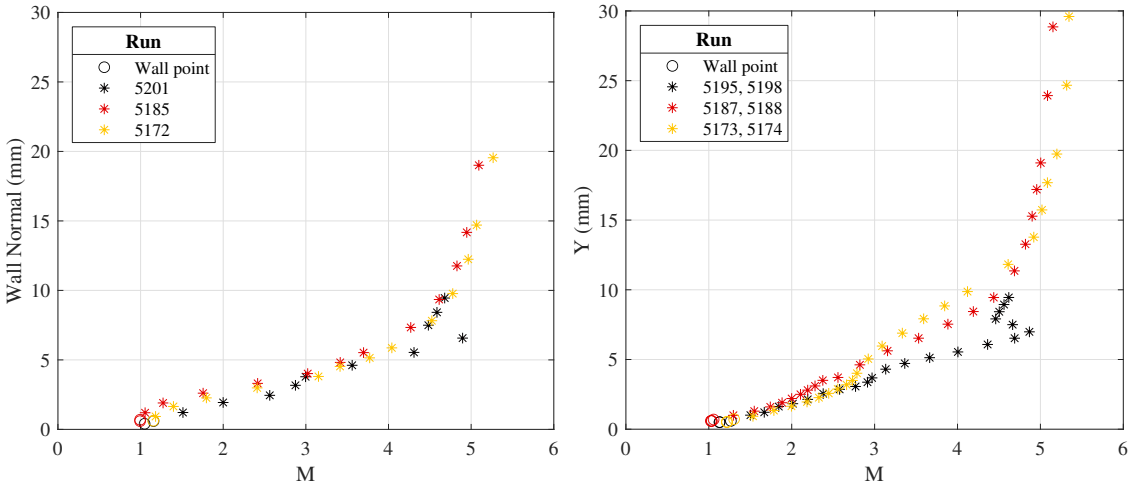

(a) Laminar, Mach number

(b) Turbulent, Mach number

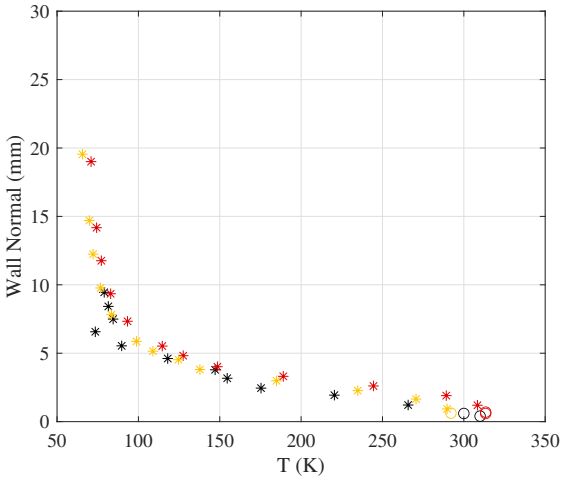

(c) Laminar, temperature

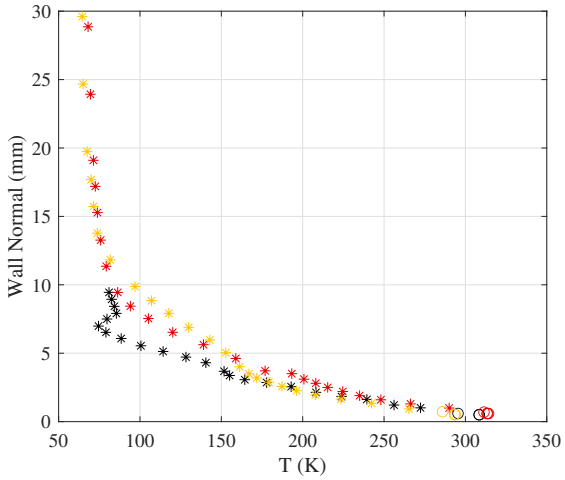

(d) Turbulent, temperature

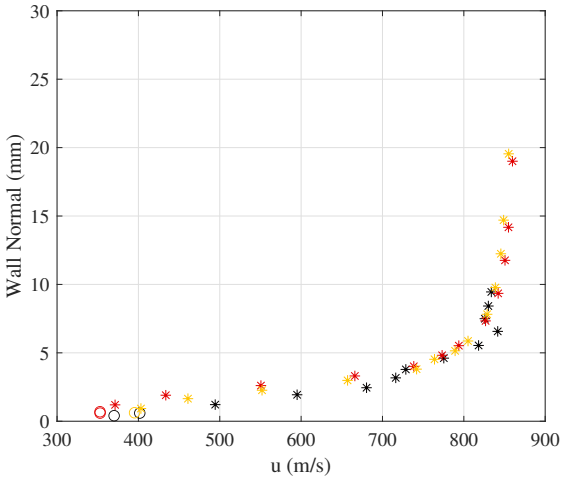

(e) Laminar, velocity

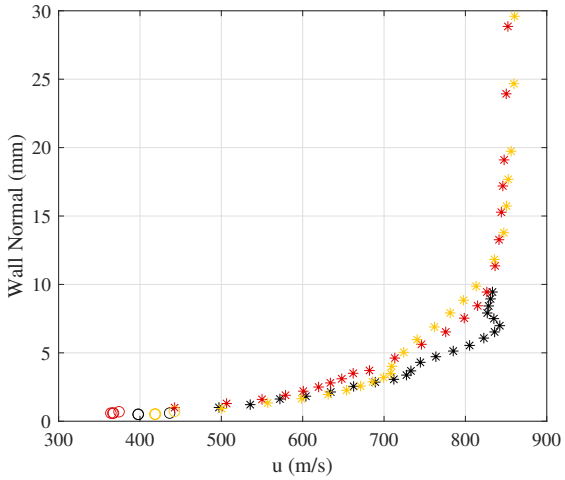

(f) Turbulent, velocity

Figure 7.58: Streamwise plots of Pitot data. All figures in the "Trough" with the plasma "Off". Same legend applies for all figures in column.

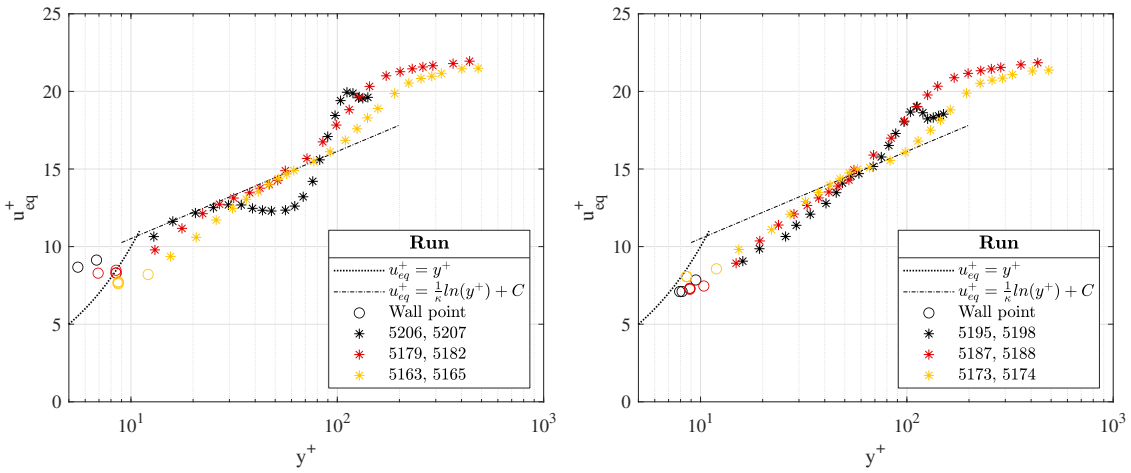

(a) Wake

(b) Trough

Figure 7.59: Streamwise plots of Pitot inner variable data. All figures had the plasma "Off".

7.3.5.3 *Freestream Mach Number Results*

The freestream Mach number test produced complex results, shown in Figure 7.60. There were two trends to consider, the amount of variation in each result, and its response as the Reynolds number changed. The $P_{o,TS}/P_{TS}$ (TS- test section, SC- settling chamber) result showed the most sensitivity to the Reynolds number, followed by the $P_{o,SC}/P_{TS}$ result, and lastly the $P_{o,TS}/P_{o,SC}$ result. Figure 7.60(b) was produced to elucidate these findings by plotting each pressure reading normalized by its value when the tunnel started. It shows that the stagnation pressures track one another closely, maintaining a near-constant pressure ratio. The static pressure readout defied this trend, growing $\sim 50\%$ more than the stagnation pressures. The reason for this sensitivity remained under investigation at the time of publication.

Still, the variation in the static pressure explained why the Mach numbers calculated using P_{TS} were the most for susceptible to change. This effect was enhanced in the Mach number calculated entirely from TS instruments. This was attributed to the role Reynolds number had on the boundary layer. As it was increased, the flow's inertial forces dominated its viscous forces, so the boundary layer thinned; this was captured in the laminar equation $\delta \propto \frac{M_e^2\sqrt{x}}{\sqrt{Re}}$ [6] (Re refers to the unit Reynolds number). Here the thinning boundary layer would affect the nozzle's effective area ratio. Both TS instruments would be affected by this behavior at the nozzle exit, while the SC probe would be largely insulated from it, producing a more invariant Mach number. The linearly-scaling 0.5% error of the MKS Baratron 631C-10 may have had some effect, but was likely too small to be the sole source of the trend.

While the variation in the Mach number could be explained, the general trend, that the Mach number decreased with as the Reynolds number grew, could not. As the boundary layer thinned, the Mach number should have increased, with the exception of the boundary layer rapidly thickening as the flow became turbulent at $Re = 3-4\times10^6/\text{m}$ [245]. In the case of the turbulent flow, it may have been that the transition point in the nozzle moved upstream, which gave the boundary layer more time to develop and grow despite the higher Reynolds number. Another possible explanation would be that the laminar flow in the nozzle's throat was proportionally affected more than the exit

area ratio, effectively driving down the cumulative area ratio. A final theory would be that as the tunnel was run, it heated slightly, increasing the speed of sound and thereby lowering the Mach number, but in constant Reynolds number tests the Mach number remained constant.

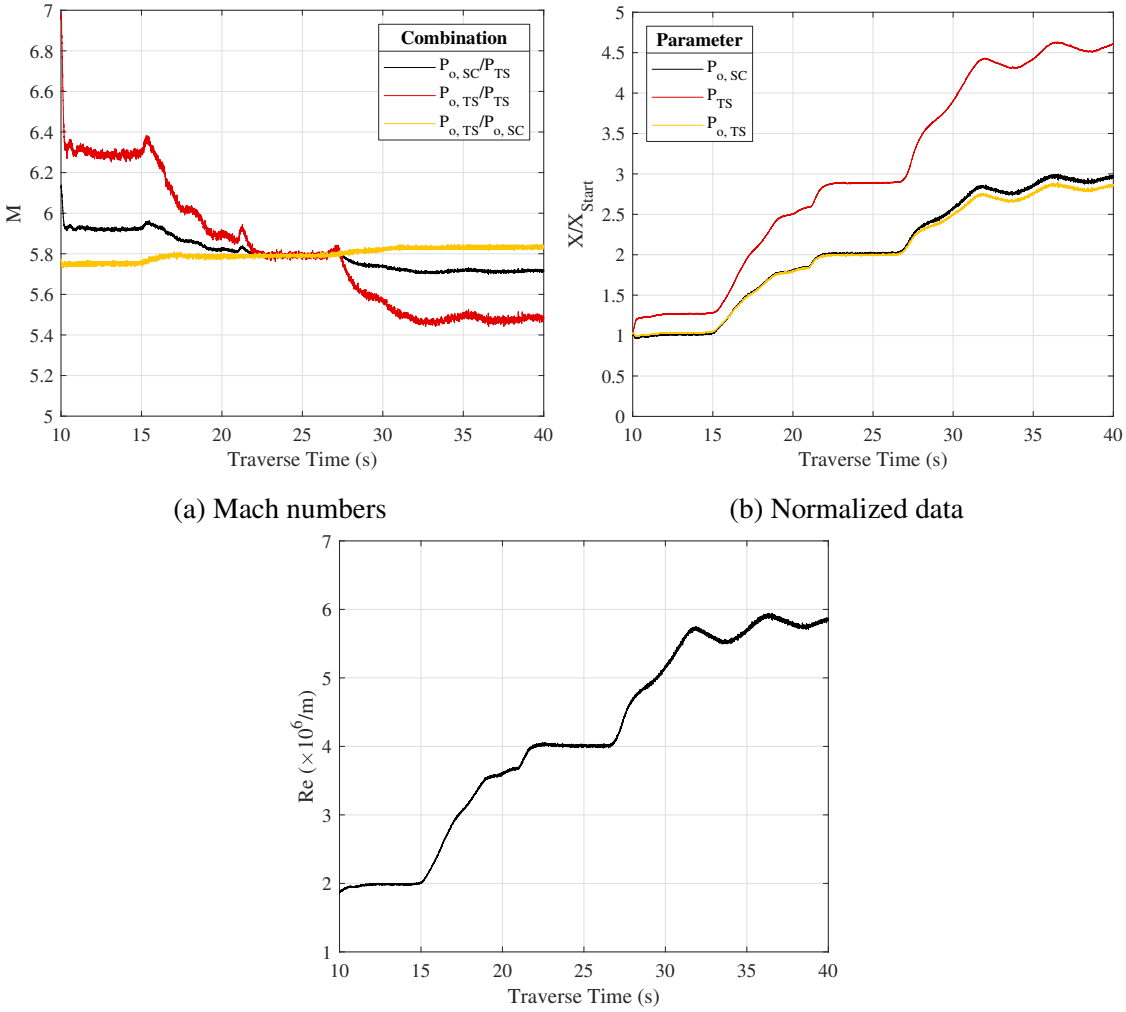

(a) Mach numbers

(b) Normalized data

(c) Reynolds number

Figure 7.60: Tunnel Mach number calculated from various pressure sources.

As part of the development of the PLIF technique, Buen [49] made freestream temperature and velocity measurements of the ACE tunnel at comparable Reynolds numbers. The former were mostly to measure freestream fluctuations and the uncertainty of the technique, however, because

to make a thermometry measurement a known temperature must be input, and the only reasonable input for the entire homogeneous data set was the NALDAQ's calculated temperature; as such the freestream temperature 57.35K from Table 4.1 was used hereafter. The velocimetry results from a spanwise (across the test section) and top-down (from the ceiling to the floor) test were 869.8 ± 7.7 and $822.5 \pm 9.0\text{m/s}$ respectively. Combined with the NALDAQ's temperature, the Mach number ranged from $M = 5.42 - 5.73$, only the latter of which was feasible and matched both the Pitot probe's and NALDAQ's results; no explanation was offered in [49] for the discrepancy in the top-down measurement. Additionally, the temperature fluctuations in the core of the NO cloud were $2 - 8\%$ and the velocity fluctuations were $0.5 - 1\%$ for both the spanwise and top-down techniques [49]; the large temperautre fluctuations were attributed to the uncertainty of the technique. What was worth noting was that, for the spanwise measurement, the velocity tended to grow as the run progressed, both in the NALDAQ and MTV data. Buen [49] attributed this behavior to the tunnel heating, but it could also have occurred due to the tunnel operator increasing the stagnation pressure, and thereby changing the velocity, to maintain the Mach number as the temperature elevated. Were it solely due to tunnel heating, then at the very least the heating's effect on the freestream temperature dominated any effect on the velocity, as the Mach number was known to fall during a run.

In summation, the Pitot-Pitot data confirmed the tunnel's standard calculation of the Mach number to be 5.7 at the test condition of $6 \times 10^6/\text{m}$ to within $\sim 2\%$, though further understanding of the behavior of the Mach number was warranted. These findings were abetted by PLIF diagnostics. As a final note, it was interesting to see the delay in the response of the static pressure data as the MKS Baratron 631C-10 vacuumed out manifest in the Mach numbers as a brief spike as the settling chamber pressure was increased; neither Pitot tube showed evidence of a delayed response.

7.4 Advanced Optical Techniques

The techniques in this section were well-established in hypersonic wind tunnel testing, but the results presented were the first from the ACE tunnel. As such they are distinguished from other, more standard optical techniques like schlieren imaging or surface profilometry. The data were

relevant to the behavior of the plasma, the flow physics in the boundary layer, and the system's nonequilibrium.

7.4.1 OES Results

The OES data can be split into three parts, the HCLs' spectra, the broadband data taken with the OceanOptics spectrometer, and the rotationally-resolved data taken with the Spex spectrograph. The broadband measurements were useful for identifying species and their degree of excitation as well as studying the effect of general parameters including flow condition and measurement location. Rotationally-resolved data were collected to allow estimation of the bulk plasma temperature to determine if it would produce a significant and undesirable thermal perturbation. The spectra from the HCLs were also recorded using both techniques; the broadband data provided the location of relevant lines, and then certain lines of interest were probed to provide a measurement of the instruments' resolutions.

The test matrix for ACE tunnel spectroscopy measurements is shown in Table 7.22, and the corresponding plasma conditions in Table 7.23 and Figure 7.61.

No.	Resolution	Location	Trip	Nitric Oxide	Run/Date
1	Broadband	Positive column	Laminar	Yes	4921, 8/31/2021
2	Broadband	Negative glow	Laminar	Yes	4919, 8/30/2021
3	Broadband	Positive column	Laminar	No	4922, 8/31/2021
4	Broadband	Negative glow	Laminar	No	4918, 8/30/2021
5	Broadband	Positive column	Turbulent	No	4923, 8/31/2021
6	Broadband	Negative glow	Turbulent	No	4917, 8/30/2021
7	Resolved	Positive column	Laminar	No	4929, 9/2/2021
8	Resolved	Negative glow	Laminar	No	4930, 9/2/2021
9	Resolved	Positive column	Turbulent	No	4928, 9/2/2021
10	Resolved	Negative glow	Turbulent	No	4935, 9/3/2021

Table 7.22: OES test matrix.

No.	Current (mA)	Power Supply Voltage (V)	Power Supply Power (W)	Plasma Voltage (V)	Plasma Power (W)
1	93.5	1427	133.5	489.6	45.8
2	94.2	1433	135.0	487.6	45.9
3	93.9	1427	133.9	485.3	45.6
4	93.9	1427	134.0	484.6	45.5
5	95.9	1430	137.2	468.5	44.9
6	95.0	1426	135.5	472.5	44.9
7	93.8	1426	133.7	485.5	45.5
8	93.9	1427	134.0	485.4	45.6
9	95.5	1429	136.5	471.4	45.0
10	95.8	1428	136.9	467.1	44.8
Average					
	94.5	1428	135.0	479.7	45.4

Table 7.23: Plasma conditions for OES campaign.

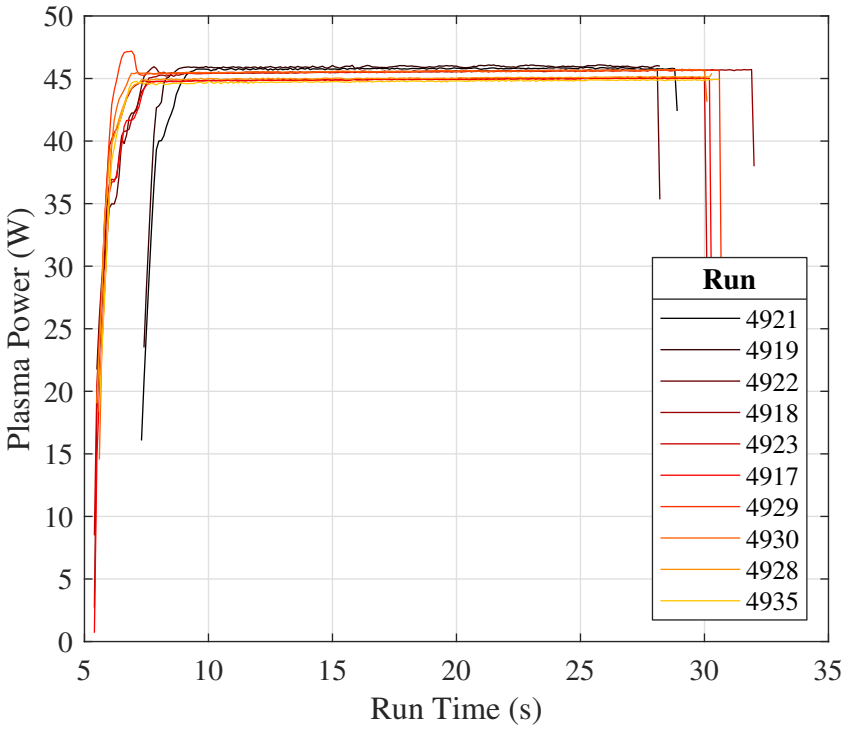

Figure 7.61: Plasma power traces for OES runs.

7.4.1.1 HCL Spectra

It was first necessary to measure the performance of the HCLs. The $Hg-Ar$ lamp was used to calibrate the OceanOptics USB2000+, then broadband measurements were taken of the remainder of the lamps. This provided the capability to check for metal lines in the plasma such as *Cu* sputtered from the electrodes, isolated peaks to determine both instruments' resolutions, and aided with the calibration of the Spex spectrograph. The full broadband results for each of the four HCLs are shown in Figure 7.62; these plots were normalized by the absolute maximum intensity in the entire spectra. In general, the lines below 600nm were attributed to the metal cathode while those above 600nm were attributed to the inert gas. This was why the *Rh*, *Ti*, and *Cu* plots all had the same IR spectra, they all used *Ne* as their fill gas. Figure 7.63 focuses on the UV region of interest; here the data were normalized by the maximum intensity in the bandwidth shown. This was appropriate because these data were taken by maximizing the output in the region shown and letting the brighter IR spectra saturate in order to provide additional clarity in the UV region, that of the greatest relevance to the plasma.

While these data mostly served as a reference and as a calibration source, there were several additional findings. Figure 7.63(a) shows a strong, isolated spike in the Hg spectra at 365.02nm (according to the NIST tables[1] discussed in Section 6.7). This was in a good position for both the calibration and resolution measurement of the Spex spectrograph. Indeed, the same line was used to measure the resolution of the OceanOptics spectrometer as well. For the OceanOptics spectrometer, the isolated *Ne* line at 692.95nm (again, from NIST) shared between the *Rh*, *Ti*, and *Cu* lamps provided another point. Using the dataset that maximized the signal of each line and taking the average of the results from all four lamps yielded a resolution of $[Hg, Rh, Ti, Cu] = [2.5039, 2.1443, 2.2021, 2.1866]\text{nm} \rightarrow 2.2592\text{nm}$. The four runs with the Spex spectrometer and Hg lamp yielded a resolution of $[4929, 4930, 4928, 4935] = [0.0804, 0.0727, 0.0804, 0.0770]\text{nm} \rightarrow 0.0776\text{nm}$; it was unknown why this value differed from the 0.025nm reported by Hsu [116]. Nevertheless the Spex spectrograph had $\sim 30\times$ the resolution of the broadband spectrometer, under-

[1] https://www.nist.gov/pml/handbook-basic-atomic-spectroscopic-data

scoring its value and enhanced capability.

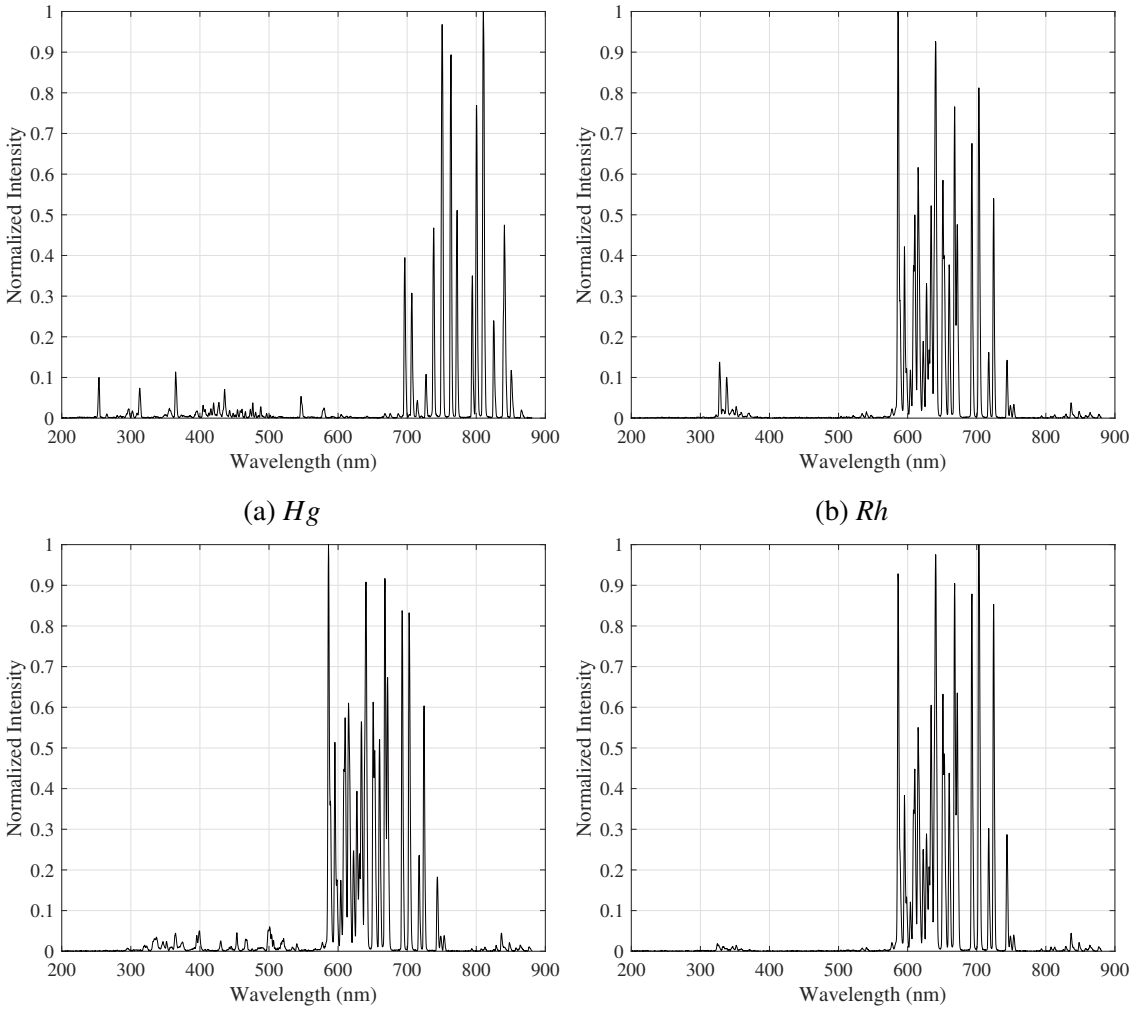

(a) Hg (b) Rh

(c) Ti (d) Cu

Figure 7.62: Broadband spectra of HCLs. Data normalized by maximum intensity in range.

7.4.1.2 Broadband Spectra

The broadband plasma spectra addressed several fundamental questions. Note that for the following figures the data were normalized by each run's maximum intensity in the full spectra. Figure 7.64 shows that the presence of the trips had no measurable effect on the negative glow or positive column. This was somewhat surprising, because the trips did have a visible impact on

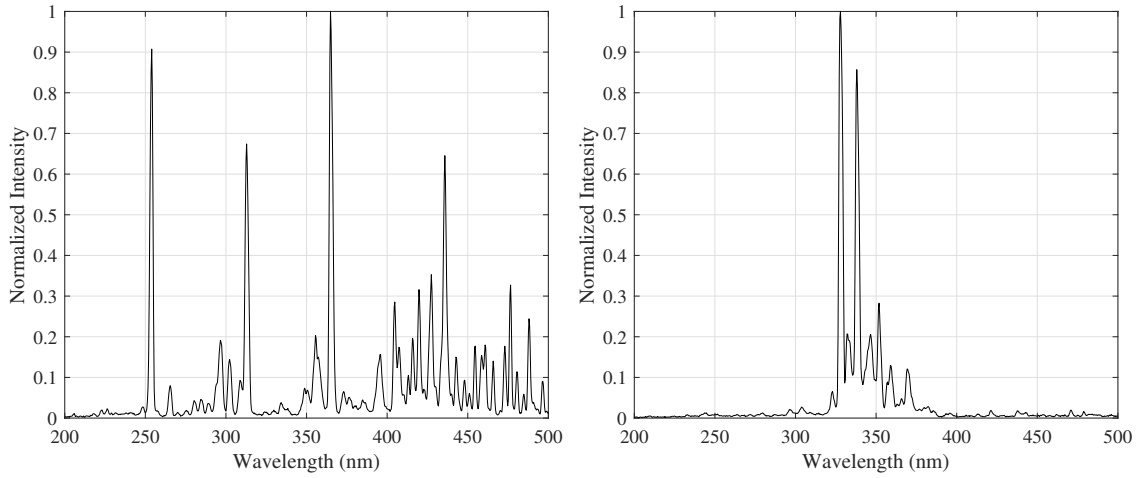

(a) Hg (b) Rh

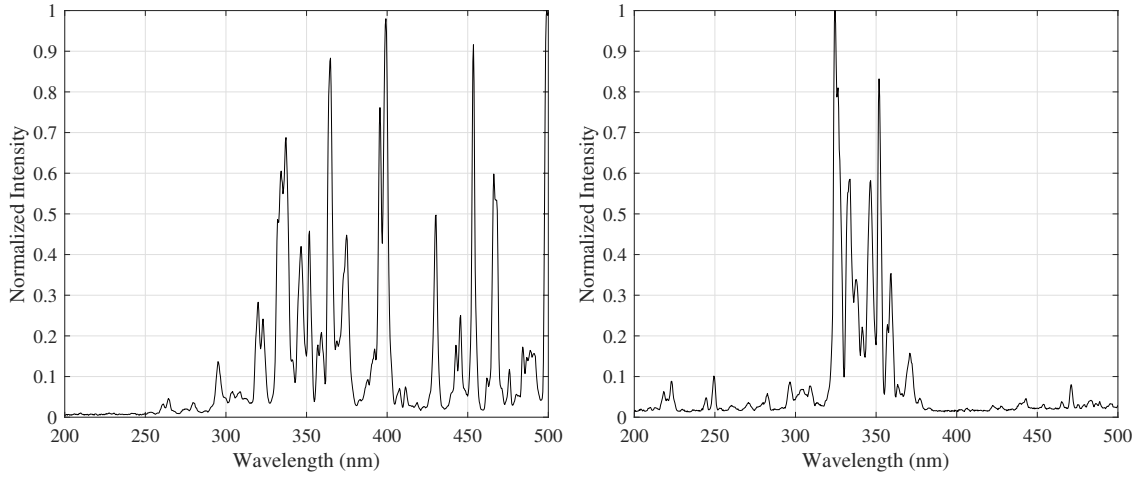

(c) Ti (d) Cu

Figure 7.63: Focused spectra of HCLs. Data normalized by maximum intensity in range.

the plasma's shape and color; further investigation on the bulk temperature was used to confirm this result, and this will be discussed shortly. For now, however, it was no longer necessary to distinguish between the two cases. The performance of negative glow and positive column is compared in Figure 7.65. There was a series of three lines present only, or at least predominantly, in the negative glow. This was the first negative system $N_2^+\left(B^2\Sigma \rightarrow X^2\Sigma\right)$, and the behavior followed from the theory captured in Figure 2.13. Recall from Section 2.4 that the positively charged ions were expected to aggregate above the cathode, so it followed purely from the perspective of number density that their spectra should be strongest in this region. Rajzer [224] offered such effects as

this and the high bulk and electron temperatures above the cathode as explanations for the color difference between the negative glow and the positive column and suggested these same effects could lead to differences in the spectra as well. All told this figure was predicted from plasma theory. The difference in the signal also ensured that the collimator was not so large as to fully conflate the two regions.

Figure 7.66 studies the effects of a 10% *NO* injection to see if the *NO* was directly excited by the plasma as Hsu [116] observed. Its results are both clear and provocative: in both the negative glow and positive column regions the *NO* was electronically excited by the plasma. The results even track those of Figure 2.13 in that the hotter, higher energy region produced more intense lines.

Buen [49] attributed the vibrational excitation of *NO* through the plasma, as observed through PLIF thermometry, to one of two processes, inelastic scattering (Equation 7.1) and/or electron-impact ionization (Equation 7.2)

$$NO^{v=0} + e^- \rightarrow NO^- \rightarrow NO^{v=1} + e^- \tag{7.1}$$

$$NO\,X^2\Pi + e^- \rightarrow NO\,A^2\Sigma^+ + e^- \tag{7.2}$$

The latter pathway would produce $NO^{v=1}\,X^2$ through fluoresence and collisional quenching. Song et al. [260] stated the resonant absorption energy range for the inelastic scattering process was $0.5-2$eV with an absorption cross-section of $\sim 2-5\times10^{-16}$cm^2. The absorption energy range for the electron-impact ionization had a maximum of 1.9eV with an absorption cross-section of 1.1×10^{-17}cm^2. From the characteristic parameters listed by Roth [228], the glow discharge's temperature of $1-2$eV was well-suited to excite these transitions. The spectrometers here could only study the fluorescence, providing little guidance as to the source of the initial excitation, but owing to the lower absorption cross-section and upper energy limit of the electron-impact ionization process, Buen [49] concluded the inelastic scattering process was likely the dominant source of *NO* excitation within the plasma.

An unexpected finding was the presence of *NO* lines even in the absence of injected gas. This

was not due to leftover gas in the chamber because the first run in the series, Run 4918, did not have NO and occurred months and many runs after the last NO run. Furthermore, NO venting procedures were built into the post-run procedure whenever the gas was injected, so none should ever be left in the line. A pickup run where the NO injection was started halfway through the run confirmed the lines were indeed excited NO because the small lines grew in intensity after the NO was introduced. The HCL spectra in Figure 7.63(d) shows these are not lines from sputtered Cu.

The question became, then, where did the NO come from? Its formation required the presence of atomic N and O, but the ACE tunnel is a cold blowdown facility and should not have produced temperatures at any point in the entire air supply system or across the shock high enough to dissociate N_2 or even O_2. Recall from Figure 2.6 these species dissociate at ~ 4000K and ~ 2500K respectively, though from Figure 2.8, some N_2 dissociation is possible at $\lesssim 2000$K [6], especially at the low pressures observed in the ACE tunnel. Taken together, this could imply a lower limit for the plasma's internal temperature, that in the nonequilibrium of the plasma, vibrational temperatures could reach these temperatures and been sufficiently excited enough to cause dissociation; because electron temperatures on the order of $1-2$eV corresponding to $11604.5-23209.1$K were expected [228], vibrational modes $\mathscr{O}(1000\text{K})$ were reasonable.

An alternative hypothesis comes from the work of Kossyi et al. [148], who identifies hundreds of reactions and their rate constants in air plasmas, including those involving N, O, and NO. These reactions illustrate the complexity of plasma chemistry, and show ionization, recombination, electronic excitation, *etc.* were all equally valid and significant contributors to the formation of NO. These reactions may not have required excessively high neutral molecule internal temperatures. Either way, the spectroscopy available did conclude NO was being formed, and that the plasma was the most likely source of the constituent atoms, specifically the negative glow where the electrons are more energetic. Further work to resolve the vibrational temperature through OES could further clarify the mechanism by which NO formation occurred.

Comparing the spectra in Figure 7.66(c) to the NIST tables, O lines were present at 777.19 and 844.63/844.64/844.68nm and N lines were present at 821.63 and 868.03/868.34nm. As expected,

these lines faded away in the positive column, Figure 7.66(d); the unidentified bands at 600, 675, and 750nm, perhaps carbon bands from burning PEEK between the electrodes or N_2 first positive bands generated by the anode, did seem to become stronger in the positive column, defying the general trend. That the data overlapped so well between the cases with and without *NO* injection also showed the *NO* was not being dissociated. This was an unexpected finding, not least because the OceanOptics spectrometer has $< 30\%$ efficiency above 575nm. It showed that the plasma, though it may have been, weak and ro-translationally cold, had sufficient energy to break apart very stable molecules and thereby foment species recombination. This would imply that a sufficiently strong plasma could remove the need for any *NO* injection for PLIF measurements. It also suggests that the *NO* that was probed with PLIF was being electronically excited by the plasma, not just vibrationally excited by relaxing *NO* or the laser, complicating the system's thermodynamics.

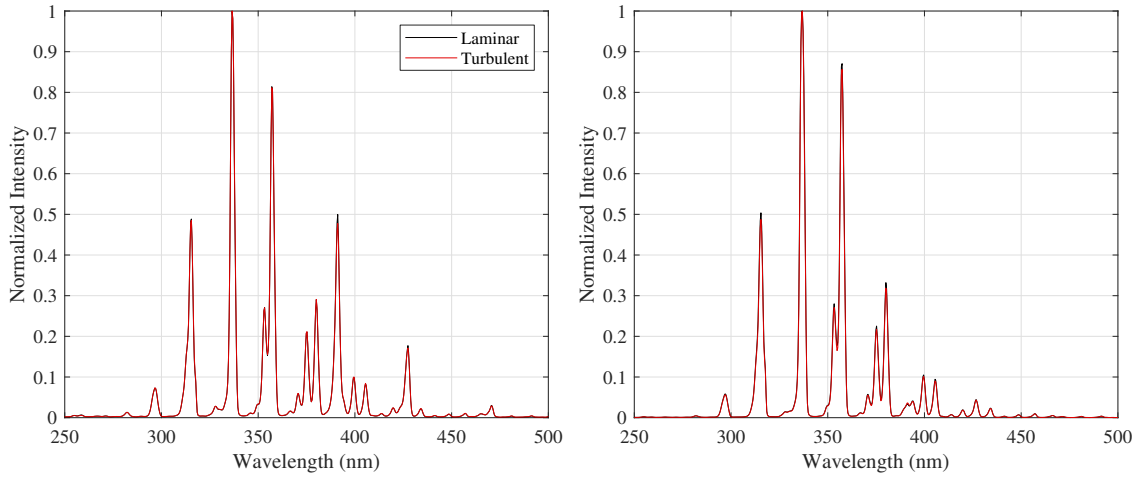

(a) Negative glow

(b) Positive column

Figure 7.64: Comparison between spectra of laminar and turbulent flow.

7.4.1.3 Spectra for Thermometry

N2SPECFIT was run for the rotational lines of the $N_2\left(C^3\Pi_u \rightarrow B^3\Pi_g\right)$ $(v',v'') = (0,2)$ band (notation from [98]). The average of the twenty acquisitions were background subtracted by the

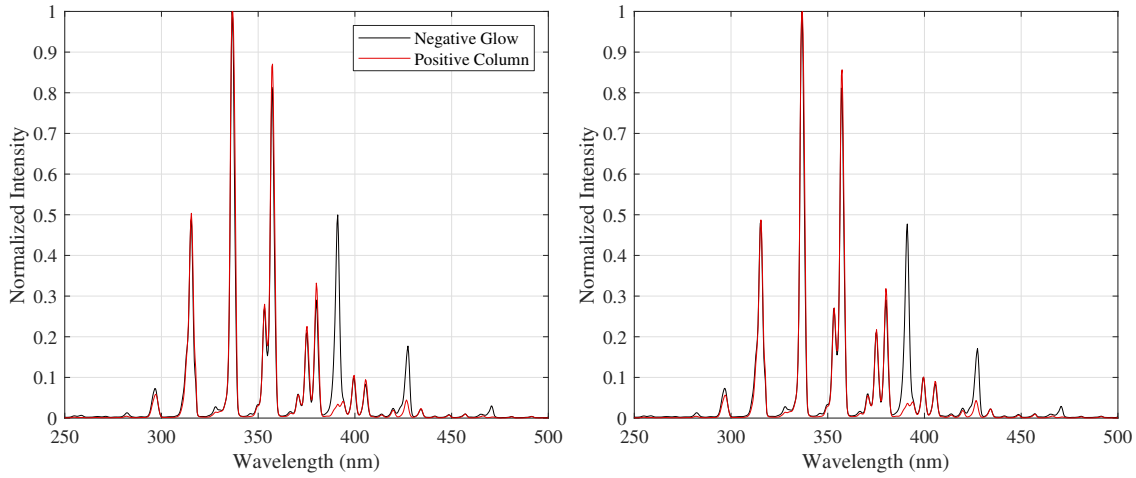

(a) Laminar (b) Turbulent

Figure 7.65: Comparison between spectra of negative glow and positive column.

mean of the twenty background frames. The maximum of resulting single spectra was used to normalize the data from zero to one. The standard deviation for each pixel was calculated from the result of subtracting the mean background signal from each spectra, then again normalizing by the maximum of the average background subtracted spectra. Despite the careful calibration and background subtraction, the best results were obtained when the program was allowed to calculate and apply a small wavescale shift and dark current offset. Similarly, omitting the vibrational peaks and fitting only the rotational lines of the aforementioned band were analyzed produced the strongest fits. The reason for this limitation was unknown, but including the vibrational peaks caused the program to converge on an incorrect wavescale shift, perhaps because the code tried to use the few and broad vibrational peaks to determine the shift instead of the more numerous rotational lines. Nevertheless, because the goal was only ever to determine a rotational temperature, cutting the vibrational peaks to improve the accuracy of the ro-translational temperature was a worthwhile sacrifice. The $(v', v'') = (0, 2)$ band's rotational lines were used because it was the dominant peak in the observed spectra.

There are three relevant mechanisms by which a spectra can broaden itself, natural (lifetime), Doppler, and pressure (collisional) broadening [86]. The first is mostly attributed to the uncertainty

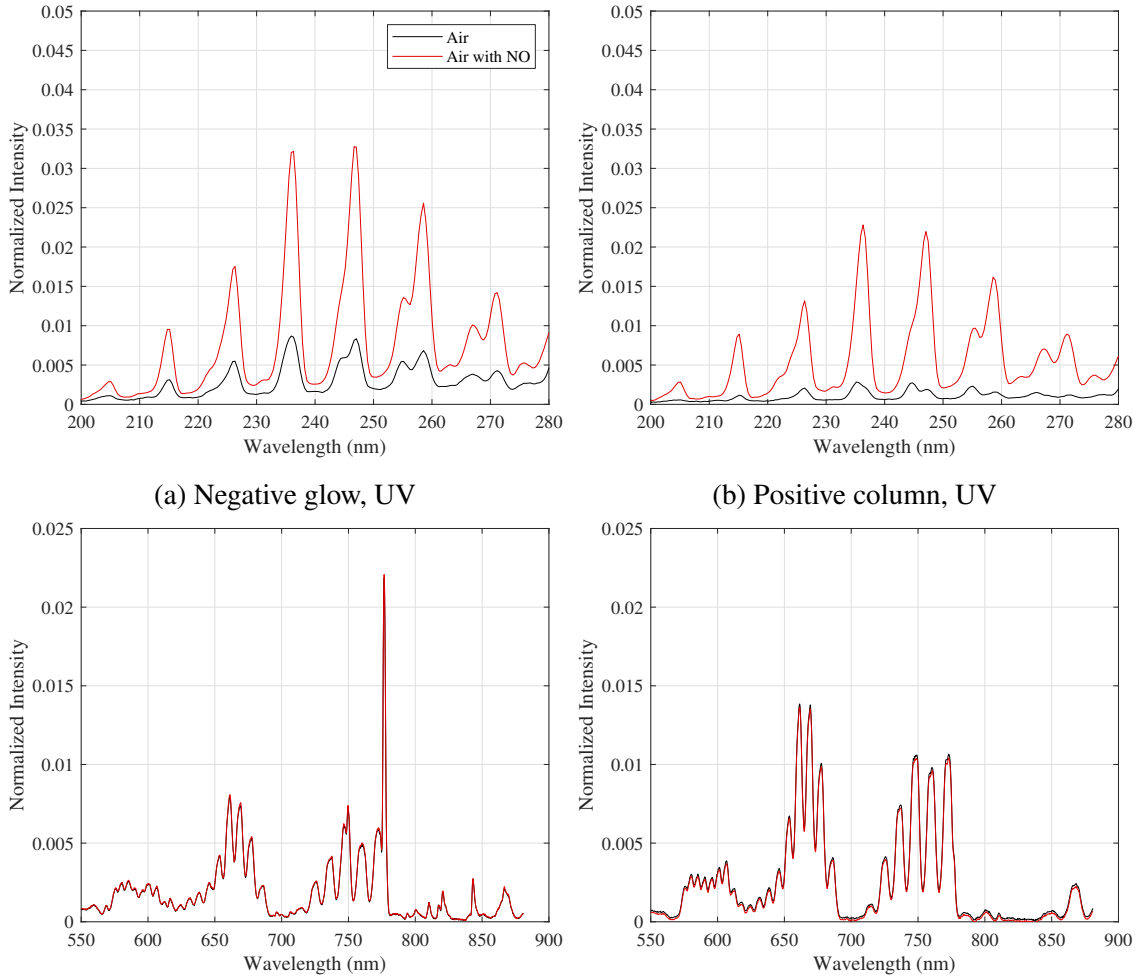

(a) Negative glow, UV

(b) Positive column, UV

(c) Negative glow, Vis-IR

(d) Positive column, Vis-IR

Figure 7.66: Comparison between spectra of air and air mixed with *NO*.

arising from the short lifetime of the upper state of the transition, but can often be neglected [86]; it was not even included as a correction in N2SPECFIT. Doppler broadening arises as gas molecules move towards and away from the detector, shifting their frequencies relative to the observer; Ellis et al. [86] write that this is perhaps the most common broadening mechanism, and it is especially pervasive in UV spectroscopy. For gases in thermal equilibrium this will manifest as a one-dimensional Maxwellian-Bolztmann distribution and could be included in the simulation with an assumed Gaussian profile shape [113]. Like lifetime broadening, collisions between the gas or the wall which depopulate states add to the overall uncertainty of the measurement and

produce so-called pressure broadening; this is often accounted for by assuming a Lorenztian profile [215]. N2SPECFIT allowed the use of either a triangular, Gaussian, or "pseudoVoigt" profile, the lattermost being a convolution of the Gaussian and Lorenztian profiles which the user could adjust to capture their system's unique physics. Ultimately the best results were found with the a purely Gaussian instrument lineshape function with the Spex spectrograph's 0.0776nm FWHM resolution.

Figure 7.67 shows the detailed view of the $(v',v'') = (0,2)$, $(1,3)$, $(2,4)$, $(3,5)$ vibrational bands of the second positive system (in order of decreasing wavelength). Because this data was taken in the negative glow, some rotational lines from the $(v',v'') = (0,0)$ band of the first negative system were visible; as expected, these were absent in positive column data. The cause of the bumps slightly to the right of each of the vibrational bands was unknown, but these regions were cut from the temperature fitting and are therefore of minor importance to the main objectives.

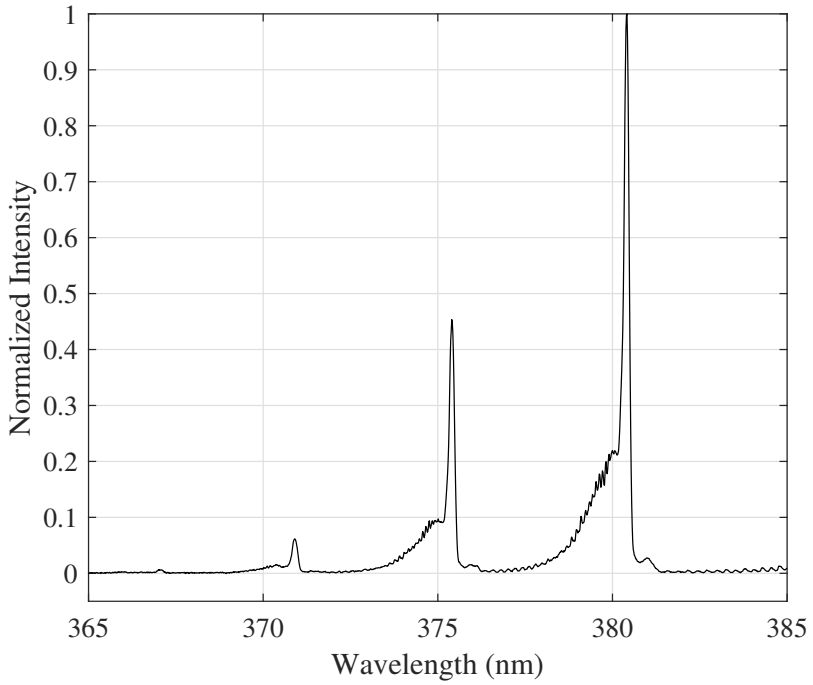

Figure 7.67: Full view of rotationally resolved spectra. Data taken from the "Negative Glow", "Turbulent" run. Data normalized by each run's maximum intensity in full spectra.

The temperature fitting results are shown in Figure 7.68 and quantified in Table 7.24. While there were some offshoots at high wavelengths and the undershoots at lower wavelengths, overall in each case the fit was strong. That being said, the fits produced a spread with no discernible pattern between $315-340$K. While N2SPECFIT did provide some uncertainty, the differences between the temperatures exceeded this margin. That the "Laminar" and "Turbulent" runs yielded different results for the same region despite any notable difference in the broadband spectra reviewed above suggested the variation was indeed due to different convergence conditions in the software. Other possible sources of error could include vibration in the plate (though the diameter of the collimating lens should have been large enough to capture the entire plasma regardless of any such movement), poor estimation of the spectrometer's resolution, or slight differences in the tunnel's conditions between runs. The lattermost idea could be probed with repeated testing at the same condition. For the fidelity of this report, however, estimating the bulk temperature of a glow discharge through a sheath, boundary layer, entropy layer, and wake, it is enough to say the plasma was approximately 330 ± 15K. Put more practically and qualitatively, the bulk of the plasma is likely to be on the order of the temperature of the hot wall and therefore is unlikely to produce a strong thermal perturbation.

Run	**Temperature (K)**	χ^2_{Red}	**Dark current offset (normalized intensity)**	**Wavescale shift (nm)**
4930	328.3 ± 2.17	2.106	$0.371 \times 10^{-2} \pm 0.185 \times 10^{-3}$	$0.499 \times 10^{-1} \pm 0.581 \times 10^{-3}$
4929	330.9 ± 1.92	2.791	$0.244 \times 10^{-2} \pm 0.153 \times 10^{-3}$	$0.491 \times 10^{-1} \pm 0.517 \times 10^{-3}$
4935	313.8 ± 1.97	2.180	$0.333 \times 10^{-2} \pm 0.164 \times 10^{-3}$	$0.500 \times 10^{-1} \pm 0.579 \times 10^{-3}$
4928	341.6 ± 2.18	2.331	$0.234 \times 10^{-2} \pm 0.176 \times 10^{-3}$	$0.549 \times 10^{-1} \pm 0.531 \times 10^{-3}$

Table 7.24: OES temperature fitting results.

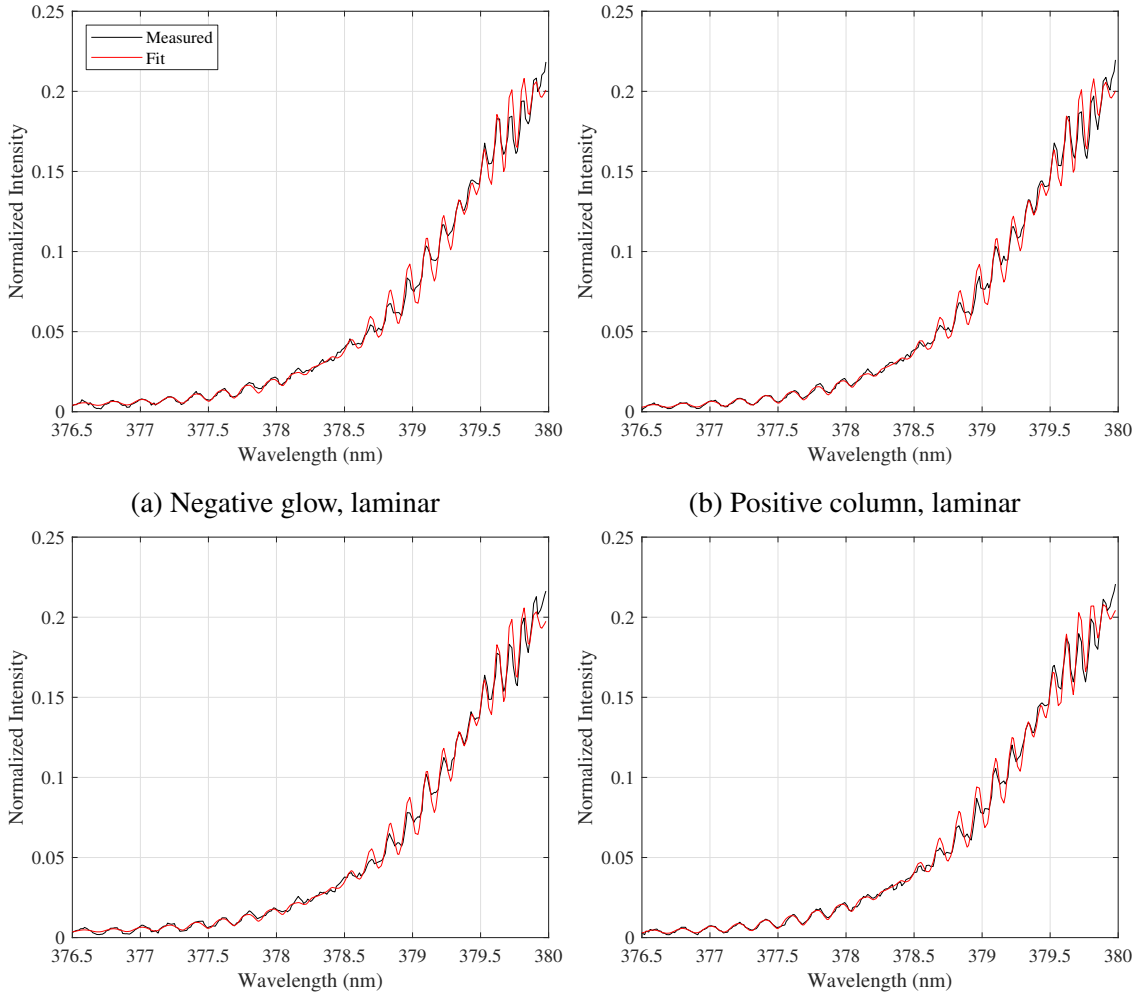

(a) Negative glow, laminar

(b) Positive column, laminar

(c) Negative glow, turbulent

(d) Positive column, turbulent

Figure 7.68: Ro-translational temperature fits of rotationally resolved $(v', v'') = (0, 2)$ band. Data normalized by each run's maximum intensity in full spectra.

7.4.2 PLIF Results

The results of the three PLIF campaigns are split into individual sections below corresponding to the rotational thermometry, vibrational thermometry, velocimenty, and spanwise velocimetry; flow visualization is discussed throughout, but especially in the rotational thermometry and spanwise velocimetry sections. The implementation, development, and analysis of these techniques and their corresponding data was the sole focus of Buen's [49] doctoral research, and as such a more detailed discussion is found therein. The goal here was an interpretation of the results in

the context of turbulent boundary layers, especially as the data informed the above theories and techniques. Of special interest was the off-body measurement of fundamental variables (*i.e.*- u and T) and their fluctuations, as well as the NEQ measurements of T_{NO}^{vib} along the test article.

7.4.2.1 Rotational Thermometry

The rotational thermometry campaign measured the thermal boundary layer as it developed along the plate. Measurement of this profile was useful in its own right, but its impact was multiplied owing to the necessity of temperature when calculating other variables such as density and viscosity. Of special interest was the measurement of the temperature just downstream of the glow discharge; the sensitivity of PLIF thermometry and its immunity to electromagnetic interference made it uniquely suited to this task. Additionally, because planar (sheet width $\sim 800\mu$m [49]) measurements were made, the raw data acted as spatially resolved flow visualization. The test matrix for this campaign is shown in Table 7.25, and the corresponding plasma conditions in Table 7.26 and Figure 7.69.

No.	Location	Trips	Plasma	Run/Date
1	Forward, wake	Laminar	Off	4608, 1/14/2021
2	Forward, wake	Turbulent	Off	4610, 1/16/2021
3	Forward, trough	Turbulent	Off	4615, 1/19/2021
4	Forward	Laminar	On	4609, 1/15/2021
5	Forward, wake	Turbulent	On	4613, 1/18/2021
6	Forward, trough	Turbulent	On	4614, 1/18/2021
7	Back, wake	Laminar	Off	4621, 1/22/2021
8	Back, wake	Turbulent	Off	4616, 1/19/2021
9	Back, trough	Turbulent	Off	4619, 1/21/2021
10	Back, wake	Laminar	On	4620, 1/21/2021
11	Back, wake	Turbulent	On	4617, 1/20/2021
12	Back, trough	Turbulent	On	4618, 1/20/2021

Table 7.25: PLIF rotational thermometry test matrix.

For each case instantaneous and mean "Hot" images are shown for flow visualization, rotated and cropped but otherwise just as they appeared out of the ICCDs. The corresponding instanta-

No.	Current (mA)	Power Supply Voltage (V)	Power Supply Power (W)	Plasma Voltage (V)	Plasma Power (W)
4	94.1	1430	134.6	486.5	45.8
5	95.0	1434	136.3	481.0	45.7
6	95.0	1432	136.1	478.7	45.5
10	95.2	1446	137.7	490.9	46.7
11	94.9	1430	135.8	478.3	45.4
12	94.9	1432	135.8	479.9	45.5
Average					
	94.9	1434.1	136.0	482.6	45.8

Table 7.26: Plasma conditions for PLIF rotational thermometry campaign.

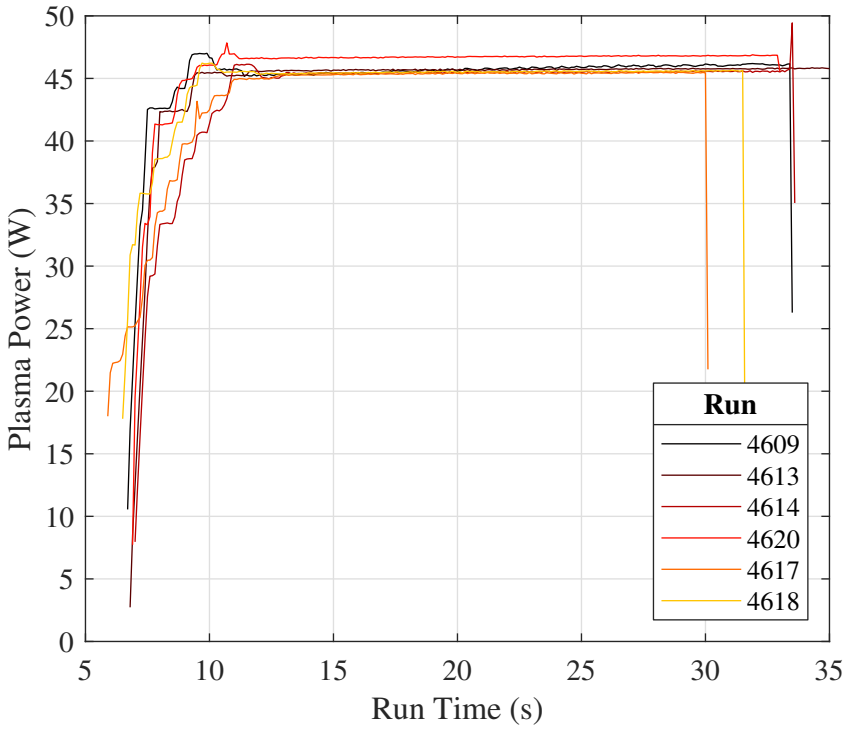

Figure 7.69: Plasma power traces for PLIF rotational thermometry runs.

neous and mean temperature maps were also provided next, as well as the mean (RMS) fluctuations and uncertainty maps. Gaps in the instantaneous temperature due to low signal or nonphysical results were filled with black space. The RMS of the fluctuations $T' = T - \overline{T}$ was provided because the mean of the Reynolds averaged data should be, and in fact was, zero. The calculation of un-

certainty is described in [49]. All of these data are contained in Figures 7.71-7.82, but they are succinctly summarized in Figure 7.70, which collapses the 2D maps into boundary layer profiles and compares the effect of plasma and location; here the fluctuation profile is the average of the RMS along the streamwise direction.

It is noted that the error bars on the mean temperature and fluctuation profiles in Figure 7.70 were not calculated from the 2D uncertainty image for the corresponding run (Figures 7.71-7.82(f)). Instead, new uncertainties were calculated when the mean temperature (d) and fluctuation (e) 2D maps were horizontally averaged to produce the boundary layer profiles. While this greatly simplified the calculation of the error bars, it meant effectively taking and "average of an average", which Buen [49] stated led to a conservative estimation of the total error. More formally, the results from each row of pixels in each frame of a run should have been used as this would yield a more complete representation of the statistics, but such rigor was taken in neither [49] nor here.

The condensed data in Figure 7.70 answers several general questions. Perhaps the clearest is the plasma's inefficacy in perturbing the boundary layer, either its temperature or its fluctuations. Recall from Section 2.3.5 that in the work of [95], a strong RF plasma increased the vibrational temperature of N_2, which then relaxed via H_2O to increase the bulk ro-translational temperature of the air, increasing its viscosity, and thereby reducing the turbulent fluctuations. Be it due to the weaker plasma used, the absence of water in the dry air air supply, or large mean free path in the ACE test section, this process was not appreciably replicated here. In nearly all cases, the the plasma "Off" and "On" cases fell within one another's uncertainties. Even at the wall, where there should have been some collisional quenching of the vibrationally excited N_2, any change was well within the uncertainty limits. There was a delicate balance between sizing the plasma to instill NEQ and thermally perturbing the flow, and a more conservative power supply was used to aim for the former, rather than the later as the goal of this work was to study NEQ, not flow control. The spectroscopic measurements in Section 7.4.1 confirmed N_2 was indeed being excited, so either an insufficient amount of it existed to meaningfully heat the boundary layer, or it remained frozen; given the calculations in [116], Buen [49], and Chapter 8 the latter case was more probable.

The boundary layer growth was clearest in the turbulent flows, and indeed there was little difference between the wake and trough cases, at least as viewed from these averaged profiles. While this was expected in the more isotropic downstream location, it did confirm that the trip's vortices were indeed breaking down even by this upstream location (see Section 7.3.1). In these cases, the fluctuation profiles provided the clearest demarcation of the boundary layer's edge as the temperature profiles tended to rise slowly but consistently well above the expected edge. This result, $\sim$ 12.5mm, agrees well with the other off body diagnostics available, schlieren imaging, CFD, and Pitot pressure. While the uncertainty in the fluctuation profiles increased considerably near the wall, approaching 50% in places, it was encouraging to see the general shape of the turbulent fluctuation profiles peak near the middle of the boundary layer then fall back towards the wall as they passed from the overlap region into the laminar sublayer; Buen [49] attributed the high uncertainty in this region to low signal and surface reflections.

The lack of growth of the laminar thermal boundary layer was initially surprising, until one recalls the presence of the entropy layer seen in the schlieren data in Section 7.3.2. It sat $\sim$ 5mm above the surface all along the length test article. Here it acted to mask the laminar flow's thermal boundary layer. That the laminar cases' fluctuations matched the tripped cases' at the "Front" test location abetted the claim the flow was still transitioning and was not fully turbulent; the clearest difference between the laminar and tripped cases at this location would be that the temperature and fluctuation profiles for the tripped boundary layers were slightly thinner.

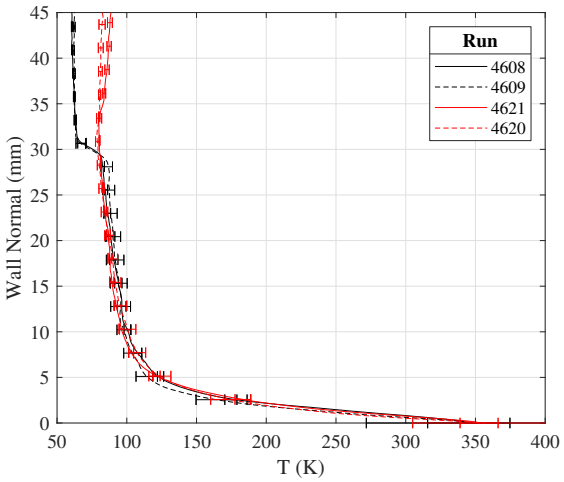

(a) Laminar, temperature

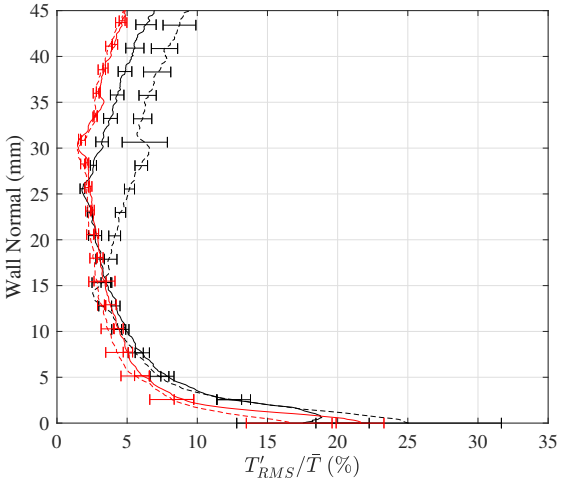

(b) Laminar, fluctuation

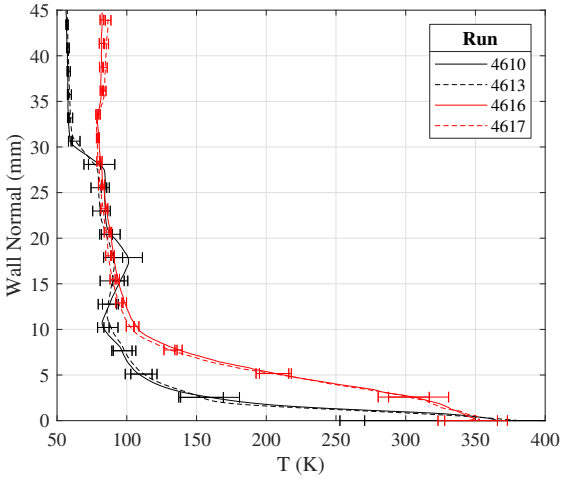

(c) Turbulent wake, temperature

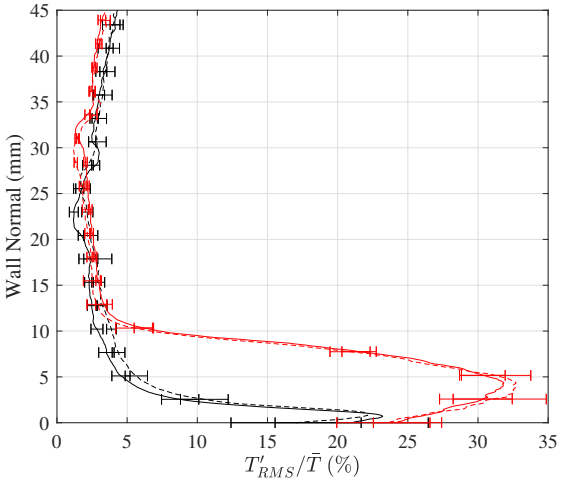

(d) Turbulent wake, fluctuation

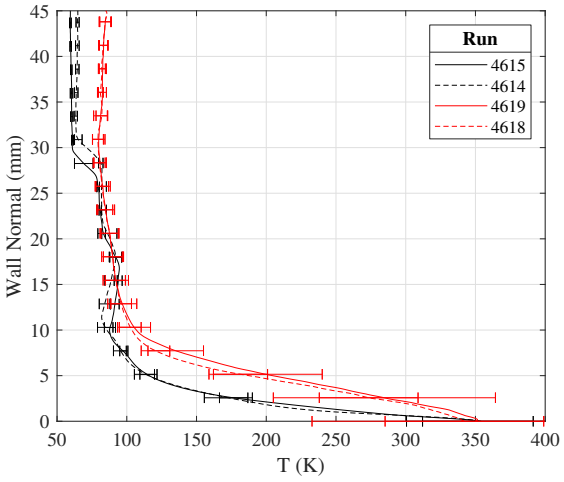

(e) Turbulent trough, temperature

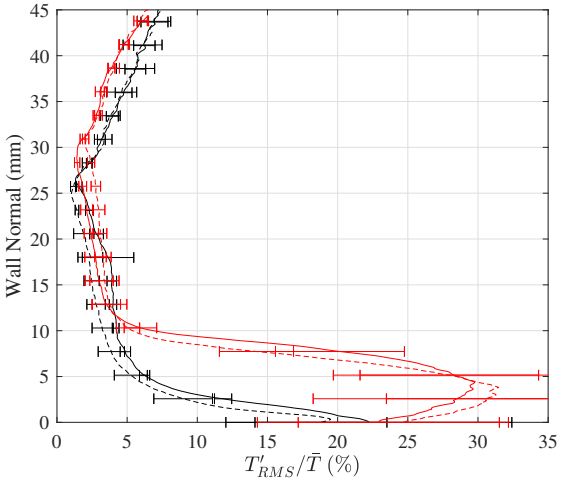

(f) Turbulent trough, fluctuation

Figure 7.70: PLIF rotational thermometry: temperature and fluctuation profile comparison; error bars were set from the corresponding mean temperature and fluctuation images. Same legend applies to all figures in a row.

The raw fluorescence images and temperature maps provide greater context for the behavior studied in the above profiles. The simplest case with which to start would be the laminar flow in the upstream test location. Here the mean fluorescence image shows the strong rise in signal across the bow shock, as well as the presence of weaker Mach waves stemming from slight steps at the interface of the PEEK insert, electrodes, trip insert, and window. The large rise in signal from the bow shock stemmed from the increase in both pressure, temperature, and density it produced. For an idealized flow at $M = 5.7$ and $\delta = 2.75°$, $P_2/P_1 = 1.458$ and $T_2/T_1 = 1.115$ and $\rho_2/\rho_1 = 1.307$ [128]. This improved signal led Buen [49] to use the post-shock region as the known calibration temperature in the thermometry calculations. They adjusted this temperature until the pre-shock temperature was 58K; as a check, under these conditions the wall temperature approached the 360K measured on the glass with a thermocouple, at least with the measurement uncertainty. What remained unclear, however, was why the temperature jump across the shock went from ~ 64 (accounting for the slight rise in the freestream) to ~ 82K, or $T_2/T_1 = 1.281$. Moreover, that the temperature rose at all above the shock was unexpected. The best theories at present include nonuniform gas seeding leading to the formation of nascent N_xO_y species, NO dimer breakup across the shock, and shock curvature causing deviation from the ideal 11.95°. Buen [49] extensively explored the first two cases and found they could be meaningful, and a rough measurement from Figure 7.71(b) yielded a shock angle of $\sim 12.5°$ ($T_2/T_1 = 1.149$), so a convolution of all effects was likely. Buen [49] also attributed the steady rise in temperature moving towards but above the boundary layer to the series of weak Mach waves and the local minimum in the laminar fluctuation profiles in the upstream location to the location of the calibration region. Finally, O'Byrne et al. [208] reminds readers that horizontally averaging an angled shock causes its temperature jump to spread and appear continuous.

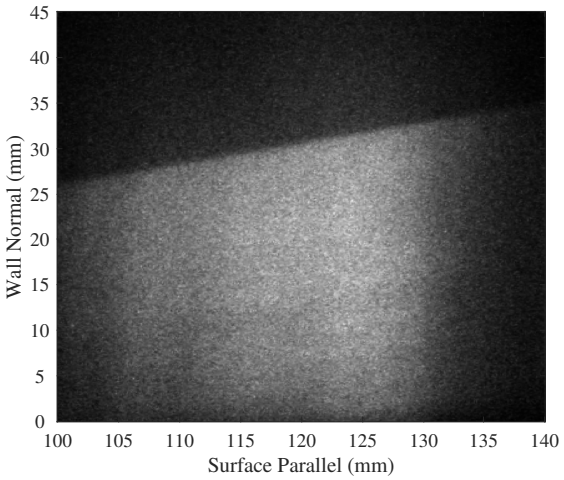

(a) Instantaneous "hot" image

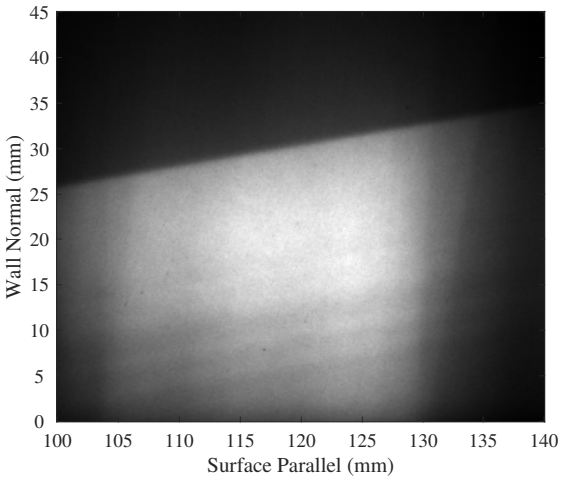

(b) Mean "hot" image

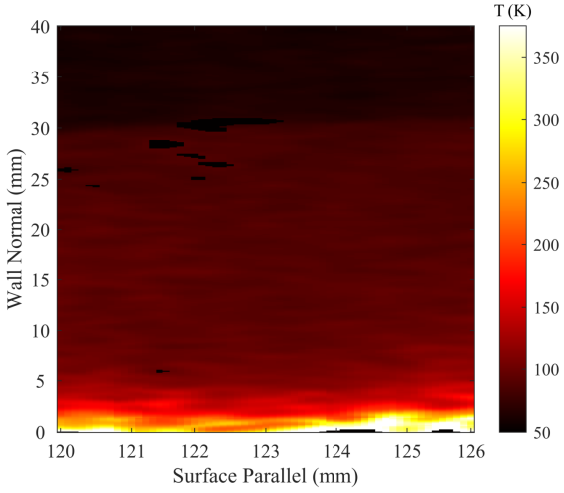

(c) Instantaneous temperature map

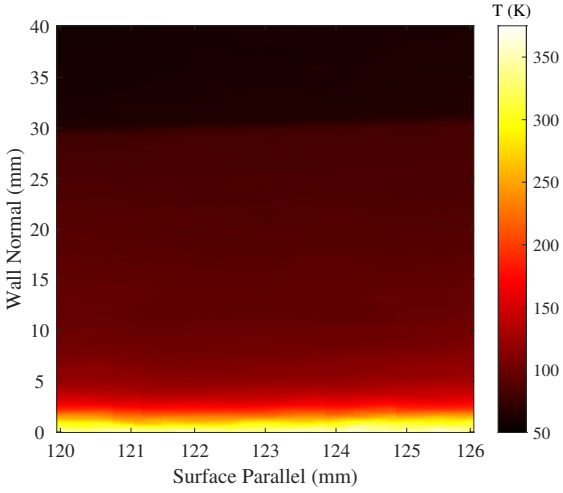

(d) Mean temperature map

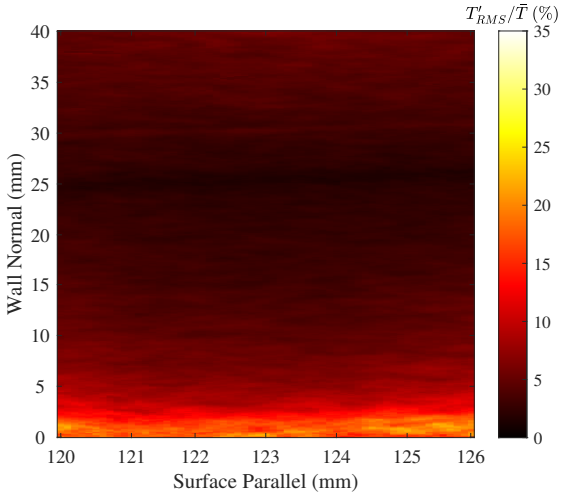

(e) Mean fluctuation map

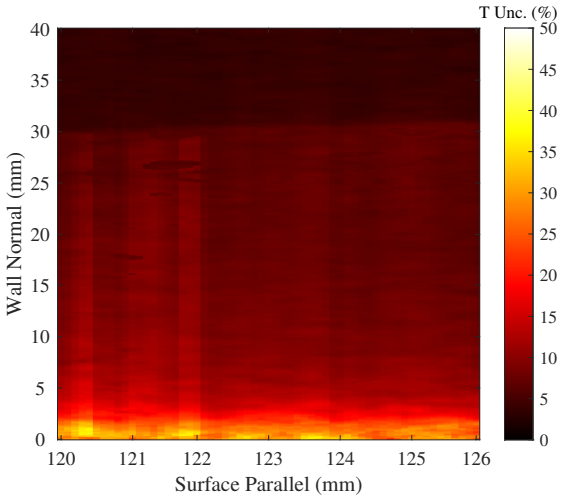

(f) Mean uncertainty map

Figure 7.71: PLIF rotational thermometry, Run 4608: upstream; laminar; plasma off.

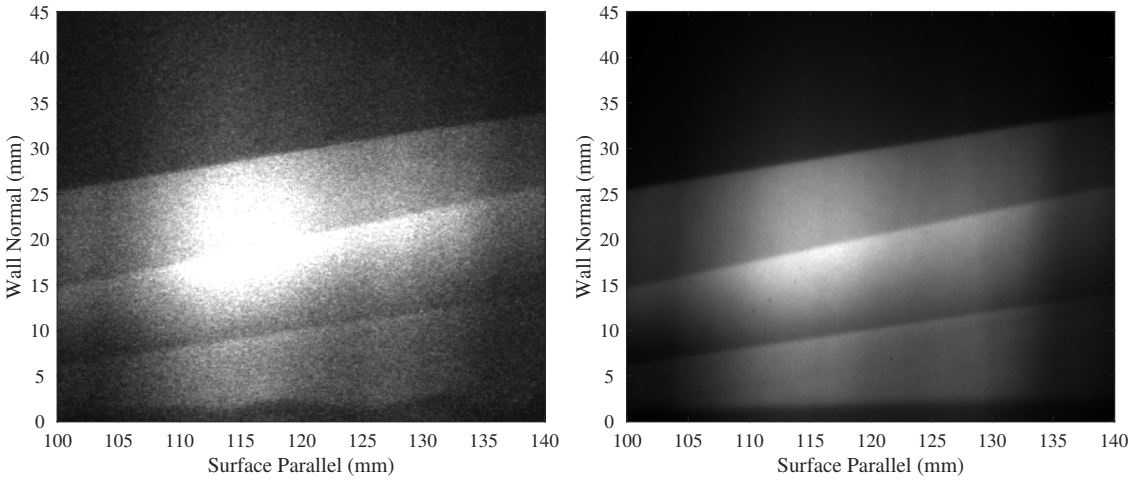

(a) Instantaneous "hot" image

(b) Mean "hot" image

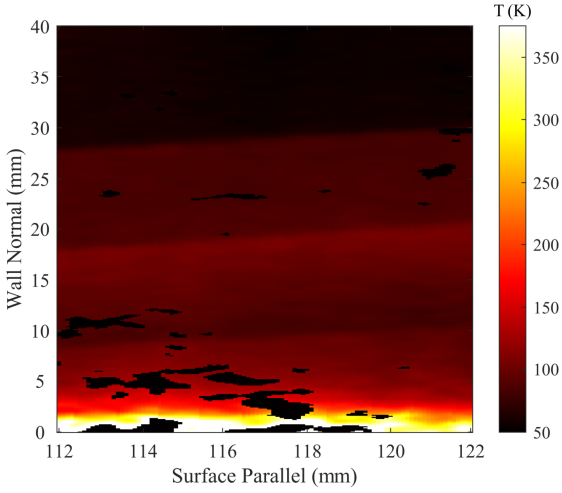

(c) Instantaneous temperature map

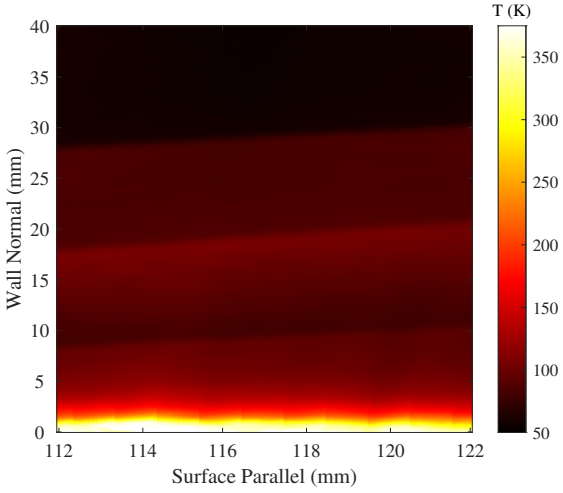

(d) Mean temperature map

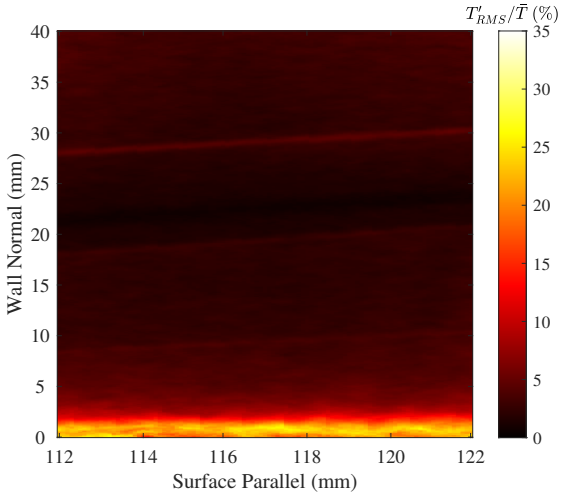

(e) Mean fluctuation map

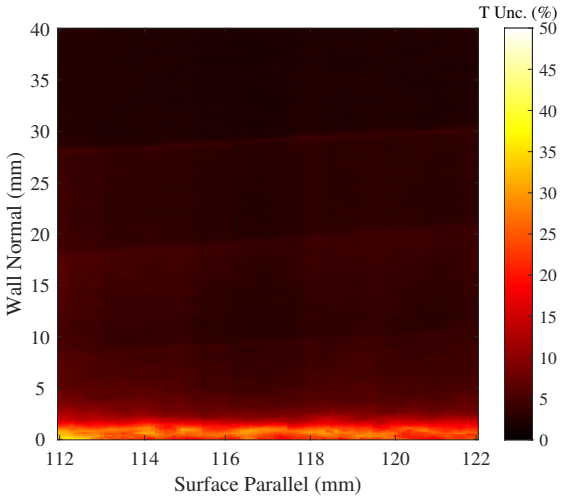

(f) Mean uncertainty map

Figure 7.72: PLIF rotational thermometry, Run 4610: upstream; turbulent wake; plasma off.

The insertion of the trips added a separation/reattachment shock below the bow shock, followed by a shear layer formed by the counter-rotating vortices exchanging slow, hot surface air with fast, cool edge air [243]; this complex shock structure is shown with better optical access with the schlieren data in Section 7.3.2. These physics tended to obscure the Mach waves, but they were indeed present, most visibly in the average turbulent trough fluorescence images, Figures 7.73 and 7.76. Of particular interest was the decrease in temperature downstream of the separation/reattachment shock. Buen [49] follows O'Byrne et al. [208], who used PLIF thermometry to study laminar flow on a flat plate and attributed the fall in temperature between the bow shock and wall to expansion as the flow turned from the shock to follow the wall. Still, one would have expected the vortices to have spread the perceived thermal boundary layer as they exchanged hot and cold gas from the wall and edge, but evidently this did not occur; that being said, this process may be at least partially responsible for the lack of Mach waves in the "Wake" case.

Much of the same behavior was observed in the upstream "Trough" data, though as Buen [49] notes the temperature jumps across the shocks were less severe. That there were even shocks at all is important, because it showed that the trips did not act individually and instead merged together to create a single, albeit complex, shock structure along their entire surface. Only a spatially-resolved flow visualization technique could have produced this finding. It was also interesting to observe the presence of regular, wave-like structures in the instantaneous wake images, Figures 7.73 and 7.73. These were a clear indication of the singular behavior of the trips as they were absent in the trough images, and that they appeared regular showed again that the flow was transitioning and not yet fully turbulent. Nevertheless, they appeared to have little tangible impact on the temperature because, as was mentioned above, there was little difference between the mean temperature and fluctuation images. Finally, that the signal dropped so low near the wall, even for these "Hot" images, reinforced the challenge of near-wall PLIF measurements.

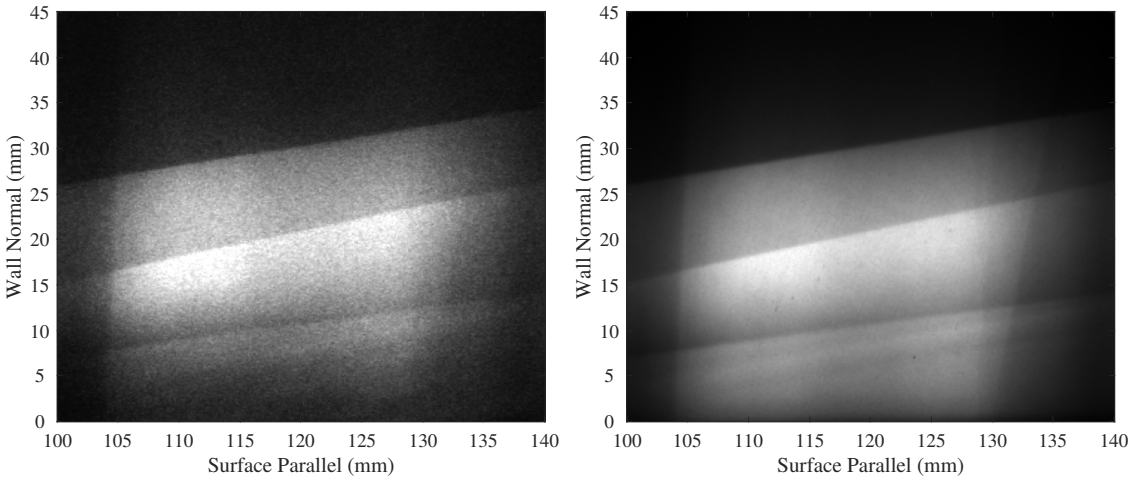

(a) Instantaneous "hot" image

(b) Mean "hot" image

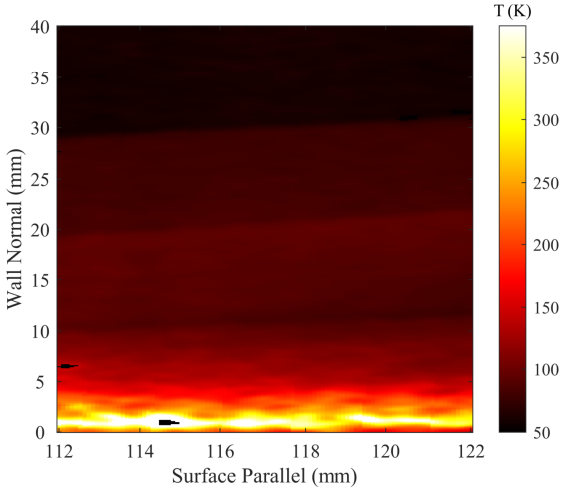

(c) Instantaneous temperature map

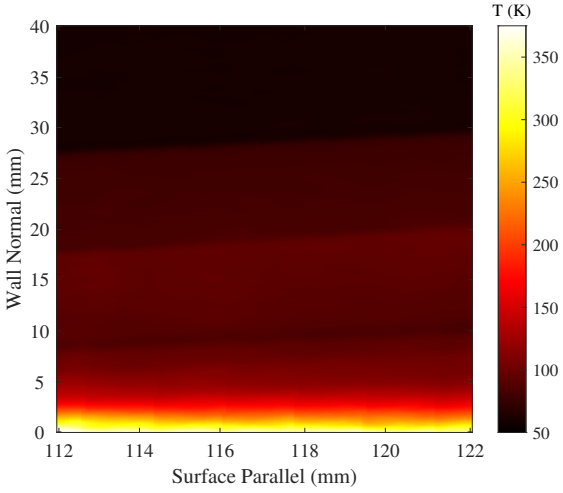

(d) Mean temperature map

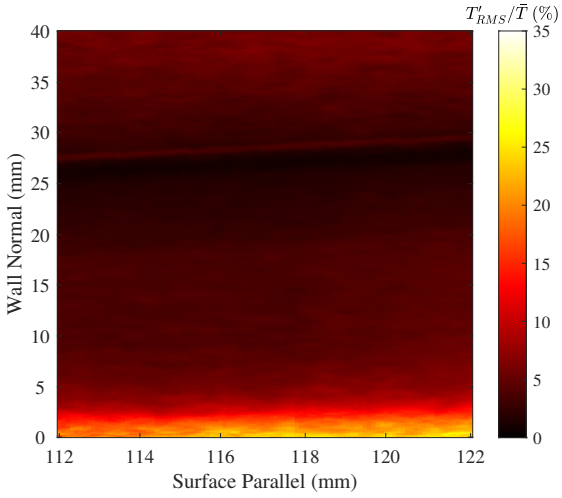

(e) Mean fluctuation map

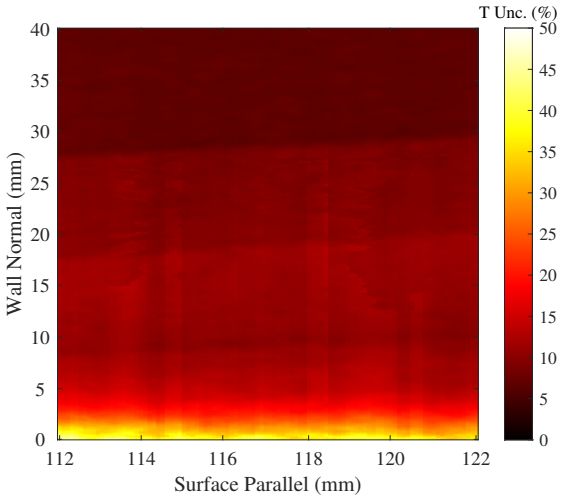

(f) Mean uncertainty map

Figure 7.73: PLIF rotational thermometry, Run 4615: upstream; turbulent trough; plasma off.

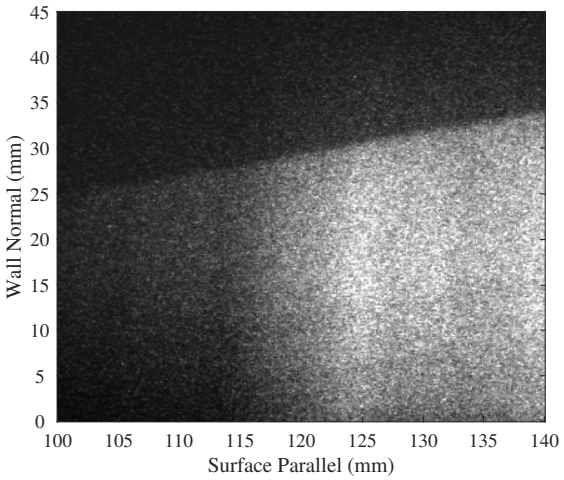

(a) Instantaneous "hot" image

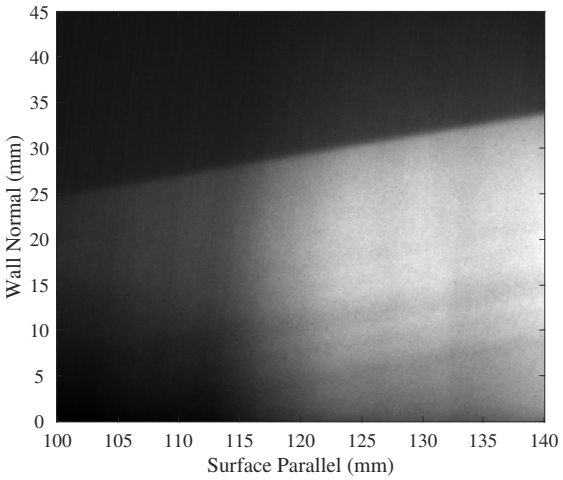

(b) Mean "hot" image

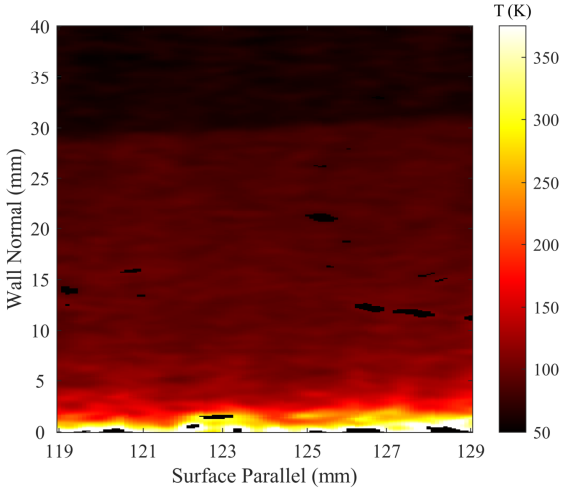

(c) Instantaneous temperature map

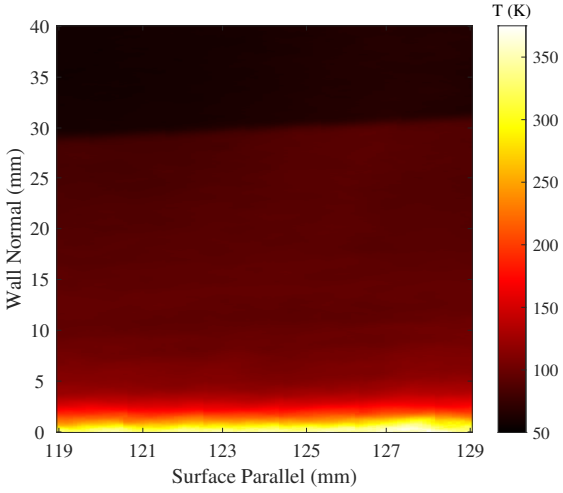

(d) Mean temperature map

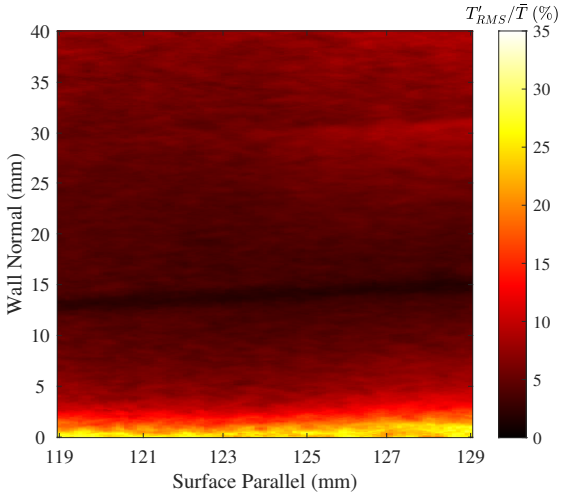

(e) Mean fluctuation map

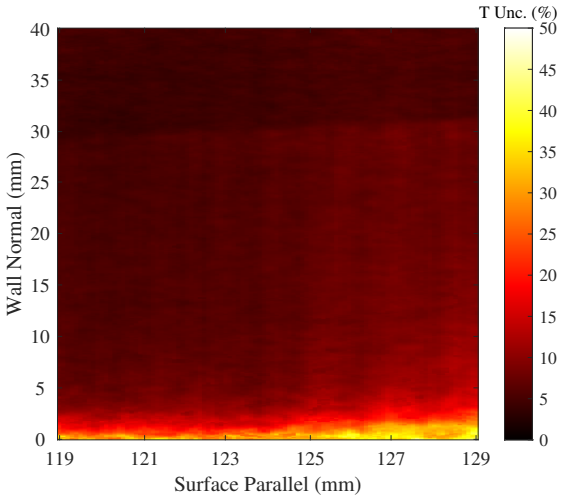

(f) Mean uncertainty map

Figure 7.74: PLIF rotational thermometry, Run 4609: upstream; laminar; plasma on.

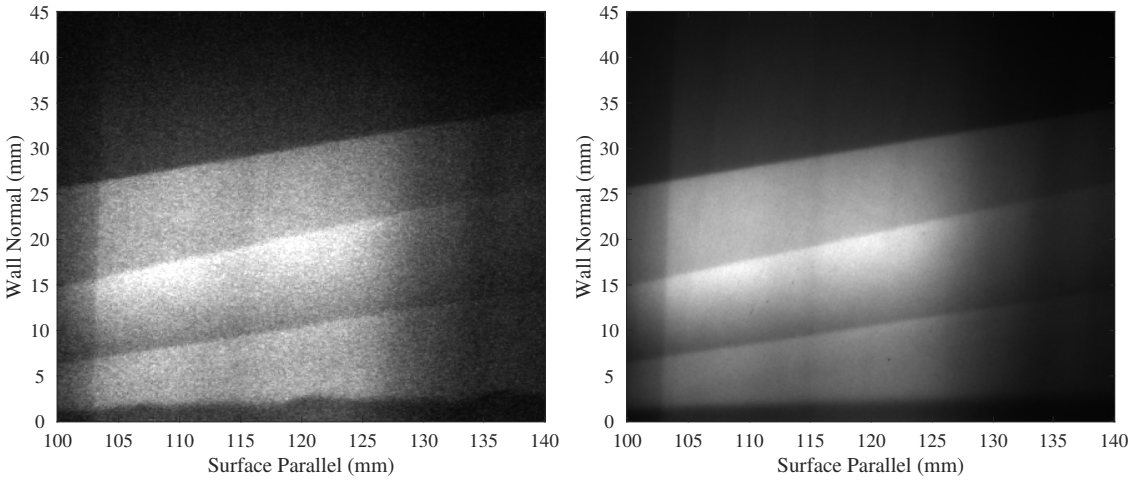

(a) Instantaneous "hot" image

(b) Mean "hot" image

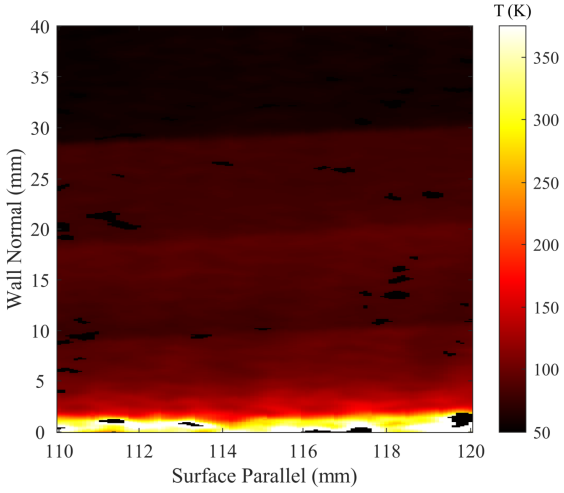

(c) Instantaneous temperature map

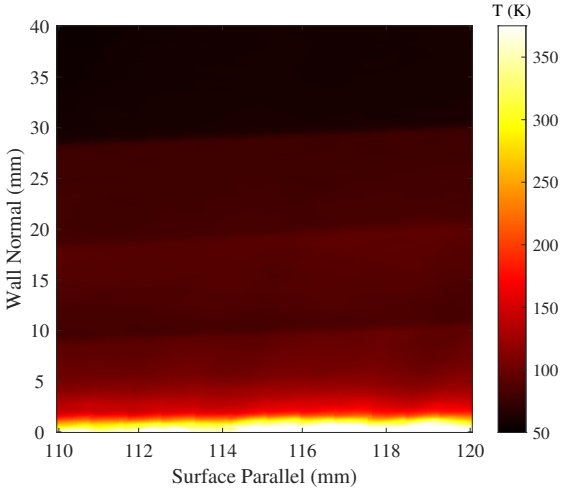

(d) Mean temperature map

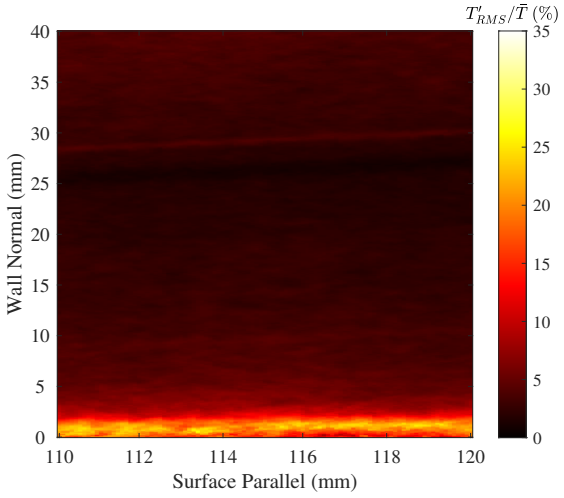

(e) Mean fluctuation map

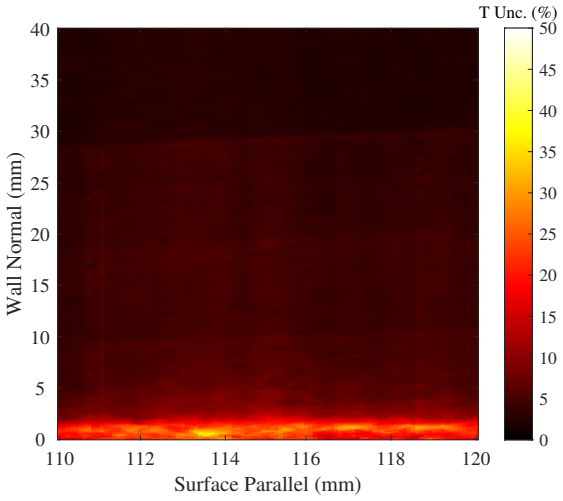

(f) Mean uncertainty map

Figure 7.75: PLIF rotational thermometry, Run 4613: upstream; turbulent wake; plasma on.

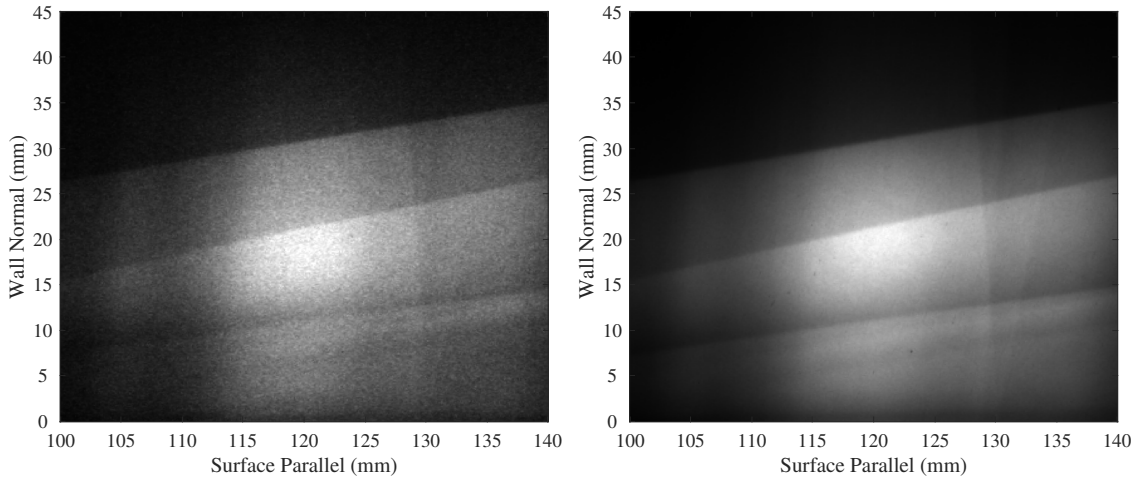

(a) Instantaneous "hot" image

(b) Mean "hot" image

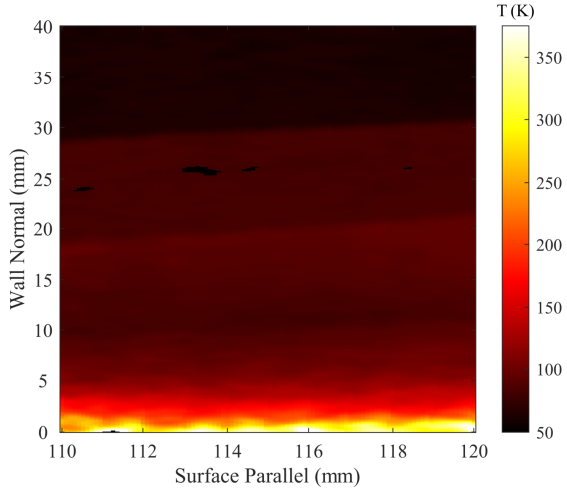

(c) Instantaneous temperature map

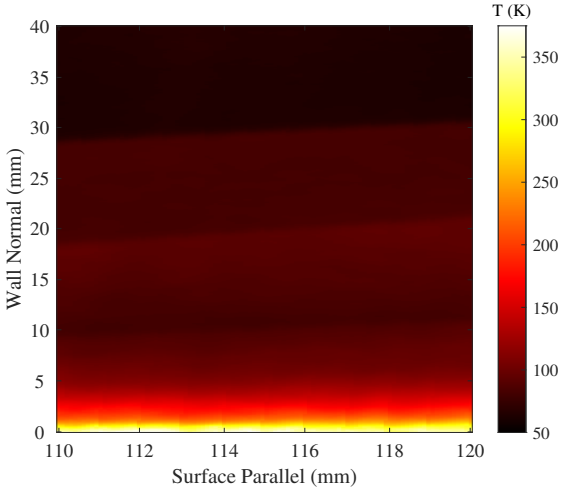

(d) Mean temperature map

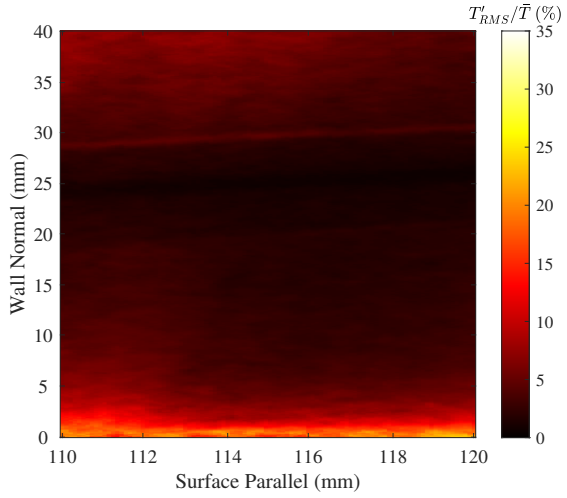

(e) Mean fluctuation map

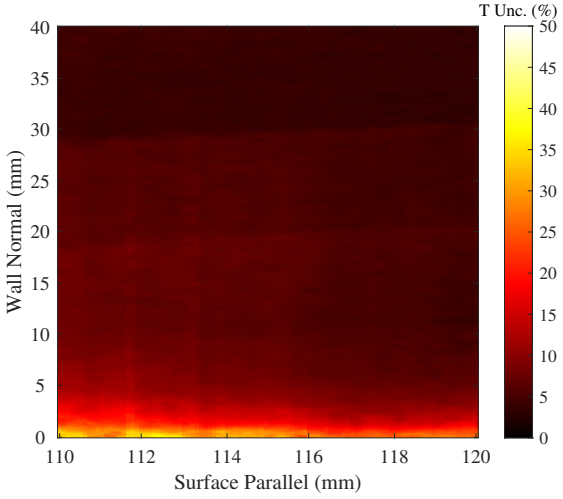

(f) Mean uncertainty map

Figure 7.76: PLIF rotational thermometry, Run 4614: upstream; turbulent trough; plasma on.

The largest change in the downstream test location came from the raw fluorescence images. By this point, the bow and trip shocks were well above the cameras' field of view, making measurement of the freestream temperature impossible. To circumvent this, Buen [49] used the result for the post-bow shock temperature from the upstream cases, 82K, for all downstream analyses; this did not account for the temperature rise across the trip shocks. The known shock from the junction between the ACE tunnel's nozzle and test section was also present; recall that when positioning the test article, great care was taken to avoid this known aberration. Here the temperature did rise slightly, $\sim$ 2K the flow moved across this shock. In the laminar cases, there was no evidence of the entropy layer. Meanwhile, in all turbulent cases, the instantaneous images provided excellent, frozen images of the turbulent boundary layer. The classical elements such as the chaotic appearance, entrained eddies, varying length scales, superlayer, *etc.* were all present [293, 55, 221], and the common appearance between the wake and trough images conveyed the flow's spanwise homogeneity, suggesting it was truly fully developed.

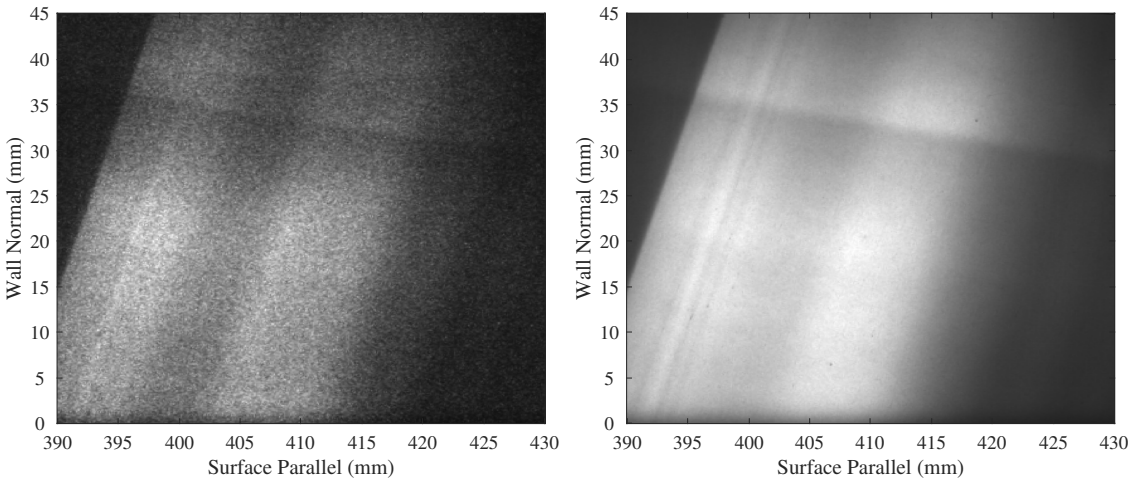

(a) Instantaneous "hot" image

(b) Mean "hot" image

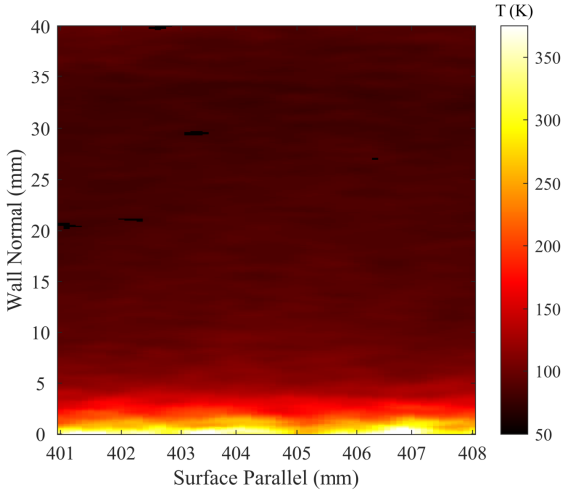

(c) Instantaneous temperature map

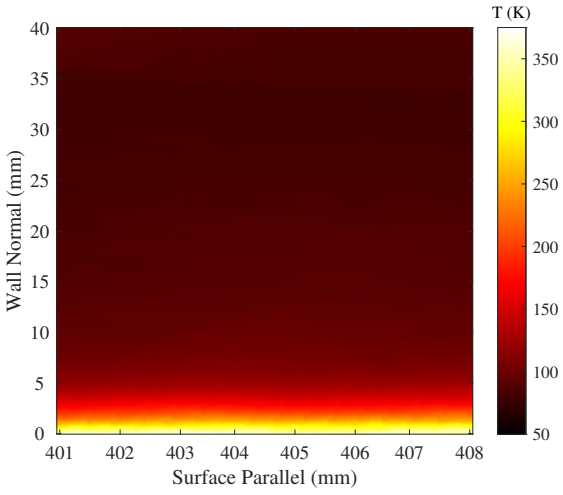

(d) Mean temperature map

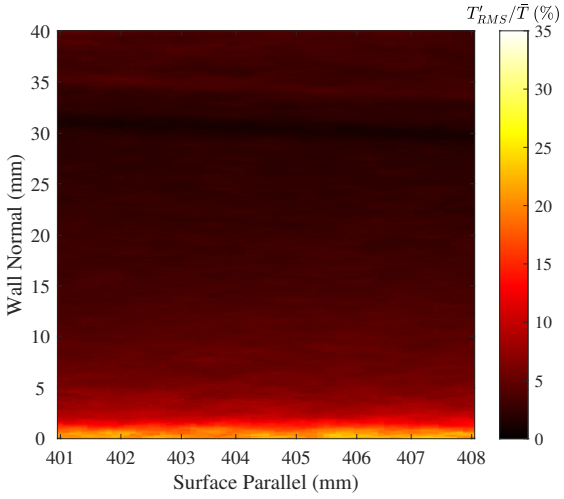

(e) Mean fluctuation map

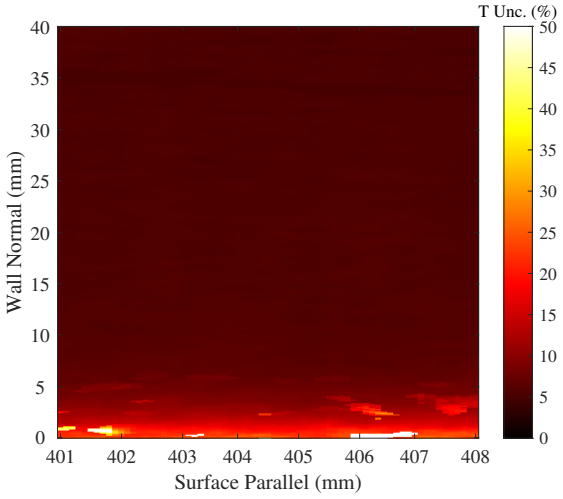

(f) Mean uncertainty map

Figure 7.77: PLIF rotational thermometry, Run 4621: downstream; laminar; plasma off.

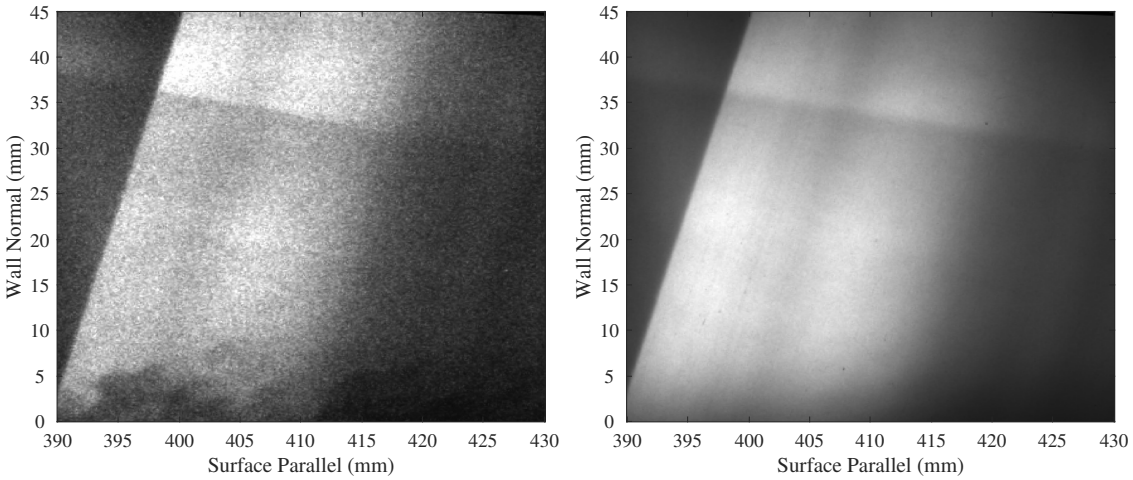

(a) Instantaneous "hot" image

(b) Mean "hot" image

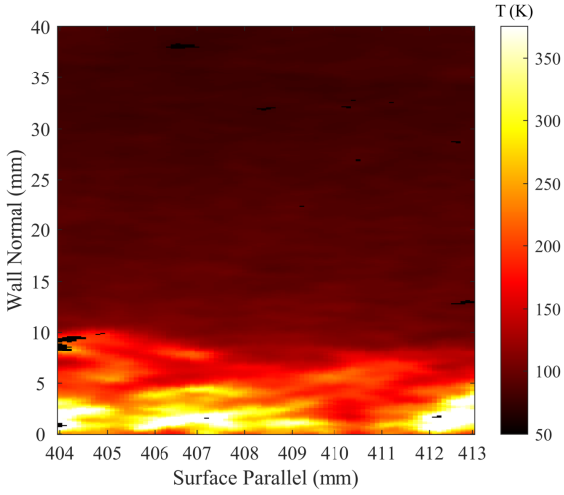

(c) Instantaneous temperature map

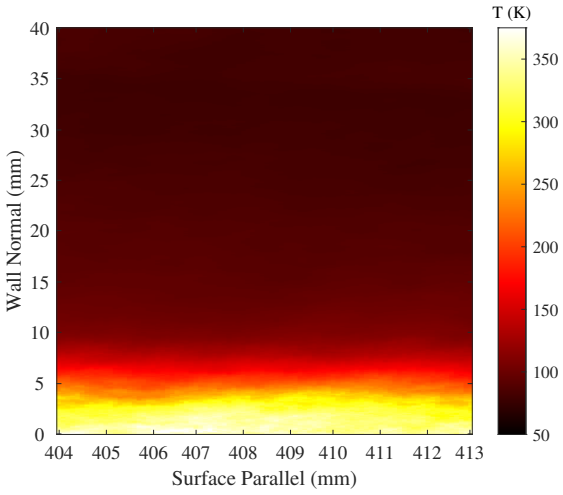

(d) Mean temperature map

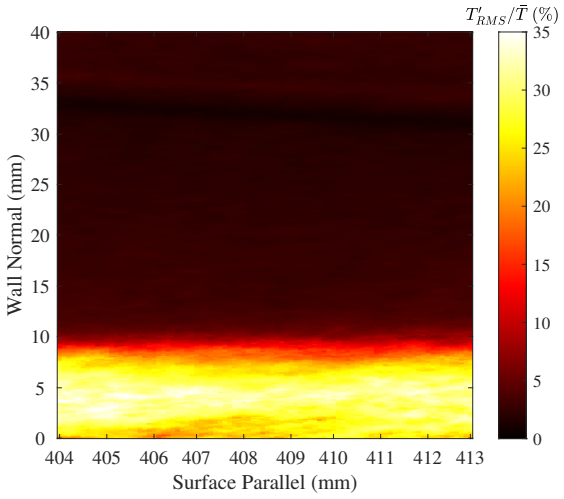

(e) Mean fluctuation map

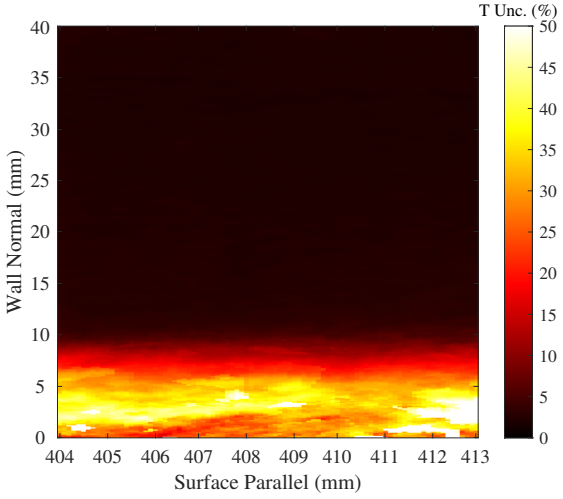

(f) Mean uncertainty map

Figure 7.78: PLIF rotational thermometry, Run 4616: downstream; turbulent wake; plasma off.

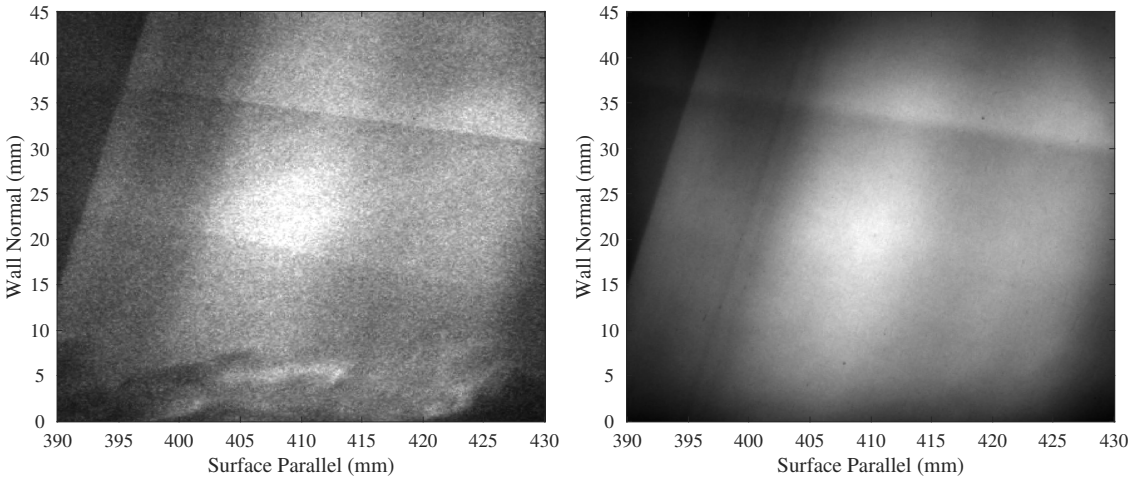

(a) Instantaneous "hot" image

(b) Mean "hot" image

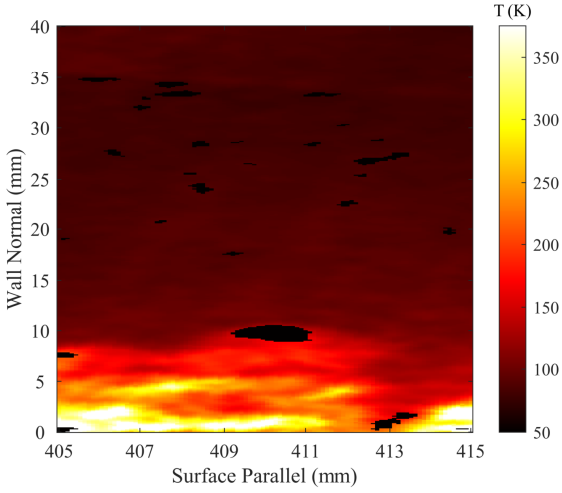

(c) Instantaneous temperature map

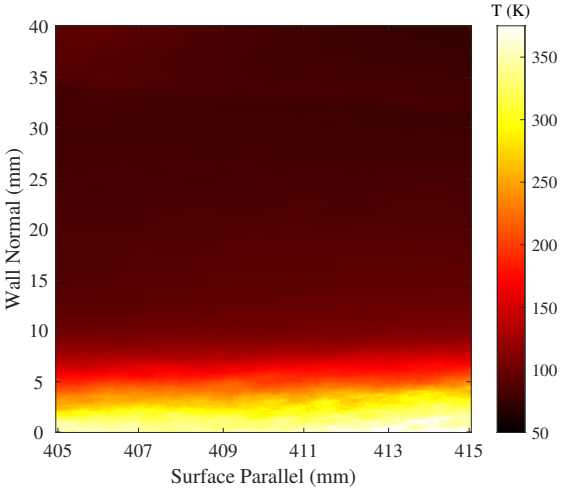

(d) Mean temperature map

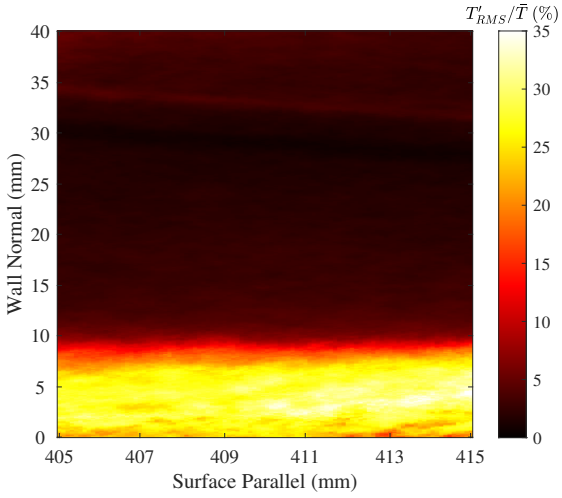

(e) Mean fluctuation map

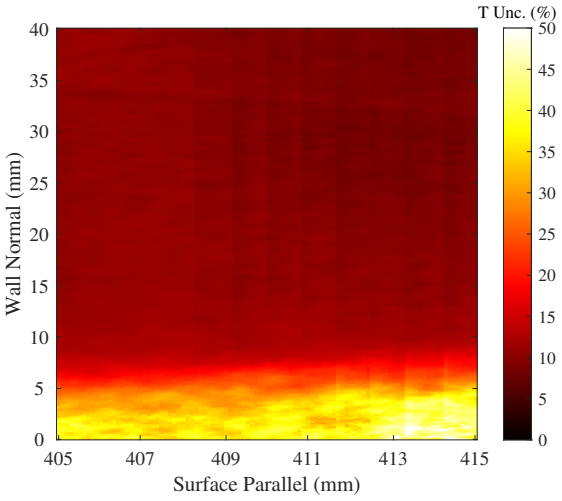

(f) Mean uncertainty map

Figure 7.79: PLIF rotational thermometry, Run 4619: downstream; turbulent trough; plasma off.

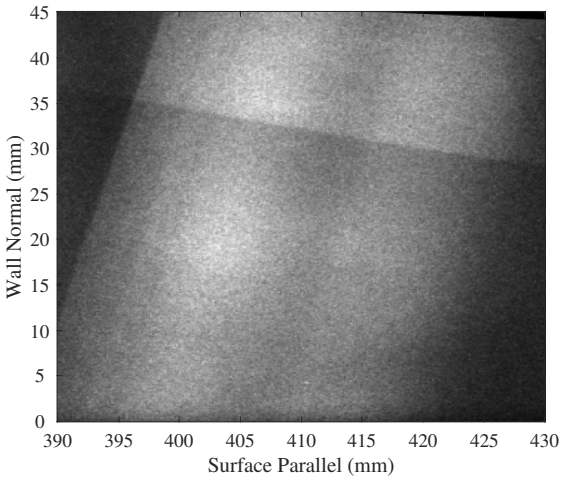

(a) Instantaneous "hot" image

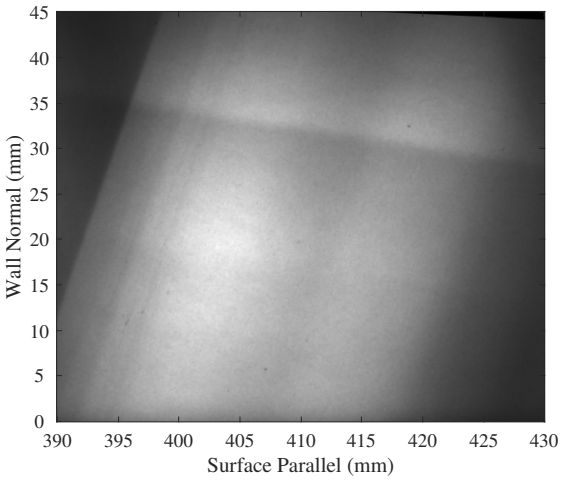

(b) Mean "hot" image

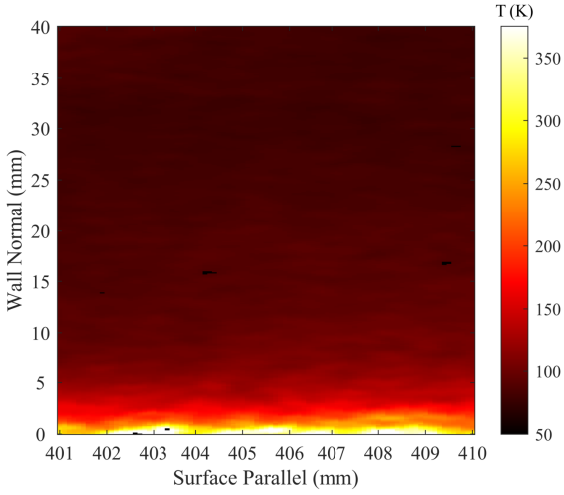

(c) Instantaneous temperature map

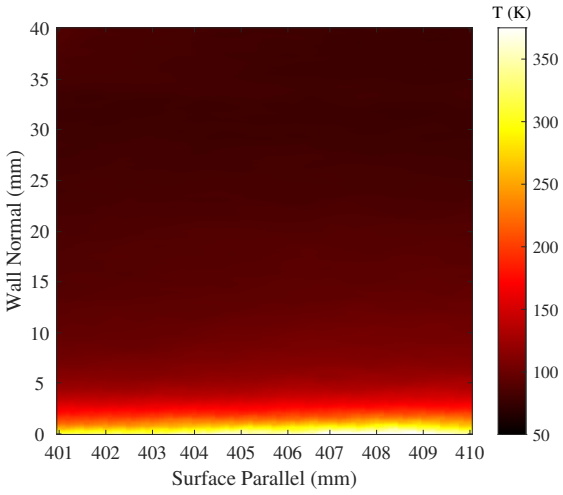

(d) Mean temperature map

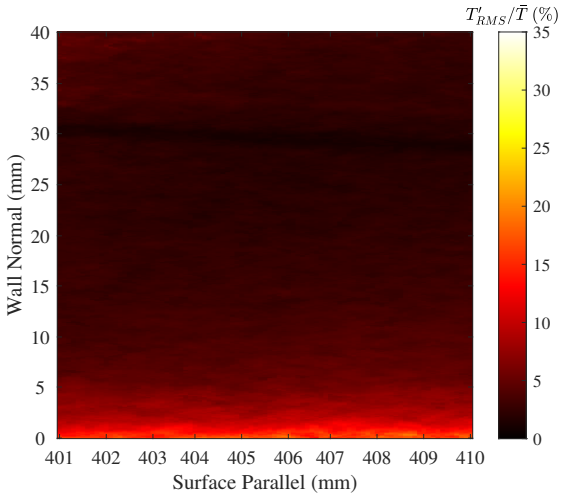

(e) Mean fluctuation map

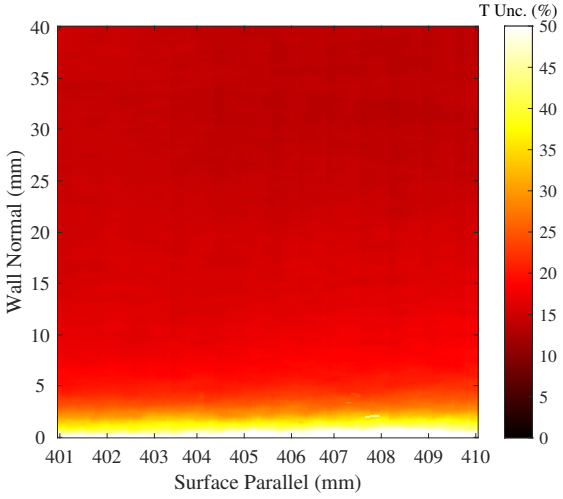

(f) Mean uncertainty map

Figure 7.80: PLIF rotational thermometry, Run 4620: downstream; laminar; plasma on.

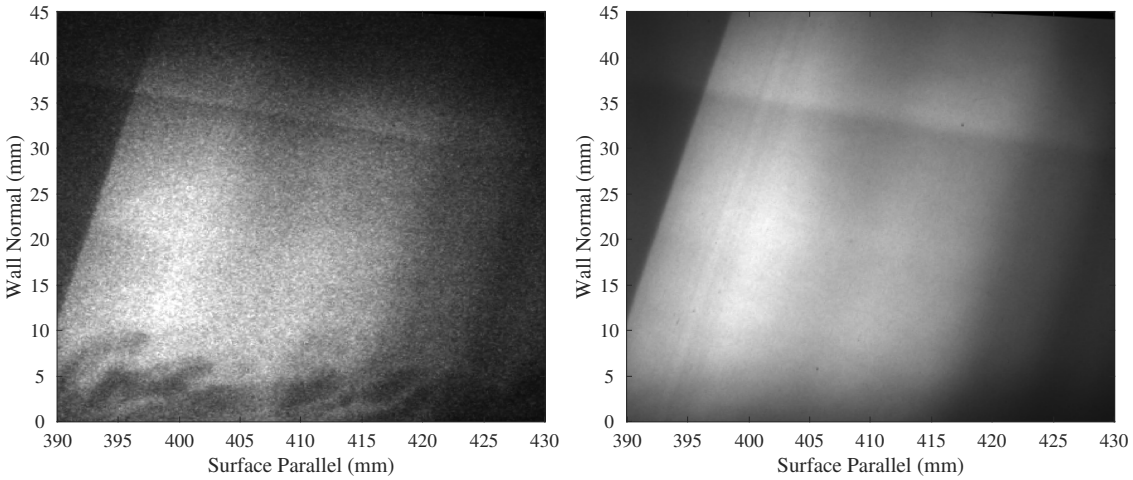

(a) Instantaneous "hot" image

(b) Mean "hot" image

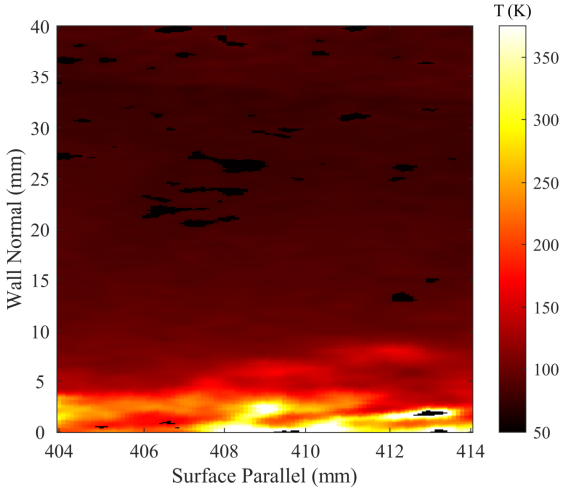

(c) Instantaneous temperature map

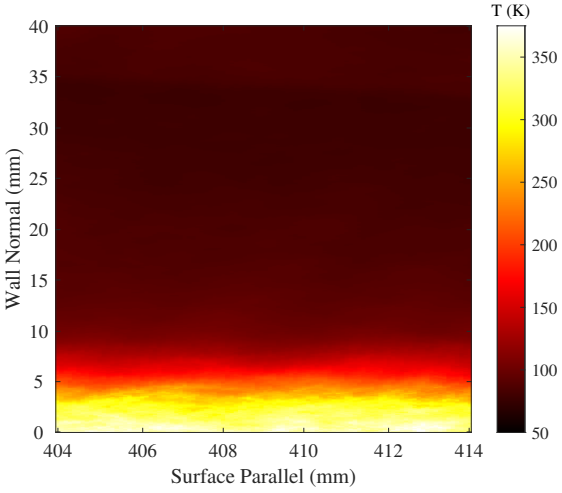

(d) Mean temperature map

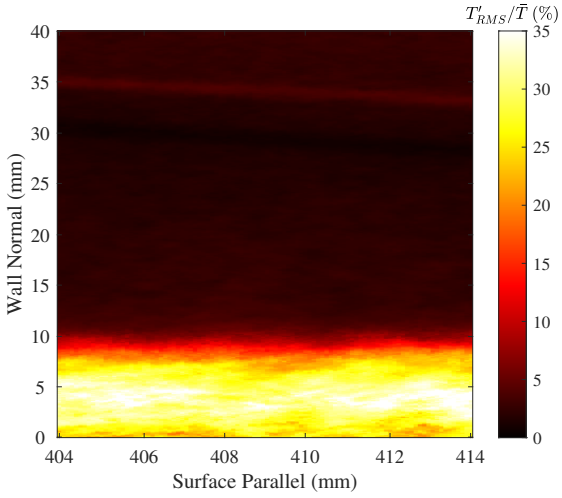

(e) Mean fluctuation map

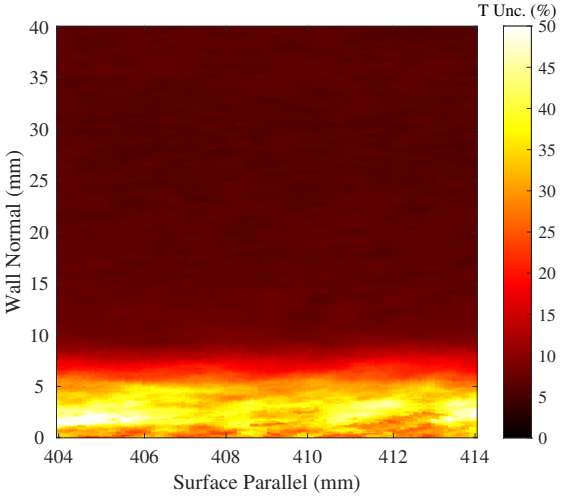

(f) Mean uncertainty map

Figure 7.81: PLIF rotational thermometry, Run 4617: downstream; turbulent wake; plasma on.

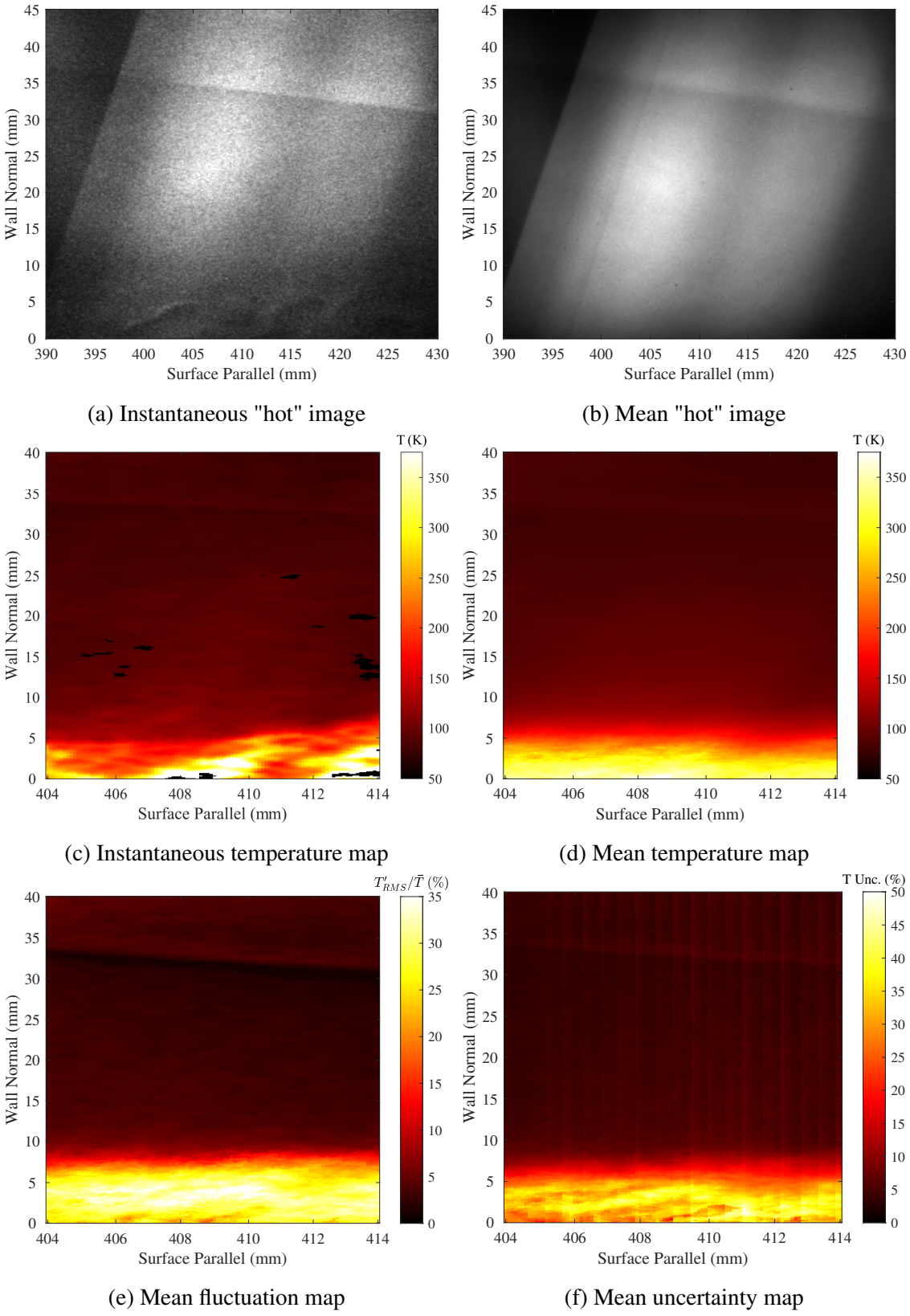

(a) Instantaneous "hot" image

(b) Mean "hot" image

(c) Instantaneous temperature map

(d) Mean temperature map

(e) Mean fluctuation map

(f) Mean uncertainty map

Figure 7.82: PLIF rotational thermometry, Run 4618: downstream; turbulent trough; plasma on.

7.4.2.2 Vibrational Thermometry Results

These data represented the first ever known, direct measurement of the development of a vibrational temperature boundary layer in a hypersonic blow down wind tunnel, at least with the PLIF technique. This campaign began when "noise" was observed in the "Read" images of preliminary MTV tests. Why did the sheet probing vibrationally excited species extend beyond the tagged "Write" line in Section 7.4.2.3? And why was the signal near the wall so much brighter when the plasma was on? The realization that not only did $NO^{v=1}$ exist in the freestream, but was being produced by the plasma was perhaps the greatest moment of discovery in this entire body of work. It is with this enthusiasm the data were analyzed. Note that a more contextualized discussion of the results in regard to the diffusion and mixing processes in the boundary layers, the relaxation pathways of $NO^{v=1}$, the degree of vibrational slip at the wall, and the performance of the plasma is contained in Chapter 8; the results here only introduce the data and make generalized observations.

These tests were conducted after the rotational thermometry and velocimetry campaigns showed there was no effect of being in the on- or off-centerline location, so the "Trough" runs were cut from the standard test matrix for time. In their place, measurements were taken at the "Middle" test location $\sim$ 260mm from the leading edge so as to better capture the evolution of the vibrational temperature boundary layer along the plate. Of course, studies of the roles of the trips and the plasma were included. The final test matrix is shown in Table 7.25, and the corresponding plasma conditions are shown in Table 7.28 and Figure 7.83.

Before starting, note that the results shown below used $T^v_{e,NO} = 230$K to be consistent with Buen's [49] the assumptions and analyses. However, the same figures are re-plotted for $T^v_{e,NO} = T^v_{e,N_2,O_2} = 358$K in Appendix A, and the consequences of the choice of $T^v_{e,NO}$ are discussed via a comparison of the results in Chapter 8. For now, although scaling PLIF data is a nonlinear process and the temperature ranges changed depending on $T^v_{e,NO}$, the same line shapes and trends held for both data sets, so most of the relative analysis below can readily be extended from one case to the other. It must also be understood that the actual T^v_{NO} most likely fell between the bounds generated by these two edge conditions.

No.	Location	Trips	Plasma	Run/Date
1	Forward	Laminar	Off	4678, 3/26/2021
2	Forward	Turbulent	Off	4681, 3/27/2021
3	Forward	Laminar	On	4679, 3/27/2021
4	Forward	Turbulent	On	4682, 3/28/2021
5	Middle	Laminar	Off	4688, 3/30/2021
6	Middle	Turbulent	Off	4691, 3/31/2021
7	Middle	Laminar	On	4687, 3/30/2021
8	Middle	Turbulent	On	4690, 3/31/2021
9	Back	Laminar	Off	4685, 3/29/2021
10	Back	Turbulent	Off	4684, 3/29/2021
11	Back	Laminar	On	4686, 3/30/2021
12	Back	Turbulent	On	4683, 3/29/2021

Table 7.27: PLIF *NO* vibrational thermometry test matrix.

No.	Current (mA)	Power Supply Voltage (V)	Power Supply Power (W)	Plasma Voltage (V)	Plasma Power (W)
3	94.5	1439	136.0	491.0	46.4
4	95.3	1433	136.6	477.3	45.5
7	95.5	1451	138.5	492.7	47.1
8	95.4	1440	137.4	482.8	46.1
11	95.5	1451	138.5	493.9	47.1
12	95.5	1443	137.8	484.8	46.3
Average					
	95.3	1442.8	137.5	487.1	46.4

Table 7.28: Plasma conditions for PLIF vibrational thermometry campaign.

As with the rotational thermometry, it was helpful to first consider the mean boundary layer profiles before analyzing the 2D images for each run individually. As in Section 7.4.2.1, it is noted that the error bars on the profiles came from the corresponding run's mean temperature and fluctuation images, not the uncertainty image; these 2D maps will be introduced shortly. The laminar profiles are shown in Figure 7.84. With the plasma off, the profiles at all three locations and their corresponding fluctuations matched to within the uncertainty of the measurement. There was a decay in the temperature as the flow approached the wall, which Buen [49] attributed to either a

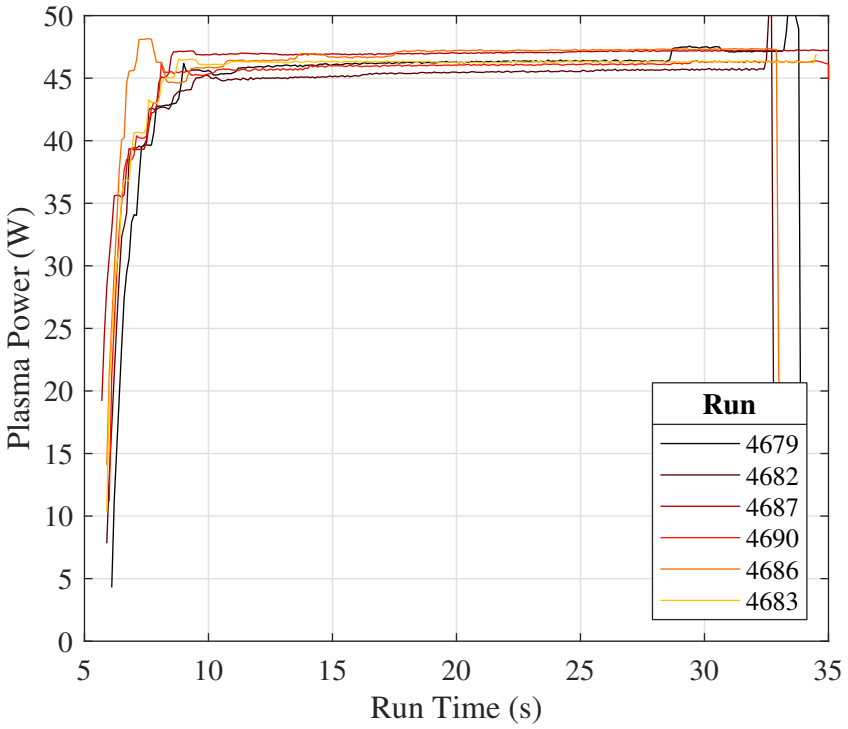

Figure 7.83: Plasma power traces for PLIF vibrational thermometry runs.

temperature gradient in the freestream (recall that the test article was mounted 25.4mm below the tunnel centerline) or the progressive activation of the VT and VV relaxation pathways as the ro-translational temperature increased towards the boundary layer. The N_xO_y species formed due to injecting NO at 15% may have exacerbated any effect of being off-centerline. Without freestream T^v_{NO} measurements, the exact source of the decay was difficult to explain, but the increased rate of said decay between $2.5-5$mm was likely due to VT and VV relaxation; using the ro-translational thermometry results to calculate the energy exchange rates through the boundary layer, Buen [49] found the efficacy of many of the relaxation pathways to increase by several orders of magnitude in this range, but the dominant NO VT and $NO-O_2$ VV reactions were relatively unaffected, rising $\mathcal{O}(10-100\times)$. An alternative explanation for the vibrational temperature deficit near the wall could be some effect due to the shock curvature at the leading edge and the corresponding entropy layer observed in Section 7.3.2, but such a process was less understood. The slight recovery below $\sim$ 1mm was likely due to the partial satisfaction of the no-slip condition. The mechanisms behind

these profiles' behavior, especially in the context of vibrational relaxation, are directly analyzed in Chapter 8.

The introduction of the plasma fomented a general trend in the laminar boundary layer. Indeed, the vibrational temperature boundary layer seemed to be growing alongside the laminar velocity boundary layer, thickening as it traveled along the test article. In doing so, the temperature dropped from a peak of ~ 275K ~ 1mm above the surface at the first test location, to ~ 260K ~ 2mm above the surface at the second test location, and finally ~ 250K ~ 2mm above the surface at the final test location. While the temperature peak did not move appreciably between the "Middle" and "Back" test locations, in the "Front" test location the peak temperature corresponded well with the observed height of the plasma's cathode layer, and the short distance between the plasma and test location left little room for relaxation or boundary layer growth. Above ~ 10mm the plasma "Off" and "On" cases appeared identical. Between $\sim 5 - 10$mm the general shape of each location's curve was maintained, but they appeared consistently ~ 5K colder when the plasma was on, a small but meaningful amount.

That the vibrational temperature boundary layer thickness matched the ro-translational boundary layer's thickness was expected. In order to explain the motion of the peak temperature, Buen [49] performed some calculations using Fick's Law of Diffusion and found it was a decent explanation for the observed results. When added to the boundary layer growth, this helped explain how any why the peak vibrational temperature moved up from the wall. That the vibrational temperature dropped could either have been due to this same diffusive pathway or vibrational relaxation, but the lack of meaningful difference in the ro-translational temperature profiles between the plasma "Off" and "On" cases, and the general thickening of the downstream vibrational temperature profiles, meant that should the latter case be significant, an insufficient amount of vibrational energy was relaxing to affect the gases' properties. Again, these trends will be discussed in detail in Chapter 8.

In both cases, the fluctuations increased as the flow approached the boundary layer, perhaps due to whatever trend drove down the vibrational temperature. Interestingly, the relative fluctu-

ation percentage was roughly matched in this region between the ro-translation and vibrational measurements. This was surprising, because one would expect the larger temperatures would have reduced the fluctuation percentage accordingly. Also, it was hypothesized the vibrational temperature would have been more insulated from the pressure perturbations which lead to ro-translational temperature fluctuations, but evidently this was not the case; this complex relationship was discussed in Section 2.3.6 based on the work of Khurshid and Donzis [138]. Near the wall the fluctuations did not spike to the same degree as the ro-translational case. This may be due to the increased signal in this regime; the $v = 0$ beam could be optimized for the "Hot" boundary layer (high J state), and when it was turned on the plasma directly increased the number density of vibrationally-excited target molecules for the $v = 1$ beam. Buen [49] asserted that the interface between the boundary and entropy layers was the source of fluctuation peak at $\sim$ 5mm. There was little change in the shape or magnitude of the fluctuation profiles between and of the three test locations, and the plasma seemed to have no effect as well.

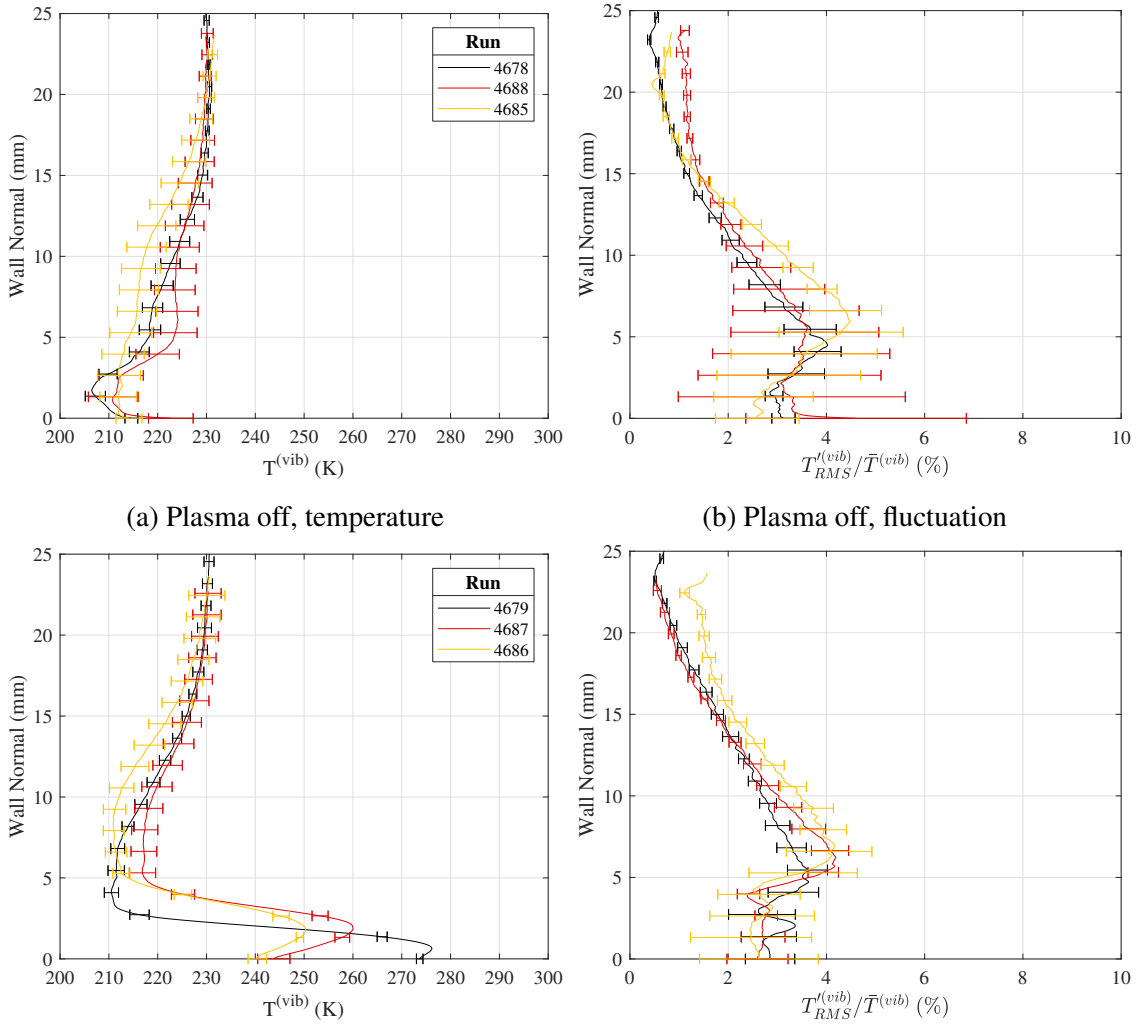

(a) Plasma off, temperature

(b) Plasma off, fluctuation

(c) Plasma on, temperature

(d) Plasma on, fluctuation

Figure 7.84: PLIF vibrational thermometry, laminar temperature profile comparison assuming $T^{v}_{e,NO} = 230K$; error bars were set from the corresponding mean temperature and fluctuation images. Same legend applies to all figures in a row.

The turbulent profiles are shown in Figure 7.85. Once again, the calculation of the error bars by Buen [49] is described in Section 7.4.2.1. The "Front/Plasma off" case agreed strongly with its laminar counterpart. The "Middle" and "Back" cases, however, did not show the same deficit below $\sim$ 5mm; they also did not show the same general decay towards the boundary layer, but this was likely due to the thickness of the boundary layer itself. All three profiles reached a wall temperature of $\sim$ 225K, which matched that of the laminar flow.

With the plasma activated, there again became a clear trend as the flow moved along the test article. The profile for the first location agreed well with the laminar case, with a peak temperature of $\sim$ 270K $\sim$ 1mm above the surface. In general, this implied that the transitional boundary layer was not yet capable of having an impact on the vibrational energy profile, but the addition of the slight "hump" in the profile at $\sim$ 3mm showed there was some effect; Buen [49] postulated this bump was due to turbulent mixing, perhaps the ejection of vibrationally hot gas from the wall and into the trips' shear layer due to the corner vortices. By the "Middle" location, the boundary layer had thickened to $\sim$ 9mm, and the temperature peaked at $\sim$ 255K at the wall; this was the only profile to peak at the wall, casting some doubt onto its veracity below $\sim$ 2mm, especially when considering the sudden and unexplained spike in its fluctuation profile in this region. By the final test location, the peak temperature was $\sim$ 240K $\sim$ 11mm from the wall, agreeing well with the ro-translational boundary layer thickness. Comparing the "Laminar" and "Turbulent" cases, it would seem the wall temperature was independent of the flow and was $\sim$ 270mm at the first test location, and then $\sim$ 240K at the second two test locations. Also, recall from Khurshid and Donzis [138] that turbulent flows should be able to store a greater degree of their energy in vibrational modes than laminar flows, potentially explaining some degree of the hotter temperatures seen in Figure 7.85 as compared to Figure 7.84; still, mixing likely played a more dominant role in the resulting temperature profiles.

Indeed, the decrease in the peak temperature and thickening of the boundary layer was attributed to turbulent mixing, or the combination of convection and diffusion [49]. Again, this would imply that the vibrational relaxation may have played a secondary role in the vibrational temperature decay, a position Buen supported with the absence of any ro-translational temperature rise along the plate. They plotted the relaxation reaction rates, now calculated using the turbulent ro-translational temperature profiles, and as with the laminar case the less important reactions had remarkable increase in efficiency. The dominant $NO\ VT$ and $NO-O_2\ VV$ reactions had the same $\mathcal{O}(10-100\times)$ increase within the boundary layer. While the exact effect of these increases was difficult to quantify given the intensity of the turbulence and lack of any perceptible impact of the

plasma in the other PLIF techniques, despite the growth of the reaction rates in the boundary layer Buen stated NO vibrational relaxation was likely to play a secondary role to turbulent mixing; the low number density of vibrationally excited NO molecules could only have lessened the impact of the relaxation. Recall that other experiments [95, 206] used a stronger plasma and more efficient relaxers like H_2O and CO_2 to foment a measurable impact from the more plentiful N_2. A more detailed analysis of these results and the mechanisms driving them is included Chapter 8.

There was surprisingly little difference in magnitude of the fluctuating profiles between the laminar and turbulent flows save for the larger boundary layer in the latter case. In all cases, the fluctuations seldom exceeded 4%. A possible explanation could be the relative invariance of the vibrational temperature to turbulent pressure fluctuations; it takes considerably more collisions to cause vibrational equilibration ($\mathscr{O}(10^4)$) than ro-translational equilibration ($\mathscr{O}(10^{0-1})$), so the timescales for the pressure perturbations and low densities in the ACE tunnel may have been such that there could be little vibrational energy exchange; possible mechanisms are provided by Khurshid and Donzis [138]. Upon entering the boundary layer, the profiles for the turbulent case appeared more constant, as one might expect for the fully developed turbulent flow; Buen [49] expected a decrease in fluctuations near the wall owing to the presence of the laminar sublayer, but the low signal in this region and presence of vibrational slip may have confounded this behavior. There was a distinct hump in both the "Laminar" and "Turbulent", plasma "On", "Front" fluctuation plots at $\sim$ 2mm; Buen [49] attributed other such bumps in these profiles to the interface of the freestream and entropy layers or the trips' wake structure, but this one remained unexplained. That it occurred so close to the cathode layer meant it may have been due to some effect of the vibrational energy seeding.

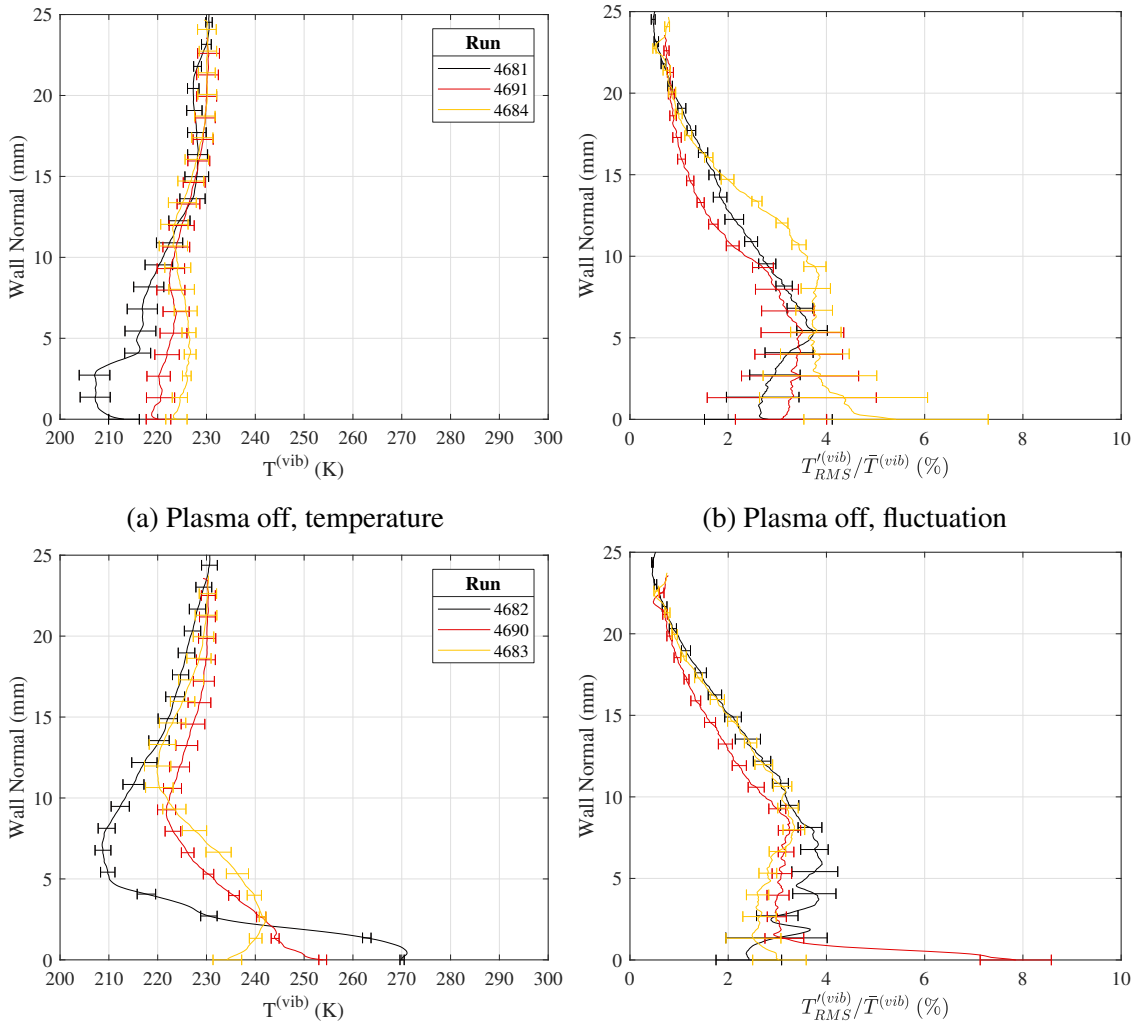

(a) Plasma off, temperature

(b) Plasma off, fluctuation

(c) Plasma on, temperature

(d) Plasma on, fluctuation

Figure 7.85: PLIF vibrational thermometry, turbulent temperature profile comparison assuming $T^{v}_{e,NO} = 230K$; error bars were set from the corresponding mean temperature and fluctuation images. Same legend applies to all figures in a row.

The individual run data is presented analogously to the ro-translational results in Figures 7.86-7.97. For each run, an instantaneous and mean fluorescence image is shown; here the $v = 1$ frame was selected because $v = 0$ images can be seen in the ro-translational results. The corresponding instantaneous 2D temperature map from this frame is provided next, as well as the mean temperature map from all of the images. The bottom row contains the RMS fluctuation ($T' = T^{v} - \overline{T}^{v}$) and mean uncertainty maps. Again, any gaps in the data were filled with solid black regions.

The laminar data showed several key trends. To begin, compare any set of raw images without and with the plasma, for example Figures 7.86(b) and 7.88(b) respectively. In the freestream, there was a gradual decrease in signal as the flow approached the wall, perhaps due to absorption, the rising temperature reducing the number density of the NO, or chemistry effects. No Mach waves were visible, likely due to their weak effect even ro-translational temperature. The main feature, however, was the bright region near the wall, contained entirely within the boundary layer, that was only present when the plasma was activated. This represented direct evidence the plasma was vibrationally exciting the NO. In those laminar runs with the plasma on it was especially clear where the boundary layer began.

The turbulent run data showed the same impact of the plasma. The instantaneous images of the fully developed turbulent boundary layer, such as 7.95(a) were particularly striking, provide excellent resolution of the turbulent structures. In the upstream location, Figure 7.89, it was interesting to view the trip shock. This shock was strong enough to be visualized, likely due to its effect on the NO's number density. However, it seemed to have little tangible effect on any of the thermometric results. This may have been due to the relative invariance of the vibrational temperature to shocks in low density blowdown facilities like the ACE tunnel[205]. An additional detail in Figure 7.89(b) was a weak glowing region between $\sim 2-4$mm; this was attributed to the trips' corner vortices convecting vibrationally excited NO out of the cathode layer [49].

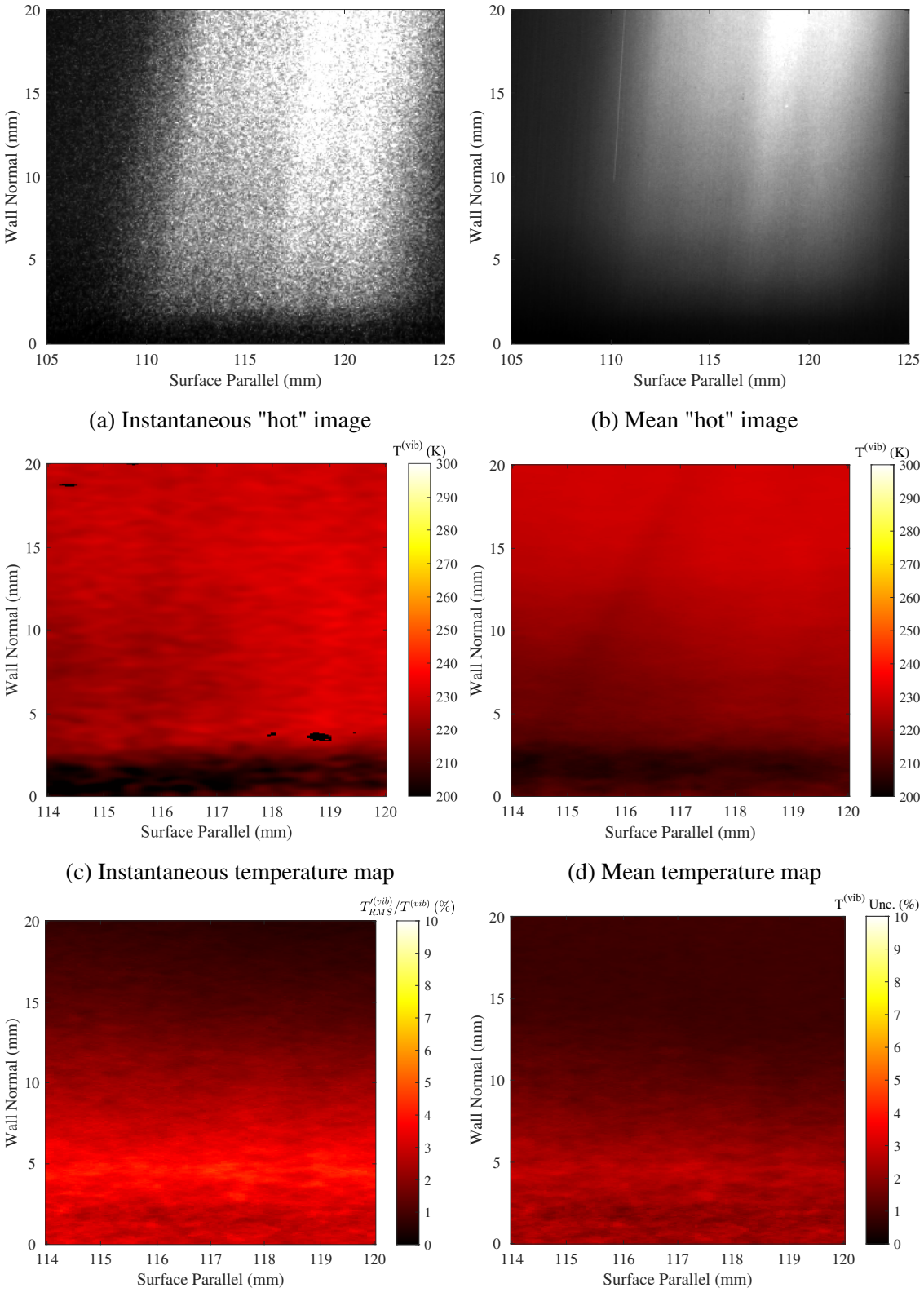

(a) Instantaneous "hot" image

(b) Mean "hot" image

(c) Instantaneous temperature map

(d) Mean temperature map

(e) Mean fluctuation map

(f) Mean uncertainty map

Figure 7.86: PLIF vibrational thermometry assuming $T^{v}_{e,NO} = 230K$, Run 4678: upstream; laminar; plasma off.

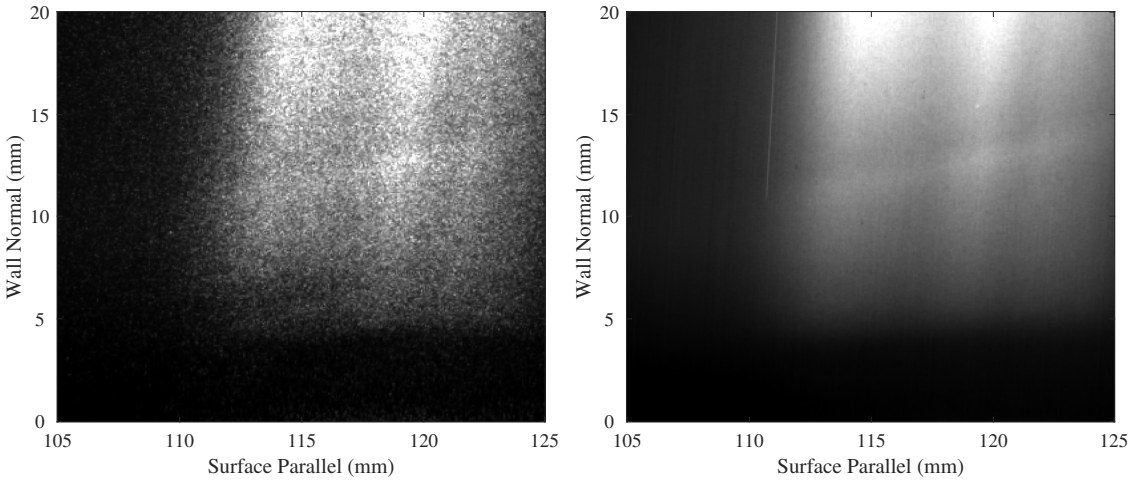

(a) Instantaneous "hot" image

(b) Mean "hot" image

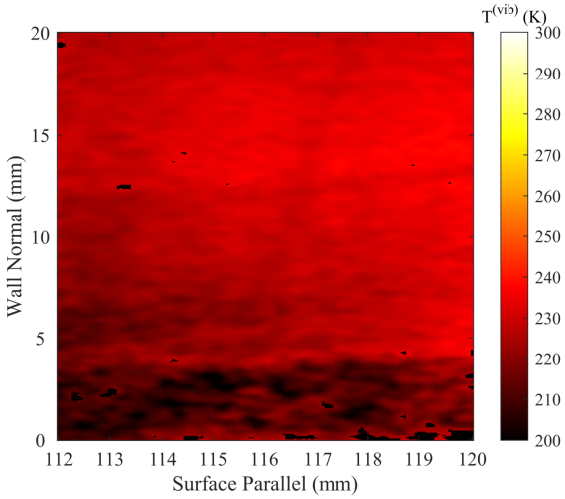

(c) Instantaneous temperature map

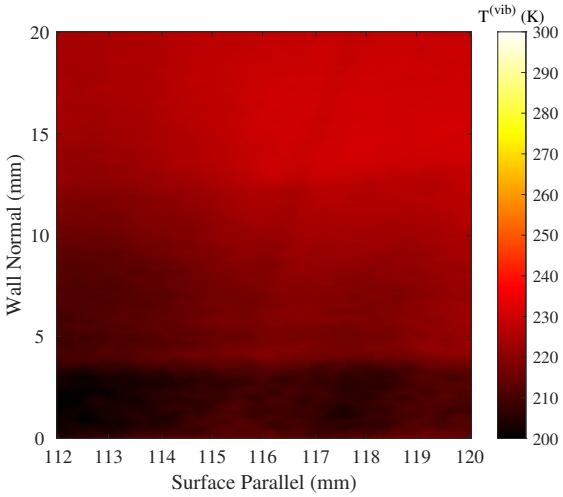

(d) Mean temperature map

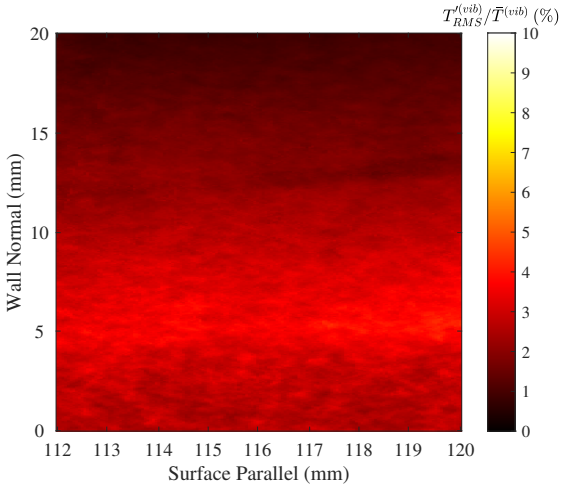

(e) Mean fluctuation map

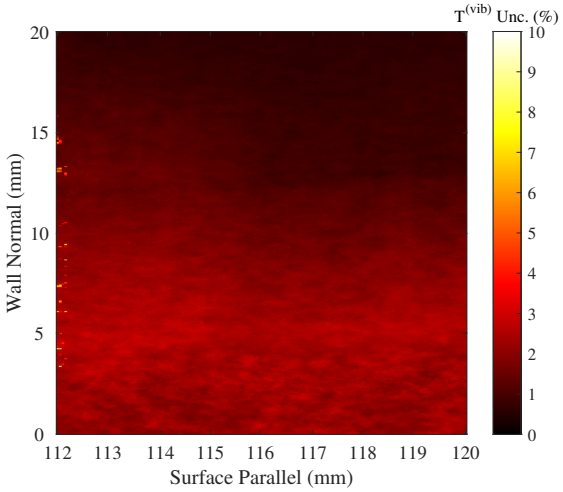

(f) Mean uncertainty map

Figure 7.87: PLIF vibrational thermometry assuming $T^{v}_{e,NO} = 230K$, Run 4681: upstream; turbulent; plasma off.

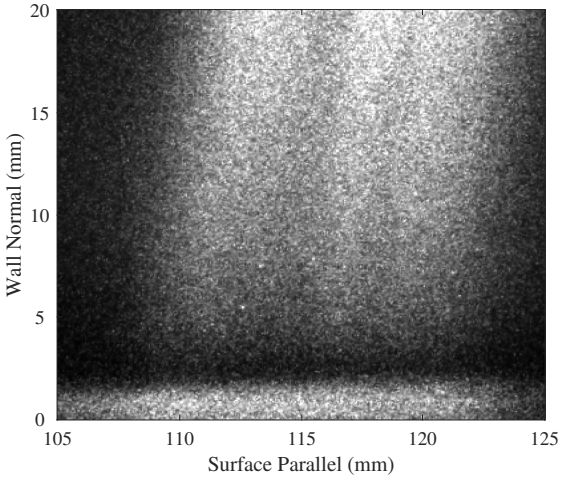

(a) Instantaneous "hot" image

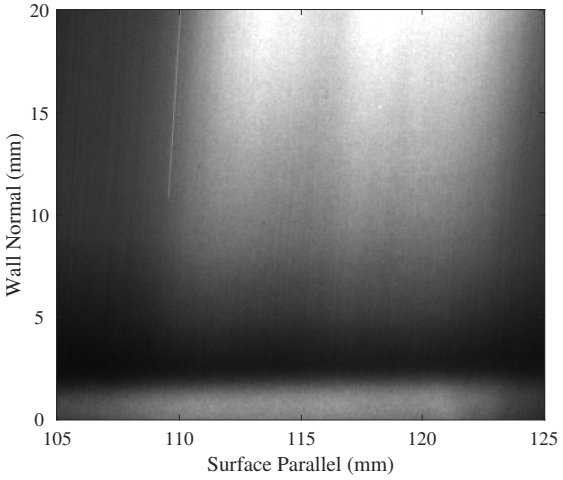

(b) Mean "hot" image

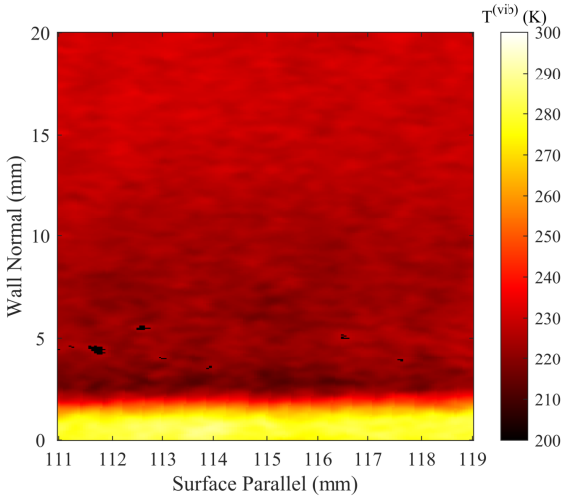

(c) Instantaneous temperature map

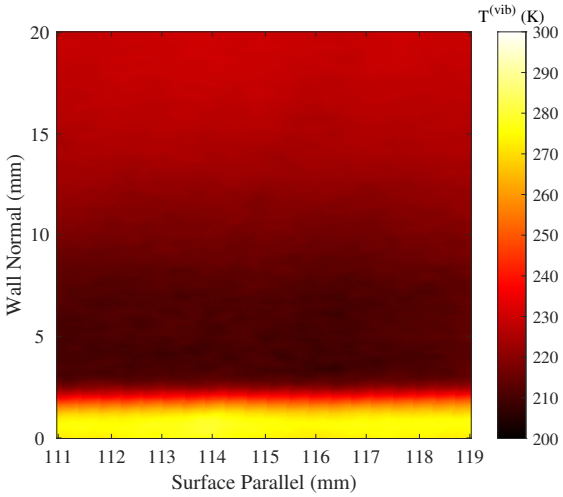

(d) Mean temperature map

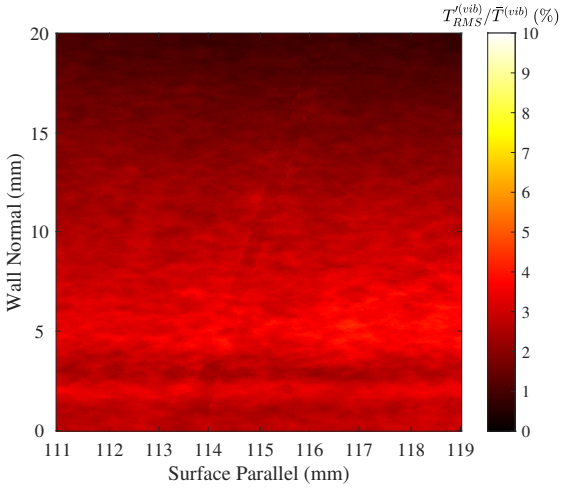

(e) Mean fluctuation map

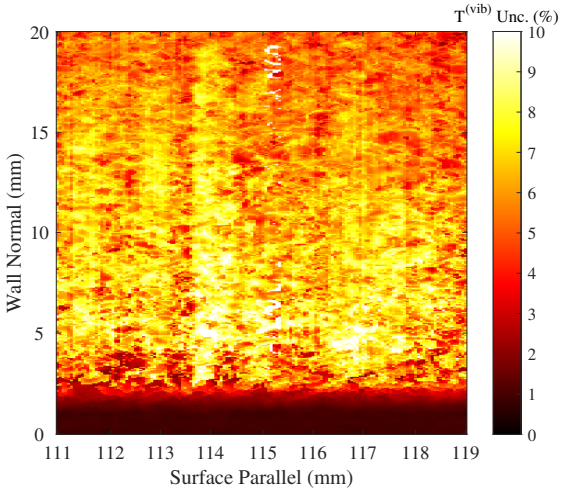

(f) Mean uncertainty map

Figure 7.88: PLIF vibrational thermometry assuming $T^{v}_{e,NO} = 230K$, Run 4679: upstream; laminar; plasma on.

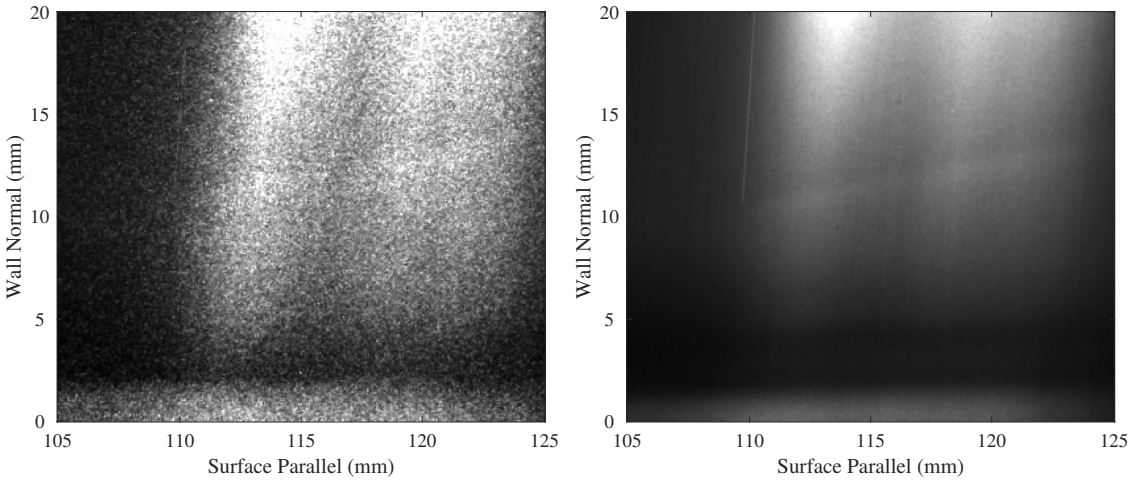

(a) Instantaneous "hot" image

(b) Mean "hot" image

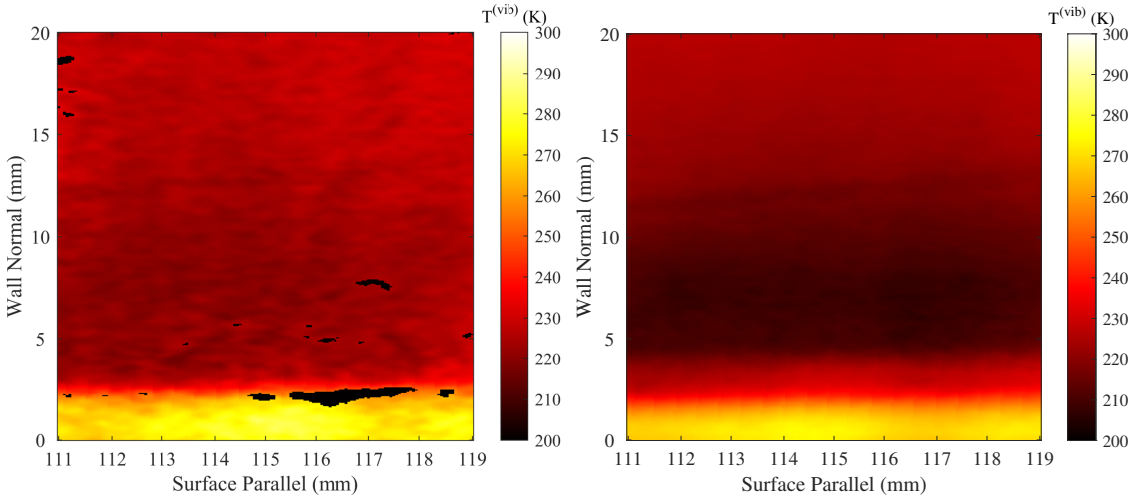

(c) Instantaneous temperature map

(d) Mean temperature map

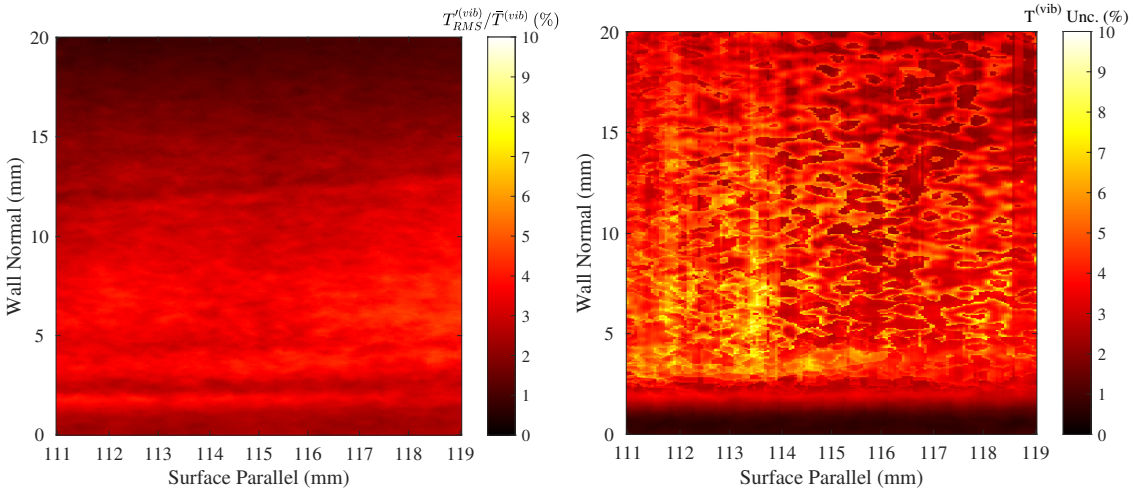

(e) Mean fluctuation map

(f) Mean uncertainty map

Figure 7.89: PLIF vibrational thermometry assuming $T^v_{e,NO} = 230K$, Run 4682: upstream; turbulent; plasma on.

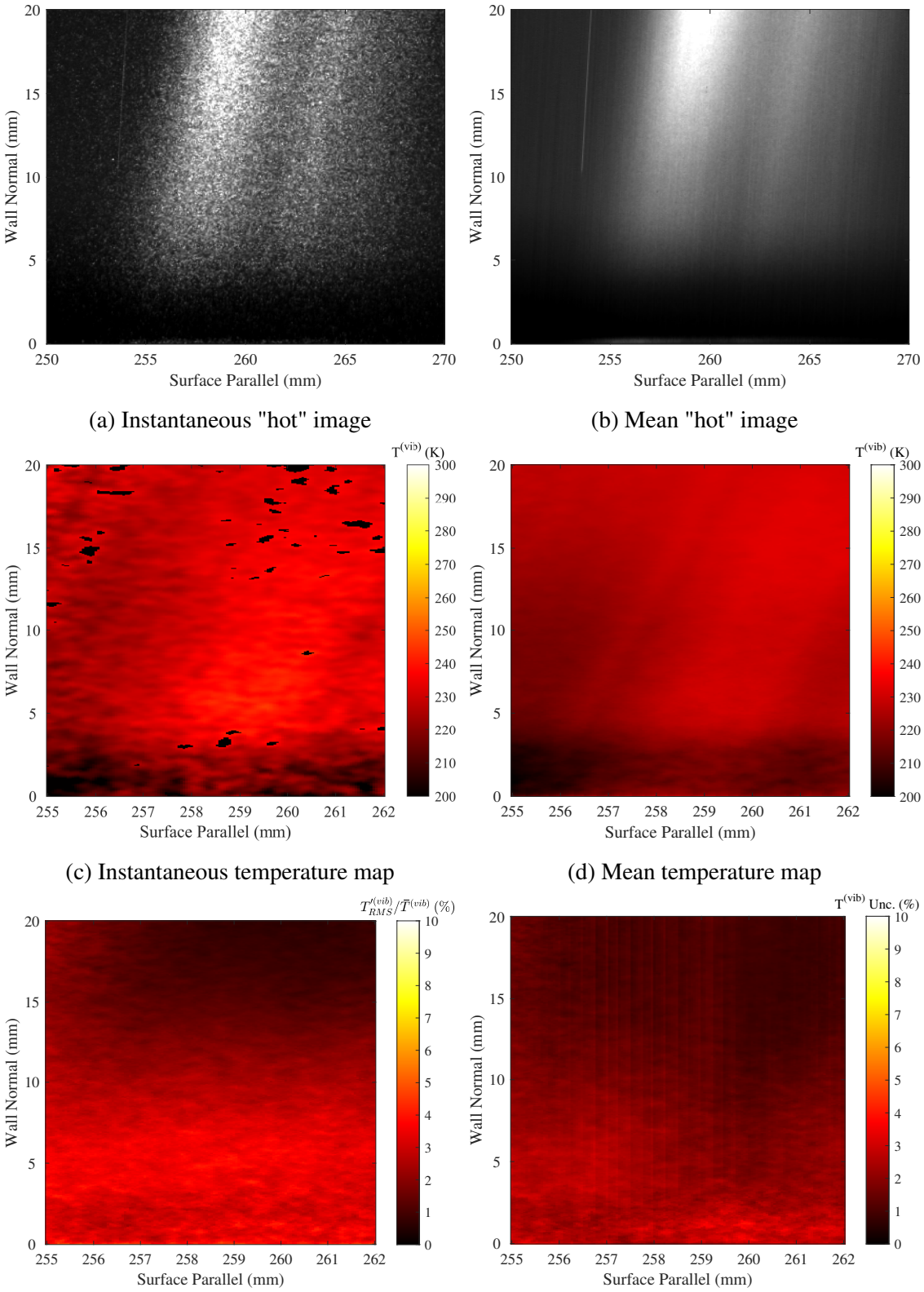

(a) Instantaneous "hot" image

(b) Mean "hot" image

(c) Instantaneous temperature map

(d) Mean temperature map

(e) Mean fluctuation map

(f) Mean uncertainty map

Figure 7.90: PLIF vibrational thermometry assuming $T^v_{e,NO} = 230K$, Run 4688: middle; laminar; plasma off.

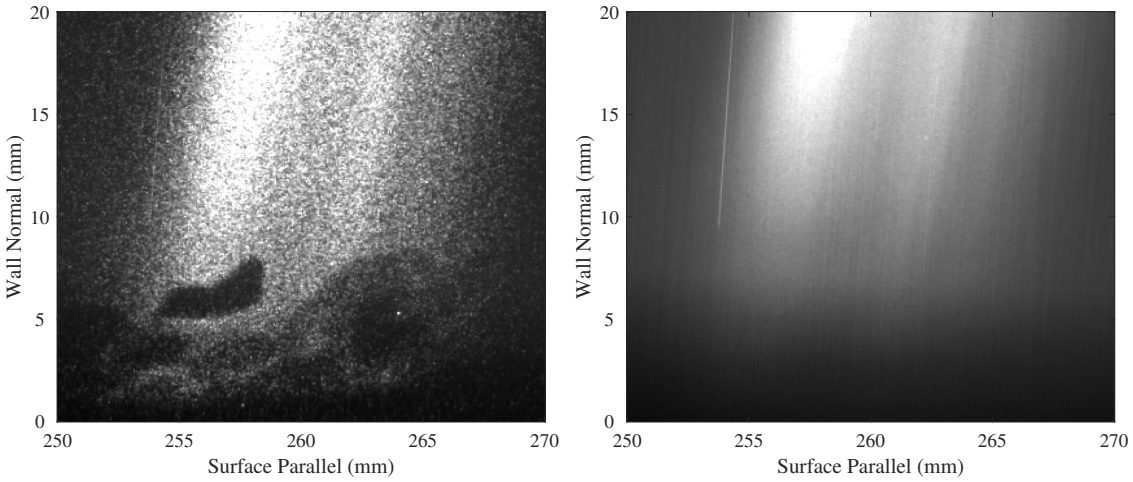

(a) Instantaneous "hot" image

(b) Mean "hot" image

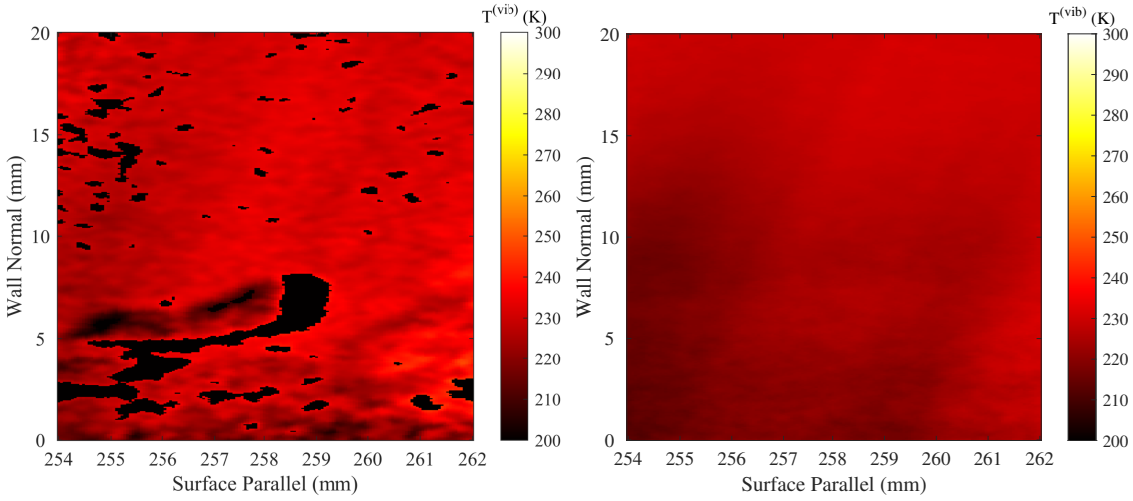

(c) Instantaneous temperature map

(d) Mean temperature map

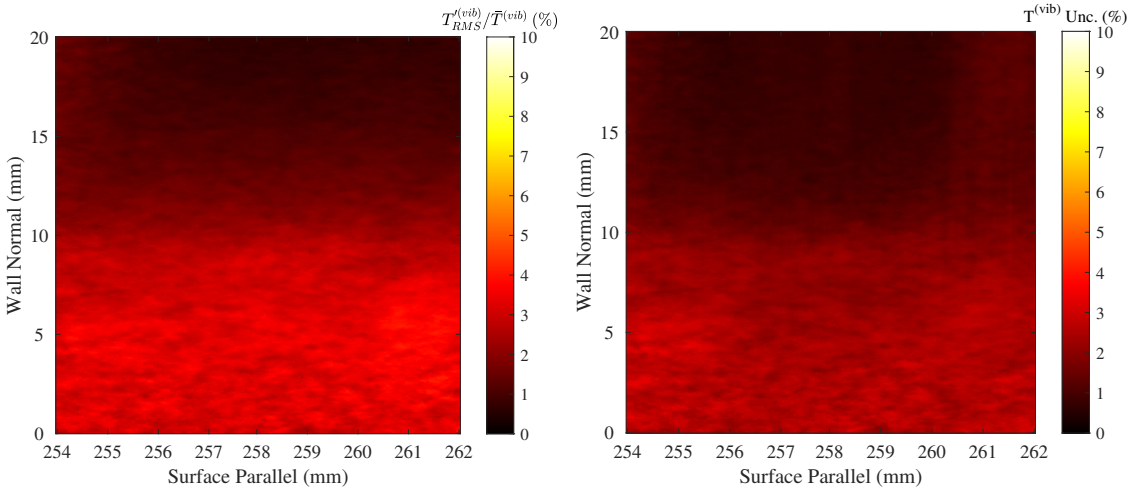

(e) Mean fluctuation map

(f) Mean uncertainty map

Figure 7.91: PLIF vibrational thermometry assuming $T^{v}_{e,NO} = 230K$, Run 4691: middle; turbulent; plasma off.

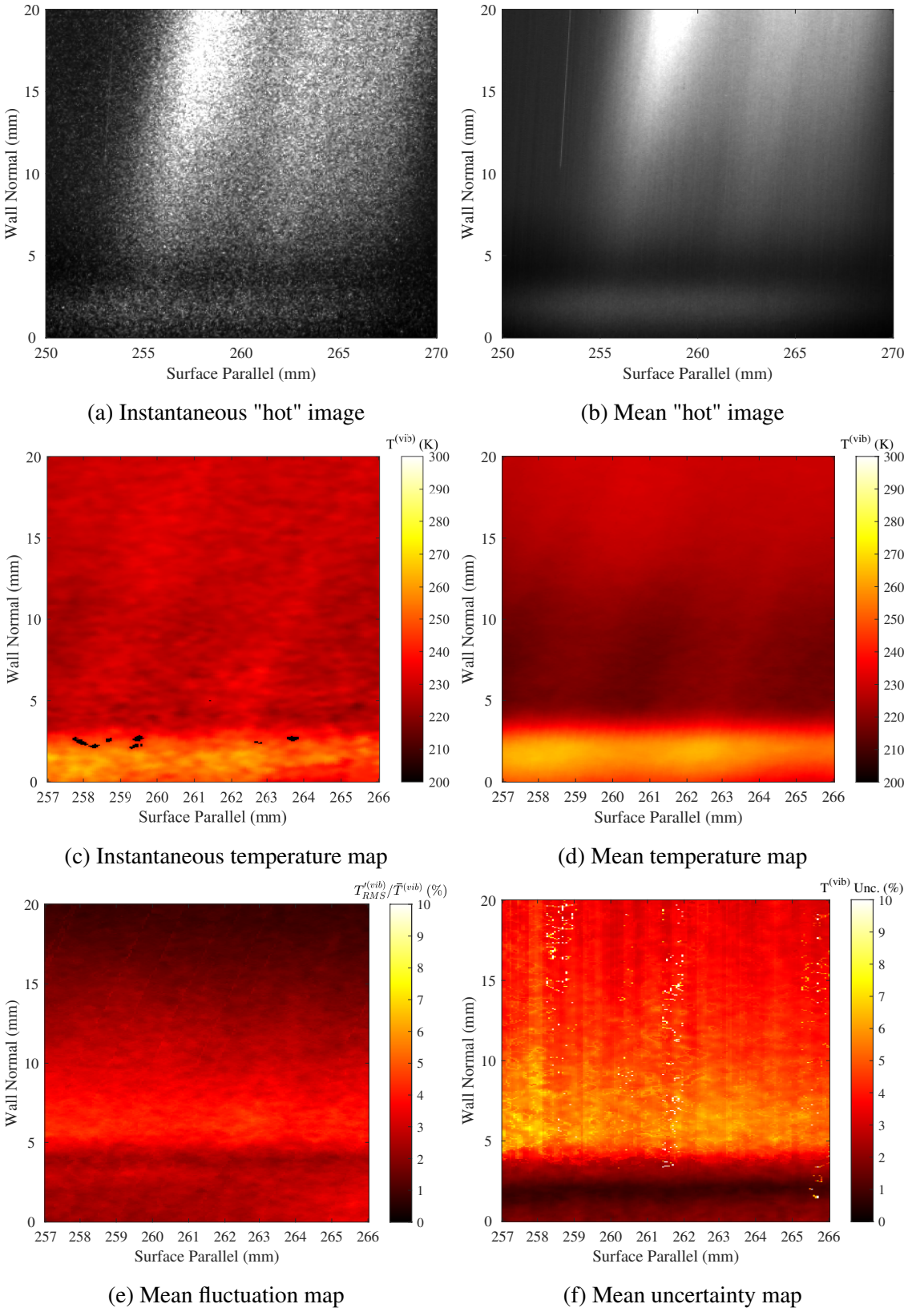

(a) Instantaneous "hot" image

(b) Mean "hot" image

(c) Instantaneous temperature map

(d) Mean temperature map

(e) Mean fluctuation map

(f) Mean uncertainty map

Figure 7.92: PLIF vibrational thermometry assuming $T^v_{e,NO} = 230K$, Run 4687: middle; laminar; plasma on.

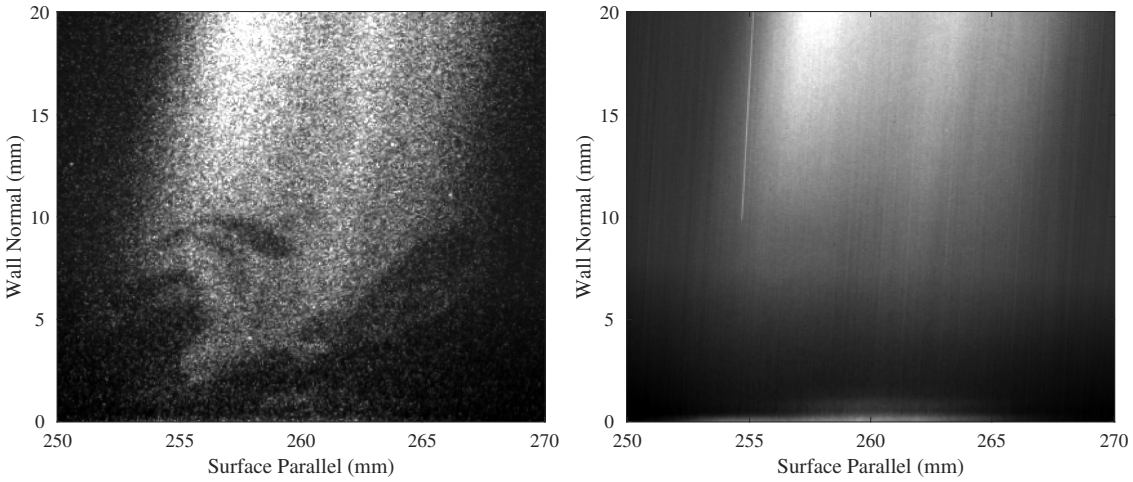

(a) Instantaneous "hot" image

(b) Mean "hot" image

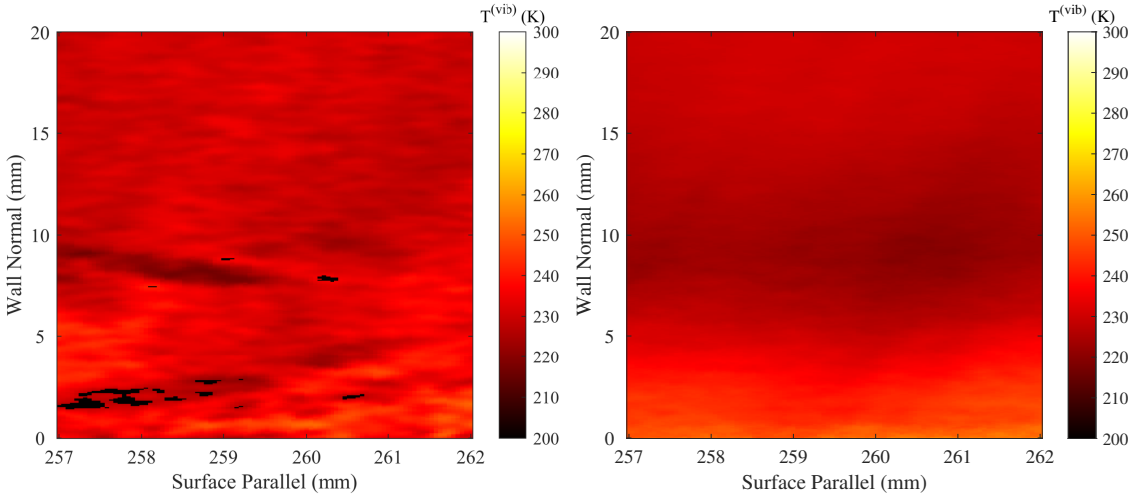

(c) Instantaneous temperature map

(d) Mean temperature map

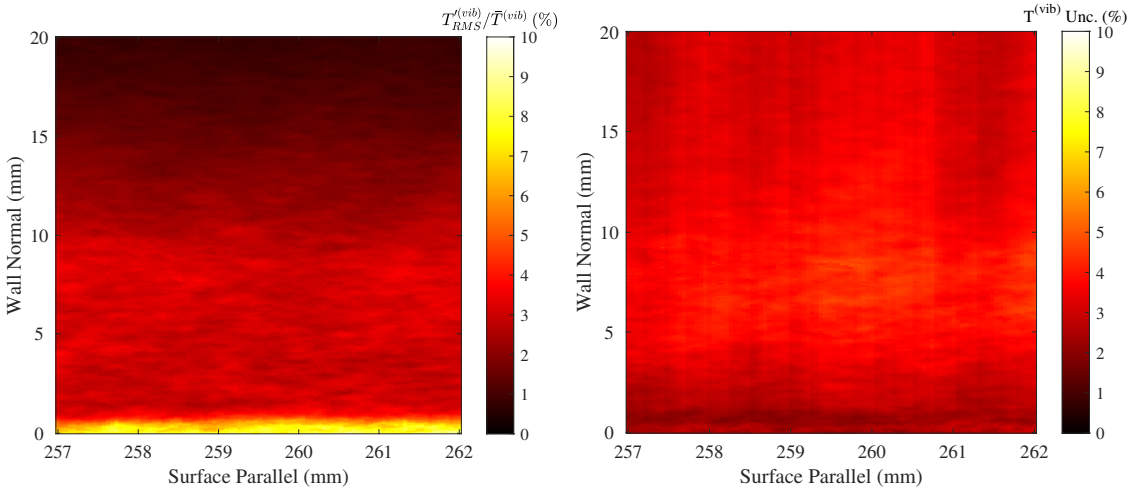

(e) Mean fluctuation map

(f) Mean uncertainty map

Figure 7.93: PLIF vibrational thermometry assuming $T^{v}_{e,NO} = 230K$, Run 4690: middle; turbulent; plasma on.

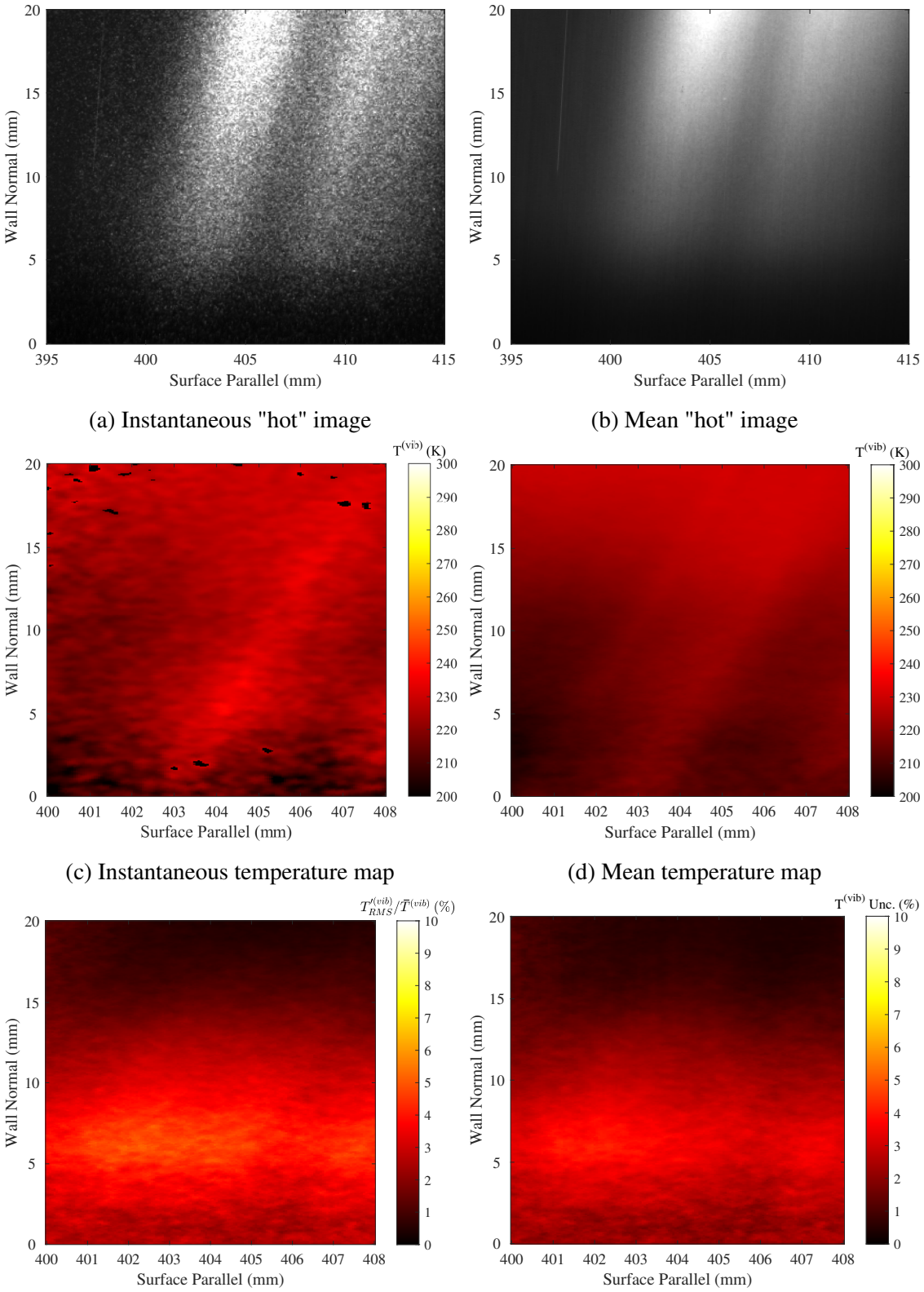

(a) Instantaneous "hot" image

(b) Mean "hot" image

(c) Instantaneous temperature map

(d) Mean temperature map

(e) Mean fluctuation map

(f) Mean uncertainty map

Figure 7.94: PLIF vibrational thermometry assuming $T^v_{e,NO} = 230K$, Run 4685: back; laminar; plasma off.

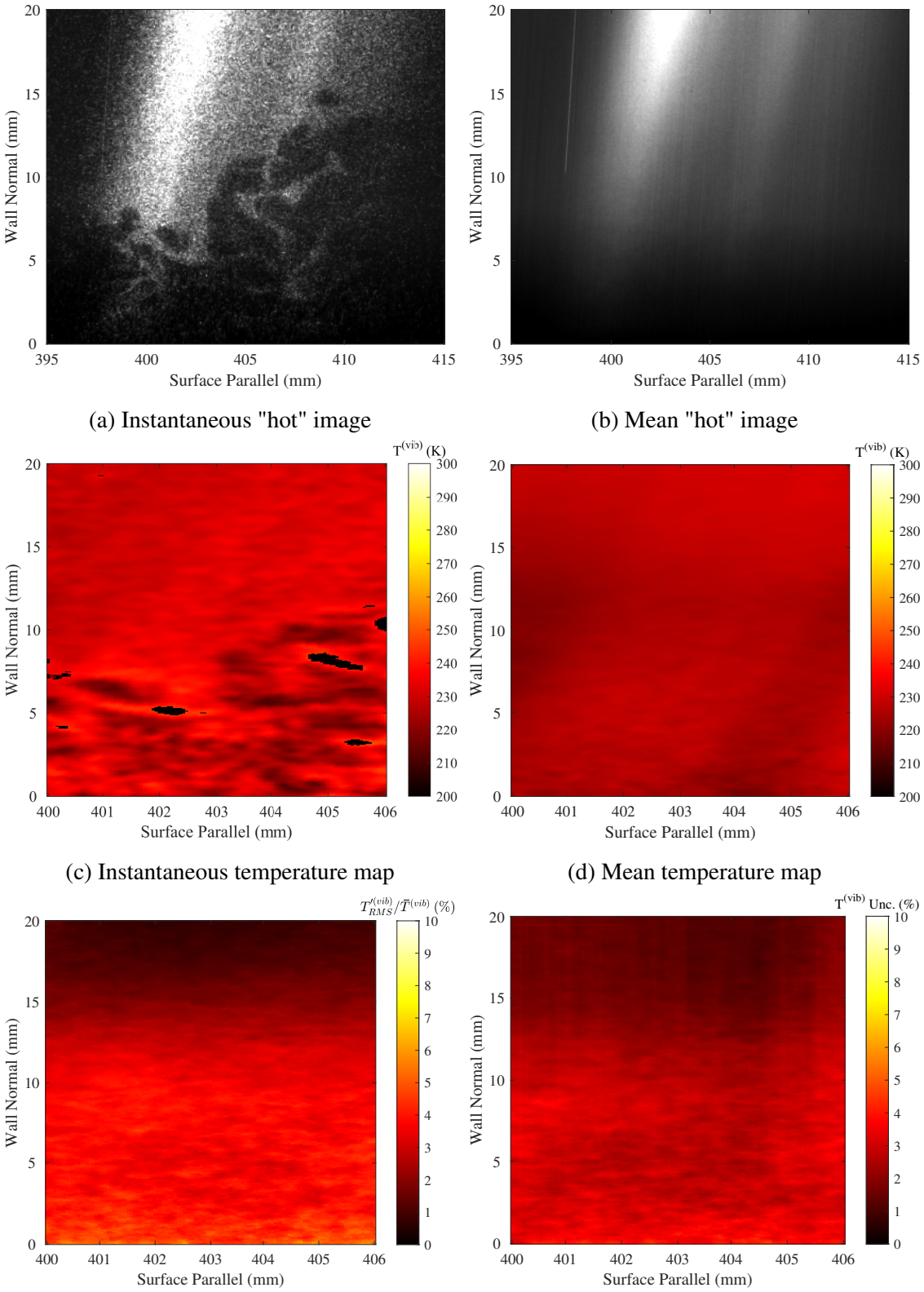

(a) Instantaneous "hot" image

(b) Mean "hot" image

(c) Instantaneous temperature map

(d) Mean temperature map

(e) Mean fluctuation map

(f) Mean uncertainty map

Figure 7.95: PLIF vibrational thermometry assuming $T^{v}_{e,NO} = 230K$, Run 4684: back; turbulent; plasma off.

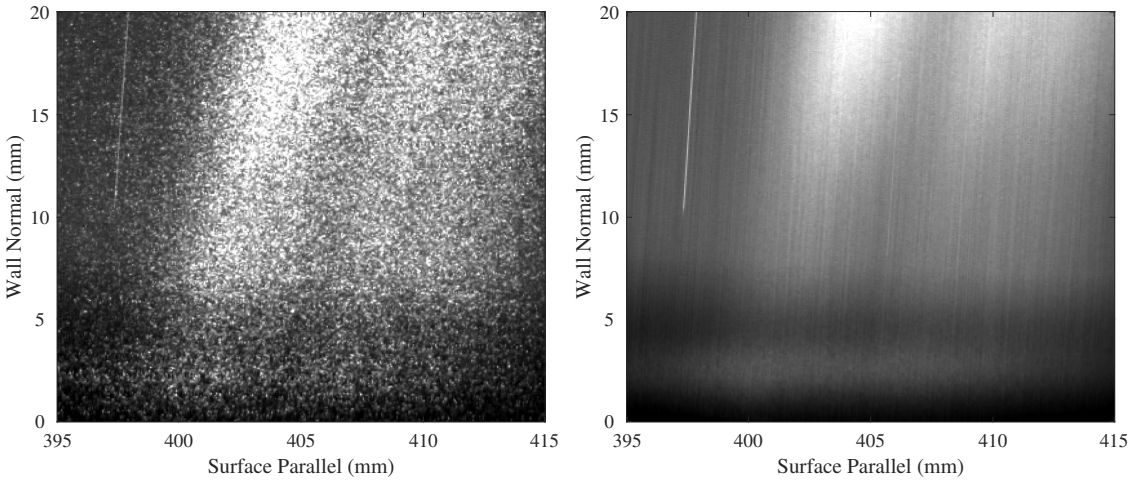

(a) Instantaneous "hot" image

(b) Mean "hot" image

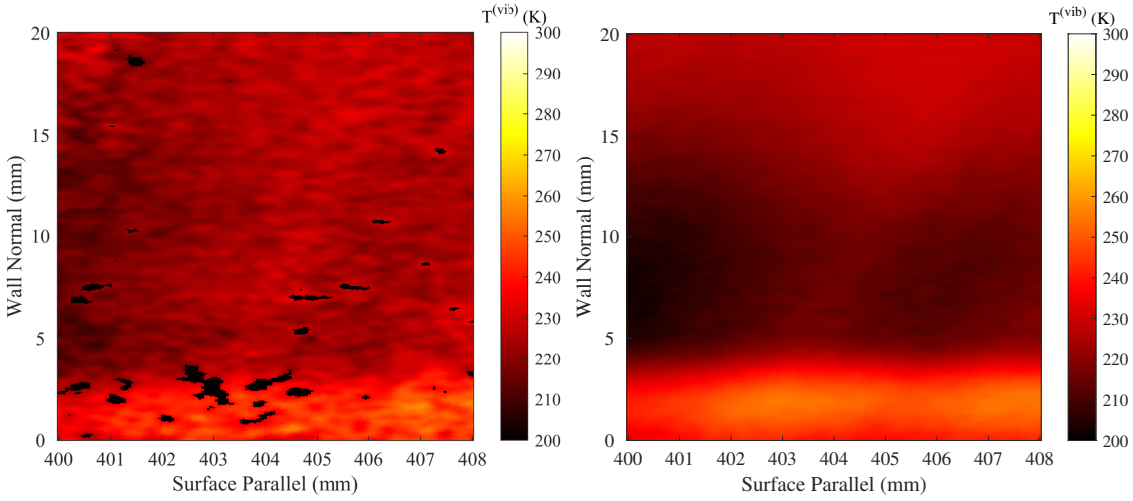

(c) Instantaneous temperature map

(d) Mean temperature map

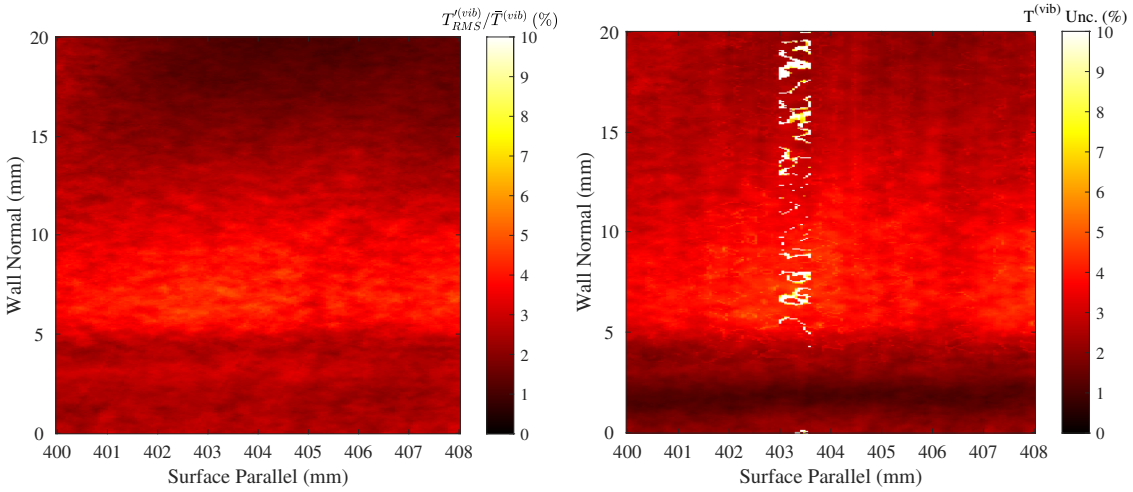

(e) Mean fluctuation map

(f) Mean uncertainty map

Figure 7.96: PLIF vibrational thermometry assuming $T^{v}_{e,NO} = 230K$, Run 4686: back; laminar; plasma on.

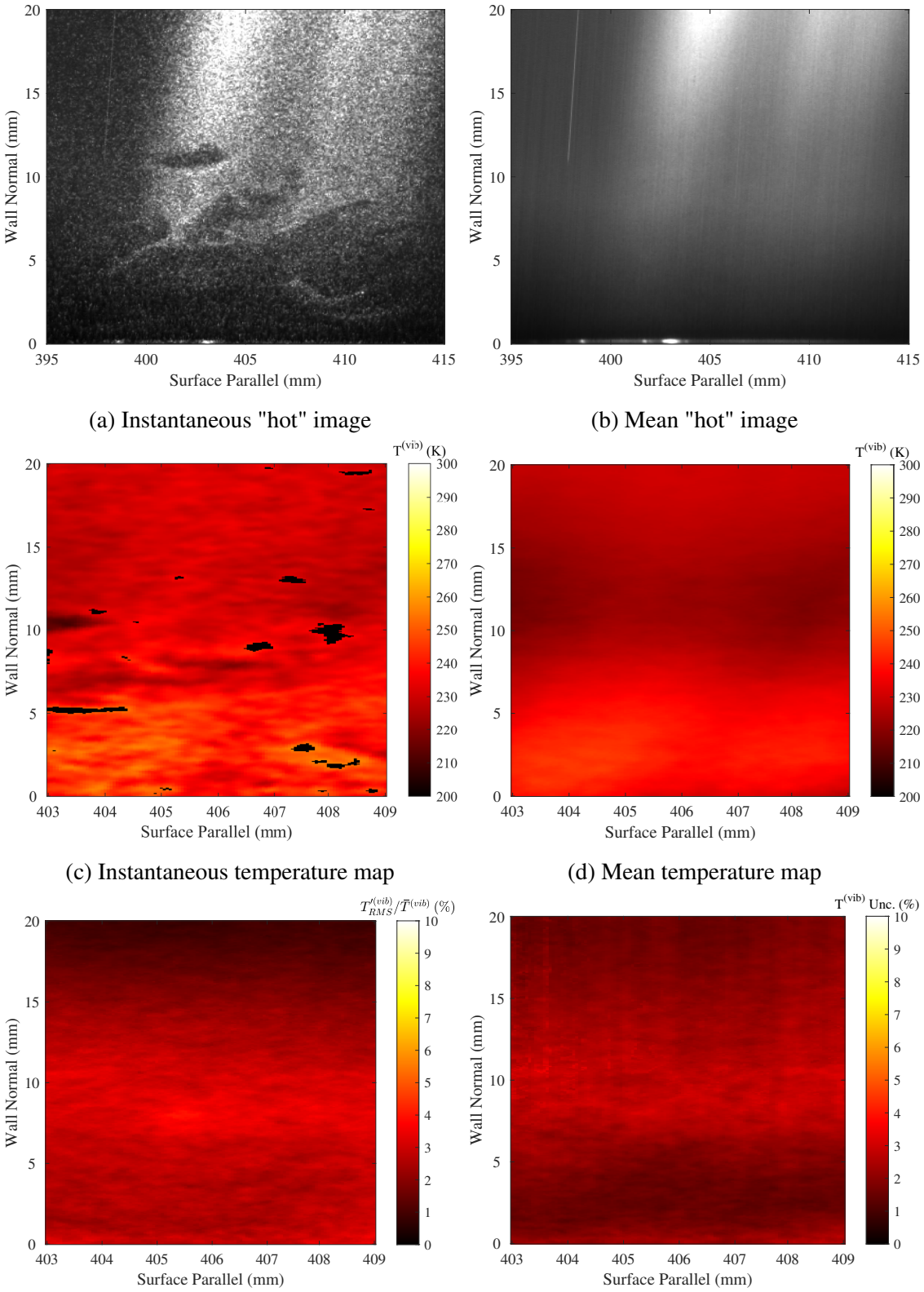

(a) Instantaneous "hot" image

(b) Mean "hot" image

(c) Instantaneous temperature map

(d) Mean temperature map

(e) Mean fluctuation map

(f) Mean uncertainty map

Figure 7.97: PLIF vibrational thermometry assuming $T^{v}_{e,NO} = 230K$, Run 4683: back; turbulent; plasma on.

7.4.2.3 Velocimetry Results

Velocity was the final fundamental, and perhaps the most classical, boundary layer variable measured. Many of the theories developed for subsonic, and then extended to supersonic, boundary layers were developed to predict the velocity profile, and as such the ability to directly and unobtrusively measure it to excellent resolution was invaluable in testing these models. As such the main goal of this campaign was to collect canonical, high-quality data that could be used to compare to past and future hypersonic turbulent boundary layer experiments and models. This included those for the shape and magnitude of the velocity fluctuation profile. The test matrix for this campaign is shown in Table 7.29, and the corresponding plasma conditions in Table 7.29 and Figure 7.98.

No.	Location	Trips	Plasma	Run/Date
1	Forward, wake	Laminar	Off	4672, 3/23/2021
2	Forward, wake	Turbulent	Off	4662, 3/18/2021
3	Forward, trough	Turbulent	Off	4664, 3/19/2021
4	Forward	Laminar	On	4671, 3/23/2021
5	Forward, wake	Turbulent	On	4661, 3/18/2021
6	Forward, trough	Turbulent	On	4663, 3/19/2021
7	Back,wake	Laminar	Off	4652, 3/15/2021
8	Back, wake	Turbulent	Off	4654, 3/16/2021
9	Back, trough	Turbulent	Off	4657, 3/17/2021
10	Back, wake	Laminar	On	4653, 3/15/2021
11	Back, wake	Turbulent	On	4655, 3/16/2021
12	Back, trough	Turbulent	On	4656, 3/16/2021

Table 7.29: PLIF velocimetry test matrix.

No.	Current (mA)	Power Supply Voltage (V)	Power Supply Power (W)	Plasma Voltage (V)	Plasma Power (W)
4	95.0	1444	137.2	490.9	46.6
5	95.2	1437	136.9	482.2	45.9
6	94.6	1433	135.6	484.0	45.8
10	95.1	1447	137.6	493.0	46.9
11	95.0	1436	136.5	483.1	45.9
12	95.1	1438	136.8	483.7	46.0
Average					
	95.0	1439.3	136.8	486.2	46.2

Table 7.30: Plasma conditions for PLIF velocimetry campaign.

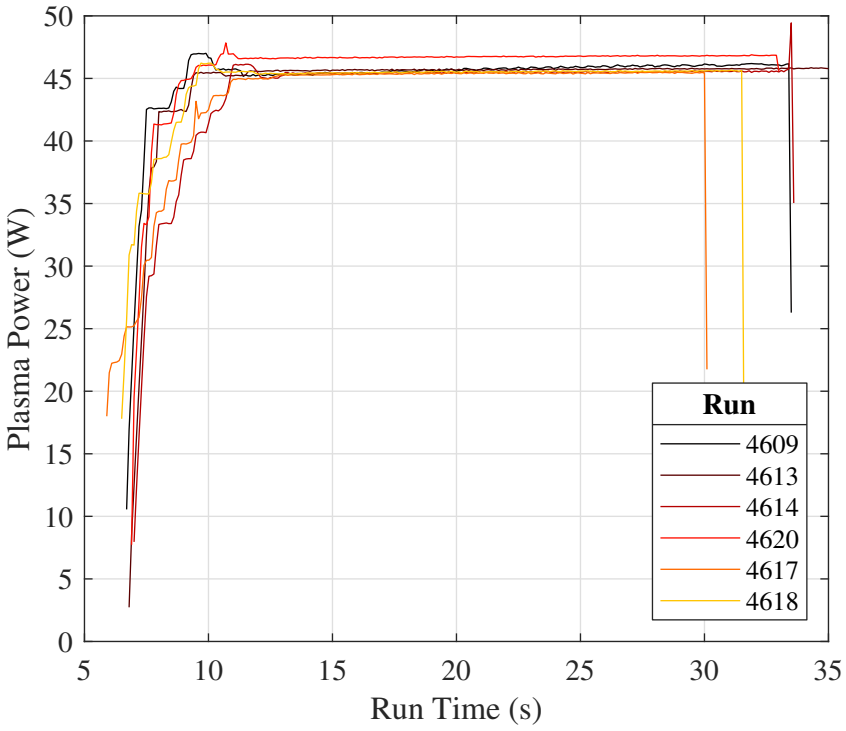

Figure 7.98: Plasma power traces for PLIF velocimetry runs.

While these detailed datasets were valuable on an individual basis, it was perhaps best to first establish general trends by looking at a cumulative comparison of the laminar, turbulent wake, and turbulent trough velocity and fluctuation profiles. These plots are contained in Figure 7.99; here the results from both lines from any given run were drawn with the same style for clarity. In general,

there was no perceptible effect of the plasma, either on the velocity profile or its fluctuations. This further supported the finding in Section 7.4.2.1 that there was little chance of relaminarization owing to $N_2^{v=1}$ relaxation, or any other species for that matter. There also appeared to be a tendency for the velocity profiles to curl towards the wall in an non-physical manner below $\sim$ 1mm from the wall. This, alongside the ostensible slip at the wall, likely stemmed from the challenge in making measurements in the near wall region owing to low signal and high noise; this manifested in the high uncertainty in this region. When reviewing these plots, it was also helpful to remember the theoretical edge velocity calculated by the boundary layer solver was 857.6m/s.

The laminar data in Figure 7.99(a) and (b) shows considerable overlap for all cases, especially after taking into account the uncertainty. In general, however, one can see that the red, downstream traces took slightly longer to reach the edge condition, $\sim$ 4mm as opposed to $\sim$ 2mm for the downstream and upstream cases respectively; these values matched the predicted boundary layer heights from other techniques (ex.- the boundary layer solver), but the lack of clarity underscored the challenge in experimentally determining the boundary layer edge. This problem was somewhat alleviated by the laminar fluctuation profile plot, wherein the departure from the perceived freestream value showed more clearly where the boundary layer started. The greater uncertainty for the upstream case may have been due to the Mach wave coming off the window/PEEK interface 97.9mm from the leading edge. Finally, Buen [49] attributed the gradual decrease in velocity as the flow approaches the boundary layer to the same series of weak Mach waves described in the rotational thermometry results, Section 7.4.2.1.

These trends were more apparent in the turbulent cases. Consider first the wake data, Figures 7.99(c) and (d). The black, upstream profiles initially sat above the red, downstream profiles, but the trend reversed at $\sim$ 3mm. Remember, a turbulent boundary layer velocity profile lays almost flat against the wall, rapidly recovering towards the edge velocity, then shifts to very gradually approach the edge velocity. In laminar boundary layer profiles, this process is more uniform through the boundary layer. These physics were displayed here. Indeed, the two cases did not overlap until $\sim$ 13mm. This was reflected in the fluctuation profile, where in the downstream location the fluc-

tuation profiles departed the edge condition at $\sim$ 13mm and in the upstream case the results more closely matched those from the laminar plot. That being said, as one would expect the magnitude of the fluctuations were larger in the tripped case as opposed to the fully laminar case. As the boundary layer became fully turbulent, the fluctuations should become zero at the wall, but this did not occur, likely due to the high uncertainty in this region. Surprisingly, in the upstream profiles there was little evidence beyond the uncertainty limits of the trip separation/reattachment shock structure, the trips' shear layer, or the wake behavior seen in Section 7.3.5. For these profiles Buen et al. [48] did attribute the slight rise in the velocity from 20 to 15mm above the surface to the expansion after the trip separation/reattachment shock and the decay above the boundary layer to the trips' shear layer. Similarly, the spread of the line-to-line data for a single run may have owed partially to the lines' $5-10$mm streamwise separation in the highly transitional region.

The trough data in Figures 7.99(e) and (f) followed the same general trends. These data appeared far more orderly, but whether this was due to the fact the trips' effects should have been weaker or there were fewer analyzable lines was unclear.

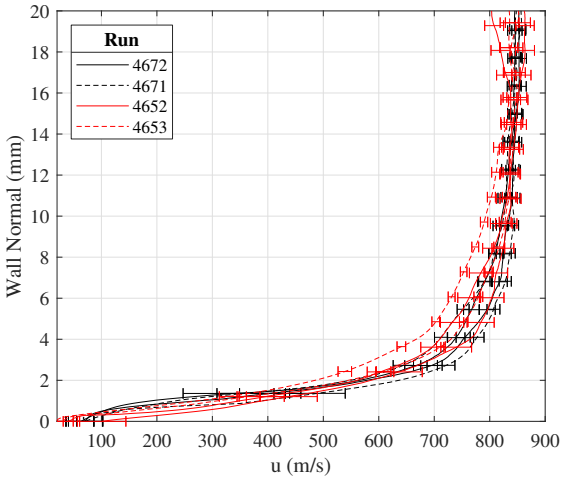

(a) Laminar, velocity

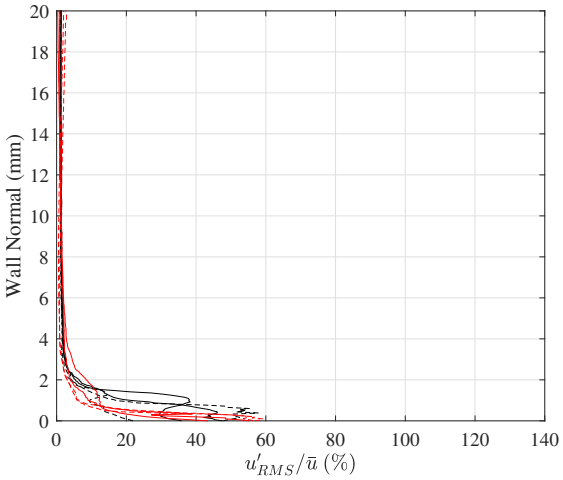

(b) Laminar, fluctuation

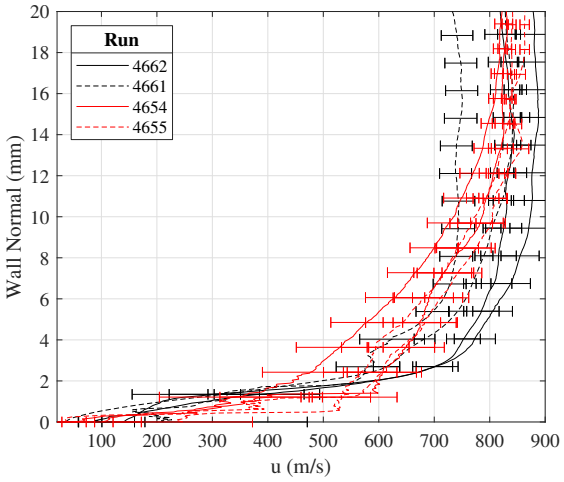

(c) Turbulent wake, velocity

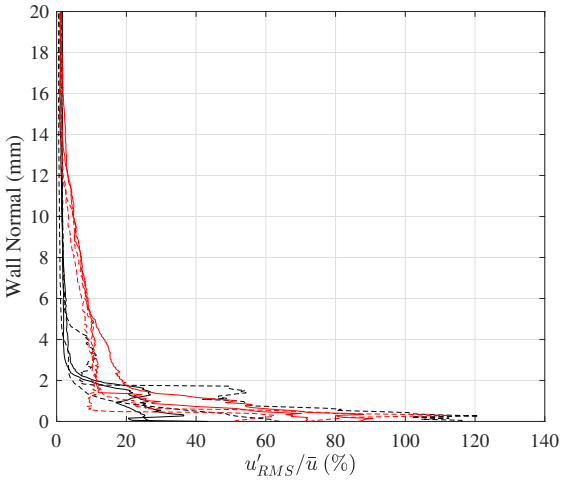

(d) Turbulent wake, fluctuation

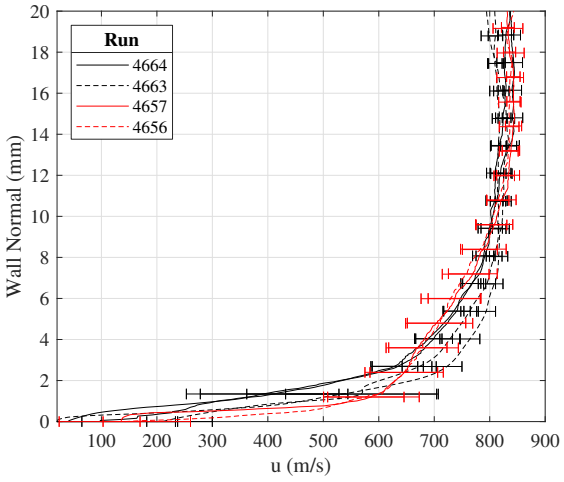

(e) Turbulent trough, velocity

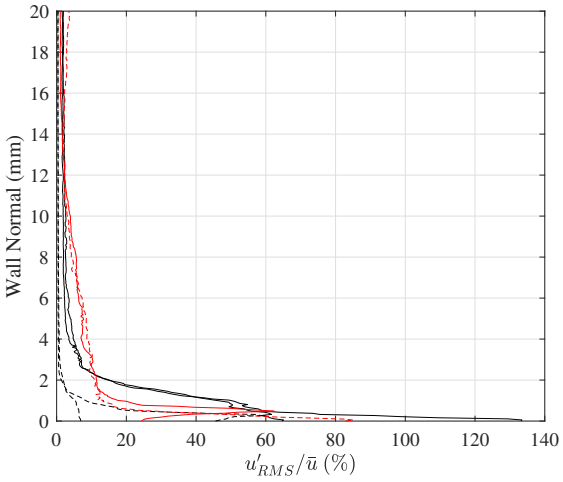

(f) Turbulent trough, fluctuation

Figure 7.99: PLIF MTV velocity and fluctuation profile comparison.

The full dataset available from each run are contained in Figures 7.100-7.111. "Write" and "Read" images are shown as they appeared out of the ICCD, the only processing being image rotation and cropping. These images underscored several experimental challenges, including: low signal near the wall; strong reflections despite the anti-reflective coating; "hot spots" on the wall from dust, burn marks, damage, *etc.* causing excessive scatter; excitation of naturally occurring vibrationally excited NO in the read images; beam spreading (the beams' waists were usually set just above the cameras' field of view). For example, the strong signal of one line could be independent of that of the other, which for Runs 4657 and 4656 manifested as only one line having sufficient accuracy for worthwhile analysis. This also meant that some of the raw images shown below appeared either too dark or too saturated, as a balance was attempted to be struck for clearly showing both lines with just one color bar; when analyzing the data, each line was separately identified using its own region of interest (see [49]). In such instances when the line locations were unclear, it is recommended to defer to the mean line location plot.

For each run, the two lines' velocity and fluctuation profiles were shown. Again, for the mean fluctuation profiles the RMS average of the temporally-fluctuating velocities $u' = u - \overline{u}$ was shown as, by definition, $\overline{u'} = 0$. Recall from Section 6.6 that during the Pitot pressure campaign, the measured Mach number was used in the second Crocco-Busemann relation to calculate the temperature profile, and from these two parameters provided the velocity profile. An analogous process was implemented here; the velocity profile for each line was inputted into Equation 2.24, and then the Mach number came from $M = u/\sqrt{\gamma R_{air} T}$. Hereafter, these parameters will be referred to as T_{C-B} and M_{C-B} respectively. Of course, here one could skip the estimation of the temperature profile and interpolate the ro-translational thermometry data from Section 6.6; in this way, one could validate the Crocco-Busemann theory. These results are subsequently denoted T_{PLIF} and M_{PLIF}. In these calculations, uncertainties were calculated by finding the extrema for the ratios in each calculation. For example,

$$T_{C-B,\,low} = T_w + (T_{aw} - T_w)\frac{u - u_{unc}}{u_e - u_{e,\,unc}} + (T_e - T_{aw})\left(\frac{u - u_{unc}}{u_e - u_{unc,\,e}}\right)^2 \tag{7.3}$$

$$M_{C-B,low} = \frac{u - u_{unc}}{\sqrt{\gamma R_{air}(T_{C-B,low})}} \tag{7.4}$$

The process was reversed for the upper limit. Due to the relatively large uncertainties, and the sensitivity of Mach number to both temperature and velocity, the more conservative approach in Section 7.3.5 yielded nonphysical results.

This form of the Crocco-Busemann equation was used because it guaranteed that at the edge of the boundary layer $u = u_e$ and $T = T_e$, regardless of data coming from different sources (PLIF thermometry, PLIF MTV, NALDAQ/theory, *etc.*); for example, T_e was set using oblique shock relations [128] and NALDAQ data for consistency with the Pitot data reduction (Section 6.6), and T_w was set from the PLIF thermometry as no single wall temperature value was hard-coded into Buen's [49] analysis. Again, for simplicity when comparing the reduced data, this was the same form used in Section 7.3.5. The adiabatic wall temperature was calculated using the PLIF results for the "PLIF" dataset, and from the NALDAQ/shock jump equations for the "C-B" dataset. This step was important, as it meant that the PLIF and Crocco-Busemann results could have different T_e, and thus different profiles. This discrepancy manifested in the data, and will be discussed shortly. Note that in the "Turbulent/Front" case, the flow was transitional, not turbulent, so using r_{turb} in T_{aw} became an unwanted but necessary approximation.

The results contained in Figures 7.100-7.111 matched the general trends discussed for Figure 7.99, but with greater clarity. Because MTV is conceptually straightforward, it was instructive to look at the raw images, then observe how the computer interpreted them in order to understand certain features; for example, the curling behavior of the velocity profiles near the wall most likely arose from ambiguity in the "Read" images.

The Crocco-Busemann-derived temperature plots differed significantly from the PLIF results. For the laminar cases, the results were decent, albeit inconsistent, below $\sim$ 6mm; even the transitional ("Turbulent/Front") boundary layers had some agreement between the two techniques despite the use of r_{turb} in T_{aw}. This was no doubt helped by the decision to use $T_{w,PLIF}$ to anchor the Crocco-Busemann results. In the fully turbulent cases, the PLIF results more gradually approached T_w, almost with a laminar profile shape. The Crocco-Busemann results, however, under predicted

these temperatures and recovered the bulk of the temperature below $\sim$ 2mm, where unfortunately the velocity data had the highest uncertainty. In general, the Crocco-Busemann profile matched the velocity data due to its explicit dependence on $\frac{u}{u_e}$. In the freestream, $T_{e,C-B} < T_{e,PLIF}$ owing to the different scaling used for the two techniques. This discrepancy led, at least in part, to the poor agreement elsewhere in the curve. The higher-than-expected value for $T_{e,PLIF}$ were discussed in Section 7.4.2.1.

Because it is a function of $\sqrt{T}$ and scales between $0-6$ instead of $360-60$K, the Mach number appeared somewhat insulated from the discrepancies in the temperature profiles. In the "Front" test locations, the profiles from at least one of the laser lines fell within the uncertainties of the PLIF and Crocco-Busemann techniques typically up to $\sim$ 5mm, and for the "Back" locations this agreement could extend up to $\sim$ 10mm. In the freestream, however, the significantly higher $T_{e,PLIF}$ drove the Mach number down to $M \approx 4.5$. The error did not stem from a lower-than-expected u_e, as in most cases u_e fell only $1-3\%$ lower than the ideal 857.6m/s, and they did reach this value including their uncertainty. Before calling M_{C-B} a resounding success, one must remember T_e was set using the theoretical result, so any agreement it had in the freestream was more a testament to the velocity data than the temperature results. Further discussion and validation of these data and theories using the Pitot probe's results is included in Section 7.5.

As a final note, in some figures (ex.- Figure 7.106(f), Run 4652), the Mach number grew erroneously high before curling back to the expected edge value. This stems back to the specific shape of the velocity profile. For whatever reason (freestream shocks, wide beams, *etc.*) the velocity profile decayed in the freestream, meaning $u_{max} \neq u_e$. However, Crocco-Busemann forces the temperature to T_e at the edge of the boundary layer, and derives temperature profile's shape entirely from the velocity profile. So, $\frac{u}{u_e} > 1$, when entered into Equation 2.24, yields $T < T_e$, a nonphysical result under the current context. For the present example, this produced $T_{min} \approx \frac{1}{2}T_e$, which, despite the $\sqrt{T}$ dependency, had a large effect on the Mach number. Thus the Mach number axes were not extended above $M = 6$ because anything above this threshold far exceeded even the nozzle's maximum Mach number and was therefore erroneous.

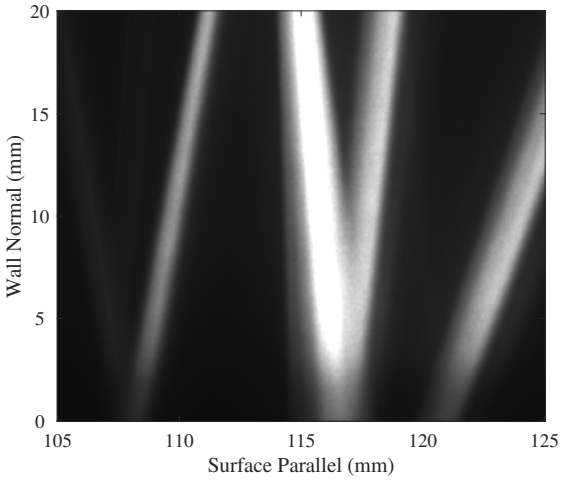

(a) Mean write image

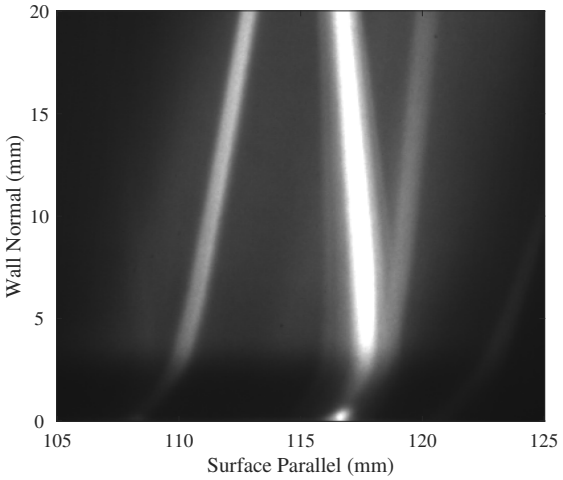

(b) Mean read image

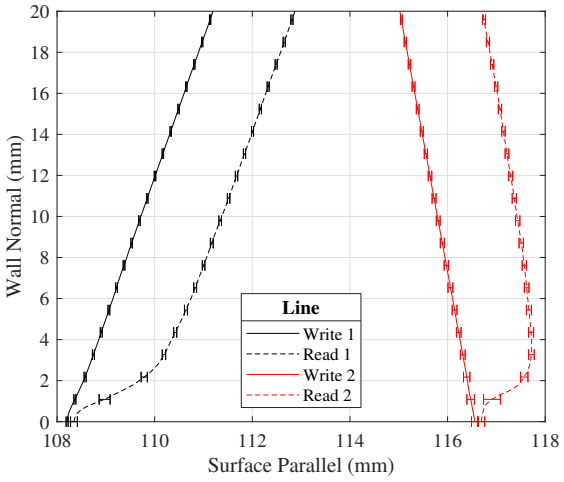

(c) Mean line locations

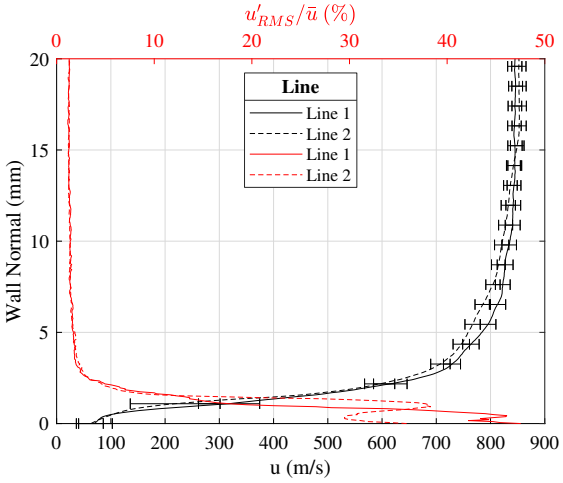

(d) Mean velocity and fluctuation profiles

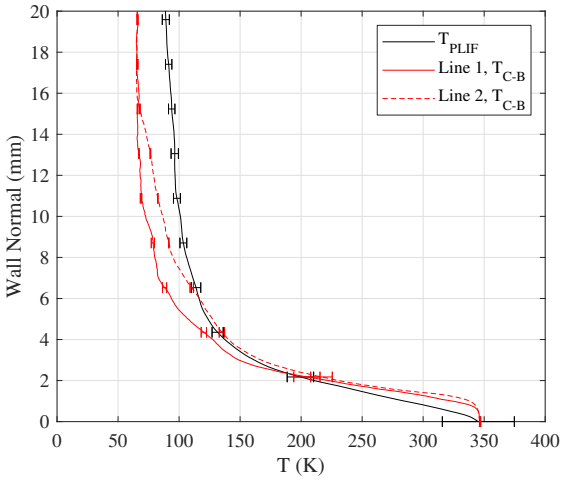

(e) Mean temperature profiles

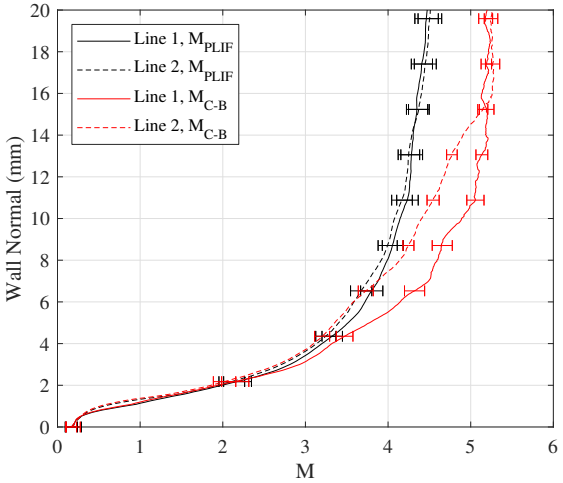

(f) Mean Mach number profiles

Figure 7.100: PLIF MTV, Run 4672: upstream; laminar; plasma off.

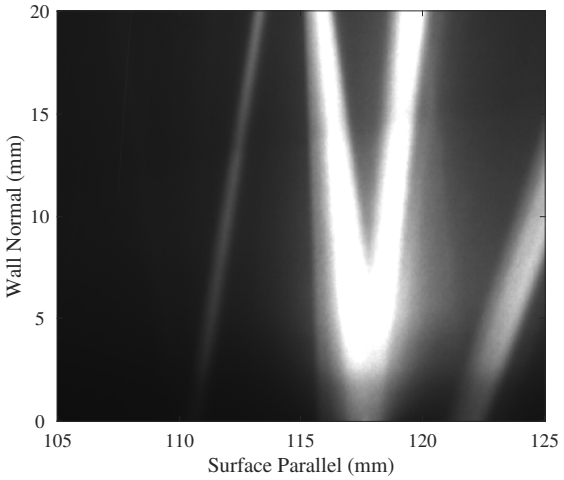

(a) Mean write image

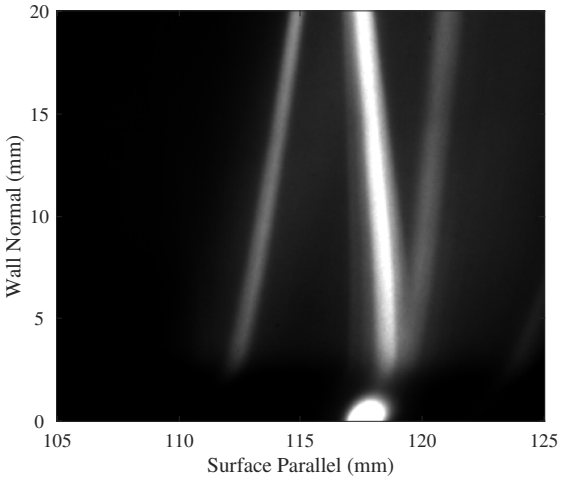

(b) Mean read image

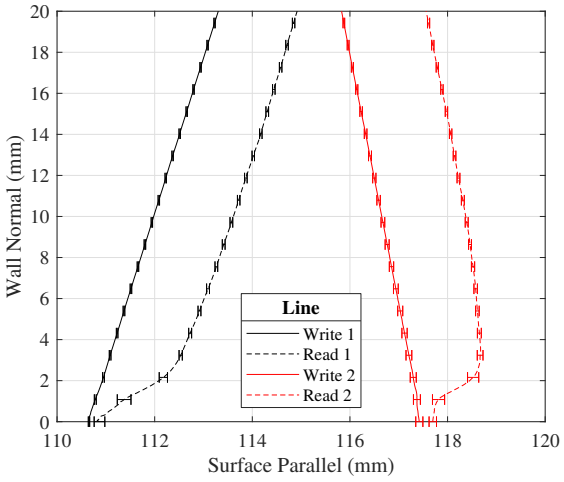

(c) Mean line locations

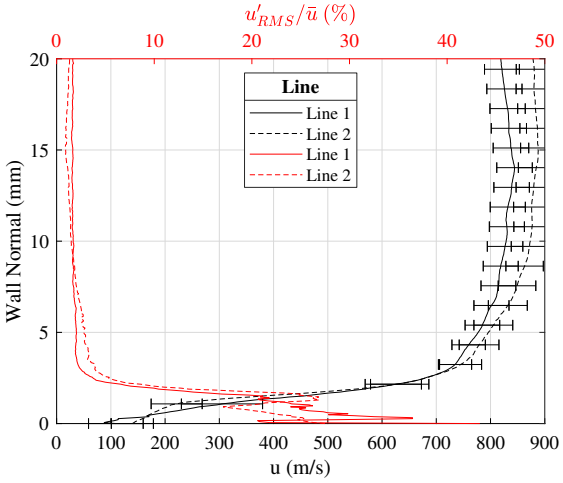

(d) Mean velocity and fluctuation profiles

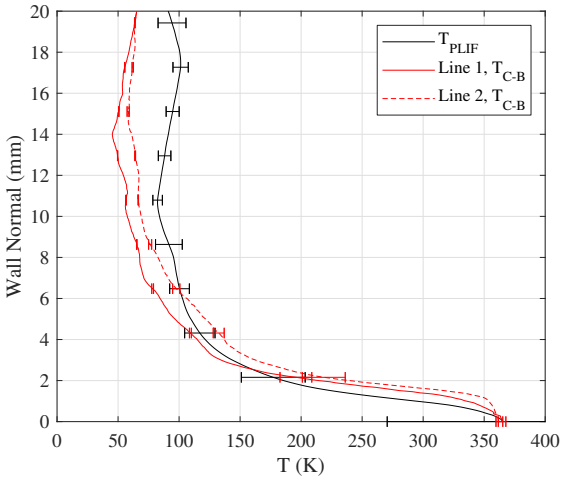

(e) Mean temperature profiles

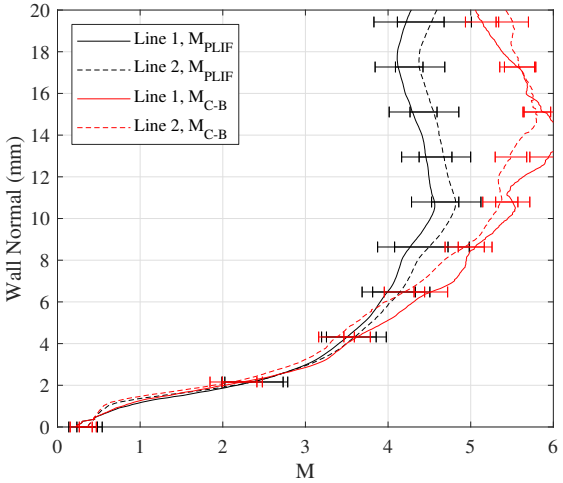

(f) Mean Mach number profiles

Figure 7.101: PLIF MTV, Run 4662: upstream; turbulent wake; plasma off.

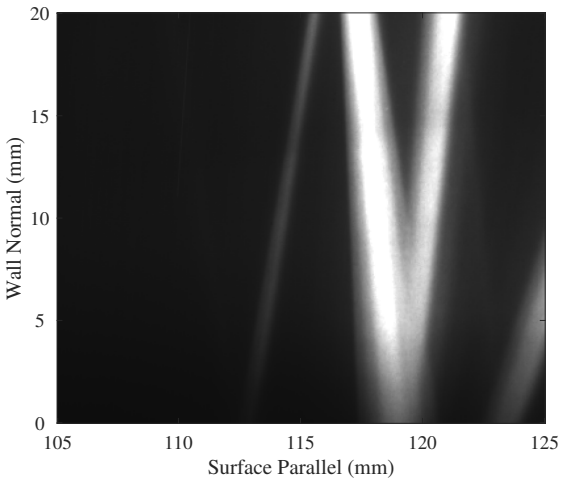

(a) Mean write image

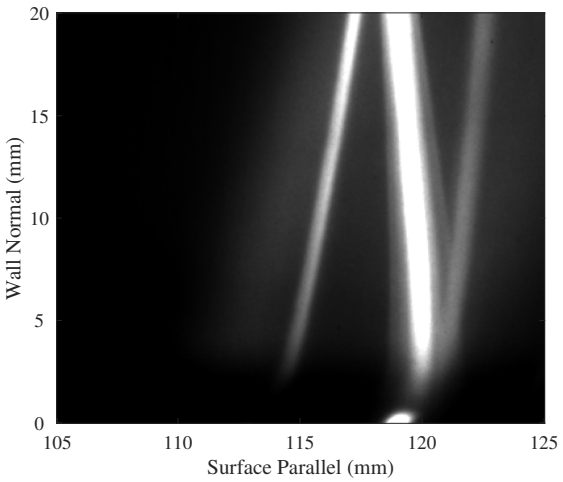

(b) Mean read image

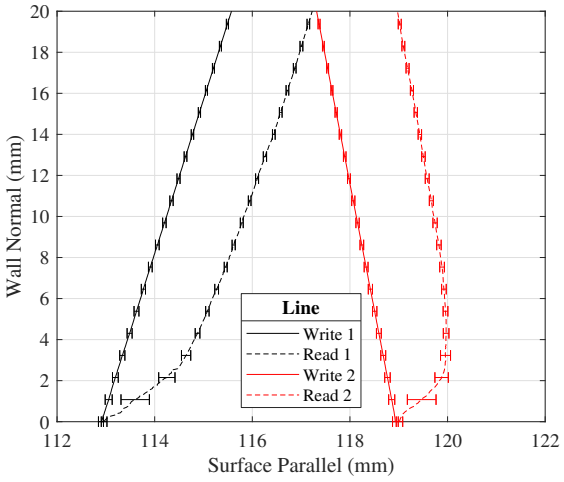

(c) Mean line locations

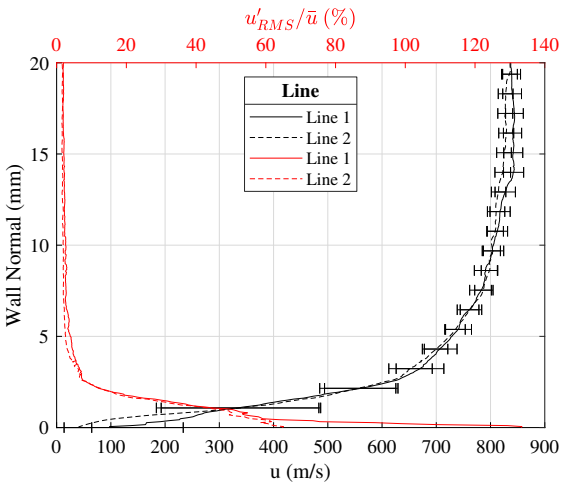

(d) Mean velocity and fluctuation profiles

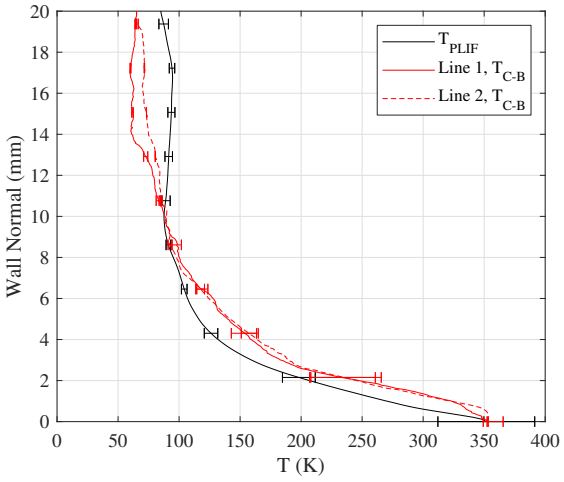

(e) Mean temperature profiles

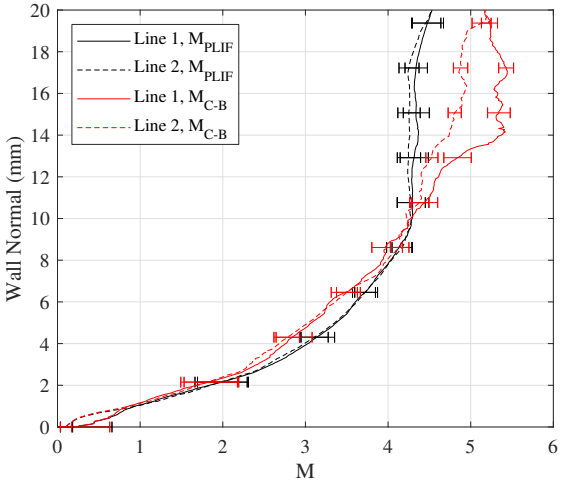

(f) Mean Mach number profiles

Figure 7.102: PLIF MTV, Run 4664: upstream; turbulent trough; plasma off.

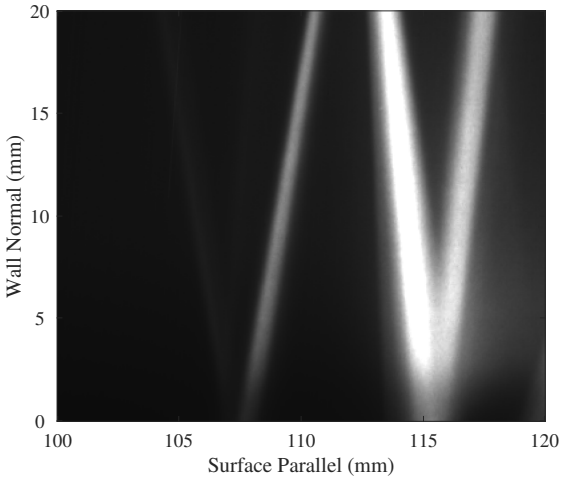

(a) Mean write image

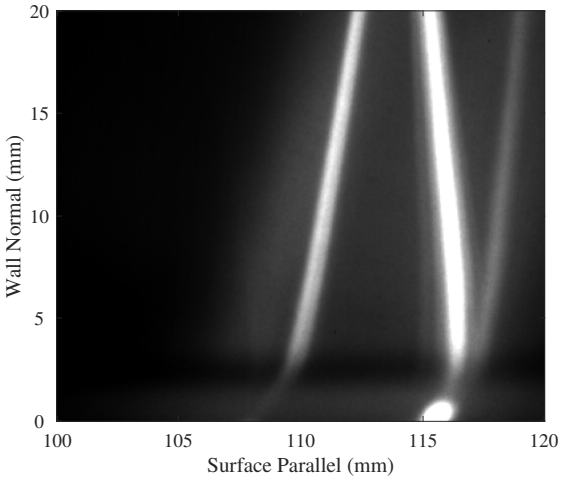

(b) Mean read image

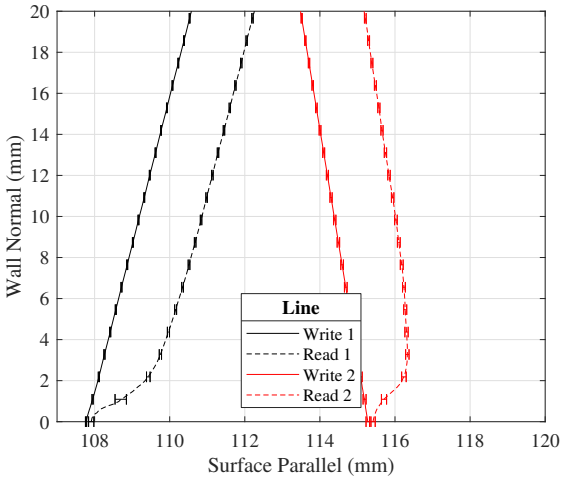

(c) Mean line locations

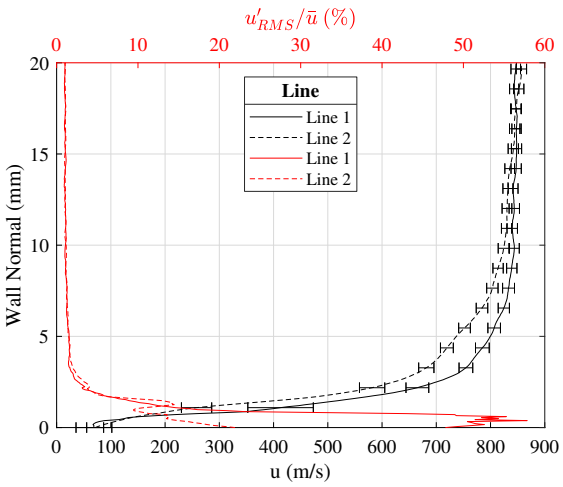

(d) Mean velocity and fluctuation profiles

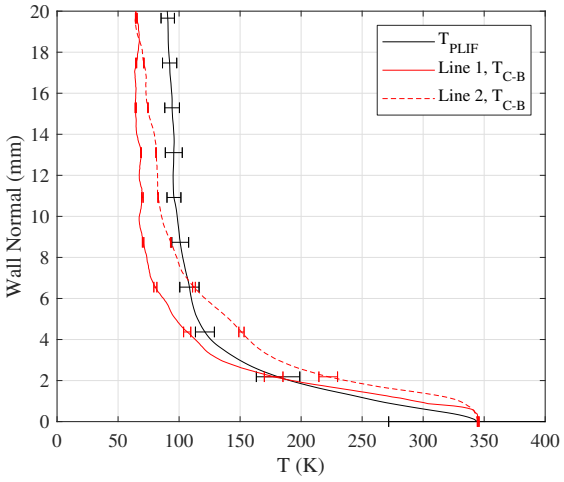

(e) Mean temperature profiles

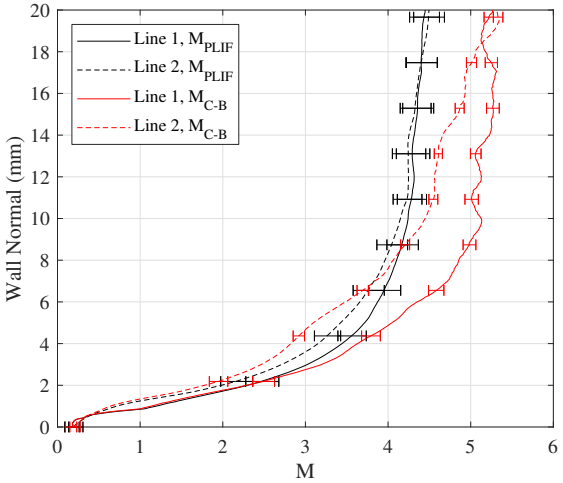

(f) Mean Mach number profiles

Figure 7.103: PLIF MTV, Run 4671: upstream; laminar; plasma on.

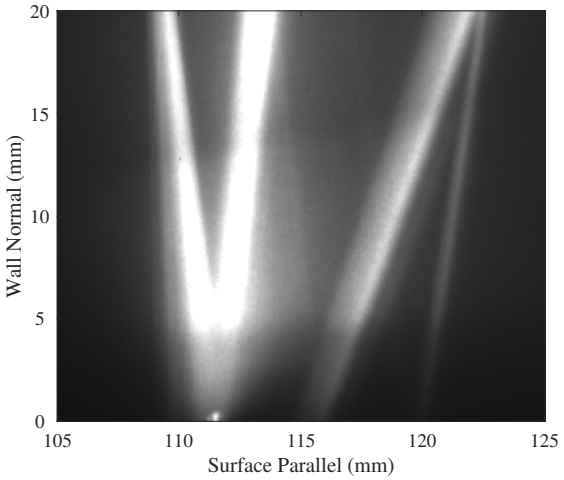

(a) Mean write image

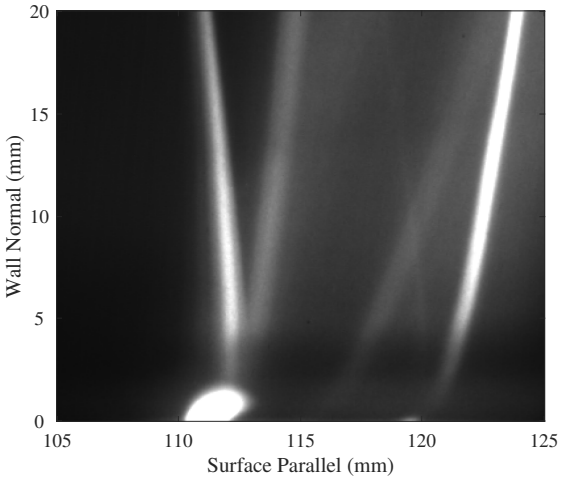

(b) Mean read image

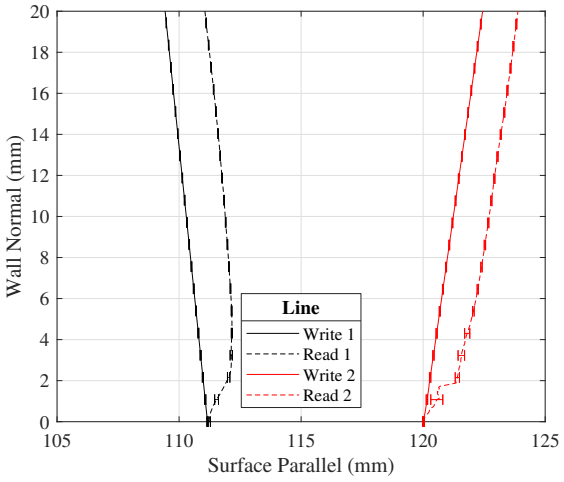

(c) Mean line locations

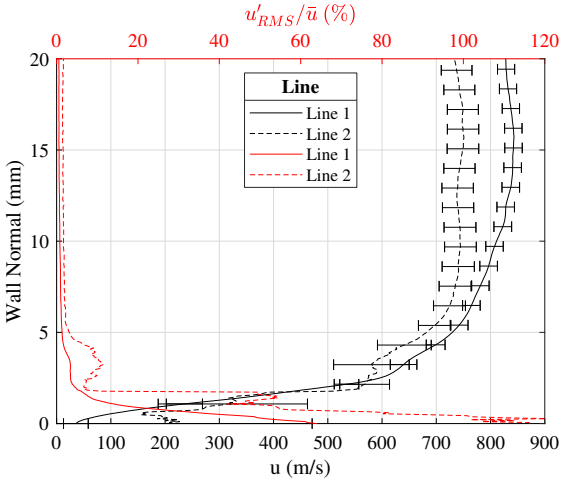

(d) Mean velocity and fluctuation profiles

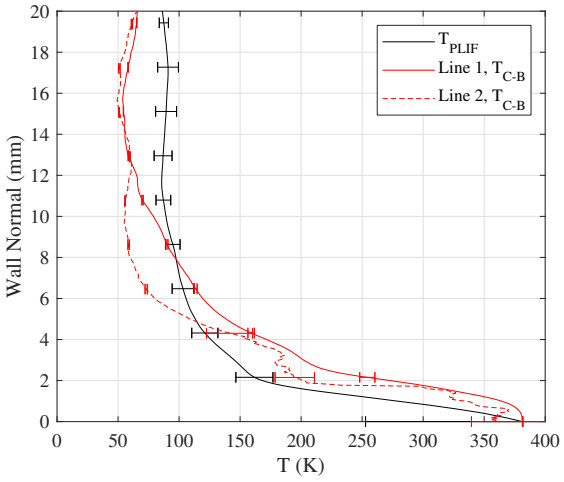

(e) Mean temperature profiles

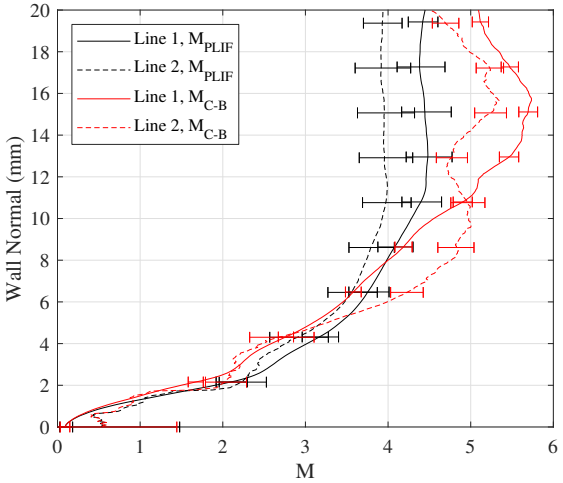

(f) Mean Mach number profiles

Figure 7.104: PLIF MTV, Run 4661: upstream; turbulent wake; plasma on.

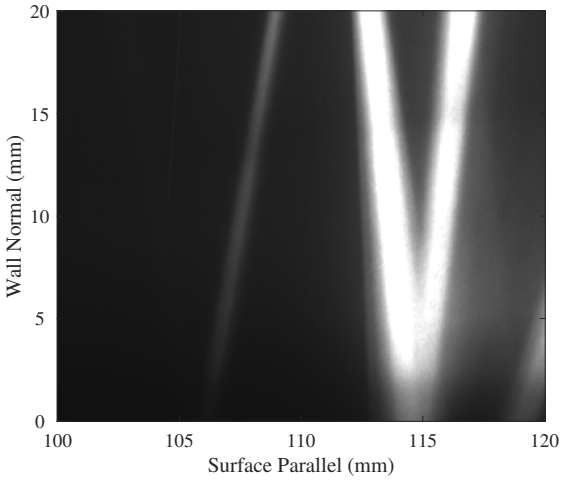

(a) Mean write image

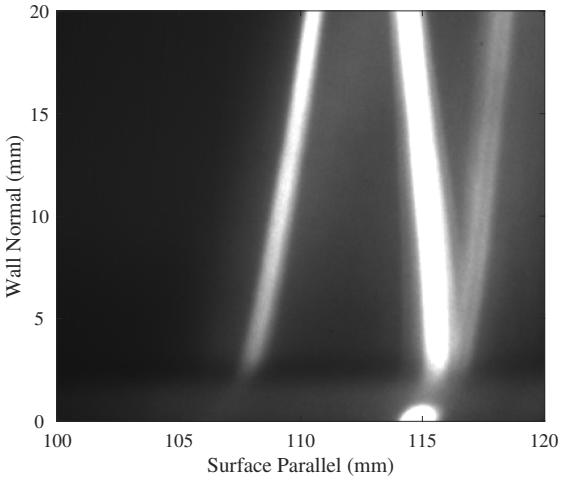

(b) Mean read image

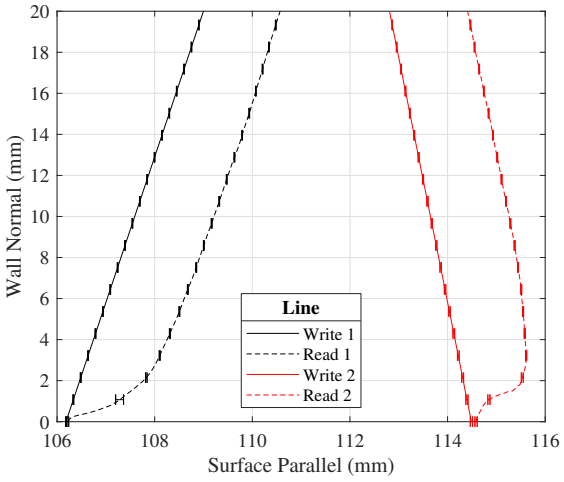

(c) Mean line locations

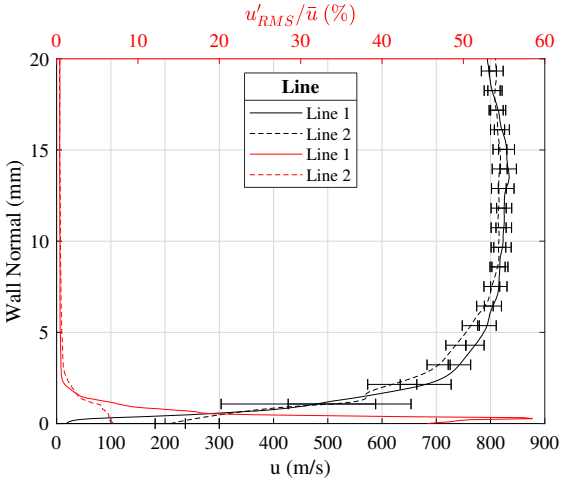

(d) Mean velocity and fluctuation profiles

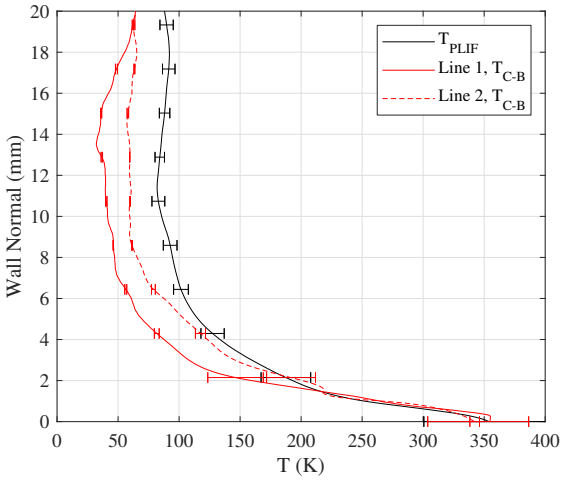

(e) Mean temperature profiles

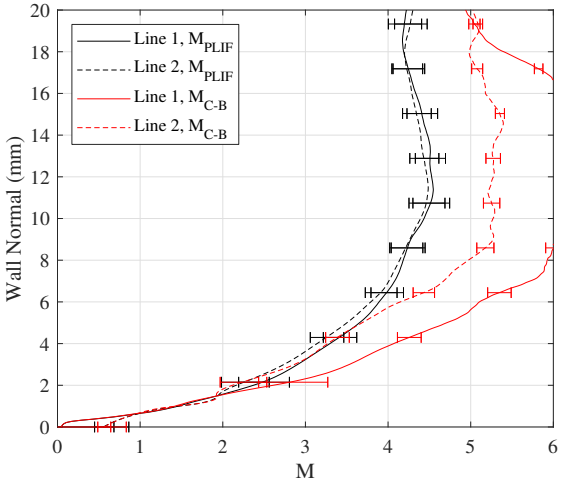

(f) Mean Mach number profiles

Figure 7.105: PLIF MTV, Run 4663: upstream; turbulent trough; plasma on.

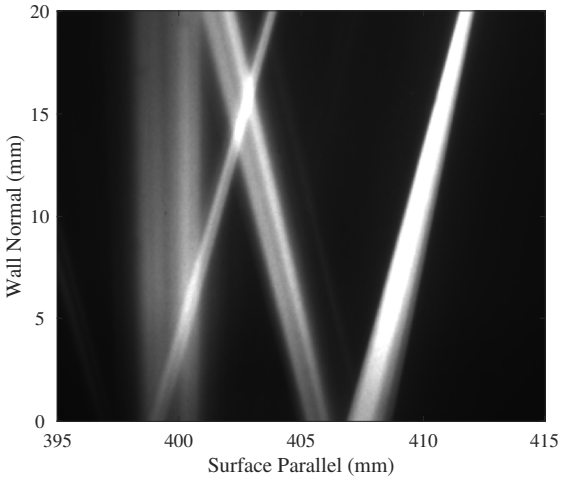

(a) Mean write image

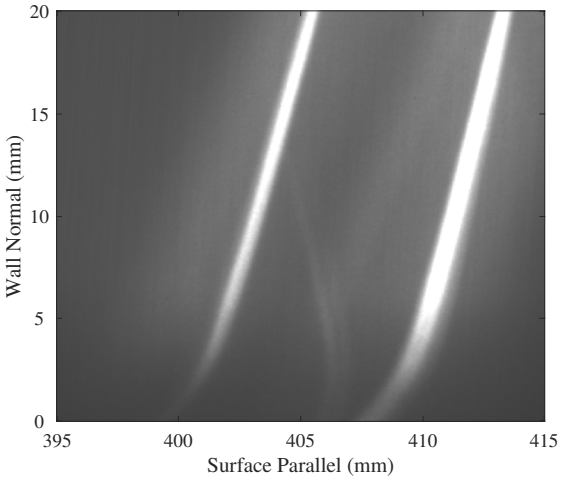

(b) Mean read image

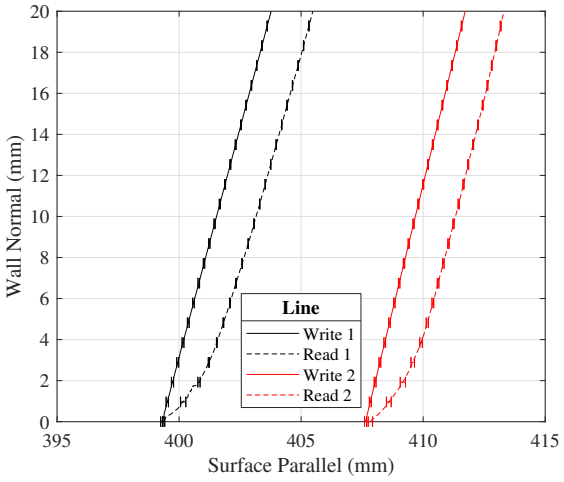

(c) Mean line locations

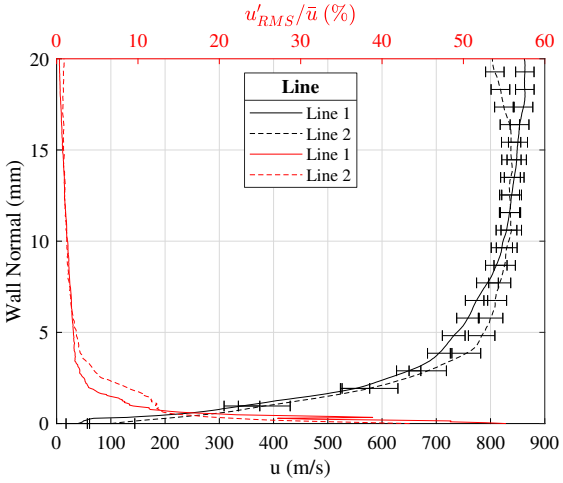

(d) Mean velocity and fluctuation profiles

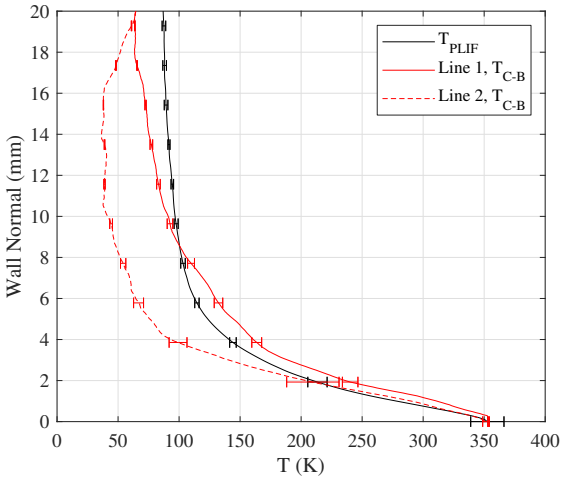

(e) Mean temperature profiles

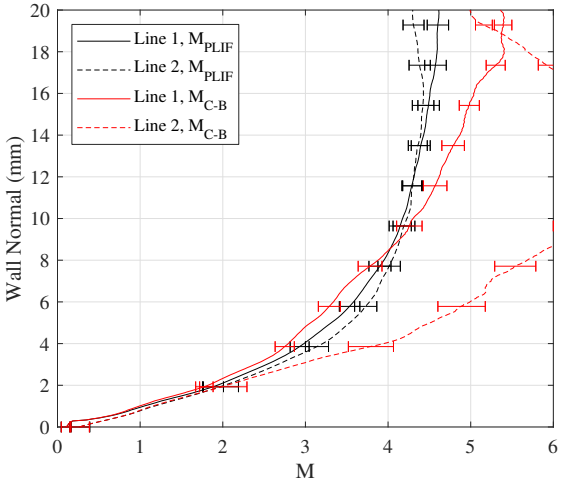

(f) Mean Mach number profiles

Figure 7.106: PLIF MTV, Run 4652: downstream; laminar; plasma off.

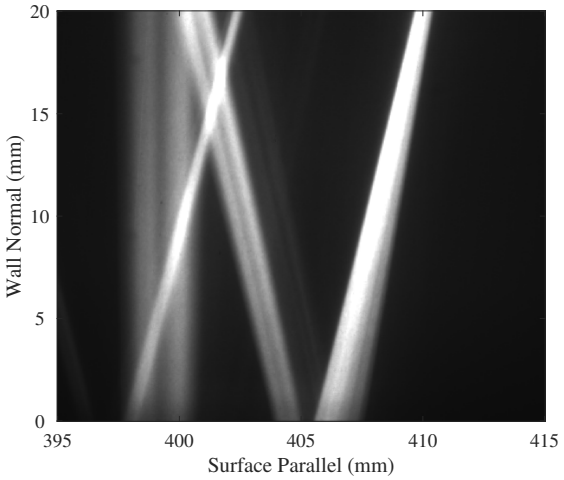

(a) Mean write image

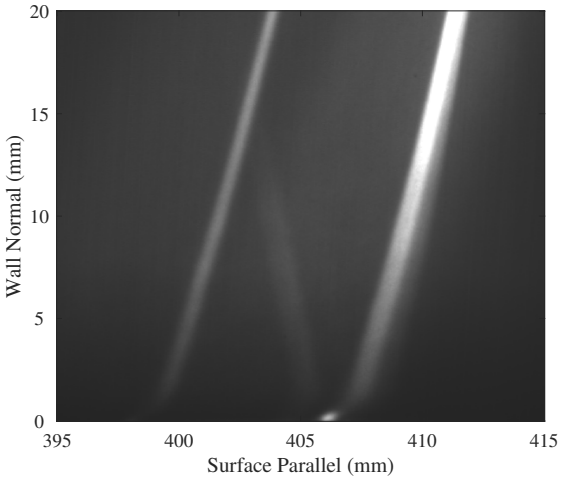

(b) Mean read image

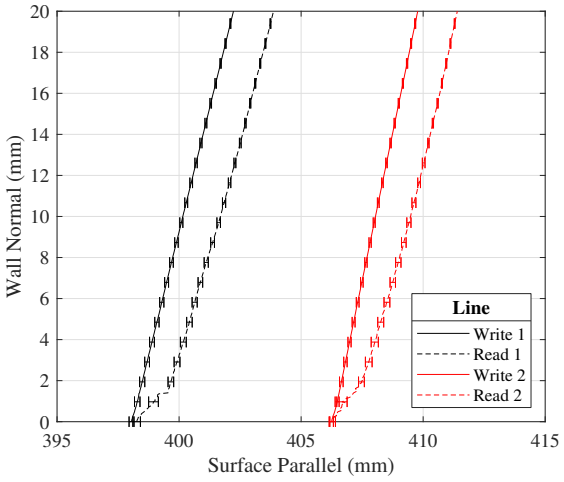

(c) Mean line locations

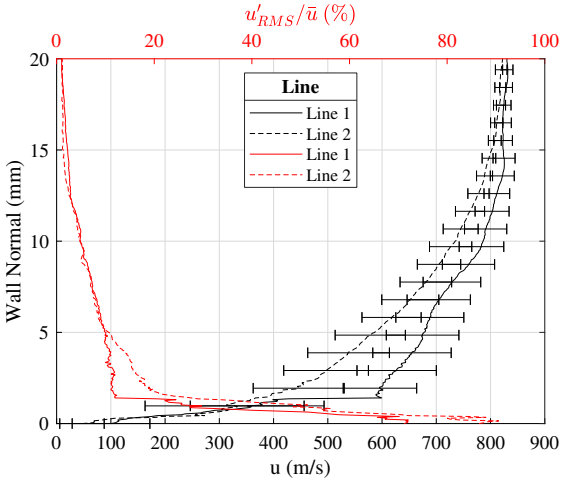

(d) Mean velocity and fluctuation profiles

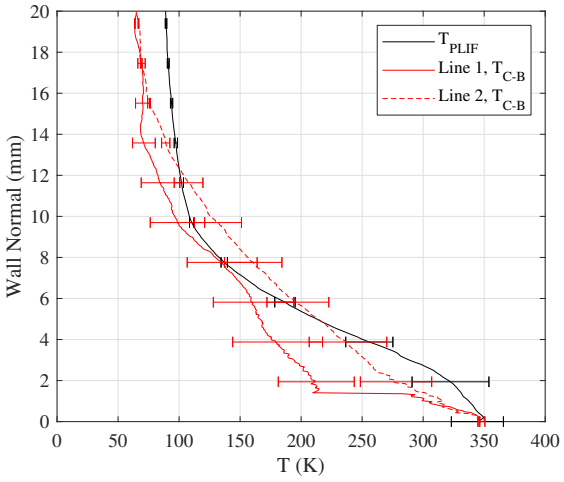

(e) Mean temperature profiles

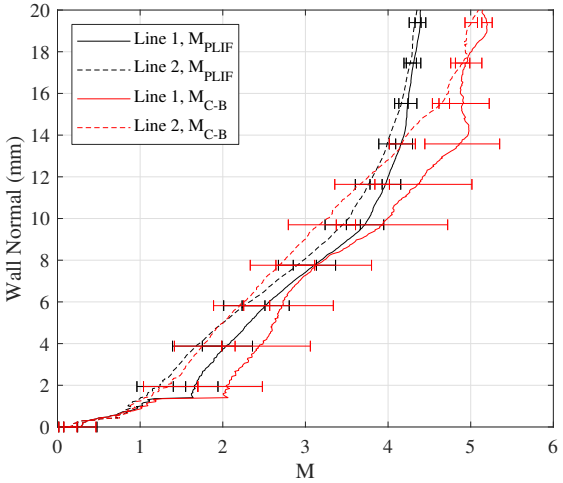

(f) Mean Mach number profiles

Figure 7.107: PLIF MTV, Run 4654: downstream; turbulent wake; plasma off.

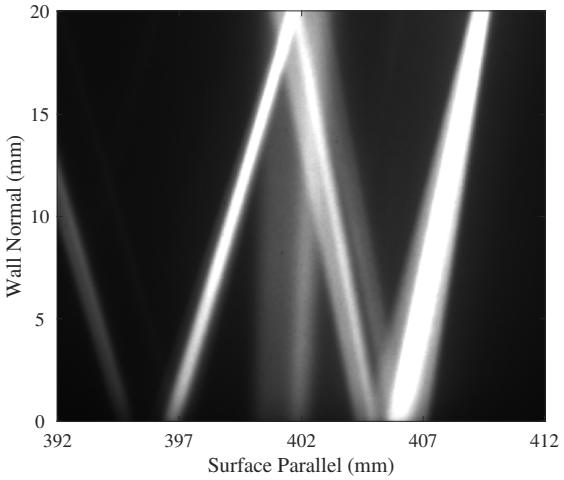

(a) Mean write image

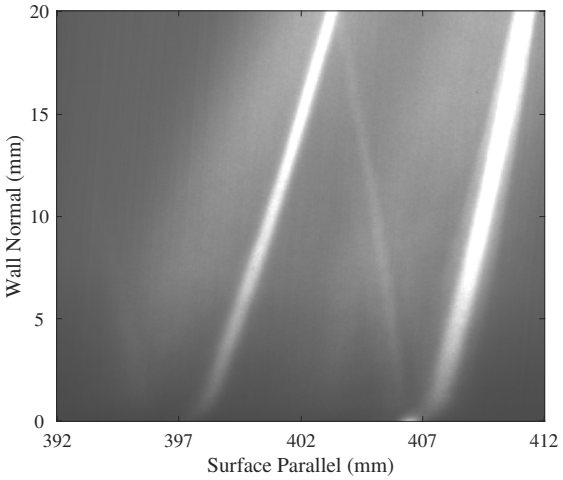

(b) Mean read image

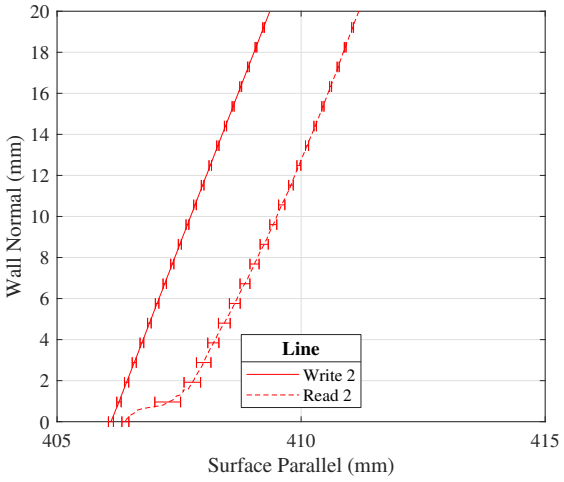

(c) Mean line locations

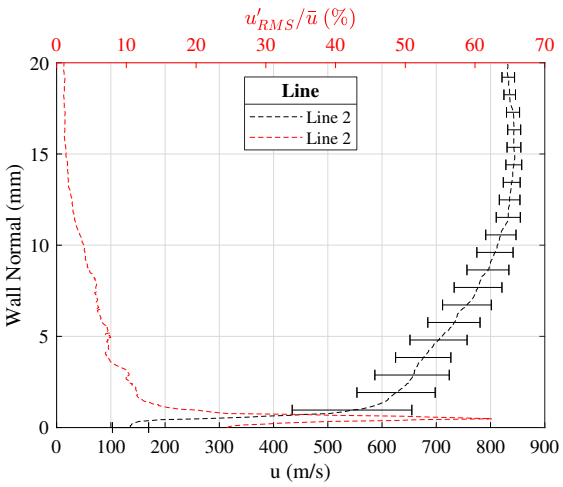

(d) Mean velocity and fluctuation profiles

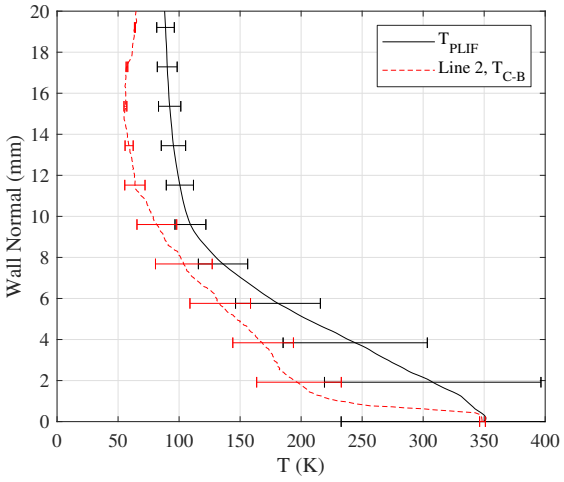

(e) Mean temperature profiles

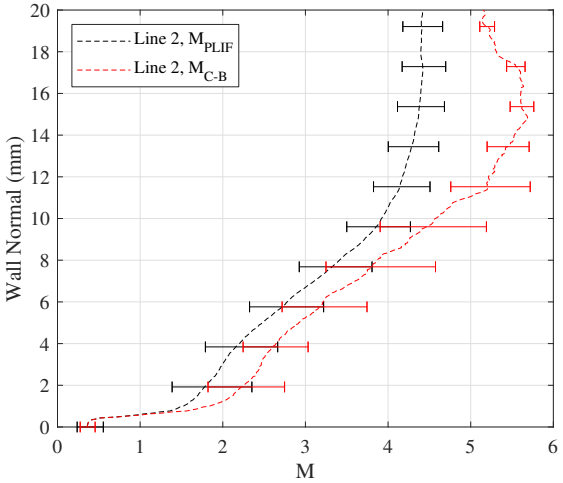

(f) Mean Mach number profiles

Figure 7.108: PLIF MTV, Run 4657: downstream; turbulent trough; plasma off.

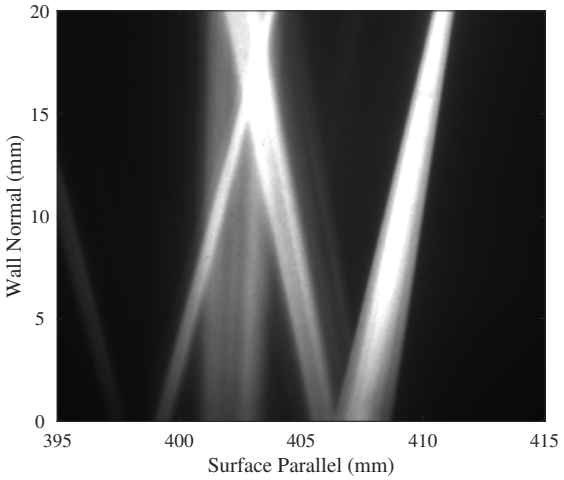

(a) Mean write image

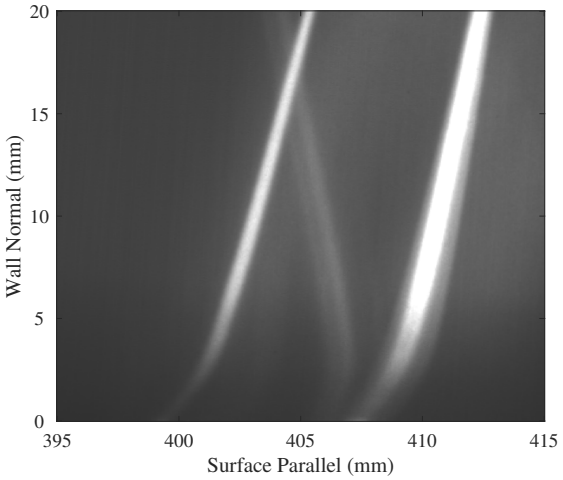

(b) Mean read image

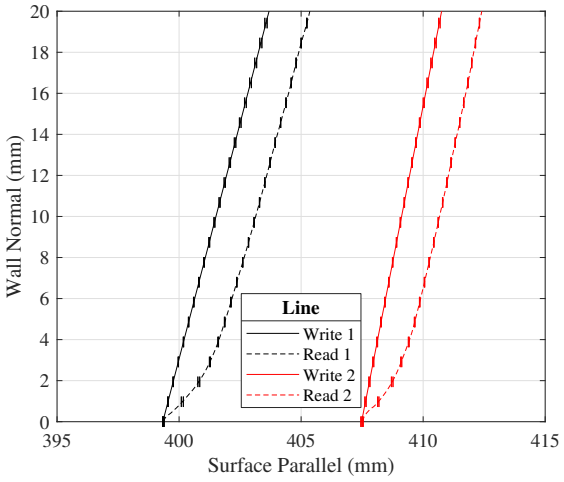

(c) Mean line locations

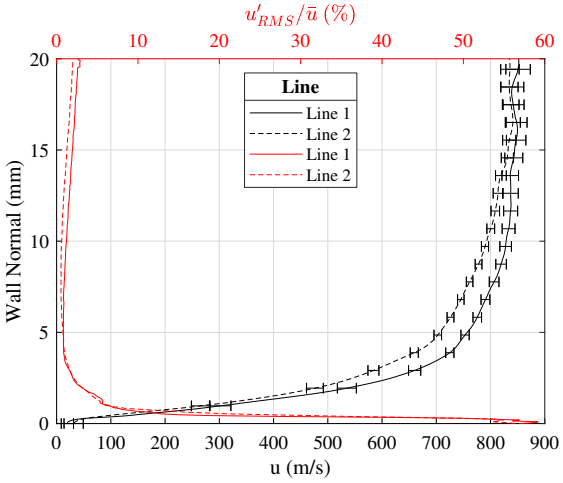

(d) Mean velocity and fluctuation profiles

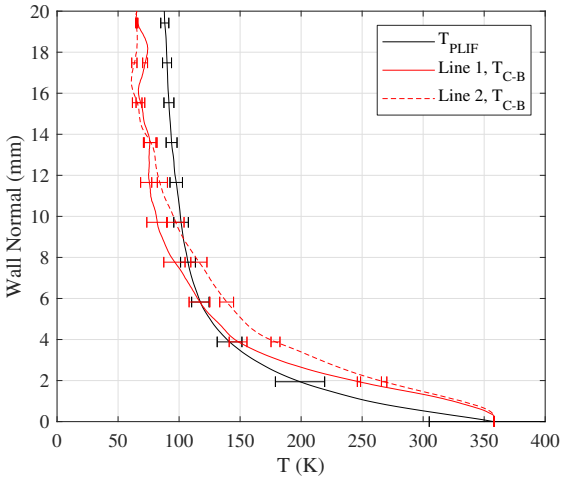

(e) Mean temperature profiles

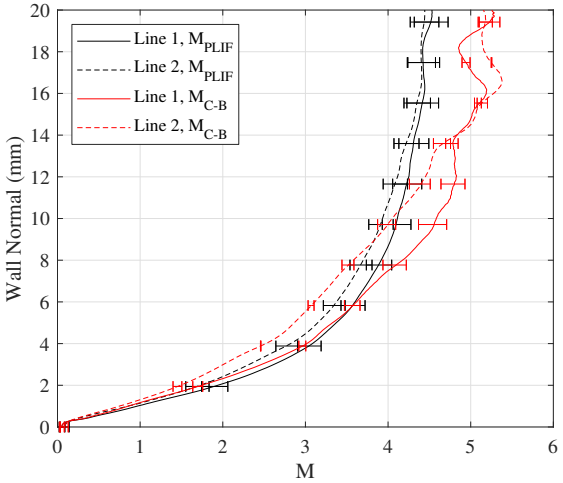

(f) Mean Mach number profiles

Figure 7.109: PLIF MTV, Run 4653: downstream; laminar; plasma on.

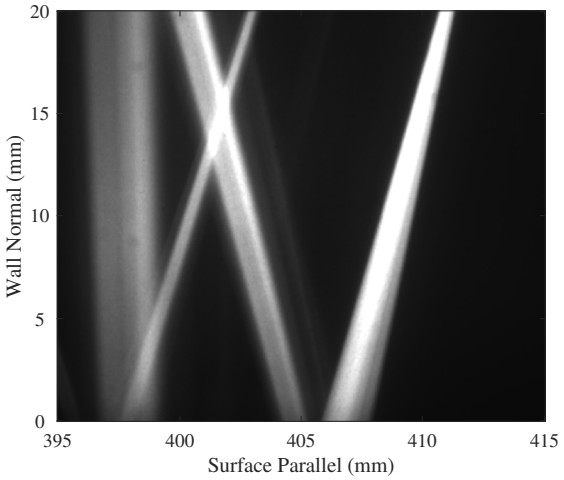

(a) Mean write image

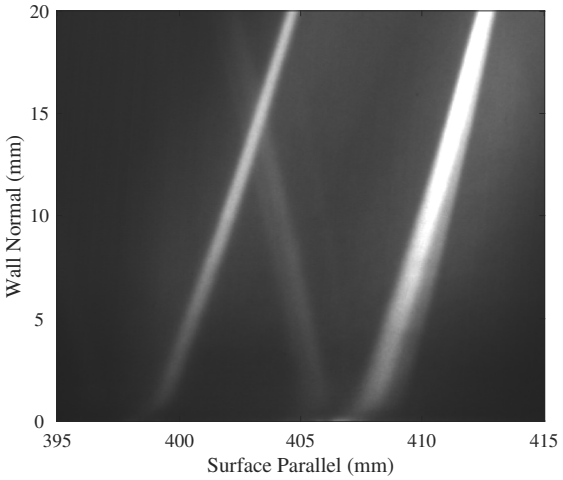

(b) Mean read image

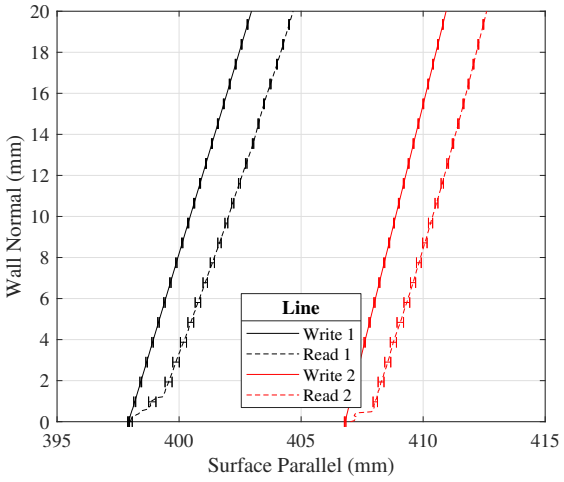

(c) Mean line locations

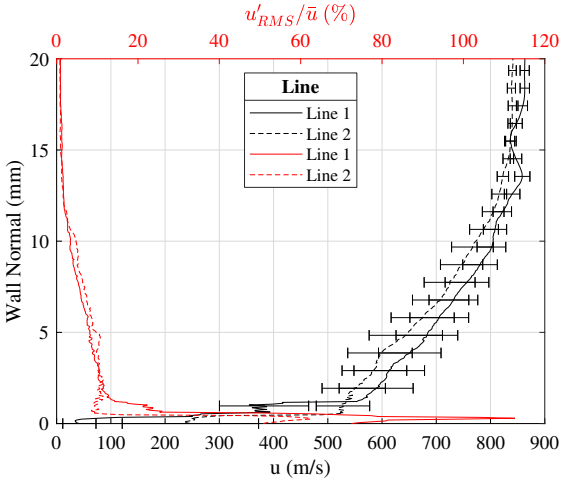

(d) Mean velocity and fluctuation profiles

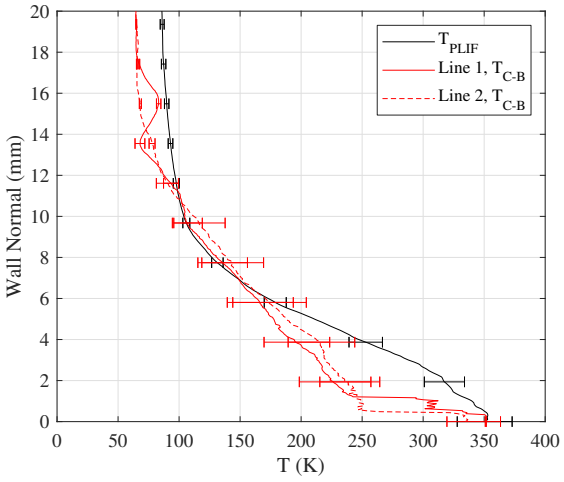

(e) Mean temperature profiles

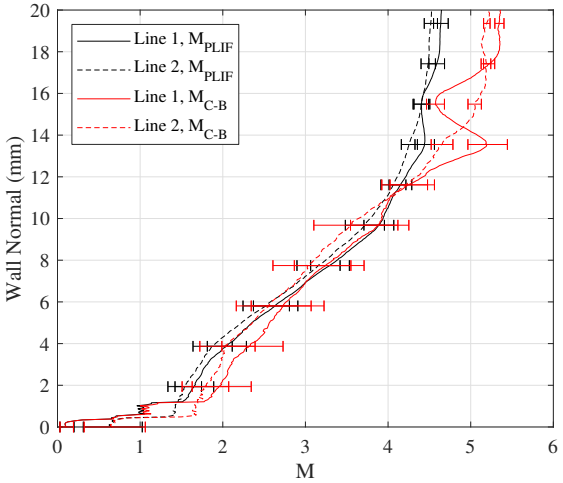

(f) Mean Mach number profiles

Figure 7.110: PLIF MTV, Run 4655: downstream; turbulent wake; plasma on.

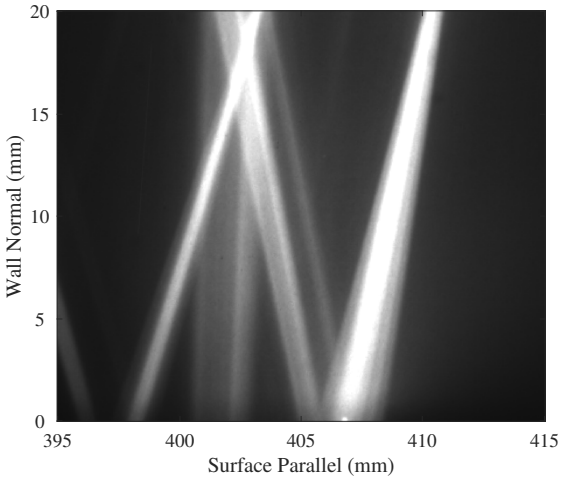

(a) Mean write image

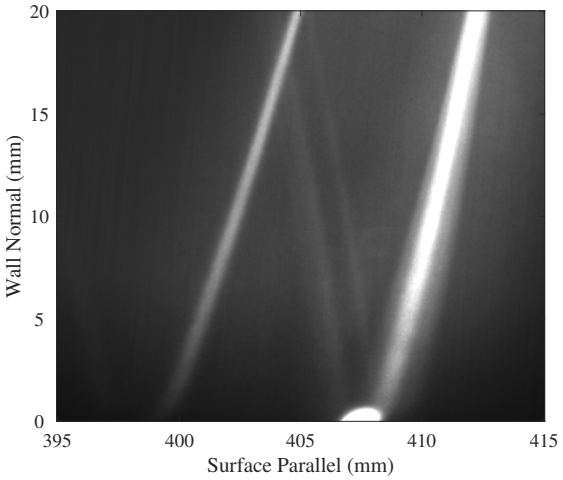

(b) Mean read image

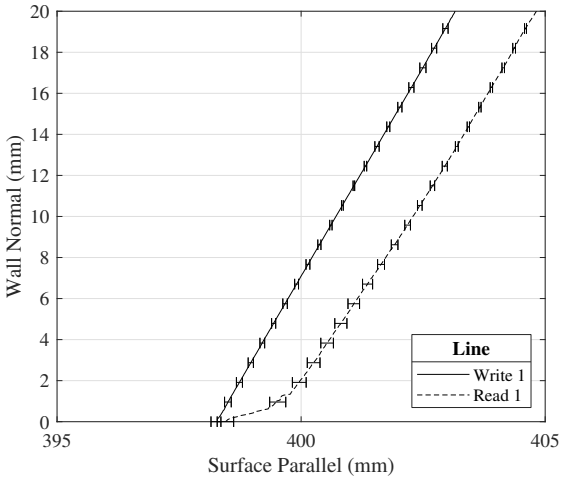

(c) Mean line locations

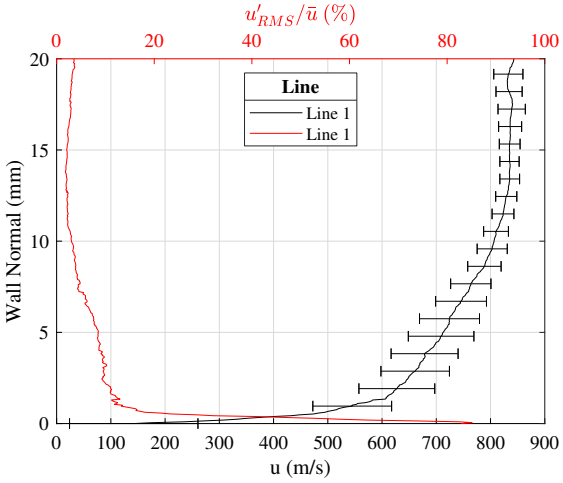

(d) Mean velocity and fluctuation profiles

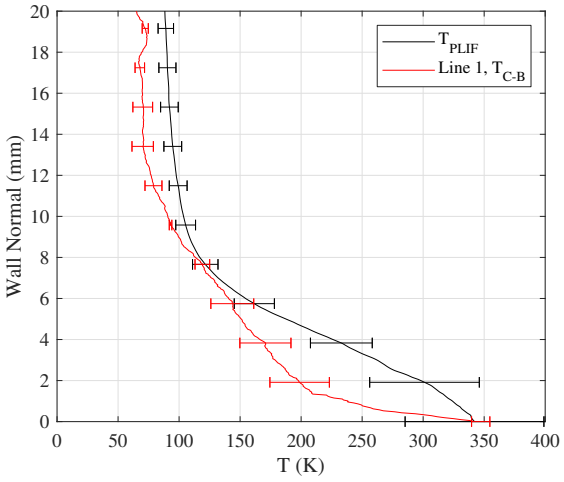

(e) Mean temperature profiles

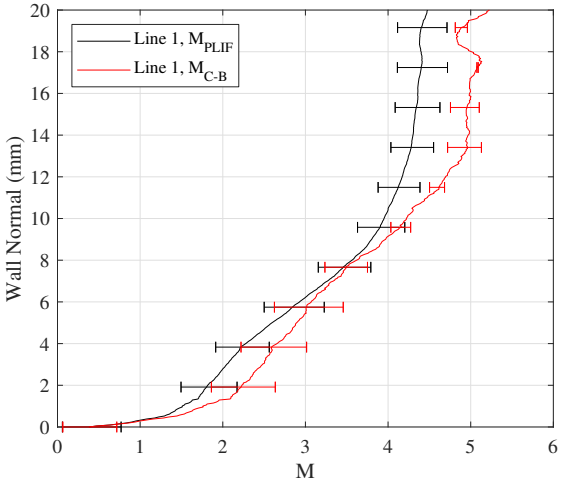

(f) Mean Mach number profiles

Figure 7.111: PLIF MTV, Run 4656: downstream; turbulent trough; plasma on.

Inner variable plots were generated using T_{PLIF} for the tripped cases. The viscosity was calculated from the temperature by blending Keyes' and Sutherland's Laws in the cold and hot regions, respectively, as was described in Chapter 5. Following the procedure outlined in 7.3.5, the τ_w was estimated using Clauser's chart method [61]. The results are shown in Figures 7.112 and 7.113 alongside the theoretical Law of the Wall ($u^+_{eq} = y^+$) and log layer ($u^+_{eq} = \frac{1}{\kappa}\ln y^+ + C$ with $\kappa = 0.41$ and $C = 4.9$, following [61, 239]) plots. The uncertainty in y^+ was too small to be shown clearly on the logarithmic axis. These plots follow the trends observed in Section 7.3.5. In the upstream location the data did not follow the expected trends because the flow was likely to be transitional, not fully turbulent; τ_w should not be trusted in this region. However, by the downstream location, it was known the boundary layer was more fully developed and turbulent. The difference between the results calculated from the PLIF and Crocco-Busemann data were generally only present in the outer layer, which was of little consequence to the region of interest.

For the wake case, the results tended to show the sensitivity of u^+_{eq} to the realities of near wall measurements. The near wall results matched those observed with the Pitot probe, and indeed were superior in the case of Figure 7.112(d), giving the impression the error in Figure 7.112(c) was largely due to a poor run; note the spread in the data in Figure 7.99(c). The downstream plots in Figure 7.113, however, were excellent and strongly correlated with the theory within the bounds shown. The deviation in the linear sublayer was likely due to the large uncertainty in the velocity data ($y^+ \approx 10 \implies y < 1\text{mm}$). Due to the spanwise homogeneity by this point on the test article, it was safe to assume these plots were representative of the true condition of the boundary layer. Note that in both cases, τ_w the results predicted by both the boundary layer solver and Pitot probe, and the same concerns about the veracity of Clauser's method remained (see Section 7.3.5).

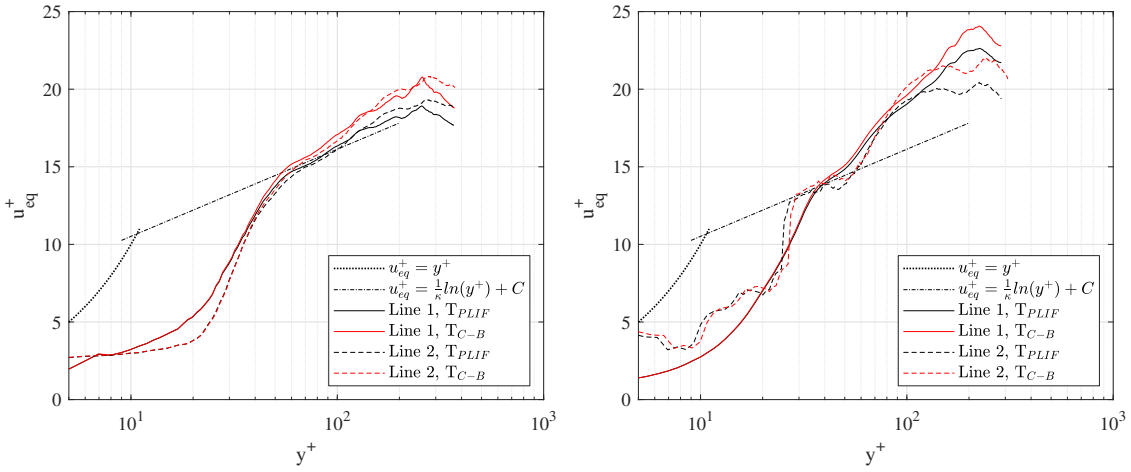

(a) Upstream, plasma off, $\tau_w \approx 23$Pa

(b) Upstream, plasma on, $\tau_w \approx 15.5$Pa

(c) Downstream, plasma off, $\tau_w \approx 13$Pa

(d) Downstream, plasma on, $\tau_w \approx 13$Pa

Figure 7.112: PLIF MTV inner variable plots, wake

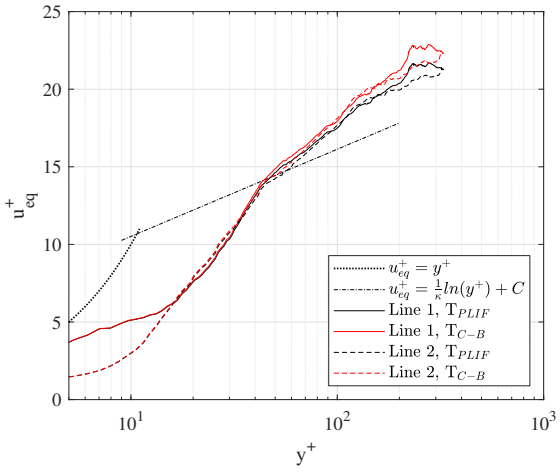

(a) Upstream, plasma off, $\tau_w \approx 17$Pa

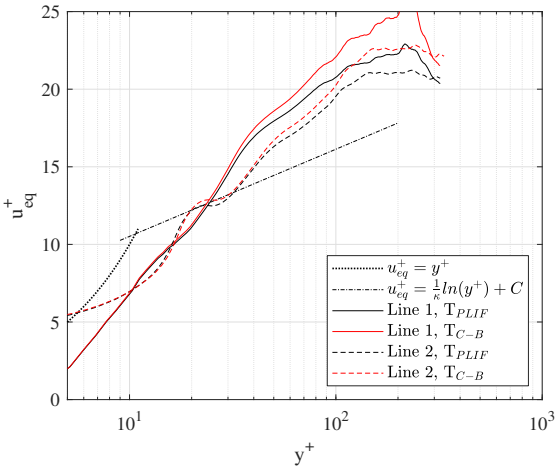

(b) Upstream, plasma on, $\tau_w \approx 16.5$Pa

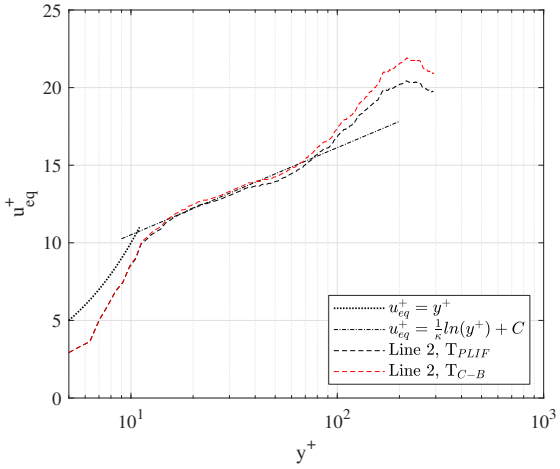

(c) Downstream, plasma off, $\tau_w \approx 15.5$Pa

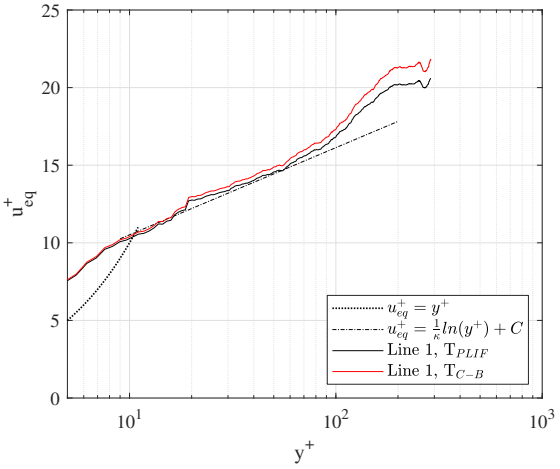

(d) Downstream, plasma on, $\tau_w \approx 15$Pa

Figure 7.113: PLIF MTV inner variable plots, trough.

7.4.2.4 Spanwise Velocimetry

The spanwise velocimetry test matrix is provided in Table 7.31. Because the focus of this campaign was to confirm there were no spanwise gradients across the plate and to study the isotropy of the turbulence, only a small number of runs were conducted. None of these runs used the plasma.

No.	Location	Trips	Run/Date
1	Forward	Laminar	4697, 4/8/2021
2	Forward	Turbulent	4695, 4/7/2021
3	Back	Laminar	4698, 4/9/2021
4	Back	Turbulent	4699, 4/9/2021

Table 7.31: PLIF spanwise velocimetry test matrix.

The data are shown in Figure 7.114. Of the four runs, only the turbulent ones yielded reliable results. The laminar runs tended to have regular changes in the velocity across the plate. The test article and tunnel shifting upon startup offered an explanation for this result. During setup, care was taken to unsure the "Write" beam and "Read" sheet were at a constant height above the plate. It was known, however, that the tunnel shifted when the flow was turned on, ruining this precise alignment. It is for this reason that during other off-body campaigns (Pitot pressure, schlieren imaging, boundary layer MTV) the wall needed to be identified for each image, but here this was impossible. Due to the thin nature of the laminar boundary layers, the velocimetry would be highly susceptible to any plate roll. Because they were thicker, measured higher off the surface, and had less of a velocity gradient in the outer layer, the turbulent profiles would be more insulated for such discrepancies; this challenge did remain, however, as a source of systematic error. What can at least be said about the laminar data is that the velocity did drop considerably between the upstream and downstream test locations, and that the fluctuations were consistently below those of the turbulent runs.

The turbulent runs yielded exciting results, especially Figure 7.114(e). One could see the

dramatic reduction in velocity as one moved into a wake. The regular spacing of these wakes matched the 6.84mm spacing of the trips. Furthermore, at the edges of each wake, where the corner vortices were present, there was a distinct spike in the velocity fluctuation on top of the already enhanced fluctuations in the wake itself. This represented direct evidence of not only the presence of the vortices, but their role in fomenting turbulence. By the downstream location described in Figure 7.114(f), the velocity dropped as the boundary layer thickened and both the velocity and fluctuation profiles homogenized. One could argue modest, regular fluctuations did indeed persist in the data, and this was observed in other data such as IR thermography (see Section 7.3.3), but it was reasonable to assume many techniques would be unable to resolve such weak and broad features.

Oversaturated instantaneous "Read" images are included in Figures 7.114(a) and (b) to show the breakdown of these vortical structures just upstream of each of the true lines. Enough naturally occurring $NO^{v=1}$ was detectable via the "Read" beam to show that in the upstream location there were orderly vortical structures, but they decayed by the downstream location; the contrast was adjusted such that these features were visible even though doing so saturated the "Write" line data. That the signal was brightest in the wakes follows from their velocity defecit as compared to the troughs. Lower velocity means higher pressure, and therefore greater NO density and signal. This effect seemed most pronounced in the trips' vortices.

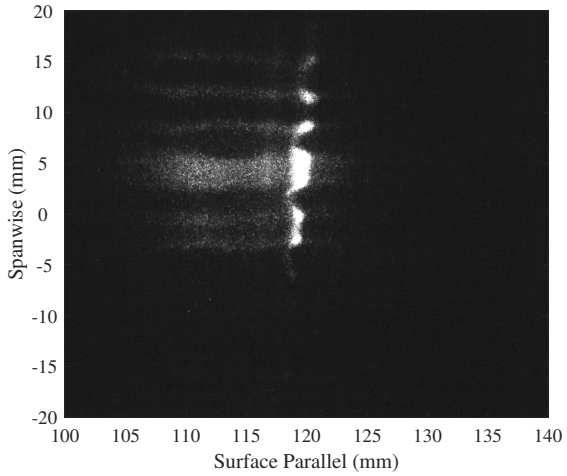

(a) Upstream instantaneous read image

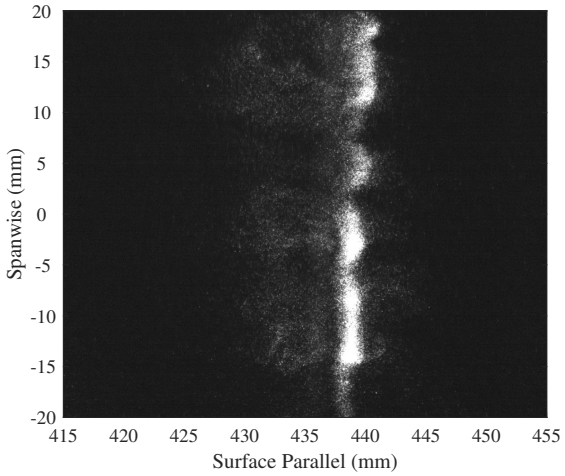

(b) Downstream instantaneous read image

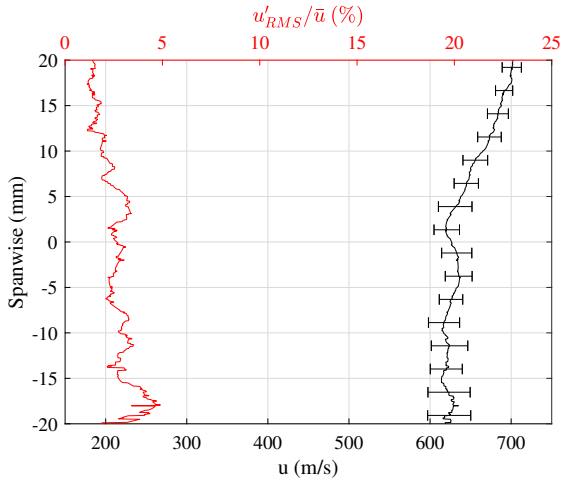

(c) Upstream laminar profiles

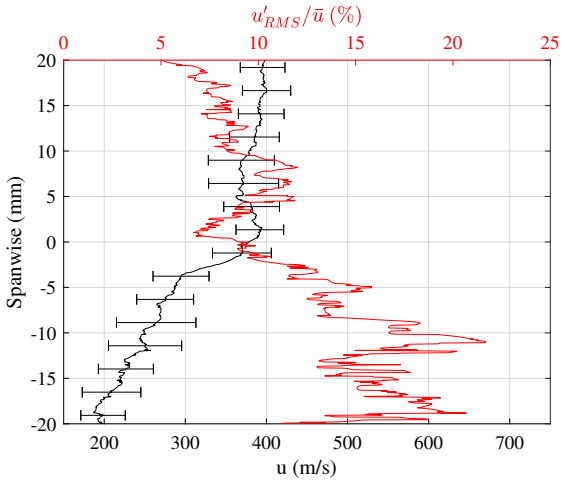

(d) Downstream laminar profiles

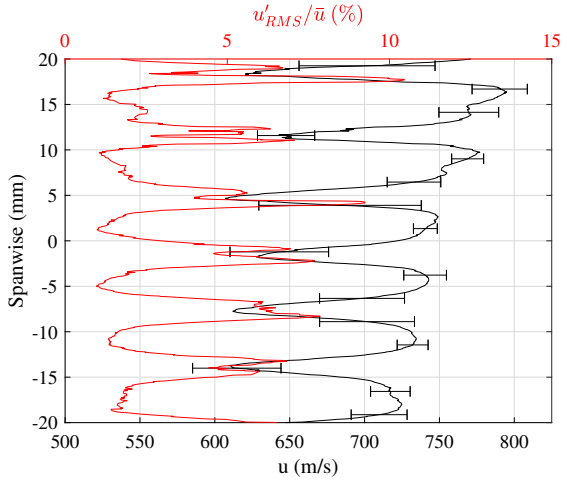

(e) Upstream turbulent profiles

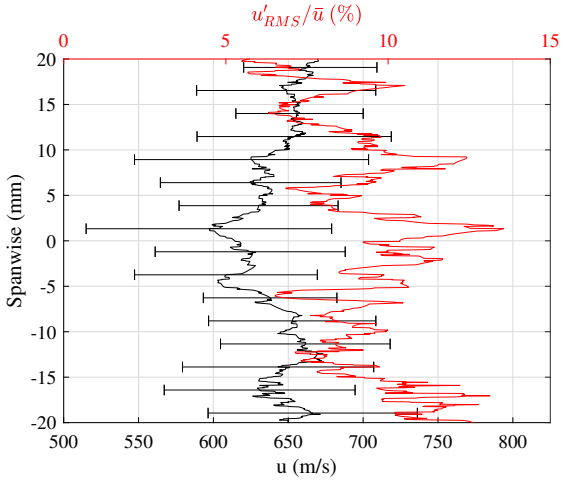

(f) Downstream turbulent profiles

Figure 7.114: Spanwise PLIF MTV.

In order to better illustrate the behavior of the trips, spanwise visualization images were taken as part of the *NO* characterization study discussed Section 4.1.3. The beams were 3 and 5mm above the plate in the upstream and downstream locations, respectively. Both beams were angled 2.75mm to match the plate's tilt, but the cameras were not for simplicity. One can see the ordered, vortical structures in the upstream image, and the chaotic, fully developed turbulence in the downstream image. The streaks in the images may have been due to *NO* clustering through the aerogrids, but more likely arose from the trips. Interestingly, the vortices seemed to be spreading at 130mm, which was observed in the oil flow results. The bias of the gas towards one side of the image may have been due to injector misalignment, and the streamwise variation of the image may have been due to plate pitch with respect to the beam. In general, the plate and tunnel tended to shift down during a test. If they pitched down as well, then in the upstream image the data is likely to be above the boundary layer until it grew large enough to reach the beam at $\sim$ 130mm; at 3mm, even under ideal conditions the beam would have been in the outer edge of the boundary layer and was taller than the trips. In the downstream image, meanwhile, a negative pitch would mean the laminar sublayer was observed past $\sim$ 445mm; this was a more likely explanation than the beam exiting the boundary layer, as the tunnel did not shift down $\mathscr{O}(1\text{cm})$, only $\mathscr{O}(1\text{mm})$.

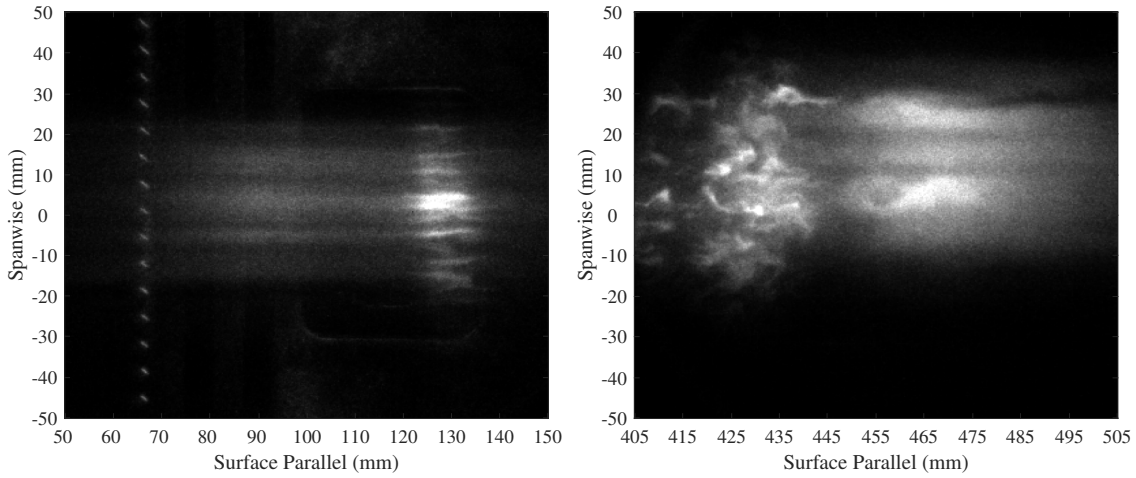

(a) Upstream (b) Downstream

Figure 7.115: Spanwise PLIF visualization.

7.5 Comparisons

The purpose of this section is to compare data collected for the same parameter by different techniques. This process can validate measurements, provide a more detailed picture of the flow physics, or motivate further work. Some comparisons were made in the above sections as each result was introduced, but here the results are directly plotted alongside one another; that being said, greater context and analysis of each individual experiment are provided in its corresponding section above. The goal here is to provide better understanding not just of the data, but the inherent strengths and weaknesses of each diagnostic.

7.5.1 Off Body Variables

Perhaps the variables of greatest interest to a turbulence model are the velocity and temperature, and by extension the Mach number. Four independent methodologies were used in this report to predict or measure these fundamental parameters: the numerical boundary layer solver; PLIF thermometry; PLIF velocimentry; and Pitot probe. Data for each of these techniques are plotted for the laminar, turbulent (wake), and turbulent (trough) cases in Figures 7.116-7.118 respectively; the inner variable plots for the turbulent cases with and without the plasma are shown in Figures 7.122 and 7.123 respectively.

As was done in their corresponding sections, the Crocco-Busemann relation was used to relate the Mach number to temperature (Pitot) or velocity to temperature (PLIF velocimetry), which allowed these techniques to produce velocity, temperature, and Mach number plots. For the PLIF measurements, when the temperature was derived from velocity via Crocco-Busemann, the label "MTV" was used, and when it came from the direct PLIF thermometry campaign the label "$\text{PLIF}_{\text{Them}}$" was used. Recall from Section 7.3.5 that the Pitot probe made measurements 140mm from the leading edge in the "Front" test location and observed a weak shock due to the static pressure tap $\sim$ 6mm from the surface, and that for "Turbulent" runs M_e was taken $\sim$ 30mm above the surface, though for consistency with other techniques only 20mm of data are shown here. This meant, in general, the Pitot data might not be fully converged on its edge condition in the

plots shown, even though theoretically no boundary layer should have been $>$ 15mm. Also, the "Trough" PLIF measurements were conducted between the first and second trip, while the Pitot's "Trough" measurements were conducted between the second and third trip. Finally, the for the "Turbulent/Front" cases r_{turb} was used in T_{aw} in the Crocco-Busemann equation when this location was only transitional, an approximation born of necessity.

It is important to remember the variable directly measured by the experimental techniques: Pitot probes measure Mach number; PLIF thermometry temperature; PLIF MTV velocity; PLIF thermometry and MTV combine to provide Mach number. Any variables produced outside of these fundamental results are subject to assumptions. Perhaps the most relevant is the definition of boundary conditions for the wall and freestream temperature used in the Crocco-Busemann equation (2.24). Recall that in both cases T_w was taken from experimental measurements, and T_e (and u_e, for the Pitot probe implementation) came from the NALDAQ and oblique shock relations. Analogously, T_e was set in the PLIF thermometry results to provide realistic values for T_w, which, for any of the reasons discussed in Section 7.4.2.1 and in [49], led to a higher-than-expected value for T_e. All of this to say that when comparing the data, the best gauge of the performance of a technique is to study its original and unprocessed form. Otherwise, one must be cognizant of the limitations of the assumptions applied.

Finally, note that deviations from the expected theory, especially in the MTV temperature results in Figures 7.116(f) and 7.121(e) and in the inner variable plots in Figures 7.122 and 7.123 were discussed in their corresponding sections. Briefly, issues with the former stemmed from unexpected shaped of the MTV profile and issue with the later may be due to wake, transition, or low density effects in the boundary layer, continued turbulence development, or issues with Clauser's method for estimating τ_w.

The analysis begins with the identification of a global trend, that the numerical boundary layer solver tended to under predict the size of the boundary layer, and miss the gradual slope from the boundary layer to the freestream. This was unfortunate but not surprising, as it was a purely theoretical code which neglected: leading edge bluntness; entropy layer effects; shock curvature;

viscous/inviscid interaction pressure features at the leading edge; transition; Mach waves due to seams at junctions in the test article; and for turbulent flows trip effects (wakes, shock structure, shear layer, 3D effects). In practice, no doubt some of these features were more important than others, but any one of them would complicate the final result. It is tempting to view the numerical results as the "correct answer", but one must recognize their own unique limitations.

The experimental analysis should begin with the "Laminar" plots in Figure 7.116. The velocity data show excellent agreement between all three velocimetry techniques. The Pitot data, derived from the Mach number, captured the same shape observed in the MTV data, with the exception of the bump at $\sim$ 6mm in the "Front" test location due to the static pressure port. Between $\sim 2-5$mm, the experimental techniques had decent agreement with the PLIF thermometry data. Caution should be exercised before declaring the MTV and Pitot results in complete agreement as both rely on Crocco-Busemann assumptions to produce temperature data and were forced to effectively the same T_e; this forcing was validated by the Pitot measurements for M_e matching the theoretical result far from the wall, even with the trips installed. The agreement, especially in the "Front" location, was striking. Thus it makes sense that parameters that agreed well in both u and T should match in M. The nonphysical result in the MTV data at the "Back" test location stemmed from the unique shape of the velocity profile via a process described in Section 7.4.2.3. As expected, the PLIF and Pitot Mach numbers agree well in the boundary layer, but the PLIF result under predicts the Pitot-validated M_e, again pointing to a problem in T_e from the PLIF thermometry data.

The "Turbulent/Wake" data from Figure 7.117 are analyzed next. Immediately one sees that the PLIF data completely misses the trips' wake structure in the "Front" test location. This was unexpected, but it was hypothesized that the Pitot data was especially sensitive to this pressure effect in a way the laser diagnostics were not. Alternatively, the Pitot probe may have been large enough to "smear" physics in this complex region, while the PLIF results would have better resolution. In general, the agreement in the velocity data was not as strong as in the "Laminar" case, especially in the "Back" test location. For the "Front" test location, the MTV and $\text{PLIF}_{\text{Therm}}$ temperature

results had decent agreement between $\sim 2-6$mm, and the Pitot data eventually fell between them from $\sim 6-10$mm. Any discrepancies between these MTV and $\text{PLIF}_{\text{Therm}}$ data were masked in the Mach number, which agreed analogously up to ~ 10mm. PLIF thermometry of the fully turbulent boundary layer in the "Back" location produced a thermal boundary layer far larger than that predicted by either Crocco-Busemann technique. That being said, at least one PLIF line did agree with the Pitot data to within the uncertainty. As expected then, this line produced decent agreement in the Mach number profiles.

The "Turbulent/Trough" data in Figure 7.118 performed the best out of the three sets described. The Pitot probe over predicted the PLIF MTV data in the "Front" location, but it was by a consistent margin; note that the trip effect was diminished in the "Trough" as compared to the "Wake". However, the PLIF MTV, Pitot, and even numerical velocity data in the "Back" location matched almost perfectly. With such excellent agreement in both cases, one would expect the temperature profiles to match, and indeed they did. While the Pitot data actually more closely matched the PLIF thermometry result through the boundary layer in the "Front" location, all three techniques agreed well up to ~ 10mm. In the "Back" location, MTV data agreed nearly perfectly with the simulation, and the Pitot data split the MTV and $\text{PLIF}_{\text{Therm}}$ results. This made sense, because the simulation and MTV data matched so closely, so the Crocco-Busemann derived temperature should fit the computational result; this validated the Crocco-Busemann approach. The temperature profile's shape from all four curves matched. The Mach number fit similarly excellently; all three experimental techniques agreed at both the "Front" and "Back" locations up to ~ 10mm.

It is unclear why the "Trough" data so soundly outperformed the "Wake" data. To check if it was simply a coincidence, the plasma "On" data is included in Figures 7.119 through 7.121, taking advantage of the fact that the plasma had no tangible effect on these parameters. The results not only support the aforementioned trends, but in fact the agreement was even better in some cases. It was interesting to note the slight presence of the shear layer in the "Front" test location in the laser diagnostics results; this validated the physics captured by the Pitot probe, but it was unclear why the result was only visible in the plasma "On" data.

Finally, for completeness, the inner variable plots from the plasma "Off" and "On" cases are included in Figures 7.122 and 7.123 respectively. Due to the variability inherent to Clauser's method and the heavy scaling applied, these data are not too instructive. For clarity, data from the transitional flows in the "Front" test location were not shown, as the scaling only was appropriate for turbulent flows.

Overall these results were highly encouraging. They suggested that with proper scaling in the freestream, all three experimental techniques were working well; the simulation results were somewhat lacking owing to their known simplicity. The agreement in the boundary layer especially was strong. The results underscored the importance of confirming results as every tool has its own strengths and weaknesses: the simulations could not capture all of the flow's physics; the PLIF thermometry and Crocco-Busemann approach were both beholden to their scaling; the Pitot probe was very sensitive to pressure features. Even for a flat plate boundary layer, these data show accurately quantifying the flow requires the application and deep understanding of many techniques.

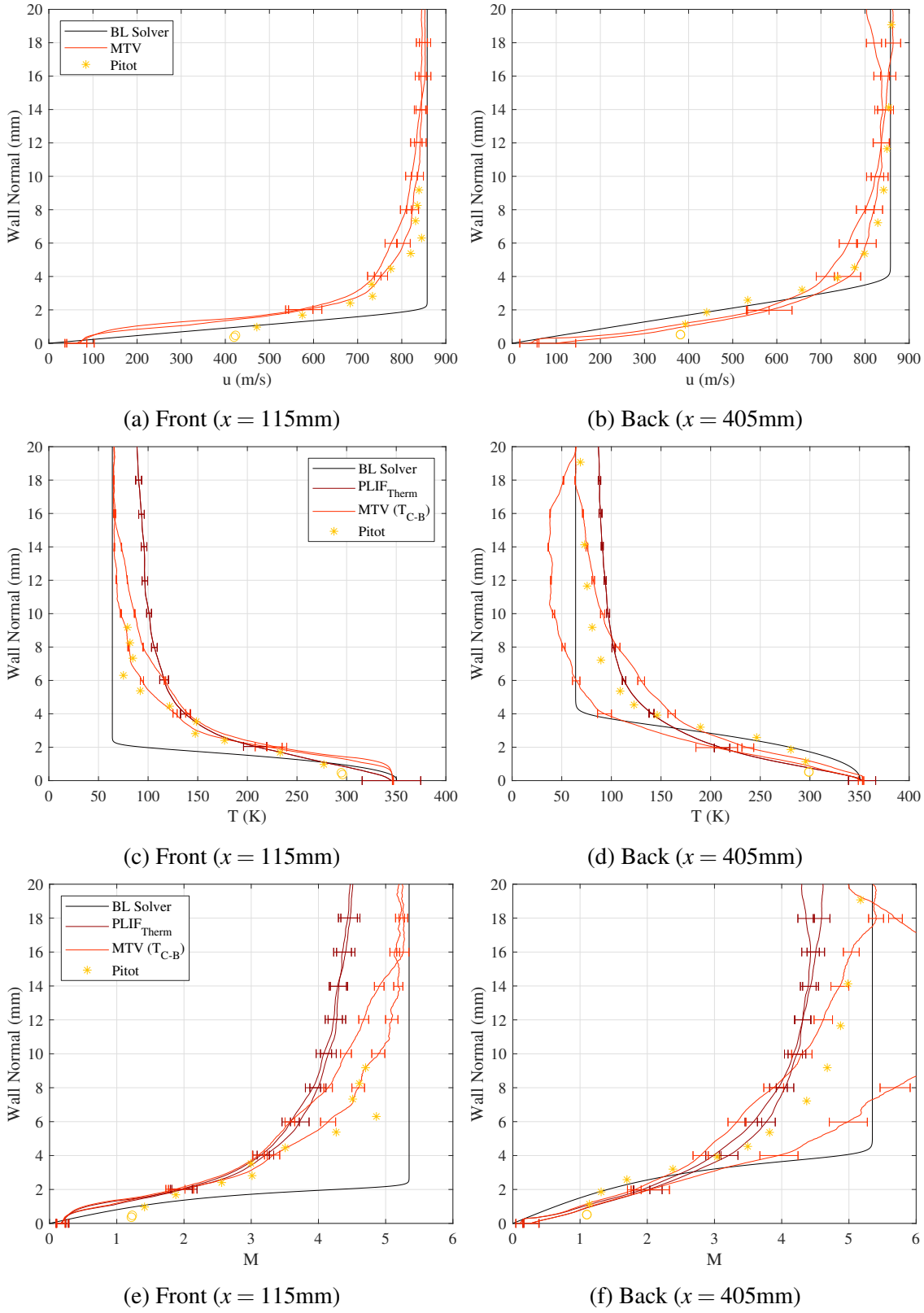

(a) Front ($x = 115$mm)

(b) Back ($x = 405$mm)

(c) Front ($x = 115$mm)

(d) Back ($x = 405$mm)

(e) Front ($x = 115$mm)

(f) Back ($x = 405$mm)

Figure 7.116: Comparison of laminar off body techniques (no plasma); same legend applies to each row.

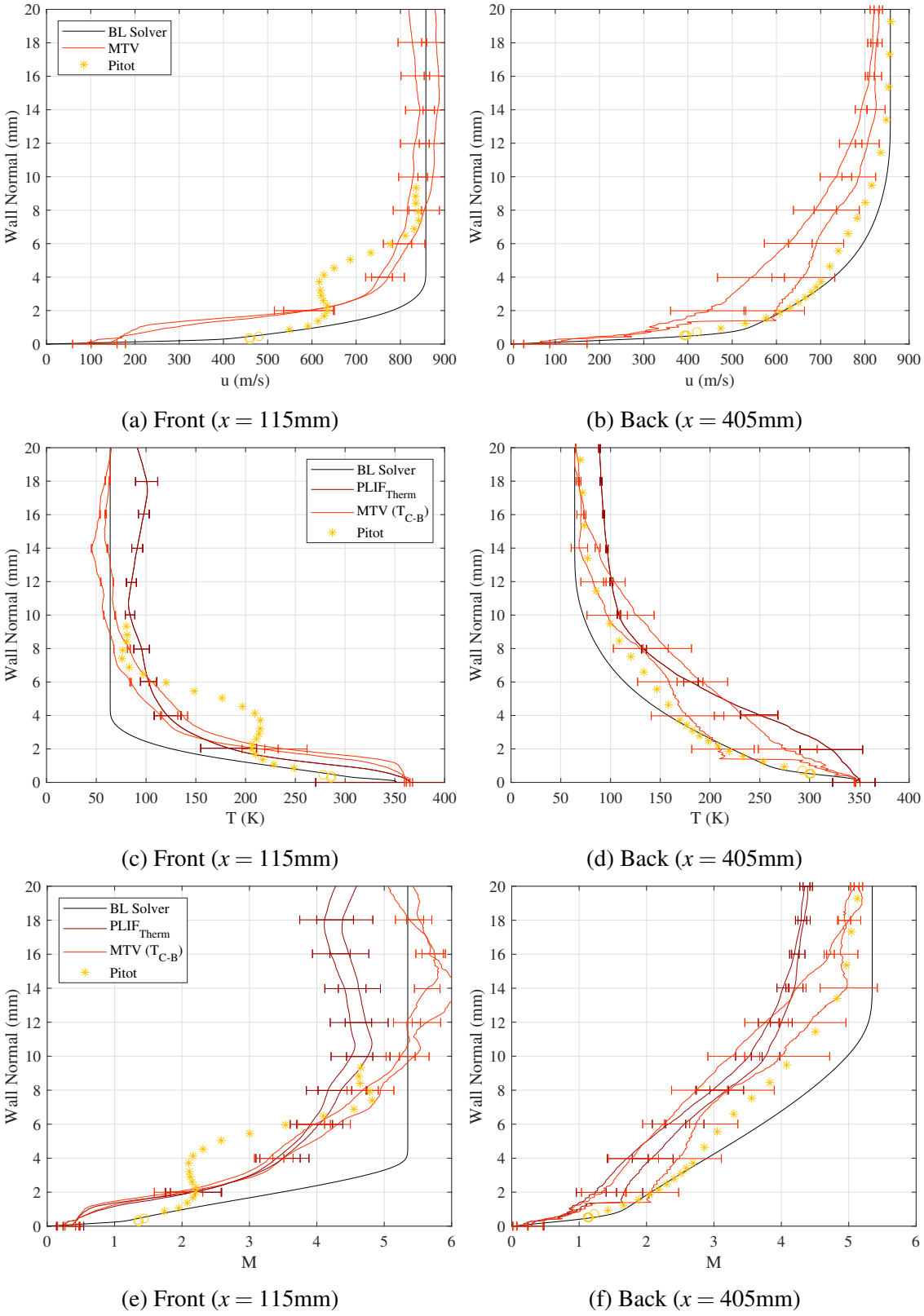

(a) Front ($x = 115$mm)

(b) Back ($x = 405$mm)

(c) Front ($x = 115$mm)

(d) Back ($x = 405$mm)

(e) Front ($x = 115$mm)

(f) Back ($x = 405$mm)

Figure 7.117: Comparison of turbulent off body techniques (wake, no plasma); same legend applies to each row.

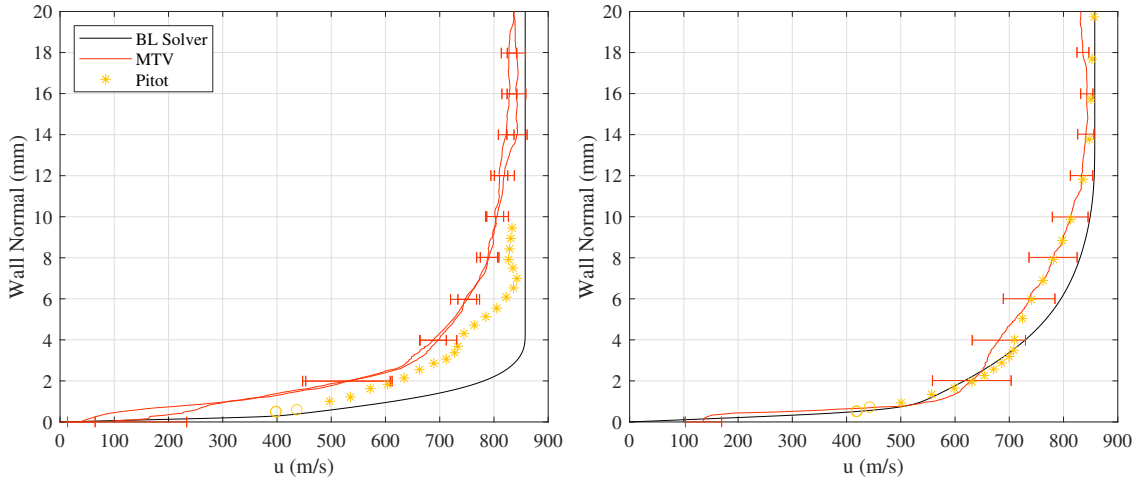

(a) Front ($x = 115$mm)

(b) Back ($x = 405$mm)

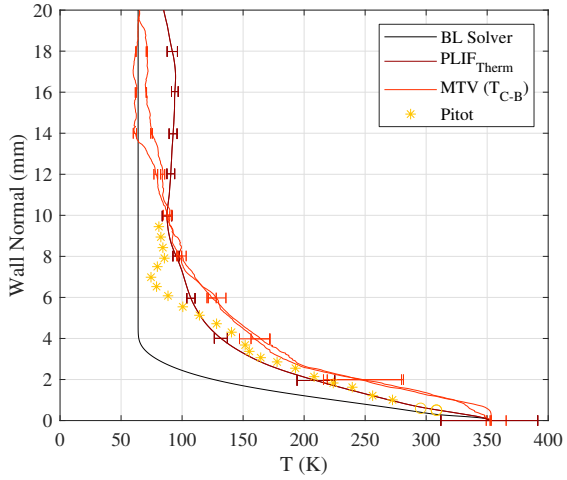

(c) Front ($x = 115$mm)

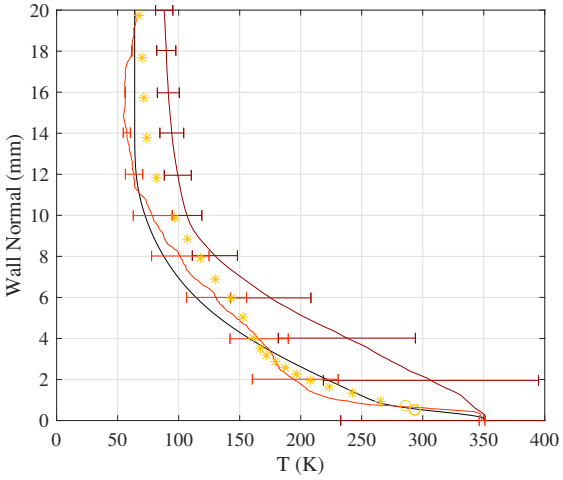

(d) Back ($x = 405$mm)

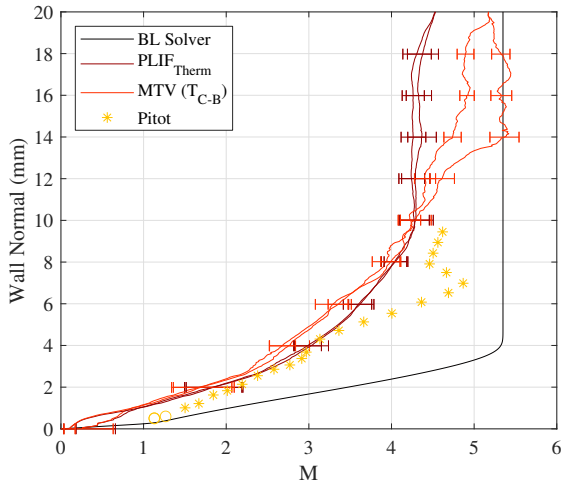

(e) Front ($x = 115$mm)

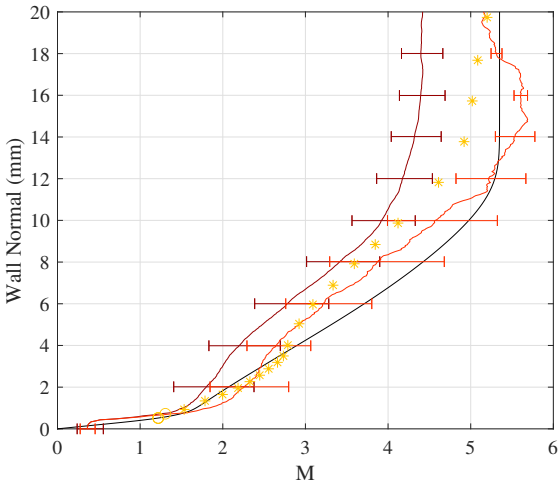

(f) Back ($x = 405$mm)

Figure 7.118: Comparison of turbulent off body techniques (trough, no plasma); same legend applies to each row.

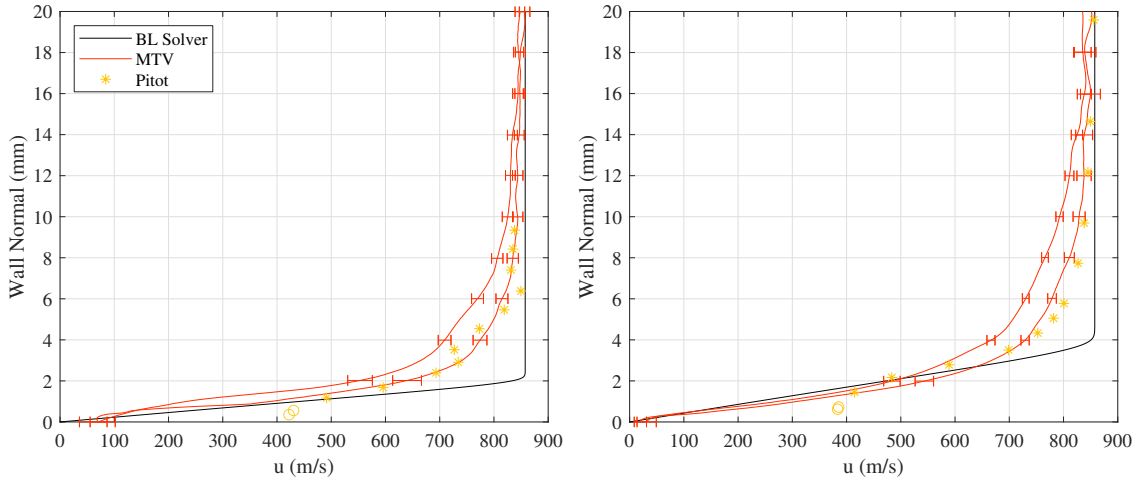

(a) Front ($x = 115$mm)

(b) Back ($x = 405$mm)

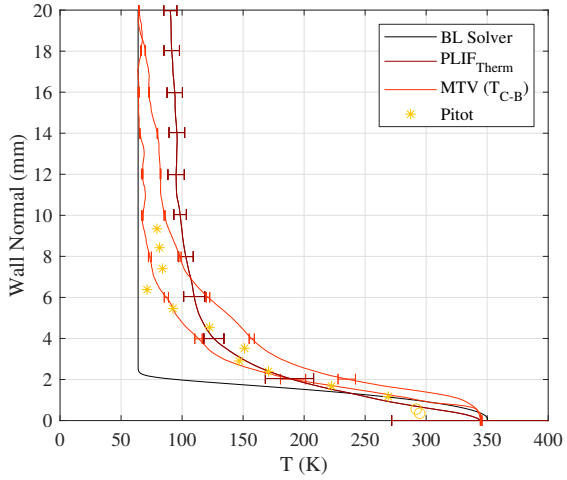

(c) Front ($x = 115$mm)

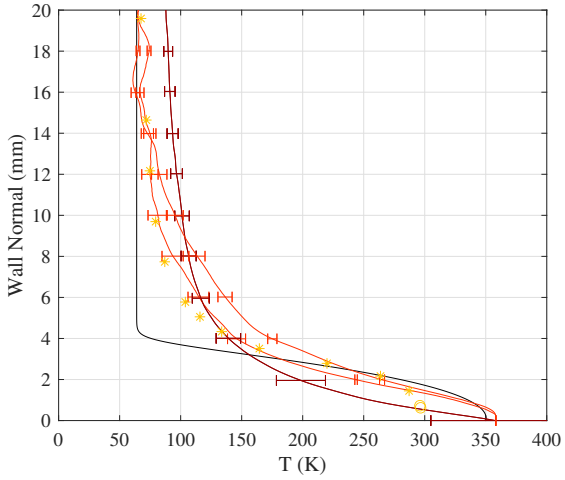

(d) Back ($x = 405$mm)

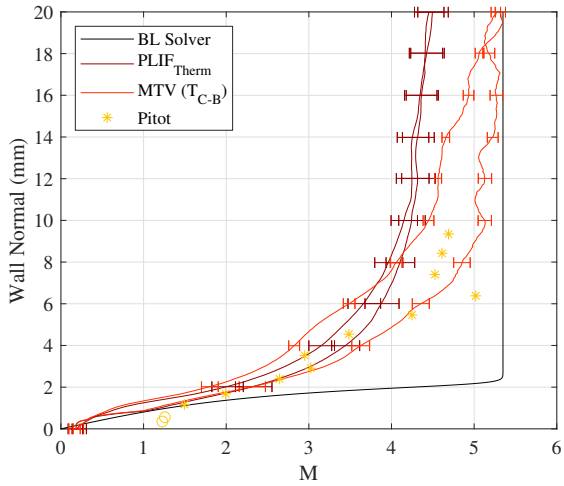

(e) Front ($x = 115$mm)

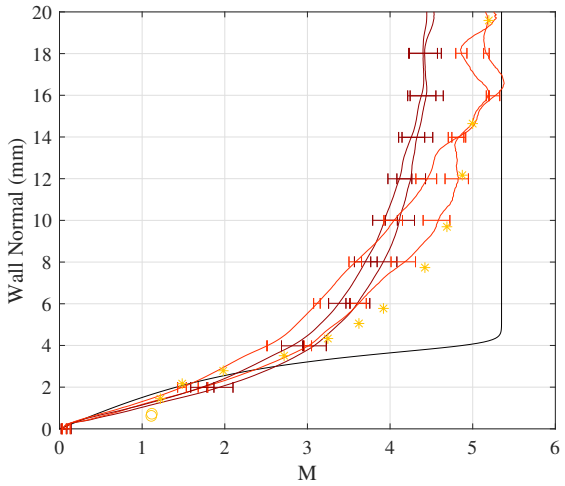

(f) Back ($x = 405$mm)

Figure 7.119: Comparison of laminar off body techniques (plasma); same legend applies to each row.

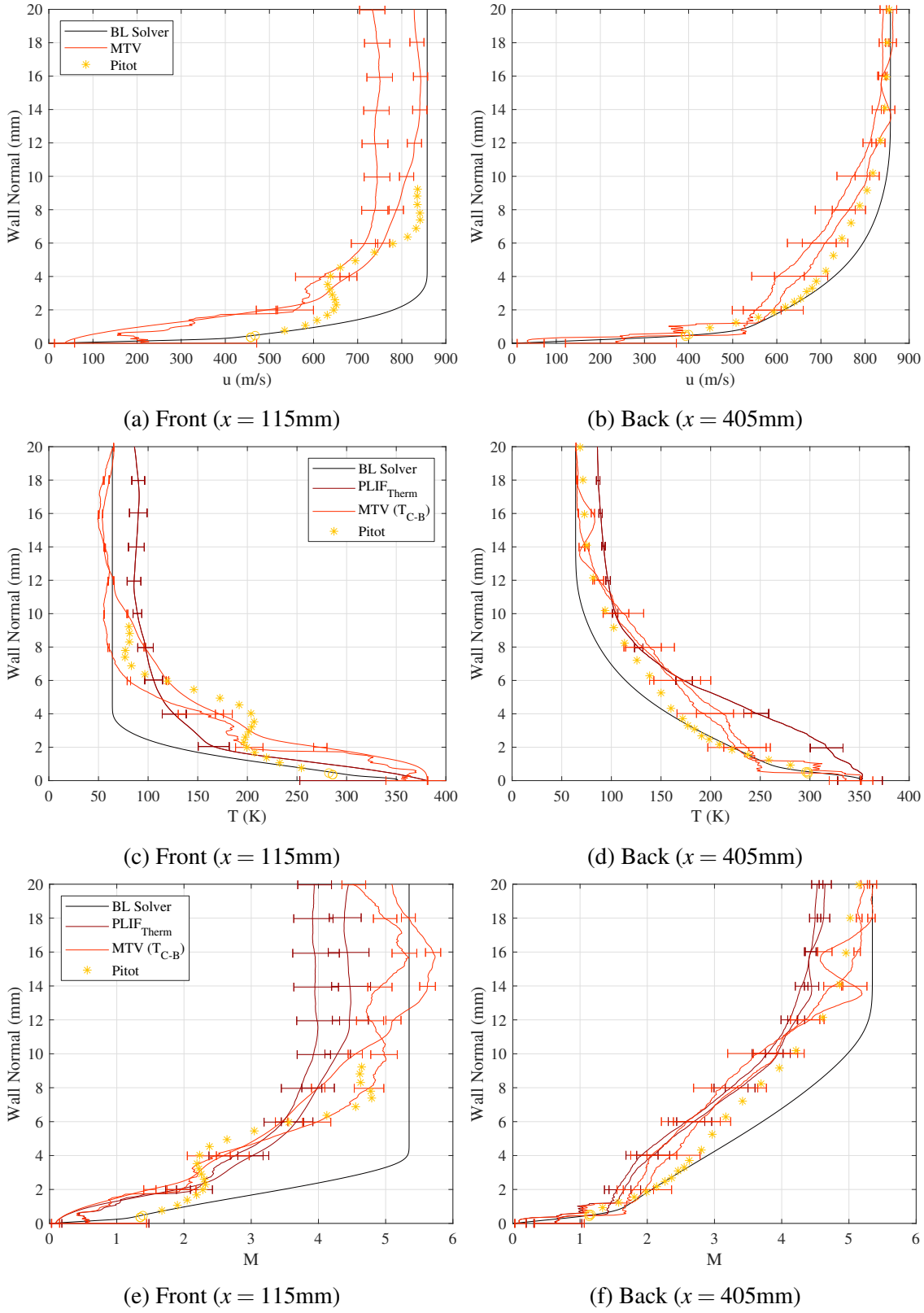

(a) Front ($x = 115$mm)

(b) Back ($x = 405$mm)

(c) Front ($x = 115$mm)

(d) Back ($x = 405$mm)

(e) Front ($x = 115$mm)

(f) Back ($x = 405$mm)

Figure 7.120: Comparison of turbulent off body techniques (wake, plasma); same legend applies to each row.

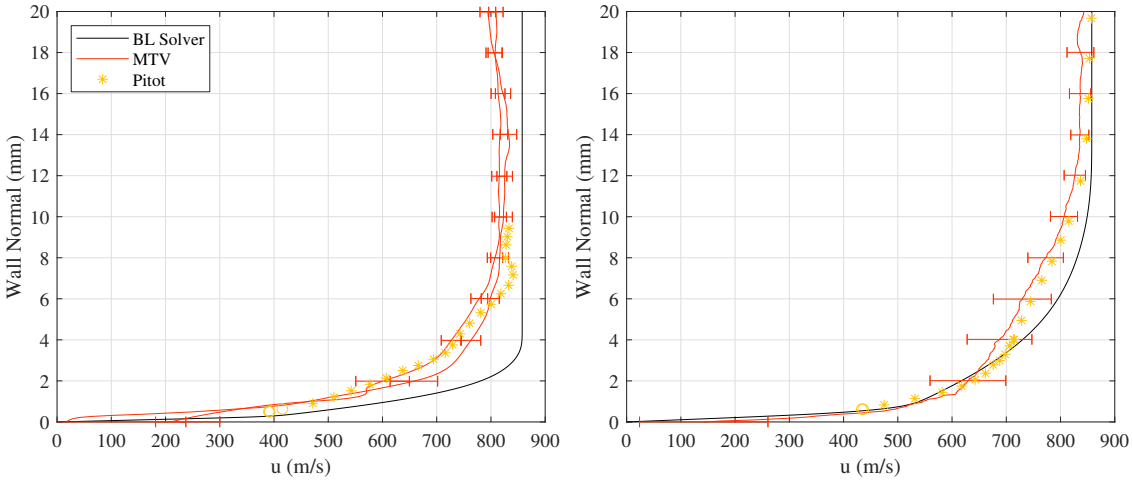

(a) Front ($x = 115$mm) (b) Back ($x = 405$mm)

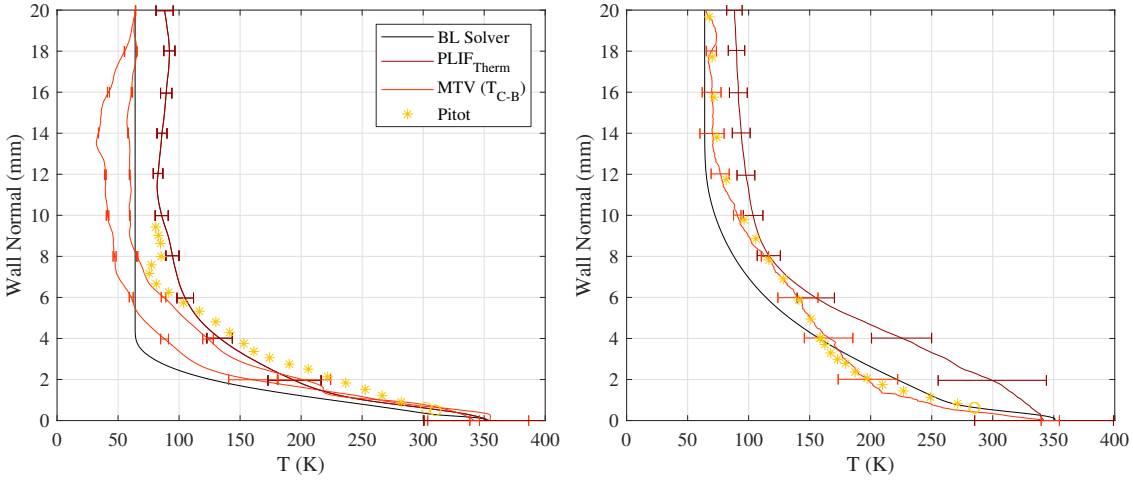

(c) Front ($x = 115$mm) (d) Back ($x = 405$mm)

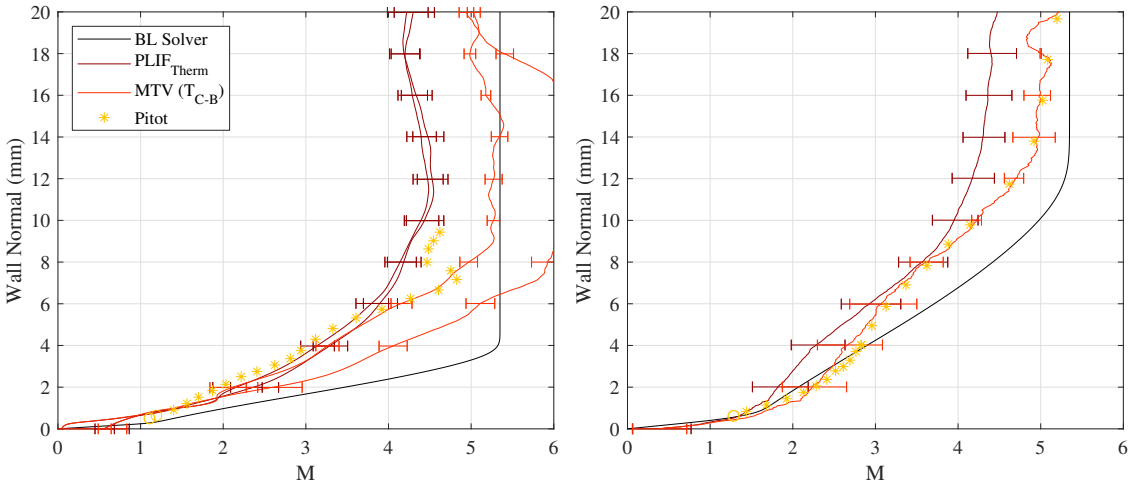

(e) Front ($x = 115$mm) (f) Back ($x = 405$mm)

Figure 7.121: Comparison of turbulent off body techniques (trough, plasma); same legend applies to each row.

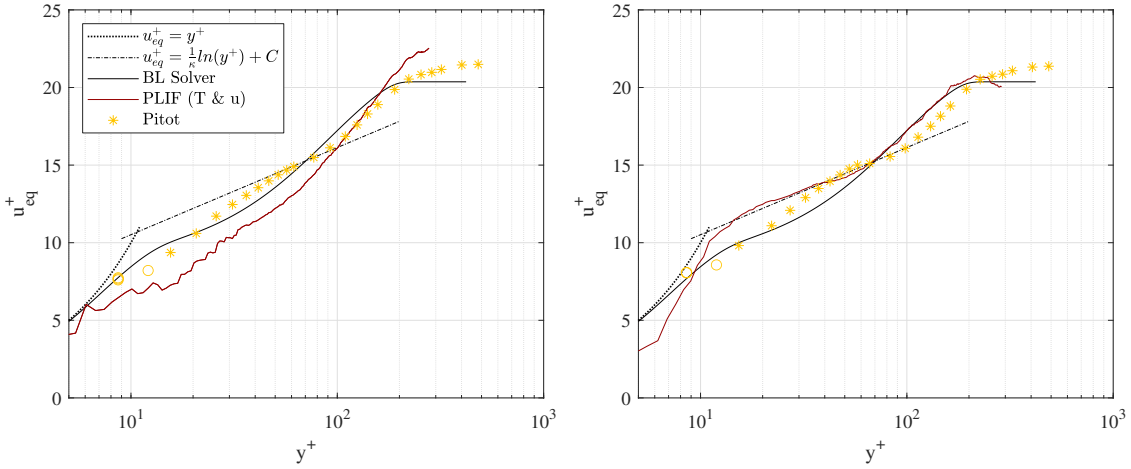

(a) Back, wake ($x = 405$mm)

(b) Back, through ($x = 405$mm)

Figure 7.122: Comparison of turbulent off body techniques, inner variable plot (no plasma); same legend applies to all figures.

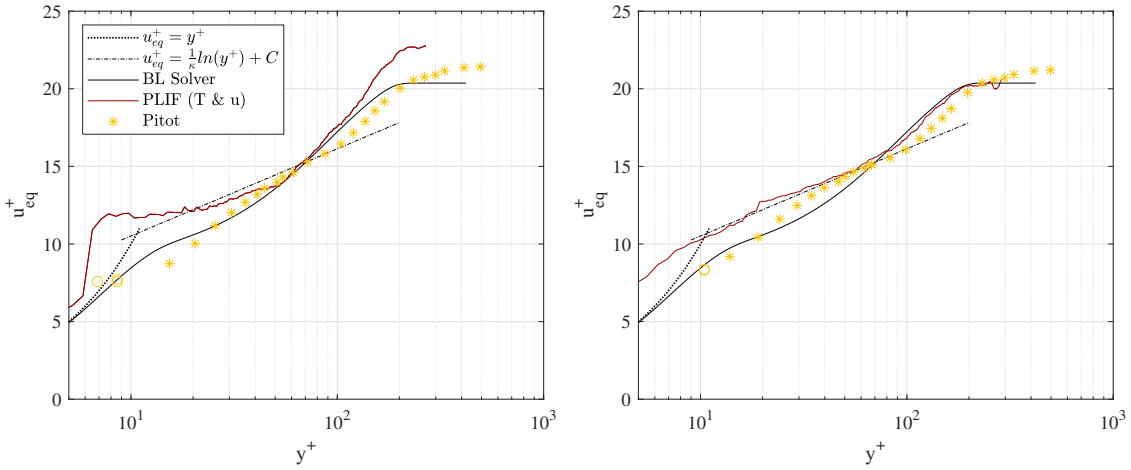

(a) Back, wake ($x = 405$mm)

(b) Back, through ($x = 405$mm)

Figure 7.123: Comparison of turbulent off body techniques, inner variable plot (plasma); same legend applies to all figures.

7.5.2 Surface Streaks

Oil flow visualization and IR thermography shared the ability to visualize fluid-wall interactions across the 2D region of interest. Summarizing the mechanisms by which this occurs, oil flows from regions of high pressure to regions of low pressure, such as along the test article or from wake to trough, while IR thermography, analogously, shows heating where wall shear stress is elevated, such as from vortical structures or turbulence.

Both techniques are dynamic, able to manifest changes in the interaction over time, so for this reason traces were taken once the flow had time to establish a trend (of particular concern for the oil flow in the low density ACE tunnel) and then at the end of the data collection cycle; thus traces were taken from the third ("Early") and final ("End") test time from the figures in the corresponding sections for a total difference of $\sim$ 10s. The IR data was normalized just like the oil flow results, and the Stanton number data was used as it clearly showed the wakes and troughs.

The results for the three test locations are shown in Figure 7.124. At all three locations, the oil flow and IR streaks were offset by half a wavelength such that a peak in the oil flow signal was in a trough in the Stanton number. The IR results in Figure 7.124(a) show the heating falls regularly behind the trips at both the start and end of the test, implying that high signal in IR corresponds to the trips' wakes. Visual inspection of the oil flow data in Section 7.3.1 shows that everywhere but a portion of the "Front" test location, the oil collected in the troughs. Taken together, this implied that the wakes formed by the trips caused higher pressures due to their velocity deficit (see also Section 7.4.2.4) which pushed oil into the troughs and led to increased skin friction due to turbulent heating. These trends persisted along the length of the test article, but by the "Back" test location their effect was diminished as the flow become more isotropic.

One trace defied the analysis just introduced, the "End" oil flow trace at the "Front" test location. Recall from Section 7.3.1 how the transition process became visible once the bulk of the oil had been removed from the plate. It remained unclear if the unexpected, in some places inverse, trends were due to a thin oil residue being left behind by the flow or just the ability for weaker trends to be given time to manifest, but nevertheless here one can see that the peaks were produced

not only offset half a wavelength from those from the "Early" trace, but they lined up well with the peaks in the IR data. This suggested that the trips' wakes were indeed being visualized with the oil flow technique at this upstream location at the end of the run.

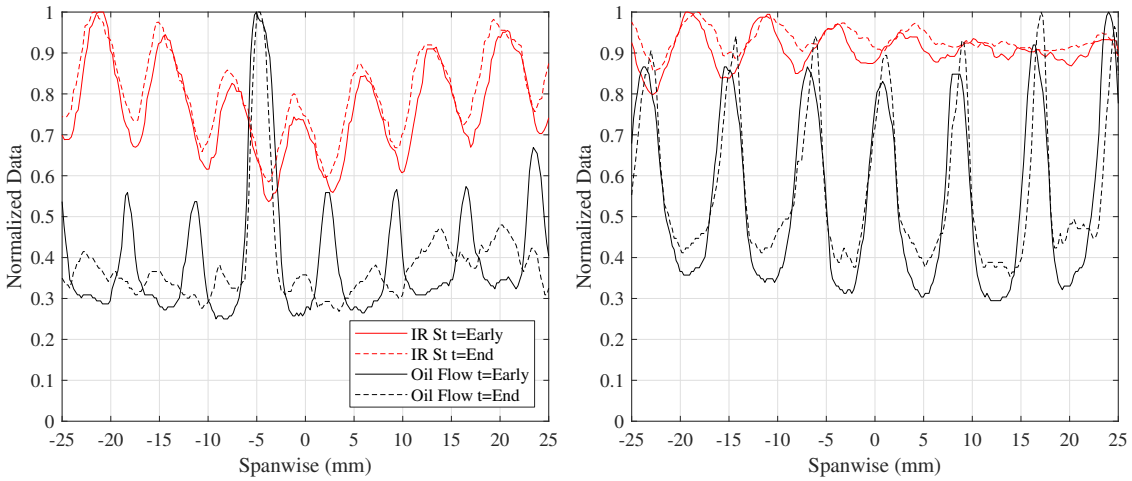

(a) Front ($x = 115$mm) (b) Middle ($x = 260$mm)

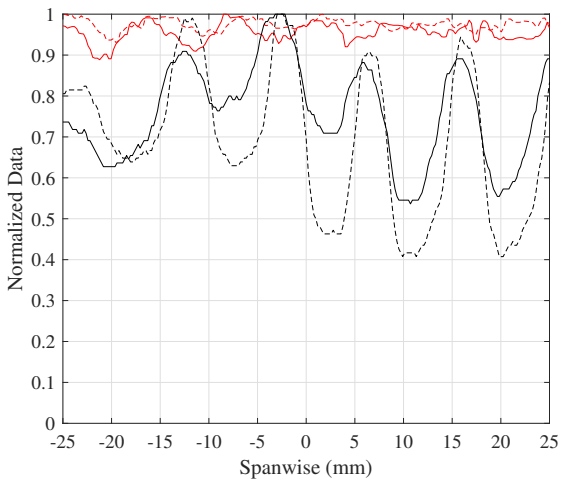

(c) Back ($x = 405$mm)

Figure 7.124: Comparison of surface streak visualization techniques; same legend applies to all figures.

7.5.3 Wall Variables

Here predictions, measurements, and calculations of the wall heat flux, Stanton number, and wall shear stress are compared. Data was provided from the numerical boundary layer solver, IR thermography, Pitot probe, and PLIF velocimetry. These results, especially those for the wall shear stress, were discussed in great detail in the aforementioned sections. The goal here was to visualize the trends in the data to further support these arguments.

Data were provided for both plasma "Off and On" cases under the understanding that its presence had little impact on these parameters. For the IR data, the final 2D frame for which trace data was shown in Section 7.3.3 was averaged along its span to provide a streamwise plot of the variable of interest; this trace was then averaged with its corresponding plasma "Off/On" partner to attempt to account for the large run-to-run variability in these parameters, especially the heat flux. Recall that the IR results were limited by the placement of the thermocouples, and that the Stanton number for the turbulent case near the leading edge was suspect as the flow was likely transitional, but the turbulent recovery factor was used. Finally, the simulations were extended to cover the range observed with the IR camera using the same settings as in Section 7.1 and a "Gradient Diffusion" heat flux calculation with the "Cebeci-Smith" turbulence model.

The IR data, Figure 7.125(a-b), are discussed first. The data showed that near the leading edge the experiment did not match the simulations. For the turbulent case, this could either be attributed to any number of factors, including: the code's inability to actually simulate transition; the physical 3D trip effects; the high heating due to the thin PEEK and closeness to the stainless steel frame; the exposure of both sides of the PEEK to the flow; the codes constant 350K boundary condition; leaving the test article in the tunnel during preheat; using r_{turb} in the data reduction code for this transitional region; *etc.*. Many of these same arguments could be extended to the laminar case in the same region.

However, farther from this dynamic region the results found much greater agreement, especially for the turbulent case. For the laminar case, the code under predicted the heat flux, and thereby the Stanton number, by a factor of two. Some testing showed reducing the wall tempera-

ture in the simulation could partially account for this discrepancy; because the heating was already so low in the "Laminar" case and both q_w and St are so sensitive to T_w, a change of only a few Kelvin in T_W could change q_w by $\sim 100\mathrm{W/m^2}$, thereby affecting the perceived difference between the results. Run-to-run repeatability could also partially explain the error; where the laminar data overlap at $\sim 375\mathrm{K}$ there was a large enough discrepancy to include the simulation's results in the margin of error. The turbulent case performed much better, perhaps because the large magnitude of heating better masked discrepancies; a difference of $\sim 100\mathrm{W/m^2}$ is a 50% error if $q_w = 200W/m^2$ but only 10% if $q_w = 1000W/m^2$. In either case, these results were encouraging and showed that given sufficient time for both the simulation and flow to develop past regions of high complexity, the simple numerical boundary layer solver did as decent a job of predicting wall heat flux and Stanton number as one could realistically hope.

The shear stress results in Figure 7.125(c) were discussed in Section 7.3.5.1. Summarizing, the laminar results were likely hindered by the assumed plate temperatures, both when analyzing the experimental data and also when setting T_w in the boundary layer solver. The turbulent data were all converging as the flow traveled downstream, which may have been evidence it was not yet entirely fully developed. The results using Clauser's method from the Pitot and PLIF data had close agreement, which was encouraging. Just as for the laminar case, that the Reynolds Average (RA) and van Driest II (VD) techniques data better matched the simulation towards the end of the test domain likely stemmed from the strong agreement in the heat flux at this point; to that end, the discrepancy at the leading edge could well have been due to the assumption of fully developed turbulence at the "Front" test location. It is noted that the boundary layer solver may have been slightly overpredicting τ_w as the boundary layer profile at the "Back" test location did not reach the log layer theory (see Figure 7.6); an alternative explanation may have been the low densities in the ACE tunnel being outside the range for which the Cebeci-Smith model was developed. Details aside, the wall shear stress was likely $5\mathrm{Pa} < \tau_w < 10\mathrm{Pa}$ and $17\mathrm{Pa} < \tau_w < 22\mathrm{Pa}$ for the laminar and turbulent flows respectively.

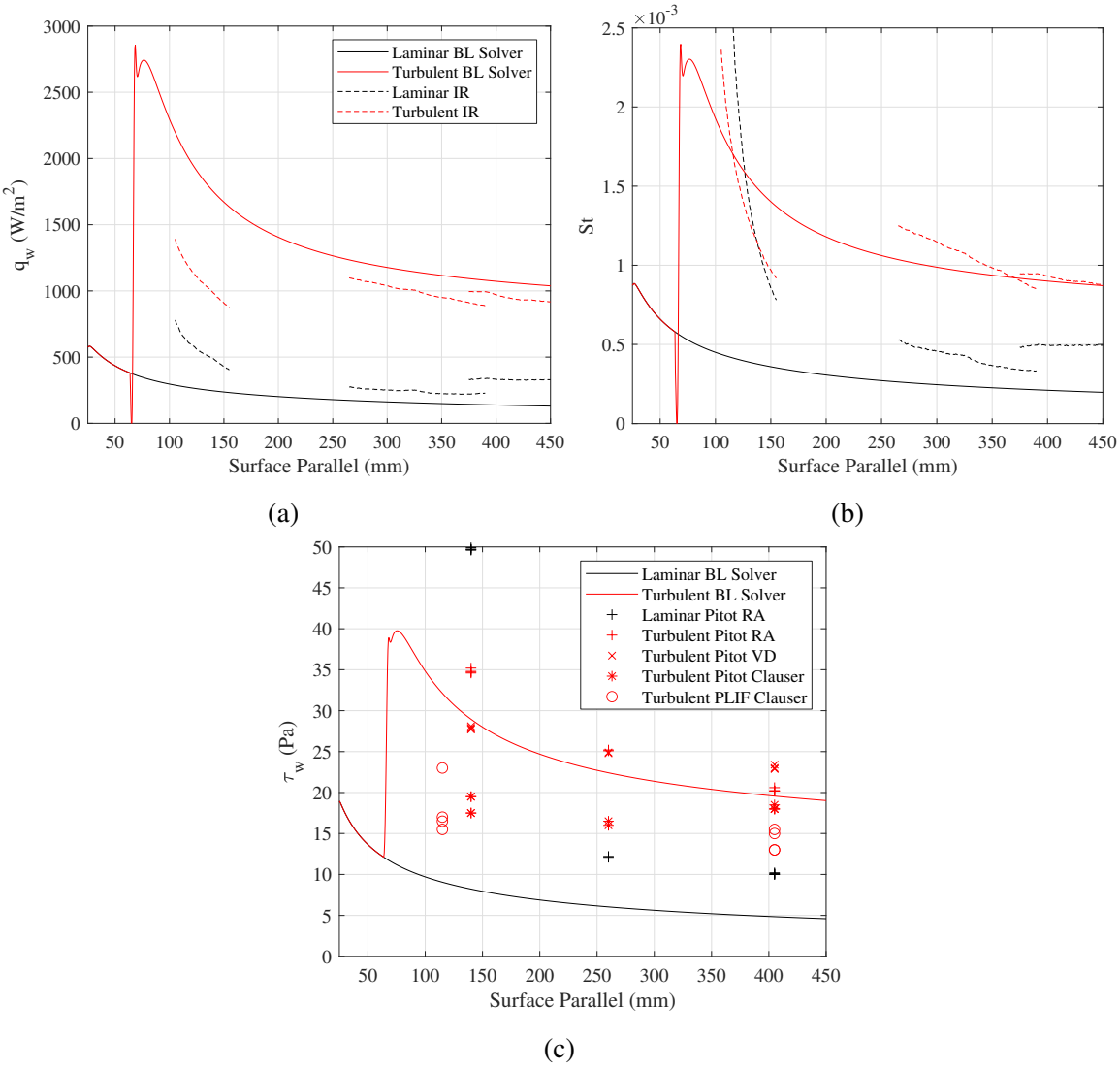

Figure 7.125: Comparison of wall variable measurement techniques; same legend applies to (a) and (b).

8. SYNTHESIS

Recall from Sections 2.3.6 and 2.3.5 the interest in relating the vibrational relaxation and turbulence timescales. Understanding the dynamics of vibrational decay and how it affected turbulence was a key research goal because whether the turbulence was frozen with respect to the vibrational decay, *vice versa*, or some combination of the two could explain some of the physics observed in the boundary layer as in [95, 138]. This section leveraged all elements of the work previously discussed in this report as organized in Figure 1.3: nonequilibrium experimentation; turbulence experimentation; and turbulence modeling. Although every piece of data thus presented and introduced here suggested the N_2 and O_2 were indeed frozen, the vibrationally excited NO acted as a more reactive proxy, and one which could be measured with the already familiar PLIF technique. A definitive, quantitative answer remained elusive, but through careful analysis of the above data and integration of several of the techniques developed throughout this report some conclusions could be drawn.

8.1 Vibrational Nonequilibrium Solver

Perhaps the most useful synthesis to address this research goal was that of the numerical boundary layer solver's results, sufficiently validated for these qualitative discussions, with the vibrational relaxation modeling Buen [49] used to estimate the species' vibrational temperatures along the ACE tunnel's nozzle. The resulting code, and the thermodynamics therein, will be described in greater detail than was originally necessary for Section 6.8.2 because it played a central role in this discussion. At its core, the program took a temperature, time (x/u), and pressure distribution and calculated the vibrational temperatures from these parameters. One will notice that all of these data were readily available along the test article via the boundary layer solver. And so it was a simple act to modify Buen's code to interpolate the numerical data at sufficient temporal resolution to model vibrational temperature evolution along the test article, creating a 2D solution.

All that remained was to provide an initial vibrational temperature resolution for the three

species. For N_2 and O_2 in the plasma "Off" case one could simply assume they were frozen at the nozzle's throat temperature of $T^v_{N_2,O_2} = 358$K, a solid assumption given the analysis by Buen [49]; this assumed full thermal slip at the wall, but coincidentally the freestream and wall temperatures were remarkably similar so any recovery would be small regardless, especially for the "Laminar" case. Really, then, the only free variable was the initial T^v_{NO}, which could either be set from the PLIF measurements or assumed to be in perfect equilibrium with the other species.

With this the simulation could begin. For simplicity's sake, this walk-through was restricted to a single height off the surface, effectively re-creating the 1D nozzle problem from Section 6.8.2, with the understanding that one could iterate over all heights in the domain to create a 2D solution. All interpolation steps were similarly omitted, but it was important to consider the system's spatial/temporal time scale. It will be seen shortly the reaction rate constants were small, so sufficient grid resolution was necessary to accurately capture the chemistry. Ultimately a value of $\Delta t = 1 \times 10^{-9}$s was used, matching the resolution in Buen's code. It was trivial to calculate for each grid point $\Delta x = u\Delta t$, and then to interpolate the boundary layer solver data for this Δx. However, near the wall the velocities became so small that tens of millions of grid points were necessary to resolve the entire domain from $x = 115 - 405$mm. For this reason, the first 25 grid points were truncated, though thanks to the clustered spacing < 0.5mm of data were removed.

The code considered the same twelve reactions tabulated in Table 2.2. Summarizing, for the three species there were nine VT reactions ($X^{v=1} + Y \rightarrow Y + X$) and three VV reactions ($X^{v=1} + Y \rightarrow Y^{v=1} + X$). For example, consider the reaction $NO^{v=1} + O_2 \rightarrow O_2^{v=1} + NO$ with forward and reverse reaction rate constants k_f and k_r respectively. The rate of change in $[NO^{v=1}]$ from this reaction can be found from $\frac{d[NO^{v=1}]}{dt} = -k_f[NO^{v=1}][O_2] + k_r[NO][O_2^{v=1}]$. Adding the losses from all of the other reactions, one can calculate a cumulative $\frac{d[NO^{v=1}]}{dt}$, and so on for $\frac{d[N_2^{v=1}]}{dt}$ and $\frac{d[O_2^{v=1}]}{dt}$.

As was discussed in Section 6.8.2, the reaction rate constants were calculated according to

$$k_{VT,v=1} = \frac{k_B T}{pt(T)\left(1 - e^{-\theta_v/T}\right)}$$

where θ_v was the vibrational characteristic temperature and $pt(T)$ were constants taken from [53]; the same source also provided equations for $k_{VV,v=1}$. $\theta_v = \Delta E/k_B$, and for N_2, O_2, and NO $\Delta E = 2358.57$, 1580.19, and 1904.04cm^{-1} respectively [109]. Following [116, 49] the reverse reaction rate constants were calculated to be $k_r = k_f \exp\left(-\frac{\theta_v}{T}\right)$ from detailed balance. Using these data, if the initial populations of the vibrationally excited species were known, their evolution along the test domain could readily be calculated using the boundary layer solver's temperature data. It is noted that these rate constants were only applicable for exchanges between the ground and first vibrational states, limiting the code to the low temperature environments in the ACE tunnel. Furthermore, these values were taken outside of their calibrated temperature range due to the unique conditions in the ACE tunnel's freestream.

Clearly proper estimation of the initial $v = 1$ populations was critical. To achieve this, the code made the necessary assumption that each species was in thermal equilibrium with itself; again, the purpose of the code was to decipher trends, not perfectly predict the exact temperatures, and at low T^v this was not such an egregious simplification. The population fractions for the first twenty vibrational levels v of each species m were calculated and the corresponding energy for each was found from

$$\Delta E_{m,v} = \Delta E(v+0.5) - \Delta E^{ex}(v+0.5)^2 \tag{8.1}$$

where the anharmonic vibration constant ΔE^{ex} was 14.324, 11.98, and 14.1cm^{-1} for N_2, O_2, and NO respectively. This equation represents an improvement over the simple harmonic oscillator model contained in the first term from Section 2.3 by adding an anharmonic correction via the second term (see [11]). The Boltzmann population distributions were then calculated from $N_{m,v}^{Boltz} = \exp\left(-\frac{\Delta E_v}{k_B T}\right)$ and the population fractions of each level were found by simply dividing $N_{m,v}^{Boltz}$ by the sum over all v. The total number density of each species was calculated from the ideal gas law $N_m = \frac{P}{k_B T}$ and the ratio of the species for a given injected $[NO]$. With the Boltzmann population fractions and true number densities known, one could easily calculate all the requisite number densities $N_{m,v} = n_{m,v}^{Boltz} N_m$.

For all subsequent iterations, after the changes in the populations of the ground and vibra-

tionally excited molecules were found the population fractions $n_{m,v}$ were calculated from $N_{m,v}/\sum_{m=1}^{3}\sum_{v=0}^{1}N_{m,v}$ for the next streamwise location. This is one simplification which limited the code to low temperature applications, as for higher T^v the populations of $v = 2-19$ would be significant and could not be neglected. Again, another reason this code was limited to such applications was because the rate constants were only provided for the $v = (0,1)$ reactions, so to model relaxation from higher vibrational energy levels would require additional equations.

With the populations of each species known, the vibrational energy for a given species was calculated from the Boltzmann equation

$$T_m^v = -\frac{\Delta E_v}{k_B \ln\left(\frac{N_m^{v=1}}{N_m^{v=0}+N_m^{v=1}}\right)} \tag{8.2}$$

where ΔE in J, as hard-coded by Buen [49], was 4.62796×10^{-20}, 3.09116×10^{-20}, and 3.72601×10^{-20}J for N_2, O_2, and NO.

These equations were sufficient to replicate the bulk of the code, with the remaining work mostly pertaining to keeping track of the number densities for the ground and excited vibrational state for each species for a given condition in the flow. This was a simple tool which relied on heavy simplifications, but it was this very simplicity which made modeling the complex environment in this report tractable to at least a first approximation. Indeed, the general trends observed from these efforts were illuminating.

8.2 Simulated Vibrational Temperature Evolution: Simple Case

It would be prudent to begin any analysis with the simplest case. The "Laminar/Plasma Off" case was simulated and the results shown in Figure 8.1. It is noted that only the NO demonstrated any tangible change, the other species were almost entirely frozen throughout the entire test domain. Figure 8.1(a) assumed $T_{e,NO}^v = 230K$, and one could see that the simulated vibrational temperature far exceeded that measured with PLIF.

Indeed, while there was some slight change in the profile, in general it seemed the temperatures were being driven to the edge condition $T_{NO}^v \rightarrow T_{e,NO}^v$. However, in the simulation T_{NO}^v rose

dramatically, approaching either T_w or $T^v_{N_2,O_2}$. This was an important result. If the experiments indicated the temperature profile was slightly approaching its edge condition, and the simulations indicated the profile should have been approaching $\sim$ 350K, that would suggest the assumption that $T^v_{e,NO} = 230K$ was flawed, and the NO was vibrationally equilibrated with the N_2 and O_2 at 358K in the freestream. Remember, $T^v_{e,NO}$ was manually set in the PLIF data reduction code, and while it was fixed according to the best educated guess, $T^v_{e,NO}$ was simply not as well predicted from theory as the ro-translational temperature. One can immediately see in Figure 8.1(b) that when $T^v_{e,NO} = T^v_{e,NO} = 358$K, though there was still a discrepancy in the boundary layer, the agreement was greatly improved. In practice, it was most likely that 230K $\leq T^v_{NEQ} \leq$ 358K, and until further experimentation or theory comes out to address this uncertainty the values in Section 7.4.2.2 and Appendix A must similarly be treated as limits of the true result and used more for the identification of trends then precise quantification.

Because $T_w \approx T^v_{N_2,O_2}$ it was difficult to tell if the NO was equilibrating with the N_2 and O_2 or with the wall. For this reason, the simulation was run again for $T^v_{N_2,O_2} = 500K$, a conservative "Hot" case. The results in Figure 8.1(c) show the NO was attempting to equilibrate with the N_2 and O_2 because it exceeded the boundary layer temperatures. However, the process that led to the equilibration, to be hypothesized shortly, was not completely dominant because the NO was unable to reach $T^v_{N_2,O_2}$. There was sufficient space in the domain for this to occur as the results at 260mm were very close to those at 405mm, and the ro-translational temperatures between the "Middle" and "Back" cases were also similar. It was possible instead that at elevated temperatures competing mechanisms existed which drove $T^v_{e,NO}$ towards a steady state between the bath gases' rotational and vibrational temperatures. Work in the next subsection addresses these pathways. Before moving on it is at least worth noting that even in the case of $T^v_{NO} = 230$K some degree of wall quenching to satisfy the no-slip condition must be considered, that although σ_v is probably $\neq 1$ it is certainly > 0.

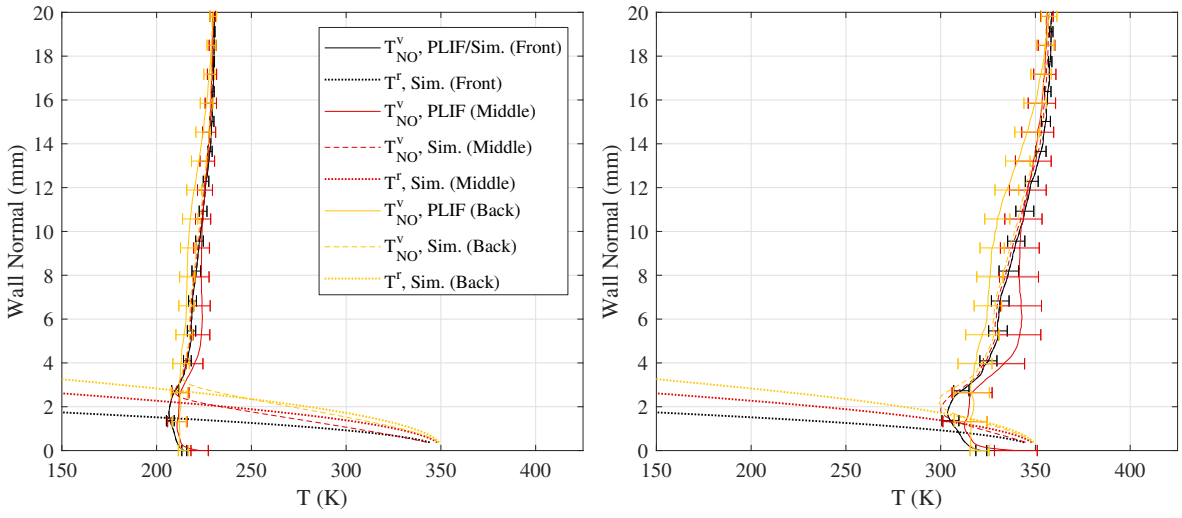

(a) $T^v_{e,NO} = 230K$, $T^v_{e,N_2} = T^v_{e,O_2} = 358K$

(b) $T^v_{e,NO} = 358K$, $T^v_{e,N_2} = T^v_{e,O_2} = 358K$

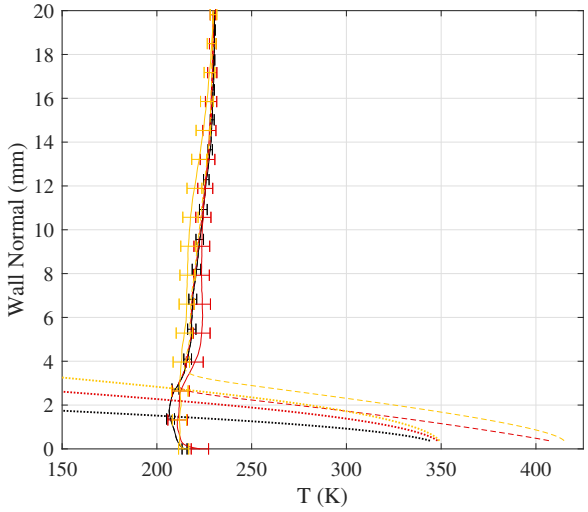

(c) $T^v_{e,NO} = 230K$, $T^v_{e,N_2} = T^v_{e,O_2} = 500K$

Figure 8.1: Comparison of simulated and measured T^v_{NO} through the laminar boundary layer with the plasma off; same legend applies to all figures.

8.3 Energy Pathways

Why did the equilibration turn on in the boundary layer? Why was only the *NO* affected? Through what mechanisms did the exchange occur? These questions were addressed by delving deeper into the thermodynamics. The reaction rate constants for the "Laminar/Plasma Off" and "Turbulent/Plasma Off" cases are plotted in Figure 8.2(a) and (b) respectively with the temperature

taken from the respective simulation 405mm from the leading edge. Note that owing to the equations provided by Candler et al. [53], the reaction rate constants were identical for all VT reactions starting from the same excited species (ex.- $NO^{v=1} + N_2$, $NO^{v=1} + O_2$, $NO^{v=1} + NO$) and thus are listed based only on the excited species.

From this figure one can see that the elevated temperatures in the boundary layer allowed the reactions to activate near the wall, some rising dozens of orders of magnitude; again, due to necessity these reaction constants were calculated outside of their calibrated temperature range. The three dominant energy pathways near the wall were, in order: 1) Vibrational energy exchange from NO to O_2; 2) Collisional vibrational relaxation of NO; 3) Vibrational energy exchange from O_2 to NO (the reverse of Reaction 1).

Upon first inspection, these data would suggest NO should be losing vibrational energy, not gaining it. But consider the relative concentration of NO, just $\sim 0.15\%$. This meant there would be $> 100\times$ as much vibrationally excited O_2 in the boundary layer than NO, even before one considered $\theta_{v,O_2} < \theta_{v,NO}$ and that O_2 may well have been at a higher vibrational temperature in the first place. Therefore, the relative likelihood of the first two most dominant reactions occurring dropped significantly. Put another way, in general NO wanted to give O_2 more vibrational energy than it received, but there were $> 100\times$ more reactant O_2 molecules for the reverse reaction to use, and often higher temperatures as well. Finally, whatever O_2 the NO did excite via Reaction 1 efficiently passed that energy back to the NO through Reaction 3. This, coupled with some NO excitation through energy exchange with vibrationally excited N_2, manifested as the rise in temperature seen in Figure 8.1.

8.4 Simulated Vibrational Temperature Evolution: Include Mixing

One could justifiably look at the data in Figure 8.1 and ask to what extent diffusion, mixing, and boundary layer growth affected the results. This became even more relevant with the introduction of the plasma, which nonuniformly seeded vibrational energy into the flow; a discussion of the effect of the plasma was reserved for later in this section. While Buen [49] did attempt to quantify diffusion using a version of Fick's Law, here it was sufficient to remain qualitative. Noting the

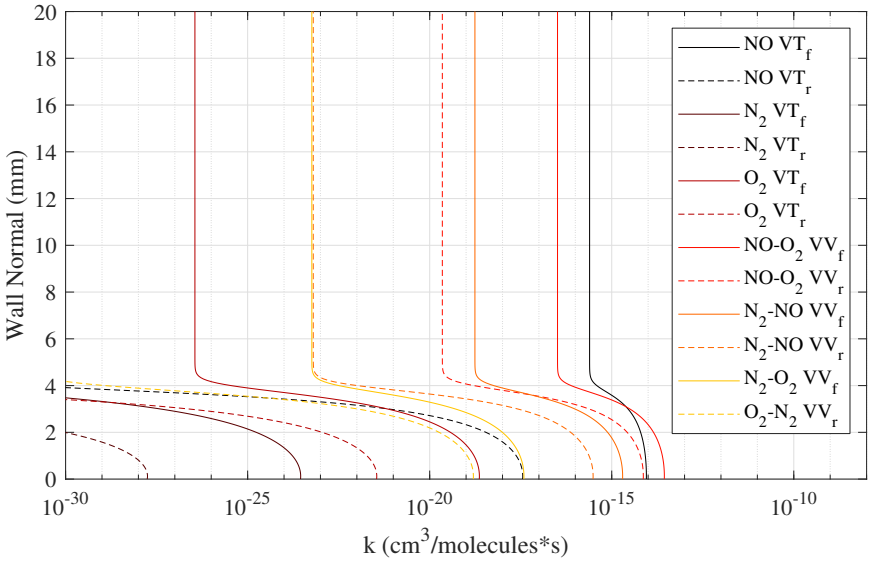

(a) Laminar

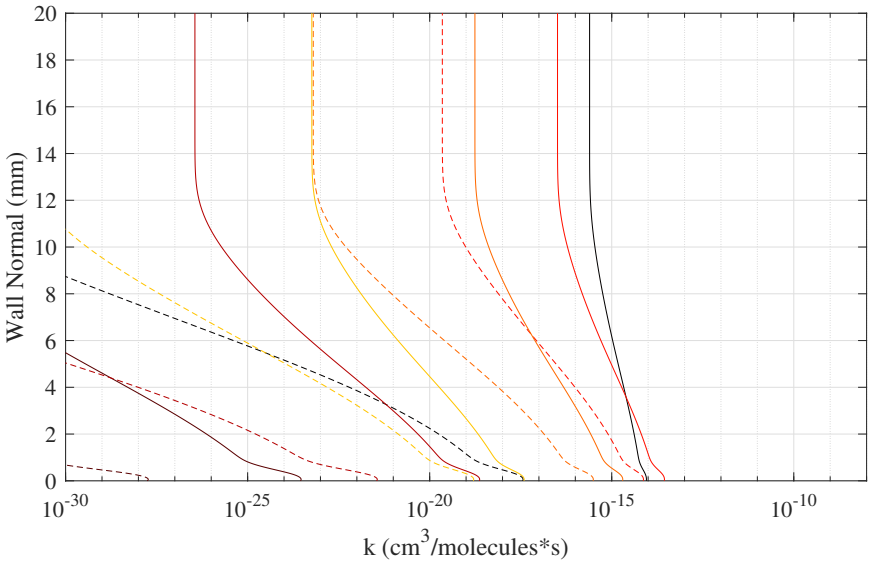

(b) Turbulent

Figure 8.2: Reaction rate constants through the boundary layer; same legend applies to all figures.

boundary layer growth seen with the numerical boundary layer solver, it was sufficient in the laminar case to say the vibrational energy profile evolved as the boundary layer grew. In this "Low Mixing" case, one can see it did not reach the edge condition in the boundary layer, though it did approach it.

Mixing was effectively "turned on" via the installment of the trips. The results from the "Tur-

bulent/Plasma Off" case are shown in Figure 8.3. It became immediately clear that with mixing turned on, the T^v_{NO} profiles solidly reached the edge conditions. The close agreement between the simulation and experimental results in Figure 8.3(b) further supported the notion that $T^v_{e,NO}$ and $T^v_{N_2,O_2}$ became much closer to the edge condition, approaching $T^v_{e,NO} \approx T^v_{N_2,O_2}$. The "Hot" results shown in Figure 8.3(c) were included for completeness. So, without mixing the T^v_{NO} profiles approached the edge condition, be it due to thermodynamic effects or diffusion. However, once turbulent mixing was introduced the profiles almost perfectly reached their edge condition. Taken together, this would suggest that turbulent mixing was occurring at a timescale comparable, if not faster than the relaxation, a concept which requires some quantification.

8.5 Time Scales

Order-of-magnitude estimates for relaxation and flow timescales were calculable. The vibrational relaxation time scale was estimated by calculating the Landau-Teller relaxation time scale, $NO\ VT_f$ in Figure 8.2. This was completed using [214]

$$\tau = \left\{ N_m k_f \left[1 - \exp\left(-\frac{\theta_v}{T} \right) \right] \right\}^{-1} \tag{8.3}$$

where N_m is the number density of species considered, N_2, O_2, and NO. These results were calculated using the reaction rate constants and temperature 405mm from the leading edge and are shown in Figure 8.4. These data reinforced the idea that N_2 was completely frozen, though the extent predicted likely stemmed from using reaction rate constants calculated outside of their calibrated range. Still, near the wall where temperatures were more reasonable, one could see that NO and O_2 would relax in $\mathscr{O}(1 \times 10^{-3})$ and $\mathscr{O}(1 \times 10^{-1}\text{s})$ respectively. Remember, this only considered self-relaxation (ex.- $NO^{v=1} + NO$), while the rate constants for the VT processes were shared by the other collisional pathways (ex.- $NO^{v=1} + N_2$ and $NO^{v=1} + O_2$). Owing to the higher concentrations of the N_2 and O_2, one could say that the true thermodynamic time scales were smaller than that of Landau-Teller, perhaps even by several orders of magnitude.

Various flow time scales could be similarly predicted. The flow-over-body time scale was

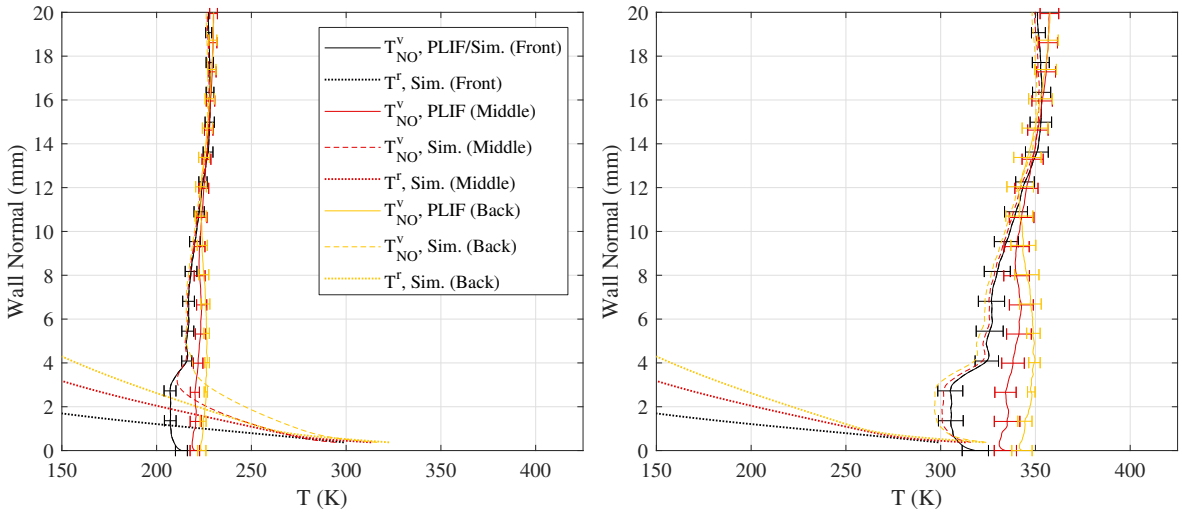

(a) $T^v_{e,NO} = 230K$, $T^v_{e,N_2} = T^v_{e,O_2} = 358K$

(b) $T^v_{e,NO} = 358K$, $T^v_{e,N_2} = T^v_{e,O_2} = 358K$

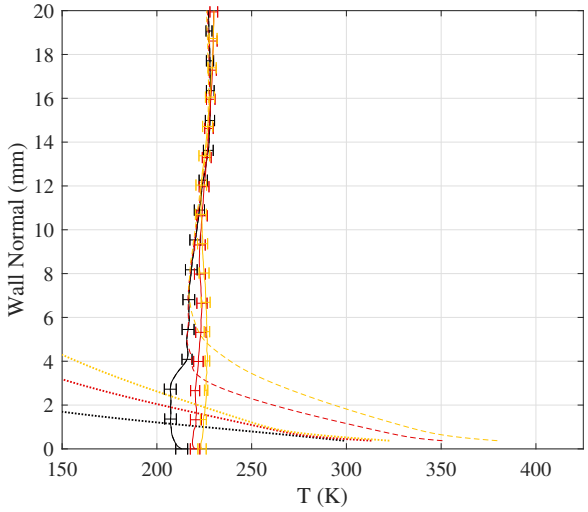

(c) $T^v_{e,NO} = 230K$, $T^v_{e,N_2} = T^v_{e,O_2} = 500K$

Figure 8.3: Comparison of simulated and measured T^v_{NO} through the turbulent boundary layer with the plasma off; same legend applies to all figures.

$\tau_F = \frac{l_{body}}{u_e} \approx 0.5\text{m}/1000\frac{\text{m}}{\text{s}} \approx 5\times10^{-4}\text{s}$; it would be even higher in the boundary layer. For turbulent flows, additional classical time scales were calculable. The large eddy turnover timescale [221], $\tau_E = \frac{\delta}{u_e} \approx 0.01\text{m}/1000\frac{\text{m}}{\text{s}} \approx 1\times10^{-5}\text{s}$. The smallest timescale, the Kolmogorov timescale $\tau_\eta = \left(\frac{\nu}{\varepsilon}\right)^{\frac{1}{2}}$ (see [221]) required some additional modeling. From [239] $\varepsilon \approx C_D\frac{K^{T\frac{3}{2}}}{l}$ where $C_D \approx 0.09$. For flows over flat plates, the turbulent kinetic energy K^T could be modeled from Bradshaw et al. [44] as $a_1\rho K^T = \tau^T_{xy}$ where $a_1 = \sqrt{C_D} \approx 0.3$ [136]. Also from [239], $l_m \approx C_D^{-1/4}l$. Now, assuming

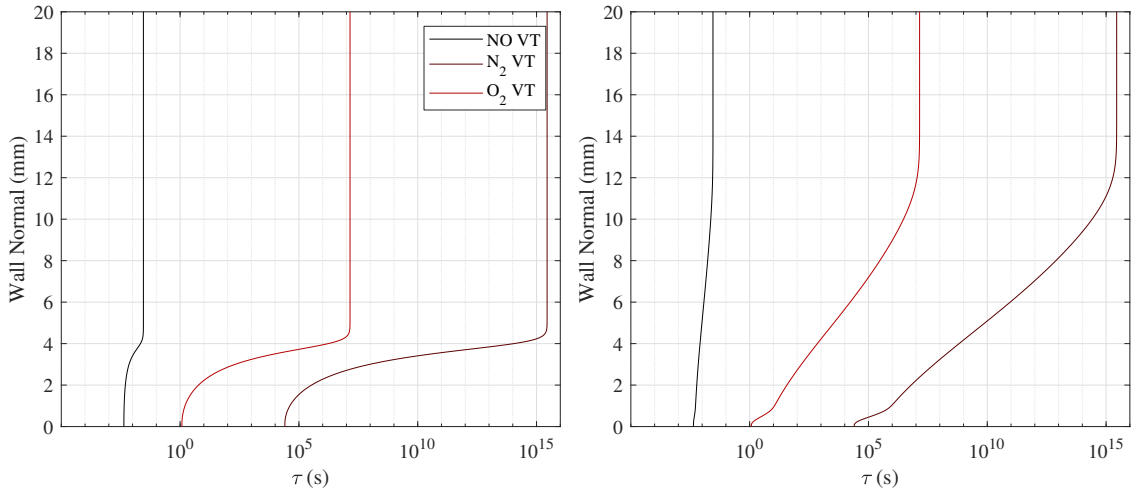

(a) Laminar (b) Turbulent

Figure 8.4: Landau-Teller vibrational relaxation times through the boundary layer; same legend applies to all figures.

for the log layer of an adiabatic flow (which the current problem nearly is), one can take $\nu = \nu_w$, $\tau_{xy}^T = \tau_w$, and $l_m \approx \kappa y$ where $\kappa \approx 0.41$ [65]. Finally, recalling $u^* = \sqrt{\frac{\tau_w}{\rho}}$ and assuming this incompressible formulation holds ($\rho_w \approx \rho$), one can write

$$\varepsilon \approx C_D \frac{K^{T\frac{3}{2}}}{l} \approx C_D \frac{K^{T\frac{3}{2}}}{C^{\frac{1}{4}}\kappa y} \approx \frac{C^{\frac{3}{4}}}{\kappa y}\left(\frac{\tau_w}{a_1\rho}\right)^{\frac{3}{2}} \approx \frac{C^{\frac{3}{4}}}{\kappa a^{\frac{3}{2}}}\frac{(u^*)^3}{y} \approx 2.5\frac{(u^*)^3}{y}$$

Using the results from the numerical boundary layer solver, one can therefore write

$$\tau_\eta \approx \left(\frac{0.003\frac{\mathrm{m}^2}{\mathrm{s}}}{2.5\frac{(u^*)^3}{y}}\right)^{\frac{1}{2}} \approx \left(\frac{0.003\frac{\mathrm{m}^2}{\mathrm{s}}}{2.5\frac{\left(50\frac{\mathrm{m}}{\mathrm{s}}\right)^3}{0.005\mathrm{m}}}\right)^{\frac{1}{2}} \approx 5\times10^{-6}\mathrm{s}$$

Finally, the Taylor microscale acts as the boundary between inertia and viscosity dominated regimes (see [221]). This timescale can be found from $\tau_\lambda = \frac{\lambda}{u'_{RMS}}$ where $\lambda = \left(10\nu\frac{K^T}{\varepsilon}\right)^{\frac{1}{2}}$; one can write under the present simplifications and assumptions $\tau_\lambda \approx \frac{\lambda}{K^{T\frac{1}{2}}} \approx \frac{\left(10\nu\frac{K^T}{\varepsilon}\right)^{\frac{1}{2}}}{K^{T\frac{1}{2}}} \approx \sqrt{10}\tau_\eta \approx 1\times10^{-5}\mathrm{s}$.

These results are summarized in Table 8.1. They suggested that vibrational relaxation would be frozen with respect to the turbulence, but not the flow itself, at least not near the wall. Again,

however, one must remember that the cross-species reactions with O_2 were dominant and likely faster than the $NO\ VT$ reaction modeled with Landau-Teller. Even if they were just one or two orders of magnitude faster, then the vibrational relaxation and turbulence effects would be of the same order of magnitude, allowing for some interplay between the two. Again, near the wall some degree of quenching must be considered, though ascribing a single time scale to this process is challenging; note that for vibrationally hot flows like those with the plasma on, the wall would likely act as a vibrational energy sink and would not participate in the chemistry modeled above.

$\tau_{L-T,NO}$	τ_F	τ_E	τ_η	τ_λ
1×10^{-3}	5×10^{-4}	1×10^{-5}	5×10^{-6}	1×10^{-5}

Table 8.1: Estimated chemistry and flow time scales.

8.6 Simulated Vibrational Temperature Evolution: Include Plasma

The data thus presented have suggested that in turbulent boundary layers mixing and near-equilibrium conditions have led to negligible changes in the vibrational energy profile. Does this mean no meaningful development of vibrational energy in a hypersonic boundary layer was recorded? Fortunately, data for boundary layers with significant thermal perturbation were available owing to the glow discharge; these plasma "On" data, Figures 7.84(b)/A.1(b) and 7.85(b)/A.2(b), show the development in a truly nonequilibrium environment. In Hsu [116] and Fuller et al. [95] it was estimated, and where possible supported by measurement, that for an air mixture containing 1% NO at 30Torr and $T^r \approx 335$ and for a 300W RF plasma that $T^v_{N_2} = 1700$K, $T^v_{O_2} = 800$K, and $T^v_{NO} = 2000$K; it is noted that in their subsequent models, Hsu assumed vibrational equilibrium at 2000K. Due to the higher pressures and lower velocities in this experiment, one would expect it to be more equilibrated than that in the current work, even though the comparatively low powered (47W) DC glow discharge was incapable of reaching as high of vibrational temperatures, as confirmed with PLIF. The point here is that a plasma can introduce a high de-

gree of nonequilibrium, perhaps most critically between the reactive O_2 and NO species. Also, the vibrational temperatures measured by PLIF were tractable for the low temperature solver available.

Because of the complexity of including both mixing and thermal nonequilibrium, it was decided to first simulate a purely theoretical case. The code was modified to set $T^v_{NO} = T^v_{N_2} = 500\text{K}$ and $T^v_{O_2} = 358\text{K}$ to mimic a case where the O_2 was "Cold". No experimental PLIF data was used because the goal was to determine whether or not the NO was frozen, not necessarily to replicate any experimental data. The results in Figure 8.5 show that the NO was indeed capable of losing vibrational energy; it is noted that the N_2 was, predictably, frozen. That the T^v_{NO} reached a lower temperature in the "Laminar" case was due to the activation of the reaction rate constants in the thinner but hotter boundary layer.

These results suggested that the decay in vibrational energy seen in Figures 7.84(b)/A.1(b) and 7.85(b)/A.2(b) cannot be said to solely exist due to diffusion, boundary layer growth, or mixing. Within the boundary layer, in the amount of time the excited species remained on the plate, the same vibrational relaxation pathways identified above were occurring to a significant degree.

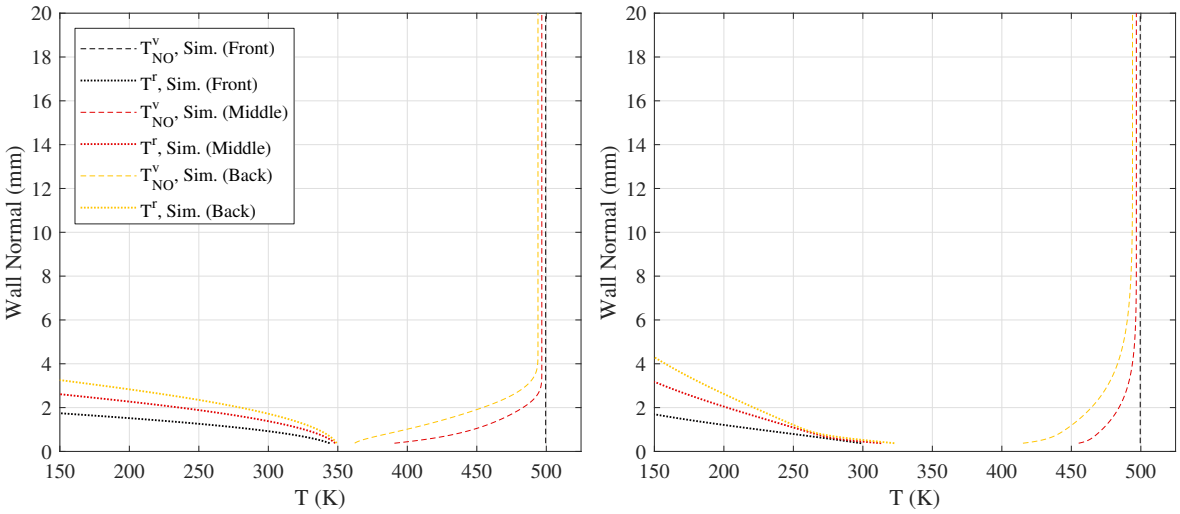

(a) Laminar

(b) Turbulent

Figure 8.5: Theoretical simulation of vibrational energy decay in a boundary layer in thermal nonequilibrium; same legend applies to all figures.

With the theory understood, the code was applied to the real PLIF data; appreciate that this result was the culmination of the synthesis of the turbulence theory, classical experiments, and nonequilibrium experiments. Following [116], it was assumed that the NO and N_2 vibrational profiles would be identical and taken from the PLIF data, and that the O_2 profile would be fixed at a constant 358K. The results were plotted in Figure 8.6.

The results assuming $T^v_{e,NO} = 230$K were mostly included for completeness, as demonstrated the same issues seen in Figures 8.1(a) and 8.3(a). The most exciting data was found when $T^v_{e,NO} =$ 358K. Consider Figure 8.6(c). The temperature peaks within the boundary layer were reasonably well predicted by the code; accounting for the heavy simplifications taken to produce a numerical result, this degree of agreement must be considered solid. The discrepancy near the wall may have been due to the numerical boundary layer solver under predicting the size of the temperature and velocity boundary layers, a fact heavily discussed in Section 7.5.1. The matching peaks and general shape of the curves lent credence to this explanation. Alternatively, it could have been due to the numerical approach over predicting the amount of equilibration with the wall, but as this feature was not observed in the turbulent case this interpretation seemed less likely. Nevertheless, the agreement suggested that in a low mixing environment, vibrational relaxation was the dominant mechanism for energy redistribution.

The results thus far offered an explanation for why, at no point in any of the above campaigns, there was no measurable effect of the plasma on the turbulence. Most of the plasma's energy went into N_2 and NO excitation, and while the latter was able to demonstrate some degree of relaxation, all of the analyses in this section point towards the N_2 being frozen. Thus the bulk of the vibrational excitation being instilled by the plasma was incapable of transferring to the ro-translational states. Because this process could not occur, the viscosity, Reynolds number, and turbulent kinetic energy were unaffected by the plasma, breaking the chain identified by Fuller et al. [95]. Furthermore, the plasma's power and temperature was too low to perturb the flow via Joule or cathode heating as observed in the experiments in Section 2.4.4. The effect of any relaxation of the NO, however, was limited simply by its low concentration and vibrational temperature. This in an of itself was

an important conclusion.

The turbulent case in Figure 8.6(d) appeared to have far worse agreement. The profile shape at the "Front" test location seemed to be imprinted on the rest of the boundary layer. To address this concern, the data are re-plotted starting the simulations in the "Middle" test location, 260mm from the leading edge in Figure 8.7; the flow should be fully turbulent by this point, not transitional as in the "Front" test location. Again, focusing on the results for $T^v_{e,NO} = 358$K ((c) and (d)), one can see that due to the closeness of the vibrational temperature profiles between the "Middle" and "Back" test locations, here the predictions show better agreement with the experiment in the "Back" test location than those in Figure 8.6. As before, near the wall T^v_{NO} was under predicted perhaps due to the reaction rate constants or velocity profiles used; as the boundary layer solver under predicted the height of the boundary layer, the velocity at any given height above the wall was low, meaning there was more time for relaxation to occur than there would be in the actual experiment. This effect went away as the relaxation began to freeze approaching the freestream. Here again, in the turbulent case (d) the effect of the plasma extended further and further into the freestream as the flow moved along the test article. Because the relaxation reactions were "turned off" far from the wall due to the low ro-translational temperatures, this was likely due to turbulent mixing and diffusion. In a way, the boundary layer was almost split between thermodynamic dominance near the wall and turbulence dominance near the freestream. In practice, all but the most specialized RANS models would likely struggle to capture the complex, 3D wake-driven turbulence actually measured on the plate, let alone couple it to thermal nonequilibrium, which lead to the worse agreement in the "Turbulent" case as compared to the "Laminar" case.

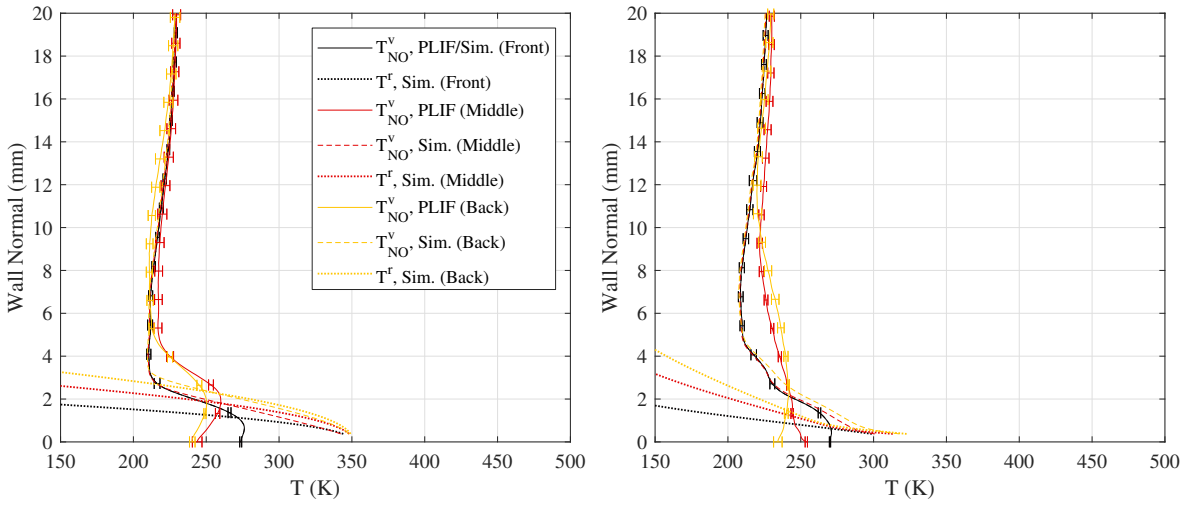

(a) Laminar, $T^v_{e,NO} = T^v_{e,N_2} = 230\text{K}$, $T^v_{e,O_2} = 358\text{K}$

(b) Turbulent, $T^v_{e,NO} = T^v_{e,N_2} = 230\text{K}$, $T^v_{e,O_2} = 358\text{K}$

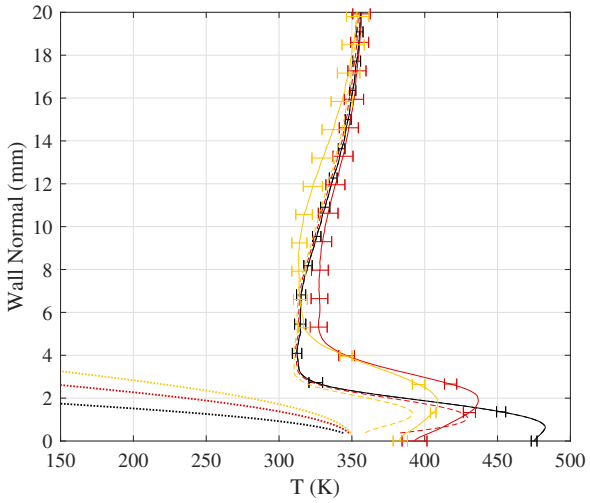

(c) Laminar, $T^v_{e,NO} = T^v_{e,N_2} = T^v_{e,O_2} = 358\text{K}$

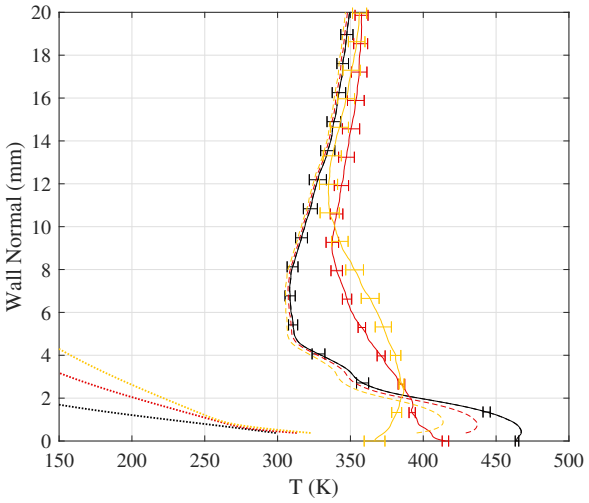

(d) Turbulent, $T^v_{e,NO} = T^v_{e,N_2} = T^v_{e,O_2} = 358\text{K}$

Figure 8.6: Comparison of simulated and measured T^v_{NO} through the laminar and turbulent boundary layers with the plasma on starting 115mm from the leading edge; same legend applies to all figures.

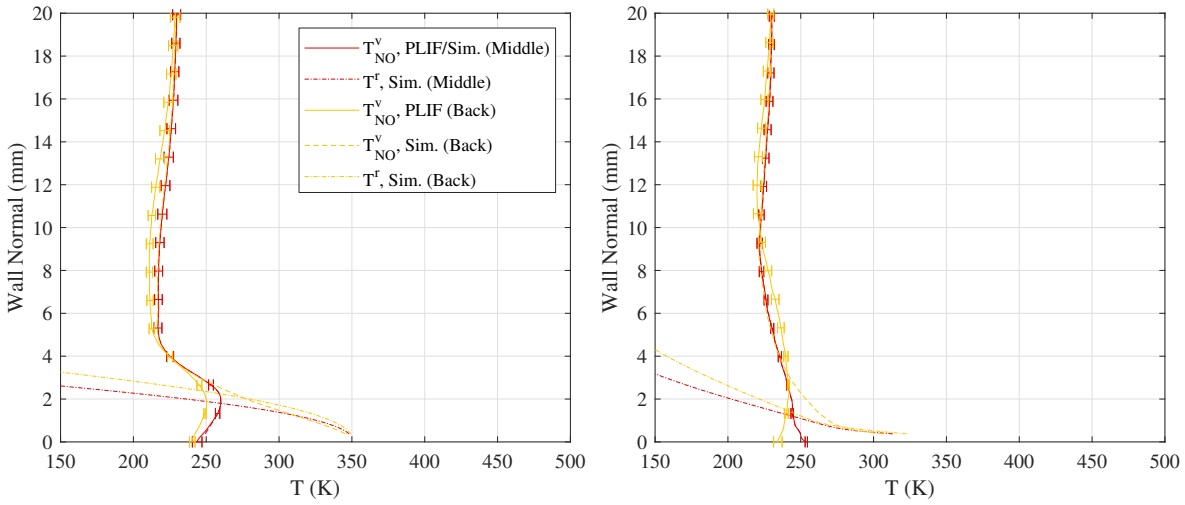

(a) Laminar, $T^v_{e,NO} = T^v_{e,N_2} = 230\text{K}$, $T^v_{e,O_2} = 358\text{K}$ (b) Turbulent, $T^v_{e,NO} = T^v_{e,N_2} = 230\text{K}$, $T^v_{e,O_2} = 358\text{K}$

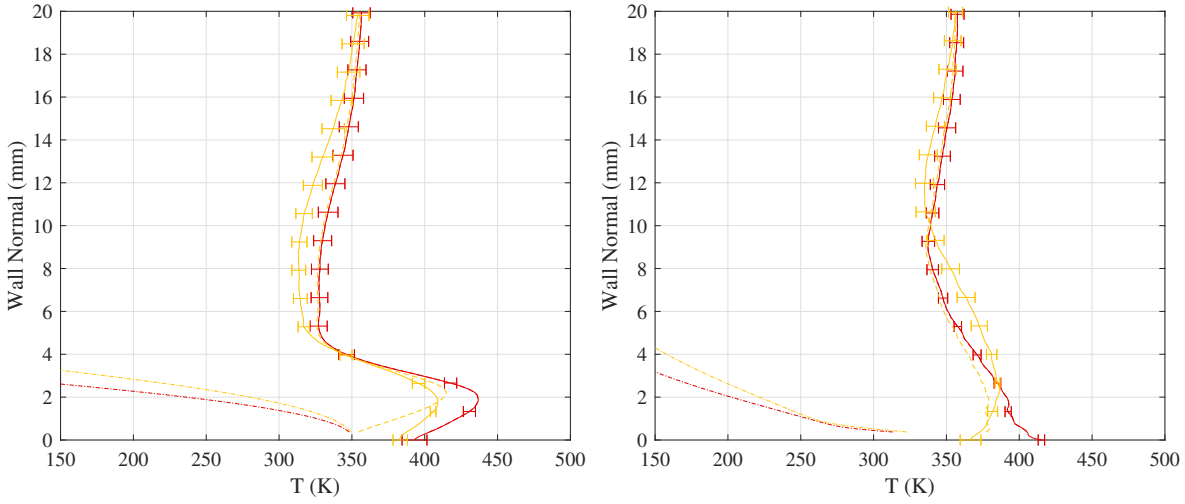

(c) Laminar, $T^v_{e,NO} = T^v_{e,N_2} = T^v_{e,O_2} = 358\text{K}$ (d) Turbulent, $T^v_{e,NO} = T^v_{e,N_2} = T^v_{e,O_2} = 358\text{K}$

Figure 8.7: Comparison of simulated and measured T^v_{NO} through the laminar and turbulent boundary layers with the plasma on starting 260mm from the leading edge; same legend applies to all figures.

This underscored the core of this report: vibrational energy in turbulent hypersonic boundary layers requires improved modeling. The data presented here represented a solid resource for exploration of the theory and validation of such a model, and a pathway to derive an energy flux-driven model was provided in Chapter 3. Would such a model be appropriate for this environment, with its vortical structures and nonuniform particle tagging, or would its omission of diffusion limit its accuracy? What other reductions would be necessary to close the nonequilibrium conservation equations in Section 2.3.4? Would existing DNS codes be capable of predicting the data at the "Back" test location given the results at the "Front" test location? If given the results from the leading edge? Would injection of a rapid relaxer species like CO_2 as in [206] allow the relaminarization pathway identified by Fuller et al. [95] to occur? Could a better prediction of the relaxation or turbulence time scales be produced? Not one of these questions was trivial, but it was hoped the the data contained in this long report would be useful in addressing them, or at least serve to motivate future research.

9. CONCLUSIONS AND FUTURE WORK

Recall this work's objectives: 1) Produce a test article capable of canonical boundary layers, excitation of thermal nonequilibrium, and both modern physical and optical diagnostics; 2) Re-derive the algebraic energy flux model in great detail; 3) Create a database of experimental turbulence data to validate turbulence models; 4) Extend this database to flows in thermal nonequilibrium. Taken together, the goal was to provide a database of parameters collected in a hypersonic turbulent boundary layer with and without thermal nonequilibrium to improve understanding and modeling of these environments. Despite its recognized critical importance, there was little to no canonical experimental data of these flows in thermal nonequilibrium for validation of proposed theories and models, hindering progress. Therefore this work served the broader community by encouraging the development of low cost predictions of aerodynamic heating, and thereby more judicious use of high fidelity computations when designing thermal protection systems.

Each of the research objectives are separately discussed. Section 4.4 covered the design of the test article, from its pedigree to its current features. Particular interest was paid to the leading edge, trips, and electrodes, as these features would directly control the quality of the boundary layer produced and thereby that of the entire experimental campaign. Novel design elements included the vibration-resistant, translatable struts and the inclusion of mounted optics, both of which were added to allow for an array of laser diagnostics to be performed both across and through the boundary layer. The success of the test article was quantified in Section 7.2 wherein the plasma was characterized using circuit measurements, the trip efficacy was tested with IR thermography, and the leading edge uniformity was confirmed using surface profilometry.

Chapter 3 covered the justification, derivation, and implementation of an algebraic energy flux model for flows in thermal equilibrium. The results matched those of the source material [38] on which they were meant to elaborate. The theory was extended for the first time to a flow in a favorable pressure gradient as well, and its results were encouraging [46]. The AEF model was included in the novel boundary layer solver covered in Chapter 5 and its results discussed in

Section 7.1. The comparisons in Section 7.5 validated the code's results to a reasonable degree and highlighted potential areas for improvement.

Future work in this research objective would extend the exact same mathematical machinery to a flow in thermal nonequilibrium using the modified conservation equations were written in Section 2.3.4. Because a solution is known to exist [37] and such rigor was provided for the equilibrium counterpart, a successful outcome is expected. Once complete, what will remain is the implementation and tuning of the model in a CFD code and validation with DNS and experimental data, a sample of the latter being provided here. Though this task did not fit into the current research schedule, it is hoped the instructions for deriving the equilibrium AEF model and steps to include it in a RANS solver in Chapters 3 and 5 respectively were sufficient to guide this effort. Without considering thermal nonequilibrium, the work in Chapter 3 pointed to the need for improved hypersonic Reynolds stress models and showed areas where the present model could be enhanced such as its performance near the wall or the use of the weak (mechanical) equilibrium assumption in the presence of pressure gradients.

Chapter 6 described all of the experimental techniques employed to analyze the test environment, the reason for their use, and the steps taken to implement them. These techniques produced the data in Chapter 7 which covered: the wall temperature, heat flux, and shear stress; the freestream velocity, temperature, and Mach number; the plasma's power, constituents, and temperature; freestream Pitot and surface pressure measurements; high-frequency pressure measurements; boundary layer and shock visualization; leading edge uniformity and roughness. The temperature, velocity, Mach number, and pressure data were all taken to resolve the turbulent fluctuations, and data was taken at up to six test locations along the streamwise and spanwise direction for the laminar/turbulent and plasma off/on cases. Thus, through a variety of techniques, including some redundant measurements, the flow was exceptionally well characterized.

The future worth of the test article for continuing experimentation has already been proven. The development of PLIF diagnostics in the ACE tunnel has continued, with with the first 1D VENOM measurement already having been completed. A complete VENOM campaign is planned at the

same conditions covered in this report, poised to add $\overline{u'T'}$ measurements to the existing database; such a direct measurement of the streamwise energy flux would prove critical for validation of the AEF model. These experiments may be extended to 2D VENOM measurements, and perhaps even the theorized vibrational VENOM. The broader NAL community has shown an interest in working with this model as well because the flow is so well characterized and understood. Members Texas A&M University's Aerospace Laboratory for Lasers, ElectroMagnetics and Optics have used it as a canonical environment for the first femtosecond laser electronic excitation tagging and filtered Rayleigh scattering experiments in the ACE tunnel, adding to the many "firsts" it has facilitated. While this test article persists as a natural choice for shaking down a new diagnostic in a hypersonic boundary layer, as new wind tunnel models are made for other researchers' specific needs, evidence of the features tested and lessons learned with this test article persist in the new designs.

Finally, the plasma was used to allow the study the effect of simple, controlled vibrational nonequilibrium in a hypersonic TBL. Specifically, PLIF thermometry of T^v_{NO} was especially successful in studying the effect of the nonequilibrium by measuring the change in the vibrational temperature along the test article and through the boundary layer. These measurements represent the first known such measurement. The unique time scales of $NO^{v=1}$ relaxation were estimated to be at least comparable to the flow over the test article, leaving the potential open for turbulence and nonequilibrium coupling. All evidence suggested that this would not have been observed with N_2 or O_2, which were likely thermally frozen; this freezing of the dominant species and the low concentration of the relaxing NO meant that the re-laminarization process identified in [95] could not occur, a finding supported the data. That these data leveraged the data from the numerical boundary layer solver, experimental PLIF measurements, and thermodynamic and turbulence theories in their analyses united the three fields at the core of this work.

These results provided fertile ground for future analyses. The simple models of the flow in Chapter 8 already showed partial success in predicting the vibrational relaxation along the test domain, and the limits of the RANS model in a complex turbulent environment. Ideally the initial conditions, set by all of the techniques covered so far, would be sufficient to allow a dedicated

numerical study of the problem, one which could match the measurements at the final test location. The data may also inform additional exploration of the reaction time scales and validate novel vibrational energy turbulence models.

In summary, the research objectives were met and progress was made in three constituent fields of hypersonic turbulent flows as identified in Figure 1.3: turbulence modeling; turbulence experimentation; and thermal nonequilibrium. A methodology for deriving algebraic energy flux models was presented and made amenable to further expansion. A test article and TBL were produced and thoroughly characterized to provide a wealth of canonical turbulence data; these data were valuable in their own right, but acted as a control case for those runs with the plasma turned on. The plasma and PLIF techniques were able to introduce and explore a controlled, repeatable, and relatively simple nonequilibrium environment.

These results will improve turbulence modeling in hypersonic environments, both with and without thermal nonequilibrium, by supplying an array of data where the literature is wanting. It is sincerely hoped this work will serve to advance that wonderfully human endeavor to fly faster, higher, and farther.

REFERENCES

[1] Igor Adamovich, SD Baalrud, Anemie Bogaerts, PJ Bruggeman, M Cappelli, Vittorio Colombo, Uwe Czarnetzki, Ute Ebert, JG Eden, Pietro Favia, et al. The 2017 plasma roadmap: Low temperature plasma science and technology. *Journal of Physics D: Applied Physics*, 50(32):323001, 2017.

[2] Jerry M Allen. Evaluation of preston tube calibration equations in supersonic flow. *AIAA Journal*, 11(11):1461–1462, 1973.

[3] E. Clay. Anderson and Clark H. Lewis. *Laminar or turbulent boundary-layer flows of perfect gases or reacting gas mixtures in chemical equilibrium*. National Aeronautics and Space Administration, 1971.

[4] John D Anderson. *Computational fluid dynamics: the basics with applications*. McGraw-Hill, 1995.

[5] John D Anderson. *Modern compressible flow*. McGraw-Hill, 3 edition, 2003.

[6] John D. Anderson. *Hypersonic and high-temperature gas dynamics*. American Institute of Aeronautics and Astronautics, Inc., 2019.

[7] C. J. Arisman, C. T. Johansen, B. F. Bathel, and P. M. Danehy. Investigation of gas seeding for planar laser-induced fluorescence in hypersonic boundary layers. *AIAA Journal*, 53(12): 3637–3651, 2015. doi: 10.2514/1.j053892.

[8] CJ Arisman and Craig T Johansen. Nitric oxide chemistry effects in hypersonic boundary layers. *AIAA Journal*, 53(12):3652–3660, 2015.

[9] CJ Arisman, CT Johansen, WC Galuppo, and A McPhail. Nitric oxide chemistry effects in hypersonic boundary layers. In *43rd AIAA Fluid Dynamics Conference*, 2013. Paper no. 3104.

[10] F W Aston. The distribution of electric force in the crookes dark space. *Proceedings of the Royal Society of London. Series A, Containing Papers of a Mathematical and Physical Character*, 84(573):526–535, 1911. doi: 10.1098/rspa.1911.0005.

[11] P. W. Atkins and Julio De Paula. *Physical chemistry for the life sciences*. Oxford University Press, 2011.

[12] B. Baldwin and H. Lomax. Thin-layer approximation and algebraic model for separated turbulentflows. *16th Aerospace Sciences Meeting*, 1978. doi: 10.2514/6.1978-257.

[13] Gordon M. Barrow. *Introduction to molecular spectroscopy*. McGraw-Hill, 1962.

[14] Gordon M. Barrow. *Structure Of Molecules*. W.A. Benjamin, 1964.

[15] Henry E Bass. Absorption of sound by air: high temperature predictions. *The Journal of the Acoustical Society of America*, 69(1):124–138, 1981.

[16] Brett Bathel, Paul Danehy, Jennifer Inman, Stephen Jones, Christopher Ivey, and Christopher Goyne. Multiple velocity profile measurements in hypersonic flows using sequentially-imaged fluorescence tagging. In *48th AIAA Aerospace Sciences Meeting Including the New Horizons Forum and Aerospace Exposition*, 2010. Paper no. 1404.

[17] Brett Bathel, Paul Danehy, Jennifer Inman, Anthony Watkins, Stephen Jones, William Lipford, Kyle Goodman, Christopher Ivey, and Christopher Goyne. Hypersonic laminar boundary layer velocimetry with discrete roughness on a flat plate. In *40th Fluid Dynamics Conference and Exhibit*, 2010. Paper no. 4998.

[18] Brett Bathel, Craig Johansen, Paul Danehy, Jennifer Inman, Stephen Jones, and Christopher Goyne. Hypersonic boundary layer transition measurements using $no_2 \rightarrow no$ photodissociation tagging velocimetry. *41st AIAA Fluid Dynamics Conference and Exhibit*, 2011. doi: 10.2514/6.2011-3246.

[19] Brett Bathel, Paul Danehy, Craig Johansen, Stephen Jones, and Christopher Goyne. Hypersonic boundary layer measurements with variable blowing rates using molecular tagging velocimetry. *28th Aerodynamic Measurement Technology, Ground Testing, and Flight Testing Conference*, 2012. doi: 10.2514/6.2012-2886.

[20] Brett Bathel, Paul Danehy, Stephen Jones, Craig Johansen, and Christopher Goyne. Trip-induced transition measurements in a hypersonic boundary layer using molecular tagging velocimetry. In *51st AIAA Aerospace Sciences Meeting including the New Horizons Forum*

and Aerospace Exposition, 2013. Paper no. 42.

[21] Brett Bathel, Craig Johansen, Paul Danehy, Jennifer Inman, and Stephen Jones. Review of fluorescence-based velocimetry techniques to study high-speed compressible flows. In *51st AIAA Aerospace Sciences Meeting including the New Horizons Forum and Aerospace Exposition*, 2013. Paper no. 339.

[22] Brett F. Bathel, Paul M. Danehy, Jennifer A. Inman, Stephen B. Jones, Christopher B. Ivey, and Christopher P. Goyne. Velocity profile measurements in hypersonic flows using sequentially imaged fluorescence-based molecular tagging. *AIAA Journal*, 49(9):1883–1896, 2011. doi: 10.2514/1.j050722.

[23] Brett F Bathel, Prahladh S Iyer, Paul M Danehy, Jennifer A Inman, Stephen B Jones, Krishnan Mahesh, and Craig T Johansen. Comparing experiment and computation of hypersonic laminar boundary layers with isolated roughness. In *52nd Aerospace Sciences Meeting*, 2014. Paper no. 0236.

[24] SB Bayram and MV Freamat. Vibrational spectra of n2: An advanced undergraduate laboratory in atomic and molecular spectroscopy. *American Journal of Physics*, 80(8):664–669, 2012.

[25] William Bennett, James Menart, Mike McFarland, and Kelly Campbell. Heating and force study of the ability of plasma discharges to modify air flows. In *46th AIAA Aerospace Sciences Meeting and Exhibit*, 2008. Paper no. 1097.

[26] Steven J Beresh, John F Henfling, Russell W Spillers, and Brian OM Pruett. Fluctuating wall pressures measured beneath a supersonic turbulent boundary layer. *Physics of Fluids*, 23(7):075110, 2011.

[27] Karen T Berger, Kevin E Hollingsworth, Shelia A Wright, and Shann J Rufer. Nasa langley aerothermodynamics laboratory: hypersonic testing capabilities. In *53rd AIAA aerospace sciences meeting*, 2015. Paper no. 1337.

[28] Scott Berry, Robert Nowak, and Thomas Horvath. Boundary layer control for hypersonic airbreathing vehicles. In *34th AIAA Fluid Dynamics Conference and Exhibit*, 2004. Paper

no. 2246.

[29] Scott A. Berry, Aaron H. Auslender, Arthur D. Dilley, and John F. Calleja. Hypersonic boundary-layer trip development for hyper-x. *Journal of Spacecraft and Rockets*, 38(6): 853–864, 2001. doi: 10.2514/2.3775.

[30] Mitchel H Bertram. Investigation of the pressure-ratio requirements of the langley 11-inch hypersonic tunnel with a variable-geometry diffuser. Technical report, National Advisory Committe for Aeronautics RM L50I13, Langley Air Force Base, VA, 1950.

[31] Graham Black, Henry Wise, Samuel Schechter, and Robert L Sharpless. Measurements of vibrationally excited molecules by raman scattering. ii. surface deactivation of vibrationally excited n_2. *The Journal of Chemical Physics*, 60(9):3526–3536, 1974.

[32] Vernon Blackman. Vibrational relaxation in oxygen and nitrogen. *Journal of Fluid Mechanics*, 1(1):61–85, 1956.

[33] B. F. Blackwell. *The turbulent boundary layer on a porous plate: an experimental study of the heat transfer behavior with adverse pressure gradients*. PhD thesis, Stanford University, Stanford, CA, 1973.

[34] F. Blottner. Nonequilibrium laminar boundary-layer flow of ionized air. *Aerospace Sciences Meeting*, 2(11), Nov 1964. doi: 10.2514/6.1964-41.

[35] Matthew P. Borg and Roger L. Kimmel. Simultaneous infrared and pressure measurements of crossflow instability modes for hifire-5. *54th AIAA Aerospace Sciences Meeting*, 2016. doi: 10.2514/6.2016-0354.

[36] J. Boussinesq. Théorie de l'écoulement tourbillant. *Memoires Presentes par Diverse Savants à l'Academie des Sciences de l'Institut de France*, 23:46, 2003.

[37] R Bowersox, S North, and R Srinivasan. High-speed free shear layers with molecular non-equilibrium: An example of the fluids information triad (invited). *AIAA Paper*, 685, 2008.

[38] Rodney D. W. Bowersox. Extension of equilibrium turbulent heat flux models to high-speed shear flows. *Journal of Fluid Mechanics*, 633:61–70, 2009. doi: 10.1017/s0022112009007691.

[39] C. F. Boyd and A. Howell. Numerical investigation of one-dimensional heat flux calculations. Technical report, Naval Surface Warfare Center Dahlgren Division, Silver Springs, MD, 1994.

[40] I Boyd, Wyatt Phillips, Deborah Levin, I Boyd, Wyatt Phillips, and Deborah Levin. Sensitivity studies for prediction of ultra-violet radiation in nonequilibrium hypersonic bow-shock waves. In *35th Aerospace Sciences Meeting and Exhibit*, 1997. Paper no. 131.

[41] Iain D Boyd and Thomas E Schwartzentruber. *Nonequilibrium Gas Dynamics and Molecular Simulation*, volume 42. Cambridge University Press, 2017.

[42] Peter Bradshaw. The strategy of calculation methods for complex turbulent flows. Technical Report 73-05, Imperial College Aero. Report, 1973.

[43] Peter Bradshaw. Compressible turbulent shear layers. *Annual Review of Fluid Mechanics*, 9(1):33–52, 1977.

[44] Peter Bradshaw, DH Ferriss, and NP Atwell. Calculation of boundary-layer development using the turbulent energy equation. *Journal of Fluid Mechanics*, 28(3):593–616, 1967.

[45] JM Brooks, AK Gupta, MS Smith, and EC Marineau. Particle image velocimetry measurements of mach 3 turbulent boundary layers at low reynolds numbers. *Experiments in Fluids*, 59(5):1–15, 2018.

[46] Casey Broslawski, Bryan Morreale, Rodney D Bowersox, Gary Nicholson, and Lian Duan. Further validation and implementation of an algebraic energy flux model for high speed gaseous shear flows. In *AIAA SCITECH 2022 Forum*, page 0340, 2022.

[47] Sanborn C. Brown. *Basic data of plasma physics*. Technology Press of MIT, 1959.

[48] Zachary D. Buen, Casey Broslawski, Madeline Smotzer, Jason E. Kuszynski, Simon North, and Rodney D. Bowersox. Towards vibrationally excited nitric oxide monitoring (venom) in a laminar, hypersonic boundary layer. *AIAA Scitech 2020 Forum*, 2020. doi: 10.2514/6.2020-1275.

[49] Zachary Daniel Buen. *Implementation of NO LIF Diagnostics to Characterize the Role of Thermal Non-Equilibrium within a Hypersonic Turbulent Boundary Layer*. PhD thesis,

Texas A&M University, College Station, TX, 12 2021.

[50] Ross A Burns, Heeseok Koo, Venkatramanan Raman, and Noel T Clemens. Improved large-eddy simulation validation methodology: application to supersonic inlet/isolator flow. *AIAA Journal*, 53(4):817–831, 2015.

[51] A. Busemann. *Handbuch der Physik*, volume 4. Geest and Portig, 1931.

[52] Graham Candler and John Perkins. Effects of vibrational nonequilibrium on axisymmetric hypersonic nozzle design. In *29th Aerospace Sciences Meeting*, 1991. Paper no. 297.

[53] Graham V Candler, J Daniel Kelley, Sergey O Macheret, Mikhail N Shneider, and Igor V Adamovich. Vibrational excitation, thermal nonuniformities, and unsteady effects on supersonic blunt bodies. *AIAA journal*, 40(9):1803–1810, 2002.

[54] T. Cebeci. Calculation of compressible turbulent boundary layers with heat and mass transfer. *AIAA Journal*, 9(6):1091–1097, 1971. doi: 10.2514/3.49920.

[55] Tuncer Cebeci and Apollo M. O. Smith. *Analysis of Turbulent Boundary Layers*. Acad. Pr., 1974.

[56] S. Cerasuolo. *Heat Flux Measurements by Infrared Thermography in the Boeing/AFOSR Mach 6 Quiet Tunnel*. PhD thesis, University of Naples Federico II, Naples, NA, 6 2016.

[57] Galina Chaban, Richard Jaffe, David Schwenke, and Winifred Huo. Dissociation cross sections and rate coefficients for nitrogen from accurate theoretical calculations. In *46th AIAA Aerospace Sciences Meeting and Exhibit*, 2008. Paper no. 1209.

[58] Amanda Chou, Andrew Leidy, Rudolph A King, Brett F Bathel, and Gregory Herring. Measurements of freestream fluctuations in the nasa langley 20-inch mach 6 tunnel. In *2018 Fluid Dynamics Conference*, 2018. Paper no. 3073.

[59] P Yo Chou. On velocity correlations and the solutions of the equations of turbulent fluctuation. *Quarterly of Applied Mathematics*, 3(1):38–54, 1945.

[60] J. Clarke and M. McChesney. *The Dynamics of Real Gases*. Butterworths Scientific Publications, 1964.

[61] Francis H. Clauser. The turbulent boundary layer. *Advances in Applied Mechanics Advances*

in Applied Mechanics Volume 4, page 1–51, 1956. doi: 10.1016/s0065-2156(08)70370-3.

[62] Ti Coakley. Turbulence modeling methods for the compressible navier-stokes equations. In *16th Fluid and Plasmadynamics Conference*, pages 83–1693, 1983.

[63] James Dillon. Cobine. *Gaseous conductors: theory and engineering applications*. Dover, 1958.

[64] Clarence B. Cohen and Eli Reshotko. *Similar solutions for the compressible laminar boundary layer with heat transfer and pressure gradient*. National Advisory Committee for Aeronautics, 1955.

[65] Donald Coles. The law of the wake in the turbulent boundary layer. *Journal of Fluid Mechanics*, 1(2):191–226, 1956. doi: 10.1017/s0022112056000135.

[66] PS. Corrsin and A. L. Kistler. The free-stream boundaries of turbulent flows. Technical Report TN 3133, National Advisory Committee for Aeronautics, 1954.

[67] Stuart A Craig and William S Saric. Experimental study of crossflow instability on a mach 6 yawed cone. In *45th AIAA Fluid Dynamics Conference*, page 2774, 2015.

[68] Brian K. Crawford, Glen T. Duncan, David E. West, and William S. Saric. Laminar-turbulent boundary layer transition imaging using ir thermography. *Optics and Photonics Journal*, 03(03):233–239, 2013. doi: 10.4236/opj.2013.33038.

[69] Brian K. Crawford, Glen T. Duncan, David E. West, and William S. Saric. Large-span, non-contact surface profilometry for laminar-flow diagnostics. *30th AIAA Aerodynamic Measurement Technology and Ground Testing Conference*, 2014. doi: 10.2514/6.2014-2940.

[70] L. Crocco. Sulle trasmissione del calore da una lamina piana a un fluido scorrente as alta velocita. *L'Aerotecnica*, 12:181–197, 1932.

[71] John W Daily. Saturation effects in laser induced fluorescence spectroscopy. *Applied Optics*, 16(3):568–571, 1977.

[72] Bart J Daly and Francis H Harlow. Transport equations in turbulence. *The physics of fluids*, 13(11):2634–2649, 1970.

[73] Paul Danehy, Aiyana Garcia, Steve Borg, Artem Dyakonov, Scott Berry, Jennifer Inman,

and David Alderfer. Fluorescence visualization of hypersonic flow past triangular and rectangular boundary-layer trips. In *45th AIAA Aerospace Sciences Meeting and Exhibit*, 2007. Paper no. 536.

[74] Paul Danehy, Brett Bathel, Christopher Ivey, Jennifer Inman, and Stephen Jones. No plif study of hypersonic transition over a discrete hemispherical roughness element. In *47th AIAA Aerospace Sciences Meeting Including The New Horizons Forum and Aerospace Exposition*, 2009. Paper no. 394.

[75] Paul Danehy, Christopher Ivey, Brett Bathel, Jennifer Inman, Stephen Jones, Naibo Jiang, Matt Webster, Walter Lempert, Joseph Miller, Terry Meyer, et al. Orbiter blt flight experiment wind tunnel simulations: Nearfield flowfield imaging and surface thermography. In *48th AIAA Aerospace Sciences Meeting Including the New Horizons Forum and Aerospace Exposition*, 2010. Paper no. 1571.

[76] Paul Danehy, Christopher Ivey, Jennifer Inman, Brett Bathel, Stephen Jones, Naibo Jiang, Matt Webster, Walter Lempert, Joseph Miller, Terry Meyer, et al. High-speed plif imaging of hypersonic transition over discrete cylindrical roughness. In *48th AIAA Aerospace Sciences Meeting Including the New Horizons Forum and Aerospace Exposition*, 2010. Paper no. 703.

[77] Paul M. Danehy, Sean Obyrne, A. Frank, P. Houwing, Jodie S. Fox, and Daniel R. Smith. Flow-tagging velocimetry for hypersonic flows using fluorescence of nitric oxide. *AIAA Journal*, 41(2):263–271, 2003. doi: 10.2514/2.1939.

[78] S. Deiwert and G. Candler. Reacting flows: Special course on three-dimensional supersonic/hypersonic flows including separation. Technical Report AGARD Report No. 764, NASA Ames Research Center, 1989.

[79] W. J. Devenport and J. A. Schetz. Boundary layer codes for students in java. *Forum on Advances in Fluids Enigneering*, 1998. Paper FEDSM98-5139.

[80] W. J. Devenport and J. A. Schetz. Boundary layer computer codes in java. *Zeitschrift fur Angewandete Mathematik und Mechanik*, pages S919–920, 2001. Supplement 4.

[81] Diego A Donzis and Agustin F Maqui. Statistically steady states of forced isotropic turbulence in thermal equilibrium and non-equilibrium. *Journal of Fluid Mechanics*, 797: 181–200, 2016.

[82] W. H. Dorrance. *Viscous Hypersonic Flow*. McGraw-Hill, 1962.

[83] Anubhav Dwivedi, Casey J. Broslawski, Graham V. Candler, and Rodney D. Bowersox. Three-dimensionality in shock/boundary layer interactions: a numerical and experimental investigation. *AIAA Aviation 2020 Forum*, Jun 2020. doi: 10.2514/6.2020-3011.

[84] Alan C. Eckbreth. *Laser diagnostics for combustion temperature and species*. Abacus Press, 1988.

[85] E. R. G. Eckert. Engineering relations for friction and heat transfer to surfaces in high velocity flow. *Journal of Aeronautical Science*, pages 858–587, 1955.

[86] Andrew M Ellis, Miklós Fehér, and Timothy G Wright. *Electronic and Photoelectron Spectroscopy: Fundamentals and Case Studies*. Cambridge University Press, 2005.

[87] Jordi Estevadeordal, Sivaram Gogineni, Roger Kimmel, and James Hayes. Schlieren imaging in hypersonic plasmas. In *42nd AIAA Aerospace Sciences Meeting and Exhibit*, 2004. Paper no. 1139.

[88] F. Faa di Bruno. Sullo sviluppo delle funzioni (on the development of functions). *Annali di Scienze Matematiche e Fisiche*, 6:479–480, 1885. doi: LCCN06036680.

[89] A. Favre. Statistical equations of turbulent gases. *SIAM Problems of Hydrodynamics and Continuum Mechanics*, 1969.

[90] H. H. Fernholz and P. J. Finley. *Critical Commentary on Mean Flow Data for Two-Dimensional Compressible Turbulent Boundary Layers*, volume AGARDograph 253. 1980.

[91] D. H. Ferris. Preston tube measurements in turbulent boundary layers and fully developed pipe flow. Technical Report C.P. No. 831, Ministry of Aviation Aeronatucal Research Council Current Papers, 1965.

[92] Gordon Francis. *Ionization Phenomena in Gases*. Butterworth, 1960.

[93] K. Fujii and H. G. Hornung. A procedure to estimate the absorption rate of sound propagat-

ing through high temperature gas. Technical Report Tech. rep., GALCIT TR FM 2001-004, California Institute of Technology Langley, 2001.

[94] T. J. Fuller. *Experimental Analysis of the Effect of Vibrational Non-Equilibrium on the Decay of Grid-Generated Turbulence*. PhD thesis, Texas A&M University, College Station, TX, 8 2009.

[95] Timothy J Fuller, Andrea G Hsu, Rodrigo Sanchez-Gonzalez, Jacob C Dean, Simon W North, and Rodney DW Bowersox. Radiofrequency plasma stabilization of a low-reynolds-number channel flow. *Journal of fluid mechanics*, 748:663, 2014.

[96] TB Gatski and CG Speziale. On explicit algebraic stress models for complex turbulent flows. *J. Fluid Mech*, 254:59–78, 1993.

[97] Amos Gilat and Vish Subramaniam. *Numerical Methods for Engineers and Scientists: an Introduction with Applications using Matlab*. John Wiley & Sons, 2014.

[98] Forrest R. Gilmore, Russ R. Laher, and Patrick J. Espy. Franck–condon factors, r-centroids, electronic transition moments, and einstein coefficients for many nitrogen and oxygen band systems. *Journal of Physical and Chemical Reference Data*, 21(5):1005–1107, 1992. doi: 10.1063/1.555910.

[99] Sharath S Girimaji and S Balachandar. Analysis and modeling of buoyancy-generated turbulence using numerical data. *International journal of heat and mass transfer*, 41(6-7): 915–929, 1998.

[100] P. Gnoffo, R. Gupta, and J. Shin. Conservation equations and physical models for hypersonic air flows and thermal and chemical non-equilibrium. Technical Report TP No. 2867, NASA Langley, 1989.

[101] Dan M. Goebel and Ira Katz. *Fundamentals of electric propulsion: ion and Hall thrusters*. Wiley, 2008.

[102] Sanford Gordon and Bonnie J. McBride. Computer program for calculation of complex chemical equilibrium compositions and applications. i. analysis. Technical Report Refence Publication 1311, NASA Lewis, 1984.

[103] Paul S. Granville. Baldwin-lomax factors for turbulent boundary layers in pressure gradients. *AIAA Journal*, 25(12):1624–1627, 1987. doi: 10.2514/3.9834.

[104] Wendy I Grosser. Factor influencing pitot probe centerline displacement in a turbulent supersonic boundary layer. Technical Report Technical Memorandum 107341, NASA Lewis, January 1997.

[105] A. Gülhan and S. Braun. An experimental study on the efficiency of transpiration cooling in laminar and turbulent hypersonic flows. *Experiments in Fluids*, 50(3):509–525, 2010. doi: 10.1007/s00348-010-0945-6.

[106] K Hanjalić and Brian Edward Launder. Contribution towards a reynolds-stress closure for low-reynolds-number turbulence. *Journal of Fluid Mechanics*, 74(4):593–610, 1976.

[107] Ronald E. Hanson, Howard P. Buckley, and Philippe Lavoie. Aerodynamic optimization of the flat-plate leading edge for experimental studies of laminar and transitional boundary layers. *Experiments in Fluids*, 53(4):863–871, 2012. doi: 10.1007/s00348-012-1324-2.

[108] W. Hayes and R. Probstein. *Hypersonic flow theory*. Academic Press, 1959.

[109] Gerhard Herzberg. *Molecular spectra and molecular structure: I: Spectra of diatomic molecules*, volume 1. Van Nostrand, 1950.

[110] Joseph Hilsenrath, Charles W. Beckett, William S. Benedict, Lilla Fane, Harold J. Hoge, Joseph S. Masi, Ralph L. Nuttell, Yoram S. Touloukian, and Harold W. Woolley. *Tables of Thermodynamic and Transport Troperties: of Air, Argon, Carbon Dioxide, Carbon Monoxide, Hydrogen, Nitrogen, Oxygen, and Steam*. Pergamon Press, 1960.

[111] C. Hirschen and A. Gülhan. Infrared thermography and pitot pressure measurements of a scramjet nozzle flowfield. *Journal of Propulsion and Power*, 25(5):1108–1120, 2009. doi: 10.2514/1.41787.

[112] Jerrod W. Hofferth. *Boundary-Layer Stability and Transition on a Flared Cone in a Mach 6 Quiet Wind Tunnel*. PhD thesis, Texas A&M University, College Station, TX, 8 2013.

[113] J Michael Hollas. *Modern Spectroscopy*. John Wiley & Sons, 2004.

[114] Edward J. Hopkins and Earl R. Keener. Study of surface pitots for measuring turbulent skin

friction at supersonic mach numbers. Technical Report TN D-3478, National Aeronatics and Space Administration, 1966.

[115] Alec Houpt, Brock Hedlund, Sergey Leonov, Timothy Ombrello, and Campbell Carter. Quasi-dc electrical discharge characterization in a supersonic flow. *Experiments in Fluids*, 58(4), 2017. doi: 10.1007/s00348-016-2295-5.

[116] Andrea Hsu. *Application of Advanced Laser and Optical Diagnostics Towards Non-Thermal Equilibrium Systems*. PhD thesis, Texas A&M University, College Station, TX, 5 2009.

[117] Andrea G Hsu, Ravi Srinivasan, Rodney DW Bowersox, and Simon W North. Molecular tagging using vibrationally excited nitric oxide in an underexpanded jet flowfield. *AIAA journal*, 47(11):2597–2604, 2009.

[118] Junji Huang, Gary L Nicholson, Lian Duan, Meelan M Choudhari, and Rodney D Bowersox. Simulation and modeling of cold-wall hypersonic turbulent boundary layers on flat plate. In *AIAA Scitech 2020 Forum*, 2020. Paper no. 0571.

[119] PG Huang. Physics and computations of flows with adverse pressure gradients. In *Modeling Complex Turbulent Flows*, pages 245–258. Springer, 1999.

[120] Adam M Hurst, Steve Carter, Doug Firth, Alan Szary, and Joe VanDeWeert. Real-time, advanced electrical filtering for pressure transducer frequency response correction. In *ASME Turbo Expo 2015: Turbine Technical Conference and Exposition*. American Society of Mechanical Engineers Digital Collection, 2015.

[121] C. R. Illingworth. Some solutions of the equations of flow of a viscous compressible fluid. *Mathematical Proceedings of the Cambridge Philosophical Society*, 46(3):469–478, 1950. doi: 10.1017/s0305004100025986.

[122] H Itoh and M Mizoguchi. Potential of glow-discharge flow measurement in hypersonic low-density flows. *AIAA Journal*, 58(1):291–303, 2020.

[123] Richard Jaffe, David Schwenke, Galina Chaban, and Winifred Huo. Vibrational and rotational excitation and relaxation of nitrogen from accurate theoretical calculations. In *46th AIAA Aerospace Sciences Meeting and Exhibit*, 2008. Paper no. 1208.

[124] Richard Jaffe, David Schwenke, and Galina Chaban. Theoretical analysis of n_2 collisional dissociation and rotation-vibration energy transfer. In *47th AIAA Aerospace Sciences Meeting including The New Horizons Forum and Aerospace Exposition*, 2009. Paper no. 1569.

[125] Richard Jaffe, David Schwenke, and Galina Chaban. Vibration-rotation excitation and dissociation in $n_2 - n_2$ collisions from accurate theoretical calculations. In *10th AIAA/ASME Joint Thermophysics and Heat Transfer Conference*, 2010. Paper no. 4517.

[126] Naibo Jiang, Matthew Webster, Walter Lempert, Joseph Miller, Terrence Meyer, and Paul Danehy. Mhz-rate no plif imaging in a mach 10 hypersonic wind tunnel. In *48th AIAA Aerospace Sciences Meeting Including the New Horizons Forum and Aerospace Exposition*, 2010. Paper no. 1407.

[127] Craig Johansen and Paul Danehy. Numerical investigation of plif gas seeding for hypersonic boundary layer flows. In *50th AIAA Aerospace Sciences Meeting Including the New Horizons Forum and Aerospace Exposition*, 2012. Paper no. 1057.

[128] James E.A. John and Theo G. Keith. *Gas Dynamics*. Pearson Prentice Hall, 3 edition, 2006.

[129] F Llewellyn Jones and AB Parker. Electrical breakdown of gases. i. spark mechanism in air. *Proceedings of the Royal Society of London. Series A. Mathematical and Physical Sciences*, 213(1113):185–202, 1952.

[130] WP Jones and Brian Edward Launder. The prediction of laminarization with a two-equation model of turbulence. *International journal of heat and mass transfer*, 15(2):301–314, 1972.

[131] Ree Jongbaik. Theoretical investigation of the vibrational relaxation of $no(v = 1-7)$ in collisions with o_2 and n_2. *Bulletin of the Korean Chemical Society*, 14(1):47–52, 1993.

[132] Thomas J. Juliano, Laura Paquin, and Matthew P. Borg. Measurement of hifire-5 boundary-layer transition in a mach-6 quiet tunnel with infrared thermography. *54th AIAA Aerospace Sciences Meeting*, 2016. doi: 10.2514/6.2016-0595.

[133] B. A. Kader. Temperature and concentration profiles in fully turbulent boundary layers. *International Journal of Heat and Mass Transfer*, 24(9):1541–1544, 1981. doi: 10.1016/0017-9310(81)90220-9.

[134] Georgi Kalitzin, Gorazd Medic, Gianluca Iaccarino, and Paul Durbin. Near-wall behavior of rans turbulence models and implications for wall functions. *Journal of Computational Physics*, 204(1):265–291, 2005.

[135] M Kandula and D Wilcox. An examination of k-ω turbulence model for boundary layers, free shear layers and separated flows. In *Fluid Dynamics Conference*, pages 95–2317, 1995.

[136] Anthony Keating, Giuseppe De Prisco, and Ugo Piomelli. Interface conditions for hybrid rans/les calculations. *International journal of heat and fluid flow*, 27(5):777–788, 2006.

[137] Earl R. Keener and Edward J. Hopkins. Use of preston tubes for measuring hypersonic turbulent skin friction. In *4th Aerodynamic Testing Conference*, number 69-345, 1969.

[138] Sualeh Khurshid and Diego A Donzis. Decaying compressible turbulence with thermal non-equilibrium. *Physics of Fluids*, 31(1):015103, 2019.

[139] Roger Kimmel, James Hayes, James Menart, and Joseph Shang. Effect of surface plasma discharges on boundary layers at mach 5. In *42nd AIAA Aerospace Sciences Meeting and Exhibit*, 2004. Paper no. 509.

[140] Roger L Kimmel, James R Hayes, James A Menart, and Joseph Shang. Effect of magnetic fields on surface plasma discharges at mach 5. *Journal of spacecraft and rockets*, 43(6): 1340–1346, 2006.

[141] Tibor Kiss and Joseph A. Schetz. Rational extension of the clauser eddy viscosity model to compressible boundary-layer flow. *AIAA Journal*, 31(6):1007–1013, 1993. doi: 10.2514/3.11722.

[142] P. S. Klebanoff. Characteristics of a compressible turbulent boundary layer with zero pressure gradient. Technical Report 1247, National Advisory Committee for Aeronautics, 1955.

[143] Johan C Kok. Resolving the dependence on freestream values for the k-ω turbulence model. *AIAA journal*, 38(7):1292–1295, 2000.

[144] A. N. Kolmogorov. Equations of turbulent motion of an incompressible fluid. *Izvestia Academy of Sciences, USSR; Physics*, 6(1 and 2):56–58, 1936.

[145] Andrey Nikolaevich Kolmogorov. The local structure of turbulence in incompressible vis-

cous fluid for very large reynolds numbers. *Cr Acad. Sci. URSS*, 30:301–305, 1941.

[146] Andrey Nikolaevich Kolmogorov. Dissipation of energy in locally isotropic turbulence. *Comptes Renduc de l'Acadamie Des Sciences de l'U.R.S.S.*, 32(16):301–305, 1941.

[147] J Kosanetzky, U List, W Urban, H Vormann, and EH Fink. Vibrational relaxation of no (x2π, υ= 1) studied by an ir-uv-double-resonance technique. *Chemical Physics*, 50(3):361–371, 1980.

[148] IA Kossyi, A Yu Kostinsky, AA Matveyev, and VP Silakov. Kinetic scheme of the non-equilibrium discharge in nitrogen-oxygen mixtures. *Plasma Sources Science and Technology*, 1(3):207, 1992.

[149] Mikhail Kotov, Pavel Kozlov, Larisa Ruleva, Sergey Solodovnikov, and Sergey Surzhikov. Experimental study of the electrical and spectroscopic characteristics of glow discharge. In *48th AIAA Plasmadynamics and Lasers Conference*, 2017. Paper no. 3157.

[150] Lev Landau and Edward Teller. Zur theorie der schalldispersion. *Phys. Z. Sowjetunion*, 10 (1):34–43, 1936.

[151] BE Launder. Fifth biennial colloquium on computational fluid dynamics. In *Manchester Institute of Science and Technology, England*, 1992.

[152] Brian Edward Launder. An introduction to single-point closure methodology. In *An Introduction to the Modelling of Turbulence*, number Lecture Series 1987-06, Rhode-Saint-Genese, Belgium, 1987. Von Karman Inst. for Fluid Dynamics. Also available as UMIST Mech. Eng. Dept. Report TFD/87/7.

[153] Brian Edward Launder. On the computation of convective heat transfer in complex turbulent flows. *Journal of Heat Transfer*, 110(4b):1112–1128, 11 1988.

[154] Brian Edward Launder and Bahrat I Sharma. Application of the energy-dissipation model of turbulence to the calculation of flow near a spinning disc. *Letters in heat and mass transfer*, 1(2):131–137, 1974.

[155] Brian Edward Launder, G Jr Reece, and W Rodi. Progress in the development of a reynolds-stress turbulence closure. *Journal of fluid mechanics*, 68(3):537–566, 1975.

[156] Normand M Laurendeau. Temperature measurements by light-scattering methods. *Progress in Energy and Combustion Science*, 14(2):147–170, 1988.

[157] Christophe O Laux. Radiation and nonequilibrium collisional-radiative models. *von Karman Institute Lecture Series*, 7, 2002.

[158] CO Laux. Optical diagnostics and collisional-radiative models. *VKI LS Course on hypersonic entry and cruise vehicles, Palo Alto, California, USA*, 2008.

[159] Michael P Lee, Brian K McMillin, and Ronald K Hanson. Temperature measurements in gases by use of planar laser-induced fluorescence imaging of no. *Applied Optics*, 32(27): 5379–5396, 1993.

[160] Andrew Leidy. *An Experimental Characterization of 3-D Transitional Shock Wave Boundary Layer Interactions at Mach 6*. PhD thesis, Texas A&M University, College Station, TX, 5 2019.

[161] Andrew Leidy, Ian Neel, Rodney D. Bowersox, and John D. Schmisseur. Influence of perturbations on 3-d hypersonic shock laminar boundary interactions. *55th AIAA Aerospace Sciences Meeting*, 2017. doi: 10.2514/6.2017-1685.

[162] Michael A. Lieberman and Allan J. Lichtenberg. *Principles of plasma discharges and materials processing*. Wiley-Interscience, 2 edition, 2005.

[163] W. W. Liou and T. H. Shih. On the basic equations for the second-order modeling of compressible turbulence. Technical Report TM 105277, NASA Lewis Research Center, Institute for Compressible Mechanics in Propulsion and Center for Modeling of Turbulence and Transition, Cleveland, OH, 1950.

[164] ED Lozanskiœ and OB Firsov. Theory of sparks, 1975.

[165] RL Macdonald, RL Jaffe, DW Schwenke, and M Panesi. Construction of a coarse-grain quasi-classical trajectory method. i. theory and application to n2-n2 system. *The Journal of chemical physics*, 148(5):054309, 2018.

[166] Sergey O Macheret, Mikhail N Shneider, and Richard B Miles. Magnetohydrodynamic and electrohydrodynamic control of hypersonic flows of weakly ionized plasmas. *AIAA Journal*,

42(7):1378–1387, 2004.

[167] Thierry E Magin, Marco Panesi, Anne Bourdon, Richard L Jaffe, and David W Schwenke. Coarse-grain model for internal energy excitation and dissociation of molecular nitrogen. *Chemical Physics*, 398:90–95, 2012.

[168] Chi Mai. *Near-Region Modification of Total Pressure Fluctuations by a Normal Shock Wave in a Low-Density Hypersonic Wind Tunnel*. PhD thesis, Texas A&M University, College Station, TX, 5 2014.

[169] George Maise and Henry Mcdonald. Mixing length and kinematic eddy viscosity in a compressible boundary layer. *AIAA Journal*, 6(1):73–80, 1968. doi: 10.2514/3.4443.

[170] M. R. Malik. Numerical methods for hypersonic boundary layer stability. *Journal of Computational Physics*, 86(2):376–413, 1990. doi: 10.1016/0021-9991(90)90106-b.

[171] Connor C McDougall, W Schuyler Hinman, Craig T Johansen, Brett F Bathel, Jennifer A Inman, and Paul M Danehy. Quantitative analysis of planar laser-induced fluorescence measurements in a hypersonic boundary layer. In *19th international symposium on the application of laser and imaging techniques to fluid mechanics*, 2018.

[172] Connor C McDougall, William S Hinman, Craig T Johansen, Brett F Bathel, Jennifer A Inman, and Paul M Danehy. Nitric oxide planar laser-induced fluorescence thermometry measurements in a hypersonic boundary layer. In *2018 aerodynamic measurement technology and ground testing conference*, 2018. Paper no. 3629.

[173] Connor C McDougall, W Schuyler Hinman, Craig T Johansen, Brett F Bathel, Jennifer A Inman, and Paul M Danehy. Evaluation of nitric oxide laser-induced fluorescence thermometry techniques in a hypersonic boundary layer. *Experiments in Fluids*, 61(4):1–19, 2020.

[174] Brianne McManamen. *Velocity and Temperature Measurements in a High Mach Number Shock-Turbulence Interaction*. PhD thesis, Texas A&M University, College Station, TX, 12 2019.

[175] John Millar Meek and John Drummond Craggs. Electrical breakdown of gases. 1953.

[176] James Menart, Joseph Shang, Sean Henderson, Andrew Kurpik, Roger Kimmel, and James

Hayes. Survey of plasmas generated in a mach 5 wind tunnel. In *41st Aerospace Sciences Meeting and Exhibit*, 2003. Paper no. 1194.

[177] James Menart, Sean Henderson, Joseph Shang, Roger Kimmel, Jim Hayes, and Carl Atzbach. Study of surface and volumetric heating effects in a mach 5 flow. In *35th AIAA Plasmadynamics and Lasers Conference*, 2004. Paper no. 2262.

[178] James Menart, Joseph Shang, C Atzbach, S Magoteaux, M Slagel, and B Bilheimer. Total drag and lift measurements in a mach 5 flow affected by a plasma discharge and a magnetic field. In *43rd AIAA Aerospace Sciences Meeting and Exhibit*, 2005. Paper no. 947.

[179] James Menart, Scott Stanfield, Joseph Shang, Roger Kimmel, and James Hayes. Study of plasma electrode arrangements for optimum lift in a mach 5 flow. In *44th AIAA aerospace sciences meeting and exhibit*, 2006. Paper no. 1172.

[180] Jim Menart, Joseph Shang, Roger Kimmel, and Jim Hayes. Effects of magnetic fields on plasmas generated in a mach 5 wind tunnel. In *34th AIAA Plasmadynamics and Lasers Conference*, 2003. Paper no. 4165.

[181] Florian R Menter. Improved two-equation k-omega turbulence models for aerodynamic flows. Technical Report TM-103975, NASA, 1992.

[182] Florian R Menter. Two-equation eddy-viscosity turbulence models for engineering applications. *AIAA journal*, 32(8):1598–1605, 1994.

[183] Florianr Menter. Zonal two equation kw turbulence models for aerodynamic flows. In *23rd fluid dynamics, plasmadynamics, and lasers conference*, number 93-2906, 1993.

[184] JG Méolans. Thermal slip boundary conditions in vibrational nonequilibrium flows. *Mechanics Research Communications*, 30(6):629–637, 2003.

[185] Parviz Moin and Krishnan Mahesh. Direct numerical simulation: A tool in turbulence research. *Annual Review of Fluid Mechanics*, 30(1):539–578, 1998. doi: 10.1146/annurev.fluid.30.1.539.

[186] A Montello, M Nishihara, JW Rich, IV Adamovich, and WR Lempert. Nitrogen vibrational population measurements in the plenum of a hypersonic wind tunnel. *AIAA journal*, 50(6):

1367–1376, 2012.

[187] Aaron Montello, Munetake Nishihara, J William Rich, Igor Adamovich, and Walter Lempert. Picosecond used-cars for simultaneous rotational/translational and vibrational temperature measurement of nitrogen in a nonequilibrium mach 5 flow. In *50th AIAA Aerospace Sciences Meeting including the New Horizons Forum and Aerospace Exposition*, 2012. Paper no. 239.

[188] M. V. Morkovin. *Effects of Compressibility on Turbulent Flow*, page 367–380. Centre National de la Recherche Scientifique, Paris, 1962.

[189] James N Moss and Graeme A Bird. Direct simulation monte carlo simulations of hypersonic flows with shock interactions. *AIAA journal*, 43(12):2565–2573, 2005.

[190] A Munafo, M Panesi, and TE Magin. Boltzmann rovibrational collisional coarse-grained model for internal energy excitation and dissociation in hypersonic flows. *Physical Review E*, 89(2):023001, 2014.

[191] Bala Muralikrishnan and Jay Raja. *Computational Surface and Roundness Metrology*. Springer, 2009.

[192] H Nassar, S Pellerin, K Musiol, O Martinie, N Pellerin, and JM Cormier. N2+/n2 ratio and temperature measurements based on the first negative n2+ and second positive n2 overlapped molecular emission spectra. *Journal of Physics D: Applied Physics*, 37(14):1904, 2004.

[193] Dominik Neeb, Dominik Saile, and Ali Gülhan. Experiments on a smooth wall hypersonic boundary layer at mach 6. *Experiments in Fluids*, 59(4):1–21, 2018.

[194] Ian Neel. *Influence of Environmental Distrubances on Hypersonic Crossflow Instability on the HiFIRE-5 Elliptic Cone*. PhD thesis, Texas A&M University, College Station, TX, 5 2019.

[195] Ian T Neel, Andrew Leidy, Rodney D Bowersox, and Nathan R Tichenor. Hypersonic boundary layer with streamline curvature-driven adverse pressure gradient. In *8th AIAA Flow Control Conference*, page 4248, 2016.

[196] Ian T. Neel, Andrew Leidy, and Rodney D. Bowersox. Preliminary study of the effect of

environmental disturbances on hypersonic crossflow instability on the hifire-5 elliptic cone. *55th AIAA Aerospace Sciences Meeting*, 2017. doi: 10.2514/6.2017-0767.

[197] Aaron G Neville, Ioannis Nompelis, Pramod K Subbareddy, and Graham V Candler. Effect of thermal non-equilibrium on decaying isotropic turbulence. In *AIAA Aviation 2014-7th AIAA Theoretical Fluid Mechanics Conference 2014*. American Institute of Aeronautics and Astronautics Inc., 2014.

[198] Aaron G Neville, Ioannis Nompelis, Pramod K Subbareddy, and Graham V Candler. Thermal non-equilibrium effects in turbulent compressible shear flows. In *45th AIAA Fluid Dynamics Conference*, 2015. Paper no. 3218.

[199] Gary Nicholson, Junji Huang, Lian Duan, and Meelan M Choudhari. Simulation and modeling of hypersonic turbulent boundary layers subject to adverse pressure gradients due to streamline curvature. In *AIAA AVIATION 2021 FORUM*, page 2891, 2021.

[200] Gary Nicholson, Junji Huang, Lian Duan, Meelan M Choudhari, and Rodney D Bowersox. Simulation and modeling of hypersonic turbulent boundary layers subject to favorable pressure gradients due to streamline curvature. In *AIAA Scitech 2021 Forum*, page 1672, 2021.

[201] Gary L Nicholson, Junji Huang, Lian Duan, Meelan M Choudhari, Bryan Morreale, and Rodney D Bowersox. Budgets of reynolds stresses and turbulent heat flux for hypersonic turbulent boundary layers subject to pressure gradients. In *AIAA SCITECH 2022 Forum*, page 1059, 2022.

[202] EE Nikitin and J Troe. 70 years of landau–teller theory for collisional energy transfer. semiclassical three-dimensional generalizations of the classical collinear model. *Physical Chemistry Chemical Physics*, 10(11):1483–1501, 2008.

[203] M Nishihara, K Takashima, N Jiang, WR Lempert, IV Adamovich, and JW Rich. Development of a mach 5 nonequilibrium wind tunnel. In *48th Aerospace Sciences Meeting and Exhibit*. American Institute of Aeronautics and Astronautics Inc., 2010. Paper no. 1567.

[204] Munetake Nishihara, Keisuke Takashima, Naibo Jiang, Walter Lempert, Igor Adamovich,

and J Rich. Nonequlibrium flow characterizarion in a mach 5 wind tunnel. In *10th AIAA/ASME Joint Thermophysics and Heat Transfer Conference*, 2010. Paper no. 4515.

[205] Munetake Nishihara, Keisuke Takashima, Naibo Jiang, WR Lempert, IV Adamovich, JW Rich, S Doraiswamy, and GV Candler. Development of a mach 5 nonequilibrium-flow wind tunnel. *AIAA journal*, 50(10):2255–2267, 2012.

[206] Munetake Nishihara, Igor V Adamovich, Walter R Lempert, and JW Rich. Effect of accelerated vibrational relaxation on a supersonic shear layer. *AIAA Paper*, 577, 2015.

[207] Ioannis Nompelis, Graham V Candler, and Michael S Holden. Effect of vibrational nonequilibrium on hypersonic double-cone experiments. *AIAA journal*, 41(11):2162–2169, 2003.

[208] S O'Byrne, PM Danehy, and AFP Houwing. Plif temperature and velocity distributions in laminar hypersonic flat-plate flow. In *20th International Congress on Instrumentation in Aerospace Simulation Facilities, 2003. ICIASF'03.*, pages 136–147. IEEE, 2003.

[209] Jean Olbregts. Termolecular reaction of nitrogen monoxide and oxygen: a still unsolved problem. *International journal of chemical kinetics*, 17(8):835–848, 1985.

[210] David G Ortiz-Suslow and Qing Wang. An evaluation of kolmogorov's- 5/3 power law observed within the turbulent airflow above the ocean. *Geophysical Research Letters*, 46 (24):14901–14911, 2019.

[211] Grant Palmer. *Technical Java: developing scientific and engineering applications*. Prentice Hall, 2003.

[212] M Panesi, A Munafò, TE Magin, and RL Jaffe. Nonequilibrium shock-heated nitrogen flows using a rovibrational state-to-state method. *Physical Review E*, 90(1):013009, 2014.

[213] Marco Panesi, Richard L Jaffe, David W Schwenke, and Thierry E Magin. Rovibrational internal energy transfer and dissociation of $n_2(^1\sigma_g^+) - n(^4s_u)$ system in hypersonic flows. *The Journal of chemical physics*, 138(4):044312, 2013.

[214] Chul Park. *Non-Equilibrium Hypersonic Aerothermodynamics*. Wiley & Sons, 1990.

[215] G Peach. Theory of the pressure broadening and shift of spectral lines. *Advances in Physics*, 30(3):367–474, 1981.

[216] A. S. Petrusev, S. T. Surzhikov, and J. S. Shang. A two-dimensional model of glow discharge in view of vibrational excitation of molecular nitrogen. *High temperature*, 44(6):804–813, 2006.

[217] Sergio Pirozzoli, F Grasso, and TB Gatski. Direct numerical simulation and analysis of a spatially evolving supersonic turbulent boundary layer at m= 2.25. *Physics of fluids*, 16(3): 530–545, 2004.

[218] Jonathan Poggie. Compressible turbulent boundary layer simulations: resolution effects and turbulence modeling. In *53rd AIAA Aerospace Sciences Meeting*, 2015. Paper no. 1983.

[219] E. Pohlhausen. Der wärmeaustausch zwischen festern körpen und fl ussigkeiten mit kleiner reibung und kleiner wärmeleitung. *Zeitschrift für Angewandte Mathematik und Mechanik*, 1:115–121, 1921.

[220] Alan Pope and Kennith L. Goin. *High-speed wind tunnel testing*. Krieger, 1965.

[221] S. B. Pope. *Turbulent Flows*. Cambridge University Press, 2015.

[222] L. Prandtl. Über flüssigkeitsbewegung bei sehr kleiner reibung. *Proc. Third Int. Math. Congr. Heidelberg*, 1904.

[223] JoH Preston. The determination of turbulent skin friction by means of pitot tubes. *The Aeronautical Journal*, 58(518):109–121, 1954.

[224] Jurij P. Rajzer. *Gas discharge physics*. Springer, 1991.

[225] Eli Reshotko and Anatoli Tumin. Role of transient growth in roughness-induced transition. *AIAA Journal*, 42(4):766–770, 2004. doi: 10.2514/1.9558.

[226] O. Reynolds. On the extent and action of the heating surface for steam boilers. *Manchester Lit. Philos. Soc.*, 14:7–12, 1874.

[227] W. Rodi. A new algebraic relation for calculating the reynolds stresses. *ZAMM - Journal of Applied Mathematics and Mechanics / Zeitschrift für Angewandte Mathematik und Mechanik*, 56(S1), 1976. doi: 10.1002/zamm.19765613093.

[228] John Reece Roth. *Industrial plasma engineering*, volume 1: PRinciples. Inst. of Physics Publ., 1995.

[229] JC Rotta. Statistische theorie nichthomogener turbulenz. *Zeitschrift für Physik*, 129(6): 547–572, 1951.

[230] JC Rotta. über eine methode zur berechnung turbulenter scherströmungen. Technical Report 69 A 14, Aerodynamische Versuchanstalt Göttingen, 1968.

[231] Christopher Roy and Frederick Blottner. Review and assessment of turbulence models for hypersonic flows: 2d/asymmetric cases. In *44th AIAA Aerospace Sciences Meeting and Exhibit*, 2006. Paper no. 713.

[232] Morris W Rubesin and HA Johnson. A critical review of skin-friction and heat-transfer solutions of the laminar boundary layer of a flat plate. *Trans. ASME*, 71(4):383–388, 1949.

[233] Carson L. Running, Michael J. Thompson, Thomas J. Juliano, and Hirotaka Sakaue. Boundary-layer separation detection for a cone at high angle of attack in mach 4.5 flow with pressure-sensitive paint. *47th AIAA Fluid Dynamics Conference*, 2017. doi: 10.2514/6.2017-3120.

[234] PG Saffman. Development of a complete model for the calculation of turbulent shear flows. In *Chapter II of Statistical mechanics and Dynamical Systems by David Ruelle and papers from the 1976 Duke Turbulence Conference, Duke University Mathematics Series III*, 1976.

[235] Rodrigo Sanchez-Gonzalez. *Advanced Laser Diagnostics Development for the Characterization of Gaseous High Speed Flows*. PhD thesis, Texas A&M University, College Station, TX, 5 2012.

[236] William S. Saric, Helen L. Reed, and Edward J. Kerschen. Boundary-layer receptivity to freestream distrubances. *Annual Review of Fluid Mechanics*, 34(1):291–319, 2002. doi: 10.1146/annurev.fluid.34.082701.161921.

[237] Robert Sauerwein and Berthold Hruschkaand. Influence of molecular vibrational energy accommodation modeling on cone surface heat flux at mach 10. *Journal of Energy and Power Engineering*, 10:660–666, 2016.

[238] S. A. Schaaf and P. L. Chambre. *Rarefied Gas Dynamics*. Princeton University Press, 1966.

[239] Joseph A. Schetz and Rodney D. W. Bowersox. *Boundary layer analysis*. American Institute

of Aeronautics and Astronautics, 2012.

[240] David W Schwenke. Dissociation cross sections and rates for nitrogen. Technical Report RTO-EN-AVT-162, NASA Ames Research Center, 2009.

[241] J. M. Seitzman and R. K. Hanson. Planar fluorescence imaging in gases. In A. M. K. P.Editor Taylor, editor, *Instrumentation for Flows with Combustion*, chapter 6, pages 406–466. Academic Press, 1993.

[242] VE Semenov, VG Bondarenko, VB Gildenburg, VM Gubchenko, and AI Smirnov. Weakly ionized plasmas in aerospace applications. *Plasma physics and controlled fusion*, 44(12B): B293, 2002.

[243] Michael Semper. *Examining a Hypersonic Turbulent Boundary Layer at Low Reynolds Number*. PhD thesis, Texas A&M University, College Station, TX, 8 2013.

[244] Michael Semper, Nathan Tichenor, Rodney Bowersox, Ravichandra Srinvasan, and Simon North. On the design and calibration of an actively controlled expansion hypersonic wind tunnel. *47th AIAA Aerospace Sciences Meeting including The New Horizons Forum and Aerospace Exposition*, 2009. doi: 10.2514/6.2009-799.

[245] Michael Semper, Brandon Pruski, and Rodney Bowersox. Freestream turbulence measurements in a continuously variable hypersonic wind tunnel. *50th AIAA Aerospace Sciences Meeting including the New Horizons Forum and Aerospace Exposition*, Jan 2012. doi: 10.2514/6.2012-732.

[246] Michael T. Semper and Rodney D. W. Bowersox. Tripping of a hypersonic low-reynolds-number boundary layer. *AIAA Journal*, 55(3):808–817, 2017. doi: 10.2514/1.j055341.

[247] G. S. Settles. *Schlieren and shadowgraph techniques: visualizing phenomena in transparent media*. Springer, 2013.

[248] Joseph Shang and Sergey Surzhikov. Magneto-fluid-dynamics interaction for hypersonic flow control. In *42nd AIAA Aerospace Sciences Meeting and Exhibit*, 2004. Paper no. 508.

[249] Joseph Shang, Roger Kimmel, James Menart, and John Hayes. Plasma actuator for hypersonic flow control. *43rd AIAA Aerospace Sciences Meeting and Exhibit*, page 562, 2005.

[250] Joseph Shang, Roger Kimmel, James Menart, and John Hayes. Plasma actuator for hypersonic flow control. In *43rd AIAA Aerospace Sciences Meeting and Exhibit*, 2005. Paper no. 562.

[251] Joseph Shang, George Huang, Hong Yan, Sergey Surzhikov, and Datta Gaitonde. Hypersonic flow control utilizing electromagnetic-aerodynamic interaction. In *15th AIAA International Space Planes and Hypersonic Systems and Technologies Conference*, 2008. Paper no. 2606.

[252] Joseph S Shang, Roger L Kimmel, J Menart, and Sergey T Surzhikov. Hypersonic flow control using surface plasma actuator. *Journal of Propulsion and Power*, 24(5):923–934, 2008.

[253] JS Shang and Sergey T Surzhikov. Magnetoaerodynamic actuator for hypersonic flow control. *AIAA journal*, 43(8):1633–1652, 2005.

[254] JS Shang, R Kimmel, J Hayes, Charles Tyler, and J Menart. Hypersonic experimental facility for magnetoaerodynamic interactions. *Journal of Spacecraft and Rockets*, 42(5): 780–789, 2005.

[255] JS Shang, ST Surzhikov, R Kimmel, D Gaitonde, J Menart, and J Hayes. Mechanisms of plasma actuators for hypersonic flow control. *Progress in Aerospace Sciences*, 41(8): 642–668, 2005.

[256] Ascher H. Shapiro. *The dynamics and thermodynamics of compressible fluid flow*, volume 1 and 2. John Wiley and Sons, 1953.

[257] Farhan Shakil Ahmed Siddiqui. *Boundary-Layer Instabilities on a Cooled Flared Cone at Mach 6*. PhD thesis, Texas A&M University, College Station, TX, 8 2021.

[258] Alexander J. Smits and Jean-Paul Dussauge. *Turbulent shear layers in supersonic flow*. Springer, 2 edition, 2006.

[259] RMC So, YG Lai, HS Zhang, and BC Hwang. Second-order near-wall turbulence closures-a review. *AIAA journal*, 29(11):1819–1835, 1991.

[260] Mi-Young Song, Jung-Sik Yoon, Hyuck Cho, Grzegorz P Karwasz, Viatcheslav Kokoouline,

Yoshiharu Nakamura, and Jonathan Tennyson. Cross sections for electron collisions with no, n2o, and no2. *Journal of Physical and Chemical Reference Data*, 48(4):043104, 2019.

[261] Philippe Spalart and Steven Allmaras. A one-equation turbulence model for aerodynamic flows. In *30th aerospace sciences meeting and exhibit*, 1992. Paper no. 439.

[262] D. B. Spalding. A single formula for the "law of the wall". *Journal of Applied Mechanics*, 28(3):455–458, Jan 1961. doi: 10.1115/1.3641728.

[263] Charles G. Speziale, Sutanu Sarkar, and Thomas B. Gatski. Modelling the pressure–strain correlation of turbulence: an invariant dynamical systems approach. *Journal of Fluid Mechanics*, 227:245–272, 1991. doi: 10.1017/s0022112091000101.

[264] Charles G Speziale, Ridha Abid, and E Clay Anderson. Critical evaluation of two-equation models for near-wall turbulence. *AIAA journal*, 30(2):324–331, 1992.

[265] N.P.L Staff of Aerodynamics Division. On the measurement of local surface friction on a flat plate by means of preston tubes. Technical Report R&M 3185, A.R.C, 5 1958.

[266] Scott Stanfield, James Menart, Joseph Shang, Roger Kimmel, and James Hayes. Application of a spectroscopic measuring technique to plasma discharge in hypersonic flow. In *44th AIAA Aerospace Sciences Meeting and Exhibit*, 2006. Paper no. 559.

[267] Scott Alan Stanfield II. *A Spectroscopic Investigation of a Surface-Discharge-Mode, Dielectric Barrier Discharge*. PhD thesis, Wright State University, Dayton, OH, 9 2009.

[268] Andrey Starikovskiy and Nickolay Aleksandrov. Plasma-assisted ignition and combustion. *Progress in Energy and Combustion Science*, 39(1):61–110, 2013. doi: 10.1016/j.pecs.2012.05.003.

[269] DA Storozhev and ST Surzhikov. Numerical simulation of the two-dimensional structure of glow discharge in molecular nitrogen in light of vibrational kinetics. *High Temperature*, 53 (3):307–318, 2015.

[270] S. T. Surzhikov. Numerical simulation of two-dimensional structure of glow discharge in view of the heating of neutral gas. *High temperature*, 43(6):825–842, 2005.

[271] Sergei Timofeevich Surzhikov and JS Shang. Viscous interaction on a flat plate with a

surface discharge in magnetic field. *High Temperature*, 43(1):19–30, 2005.

[272] Sergey T Surzhikov and Joseph S Shang. Two-component plasma model for two-dimensional glow discharge in magnetic field. *Journal of Computational Physics*, 199(2): 437–464, 2004.

[273] ST Surzhikov and JS Shang. The hypersonic quasineutral gas discharge plasma in a magnetic field. In *Proceedings third MIT Conference on Computational Fluid and Solid Mechanics*, pages 1004–1005, 2005.

[274] W. Sutherland. The viscosity of gases and molecular force. *Philosophy Magazine*, 5:507–531, 1893.

[275] John C. Tannehill, Dale A. Anderson, and Richard H. Pletcher. *Computational Fluid Mechanics and Heat Transfer*. Taylor and Francis, 2 edition, 1997.

[276] Michael E Tauber, Gene P Menees, and Henry G Adelman. Aerothermodynamics of transatmospheric vehicles. *Journal of Aircraft*, 24(9):594–602, 1987.

[277] H. Tennekes. *First Course in Turbulence*. MIT Press, 2018.

[278] N. R. Tichenor, R. A. Humble, and R. D. W. Bowersox. Response of a hypersonic turbulent boundary layer to favourable pressure gradients. *Journal of Fluid Mechanics*, 722:187–213, 2013. doi: 10.1017/jfm.2013.89.

[279] Nathan Tichenor. *Characterization of the Influence of a Favorable Pressure Gradient on the Basic Structure of a Mach 5.0 High Reynolds Number Supersonic Turbulent Boundary Layer*. PhD thesis, Texas A&M University, College Station, TX, 8 2010.

[280] Stephen R Turns et al. *Introduction to combustion*, volume 287. McGraw-Hill Companies, 1996.

[281] Mahinder S Uberoi. Effect of wind-tunnel contraction on free-stream turbulence. *Journal of the Aeronautical Sciences*, 23(8):754–764, 1956.

[282] E. R. van Driest. Turbulent boundary layer in compressible fluids. *Journal of the Aeronautical Sciences*, 18(3):145–160, 1951. doi: 10.2514/8.1895.

[283] E. R. van Driest. *Investigation of Laminar Boundary Layer in Compressible Fluids Using*

the Crocco Method. National Advisory Committee for Aeronautics, 1952.

[284] E. R. van Driest. On turbulent flow near a wall. *Journal of the Aeronautical Sciences*, 23 (11):1007–1011, 1956. doi: 10.2514/8.3713.

[285] E. R. van Driest. The problem of aerodynamic heating. *Aeronautical Engineering Review*, 15:26–41, 1956.

[286] Walter G. Vincenti and Charles H. Kruger. *Introduction to physical gas dynamics*. Wiley, 1965.

[287] RJ Volluz. Handbook of supersonic aerodynamics. section 20: Wind tunnel instrumentation and operation. Technical Report 1488, Bureau of Naval Weapons, January 1961.

[288] A von Engel and M Steenbeck. *Elektrische Gasentladungen. Ihre Physik und Technik*. Springer-Verlag, Berlin, 1934.

[289] Alfred von Engel. *Ionized Gases*. Clarendon Press, 2 edition, 1965.

[290] R. M. Wagnild. *High Enthalpy Effects on Two Boundary Layer Disturbances in Supersonic and Hypersonic Flow*. PhD thesis, University of Minnesota, Minneapolis, MN, 5 2012.

[291] Peter P. Wegener and R. Kenneth Lobb. An experimental study of a hypersonic wind-tunnel diffuser. *Journal of the Aeronautical Sciences*, 20(2):105–110, 1953. doi: 10.2514/8.2549.

[292] Tie Wei, Rodney Schmidt, and Patrick McMurtry. Comment on the clauser chart method for determining the friction velocity. *Experiments in fluids*, 38(5):695–699, 2005.

[293] F. M. White. *Viscous Fluid Flow*. McGraw-Hill, 3 edition, 2006.

[294] Allen Whitehead Jr. Nasp aerodynamics. In *National Aerospace Plane Conference*, 1989. Paper no. 5013.

[295] David C Wilcox. Reassessment of the scale-determining equation for advanced turbulence models. *AIAA journal*, 26(11):1299–1310, 1988.

[296] David C. Wilcox. *Turbulence Modeling for CFD*, volume 2. DCW Industries, 1998.

[297] David C. Wilcox. *Turbulence Modeling for CFD*, volume 3. DCW Industries, 2006.

[298] David C Wilcox and Morris W Rubesin. Progress in turbulence modeling for complex flow fields including effects of compressibility. (TP-1517), 1980.

[299] O. J. H. Williams, D. Sahoo, M. L. Baumgartner, and A. J. Smits. Experiments on the structure and scaling of hypersonic turbulent boundary layers. *Journal of Fluid Mechanics*, 834:237–270, 2018.

[300] James M Williamson and Charles A DeJoseph Jr. Determination of gas temperature in an open-air atmospheric pressure plasma torch from resolved plasma emission. *Journal of applied physics*, 93(4):1893–1898, 2003.

[301] John M. Wirth. Measurement of heat flux due to fin-induced shock-boundary layer interaction. Master's thesis, Texas A&M University, College Station, TX, 12 2021.

[302] J. C. Wu. *On the Finite Difference Solution of Laminar Boundary Layer Problems*. Stanford University Press, 1961.

[303] VSASTBCG Yakhot, SA Orszag, Siva Thangam, TB Gatski, and CG Speziale. Development of turbulence models for shear flows by a double expansion technique. *Physics of Fluids A: Fluid Dynamics*, 4(7):1510–1520, 1992.

[304] Yong-Liang Yu, Xian-Dong Li, Zhi-Hui Wang, and Lin Bao. Theoretical modeling of heat transfer to flat plate under vibrational excitation freestream conditions. *International Journal of Heat and Mass Transfer*, 151:119434, 2020.

[305] Mirko Zaccara, Salvatore Cerasuolo, Gennaro Cardone, Joshua B. Edelman, and Steven P. Schneider. Infrared thermography data reduction technique for heat transfer measurements in the boeing/afosr mach-6 quiet tunnel. *AIAA Scitech 2019 Forum*, 2019. doi: 10.2514/6.2019-0894.

[306] S Zeierman and M Wolfshtein. Turbulent time scale for turbulent-flow calculations. *AIAA journal*, 24(10):1606–1610, 1986.

APPENDIX A

VIBRATIONAL THERMOMETRY RESULTS ASSUMING VIBRATIONAL EQUILIBRIUM IN THE FREESTREAM

The figures in this section represent supplemental data to that presented in Section 7.4.2.2. The same raw data was used, but here the results were processed using assuming $T^v_{e,NO} = T^v_{e,N_2,O_2} = 358K$. The merit for this analysis is provided in Chapter 8. The same trends described in Section 7.4.2.2 hold, but the relative amplitude of certain features may have changed do to the nonlinear scaling in PLIF thermometry data reduction; futhermore, the no-slip boundary condition is revisited in the context of these data in Chapter 8. Both streamwise mean temperature comparison and detailed 2D images of all of the individual runs in Table 7.27 are included here. Finally, the calculation for the error bars in Figures A.1 and A.2 by Buen [49] is described in Section 7.4.2.1.

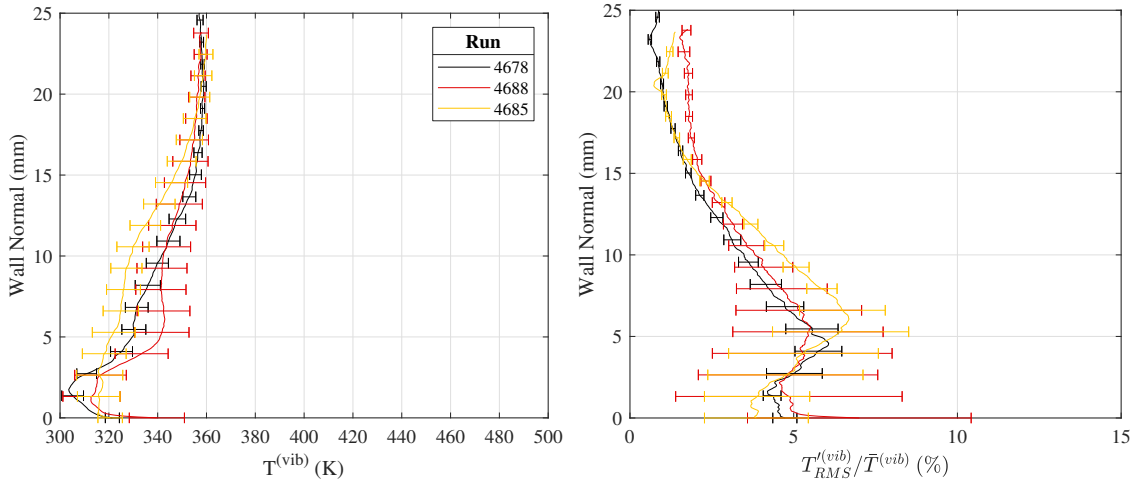

(a) Plasma off, temperature

(b) Plasma off, fluctuation

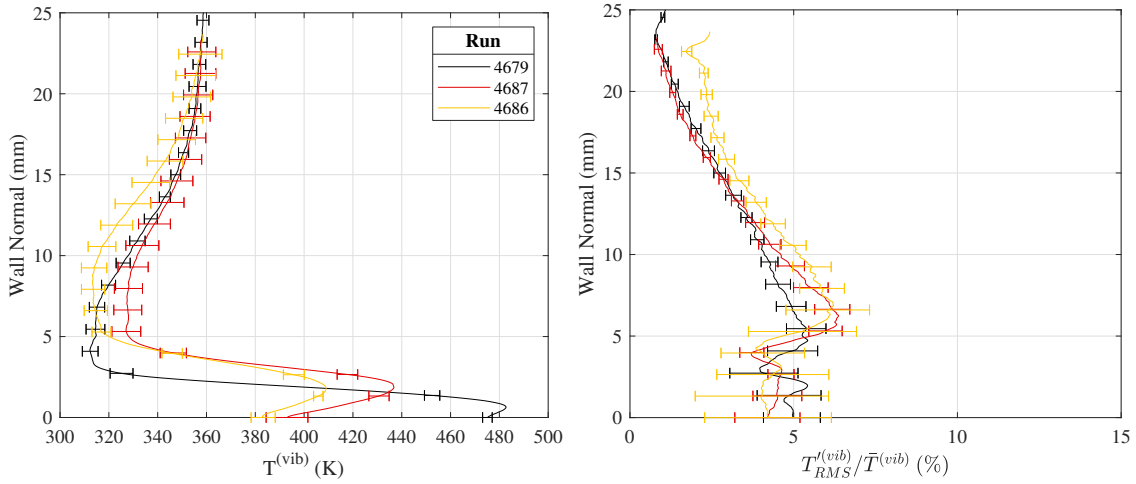

(c) Plasma on, temperature

(d) Plasma on, fluctuation

Figure A.1: PLIF vibrational thermometry, laminar temperature profile comparison assuming $T^{v}_{e,NO} = 358K$; error bars were set from the corresponding mean temperature and fluctuation images. Same legend applies to all figures in a row.

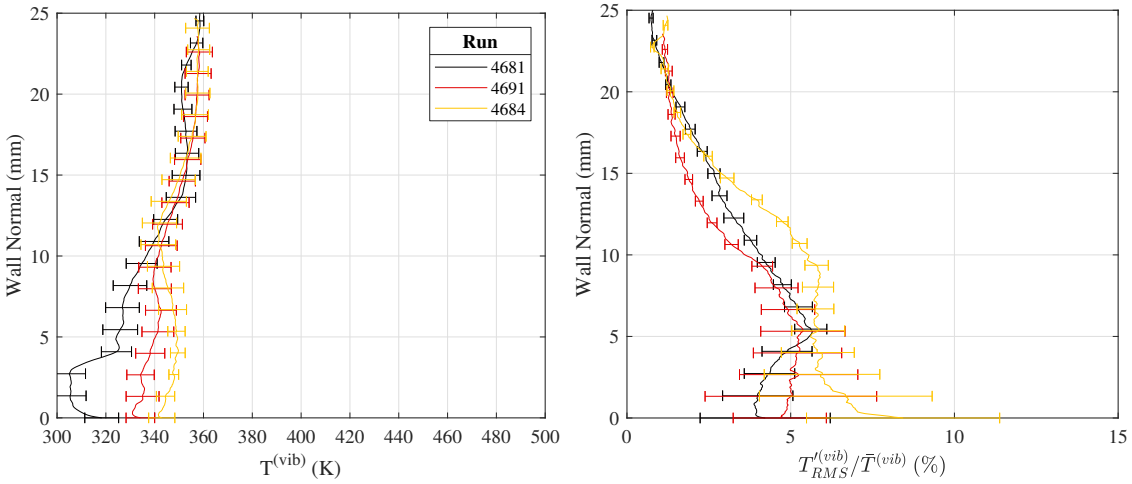

(a) Plasma off, temperature

(b) Plasma off, fluctuation

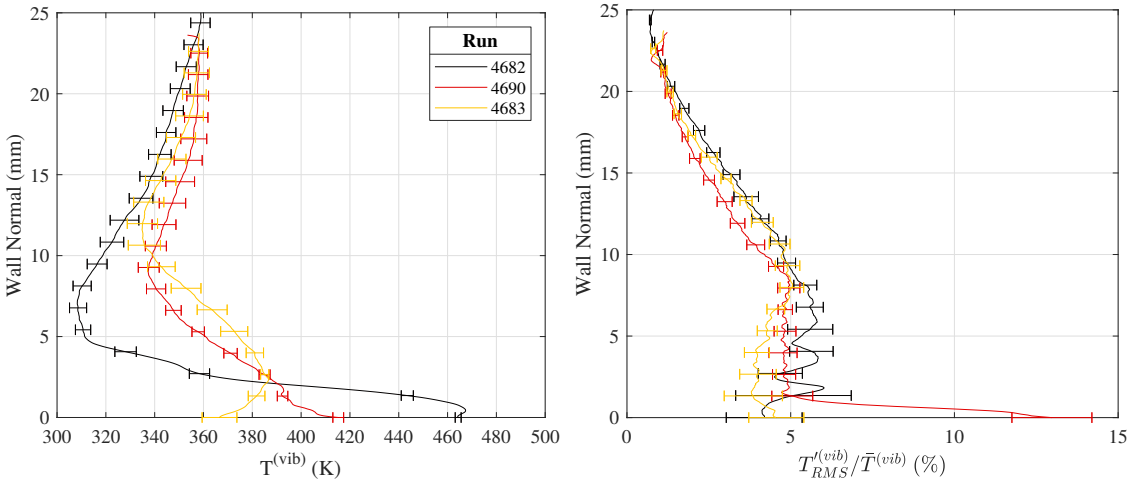

(c) Plasma on, temperature

(d) Plasma on, fluctuation

Figure A.2: PLIF vibrational thermometry, turbulent temperature profile comparison assuming $T^{v}_{e,NO} = 358K$; error bars were set from the corresponding mean temperature and fluctuation images. Same legend applies to all figures in a row.

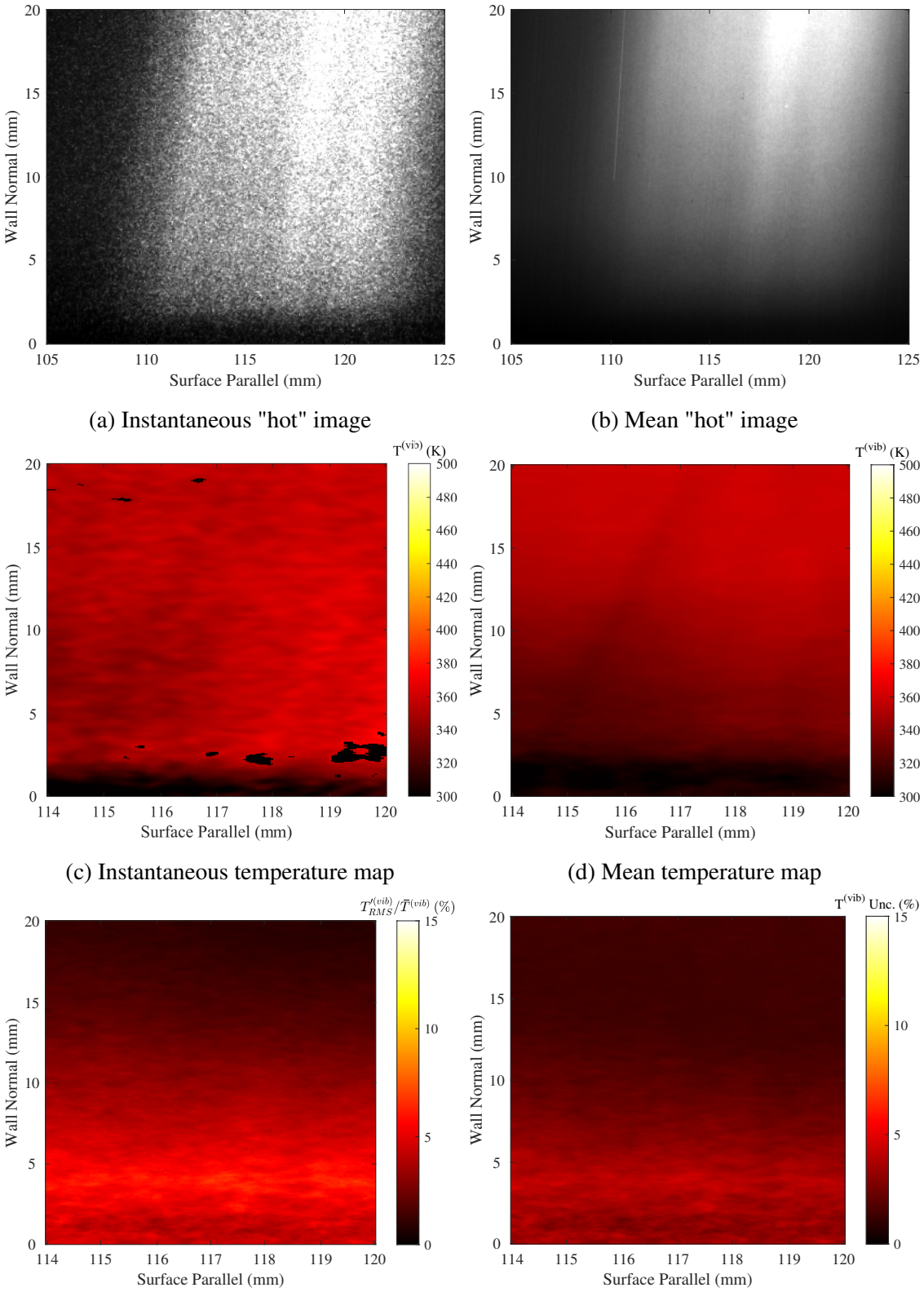

(a) Instantaneous "hot" image

(b) Mean "hot" image

(c) Instantaneous temperature map

(d) Mean temperature map

(e) Mean fluctuation map

(f) Mean uncertainty map

Figure A.3: PLIF vibrational thermometry assuming $T^{v}_{e,NO} = 358K$, Run 4678: upstream; laminar; plasma off.

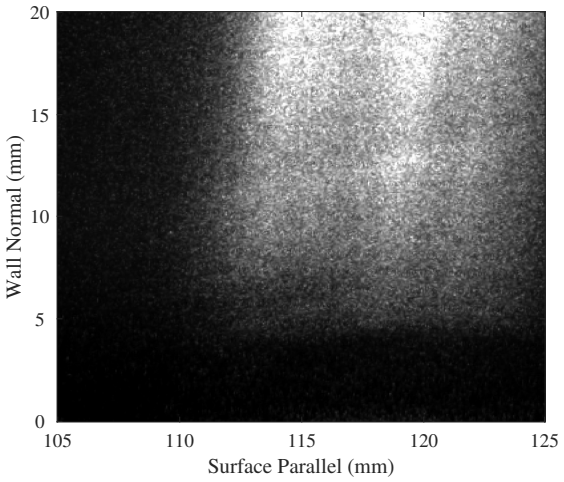

(a) Instantaneous "hot" image

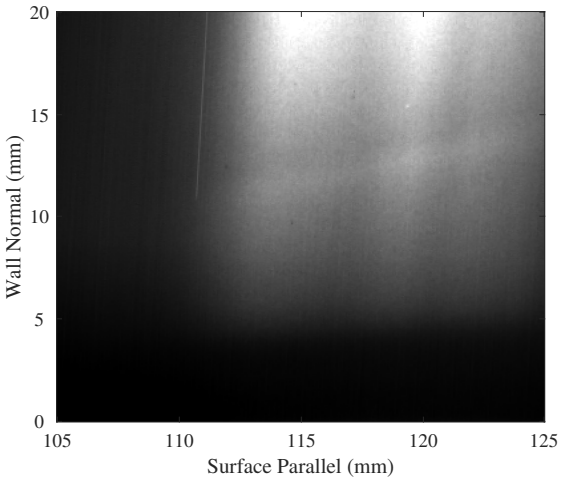

(b) Mean "hot" image

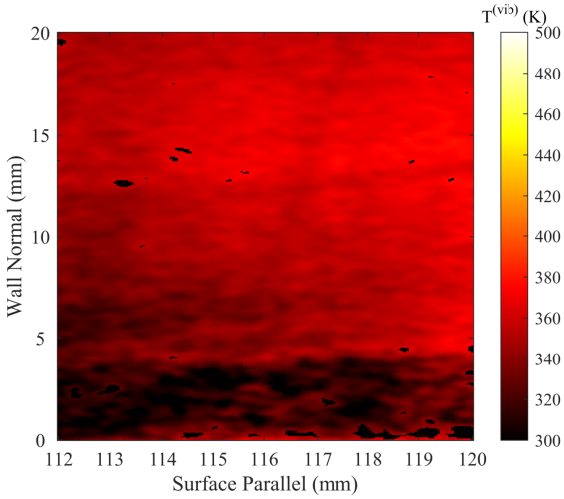

(c) Instantaneous temperature map

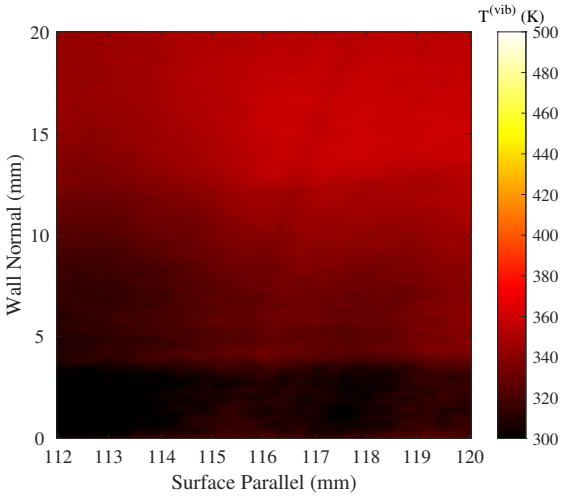

(d) Mean temperature map

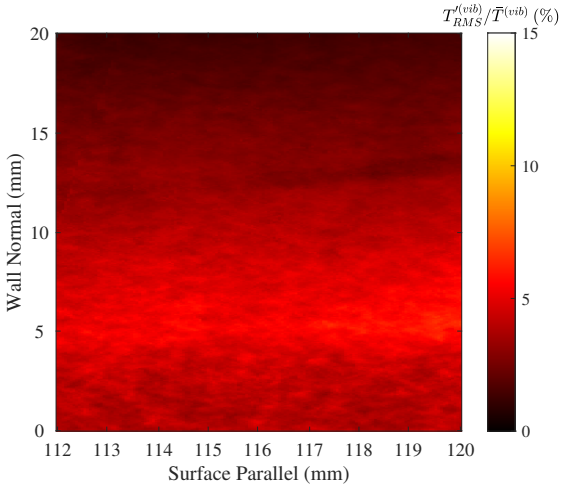

(e) Mean fluctuation map

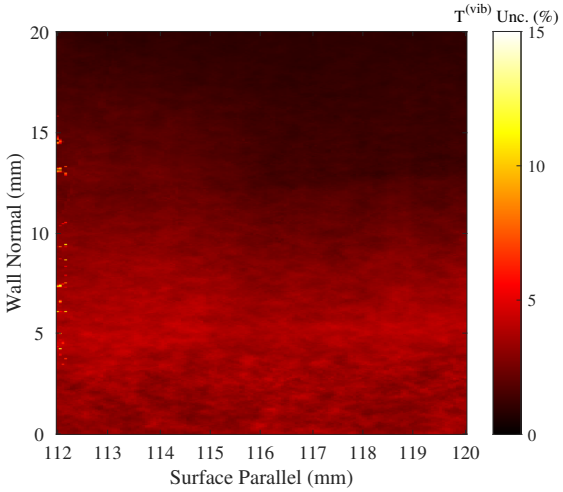

(f) Mean uncertainty map

Figure A.4: PLIF vibrational thermometry assuming $T^{v}_{e,NO} = 358K$, Run 4681: upstream; turbulent; plasma off.

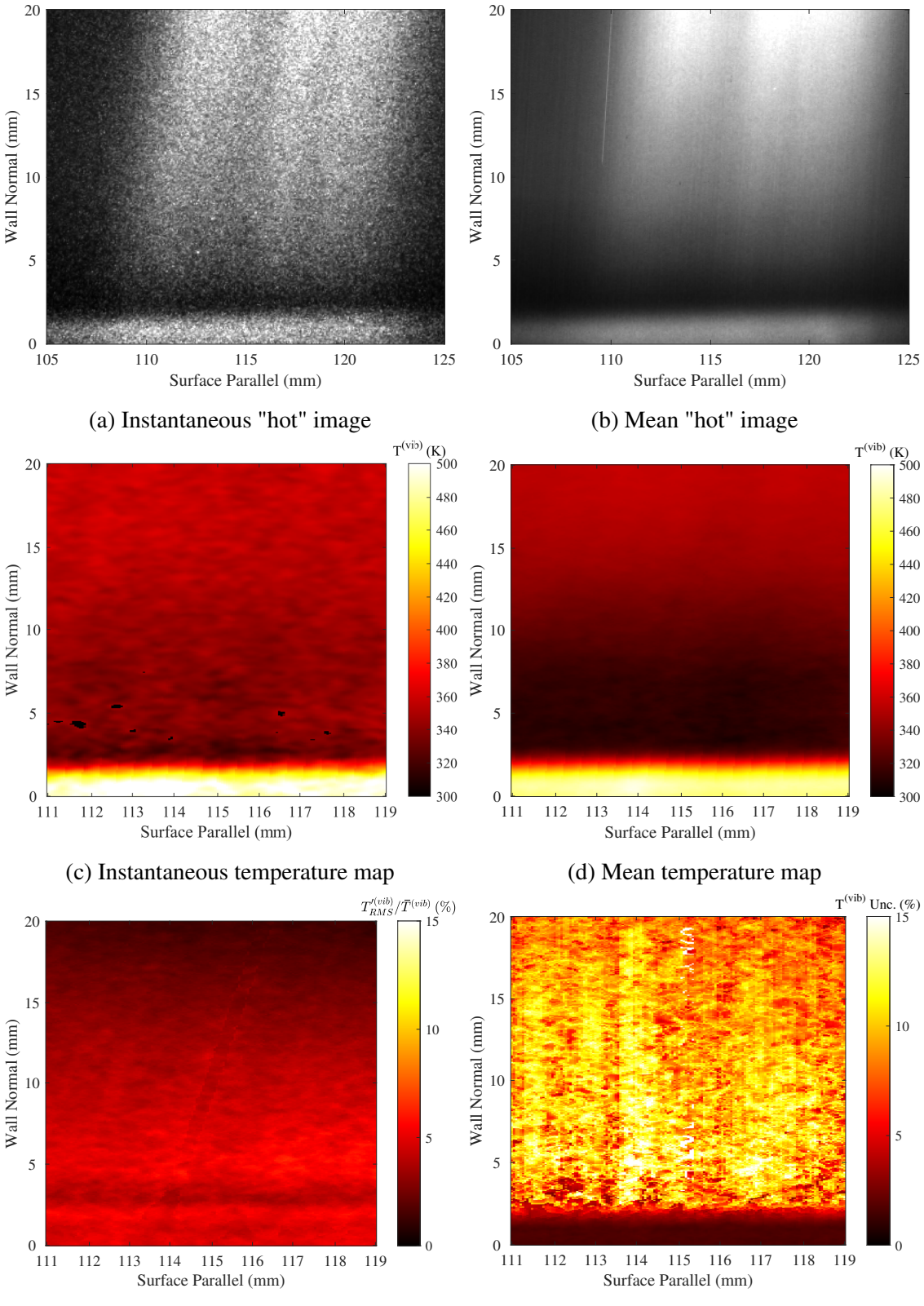

(a) Instantaneous "hot" image

(b) Mean "hot" image

(c) Instantaneous temperature map

(d) Mean temperature map

(e) Mean fluctuation map

(f) Mean uncertainty map

Figure A.5: PLIF vibrational thermometry assuming $T^{v}_{e,NO} = 358K$, Run 4679: upstream; laminar; plasma on.

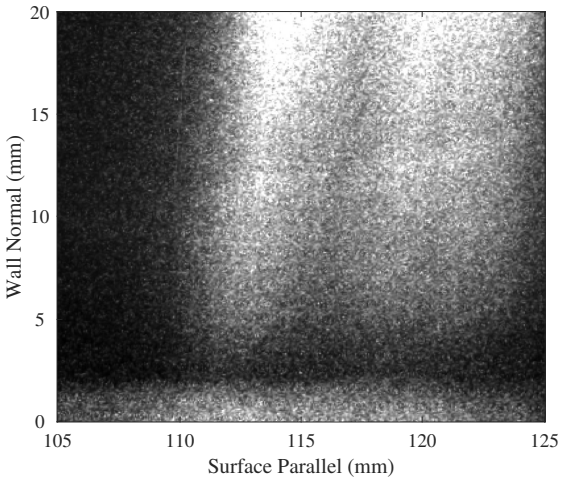

(a) Instantaneous "hot" image

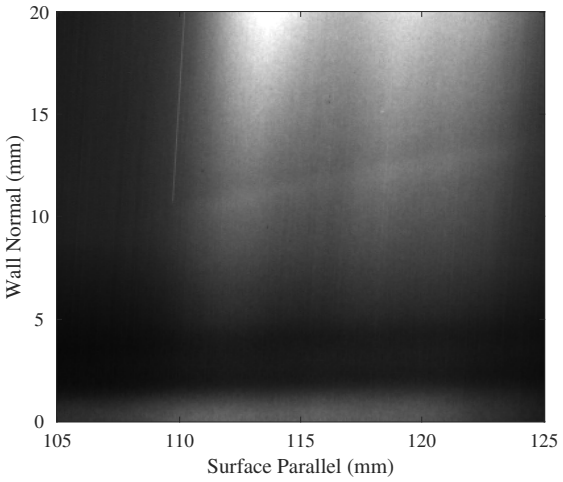

(b) Mean "hot" image

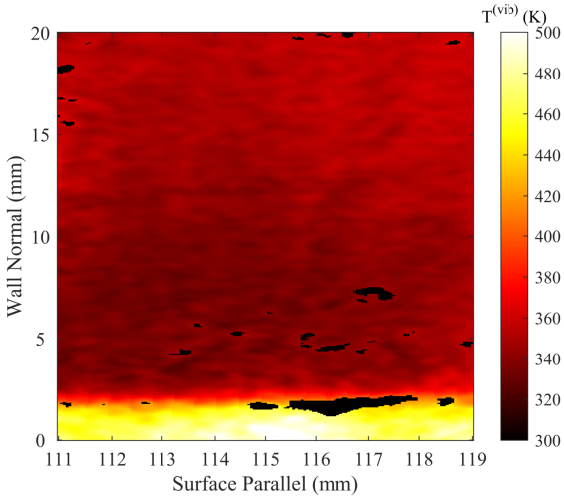

(c) Instantaneous temperature map

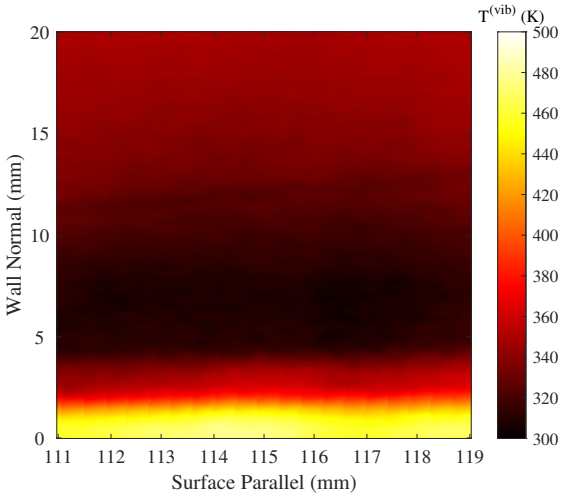

(d) Mean temperature map

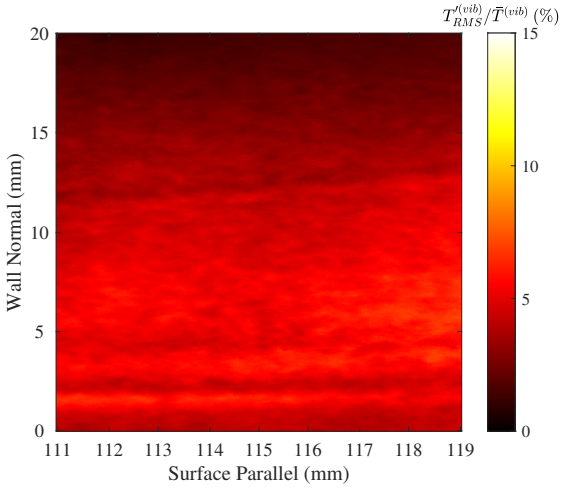

(e) Mean fluctuation map

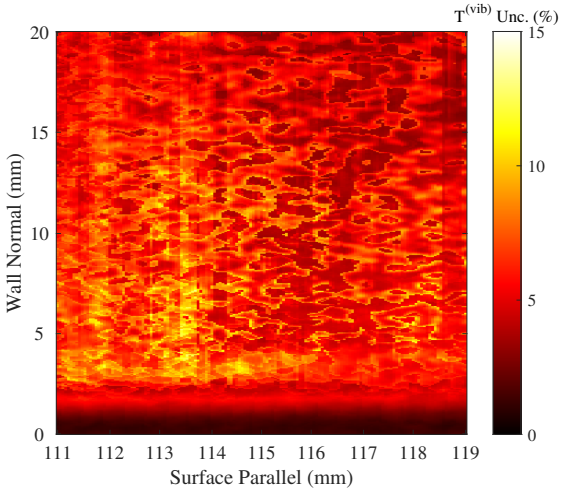

(f) Mean uncertainty map

Figure A.6: PLIF vibrational thermometry assuming $T^{v}_{e,NO} = 358K$, Run 4682: upstream; turbulent; plasma on.

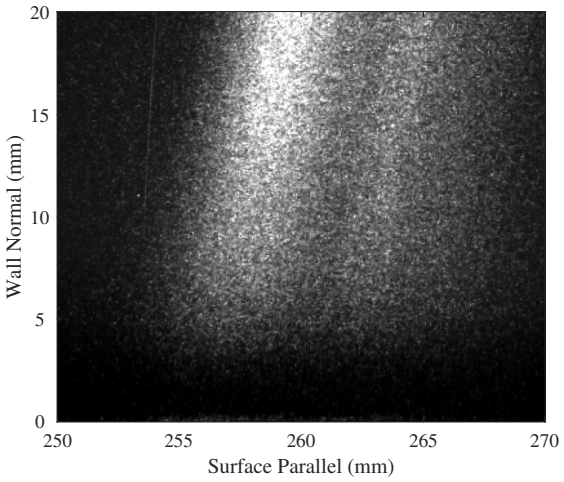

(a) Instantaneous "hot" image

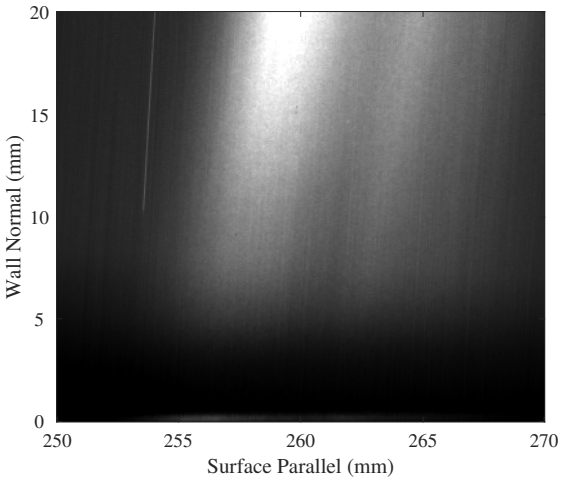

(b) Mean "hot" image

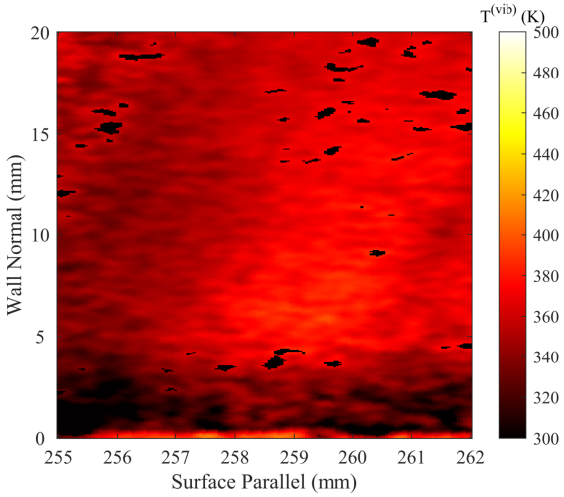

(c) Instantaneous temperature map

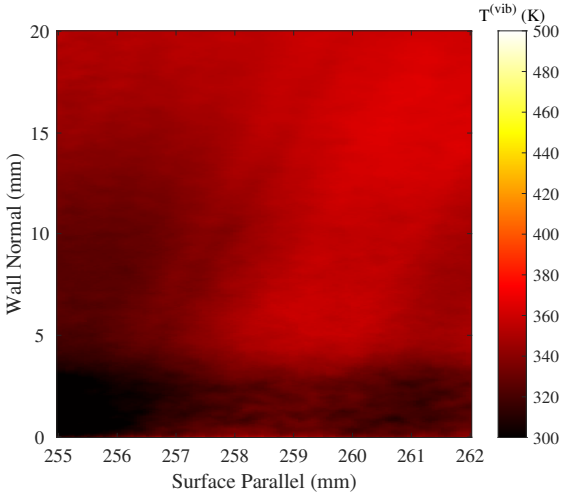

(d) Mean temperature map

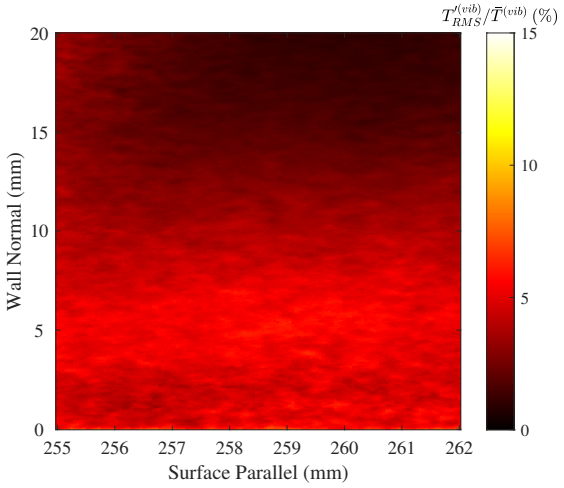

(e) Mean fluctuation map

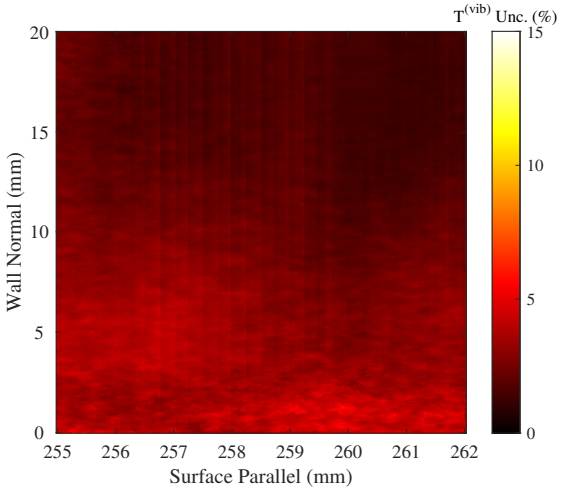

(f) Mean uncertainty map

Figure A.7: PLIF vibrational thermometry assuming $T^{v}_{e,NO} = 358K$, Run 4688: middle; laminar; plasma off.

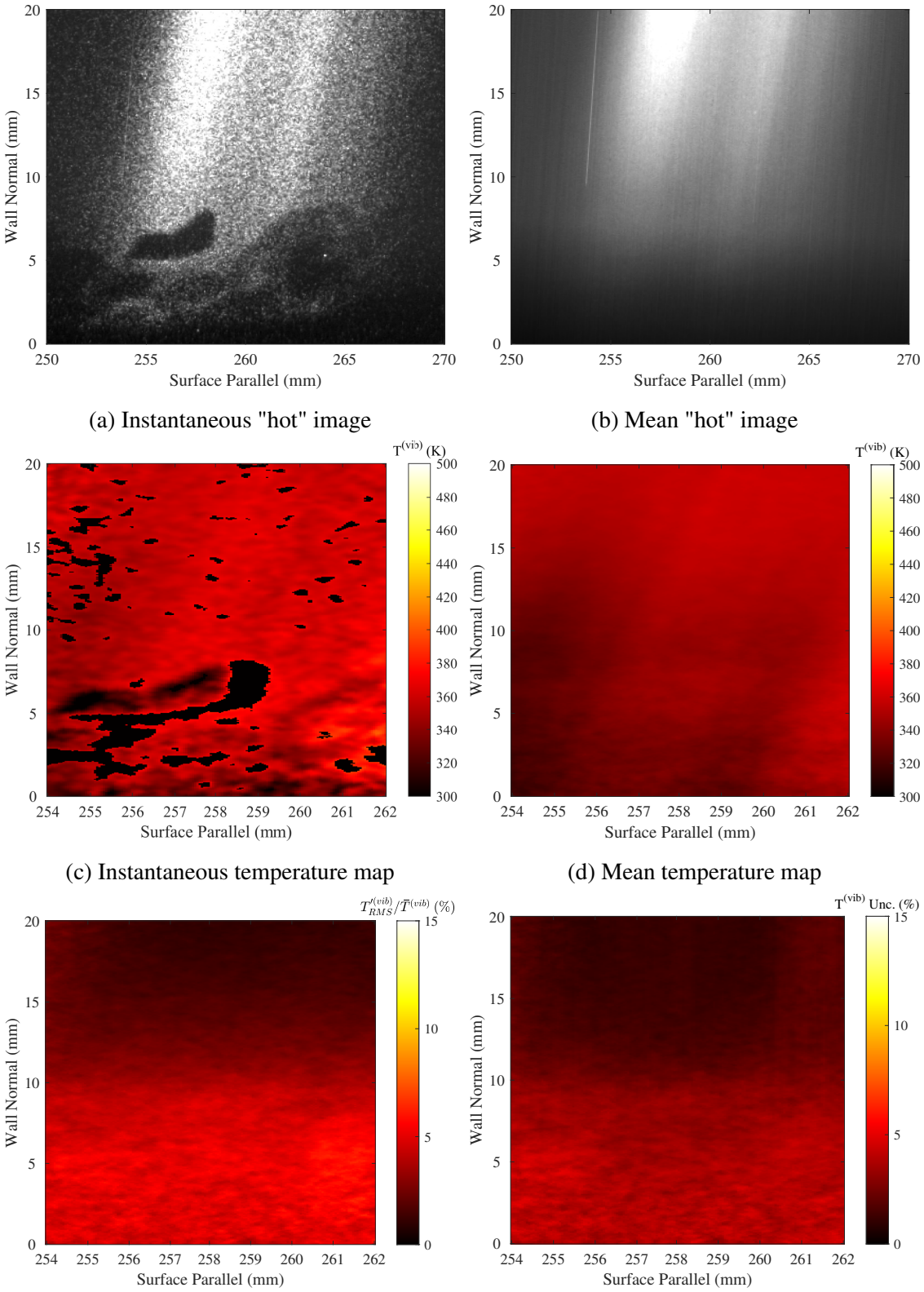

(a) Instantaneous "hot" image

(b) Mean "hot" image

(c) Instantaneous temperature map

(d) Mean temperature map

(e) Mean fluctuation map

(f) Mean uncertainty map

Figure A.8: PLIF vibrational thermometry assuming $T^{v}_{e,NO} = 358K$, Run 4691: middle; turbulent; plasma off.

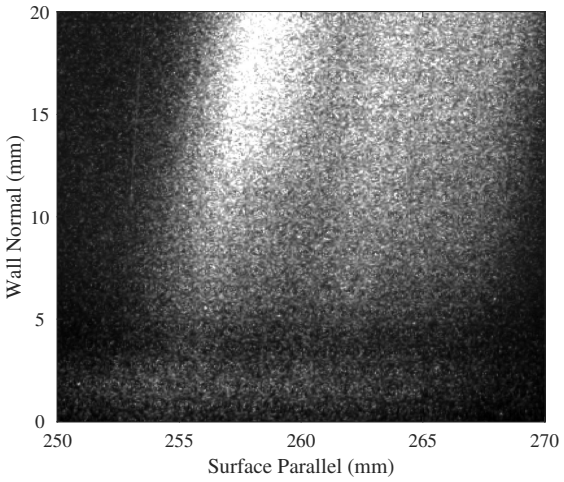

(a) Instantaneous "hot" image

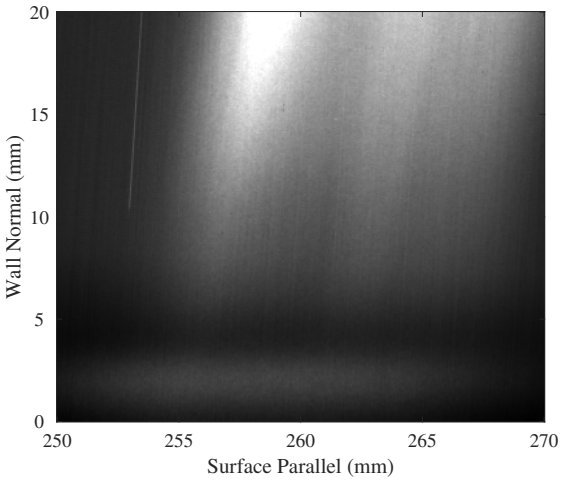

(b) Mean "hot" image

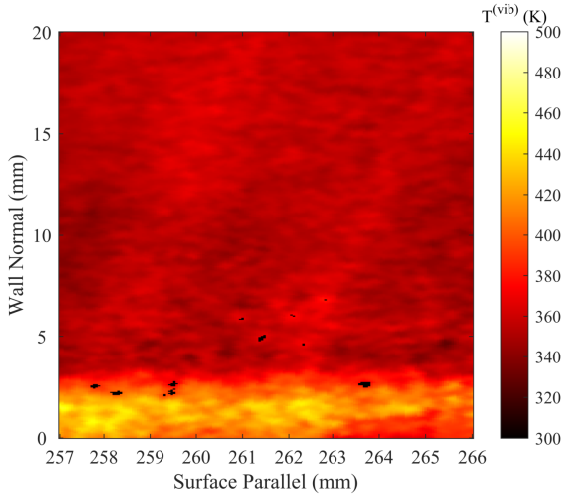

(c) Instantaneous temperature map

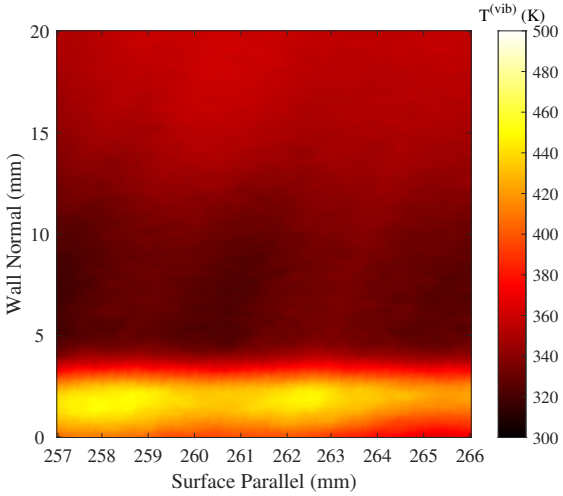

(d) Mean temperature map

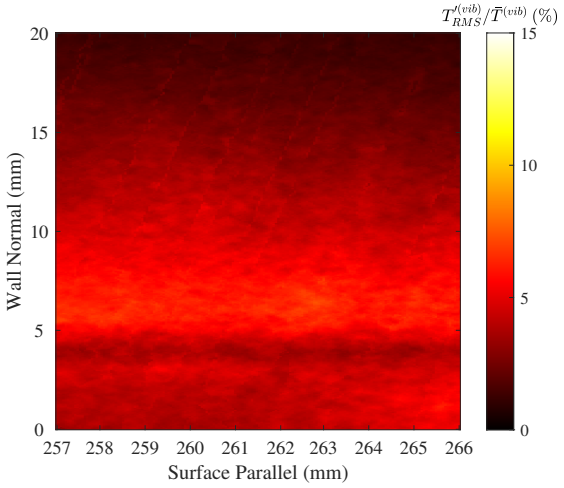

(e) Mean fluctuation map

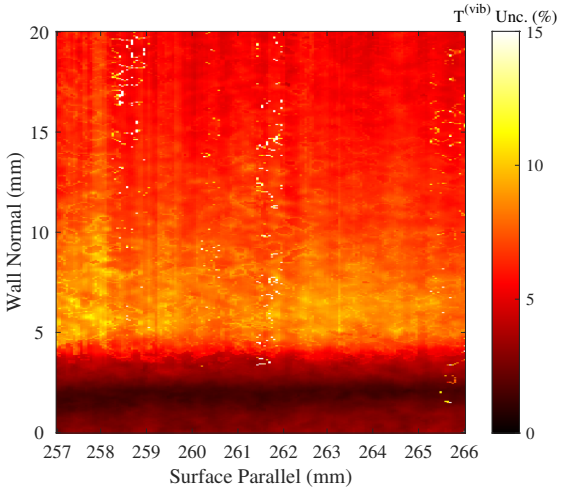

(f) Mean uncertainty map

Figure A.9: PLIF vibrational thermometry assuming $T^{v}_{e,NO} = 358K$, Run 4687: middle; laminar; plasma on.

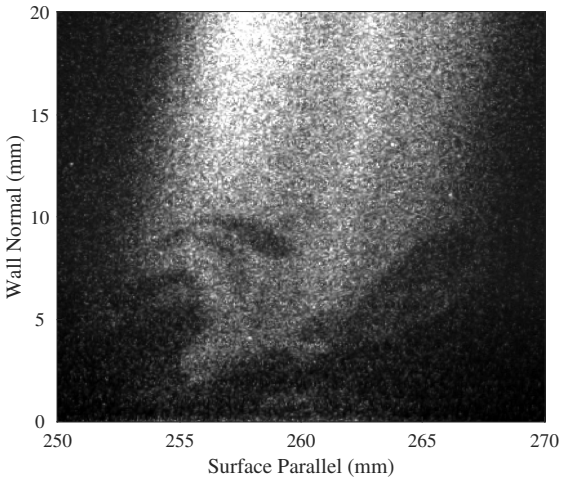

(a) Instantaneous "hot" image

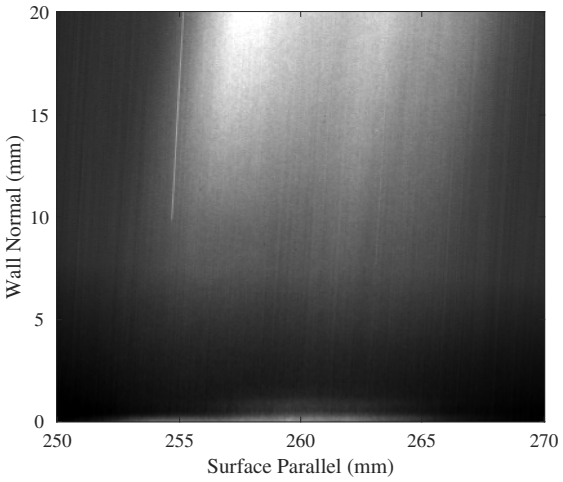

(b) Mean "hot" image

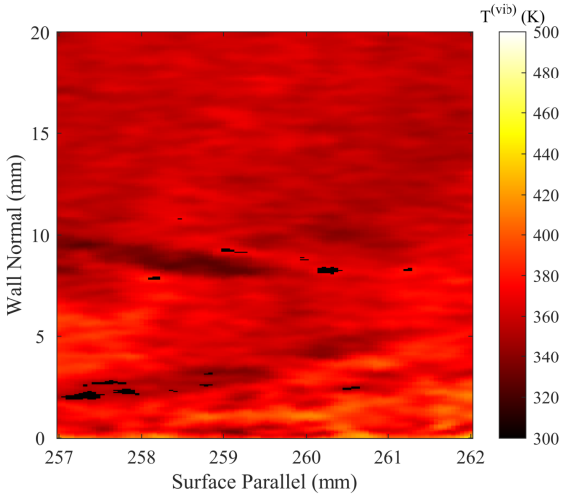

(c) Instantaneous temperature map

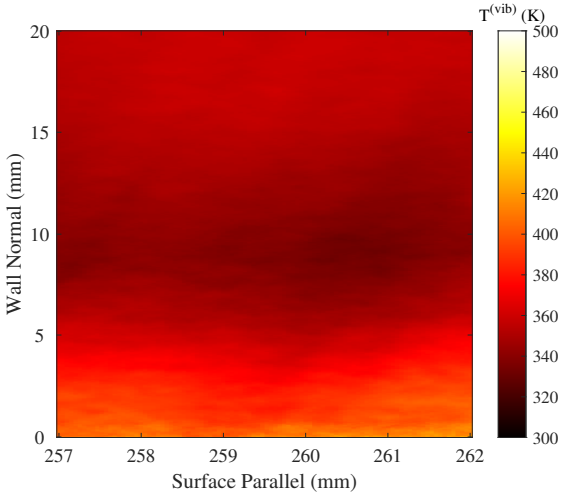

(d) Mean temperature map

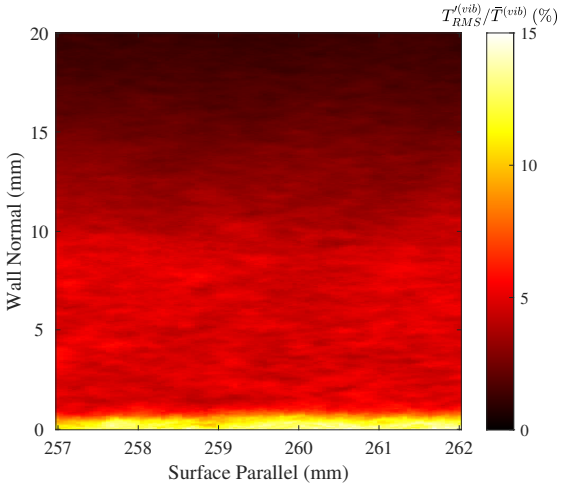

(e) Mean fluctuation map

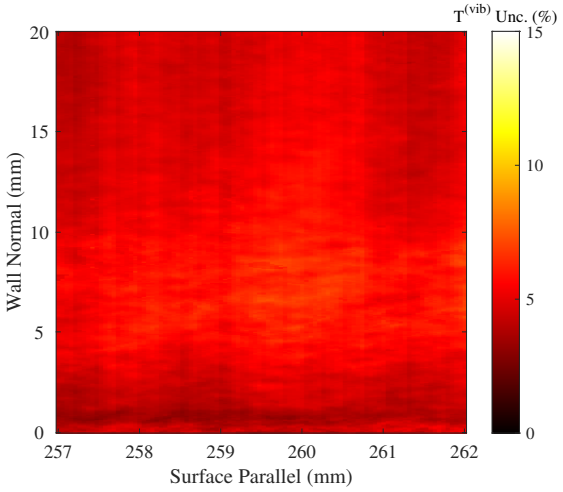

(f) Mean uncertainty map

Figure A.10: PLIF vibrational thermometry assuming $T^{v}_{e,NO} = 358K$, Run 4690: middle; turbulent; plasma on.

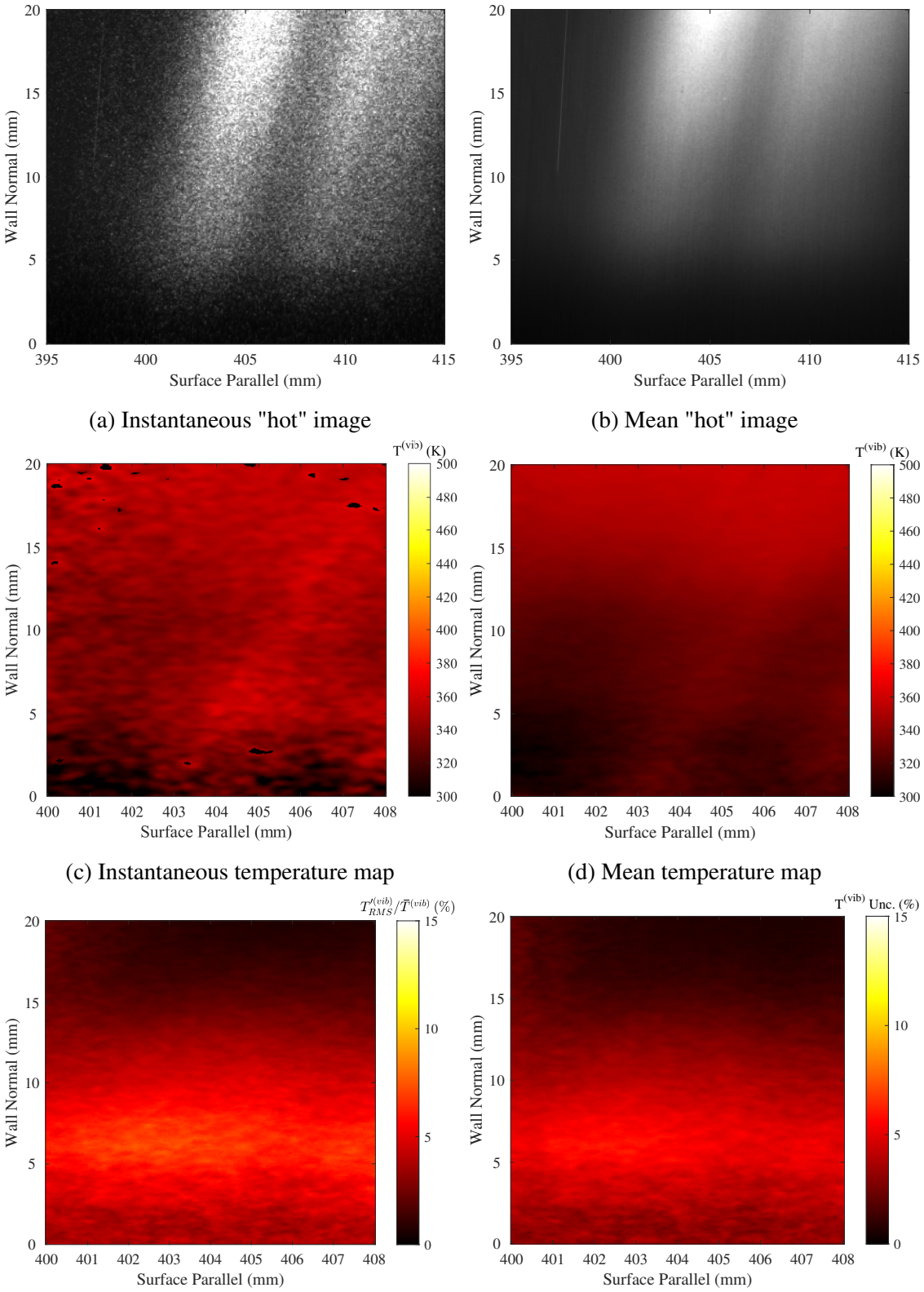

(a) Instantaneous "hot" image

(b) Mean "hot" image

(c) Instantaneous temperature map

(d) Mean temperature map

(e) Mean fluctuation map

(f) Mean uncertainty map

Figure A.11: PLIF vibrational thermometry assuming $T^{v}_{e,NO} = 358K$, Run 4685: back; laminar; plasma off.

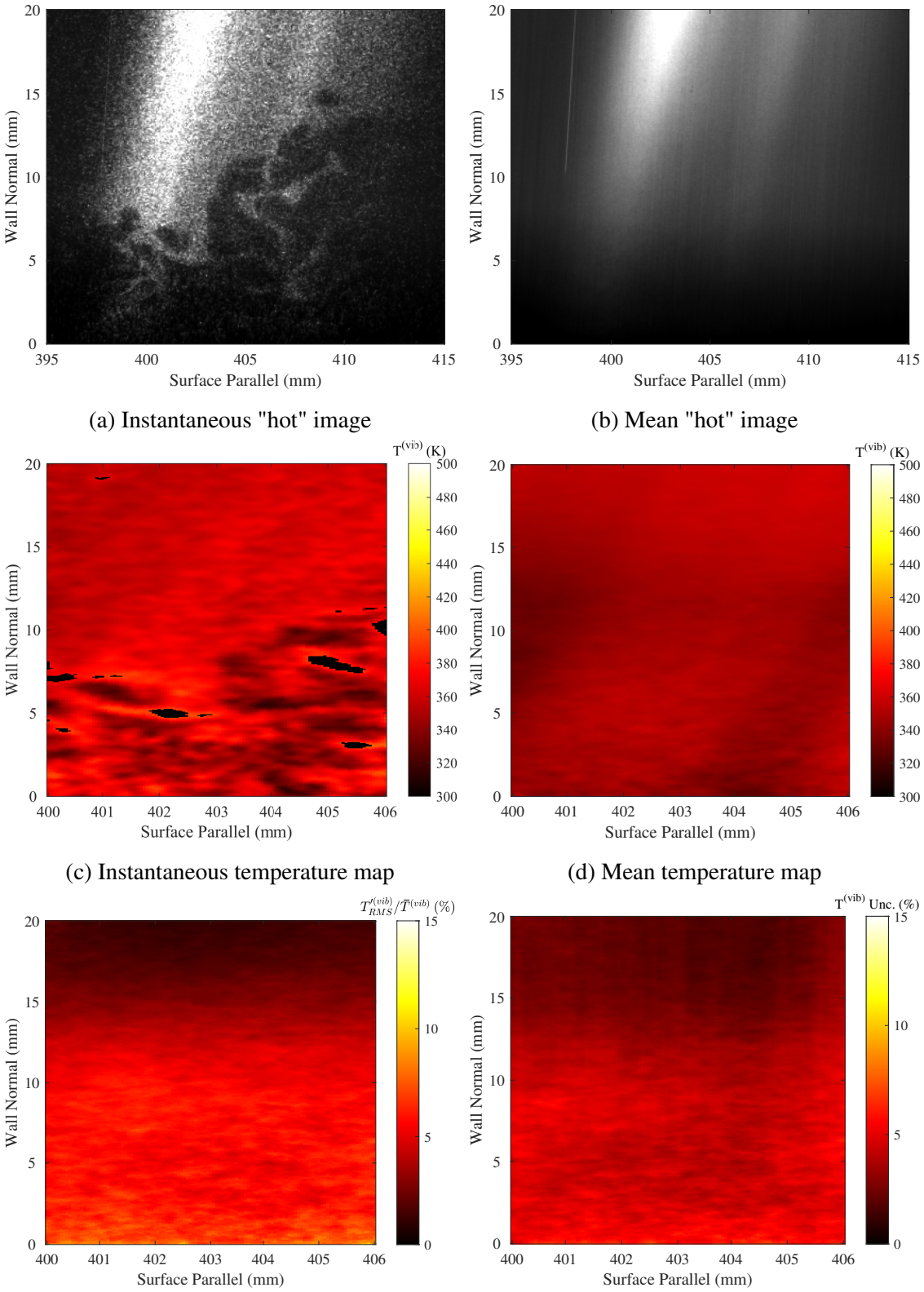

(a) Instantaneous "hot" image

(b) Mean "hot" image

(c) Instantaneous temperature map

(d) Mean temperature map

(e) Mean fluctuation map

(f) Mean uncertainty map

Figure A.12: PLIF vibrational thermometry assuming $T^{v}_{e,NO} = 358K$, Run 4684: back; turbulent; plasma off.

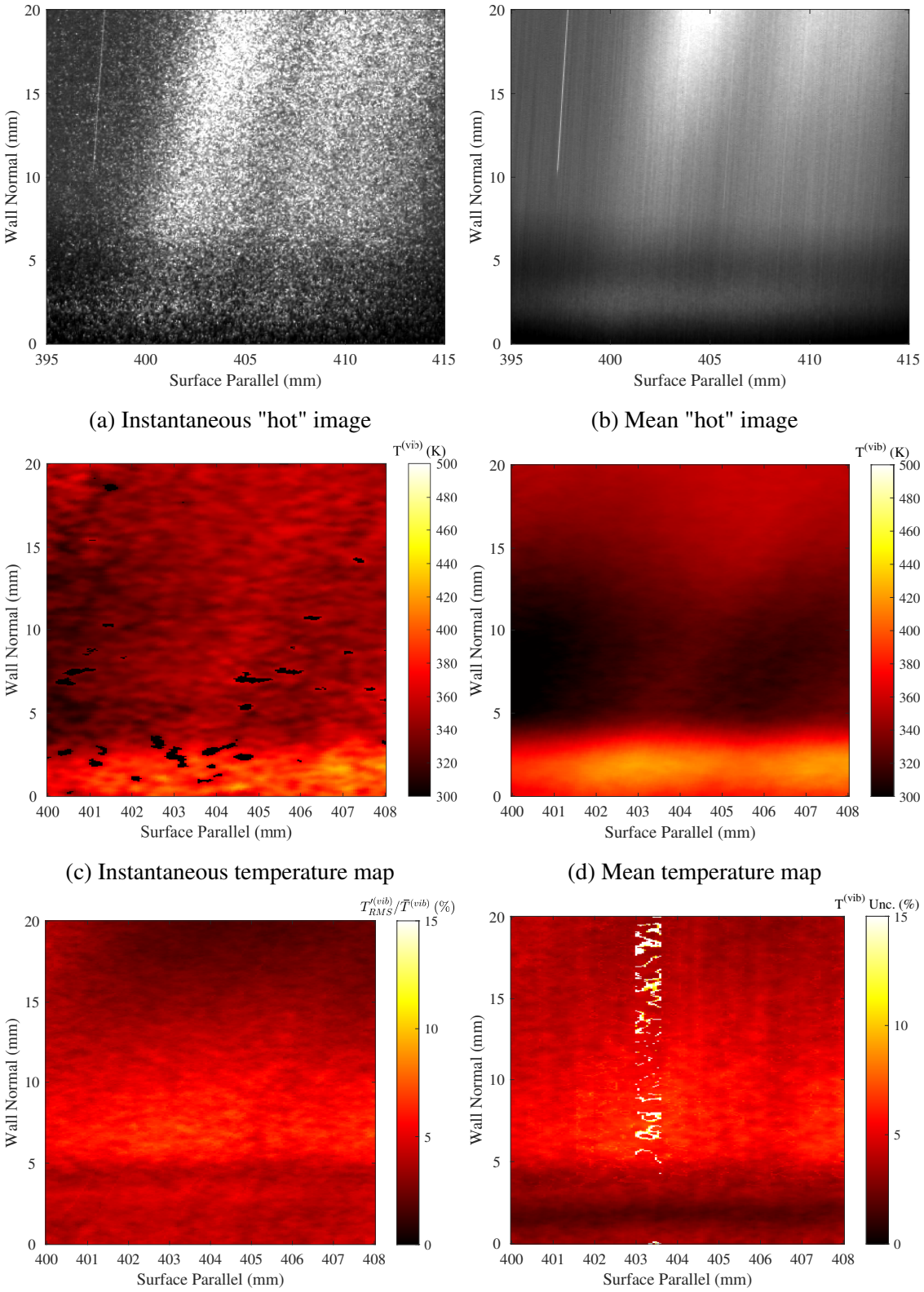

(a) Instantaneous "hot" image

(b) Mean "hot" image

(c) Instantaneous temperature map

(d) Mean temperature map

(e) Mean fluctuation map

(f) Mean uncertainty map

Figure A.13: PLIF vibrational thermometry assuming $T^{v}_{e,NO} = 358K$, Run 4686: back; laminar; plasma on.

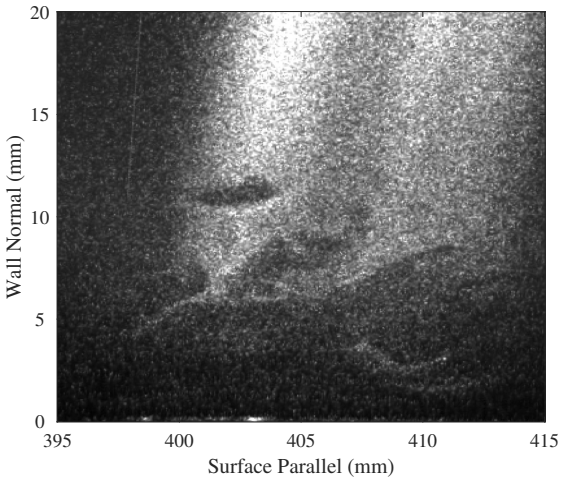

(a) Instantaneous "hot" image

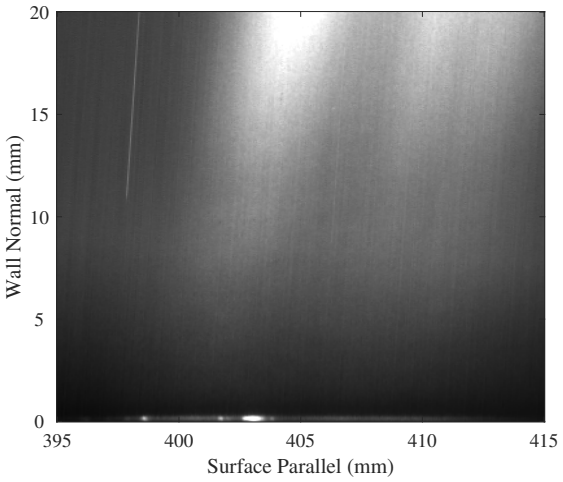

(b) Mean "hot" image

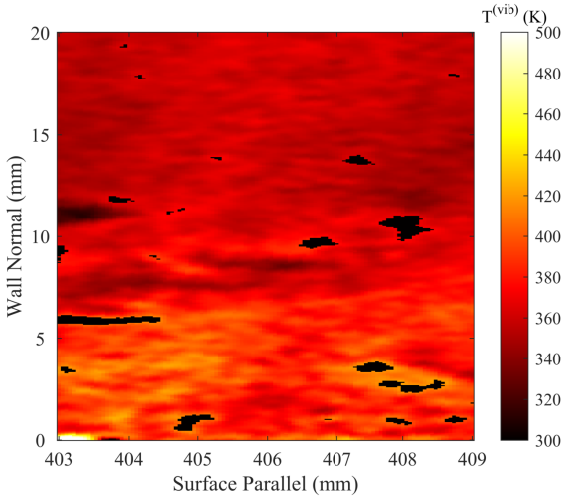

(c) Instantaneous temperature map

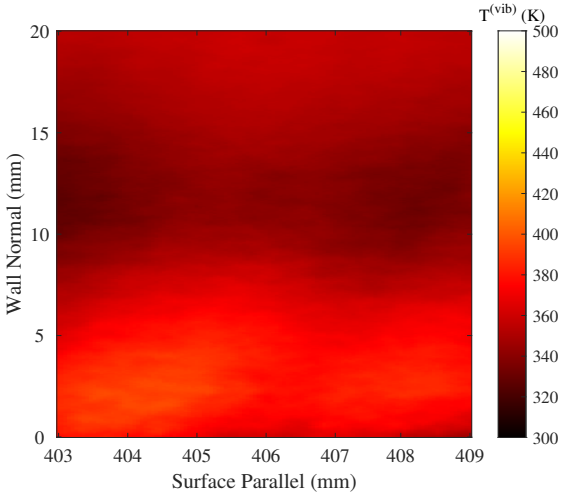

(d) Mean temperature map

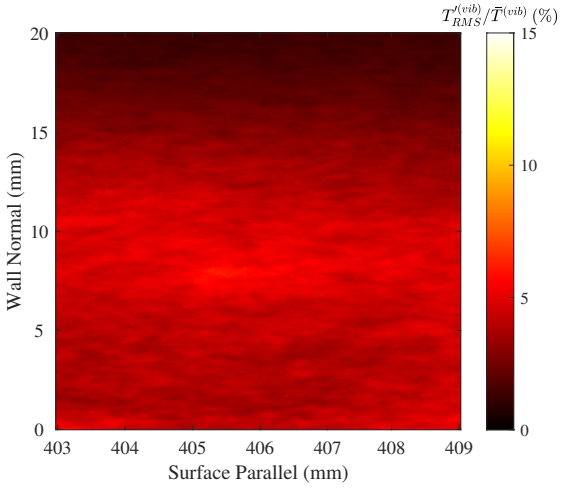

(e) Mean fluctuation map

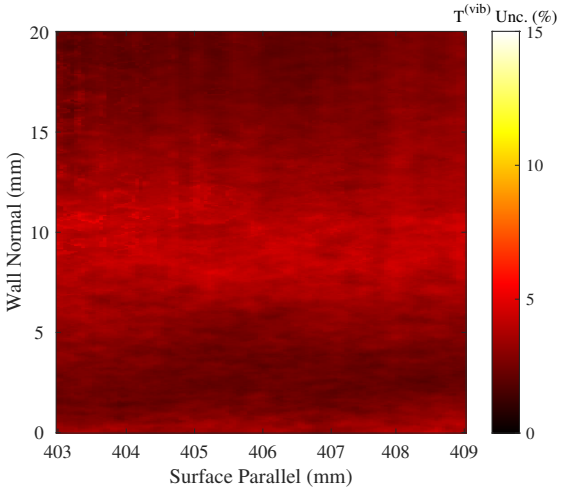

(f) Mean uncertainty map

Figure A.14: PLIF vibrational thermometry assuming $T^{v}_{e,NO} = 358K$, Run 4683: back; turbulent; plasma on.